EDITORIAL STAFF
Editor, **J. J. JAKLITSCH, JR.**
Production Editor,
STELLA ROBINSON
Editorial Prod. Asst.,
BETH DARCHI

HEAT TRANSFER DIVISION
Chairman, **F. W. SCHMIDT**
Secretary, **C. J. CREMERS**
Senior Technical Editor, **E. M. SPARROW**
Technical Editor, **W. AUNG**
Technical Editor, **B. T. CHAO**
Technical Editor, **D. K. EDWARDS**
Technical Editor, **R. EICHHORN**
Technical Editor, **J. S. LEE**
Technical Editor, **V. E. SCHROCK**
Technical Editor, **R. SIEGEL**

POLICY BOARD, COMMUNICATIONS
Chairman and Vice-President
I. BERMAN

Members-at-Large
J. W. LOCKE
J. E. ORTLOFF
M. J. RABINS
W. J. WARREN

Policy Board Representatives
Basic Engineering, **F. LANDIS**
General Engineering, **D. D. ACKER**
Industry, **M. M. LIVINGSTON**
Power, **R. E. REDER**
Research, **G. P. COOPER**
Codes and Stds., **P. M. BRISTER**
Computer Technology Com.,
A. A. SEIREG
Nom. Com. Rep.,
S. P. ROGACKI

Business Staff
345 E. 47th St.
New York, N. Y. 10017
(212) 644-7789
Mng. Dir., Publ., **C. O. SANDERSON**

OFFICERS OF THE ASME
President, **O. L. LEWIS**
Exec. Dir. & Sec'y, **ROGERS B. FINCH**
Treasurer, **ROBERT A. BENNETT**

EDITED and PUBLISHED quarterly at the offices of The American Society of Mechanical Engineers, United Engineering Center, 345 E. 47th St., New York, N. Y. 10017. *Cable address, "Mechaneer," New York. Second-class* postage paid at New York, N. Y., and at additional mailing offices.

CHANGES OF ADDRESS must be received at Society headquarters seven weeks before they are to be effective. Please send old label and new address.

PRICES: To members, $25.00, annually; to nonmembers, $50.00. Single copies, $15.00 each. Add $1.50 for postage to countries outside the United States and Canada.

STATEMENT from By-Laws. The Society shall not be responsible for statements or opinions advanced in papers or . . . printed in its publications (B 13, Par. 4).

COPYRIGHT © 1978 by the American Society of Mechanical Engineers. Reprints from this publication may be made on conditions that full credit be given the TRANSACTIONS OF THE ASME, SERIES C—JOURNAL OF HEAT TRANSFER, and the author and date of publication stated.

INDEXED by the Engineering Index, Inc.

transactions of the ASME

Published Quarterly by
The American Society of
Mechanical Engineers
Volume 101 • Number 1
February 1979

journal of heat transfer

(continued on page 37)

Downloaded 04 Feb 2011 to 194.85.80.107. Redistribution subject to ASME license or copyright; see http://www.asme.org/terms/Terms_Use.cfm

TECHNICAL NOTES

DISCUSSIONS

ANNOUNCEMENTS

R. S. Basu
J. V. Sengers
Institute for Physical Science and Technology,
University of Maryland,
College Park, MD 20742

Viscosity of Nitrogen near the Critical Point

The viscosity of fluids exhibits an anomalous enhancement near the gas-liquid critical point. It is shown that the behavior of the viscosity of nitrogen as observed experimentally by Zozulya and Blagoi is consistent with current theoretical predictions. An equation is proposed for the viscosity of nitrogen that incorporates the observed critical enhancement in the viscosity near the critical point.

Introduction

Many thermophysical properties exhibit an anomalous behavior in the vicinity of the critical point. For instance, the isothermal compressibility, the thermal expansion coefficient and the specific heat of fluids all diverge at the gas-liquid critical point. During the past years considerable progress has been made in developing equations of state that characterize the thermodynamic behavior of fluids near the critical point [1]. Anomalous effects are also encountered when one studies the behavior of the thermal conductivity and the viscosity of fluids near the critical point [2]. The present paper is concerned with the formulation of a quantitative description of the critical enhancement in the shear viscosity of fluids near the gas-liquid critical point.

The critical point is a point of marginal thermodynamic stability. In the vicinity of the critical point, large-scale density fluctuations are present in the fluid. The spatial extent of these fluctuations may be characterized by a correlation length ξ. Near the critical point this correlation length becomes much larger than the intermolecular distances and the intermolecular interaction range, and the behavior of the fluid becomes that of a system of clusters. States in the vicinity of the critical point correspond to different cluster sizes and the different thermodynamic states can be interrelated by scaling laws. Moreover, the properties of a system of clusters become independent of the microscopic nature of the constituent particles. This principle is commonly referred to as critical-point universality [3]. From a practical point of view, universality of critical behavior implies that the same methods can be used to correlate thermophysical property data of a large number of fluids near the critical point.

The thermal conductivity exhibits a critical enhancement in a large range of densities and temperatures around the critical point [4]. In recent years equations representing the critical enhancement of the thermal conductivity of fluids, including nitrogen, have been formulated [5, 6].

Unlike the thermal conductivity, the critical enhancement of the viscosity of fluids is restricted to a narrow range of temperatures near the critical temperature. While a critical enhancement in the thermal conductivity of fluids has been noticed up to temperatures 20 percent above the critical temperature, the critical enhancement in the viscosity of fluids like nitrogen only appears at temperatures less than three percent from the critical temperature. Nevertheless, both theoretical and experimental evidence indicate that the shear viscosity diverges at the critical point. Because of the large compressibility, experimental methods, such as the capillary flow method for measuring the viscosity, become inaccurate in the critical region. Moreover, the viscosity is often measured as a function of pressure, and additional inaccuracies are introduced in converting the experimental pressures into densities. Nevertheless, careful experiments for such fluids as carbon dioxide [7, 8] argon and ethane [9], steam [10], ethylene [11] and nitrogen [12] have now definitely established the ex-

---

Contributed by the Heat Transfer Division and presented at the Winter Annual Meeting, San Francisco, California, December 10–15, 1978 of THE AMERICAN SOCIETY OF MECHANICAL ENGINEERS. Manuscript received by the Heat Transfer Division Sept. 7, 1978. Paper No. 78-WA/HT-38

istence of a critical enhancement in the viscosity of fluids near the gas-critical point.

In Fig. 1 we show schematically the viscosity η as a function of the density ρ at a temperature T slightly above the critical temperature T_c. In order to describe the viscosity in the critical region, we separate η into a normal or background viscosity $\bar{\eta}(\rho, T)$ and a critical enhancement or anomalous viscosity $\Delta\eta(\rho, T)$

$$\eta = \bar{\eta} + \Delta\eta \tag{1}$$

Outside the critical region, the viscosity η is to be identified with the normal viscosity $\bar{\eta}$. Inside the critical region, $\bar{\eta}$ is defined empirically by extrapolating the behavior of the normal viscosity outside the critical region into the critical region. The normal viscosity $\bar{\eta}$ may in turn be written as

$$\bar{\eta}(\rho, T) = \eta_0(T) + \eta_e(\rho, T) \tag{2}$$

where $\eta_0(T)$ is the viscosity in the limit of low densities and where $\eta_e(\rho, T)$ is commonly referred to in the engineering literature as excess viscosity. The excess viscosity is a slowly varying function of temperature and increases monotonically with density [13, 14]. The separation of the total viscosity in the critical region into a normal and an anomalous part is analogous to the separation of the thermal conductivity λ into a normal thermal conductivity $\bar{\lambda}(\rho, T)$ and an anomalous thermal conductivity $\Delta\lambda(\rho, T)$ introduced in previous publications [2, 4]

$$\lambda = \bar{\lambda} + \Delta\lambda \tag{3}$$

In formulating an equation for the viscosity in the critical region we are guided by the following principles:

a The asymptotic behavior of the equation upon approaching the critical point should be consistent with current theoretical predictions.

b The equation should reproduce currently available experimental data for the critical enhancement within their experimental accuracy.

c The equation for the critical viscosity enhancement should be consistent with the equations for the thermodynamic properties and the thermal conductivity of the fluid near its critical point. Such consistency is required for the calculation of properties such as the Prandtl number which involve both thermodynamic and transport properties.

d The equation should connect smoothly the critical behavior inside the critical region with the normal behavior outside the critical region, so that the equation can be incorporated into a comprehensive equation for the viscosity.

e Within these requirements we try to formulate an equation that is easy to use in practice.

Zozulya and Blagoi have made an extensive experimental study of the viscosity of nitrogen near the critical point [12]. They measured the viscosity as a function of density by determining the period and damping of the rotational oscillations of a stack of disks. Thus nitrogen is a possible fluid for testing the applicability of a proposed equation for the anomalous behavior of the viscosity near the critical point.

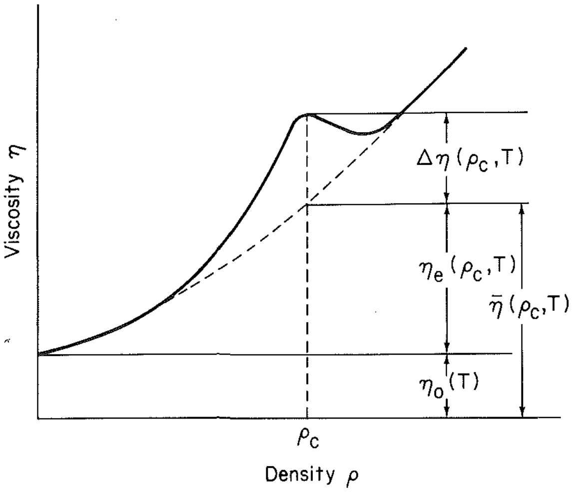

Fig. 1 **Schematic representation of the viscosity as a function of density at a temperature slightly above the critical temperature**

While the thermal conductivity λ can indeed be conveniently decomposed into the sum of a normal contribution $\bar{\lambda}$ and a critical enhancement $\Delta\lambda$ in accordance with (3), experiment [2, 15] and theory [16, 17, 18] indicate that the critical viscosity enhancement is multiplicative rather than additive. That is, the critical viscosity enhancement $\Delta\eta$, as defined in (1), is itself proportional to the viscosity $\bar{\eta}$ in the absence of the critical fluctuations. Since the viscosity of liquids is larger than that of gases, the multiplicative nature of the anomaly also explains in retrospect why the critical viscosity enhancement of binary liquids near the consolute point was discovered experimentally much earlier [15]. Thus, rather than $\Delta\eta$, we shall consider in practice the relative critical enhancement $\Delta\eta/\bar{\eta}$ or the viscosity ratio $\eta/\bar{\eta}$. Experiments indicate that the viscosity ratio $\eta/\bar{\eta}$ is larger than unity in a range around the critical point bounded approximately by

$$|(\rho - \rho_c)/\rho_c| < 0.25, \quad |(T - T_c)/T_c| < 0.03 \tag{4}$$

Theoretical Remarks

Upon approaching the critical point the relaxation rate of the large-scale fluctuations tends to zero. This phenomenon is known as the critical slowing down of the fluctuations. Because of the interaction between hydrodynamic modes, the critical slowing down of the fluctuations leads to anomalous behavior of various transport prop-

Nomenclature

B = critical amplitude of coexistence curve
c_p = specific heat at constant pressure, J kg^{-1}K^{-1}
c_v = specific heat at constant volume, J kg^{-1}K^{-1}
E_1, E_2 = parameters in critical region equation of state
k = Boltzmann's constant, 1.38066×10^{-23} J K^{-1}
$K_T = \rho^{-1}(\partial\rho/\partial P)_T$, Pa^{-1}
q = constant in viscosity equation
P = pressure, Pa
P_c = critical pressure, 3.398×10^6Pa
T = temperature, K
T_c = critical temperature, 126.20K
$\Delta T^* = (T - T_c)/T_c$
$x = \Delta T^*/|\Delta\rho^*|^{1/\beta}$
$x_0 = -x$ when $\rho = \rho_{cxc}$
β = critical exponent of coexistence curve
γ = critical exponent of χ_T^*
Γ = critical amplitude of χ_T^*
η = shear viscosity, Pa.s
$\bar{\eta}$ = normal shear viscosity, Pa.s
η_0 = shear viscosity at low density, Pa.s
η_e = excess shear viscosity, Pa.s
$\Delta\eta$ = critical viscosity enhancement, Pa.s
λ = thermal conductivity, Wm^{-1}K^{-1}
$\bar{\lambda}$ = normal thermal conductivity, Wm^{-1}K^{-1}
$\Delta\lambda$ = critical thermal conductivity enhancement, Wm^{-1}K^{-1}
Λ = constant in thermal conductivity equation
ν = critical exponent of correlation length
ξ = correlation length, m
ξ_0 = critical amplitude of ξ, m
ρ = density, kg/m^3
ρ_c = critical density, 314 kg/m^3
ρ_{cxc} = density at coexistence boundary, kg/m^3
$\Delta\rho^* = (\rho - \rho_c)/\rho_c$
ϕ = critical exponent in viscosity equation
$\chi_T = \rho^2 K_T$ = symmetrized compressibility, kg^{2}m^{-3}J^{-1}
$\chi_T^* = \chi_T P_c/\rho_c{}^2$

erties [16–18]. In fluids the property most directly affected is the thermal diffusivity $\lambda/\rho c_p$ which measures the decay rate of the entropy fluctuations [4]. Identifying the thermal diffusivity with the diffusivity of clusters with radius ξ, one concludes that the thermal diffusivity will vanish in inverse proportion to the correlation length ξ [19]. Since the specific heat c_p diverges approximately as ξ^2, it follows that the thermal conductivity λ diverges upon approaching the critical point. More specifically, the critical enhancement $\Delta\lambda$ may be represented by [4]

$$\Delta\lambda = \frac{\Lambda}{6\pi\eta\xi} kT\rho(c_p - c_v) = \frac{\Lambda}{6\pi\eta\xi}\frac{kT^2}{\rho^2}\left(\frac{\partial P}{\partial T}\right)_\rho^2 \chi_T \tag{5}$$

where $\chi_T = \rho^2 K_T$ is a symmetrized isothermal compressibility to be discussed in the next section. In the original theory the coefficient Λ in (5) was approximated by unity [16], but further investigations have indicated that it may be slightly larger than unity [5, 20–23].

As a consequence of the strong coupling between the thermal diffusive mode and the viscous mode, the critical slowing down of the fluctuations also causes a weak anomalous behavior of the shear viscosity η. A simplified theoretical treatment indicates that the relative critical enhancement $\Delta\eta/\bar{\eta}$ will diverge as [16, 24, 25]

$$\frac{\Delta\eta}{\bar{\eta}} = \frac{8}{15\pi^2}\ln(q\xi) \tag{6}$$

Here q is an undetermined system-dependent constant which arises in the theory as a cut-off wave number when integrating over the fluctuations with various wave numbers. A more detailed investigation of the equations governing the coupling of hydrodynamic modes indicates that q will in fact be a slowly varying function of density and temperature. Generalizing an argument presented by Oxtoby and Gelbart [25], an order of magnitude estimate for q may be obtained from

$$q \simeq \frac{kT\rho(c_p - c_v)}{8\pi\bar{\eta}\bar{\lambda}\xi^2} = \frac{kT^2}{8\pi\bar{\eta}\bar{\lambda}\rho^2}\left(\frac{\partial P}{\partial T}\right)_\rho^2 \frac{\chi_T}{\xi^2} \tag{7}$$

A preliminary analysis of the experimental data does indicate a divergent behavior of the viscosity which is close to logarithmic [2, 19]. More recent theoretical investigations indicate that the viscosity exhibits a slightly more general power law divergence proportional to ξ^ϕ, where ϕ is a universal exponent independent of the nature of the fluid [18]. The simplified theoretical expression (6) may be rewritten in the form of a power law by noting that

$$\frac{\eta}{\bar{\eta}} = 1 + \ln(q\xi)^\phi \simeq (q\xi)^\phi \tag{8}$$

where $\phi = 8/15\pi^2 = 0.054$. Several alternative attempts have been made to calculate the exponent ϕ from theory. The theoretical values currently available span the range [17, 18, 26]

$$0.054 < \phi < 0.065 \tag{9}$$

Correlation Length and Compressibility

In the preceding section, the critical enhancement of the transport properties was related to the correlation length ξ which diverges upon approaching the critical point. As a next step we relate this correlation length to the compressibility, thus providing consistency between the equations for the transport properties and the equation of state in the critical region.

Rather than the compressibility $K_T = \rho^{-1}(\partial\rho/\partial P)_T$, we consider the quantity $\chi_T = \rho^2 K_T$ introduced in the previous section. The reason is, that unlike K_T, χ_T is a symmetric function of $\Delta\rho^*$ in the critical region [1, 27]. We refer to χ_T as the symmetrized compressibility. In terms of reduced units, $\chi_T{}^*$ in the critical region can be represented by a scaled equation of the form [1, 27]

$$\chi_T{}^{*-1} = |\Delta\rho^*|^{\gamma/\beta}\left[h(x) - \frac{x}{\beta}h'(x)\right] \tag{10}$$

where $h'(x) = dh(x)/dx$. The variable x is defined as

$$x = \frac{\Delta T^*}{|\Delta\rho^*|^{1/\beta}} \tag{11}$$

with $\Delta T^* = (T - T_c)/T_c$ and $\Delta\rho^* = (\rho - \rho_c)/\rho_c$. The exponents β and γ are the critical exponents for the coexistence curve

$$\Delta\rho^* = \pm B|\Delta T^*|^\beta \qquad (\rho = \rho_{cxc}, T \leq T_c) \tag{12}$$

and for the power law behavior of $\chi_T{}^*$ along the critical isochore

$$\chi_T{}^* = \Gamma|\Delta T^*|^{-\gamma} \qquad (\rho = \rho_c, T \geq T_c) \tag{13}$$

An explicit, though approximate, expression for the function $h(x)$ was proposed by Vicentini, et al. [28].

$$h(x) = E_1\left(1 + \frac{x}{x_0}\right)\left[1 + E_2\left(1 + \frac{x}{x_0}\right)^{2\beta}\right]^{(\gamma-1)/2\beta} \tag{14}$$

where E_1, E_2 and x_0 are constants. This equation has been referred to either as NBS equation [27] or MLSG equation [1, 29]. The constant x_0 is chosen such that at coexistence $x = -x_0$ which implies in accordance with (12)

$$B = x_0{}^{-\beta} \tag{15}$$

The constant E_1 is related to the amplitude Γ in (13) by

$$\Gamma = x_0{}^\gamma / E_1 E_2{}^{(\gamma-1)/2\beta} \tag{16}$$

The principle of critical-point universality predicts that the critical exponents, such as β and γ, and the function $h(x)$ are universal, i.e., the same for all fluids, except for the two system-dependent scale factors B and Γ, or equivalently, x_0 and E_1 [1, 30].

At the critical isochore the correlation length diverges as

$$\xi = \xi_0|\Delta T^*|^{-\nu} \qquad (\rho - \rho_c, T \geq T_c) \tag{17}$$

In order to evaluate the correlation length at densities different from the critical we use an approximate expression introduced previously [1]

$$\xi = \xi_0(\chi_T{}^*/\Gamma)^{\nu/\gamma} \tag{18}$$

The critical exponent ν for the correlation length is related to the thermodynamic exponents β and γ by the hyperscaling relation [1]

$$\nu = (2\beta + \gamma)/3 \tag{19}$$

The scale factor ξ_0 for the correlation length can be related to the thermodynamic scale factors B and Γ by [1, 31]

$$\xi_0(B^2 P_c/\Gamma k T_c)^{1/3} = R \tag{20}$$

where R is a universal constant whose value is approximately equal to 0.7.

The validity of the scaling laws with universal critical exponent values predicted by the theory is restricted to a very small temperature range $\Delta T^* < 10^{-4}$ near the critical point [3]. Nevertheless, in the region of the critical enhancement of the viscosity, given by (4), a reasonable practical approximation is obtained by using a scaled equation of state with effective exponents [1, 27]. Effective critical region parameters, which specify the scaled equation of state (10) as well as the correlation length (18) for a large number of fluids, were presented in a previous publication [1]. The parameters needed for nitrogen are reproduced in Table 1.

Table 1 Critical region parameters for nitrogen

Critical parameters
$P_c = 3.398 \times 10^6$Pa
$\rho_c = 314.0$ kg/m^3
$T_c = 126.20$K
Critical exponents
$\beta = 0.355$
$\gamma = 1.190$
$\nu = 0.633$
Equation of state parameters
$x_0 = 0.164$
$E_1 = 2.17$
$E_2 = 0.287$
Correlation length scale factor
$\xi_0 = 1.6 \times 10^{-10}$m

We do not know a priori how close to the critical point the viscosity will approach the conjectured asymptotic behavior (8) with an exponent value ϕ predicted by theory. In fact, some of the more recent theoretical estimates [26] assume $\Delta\eta \gg \bar{\eta}$, a condition not satisfied in the range where experimental viscosity data are currently available. Our procedure here is to relate the viscosity to the correlation length as deduced from the equation of state and allow for an effective exponent ϕ to be deduced from the viscosity data.

Viscosity of Nitrogen

The viscosity of nitrogen near the critical point has been measured by Zozulya and Blagoi [12]. They determined the viscosity as a function of density along 14 different isotherms covering the range $126.16\text{K} \leq T \leq 135.00\text{K}$. The critical temperature was estimated as $T_c = (126.21 \pm 0.01)\text{K}$. A critical enhancement of the viscosity was observed in a temperature range of about 3K above the critical temperature and at densities between 250 kg/m^3 and 375 kg/m^3.

From (1) and (2) it follows that the viscosity may be decomposed as

$$\eta(\rho, T) = \eta_0(T) + \eta_e(\rho, T) + \Delta\eta(\rho, T) \tag{21}$$

The viscosity $\eta_0(T)$ of dilute nitrogen has been tabulated by Hanley and Ely [32]. In the small temperature range where the anomalous behavior of the viscosity is observed, the temperature dependence of the normal excess viscosity $\eta_e(\rho, T)$ is negligibly small. Zozulya and Blagoi report original experimental viscosity data at temperatures $T = 126.21\text{K}, 127.00\text{K}, 128.00\text{K}, 130.00\text{K}$ and 135.00K. At 130K and 135K, the critical enhancement $\Delta\eta$ has vanished completely, and the data at these temperatures may be used to determine $\eta_e(\rho, T) \simeq \eta_e(\rho)$. In addition, Zozulya and Blagoi report values for the critical enhancement $\Delta\eta$ at 126.16K, 126.18K, 126.20K, 126.22K, 126.24K, 126.26K. Using (21) we have reconverted these data into estimated values for the viscosity η itself.

In order to analyze the experimentally observed critical enhancement in terms of the conjectured behavior $\eta/\bar{\eta} = (q\xi)^\phi$, we need an explicit equation for the normal viscosity

$$\bar{\eta}(\rho, T) = \eta_0(T) + \eta_e(\rho, T) \tag{22}$$

Such an equation has been formulated by Hanley, McCarty and Haynes [6]. For a full description concerning the form of this equation and the constants used, the reader is referred to the paper by Hanley, et al. [6]. A comparison of the viscosity values predicted by this equation and the experimental data reported by Zozulya and Blagoi [12] at $T = 135\text{K}$ is presented in Fig. 2. The agreement is not perfect, but the deviations are within the claimed accuracy of two percent of the experimental data. The equation is therefore considered adequate for our purpose, and we have used it to convert the experimental viscosity data into viscosity ratios $\eta/\bar{\eta}$.

The viscosity ratios $\eta/\bar{\eta}$, thus obtained near the critical point, are plotted in Fig. 3 as a function of the correlation length ξ evaluated by the method described in the preceding section. We note that on a double logarithmic scale the data do approach a straight line within the scatter of the data upon approaching the critical point. The slope of this line yields the exponent ϕ and the intercept with the ξ-axis the constant q^{-1}.

Since the viscosity diverges at the critical point, a quantitative analysis is somewhat sensitive to the value adopted for the critical temperature T_c. This value affects ΔT^* in (11) and, hence, the value calculated for the correlation length in (8). We examined variations in T_c to determine its influence and found that the best results were obtained with $T_c = (126.201 \pm 0.004)\text{K}$; this value is in good agreement with the value $T_c = 126.20\text{K}$ found by other investigators [33].

Having determined the critical temperature, the experimental viscosity data were fitted to

$$\eta = \bar{\eta}(q\xi)^\phi \tag{23}$$

using ϕ and q as adjustable parameters. For the asymptotic behavior to be applicable, the correlation length ξ must be larger than q^{-1}. Therefore, in determining ϕ and q we restricted ourselves to the data points sufficiently close to the critical point for which $\xi \geq 30 \times 10^{-10}$ m. In fitting the viscosity data we attributed an uncertainty $\sigma = 0.015\ \eta$ to the experimental values. The values thus obtained for the parameters ϕ and q, together with the value adopted for T_c, are listed in Table 2. The value of 0.057 ± 0.007 found for the exponent ϕ is in good agreement with the exponent values predicted theoretically (cf. (9)). A theoretical estimate for the magnitude of the parameter q may be obtained from (7). For this purpose $\chi_T{}^*$ and ξ were calculated by the method described in the preceding section, the normal viscosity $\bar{\eta}$ and normal thermal conductivity $\bar{\lambda}$ were estimated from the equations proposed by Hanley, et al. [6] and $(\partial P/\partial T)_\rho$ from the equation of state proposed by Jacobsen and Stewart [33]. The values thus obtained for q^{-1} vary between 22×10^{-10}m and 31×10^{-10}m in the range of densities and temperatures of interest, to be compared with the value $q^{-1} = 22 \times 10^{-10}$m deduced from the experimental viscosity data. Keeping in mind that the theoretical estimate (7) for q is an approximate one, we conclude that the critical viscosity enhancement as observed by Zozulya and Blagoi is consistent with current theoretical predictions.

In order to obtain an equation that incorporates the appropriate critical viscosity behavior and the normal viscosity behavior outside

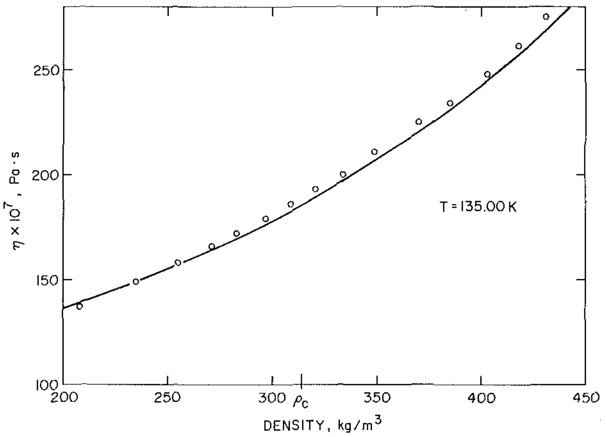

Fig. 2 The viscosity of nitrogen as a function of density at T = 135 K. The circles indicate the experimental data reported by Zozulya and Blagoi [12] and the curve represents the data predicted by the equation of Hanley, et al. [6]

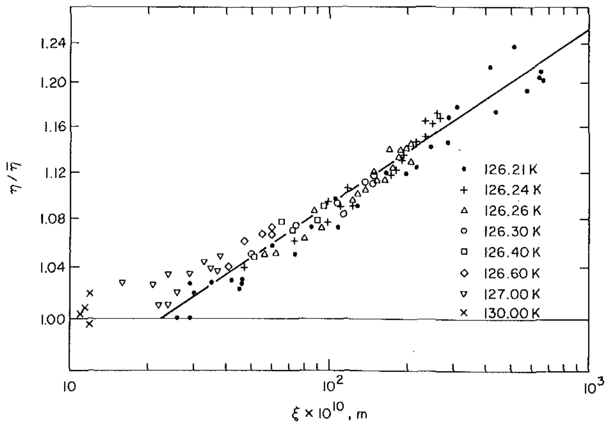

Fig. 3 Log-log plot of $\eta/\bar{\eta}$ as a function of the correlation length ξ. The intercept of the straight line with the ξ-axis gives q^{-1} and the slope gives the exponent ϕ

the critical region, we propose

$$\eta = \bar{\eta}(q\xi)^{\phi}, \qquad \text{for } q\xi \geq 1$$

$$\eta = \bar{\eta}, \qquad \text{for } q\xi \leq 1 \qquad (24)$$

with $\phi = 0.057$, $q^{-1} = 22 \times 10^{-10}$m and where $\bar{\eta}(\rho, T)$ is calculated from the equation proposed by Hanley, McCarty and Haynes [6]. Equation (24) is chosen so that the critical behavior goes over into the normal behavior without a discontinuity in η.

In Fig. 4 the viscosity of nitrogen is plotted as a function of density at a number of temperatures. The data points indicate the experimental data obtained by Zozulya and Blagoi and the curves represent the values calculated from (24). A plot of the normalized deviations $(\eta_{\rm exp} - \eta_{\rm calc})/\sigma$ is presented in Fig. 5. It is concluded that the equation reproduces the experimental data in the critical region within two standard deviations. The small systematic deviations at larger densities $\rho \approx 400$ kg/m^3 correspond to data outside the critical region. They reflect small systematic differences between the equation of Hanley, et al. and the experimental data outside the critical region.

Discussion

The critical viscosity enhancement observed by Zozulya and Blagoi for nitrogen is consistent with current theoretical predictions. The critical behavior of the viscosity can be incorporated in an equation for the normal viscosity $\bar{\eta}$ outside the critical region by the simple approximation

$$\eta = \bar{\eta}(q\xi)^{\phi} \qquad \text{for } q\xi \geq 1 \qquad (26)$$

with the values of q and ϕ as given in Table 2.

According to theoretical predictions [18], the exponent ϕ is assumed to be universal for fluids near the gas-liquid critical point and binary liquids near the consolute point. We therefore conjecture that equation (26) will be suitable to represent the viscosity of other fluids near the critical point as well, provided that q is treated as an adjustable parameter depending on the particular fluid under consideration. In fact, a preliminary analysis [34] indicates that equation (26) with about the same value of ϕ and a suitably chosen value of q can be used to represent the critical viscosity enhancement of steam as measured by Rivkin, et al. [10].

It should be noted that equation (6), which is closely similar to equation (26), has been used by D'Arrigo, et al. to analyze the critical viscosity enhancement of binary liquids as a function of temperature and concentration [35]. They find good agreement for large values of $q\xi$, but deviations for intermediate values of $q\xi$. Since the critical viscosity enhancement $\Delta\eta$ of fluids near the gas-liquid critical point is appreciably smaller than that of binary liquids near the consolute point, use of equation (26) for all values $q\xi \geq 1$, would seem to represent an adequate first approximation.

Acknowledgments

The research was supported by the NASA Lewis Research Center under grant NGR 21-002-344 and by the National Science Foundation under grant DMR 76-82345. Computer time for this project was provided by the Computer Science Center at the University of Maryland. The authors acknowledge stimulating discussions with D. L. Henry and thank R. J. Simoneau for some valuable suggestions concerning the manuscript.

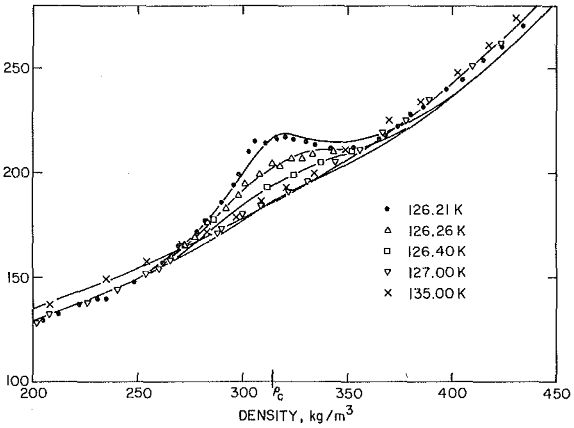

Fig. 4 Viscosity of nitrogen as a function of density at various temperatures. The data points indicate those obtained by Zozulya and Blagoi [12] and the curves are calculated from the conjectured equation (24)

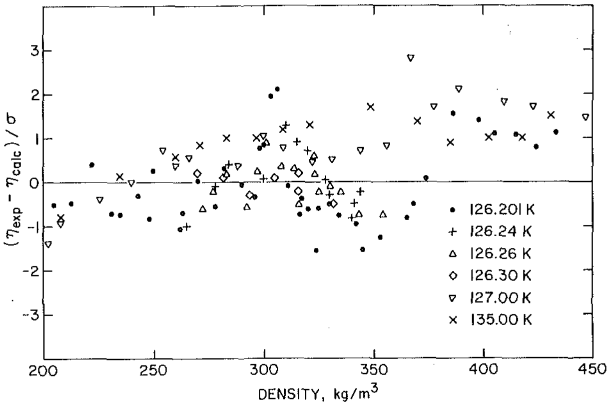

Fig. 5 Normalized deviations $(\eta_{\rm exp} - \eta_{\rm calc})/\sigma$ as a function of density

Table 2 Parameters for critical viscosity enhancement

$\phi = 0.057 \pm 0.007$
$q^{-1} = (22 \pm 5) \times 10^{-10}$m
$T_c = (126.201 \pm 0.004)$K

References

1 Sengers, J. V. and Levelt Sengers, J. M. H., "Critical Phenomena in Classical Fluids," *Progress in Liquid Physics,* C. A. Croxton, ed., Wiley, New York, 1978, pp. 103–174; "Concepts and Methods for Describing Critical Phenomena in Fluids," NASA Contractor Report 149665, National Aeronautics and Space Administration, 1977, 159 pages.

2 Sengers, J. V., "Transport Properties of Gases and Binary Liquids near the Critical State," *Transport Phenomena—1973,* J. Kestin, ed., AIP Conference Proceedings No. 11, American Institute of Physics, 1973, pp. 229–277.

3 Levelt Sengers, A., Hocken, R. and Sengers, J. V., "Critical-Point Universality and Fluids," *Physics Today,* Vol. 30, No. 12, Dec. 1977, pp. 42–51.

4 Sengers, J. V., "Transport Processes near the Critical Point of Gases and Binary Liquids in the Hydrodynamic Regime," *Berichte der Bunsen-Gesellschaft für physikalische Chemie,* Vol. 76, No. 3/4, April 1972, pp. 234–249.

5 Hanley, H. J. M., Sengers, J. V. and Ely, J. R., "On Estimating Thermal Conductivity Coefficients in the Critical Region of Gases," *Thermal Conductivity 14,* P. G. Klemens and T. K. Chu, eds., Plenum Publ. Corp., New York, 1976, pp. 383–408.

6 Hanley, H. J. M., McCarty, R. D. and Haynes, W. M., "The Viscosity and Thermal Conductivity Coefficients for Dense Gaseous and Liquid Argon, Krypton, Xenon, Nitrogen and Oxygen," *Journal of Physical and Chemical Reference Data,* Vol. 3, No. 4, 1974, pp. 979–1017.

7 Kestin, J., Whitelaw, J. H. and Zien, T. F., *Physica,* Vol. 30, No. 1, Jan. 1964, pp. 161–181.

8 Iwasaki, H. and Takahashi, M., "Viscosity of Carbon Dioxide," to be published.

9 Strumpf, H. J., Collings, A. F. and Pings, C. J., "Viscosity of Xenon and Ethane in the Critical Region," *Journal of Chemical Physics,* Vol. 60, No. 8, April 1974, pp. 1309–1323.

10 Rivkin, S. L., Levin, A. Ja., Izrailevsky, L. B. and Kharitonov, K. G., "Experimental Investigation of Viscosity of Light Water near the Critical Point and of Heavy Water in Liquid Phase and in Supercritical Region," *Proceedings of the 8th International Conference on the Properties of Water & Steam,* P. Bury, H. Perdon and B. Vodar, eds., Editions Européennes Thermiques et Industries, Paris, 1975, pp. 153–162.

11 Iwasaki, H. and Takahashi, M., "Viscosity of Ethylene," *Proceedings of the 4th International Conference on High Pressure,* Kyoto, 1974, pp.

523–529

12 Zozulya, V N and Blagoik Yu P , "Viscosity of Nitrogen near the Liquid Vapor Critical Point," *Soviet Physics—JETP,* Vol 39, No 1, July 1974, pp 99–105

13 Sengers, J V , "Transport Properties of Compressed Gases," *Recent Advances in Engineering Science,* Vol 3, A C Eringen, ed , Gordon and Breach, New York, 1968, pp 153–196

14 Diller, D E , Hanley, H J M and Roder, H M , "The Density and Temperature Dependence of the Viscosity and Thermal Conductivity of Dense Simple Fluids," *Cryogenics,* Vol 10, No 4, Aug 1970, pp 286–294

15 Sengers, J V , "Transport Properties of Fluids near Critical Points," *Critical Phenomena, Varenna Lectures,* Course LI, M S Green, ed , Academic Press, New York, 1971, pp 445–507

16 Kawasaki, K , "Mode Coupling and Critical Dynamics," *Phase Transitions and Critical Phenomena,* Vol 5A, C Domb and M S Green, eds , Academic Press, New York, 1976, pp 165–403

17 Ohta, T , "Multiplicative Renormalization of the Anomalous Shear Viscosity in Classical Liquids," *Journal of Physics C Solid State Physics,* Vol 10, No 6, March 1977, pp 791–793

18 Hohenberg, P C and Halperin, B I , "Theory of Dynamic Critical Phenomena," *Reviews of Modern Physics,* Vol 49, No 3, July 1977, pp 435–479

19 Arcovito, G , Faloci, C , Roberti, A M and Mistura, L , "Shear Viscosity of the Binary System Aniline Cyclohexane near the Critical Point," *Physical Review Letters,* Vol 22, No 20, May 1969, pp 1040–1042

20 Siggia, E D , Halperin, B I , and Hohenberg, P C , "Renormalization Group Treatment of the Critical Dynamics of the Binary Fluid and Gas Liquid Transitions," *Physical Review,* Vol 13, No 5, March 1976, pp 2110 2123

21 Basu, R S and Sengers, J V , "Thermal Conductivity of Steam in the Critical Region," *Proceedings of the 7th Symposium of Thermophysical Properties,* A Cezairliyan, ed , American Society of Mechanical Engineers, 1977, pp 822 830

22 Chen, S H , Lai, C C and Rouch, J , "Experimental Confirmation of Renormalization Group Prediction of Critical Concentration Fluctuation Rate in Hydrodynamic Limit," *Journal of Chemical Physics* Vol 68, No 4, Feb 1978, pp 1994–1995

23 Sorensen, C M , Mockler, R C and O'Sullivan, W J , "Rayleigh Line width Measurements near the Critical Point of a Binary Fluid," *Physical Review Letters,* Vol 40, No 12, March 1978, pp 777 780

24 Perl, R and Ferrell, R A , "Decoupled Mode Theory of Critical Viscosity and Diffusion in the Binary Liquid Phase Transition," *Physical Review A,* Vol 6, No 6, Dec 1972, pp 2358–2369

25 Oxtoby, D W and Gelbart, W M , "Shear Viscosity and Order Parameter Dynamics of Fluids near the Critical Point," *Journal of Chemical Physics,* Vol 61, No 7, Oct 1974, pp 2957–2963

26 Garisto, F and Kapral, R , "Vertex Corrections to the Shear Viscosity Critical Exponent," *Physical Review A,* Vol 14, No 2, Aug 1976, pp 884–885

27 Levelt Sengers, J M H , Greer, W L and Sengers, J V , "Scaled Equation of State Parameters for Gases in the Critical Region," *Journal of Physical and Chemical Reference Data,* Vol 5, No 1, 1976, pp 1–51

28 Vicentini Missoni, M , Levelt Sengers, J M H and Green, M S , "Scaling Analysis of Thermodynamic Properties in the Critical Region of Fluids," *Journal of Research of the National Bureau of Standards M,* Vol 73A, No 6, Nov -Dec 1969, pp 563–583

29 Levelt Sengers, J M H and Sengers, J V , "Universality of Critical Behavior in Gases," *Physical Review A,* Vol 12, No 6, Dec 1975, pp 2622–2627

30 Levelt Sengers, J M H , "Universality of Thermophysical Properties near Critical Points," *Proceedings of the 7th Symposium on Thermophysical Properties,* A Cezairliyan, ed , American Society of Mechanical Engineers, 1977, pp 766–773

31 Sengers, J V and Moldover, M R , "Two Scale Factor Universality near the Critical Point of Fluids," *Physics Letters,* Vol 66A, No 1, April 1978, pp 44–46

32 Hanley, H J M and Ely, J R , "The Viscosity and Thermal Conductivity Coefficients of Dilute Nitrogen and Oxygen," *Journal of Physical and Chemical Reference Data,* Vol 2, No 4, 1973, pp 735–755

33 Jacobsen, R T and Stewart, R B , "Thermodynamic Properties of Nitrogen Including Liquid and Vapor Phases from 63K to 2000K with Pressures to 10,000 Bar," *Journal of Physical and Chemical Reference Data,* Vol 2, No 4, 1973, pp 757 922

34 Watson, J T R , Basu, R S and Sengers, J V , "Viscosity of Water and Steam," Note BN 888, Institute for Physical Science and Technology, University of Maryland, College Park, MD, Sept 1978, 19 pages

35 D'Arrigo, G , Mistura, L and Tartaglia, P , "Concentration and Temperature Dependence of Viscosity in the Critical Mixing Region of Aniline Cyclohexane," *Journal of Chemical Physics,* Vol 66, No 1, Jan 1977, pp 80 84, "Concentration and Temperature Dependence of Viscosity in the Critical Region of Binary Liquid Mixtures," *Proceedings of the 7th Symposium on Thermophysical Properties,* A Cezairliyan, ed , American Society of Mechanical Engineers, 1977, pp 831, 835

D. E. Daney
P. R. Ludtke
M. C. Jones

Thermophysical Properties Division
National Engineering Laboratory
National Bureau of Standards
Boulder, Colorado 80303

An Experimental Study of Thermally-Induced Flow Oscillations in Supercritical Helium[1]

The density wave stability boundary has been experimentally determined for supercritical helium flowing in a long (L = 185 m), heated channel of high aspect ratio (L/d = 4 6 $(10)^4$) A pressure drop ratio and the fluid expansion ratio correlate the oscillation inception point data The growth of enthalpy (temperature) perturbations in a heated channel has been experimentally verified During the density wave oscillation, the channel exit temperature and inlet mass flow were observed to be in phase, and the oscillation period was close to twice the fluid transit time All three observations agree with a simple incompressible flow model Oscillation amplitudes as great as 11 K and 100 percent of inlet flow were observed

Introduction

This study of the stability of supercritical helium flowing in a heated channel was prompted by an interest in superconducting power transmission lines [1] These lines will typically be cooled by supercritical helium over the temperature range of 6 to 10K and at pressures up to 15 bar They are characterized by a high aspect ratio ($L/d \approx 10^5$) and by a low heat flux ($q \approx 10^{-5}$ W/cm^2) Of the various flow instabilities described by Boure, et al [2], the density wave instability has been considered the most common and likely to occur It is this instability that was observed and studied in our work

In the density wave instability, temperature (density) disturbances move down the heated channel at the fluid velocity, producing flow and temperature oscillations with a frequency of approximately 1/27 The amplitude of these temperature oscillations can be several Kelvin or more, making operation of the high current superconductor hazardous, if not impossible This hazard results because if the superconductor warms to its transition temperature (the temperature at which it becomes normal or nonsuperconducting), large quantities of electrical energy will be dumped into the conductor due to the discontinuous jump in its resistivity At best, an unacceptable loss of service would occur Rupture of the coolant channel due to rapid warming of the helium might also occur

At ambient temperature and above, density wave oscillations have been studied extensively in recent years [2–4], but relatively little experimental work has been reported for cryogenic fluids [5, 6] Jones and Peterson [7] have recently reported on a numerical analysis of supercritical helium flow stability using an exact equation of state, and Zuber [8] and Friedly, et al [9] have analyzed supercritical systems using an approximate two zone equation of state The effort reported here is, to our knowledge, the first experimental work on density wave oscillations in supercritical helium

It is clear from these studies that the density wave instability is a system instability which is characterized not only by the conditions in the heated section, but by the boundary conditions as well Thus control and measurement of the supply pressure and temperature and of the inlet and exit flow impedances are essential to a meaningful study

The primary goals of this work were to observe the nature of density wave oscillations in supercritical helium and to define the stability boundary so that the safe operating region for supercritical helium might be known Propagation of heat pulses or thermal waves (local temperature spikes or disturbances) was also studied, both as an aid to understanding the nature of density wave oscillations, and because of an interest in the waves themselves Analysis of superconducting to normal zone propagation in helium cooled superconductors requires detailed knowledge of such thermal wave propagation As a by product of this study, the hydraulic resistance of supercritical helium was also measured [10]

Experimental

Fig 1 is a schematic of the apparatus The 185 m long test section, which is wound in a 775 mm diameter helical coil, is fabricated from 5 lengths of 3 99 mm ID × 0 41 mm wall, type 304 stainless steel tubing It is shielded by both an outer radiation shield cooled by liquid nitrogen and by an inner shield cooled by the helium exhausted from the test section The resulting heat leak to the test section is less than 1 watt It is heated by passing current through the tube wall, giving

---

[1] This work was performed at the National Bureau of Standards under the sponsorship of the Department of Energy, Contract EA 77 A 01 6010

Contributed by the Heat Transfer Division for publication in the JOURNAL OF HEAT TRANSFER Manuscript received by the Heat Transfer Division, March 13, 1978

uniform wall heat flux and stray current paths are eliminated by dielectric joints. The aspect ratio (L/d) is 4.6 $(10)^4$ and the helix to tube diameter ratio is 194. The resulting increase in hydraulic resistance due to the curvature is about 10 percent [10, 11].

The operating range in these experiments was:

P_0	2.7 – 15 bar
T_0	4.6 – 6.0 K
$\dot{m}_1$	0.32 – 0.58 g/s
u_1	21 – 38 cm/s
Re_1	$3.2(10)^4 - 6.2(10)^4$
R	0 – 15

choked flow at exit (position e, Fig. 1)

For reference, the helium critical point is 2.22 bar and 5.2 K. The ratio of the fluid to wall heat capacity, $(\rho A_c C_p)_{He}/(\rho A_c C)_w$, is about 450 at 4 K and 140 at 10 K.

Instrumentation. Pressures are measured with variable reluctance and capacitance pressure transducers operating at ambient temperature. Temperatures are measured with germanium resistance thermometers which measure the temperature of the copper couplings between tubing lengths. The coupling-to-helium temperature difference is estimated to be 0.01 K or less. The installed thermomenter response time is estimated to be one second or less. The inlet flow is measured by a sharp-edged orifice (diameter = 1.3 mm) which was calibrated in situ against the ambient temperature thermal type mass flowmeter during steady flow. The total uncertainty in the measurements is estimated to be: P_1, 0.5 percent; ΔP_{0-1} 3 percent; ΔP_{1-6}, 200 Pa, test section temperature, 0.02 K, inlet mass flow rate, 3 percent, ambient (discharge) flow rate 0.5 percent.

Data are collected with a mini computer which gives "real time" conversion of all instrument channels to physical parameters (P, T, $\dot{m}$, etc.). A strip chart records the wave form.

Procedure. Because stable inlet boundary conditions were considered essential to a meaningful study, we held the conditions at point a (Fig. 1) constant during a particular test. This is equivalent to a near zero supply impedance. Typically, the pressure (controlled by the cold PRV [12]) was constant to within a few thousandths of a bar, and the temperature (controlled by the heater-controller), was constant to within a few hundredths K for all but the most severe oscillations.

Density wave oscillations were induced by two methods. The usual technique was to gradually increase the test section heating in a series of steps while holding the inlet valve position fixed, and adjusting the exit valve to maintain a constant inlet mass flow rate. In the alternative technique, which was used to obtain high values of the fluid expansion ratio, R, and the pressure drop ratio, ψ, the heating was increased to give the desired fluid expansion ratio. Then the inlet valve was opened (reducing the supply impedance) until oscillations occurred.

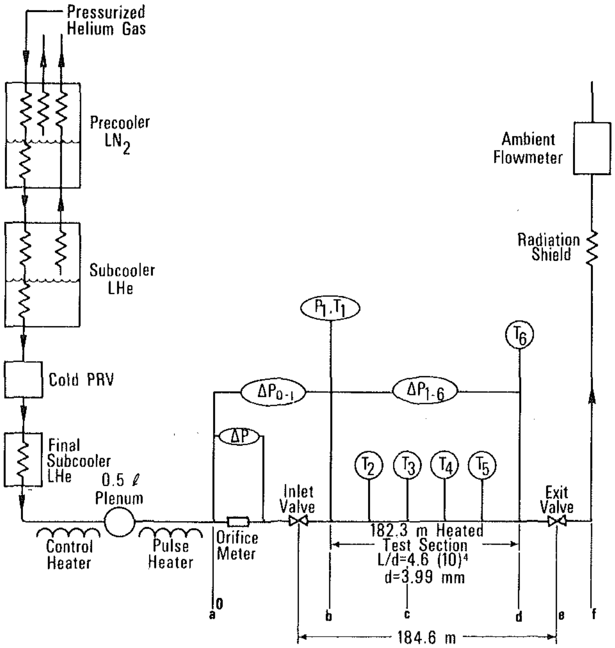

Fig. 1 Flow schematic

Selection of a stability criterion, i.e., defining the oscillation inception point, was something of a problem. Because of the low frequency of the oscillations, typically 1.5 to 3.5 mHz, more than an hour was required to follow as few as six or ten cycles. As an unstable operating point was approached, damped or weak oscillations were induced (and observed for five to ten cycles) by perturbations associated with changing the operating conditions. Thus five or six hours were required to obtain each stability point, and the time required to obtain true steady-state would have been at least several times as long—truly prohibitive in both helium and manpower costs. Instead of defining the inception of flow instability as the break in the steady-state curve of flow fluctuation versus heating rate [3], we settled on similar criteria which include a qualitative judgment about the growth or decay of

Nomenclature

A_c = cross-sectional area
A_s = channel surface area
C = specific heat
C_p = specific heat at constant pressure
d = channel diameter
f = oscillation frequency
h = specific enthalpy
L = channel length
$\dot{m}$ = mass flow rate
p = pressure
P = wetted perimeter of channel
q = wall heat flux
Q = total channel heat transfer rate
R = expansion ratio, $\Delta v_{1-6}/v_1 = \Delta v_{bd}/v_b$
Re = Reynolds number, $\dfrac{\rho u d}{\mu}$

t = time
T = temperature
u = velocity
v = specific volume
x = longitudinal position along channel
μ = viscosity
ζ = dimensionless position of the transposed critical
τ = fluid transit time
ρ = density
ψ = pressure drop ratio, $\dfrac{\Delta P_{ab} + \Delta P_{bc}}{\Delta P_{cd} + \Delta P_{de}}$
Ω = rate of fluid expansion, $\dfrac{qP}{A_c}\left(\dfrac{\partial v}{\partial h}\right)_p$

Subscripts

a–f = positions indicated in Fig. 1
c = position of the transposed or pseudo critical point—location varies with operating conditions.
h = heated
He = helium
i = inception point of oscillation (stability boundary)
m = measured
t = transposed critical point
u = unheated
w = wall
0–6 = instrument positions indicated in Fig. 1.

an oscillation. We define the following three flow classifications, quantified from our original intuitive judgments of the inception of instability.

Classification	Amplitude	
	$(\Delta\dot{m}/\dot{m})_0$	ΔT_6
Stable	<4 percent	<0.2 K
Marginal	>3 percent and ≤10 percent	>0.15 K and ≤0.26 K
Unstable	>9 percent	>0.27 K

In case of growth or decay of the oscillation, the amplitude listed is for the end of the observation period, usually six to ten cycles. The apparent overlap of the criteria is eliminated when both flow and temperature are considered. It is interesting to note that our criteria agree well with inception criteria for Freon 113 [3], where inception typically occurred at flow disturbances of about five percent of the mean flow.

Results and Discussion

General Observations. Initial difficulties experienced in obtaining steady inlet conditions suggested that a supply system which allows variation of the temperature of the fluid arriving at point a (Fig. 1) can have a destabilizing effect. For example, in flow studies which use a helium refrigerator as the supply, Hoffer and Dean [13] report multiple "reflections" of thermal waves off the final refrigerator heat exchanger.

The period required for the heated line to achieve steady-state after a change in operating conditions appeared to be many fluid transit times on some occasions, and on one occasion a combination of inlet flow drift and a slowly damped oscillation resulted in a severe excursion to zero inlet flow. It is not clear whether or not this was a true excursive (Ledinegg [2]) instability since calculations by Arp [14] indicate that this instability is not possible under the conditions of our experiments. In any case, the temperature perturbations which accompany such flow disturbances are unacceptable for superconducting applications, and their occurrence points to the need for active flow control in some cases.

Because the response time of large aspect ratio lines is much greater than normally encountered, care is necessary regarding assumptions of steady-state or assumptions of equal flow in and out. This is especially true following a change in operating conditions, e.g., an increase in the heat load. Expansion of the resident fluid can cause a large temporary imbalance in the inlet and exit flows, and failure to maintain the inlet flow by adjustment of the exit valve (or inlet restriction if appropriate) can result in high amplitude density wave oscillations—even under conditions which are stable for sustained oscillations. Although these oscillations may be damped, they are none the less damaging if the initial temperature excursion exceeds the safe operating limit.

In view of this difficulty in changing the heating rate without inducing a significant flow ($\dot{m}_0$) and temperature (T_6) perturbation, the disturbance required to trigger an oscillation was always present. Thus, an experiment generally comprised a series of progressively less damped oscillations with the final oscillations being either sustained or growing. The mode of operation usually gave only a single large sustained disturbance which set the system oscillating at its characteristic frequency. Disturbances of short duration gave spikes superimposed on the basic wave form.

Heat Pulse Behavior. There are two principle features of the density wave oscillations we observed in supercritical helium. One feature concerns the effect of the exit density on the flow and the resulting phase lag between the inlet and exit mass flow rates. The other feature is the tendency of enthalpy (temperature) perturbations to grow [7] in a heated channel. We first consider this latter feature, which is also of interest in its own right.

The growth of heat pulses, or enthalpy perturbations, occurs because an element of fluid that is less dense (warmer) than average undergoes greater than average heating per unit mass (for constant wall heat flux) as it travels down a heated channel, making it even less dense and subject to even greater heating, etc. The phenomenon can be analyzed by considering a simple linear perturbation of enthalpy and specific volume (due to a small perturbation in the heat flux, for example) in a small element of fluid in a stream with steady flow previous to the perturbation. A constant area duct and uniform heat flux, q, are assumed. For the case of negligible wall heat capacity (less than one percent of the fluid heat capacity in these experiments) and negligible axial wall conduction, the instantaneous wall temperature of a resistance-heated tube will adjust itself so as to maintain constant q for both the perturbed and unperturbed elements of the fluid. If we choose a Lagrangian method of description so that we follow a small fixed mass of perturbed fluid, the problem is greatly simplified since we need consider only the perturbed element rather than all elements.

For the Lagrangian method, the one-dimensional continuity and energy equations are

$$\rho A_c \Delta x = \Delta m = \text{constant} \tag{1}$$

$$\rho A_c \frac{dh}{dt} = qP \tag{2}$$

where Δx and Δm are the length and mass of a small element. To obtain these equations in terms of perturbed variables we write the variables h, ρ and Δx, as the sum of a steady part and a time dependent part. For example, $h = \bar{h} + h'(t)$ where $\bar{h}$ is the unperturbed value and $h'(t)$ is the perturbed value. Substituting these expressions into (1) and (2), then subtracting the unperturbed expressions yields the continuity and energy equations for the perturbed variables, which, for convenience, are expressed in terms of the specific volume perturbation, v', rather than the density perturbation.

$$\Delta x' = v' \frac{\Delta m}{A_c} \tag{3}$$

$$dh' = \frac{qP}{A_c} v' dt \tag{4}$$

The expression for heat pulse growth is obtained by dividing (4) by h' and setting $v'/h' = (\partial v/\partial h)_p$. This assumes that pressure effects are absent and that the local equation of state is identical with that for stable equilibrium. Integration of the resulting equation yields the time domain expression for the growth of an enthalpy perturbation in a heated channel in the absence of pressure effects.

$$h' = h_1' e^{\int \Omega dt} \tag{5}$$

where $\Omega \equiv qP/A_c (\partial v/\partial h)_p$ is the rate of fluid expansion and is the so-called reaction frequency introduced by Zuber [8] and used by Friedly [9] and Jones [7]. Equation (5) which is for the characteristic line, $dt = dx/u(x, t)$, indicates an enthalpy perturbation will grow exponentially with time as the fluid travels down a heated line. Because the velocity increases along the channel, the growth with respect to length will not be exponential.

Enthalpy perturbation growth may be expressed in terms of specific volume by noting in (4) that $qPdt/A_c$ is the enthalpy change per unit volume dh/v. Making this substitution gives

$$dh' = \frac{dh}{v} v'.$$

Dividing by h', setting $v'/h' = (\partial v/\partial h)_p$ and integrating results in

$$h' = h_1' \left(\frac{v}{v_1}\right). \tag{6}$$

Thus, for uniform heating, the growth of an enthalpy perturbation will go as $v = v(h)$, which is more nearly linear than exponential.

Expressed in terms of temperature, equation (5) becomes

$$T' = (C_{p1}/C_p) T_1' e^{\int \Omega dt} \tag{7}$$

where C_p is the specific heat at constant pressure.

The time, Δt, required for a square wave to pass a fixed point is easily obtained from the continuity equation. Rearranging (1) gives

$$\Delta x = \frac{v}{v_1} \Delta x_1$$

where the subscript 1 refers to the initial perturbation. Using the definition of velocity, $\Delta x = u\Delta t$ gives

$$\Delta t = \Delta t_1 \left(\frac{u_1}{u}\right)\left(\frac{v}{v_1}\right),$$

and the steady flow Eulerian continuity equation is substituted for u to obtain the final form

$$\Delta t = \Delta t_1 \left(\frac{\bar{v}_1}{\bar{v}}\right)\left(\frac{v}{v_1}\right), \tag{8}$$

where $\bar{v}$ is the unperturbed (steady-state) specific volume and v is the specific volume of the perturbed fluid. Depending on the equation of state and the operating conditions, equation (8) can give either a positive or negative change in Δt.

Fig. 2 shows the progression down the unheated test section of a thermal wave which was generated by a 20 second activation of the pulse heater. Although there is some rounding of the wave due to diffusion and wall heat transfer, there is no significant growth before position 6. A small anomalous heat leak to the end of the test section produces a slight broadening at this point. Note that the wave front is on the left side of the wave since Fig. 2 shows the response of a fixed thermometer to moving wave.

In contrast, a heat pulse traveling down a heated line, Fig. 3, exhibits rapid growth in both amplitude and time required to pass a fixed point as predicted by equations (7) and (8). The growth in Δt predicted by equation (8) for the experimental conditions is 33 percent compared to about 50 percent observed in Fig. 3. The agreement is probably as good as can be expected considering the inexact theoretical model, the irregular wave form, and the non-zero wall heat capacity. The irregular shape of the original pulse is due to flow perturbations induced by the heat pulse in the more compressible heated helium. The decay of the wave as it passes thermometer 6 results because the front of the wave arrives at the exit valve, accelerating the flow, before the remainder of the wave has passed position 6.

Density wave oscillations. The second feature of density wave oscillations which we consider is the phase or space lag between the inlet and exit mass flow rates (and other system variables as well) which is required for an oscillatory instability [8]. This feature is most easily understood by considering a simple incompressible flow model (which considers thermal expansion, but not pressure effects) with a large exit flow impedance such as was present in the experiments. Focusing our attention on the exit restriction, we note that the velocity at this point is given by

$$u_d \sim \sqrt{\frac{\Delta P_{d-f}}{\rho_d}}. \tag{9}$$

When warmer than average fluid (lower density) arrives at the exit restriction, the velocity increases, and the fluid in the line accelerates to satisfy continuity. The residence time of the fluid in the heated section decreases, resulting in less heating per unit mass and, hence, in cooler fluid delivered to the exit restriction after some time lag. As the cooler fluid flows through the exit restriction the fluid in the heated section decelerates, giving it an increased residence time and greater than average heating. Thus, a positive perturbation in the exit temperature induces a negative perturbation or reflection which arrives at the exit after the transit time of the fluid in the line. The period of the oscillation is twice the transit time, and the mass flow rate at the inlet and exit are 180 deg out of phase. This phase difference results because in the absence of pressure effects, the inlet and exit velocities are in phase, making the inlet mass flow, $\dot{m}_b$, proportional to $1/\sqrt{\rho_d}$, i.e., $\dot{m}_b \sim u_b \sim u_d \sim \sqrt{1/\rho_d}$. According to (9), however, the exit mass flow, $\dot{m}_d$, is proportional to $\sqrt{\rho_d}$, giving the 180 deg phase shift in inlet and exit mass flow rates.

Fig. 4 shows a typical density wave oscillation, composed from a strip chart trace of orifice pressure drop and thermometer resistance. In this case the instability was induced by reduction of the inlet impedance. The exit valve was adjusted at the same time so as to maintain the average flow rate constant. Note that the exit temperature and inlet flow are in phase, implying that inlet and exit mass flow rates are 180 deg out of phase—in agreement with the simple qualitative model discussed above. Although continuous traces of the exit flow were not recorded, discrete simultaneous readings of $\dot{m}_a$ and $\dot{m}_f$ were made, and these also confirm the 180 deg phase shift. The density wave oscillation shown in Fig. 5 was induced and then damped by changes in the power level. This trace shows both the growth and phase relation of the thermal wave as it progresses down the heated channel. As before, the inlet mass flow and exit temperature are nearly in phase.

Development of a stability (inception point) map for density wave oscillations in supercritical helium requires a set of scaling or correlating parameters, for which we have relied on the work of Zuber [8]. In his simplified stability analysis, Zuber assumes a two zone equation of state for a supercritical fluid. In the first (fluid) zone the specific volume is independent of enthalpy, and in the second (gas) zone the specific volume is proportional to enthalpy. The stability criterion he derives with this model (equation (VII-29) in [8]), expressed in terms more convenient to our purposes here is

$$\frac{2\Delta P_{ac}}{\Delta P_{cf}} > \left[1 + \frac{\Delta h_{bc}}{\Delta h_{cd}}\right]\left[\frac{R}{1+R}\right] \tag{10}$$

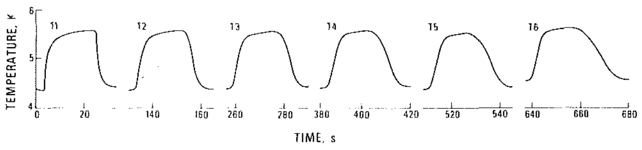

Fig. 2 Propagation of a heat pulse in unheated test section (experimental results); $P_1 = 2.87$ bar, $T_1 = 4.37$ K, $\dot{m} = 0.493$ g/s, $U_1 = 30.2$ cm/s

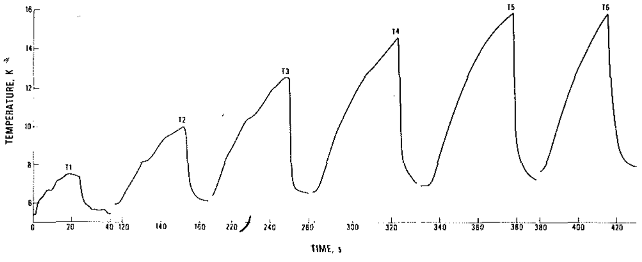

Fig. 3 Propagation of a heat pulse in a heated test section (experimental results); $P_1 = 3.93$ bar, $T_1 = 5.40$ K, $\dot{m} = .429$ g/s, $U_1 = 30.4$ cm/s, $Q = 11.1$ W

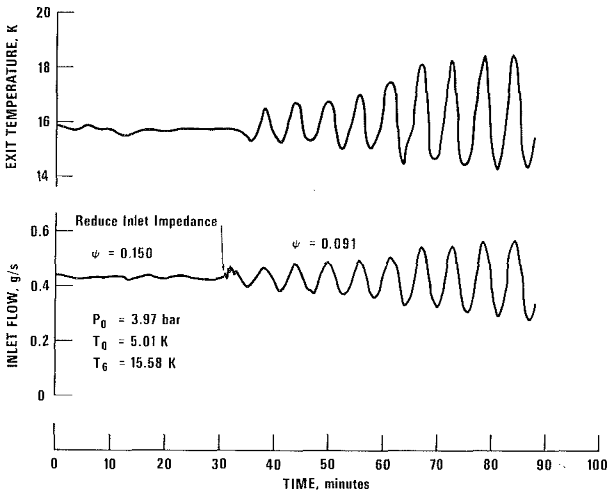

Fig. 4 Density wave oscillation induced by reducing inlet impedance, $Q = 37.2$ W

for stability.

A similar expression with an essentially linear dependence on the expansion ratio has been used by Serov and Smirnov [15].

Because (10) is based on a rather crude equation of state, it should not be expected to give a highly accurate description of the stability boundary. It does suggest, however, the use of $\Delta P_{ac}/\Delta P_{cf}$ and expansion ratio, R, as correlating parameters, taking the zone transition point c to be the transposed critical point (the locus of the specific heat maxima).

The dimensionless position of the transposed critical in the channel is determined from $\zeta = (h_c - h_b)/(h_d - h_b)$, where h_c is obtained from a plot of the transposed critical enthalpy versus pressure, and the pressure drop ratio, ψ, is given by

$$\psi \equiv \frac{\Delta P_{ab} + \Delta P_{bc}}{\Delta P_{cd} + \Delta P_{de}} = \frac{\Delta P_{ab} + \zeta \Delta P_u}{\Delta P_h - \zeta \Delta P_u + \Delta P_{de}}. \qquad (11)$$

The unheated line pressure drop, ΔP_u, is that calculated for the measured conditions at point b with $Q = 0$, whereas the heated pressure drop, ΔP_h, is the mean measured value. Because the exit flow is choked, the pressure drop to choked conditions rather than the total pressure drop is used to evaluate ΔP_{de}. Except for very low values of ψ (obtained by removing the inlet valve) ΔP_{bc} is generally less than 25 percent of ΔP_{ab}.

Even though ψ is derived from a somewhat inaccurate and crude equation of state, its use gives a rather good correlation of the stability data as shown in Fig. 6. The curve defining the stability boundary is estimated from the experimental data. The points shown are those observed closest to the stability boundary for a particular experimental run, either the last stable operating point or the first unstable point. The points marked marginal are for weakly damped or low amplitude oscillations. Thus, two or three points are shown for each run. A summary of the experimental data is given in the Appendix. Numerical results of Jones and Peterson for supercritical helium [7] are also given in Fig. 6 for comparison. These points, which were calculated for typical design and off-design conditions, are not at the stability boundary, but they do seem to indicate that the numerical calculations give conservative results, i.e., the numerical method predicts unstable conditions at lower values of fluid expansion. The numerical method requires that the stability boundary be defined as the point at which infinitesimal disturbances grow, whereas the experimental method classifies mass flow oscillation amplitudes of less than four percent as stable (see procedure section for details).

Fig. 7 compares the measured oscillation frequency to the calculated fluid transit time as a function of the degree of instability. The ordinate, $2\tau f$, is the ratio of the measured frequency to the frequency predicted by the simple incompressible flow model, $1/2\tau$. The fluid transit time, τ, is calculated from the mean measured inlet conditions (P_1, T_1 and $\dot{m}_1$) and from the heat input, $Q = \dot{m}_1(h_6 - h_1)$. The correlating parameter, R_m/R_i is the ratio of the measured fluid expansion to the fluid expansion at the oscillation inception point (stability boundary in Fig. 6). This parameter is a measure of the relative degree of instability. A value less than one denotes stable conditions, and a value greater than one denotes unstable conditions.

The principal feature of Fig. 7 is the clustering of $2\tau f$ about a value of 1.0 as predicted by the simple incompressible flow model. Although R_m/R_i is a somewhat imprecise parameter because of the uncertainty in the location of the stability boundary in Fig. 6, the trend towards a higher frequency ratio at greater degrees of instability is clear.

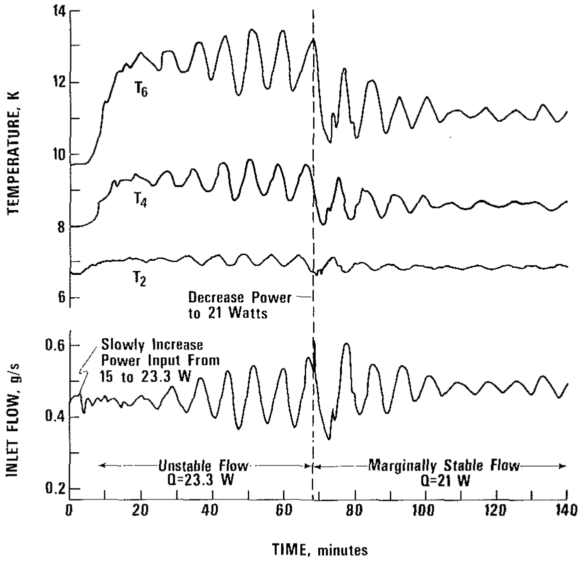

Fig. 5 Density wave oscillation, P_0 = 6.0 bar, T_0 = 5.80 K, ψ = 0.008. Power level reduction causes an unstable oscillation to become damped or marginally stable

Summary

This experimental study of flow stability of supercritical helium flowing in a long (L = 185 m, L/d = 4.6 $(10)^4$) heated channel has defined the stability boundary of density wave oscillations for the case of a choked exit restriction. The pressure drop ratio, ψ, and fluid expansion ratio, R, correlate the oscillation inception point data.

The growth of enthalpy (temperature) perturbations in a heated channel has been experimentally verified. During density wave oscillations, the channel exit temperature and inlet mass flow were observed to be in phase, and the oscillation period was close to twice the fluid transit time. All three observations agree with a simple incompressible flow model.

For superconducting power transmission lines, the application which prompted this study, density wave oscillations of the amplitude observed in this study would make operation hazardous if not impossible. Fortunately, however, the anticipated operating conditions

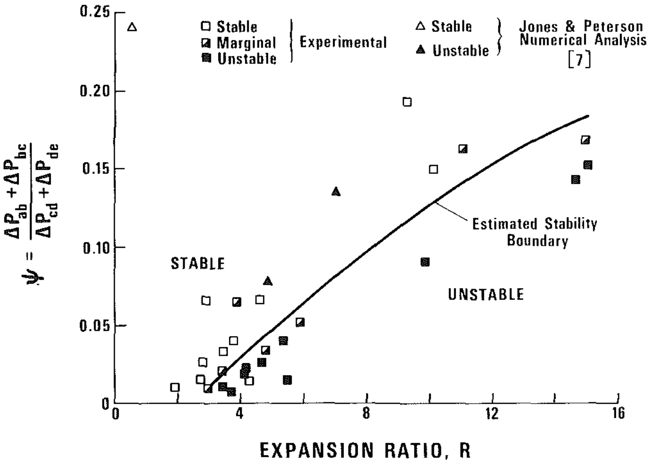

Fig. 6 Density wave stability map for supercritical helium. The curve is estimated from the experimental results

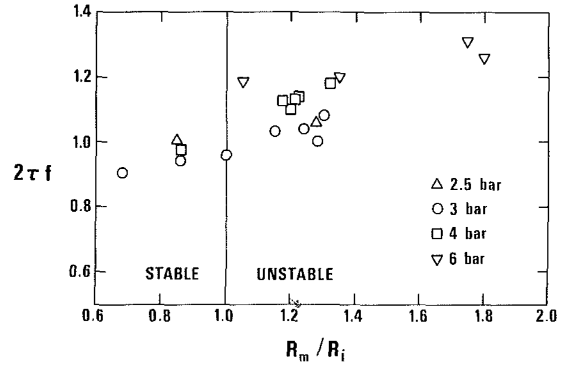

Fig. 7 Normalized frequency as a function of the degree of instability

are generally such that the fluid expansion ratios are expected to be less than 2.0—a stable condition for even low inlet impedances. Off design operating conditions which give high expansion ratios should be avoided though, and consideration should be given to active control of the helium temperature at the inlet to the transmission line so as to avoid "reflection" of temperature perturbations from the refrigerator heat exchangers.

If operation of a system under unstable conditions is anticipated, then active control of the inlet flow will be required. Uncoupling the flow rate from the exit conditions should give stable operation even for severe conditions.

Acknowledgments

We thank Vincent Arp for his interest and his helium flow computer program. The support of Eric Forsyth and Jack Jensen of Brookhaven National Laboratory is also appreciated.

References

1 Forsyth, E. B., Stewart, J. R., Williams, J. A., "Long-Distance Bulk Power Transmission Using Helium-Cooled Cables," Brookhaven National Laboratory, Upton, N.Y. 11973, Report No. BNL 20250 presented at the 1976 IEEE Underground Transmission and Distribution Conference, Atlantic City, N. J., Sept. 27–October 1, 1976.

2 Boure, J. A., Bergles, A. E., Tong, L. S., "Review of Two-Phase Flow Instability," *Nuclear Engineering and Design,* Vol. 25, No. 2, July 1973, pp. 165–192.

3 Saha, P., Ishii, M., Zuber, N., "An Experimental Investigation of Thermally Induced Flow Oscillations in Two-Phase Systems," ASME JOURNAL OF HEAT TRANSFER, Vol. 98, 1976, pp. 616–622.

4 EURATOM, *Proceedings Symposium on Two Phase Flow Dynamics,* Eindhoven, 1967.

5 Fleming, R. B., Staub, F. W., "Investigation of the Nature of Cryogenic Fluid Flow Instabilities in Heat Exchangers," General Electric Co., Schenectady, N. Y., Research and Development Center NAS 8-11422, NTIS Report No. N69-7454B, May 1966.

6 Thurston, R. S., Rogers, J. D., and Skoglund, V. J., "Pressure Oscillations Induced by Forced Convection Heating of Dense Hydrogen," *Advances in Cryogenic Engineering,* K. D. Timmerhaus, ed., Vol. 12, Plenum Press, New York, 1967, pp. 438–451.

7 Jones, M. C., Peterson, R. G., "A Study of Flow Stability in Helium Cooling Systems," ASME JOURNAL OF HEAT TRANSFER, Vol. 97, 1975, pp. 521–527.

8 Zuber, N., "An Analysis of Thermally Induced Flow Oscillations in the Near-Critical and Supercritical Thermodynamic Region," General Electric Co., Schenectady, N. Y., Research and Development Center Final Report No. NASA-CR-80609, May 1966, Contr. No. NAS 8-11422.

9 Friedly, J. C., Manganaro, J. L., Kroeger, P. G., "Approximate Criterion for Prediction of Flow Oscillations in Supercritical Fluid Heat Exchangers," *Advances in Cryogenic Engineering,* K. D. Timmerhaus, ed. Vol. 14, Plenum Press, New York, 1969, pp. 258–270.

10 Daney, D. E., Ludtke, P. R., "Friction Factors for Flow of Near-Critical Helium in Curved Tubes," *Cryogenics,* Vol. 18, 1978, pp. 345–348.

11 Ito, H., "Friction Factors for Turbulent Flow in Curved Pipes," ASME *Journal of Basic Engineering,* Vol. 81, 1959, pp. 123–133.

12 Daney, D. E., "A Cryogenic Pressure Regulator," *Cryogenics,* Vol. 18, 1978, pp. 234–235.

13 Hoffer, J. K., Dean, J. W., "Propagation of Thermal Waves in Supercritical Helium," ASME Paper No. 77-HT-76.

14 Arp, V., "Negative Differential Flow Resistance in Supercritical Helium," *Cryogenics,* Vol. 16, 1976, pp. 171–177.

15 Serov, E. P., Smirnov, O. K., *Teplofizka Vysokikh Temperatur,* Vol. 2, 1964, p. 623.

APPENDIX

Oscillation Data

Run No.	P_1 (bar)	T_1 (K)	ΔP_{01} (bar)	ΔP_{16} (bar)	T_6 (K)	P_e** (bar)	$\dot{m}_1$ (g/s)	Q (W)	f (mHz)	oscillation amplitude $\Delta\dot{m}_1/\dot{m}_1$ (percent)	ΔT_6	ρ_1 g/cm^3	$\mathrm{Re}\times10^{-4}$	ζ	ψ	R	classification
5-3	2.87	4.85	0.033	.085	7.79	1.35	0.317	10.9	1.34	12.3	0.27	0.1212	3.18	.287	0.026	4.73	unstable
5-5	3.96	5.42	0.040	.118	9.93	1.84	0.384	16.3	1.87	excursion to zero flow*		0.1123	4.04	.214	0.024	4.20	"
5-5	3.90	5.40	0.076	.184	11.23	1.79	0.430	21.8	2.36	34.0	1.83	0.1122	4.54	.177	0.041	5.35	"
5-5	3.94	5.39	0.065	.147	10.57	1.82	0.417	19.5	2.16	9.8	0.49	0.1132	4.39	.199	0.035	4.79	"
5-11	3.78	5.00	0.182	.259	15.58	1.70	0.418	32.7	2.90	35.0	2.18	0.1231	4.02	.151	0.091	9.84	"
5-12	5.99	6.03	0.042	.193	17.06	2.78	0.421	32.3	2.71	37.4	2.70	0.1121	4.20	.129	0.015	5.50	"
5-25	2.45	4.63	0.197	.285	13.26	1.05	0.397	28.2	2.71	100.0	10.91	0.1243	3.86	.139	0.145	14.68	"
5-26	3.20	5.00	0.274	.366	18.78	1.38	0.435	41.8	3.44	9.6	0.84	0.1191	4.40	.099	0.153	15.11	"
6-14	2.95	5.00	0.015	.139	7.56	1.36	0.470	15.1	1.85	29.4	0.68	0.1171	4.89	.284	0.021	4.22	"
6-15	3.99	5.21	0.012	.098	8.71	1.87	0.399	14.3	.60	21.3	0.78	0.1188	4.01	.293	0.012	3.43	"
6-15	5.96	5.80	0.014	.140	12.54	2.78	0.448	24.0	2.12	22.0	0.90	0.1176	4.35	.221	0.008	3.68	"
4-20	2.87	4.86	0.083	.119	7.07	1.33	0.444	13.3	1.46	8.3	0.21	0.1211	4.50	.335	0.066	3.93	marginally stable
4-21	2.91	4.85	0.066	.223	8.45	1.30	0.527	20.8	2.32	5.9	0.19	0.1215	5.31	.257	0.053	5.79	"
5-12	6.01	5.92	0.040	.183	16.76	2.80	0.433	33.5	2.81	26.2†	2.07†	0.1149	4.39	.146	0.015	5.53	"
5-25	2.44	4.60	0.216	.272	10.72	1.04	0.457	25.2	2.22	3.3	0.26	0.1250	4.47	.178	0.164	11.05	"
6-14	2.98	5.00	0.162	.120	6.99	1.37	0.461	12.9	1.59	10.0	0.21	0.1173	4.93	.332	0.022	3.42	"
6-15	5.94	5.80	0.016	.139	11.09	2.78	0.480	21.4	2.07	4.2	0.17	0.1174	4.79	.269	0.010	2.99	"
4-20	2.87	4.83	0.082	.098	6.49	1.37	0.446	11.1		strongly damped		0.1218	4.53	.405	0.066	2.91	stable
4-21	2.89	4.84	0.080	.211	7.44	1.28	0.576	19.0		2.0	0.09	0.1218	6.16	.309	0.067	4.64	"
5-3	2.87	4.85	0.037	.074	6.79	1.34	0.350	9.6		6.4	0.11	0.1211	3.74	.365	0.033	3.45	"
5-5	3.93	5.39	0.072	.131	9.25	1.35	0.419	17.0		3.3	0.15	0.1129	4.52	.226	0.040	3.79	"
5-11	3.67	5.00	0.296	.267	15.46	1.66	0.427	33.1		2.7	0.05	0.1224	4.28	.142	0.150	10.14	"
5-12	5.84	5.99	0.040	.154	14.17	2.83	0.426	26.3		1.2	0.07	0.1132	4.38	.176	0.015	4.27	"
5-13	14.81	6.00	0.058	.116	15.77	6.74	0.501	31.3		0.0	0.0	0.1431	3.64	.390	0.010	1.95	"
5-25	2.39	4.59	0.252	.261	9.20	1.03	0.496	23.1		2.4	0.13	0.1249	4.98	.316	0.197	9.24	"
5-26	3.17	5.00	0.299	.370	18.27	1.36	0.439	41.0		1.5	0.17	0.1189	4.60	.105	0.168	14.85	"
6-14	2.98	4.98	0.017	.113	6.41	1.40	0.498	11.5		1.8	0.05	0.1182	5.32	.409	0.028	2.64	"
6-15	3.92	5.21	0.015	.099	7.76	1.84	0.437	12.8		3.0	0.07	0.1185	4.50	.360	0.016	2.69	"

* Combined excursive and oscillatory instability.
† Grew to amplitude given and then decayed to near zero amplitude.
** Pressure at choked condition.

M. Hishida
Professor.

Y. Nagano
Assistant Professor.

Nagoya Institute of Technology,
Showa-ku, Nagoya, Japan

Structure of Turbulent Velocity and Temperature Fluctuations in Fully Developed Pipe Flow

An experimental investigation of the turbulent structure of velocity and temperature fields has been made in fully developed pipe flow of air. In the near-wall region, the coherent quasi-ordered structure plays a dominant role in the turbulent heat transport process. The turbulent axial heat flux as well as the intensities of velocity and temperature fluctuations reach their maximums in this region, but these maximum points are different. The nondimensional intensities of velocity and temperature fluctuations are well described with the "logarithmic law" in the turbulent part of the wall region where the velocity-temperature cross-correlation coefficient is nearly constant. In the turbulent core, the velocity and temperature fluctuations are less correlated. The spectra of velocity and temperature fluctuations present −1 slope at low wavenumbers in the wall region and −5/3 slope in the inertial subrange. The temperature spectrum for the inertial-diffusive subrange indicates the −8/3 power-law.

Introduction

A knowledge of the fine structure of turbulent velocity and temperature fields in fully developed pipe flow is of great importance to gain a better understanding of the complex nature of the turbulent heat transport process. Nevertheless only a limited amount of research has been done on this subject, which is mainly due to the difficulty of simultaneous velocity and temperature measurements in nonisothermal flows. For pipe flow of air, the representative works hitherto reported were those of Tanimoto and Hanratty [1], Bremhorst and Bullock [2, 3], and Carr, et al. [4]. These results, however, are considered to involve noticeable errors under many restrictions of measuring system and data processing. The structure of the wall region in particular is still a matter of speculation.

In the present study, velocity and temperature fluctuations in turbulent pipe flow of air with a uniform wall temperature have been measured by employing the two-wire probe technique recently developed by the authors [5], and significant features of the wall turbulence structure are explored such as intensities, auto-correlation functions, cross-correlation functions and spectral densities. Attention is also paid to the turbulent heat transfer associated with the bursting phenomena in the near-wall region.

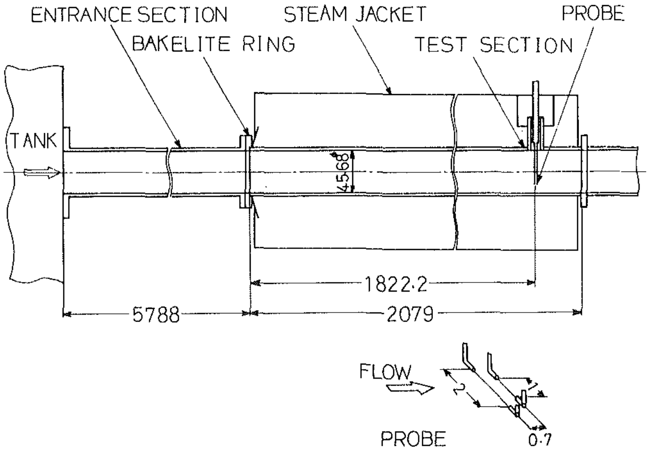

Fig. 1 Schematic of apparatus

Experimental Apparatus and Procedure

The test section, as shown in Fig. 1, was constructed from a 45.68 mm ID, 2079 mm-long reamed brass tube heated by saturated steam of atmospheric pressure and thus provided with a uniform wall temperature. At the beginning of the test section which immediately followed the unheated upstream of 127 pipe diameters, the velocity distribution showed that the flow was fully developed turbulent. Measurements were performed at a location 39.9 diameters downstream from the beginning of the test section, while the fully developed profiles of mean temperature and relevant turbulent quantities

---

Contributed by the Heat Transfer Division for publication in the JOURNAL OF HEAT TRANSFER. Manuscript received by the Heat Transfer Division December 16, 1977.

were certainly attained at a location about 21 diameters downstream [6, 7].

Velocity and temperature were simultaneously measured by the two-wire probe technique [5]. The probe consisted of 5 μm dia tungsten wires, i.e., the upstream wire was the constant current cold wire and the downstream one the constant temperature hot wire. The equations of the thermal equilibrium of hot and cold wires were solved by employing analog technique, and instantaneous velocity and temperature were simultaneously obtained. Cross-correlations between velocity and temperature fluctuations were obtained by electronic multiplication of a-c amplified separate signals of velocity and temperature. A SAICOR real time-time compression spectrum analyzer was employed to perform a spectrum analysis.

All measurements were made at a Reynolds number of 40,000.

Experimental Results

Velocity and Temperature Distributions. Radial velocity and temperature profiles normalized by centerline velocity $\overline{U}_c$ and temperature difference $\overline{T}_w - \overline{T}_c$ respectively, were shown in Fig. 2. There is an appreciable difference between velocity and temperature profiles. The effect of heat input on velocity profile becomes noticeable when approaching the wall. In the region very near the wall $y/r_0 < 0.078$, the dimensionless velocity of heated flow is higher than that of the unheated flow, thus indicating a steeper velocity gradient; in the other region ($y/r_0 > 0.078$), little effect from heat added to the velocity profile can be detected.

The universal velocity and temperature profiles were given in Fig. 3. In evaluating $\overline{U}^+$, $\overline{T}^+$ and y^+, the wall shear stress τ_w was obtained from the momentum integral equation with the measured values of pressure, velocity and temperature of air flowing through the test section, and the wall heat flux q_w was measured from the rate of condensation of the steam obtained in separated heating sections [6]. Considering the characteristics of the velocity and temperature fluctuations described later, we refer to the region $5 < y^+ < 30$ as the buffer layer, the region $30 < y^+ < 200$ as the turbulent part of the wall region, and the region $y^+ > 200$ as the turbulent core.

With heat input, the dimensionless velocity $\overline{U}^+$ is reduced in the turbulent region, and raised in the buffer layer. The chain line in Fig. 3 indicates the Prandtl-Nikuradse equation

$$\overline{U}^+ = 2.50 \ln y^+ + 5.5 \qquad (1)$$

The corresponding equation for the heated flow is reduced to

$$\overline{U}^+ = 2.50 \ln y^+ + 4.65 \qquad (2)$$

which is shown by the broken line.

The $\overline{T}^+$ data for the turbulent part of the wall region are well described with the following equation indicated by the two-dot chain line in the figure

$$\overline{T}^+ = 2.17 \ln y^+ + 4.30 \qquad (3)$$

Accordingly, from equations (2) and (3), the turbulent Prandtl

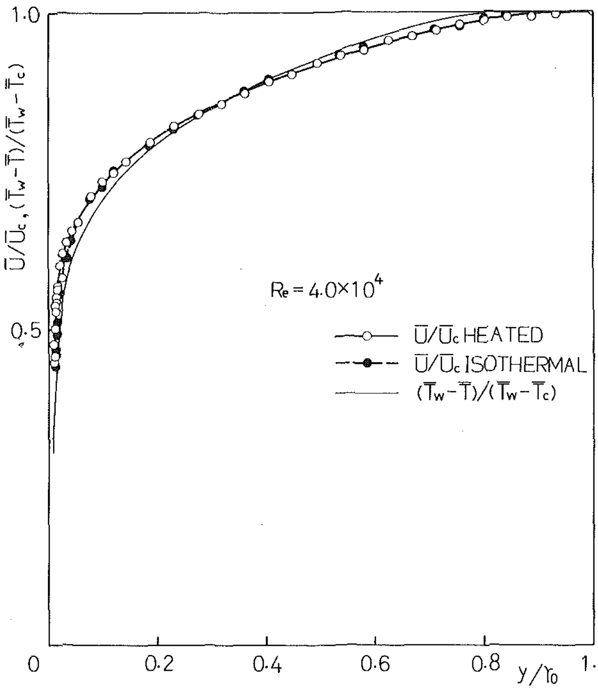

Fig. 2 Mean velocity and temperature profiles

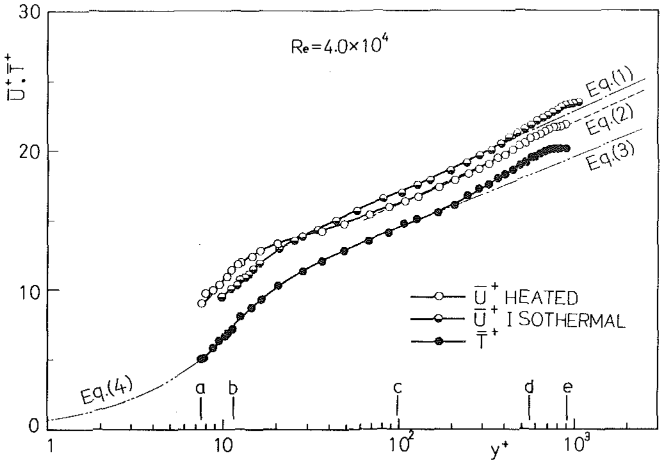

Fig. 3 Mean velocity and temperature in wall coordinates

Nomenclature

a = thermal diffusivity
c_p = specific heat at constant pressure
d = diameter of pipe
$E_t(k)$ = one-dimensional spectrum function of temperature fluctuations
$E_u(k)$ = one-dimensional spectrum function of velocity fluctuations
f = frequency
k = wavenumber = $2\pi f/\overline{U}$
Pr = Prandtl number
q_w = heat flux at wall
Re = Reynolds number = $\overline{U}_0 d/\nu$
$R_t(\tau)$, $R_u(\tau)$ = auto-correlation coefficients of t' and u', respectively
R_{ut} = cross-correlation coefficient between u' and t' = $\overline{u't'}/\sqrt{\overline{u'^2}}\sqrt{\overline{t'^2}}$
r_0 = radius of pipe
$\overline{T}$ = time averaged temperature
$\overline{T}_c$ = centerline temperature
$\overline{T}_m$ = bulk temperature
$\overline{T}_w$ = wall temperature
$\overline{T}^+$ = dimensionless temperature = $(\overline{T}_w - \overline{T})/t_*$
t' = turbulent temperature fluctuation
t_* = friction temperature = $q_w/\rho c_p u_*$
$\overline{U}$ = time averaged streamwise velocity
$\overline{U}_c$ = centerline velocity
$\overline{U}_0$ = bulk velocity at beginning of heated section
$\overline{U}^+$ = dimensionless velocity = $\overline{U}/u_*$
u' = streamwise velocity fluctuation
u_* = friction velocity = $\sqrt{\tau_w/\rho}$
y = radial distance from wall
y^+ = dimensionless distance from wall = $u_* y/\nu$
ν = kinematic viscosity
ρ = density
τ = lag time
τ_w = shear stress at wall

Physical properties of fluid are evaluated at the film temperature $\overline{T}_f = (\overline{T}_w + \overline{T}_m)/2$.

(¯) time average.

number P_{rt} becomes

$$P_{rt} = (\partial \overline{T}^{+}/\partial y^{+})/(\partial \overline{U}^{+}/\partial y^{+}) = 0.87$$

The profile of $\overline{T}^{+}$ for the buffer layer and the viscous sublayer can be derived from the semi-empirical equation for the eddy diffusivity for heat, which we have developed earlier [8], as

$$\overline{T}^{+} = \int_0^{y^+} \frac{dy^+}{1/\mathrm{Pr} + \epsilon_h/\nu} \tag{4}$$

where

$$\frac{\epsilon_h}{\nu} = \frac{0.4}{0.87} y^+ \left[1 - \exp\left(-\frac{y^+}{16}\right)\right]^3$$

This semi-empirical result, given in Fig. 3, showed good agreement with the experimental result.

Pictorial Structure Survey. Fig. 4(*a–e*) show the typical oscillograms of temperature fluctuation t', velocity fluctuation u' and cross-correlation $u't'$ at the selected locations marked by $a - e$ in Fig. 3. In these figures, t' and u' increase upward. In the buffer layer adjacent to the viscous sublayer, as seen from Fig. 4(*a*), the laminar-like flow patterns occur irregularly with minimum fluctuations (marked with ↑), which are accompanied with a decrease of velocity, an increase of temperature and cross-correlation. There also occur large fluctuations having a strong correlation with an increase of velocity and a decrease of temperature, and hence the waveforms of the velocity and temperature fluctuations become skewed on the whole. Recently, accumulated visual investigations have revealed a certain cyclic process in the wall turbulent shear flows; an outward movement of the lower momentum fluid from the wall vicinity takes place, which serves to thicken the viscous sublayer, and terminates in a burst of chaotic turbulence followed by the onset of an inrush of the higher momentum fluid toward the wall, thus again thinning the viscous sublayer [9]. The velocity and temperature fluctuations closely correlated among themselves in Fig. 4(*a*) may be regarded as the features associated with this cyclic phenomenon. With increasing y^+, as in Fig. 4(*b*) of $y^+ = 11.54$, the laminar-like flow patterns occur more seldom. The fluid-motions become predominant under the strong cross-correlation accompanying the velocity increase and the simultaneous decrease of relevant temperature. Fig. 4(*c*) shows the record at $y^+ = 99.11$ in the fully turbulent part of the wall region, in which the background turbulence is superimposed on the gentle waves with a period of about 10–30 ms. Here, fluctuations with strong correlations are composed of the fluid-motions from not only the large amplitude velocity increase and temperature decrease but, at nearly the same frequency of occurrence, from the large amplitude velocity decrease and temperature increase; hence, the skewed waveforms almost disappear. Consequently, it is seen that the turbulent mixing processes in this region result from both the fluid moving outwards from the wall and the fluid moving towards the wall. The records in the turbulent core and at the center of the pipe are shown in Figs. 4(*d*) and 4(*e*), respectively, indicating a trend towards homogeneity of the velocity and temperature fluctuations with diminishing cross-correlations.

Typical waveforms of the velocity and temperature fluctuations at $y^+ = 7.56$ in the buffer layer were presented in Fig. 5 with the enlarged time scale. Both the velocity and temperature fluctuations are constructed of the random components of high frequencies with periods of less than 1 ms superimposed on the quasi-periodic events with an average period of about 3 ms. These quasi-periodic fluctuations of velocity and temperature are closely correlated with each other and, as described later, result in the well-marked characteristics of turbulence in the near-wall region.

Intensities of Velocity and Temperature Fluctuations. Intensities of velocity and temperature fluctuations relative to local mean velocity $\overline{U}$ and local mean temperature difference $(\overline{T}_w - \overline{T})$ were shown in Fig. 6. By the addition of heat flux, relative intensities of the velocity fluctuation increase throughout the pipe section. Both $\sqrt{\overline{u'^2}}/\overline{U}$ and $\sqrt{\overline{t'^2}}/(\overline{T}_w - \overline{T})$ are seen to increase as the wall is approached and decrease monotonously to the minimums at the pipe center. The $\sqrt{\overline{t'^2}}/(\overline{T}_w - \overline{T})$ values for $y/r_0 < 0.63$ ($y^+ < 570$) are lower than the corresponding $\sqrt{\overline{u'^2}}/\overline{U}$ values, and they are almost identical

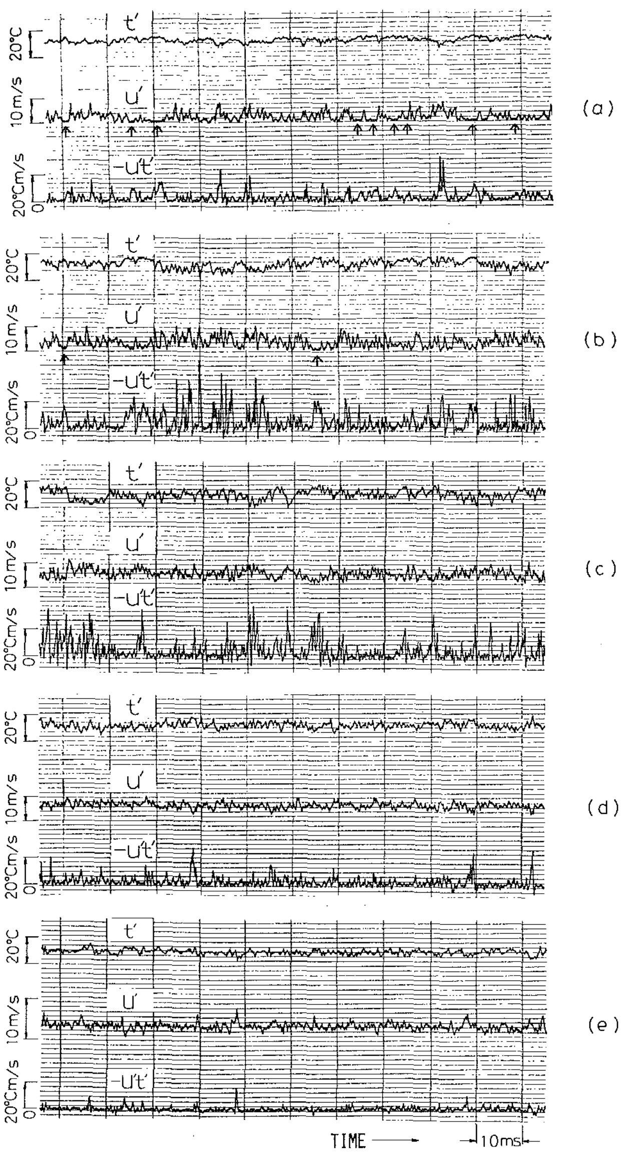

Fig. 4 Oscillograms of velocity and temperature fluctuations. (*a*) $y^+ = 7.56$ $\overline{U} = 7.49$ m/s $\overline{T}_w - \overline{T} = 13.38$°C, (*b*) $y^+ = 11.54$ $\overline{U} = 9.81$ m/s $\overline{T}_w - \overline{T} = 19.61$°C, (*c*) $y^+ = 99.11$ $\overline{U} = 13.41$ m/s $\overline{T}_w - \overline{T} = 38.02$°C, (*d*) $y^+ = 557.2$ $\overline{U} = 17.28$ m/s $\overline{T}_w - \overline{T} = 51.41$°C, (e) $y^+ = 909.1$ (pipe centerline) $\overline{U} = 18.17$ m/s $\overline{T}_w - \overline{T} = 53.08$°C

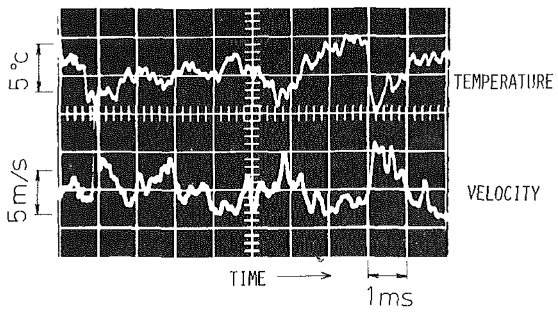

Fig. 5 Oscilloscope traces of u' and t' in near-wall region

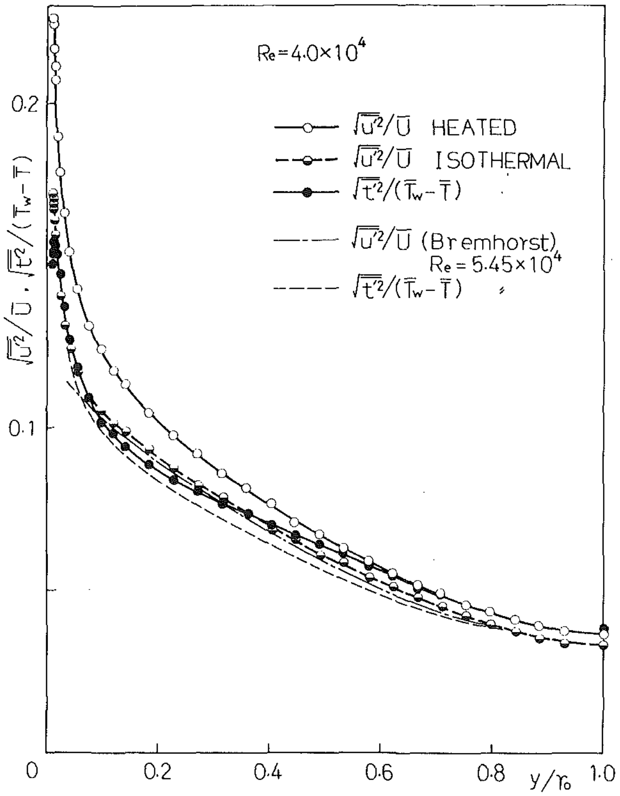

Fig. 6 Intensities of u' and t' relative to $\overline{U}$ and $\overline{T}_w - \overline{T}$

in the near-centerline region ($y/r_0 > 0.63$).

The distributions of intensities of velocity and temperature fluctuations normalized by the friction velocity u_* and friction temperature t_* are presented as a function of y/r_0 in Fig. 7. The effect of heat input on the $\sqrt{\overline{u'^2}}/u_*$ distribution is chiefly produced in the wall region, and in the core region $y/r_0 > 0.5$ ($y^+ > 450$) there is no longer a definite effect of added heat. In general the distribution curve for $\sqrt{\overline{t'^2}}/t_*$ is lower than the corresponding curve for $\sqrt{\overline{u'^2}}/u_*$, but these distributions resemble each other both qualitatively and quantitatively in the core region. The data of Bremhorst, et al. [2] differ from the present data for $\sqrt{\overline{u'^2}}/u_*$ in the region close to the wall and for $\sqrt{\overline{t'^2}}/t_*$ in the core region.

The distributions of $\sqrt{\overline{u'^2}}/u_*$ and $\sqrt{\overline{t'^2}}/t_*$ as a function of y^+ were shown in Fig. 8. These can be characterized according to the aforesaid flow regions: the buffer layer ($5 < y^+ < 30$), the turbulent part of the wall region ($30 < y^+ < 200$), and the turbulent core ($y^+ > 200$). For the last one, we further distinguish the near-centerline region specified by $y^+ > 570$ ($y/r_0 > 0.63$) from the rest. The non-dimensional intensities of both velocity and temperature fluctuations reach their maximums in the buffer layer and fall off sharply as the viscous sublayer is approached. The maximum of $\sqrt{\overline{u'^2}}/u_*$ occurs at $y^+ \simeq 19$ for the isothermal flow and at $y^+ \simeq 13$ for the heated flow, wherein the maximum value for the heated flow exceeds the corresponding isothermal value. The temperature fluctuation intensity $\sqrt{\overline{t'^2}}/t_*$ attains a maximum around the edge of the buffer layer (i.e., at $y^+ \simeq 27$), so that the position of maximum intensity does not coincide with that of turbulent velocity. In Fig. 8 the $\sqrt{\overline{u'^2}}/u_*$ values for the core region of the heated flow were plotted lower than the isothermal value, while they are identical in Fig. 7. This peculiarity stems from the temperature dependence of physical properties of fluid in evaluating y^+; i.e., for heated flow, the kinematic viscosity ν is higher than that for unheated flow, so y^+ ($= u_* y/\nu$) for heated flow becomes smaller even though the values of u_* and y are the same. In the turbulent part of the wall region, where both $\overline{U}^+$ and $\overline{T}^+$ obey the logarithmic law, the distributions of $\sqrt{\overline{u'^2}}/u_*$ and $\sqrt{\overline{t'^2}}/t_*$ are aptly described with the following logarithmic equations.

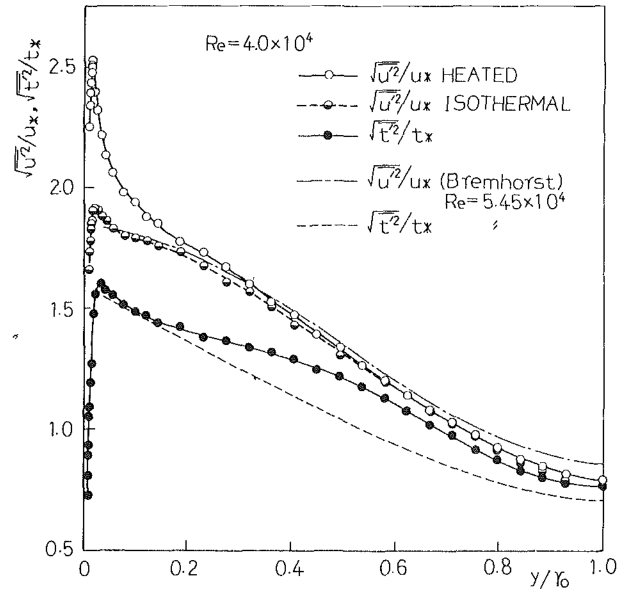

Fig. 7 Intensities of u' and t' relative to u_* and t^*

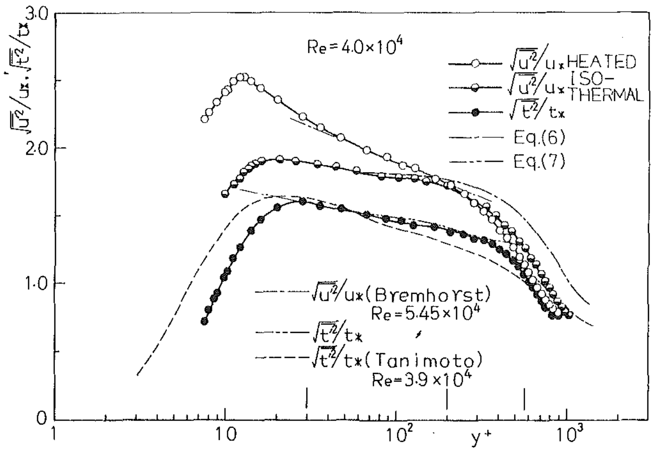

Fig. 8 Intensities of u' and t' in wall coordinates

$$\sqrt{\overline{u'^2}}/u_* = -0.277 \ln y^+ + 2.95 \tag{6}$$

$$\sqrt{\overline{t'^2}}/t_* = -0.110 \ln y^+ + 1.98 \tag{7}$$

In Fig. 8, as y^+ increases into the core region, the non-dimensional intensities of velocity and temperature fluctuations are seen to decrease rapidly, terminating in the steeper linear falling off in the near-centerline region. The results of Tanimoto, et al. [1] and Bremhorst, et al. [2] (the range of measurements: $y^+ > 52$) show substantially the same trends as the present data, but there exist noticeable differences in value. These differences might be due to the drawbacks of their measuring technique; i.e., they employed the conventional constant-current method which are bound to be erroneous due to nonlinearity of the hot-wire response and additional assumptions needed to find the sensitivities of fluctuations, as de-

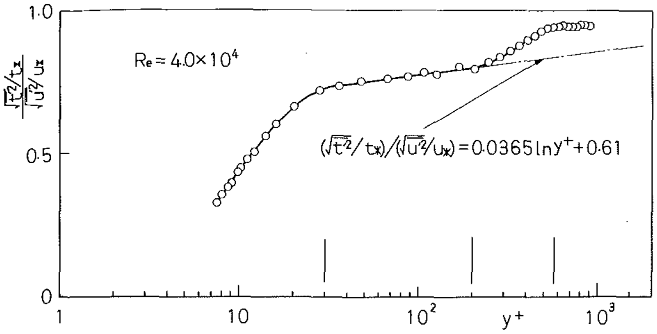

Fig. 9 Ratio of nondimensional intensity of temperature fluctuation to that of velocity fluctuation

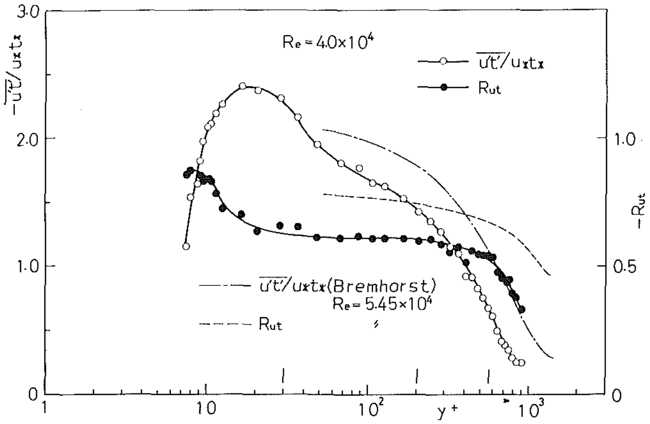

Fig. 10 Turbulent velocity-temperature correlation

scribed in the previous paper [5].

As seen from Fig. 9, the ratio of nondimensional intensities $(\sqrt{\overline{t'^2}}/t_*)/(\sqrt{\overline{u'^2}}/u_*)$ indicates the striking feature in each region. For the turbulent part of the wall region this ratio can be expressed as follows:

$$(\sqrt{\overline{t'^2}}/t_*)/(\sqrt{\overline{u'^2}}/u_*) = 0.0365 \ln y^+ + 0.61 \tag{8}$$

The peaks of nondimensional intensities of velocity and temperature fluctuations in the buffer layer disappear in their ratio, which smoothly decreases with decreasing y^+. In the near-centerline region this ratio attains a nearly constant value of 0.95.

Cross-Correlation Between Velocity and Temperature Fluctuations. The connections between velocity and temperature fluctuations are examined in the form of nondimensional correlation $\overline{u't'}/u_*t_*$ and cross-correlation coefficient $R_{ut} = \overline{u't'}/\sqrt{\overline{u'^2}}\sqrt{\overline{t'^2}}$. The nondimensional correlation yields $\overline{u't'}/u_*t_* = \rho c_p \overline{u't'}/q_w$ and hence indicates the ratio of the heat flux transported in the axial direction by turbulence to the total flux provided at the wall. Fig. 10 shows the distributions of $\overline{u't'}/u_*t_*$ and R_{ut} as a function of y^+. R_{ut} is seen to increase as the wall is approached, thus indicating the increase of highly correlated velocity and temperature fluctuations as noted in the pictorial survey. In the turbulent part of the wall region, the value of R_{ut} changes little with radial location, i.e., $R_{ut} \simeq -0.61$. As y^+ increases, R_{ut} first decreases gradually in the core region, then falls off sharply in the near-centerline region with the fluctuating velocity-temperature field approaching isotropy. This is also verified by the velocity and temperature spectra described later. It is seen that $\overline{u't'}/u_*t_*$ reaches a peak in the buffer layer, falls off rapidly as the wall is approached, and diminishes in value gradually toward the pipe center.

Velocity and Temperature Fluctuations Near the Wall. As already stated from Fig. 5, it is chiefly a rather definite sequence of ordered motions with an average period of about 3 ms that determines the velocity and temperature fluctuations in the buffer layer. In this section, the measured auto-correlation coefficients of velocity and temperature fluctuations, $R_u(\tau)$ and $R_t(\tau)$ respectively, are analyzed to grasp the essentials of velocity and temperature fluctuations very near the wall. The auto-correlation coefficients are defined as

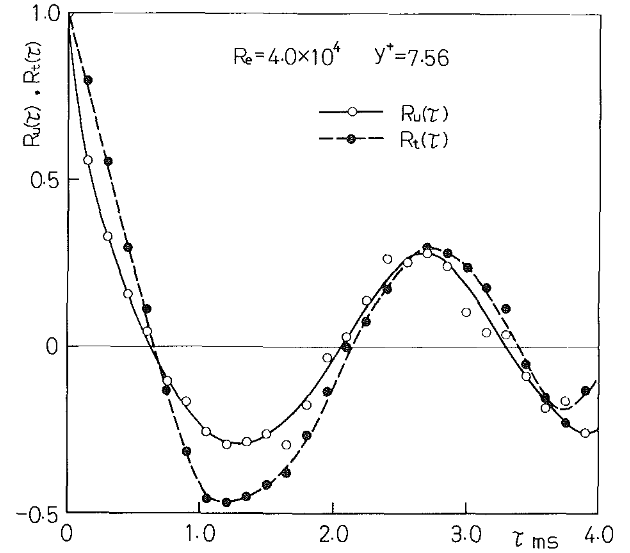

Fig. 11 Auto-correlation coefficients of velocity and temperature fluctuations in near-wall region

$$R_u(\tau) = \overline{u'(\tau')\,u'(\tau' + \tau)}/\overline{u'^2} \tag{9a}$$

$$R_t(\tau) = \overline{t'(\tau')\,t'(\tau' + \tau)}/\overline{t'^2} \tag{9b}$$

where τ is a time lag. Fig. 11 shows the sample curves of $R_u(\tau)$ and $R_t(\tau)$ calculated from the signals (shown in Fig. 5), which correspond to $y^+ = 7.56$. The sample length was chosen so as to enhance the quasi-periodic events hidden in the flow; in this case the sample length was 10 ms. The auto-correlation coefficients smoothly decrease with increasing τ, showing wavy behavior at higher lag times. This indicates incontestably that the velocity and temperature fluctuations consist of certain periodic regularities covered up with random components. In the near-wall region, the velocity and temperature fluctuations show striking resemblances among one another, and present almost the same periods of quasi-periodic events (about 2.7 ms in this example). It should be mentioned that we varied the sample lengths from 10 ms to 345 ms and found a degree of peaking in the auto-correlation coefficient curve depends on the lengths of velocity and temperature samples from which the coefficient is obtained; i.e., the peaking is less pronounced with an increase of sample length, which is exactly in accordance with the result of Kim, et al. [10, 11].

In order to investigate the contribution of these quasi-periodic events to the total powers of the fluctuations, the short-duration one-dimensional velocity and temperature spectra were calculated. The spectra were obtained by the Fourier cosine transform of the auto-correlation coefficients according to the Wiener-Khintchine's theorem. Fig. 12 shows the normalized one-dimensional spectra thus obtained from Fig. 11, where an appropriate spectral window was employed [12, 13]. Peaks in the short-time averaged spectra correspond to the waves of the auto-correlation coefficients, which is quite evident from the Wiener-Khintchine's theorem [14]. It is seen that the most energetic peaks in the spectra of both velocity and temperature occur at a frequency of approximately 370 Hz, which corresponds to the mean period of the aforementioned quasi-periodic events of 2.7 ms (= 1/370 s). This indicates that the turbulent heat transport process is dominated the most by the quasi-periodic ordered motions. Note that, because of the variation in the location of the peak in individual short-time averaged auto-correlation coefficients, the peak becomes considerably weak in the auto-correlation data obtained from a very long sample, which results in the smoothed out spectrum for a long sample. Consequently, the basic ordered patterns in the velocity and temperature fluctuations are masked in the long-duration spectra, as in fact shown in the next section.

The recent studies by Kline, et al. [10, 15] and Brodkey, et al. [16, 17] have revealed that the fairly organized cyclic motions in space and time, i.e., the bursting phenomenon, dominate the flow structure of the near-wall region in turbulent boundary layers. A survey of the highlights of the present knowledge of turbulent structure near the wall has been made by Willmarth [18]. When denoting the lag times by τ_B at which the auto-correlation coefficients $R_u(\tau)$, obtained in the previously described manner, reach the first re-rise maximums, and these ensemble average by $\overline{\tau}_B$, Kim, et al. [10, 11] have found that τ_B coincides approximately with the burst period, or the time between bursts. We regard thus obtained $\overline{\tau}_B$ as the mean burst period for the turbulent flow in a heated pipe and make a comparison with the mean burst periods $\overline{\tau}_B$ [10, 19] for the isothermal turbulent boundary layer flows along flat plates in Table 1. Here $R_\theta = \overline{U}_c\theta/\nu$ ($\overline{U}_c$ being the centerline velocity or free-stream velocity), is the momentum thickness Reynolds number and δ^* and θ denote the displacement and momentum thicknesses, respectively, which are defined for the pipe flow by:

$$\int_0^{r_0} (r_0 - y)(\rho_c\overline{U}_c - \rho\overline{U})\, dy = \int_0^{\delta^*} (r_0 - y)\rho_c\overline{U}_c\, dy$$

$$= \rho_c\overline{U}_c(r_0 - \delta^*/2)\delta^* \qquad (10)$$

$$\int_0^{r_0} (r_0 - y)\rho\overline{U}(\overline{U}_c - \overline{U})\, dy = \int_0^{\theta} (r_0 - y)\rho_c\overline{U}_c{}^2\, dy$$

$$= \rho_c\overline{U}_c{}^2(r_0 - \theta/2)\theta \qquad (11)$$

It is seen from Table 1 that, although the values of $\overline{\tau}_B$ differ by orders of magnitude with the condition of experiments, the suitably nondimensionalized periods $u_*{}^2\overline{\tau}_B/\nu$ and $\overline{U}_c\overline{\tau}_B/\delta^*$ are almost identical. The nondimensional period $u_*{}^2\overline{\tau}_B/\nu$ also agrees reasonably well with the relation evolved by Rao, et al. [20], $u_*{}^2\overline{\tau}_B/\nu = 0.65\, R_\theta{}^{0.73} = 107$. From these results it could be deduced that the quasi-periodic events of velocity and temperature in the near-wall region are the consequence of the dominant influence of the bursting phenomenon. Accordingly, judging from all the related aspects of waveforms of the velocity and temperature fluctuations, auto-correlation coefficients, and power spectra, the large amplitude velocity fluctuation closely associated with the bursting phenomenon is considered to provoke the similar large amplitude temperature fluctuation, thus governing the turbulent heat transport process in the near-wall region.

Velocity and Temperature Spectra. One-dimensional wavenumber spectra $E_u(k)$ of the velocity fluctuation, and $E_t(k)$ of the temperature fluctuation are defined so that

$$\overline{u'^2} = \int_0^\infty E_u(k)\, dk \quad \text{and} \quad \overline{t'^2} = \int_0^\infty E_t(k)\, dk$$

where k is the wavenumber, $k = 2\pi f/\overline{U}$. The normalized velocity and temperature spectra are presented in Fig. 13 and Fig. 14, respectively. In these figures, lines indicating the traditional -1, $-5/3$, and -7 power-law spectra are also included for comparison. For fluids with Prandtl numbers of less than 1, there exists, in a wavenumbers range above the inertial-convective subrange, the inertial-diffusive subrange in which molecular conduction plays an important role. The theoretical temperature spectra $E_t(k)$ for this subrange [21, 22] have been proposed in very different forms such as $E_t(k) \propto k^{-17/3}$ and $E_t(k) \propto k^{-3}$; thus, the preferable form is not yet definitively established.

The present turbulence parameters responsible for the spectrum are given in Table 2. The rate of turbulent energy dissipation ϵ and microscale λ are defined by the following, and the values in the table are semi-empirical estimates [23, 24]:

$$\epsilon = \nu\overline{(\partial u_j'/\partial x_i)(\partial u_j'/\partial x_i)} \qquad (12)$$

$$\lambda^2 = \overline{u'^2}/\overline{(\partial u'/\partial x)^2} \qquad (13)$$

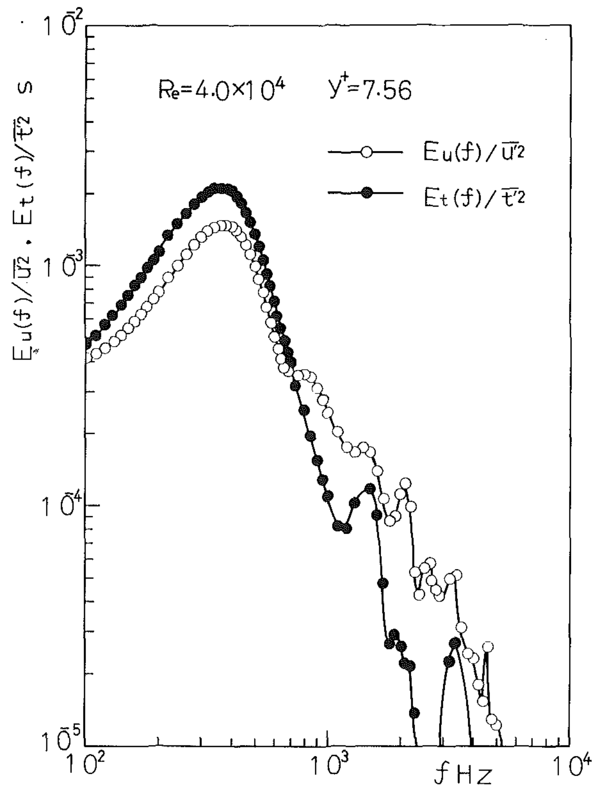

Fig. 12 Short-duration velocity and temperature spectra in near-wall region

Table 1 Comparison of mean burst period for pipe flow with those for turbulent boundary layers along flat plate

	$\overline{U}_c$ m/s	R_θ	$\overline{\tau}_B$ s	$u_*^2\overline{\tau}_B/\nu$	$\overline{U}_c\overline{\tau}_B/\delta^*$	Flow Type
Present	18.3	1080	0.0032	106	27.8	Pipe Flow (Air, Heated)
Kim et al.	0.152	1100	2.3	107	33.6	Boundary Layer (Water, Isothermal)
Ueda-Hinze	4.1	1244	0.0484	102	30.5	Boundary Layer (Air, Isothermal)

Table 2 Viscous and conductive cut-off

y/r_0	y^+	$\epsilon r_0/u_*^3$	Re_λ	k_s cm^{-1}	k_c cm^{-1}
0.0088	7.68	228	37.3	265	204
0.1095	96.03	22.8	95.4	165	127
1.0000	877.3	2.20	58.9	99	76

where x denotes the coordinate in the axial direction. The viscous cut-off occurs near $k_s = (\epsilon/\nu^3)^{1/4}$, termed the Kolmogoroff wavenumber, and the conduction cut-off [25] is proposed to be near $k_c = (\epsilon/a^3)^{1/4}$. The turbulent Reynolds number Reλ is defined so that Reλ $= \sqrt{\overline{u'^2}}\lambda/\nu$.

From Fig. 13, it is seen that the velocity spectra show the k^{-1} dependence in the low wavenumber range over most of the pipe section, and this wavenumber range broadens in the wall region where the mean velocity gradients become steeper. Although, as seen from Table 2, the estimated values of Reλ are not high enough for the requirements of Kolmogoroff's theory to be satisfied [26], the experimental result does indicate the existence of a reasonable range of wavenumbers where $E_u(k) \propto k^{-5/3}$ holds. The $-5/3$ power-law spectra are more evident in the core region $y^+ > 200$, thus indicating a trend toward local isotropy. The viscous effect becomes significant at $k \simeq$

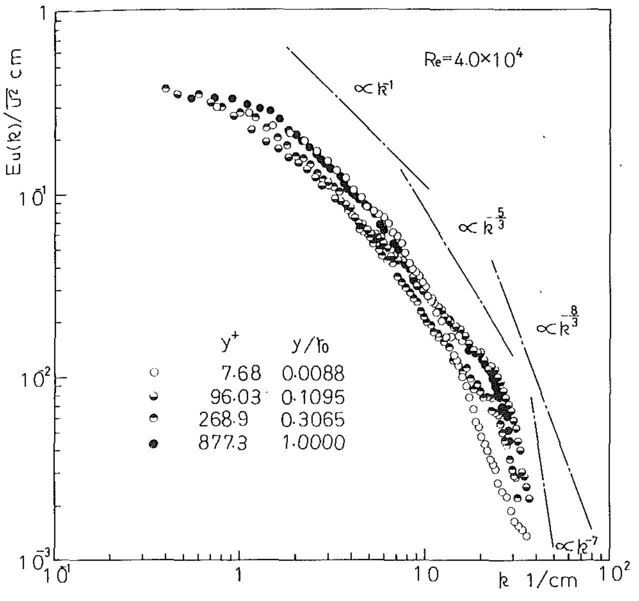

Fig. 13 Velocity fluctuation spectra

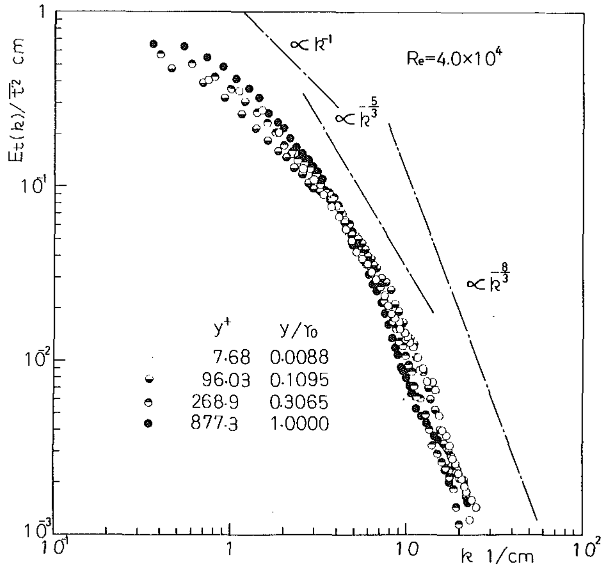

Fig. 14 Temperature fluctuation spectra

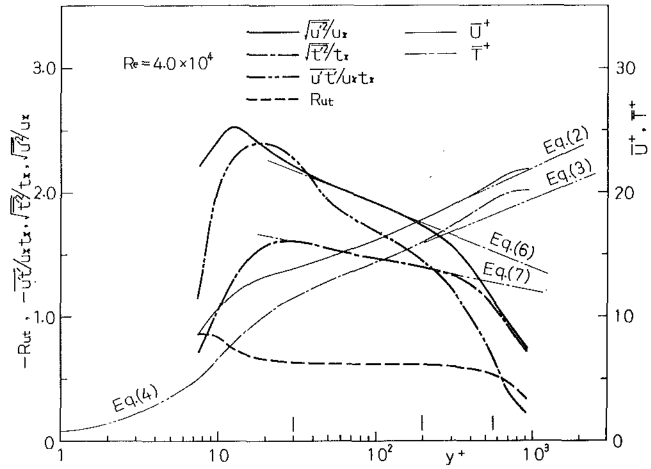

Fig. 15 Distributions of velocity, temperature, and relevant turbulent quantities

$0.1k_s$, and at higher wavenumbers the spectrum is seen to approach the k^{-7} dependence.

The temperature spectra, as shown in Fig. 14, exhibit a region with slope −1 at still lower wavenumbers than with the velocity spectra. The normalized temperature spectra are seen to be higher than the corresponding velocity spectra at low wavenumbers, and vice versa at high wavenumbers. This means that the temperature fluctuations are dominated by the even larger-scale turbulence with low wavenumbers than the velocity fluctuations. And this result has also been confirmed by the measured auto-correlations of velocity and temperature fluctuations, as given in Fig. 11, which indicate that the temperature fluctuations maintain their identity for longer time delays. There exist the −5/3 power-law spectra for the temperature fluctuations in the turbulent core, but the region of wavenumbers concerned is smaller than that for the velocity spectra. The drop from the −5/3 power-law occurs approximately at $k \simeq 0.1k_c$, beyond which the molecular conductive effect becomes important.

The measured temperature spectra in the region just above the inertial-convective subrange (the upper limit of wavenumber range being near $0.1k_c$) can be aptly expressed as follows:

$$E_t(k) \propto k^{-8/3} \tag{14}$$

Since the present result, as is evident from Fig. 14, contains the spectra for the inertial-convective subrange and equation (14) is valid only within the inertial subrange (i.e., $0.1k_c < k < 0.1k_s$), it seems to be quite legitimate to regard equation (14) as the experimental power-law form for the temperature spectrum in the inertial-diffusive subrange. Note that, however, the spectra at high wavenumbers would be attenuated somewhat by the effect of finite sensor length.

Relations of Velocity and Temperature Distributions to Fluctuating Quantities. Velocity and temperature distributions together with the intensities of fluctuating quantities were presented in Fig. 15 for ready comparison. The turbulent axial heat flux as well as the intensities of velocity and temperature fluctuations reach their maximums in the buffer layer, notwithstanding the still remaining viscous and conductive effects. The cross-correlation coefficient tends to approach −1 as the wall is approached. In the turbulent part of the wall region, where $\overline{U}^+$ and $\overline{T}^+$ exhibit logarithmic distributions, the cross-correlation coefficient attains a nearly constant value, so that the relations between velocity and temperature fluctuations are structurally similar. In the turbulent core region, where the distributions of $\overline{U}^+$ and $\overline{T}^+$ deviate from the logarithmic law, the intensities of velocity and temperature fluctuations decrease rapidly with the gradual diminution of the cross-correlation coefficient. In the near-centerline region, the intensities of velocity and temperature fluctuations fall off sharply with the constant mutual ratio (see also Fig. 9). The correlations in this region become less close, thereby indicating a trend towards isotropy.

Finally, to develop a picture of the turbulent heat transfer process, we should mention the necessity of measurements of radial velocity fluctuation v' and radial turbulent velocity-temperature correlation $v't'$. Such measurements were usually carried out by the X-wire anemometry technique [2, 3]. However, when employed in a turbulent flow near the wall, this technique is subject to serious errors due to wire-length effect and aerodynamic disturbances caused by the wire supports. So in order to obtain a knowledge of v' and $v't'$ behaviors in close proximity to the wall, we first of all have to develop a novel technique for measurements. We have been studying this measuring technique, and the results obtained are to be reported in the near future.

Conclusions

From the measurements of intensities, auto-correlations, cross-correlations, and spectra of velocity and temperature fluctuations as well as velocity and temperature distributions in turbulent pipe flow of air with uniform wall temperature, the following conclusions are established:

1 Structural features of velocity and temperature fluctuations such as waveforms, intensities, and cross-correlations make substantial differences among distinct regions of the viscous sublayer and the buffer layer, the turbulent part of the wall region, the turbulent core, and the near-centerline region.

2 In the buffer layer, the large amplitude velocity fluctuation closely associated with the bursting phenomenon provokes a similar large amplitude temperature fluctuation. The short-duration velocity and temperature spectra reach their peaks at a frequency corresponding to the mean burst period, which indicates that the bursting phenomena have a dominant influence on the turbulent heat transport process. The non-dimensional burst periods agree well with those for the isothermal turbulent boundary layer flows along flat plates.

3 With heat input, the turbulent velocity intensities increase throughout the pipe section. The intensities of both velocity and temperature fluctuations reach their maximums in the buffer layer, but the positions do not coincide with each other. The cross-correlation coefficient between velocity and temperature fluctuations increases as the wall is approached.

4 In the turbulent part of the wall region, the logarithmic law may apply to the distributions of the non-dimensional intensities of velocity and temperature fluctuations. The closely correlated velocity and temperature fluctuations in this region are composed of not only the large amplitude velocity increase and temperature decrease but, with almost the same frequency of occurrence, the large amplitude velocity decrease and temperature increase. The velocity-temperature cross-correlation coefficient keeps a constant value of -0.61.

5 In the core region, as the distance from the wall increases, the intensities of velocity and temperature fluctuations decrease with the gradual diminution of the cross-correlation coefficient. These trends become more pronounced in the near-centerline region, indicating that the turbulent velocity and temperature fields approach isotropy. In the near-centerline region, the ratio of nondimensional intensities between velocity and temperature fluctuations is held constant.

6 Both the velocity and temperature spectra indicate the existence of the -1 power-law spectrum in the wall region and the $-5/3$ power-law spectrum in the core region. The temperature spectra in the inertial-diffusive subrange vary as the $-8/3$ power of the wavenumber.

7 The normalized temperature spectra become higher than the velocity spectra at low wavenumbers, and vice versa at high wavenumbers.

References

1 Tanimoto, S., and Hanratty, T. J., "Fluid Temperature Fluctuations Accompanying Turbulent Heat Transfer in a Pipe," *Chemical Engineering Science*, Vol. 18, 1963, pp. 307–311.

2 Bremhorst, K., and Bullock, K. J., "Spectral Measurements of Temperature and Longitudinal Velocity Fluctuations in Fully Developed Pipe Flow," *International Journal of Heat and Mass Transfer*, Vol. 13, 1970, pp. 1313–1329.

3 Bremhorst, K., and Bullock, K. J., "Spectral Measurements of Turbulent Heat and Momentum Transfer in Fully Developed Pipe Flow," *International Journal of Heat and Mass Transfer*, Vol. 16, 1973, pp. 2141–2154.

4 Carr, A. D., Connor, M. A., and Buhr, H. O., "Velocity, Temperature, and Turbulence Measurements in Air for Pipe Flow With Combined Free and Forced Convection," ASME JOURNAL OF HEAT TRANSFER, Vol. 95, 1973, pp. 445–452.

5 Hishida, M., and Nagano, Y., "Simultaneous Measurements of Velocity and Temperature in Nonisothermal Flows," ASME JOURNAL OF HEAT TRANSFER, Vol. 100, 1978, pp. 340–345.

6 Hishida, M., "Turbulent Heat Transfer and Temperature Distribution in the Thermal Entrance Region of a Circular Pipe," *Bulletin of the JSME*, Vol. 10, No. 37, 1967, pp. 113–123.

7 Hishida, M., and Nagano, Y., "Structure of Turbulent Temperature and Velocity Fluctuations in the Thermal Entrance Region of a Pipe," *Proceedings of the Sixth International Heat Transfer Conference*, Canada, FC(a)-8, 1978, pp. 531–536.

8 Hishida, M., Nagano, Y., and Nakamura, Y., "Temperature Distribution in the Turbulent Boundary Layer in a Circular Pipe," *Bulletin of the JSME*, Vol. 21, No. 157, 1978, pp. 1175–1184.

9 Hinze, J. O., *Turbulence*, Second ed., McGraw-Hill, 1975, pp. 656–684.

10 Kim, H. T., Kline, S. J., and Reynolds, W. C., "The Production of Turbulence Near a Smooth Wall in a Turbulent Boundary Layer," *Journal of Fluid Mechanics*, Vol. 50, 1971, pp. 133–160.

11 Kim, H. T., "An Experimental Study of Turbulence Production Near a Smooth Wall in a Turbulent Boundary Layer With Zero Pressure-Gradient," PhD thesis, Stanford University, 1968.

12 Bendat, J. S., and Piersol, A. G., *Random Data—Analysis and Measurement Procedure*, John Wiley & Sons, 1971.

13 Schraub, F. A., and Kline, S. J., "A Study of the Structure of the Turbulent Boundary Layer With and Without Longitudinal Pressure Gradients," Mechanical Engineering Department Report MD-12, 1965, Stanford University.

14 Zaric, Z., "Wall Turbulence Studies," in *Advances in Heat Transfer*, Vol. 8, Academic Press, 1972, pp. 285–350.

15 Kline, S. J., et al., "The Structure of Turbulent Boundary Layers," *Journal of Fluid Mechanics*, Vol. 30, 1967, pp. 741–773.

16 Corino, E. R., and Brodkey, R. S., "A Visual Investigation of the Wall Region in Turbulent Flow," *Journal of Fluid Mechanics*, Vol. 37, 1969, pp. 1–30.

17 Nychas, S. G., Hershey, H. C., and Brodkey, R. S., "A Visual Study of Turbulent Shear Flow," *Journal of Fluid Mechanics*, Vol. 61, 1973, pp. 513–540.

18 Willmarth, W. W., and Bogar, T. J., "Survey and New Measurements of Turbulent Structure Near the Wall," *The Physics of Fluids*, Vol. 20, No. 10, Pt. 2, 1977, pp. S9-S21.

19 Ueda, H., and Hinze, J. O., "Fine-Structure Turbulence in the Wall Region of a Turbulent Boundary Layer," *Journal of Fluid Mechanics*, Vol. 67, 1975, pp. 125–143.

20 Rao, K. N., Narasimha, R., and Badri Narayanan, M. A., "The 'Bursting' Phenomenon in a Turbulent Boundary Layer," *Journal of Fluid Mechanics*, Vol. 48, 1971, pp. 339–352.

21 Batchelor, G. K., Howells, I. D., and Townsend, A. A., "Small-Scale Variation of Convected Quantities like Temperature in Turbulent Fluid, Part 2 The Case of Large Conductivity," *Journal of Fluid Mechanics*, Vol. 5, 1959, pp. 134–139.

22 Gibson, C. H., "Fine Structure of Scalar Fields Mixed by Turbulence, II. Spectral Theory," *The Physics of Fluids*, Vol. 11, No. 11, 1968, pp. 2316–2327.

23 Laufer, J., "The Structure of Turbulence in Fully Developed Pipe Flow," NACA Report 1174, 1954.

24 Brodkey, R. S. (ed.), *Turbulence in Mixing Operations*, Academic Press, 1975, pp. 47–119.

25 Batchelor, G. K., "Small-Scale Variation of Convected Quantities like Temperature in Turbulent Fluid, Part 1 General Discussion and the Case of Small Conductivity," *Journal of Fluid Mechanics*, Vol. 5, 1959, pp. 113–133.

26 Lawn, C. J., "The Determination of the Rate of Dissipation in Turbulent Pipe Flow," *Journal of Fluid Mechanics*, Vol. 48, 1971, pp. 477–505.

E. M. Sparrow
R. G. Kemink

Department of Mechanical Engineering
University of Minnesota,
Minneapolis, Minn. 55455

Heat Transfer Downstream of a Fluid Withdrawal Branch in a Tube

Experiments have been performed to study how fluid withdrawal at a branch point in a tube affects the turbulent heat transfer characteristics of the main line flow downstream of the branch. Air was the working fluid. The experiments were carried out for several fixed test section Reynolds numbers and at each Reynolds number the ratio of the withdrawn flow to the test section flow (hereafter designated as the flow split number) was varied systematically. Local heat transfer coefficients were determined both around circumference and along the length of the tube, and circumferential average coefficients were also evaluated. The circumferential average Nusselt numbers in the thermal entrance region are much higher than those for a conventional turbulent pipe flow having the same Reynolds number, and the differences are accentuated at higher values of the flow split number. When normalized by the corresponding fully developed value, the axial distribution of the circumferential average Nusselt number is relatively insensitive to the Reynolds number for a fixed flow split. The thermal entrance lengths, based on a five percent approach to fully developed conditions, are in the 20 to 30 diameter range, which is substantially greater than that for conventional turbulent air flows. Circumferential variations on the order of ±20 percent are induced by the fluid withdrawal process. For the most part, these variations are dissipated upstream of x/D = 10.

Introduction

Fluid withdrawal at a branch point in a tube is a common occurrence in pipeline flows as diverse as the human circulatory system and residential hot water plumbing. Typically, the branch line is oriented at right angles to the main line, but various other arrangements are also employed in practice. Even if the flow upstream of the branch is fully developed (i.e., characterized by a unidirectional axially unchanging velocity distribution), the main-line flow downstream of the branch will be highly three-dimensional. It may be expected that the heat transfer characteristics of such a disturbed, three-dimensional flow will differ markedly from those of conventional pipe flows.

Notwithstanding the frequency with which fluid withdrawal at pipeline branch points is encountered in practical applications, it appears that the heat transfer characteristics of such flows have yet to be investigated. In the present research, experiments are performed to study the heat transfer in the main-line flow downstream of a point of fluid withdrawal. In the experiments, air is delivered to a branch point via a long, insulated hydrodynamic development tube. The air enters one of the side ports of a tee, and a portion is withdrawn at the center port. The remainder exits via the other side port and passes into an electrically heated test section tube. The inflow-outflow arrangement at the tee is shown schematically in the inset of Fig. 1.

The test section was heavily instrumented so as to enable the determination of local heat transfer coefficients both around the circumference and along the length of the tube. The experiments were planned and conducted so that the effects of the fluid withdrawal on the heat transfer coefficients could be readily identified. Specifically, for a fixed test section Reynolds number, the flow through the withdrawal branch was systematically varied from zero up to the limit allowed by the apparatus. Thus, the results are parameterized by both the test section Reynolds number Re and the flow split number S defined as the ratio of the withdrawn mass flow rate to the test section mass flow rate.

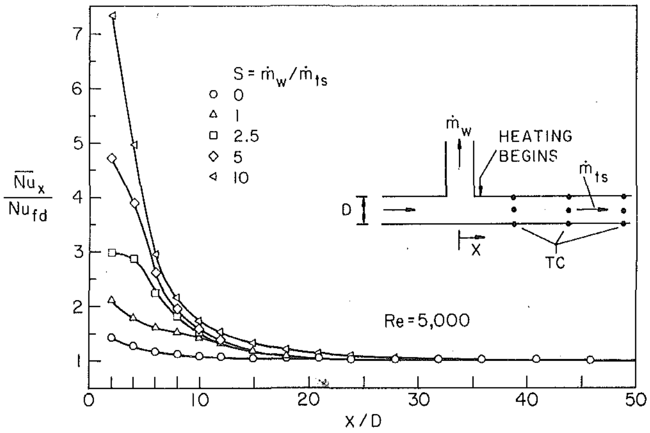

Fig. 1 Circumferential average Nusselt numbers for Re = 5,000 and for parametric values of the flow split number *S*

Contributed by the Heat Transfer Division for publication in the JOURNAL OF HEAT TRANSFER. Manuscript received by the Heat Transfer Division February 17, 1978.

The test section operating conditions spanned the range from low Reynolds number turbulent flow to intermediate Reynolds number turbulent flow, Re = 5,000 to 20,000. The flow split number ranged from zero to as high as ten. Results are presented both for the circumferential variation of the Nusselt number at successive axial stations and for the axial distribution of the circumferential average Nusselt number. Inasmuch as the latter results are of more immediate relevance to design, they are examined both from the standpoint of their dependence on the flow split number for a fixed Reynolds number and vice-versa. Thermal entrance lengths, deduced from the axial distributions, are also reported.

As was noted earlier, it appears that there is no literature information on heat transfer downstream of a withdrawal branch point in a tube. The literature on conventional uniformly heated turbulent pipe flows will be employed later for comparisons with the present results.

The Experiments

Apparatus. The experiments were performed in an open-circuit airflow system, with a steady, regulated supply of air being provided by a dryer-equipped central compressor. The air was ducted to the inlet of a heavily insulated, 100-diameters-long horizontal tube which served as a hydrodynamic development section. The downstream end of this tube mated with one of the side ports of a tee. The test section tube emanated from the other side port of the tee. It, too, was horizontal and had a length equal to 100 diameters. Both the hydrodynamic development and test section tubes were painstakingly straightened by a technique used for straightening firearm barrels and then carefully aligned so that they shared a common centerline.

As noted earlier and illustrated schematically in the inset of Fig. 1, the flow delivered to the tee by the hydrodynamic development tube was, in part, withdrawn at the center port, with the remainder passing into the test section. The center port was oriented vertically and mated with a 90-diameters-long withdrawal tube. The latter was also carefully straightened and then positioned so as to be perpendicular to the horizontal centerline of the development and test section tubes.

The heated air exiting the test section was ducted through a rotameter and then exhausted outside the laboratory. Similarly, the air from the withdrawal tube was metered by a rotameter and conveyed out of the laboratory.

The development section, test section, and withdrawal tubes were all cut from a single piece of type 304 stainless steel tubing. The bore of each tube was honed to a satin smooth finish, with a resulting inside diameter of 2.37 cm (0.933 in.). To determine the wall thickness, short axial lengths were cut from the ends of the respective tubes. With the aid of both micrometer and optical comparator measurements, it was found that there was a small, but regular variation of the wall thickness, and this was taken into account in the data reduction. The mean wall thickness was 0.0894 cm (0.0352 in.).

The tee was made of chlorinated polyvinyl chloride (cpvc), which was chosen in preference to a metal in order to minimize extraneous heat conduction from the test section. To the same end, the wall thickness of the tee was reduced to the minimum consistent with structural integrity. The tee was finish-bored to the internal diameters of the stainless steel tubes and was mated to them by lap joints, with care being taken to obtain a continuous surface at the joint. In addition, the axial length of the tee was shortened to minimize redevelopment of the flow between the center port of the tee and the onset of heating in the test section. The axial distance from the center of the tee to the start of heating was 0.76 bore diameters (Fig. 1, inset).

Fittings were attached to the respective ends of the test section tube to carry a-c electric current for the ohmic heating of the tube wall. In the design of these fittings, account was taken of the need to minimize heat conduction which might affect the temperature of the wall. In particular, had a copper or aluminum ring been affixed to each end of the tube to convey the current, conduction in the ring would have diminished otherwise existing circumferential temperature variations. In view of this, discontinuous copper rings, each consisting of twelve separate segments, were used instead of continuous rings.

Electric current was carried to (or from) each ring segment via a 0.32 cm ($1/8$ in.) diameter copper rod. The assemblage of the twelve rods at each end of the tube resembled the spokes of a wheel, especially since their outer ends terminated in a large circular copper rim to which the electrical cables were connected. With a view to preventing heat loss along the spokes from the tube to the surroundings, each of the spokes was fitted with a guard heater and a differential thermocouple. The entire spokes/rim assembly at the upstream end of the test section was embedded in silica aerogel powder, which has a thermal conductivity lower than that of air. Since the downstream spokes/rim assembly is ten diameters away from the nearest measurement station, it was sufficient to embed it in an insulation sandwich consisting of fiberglass and silica aerogel.

The development and test sections were insulated with a 20 cm (8 in.) square core of silica aerogel surrounded by a 5.08 cm (2 in.) thick casing of fiberglass. In the neighborhood of the tee and extending 30 diameters upstream and downstream of it, the aerogel was used exclusively. The downstream portions of the withdrawal pipe were insulated with fiberglass. As a further precaution against heat losses, all test section supports were plastic with knife-edge contacts.

The circumferential and axial temperature distributions on the outside surface of the test section tube were measured with a total of 139 calibrated 36-gage iron-constantan thermocouples. At each of seventeen axial stations between $x/D = 2$ and 60, eight thermocouples were deployed at 45 deg intervals around the circumference. Single thermocouples were situated at x/D = 70, 80, and 90. The junction of each thermocouple was affixed to the tube surface with copper oxide cement, which is both a good heat conductor and excellent electrical insulator.

The axial coordinates of the thermocouples were measured with respect to the center of the tee, where x was set equal to zero. In terms of this coordinate, heating was initiated at $x/D = 0.76$, so that the first set of thermocouples, i.e., at $x/D = 2$, was situated 1.24 diameters downstream of the start of heating. This arrangement is illustrated in the inset of Fig. 1. The angular positions of the thermocouples were characterized by the angle θ, with $\theta = 0$ deg at the top of the tube and $\theta = 180$ deg at the bottom.

Nomenclature

c_p = specific heat of air
D = diameter of tube bore
$\bar{h}_x$ = circumferential average heat transfer coefficient, equation (1)
$h_x(\theta)$ = local heat transfer coefficient, equation (5)
k = thermal conductivity of air
$\dot{m}_{ts}$ = test section mass flow rate
$\dot{m}_w$ = rate of mass withdrawal
Nu_{fd} = fully developed Nusselt number
$\overline{\mathrm{Nu}}_x$ = circumferential average Nusselt number at x, $\bar{h}_x D/k$
$\mathrm{Nu}_x(\theta)$ = local Nusselt number, $h_x(\theta)D/k$
$\bar{q}_x$ = circumferential average heat flux
$q_x(\theta)$ = local heat flux
Re = Reynolds number, $4\dot{m}_{ts}/\mu\pi D$
S = flow split number, $\dot{m}_w/\dot{m}_{ts}$
T_{bx} = local bulk temperature
$\overline{T}_{wx}$ = circumferential average wall temperature
$T_{wx}(\theta)$ = local wall temperature
T_∞ = temperature of surroundings
t = local wall thickness
x = axial coordinate, see inset of Fig. 1
θ = angular coordinate
μ = viscosity of air

Subscript

e = length of thermal entrance region

Measurements were also made of the inlet and outlet bulk fluid temperatures. The inlet bulk was read with the aid of a three-element thermocouple rake situated just upstream of the hydrodynamic development tube. For the outlet bulk, four thermocouples were positioned in a well-insulated multi-baffle mixing box situated just downstream of the test section tube. The rates of air flow through the test section and through the withdrawal tube were respectively measured with calibrated rotameters.

Data reduction. Two types of heat transfer coefficients were evaluated from the measured temperatures, flow rates, and power inputs. The first of these is the circumferential average coefficient $\bar{h}_x$ correspondng to a given axial station x. In general $\bar{h}_x$ varies along the length of the tube and ultimately attains a fully developed value at sufficiently large downstream distances. The second quantity is the local coefficient $h_x(\theta)$ which is specific to an angular position θ as well as to an axial station x.

Attention will first be focused on the circumferential average coefficient, which was evaluated from the definition

$$\bar{h}_x = \frac{\bar{q}_x}{\bar{T}_{wx} - T_{bx}} \tag{1}$$

where $\bar{T}_{wx}$ and $\bar{q}_x$ are, respectively, the circumferential average wall temperature and heat flux at the tube bore while T_{bx} is the bulk temperature, all at axial station x. The temperature $\bar{T}_{wx}$ was obtained by averaging the outside wall temperatures at the eight circumferential measurement points and then correcting for radial conduction in the tube wall (typically about 0.01°C (0.02°F)).

The average heat flux $\bar{q}_x$ was calculated by subtracting the heat losses $\bar{q}_{\ell x}$ from the ohmic dissipation, that is

$$\bar{q}_x = P/\pi DL - \bar{q}_{\ell x} \tag{2}$$

in which P is the power input, L and D are, respectively, the tube length and bore diameter, and both $\bar{q}_x$ and $\bar{q}_{\ell x}$ are per unit surface area at the bore. With regard to the heat losses, the net axial conduction was found by computation to be negligible. The loss from the outside of the tube to the surroundings (temperature = T_∞) was evaluated taking account of the series resistances of the insulation and the external natural convection, with $(\bar{T}_{wx} - T_\infty)$ as the thermal potential. Typically, along the length of the tube (inlet to exit), $\bar{q}_{\ell x}$ ranged from one to three percent of the power input for Re = 20,000 and from three to ten percent for Re = 5,000. Once $\bar{q}_x$ had been determined at the successive axial measurement stations, the local bulk temperature T_{bx} was obtained via the energy balance

$$T_{bx} = T_{b0} + (\pi D/\dot{m}_{ts}c_p)\int_0^x \bar{q}_x dx \tag{3}$$

in which T_{b0} is the inlet bulk temperature and $\dot{m}_{ts}$ is the mass flow rate through the test section.

The $\bar{h}_x$ values will be reported in terms of the circumferential average Nusselt number $\overline{\mathrm{Nu}}_x$ defined as

$$\overline{\mathrm{Nu}}_x = \bar{h}_x D/k \tag{4}$$

where k is thermal conductivity of air at T_{bx}.

For the local coefficient $h_x(\theta)$, the defining equation

$$h_x(\theta) = \frac{q_x(\theta)}{T_{wx}(\theta) - T_{bx}} \tag{5}$$

was employed. The basic task to be performed in evaluating this equation is to find the local heat flux $q_x(\theta)$. To this end, an energy balance was made on an element at x,θ that spans the thickness of the tube wall and has dimensions dx, $d\theta$ in the axial and angular directions. The selection of such a wall-spanning element reflects the fact that radial temperature variations in the wall are too small to have a material influence on the energy balance. Axial conduction is also negligible.

The energy balance yields

$$q_x(\theta) = (P'''tr_m)/r_i + \frac{k_w}{r_i}\frac{d}{d\theta}\left[\frac{t}{r_m}\frac{dT_{wx}}{d\theta}\right] - q_{\ell x}(\theta) \tag{6}$$

where P'' is the power input per unit volume, $t = t(\theta)$ is the local wall thickness, $r_i = D/2$ is the bore radius, and the mean radius $r_m = r_i + \frac{1}{2}t$. The thermal conductivity of the stainless steel wall is denoted by k_w. The loss $q_{\ell x}(\theta)$ from the outside of the tube to the surroundings was evaluated in a manner similar to $\bar{q}_{\ell x}$ in equation (2), but with $(T_{wx}(\theta) - T_\infty)$ as the thermal potential.

The circumferential conduction term appearing in equation (6) involves first and second derivatives of the circumferential temperature distribution. To facilitate the numerical evaluation of these derivatives, a curve fit of the measured temperatures at the eight circumferential measurement points was performed, with a cosine

$$T_{wx}(\theta) = \bar{T}_{wx} + a_1 \cos\theta \tag{7}$$

giving the truest representation of the data, where

$$a_1 = (\tfrac{1}{4})\sum_{j=1}^{8} T_{wx}(\theta_j)\cos\theta_j \tag{8}$$

in which $\theta_j = (j-1)\pi/4$. Also needed for the evaluation of equation (6) is the thickness distribution $t = t(\theta)$, which was obtained from measurement as $t = 0.0894 - 0.00559\cos\theta$, where t is in cm.

With $q_x(\theta)$ from equation (6), T_{bx} from equation (3), and $T_{wx}(\theta)$ from measurement, all the ingredients necessary to determine $h_x(\theta)$ are available. The results will be reported in terms of the circumferential local Nusselt number $\mathrm{Nu}_x(\theta)$

$$\mathrm{Nu}_x(\theta) = h_x(\theta)D/k \tag{9}$$

where, again, k corresponds to T_{bx}.

The results will be characterized by two parameters, one of which is the test section Reynolds number Re

$$\mathrm{Re} = 4\dot{m}_{ts}/\mu\pi D \tag{10}$$

with μ evaluated at the mean bulk temperature. As noted earlier, $\dot{m}_{ts}$ denotes the flow rate through the test section. The other parameter is the flow split number S, which is the ratio of the withdrawn mass flow $\dot{m}_w$ to the test section mass flow

$$S = \dot{m}_w/\dot{m}_{ts} \tag{11}$$

The Prandtl number is approximately 0.7 (air). In general, variable properties were not an important factor since the overall bulk temperature rise was about 11°C (20°F) and the wall-to-bulk temperature difference in the developed regime was about 7°C (12°F).

Results and Discussion

In the presentation of the results, the circumferential average heat transfer coefficients and their axial distribution will be dealt with first because of their more immediate relevance to practice. Thermal entrance lengths deduced from these distributions are then reported. Finally, circumferential variations of the heat transfer coefficient that are induced by the fluid withdrawal are illustrated for representative cases.

Circumferential Average Heat Transfer Coefficients. Two different approaches are used in the presentation of the circumferential average heat transfer coefficients. In the first, attention is focused on a specific test section Reynolds number, and the flow split number is varied parametrically from zero to the maximum value consistent with the capacity of the rotameter in the withdrawal line. The second approach focuses on a specific flow split and the Reynolds number is varied parametrically.

The heat transfer results for the various specific Reynolds number are presented in Figs. 1 and 2. In each figure, the ratio of the circumferential average Nusselt number $\overline{\mathrm{Nu}}_x$ to the corresponding fully developed value Nu_{fd} is plotted as a function of the dimensionless axial coordinate x/D. As noted earlier, the origin of the x coordinate is at the center of the tee and the start of heating is at $x/D = 0.76$. Each figure contains results corresponding to several values of the flow split number. Curves have been faired through the data to provide continuity.

Fig. 1 pertains to Re = 5,000 while Fig. 2 contains a pair of graphs, respectively for Re = 10,000 and 20,000. Some exploratory data runs

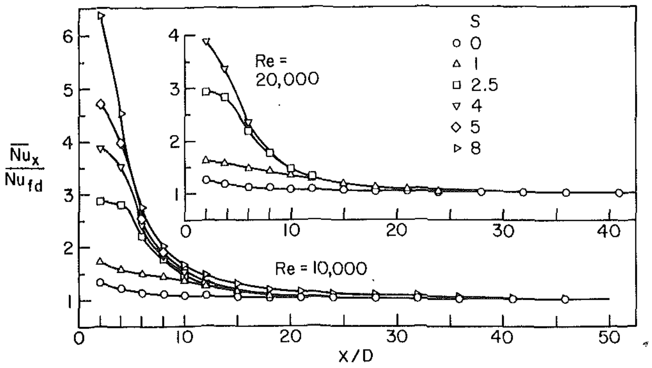

Fig. 2 Circumferential average Nusselt numbers for Re = 10,000 and 20,000 and for parametric values of the flow split number S.

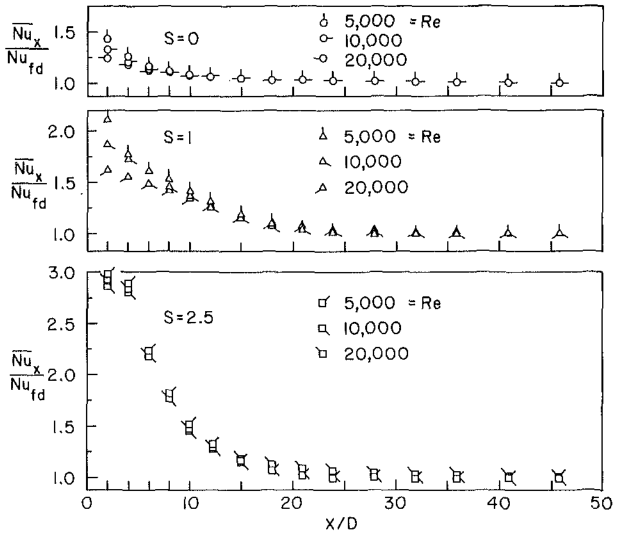

Fig. 3 Circumferential average Nusselt numbers for S = 0, 1, and 2.5 and for parametric values of the Reynolds number

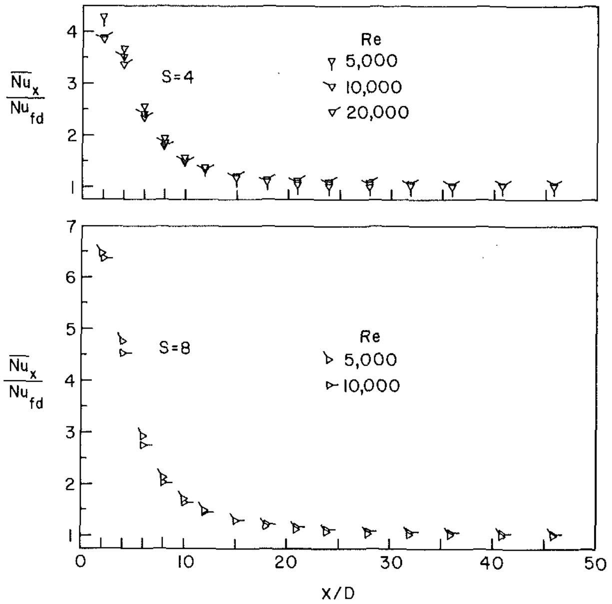

Fig. 4 Circumferential average Nusselt numbers for S = 4 and 8 and for parametric values of the Reynolds number

were also made at higher Reynolds numbers. Those results are not included here because it was not possible to satisfactorily control heat losses through the current carrying copper spokes situated at the test section inlet.

Inspection of Figs. 1 and 2 reveals a pattern which is qualitatively similar to that encountered in a conventional thermally developing flow. That is, the highest value of $\overline{\mathrm{Nu}}_x/\mathrm{Nu}_{fd}$ is attained at the onset of heating and, thereafter, the Nusselt numbers decrease with increasing downstream distance until the fully developed regime is reached. Aside from this global similarity, there are some important differences between the present results and those for the conventional entrance region.

The primary difference is that the values of $\overline{\mathrm{Nu}}_x/Nu_{fd}$ in the entrance region are much higher in the presence of fluid withdrawal. This characteristic can be readily observed in Figs. 1 and 2 by comparing the results for $S > 0$ (fluid withdrawal > 0) with those for $S = 0$ (no fluid withdrawal). The extent of the increase in the heat transfer coefficient is markedly affected by the extent of the withdrawal, i.e., by the magnitude of S; the larger the value of S, the larger is $\overline{\mathrm{Nu}}_x/\mathrm{Nu}_{fd}$. For the largest S value of these experiments ($S = 10$), the heat transfer coefficient at a point $1\frac{1}{4}$ diameters from the onset of heating is more than five times that for no fluid withdrawal.

The aforementioned increases in the transfer coefficient may be attributed to various flow field events. One of these is the secondary flow which is induced by pressure variations caused by the turning of the flow passing into the withdrawal tube. Also, fluid particles entering the test section tube carry their upstream momentum, which, in an average sense, corresponds to a Reynolds number equal to $(S + 1)$Re. Thus, high velocity fluid, albeit nonuniformly distributed, is available to participate in the heat transfer process. Finally, the turning, the secondary flow, and the subsequent readjustments of the velocity field give rise to a substantial amount of mixing which serves to enhance the heat transport.

From a superficial viewing of Figs. 1 and 2, it might appear that the successively smaller ranges of the ordinate scales imply a lesser degree of augmentation as the Reynolds number increases. In actuality, the diminishing ordinate ranges result from the fact that the maximum S values that could be attained at higher Reynolds numbers were smaller than those attainable at lower Reynolds numbers. As will shortly be demonstrated, the augmentation is not a strong function of Reynolds number in the range investigated.

In addition to the higher values of the heat transfer coefficient, another effect of fluid withdrawal in evidence in Figs. 1 and 2 is the elongation of the thermal entrance region. Therefore, the fluid withdrawal process plays the role of an effective augmentation device.

Further inspection of Figs. 1 and 2 reveals that whereas all the distribution curves display a monotonic decrease with x/D, some tend to be concave downward initially. This is especially evident for S values in the range from 2.5 to 5. This concavity is distinctly different from that of the conventional entrance region distribution and provides further testimony about the complexity of the flow processes induced by the fluid withdrawal.

Attention will now be turned to an alternate presentation of the $\overline{\mathrm{Nu}}_x$ results in which data having common values of S are brought together. Figs. 3 and 4 have been prepared for this purpose. Fig. 3 consists of three graphs, respectively for $S = 0$, 1, and 2.5, whereas Fig. 4 contains graphs for $S = 4$ and 8. In each graph, data for various Reynolds numbers are identified via specific symbols. In common with earlier figures, the results are once again plotted in the form $\overline{\mathrm{Nu}}_x/\mathrm{Nu}_{fd}$ versus x/D.

From an overall examination of Figs. 3 and 4, it is seen that in the range investigated, $\overline{\mathrm{Nu}}_x/\mathrm{Nu}_{fd}$ is not a strong function of the Reynolds number for a given value of S, especially when $S > 1$. This finding is of practical relevance inasmuch as greater sensitivity might be expected in the low Reynolds number range than at higher Reynolds numbers. Thus, in the absence of other information, it would not be unreasonable to use the results of Figs. 3 and 4 for Reynolds numbers that are higher than those for which the experiments were performed.

The results for $S = 0$ and 1 are more sensitive to Reynolds number than are those for higher values of S. For the case of no fluid withdrawal ($S = 0$), the trend with Reynolds number evidenced in Fig. 3 is altogether reasonable on the basis of prior information. The sensitivity of the $S = 1$ results can be rationalized on the basis that the withdrawn flow is not yet sufficiently dominant to fix the flow field. It is believed that the Re = 20,000 results can be used as a first approximation for higher Reynolds numbers.

The entrance region results for $S = 0$ and for Re = 10,000 and 20,000 have been compared in [1] with available experimental results [2, 3] for the thermal entrance region in a conventional turbulent air flow. The agreement is altogether satisfactory. The fully developed Nusselt numbers for Re = 10,000 and 20,000 were compared with the Petukhov-Popov correlation [4], which is applicable for Re ≥ 10,000. Agreement prevails to three percent or better. The present fully developed data also agree to within two percent with those of Black [5].

The thermal entrance length has been mentioned previously and now will be dealt with in a quantitative manner. The dimensionless entrance length $(x/D)_e$ is defined here as the downstream distance, measured from the center of the tee, where $\overline{\mathrm{Nu}}_x/\mathrm{Nu}_{fd} = 1.05$ Results based on this definition are plotted in Fig. 5 as a function of the flow split number for parametric values of the Reynolds number. The slight scatter in the data is due to inherent uncertainties involved in graphical interpolation in the flat portion of the curves of $\overline{\mathrm{Nu}}_x/\mathrm{Nu}_{fd}$ versus x/D.

Examination of the figure shows that the entrance lengths are in the 20 to 30 diameter range, which is substantially larger than the entrance length for a conventional turbulent air flow. The entrance length tends to increase with increasing fluid withdrawal, thereby reflecting the longer length of run needed to redevelop and regularize the flow downstream of the disturbance caused by the branching. In addition, the longer entrance lengths in evidence at higher Reynolds numbers are, in all likelihood, due to the diminished viscous damping of the disturbances.

It is seen from the figure that the entrance length for $S = 0$ is about 15 diameters. This is larger than the 8 to 10 diameters that is regarded as typical for conventional turbulent air flows. In examining the basis for this difference, it was found that the present data for $\overline{\mathrm{Nu}}_x/\mathrm{Nu}_{fd}$ lie a few percent above those of [2] and [3] in the range $x/D = 8$ to 15. Owing to the flatness of the $\overline{\mathrm{Nu}}_x/\mathrm{Nu}_{fd}$ versus x/D curve in that range, this small deviation is sufficient to cause a relatively large shift in the entrance length. It is believed that the small deviation of the present $\overline{\mathrm{Nu}}_x/\mathrm{Nu}_{fd}$ data from those of [2] and [3] is caused by the interruption of the wall at the center port of the tee (i.e., at the withdrawal point). This interruption alters the velocity distribution in the flow entering the test section and may, thereby, induce a longer development length.

Angular Distributions of the Transfer Coefficients. The withdrawal of fluid causes a general displacement of the flow toward the point of withdrawal, with the result that the velocity distribution at the test section inlet is not axisymmetric. As a consequence, circumferential nonuniformities of the heat transfer coefficient in the entrance region are to be expected, and representative results illustrating the angular variations are presented in Figs. 6 and 7.

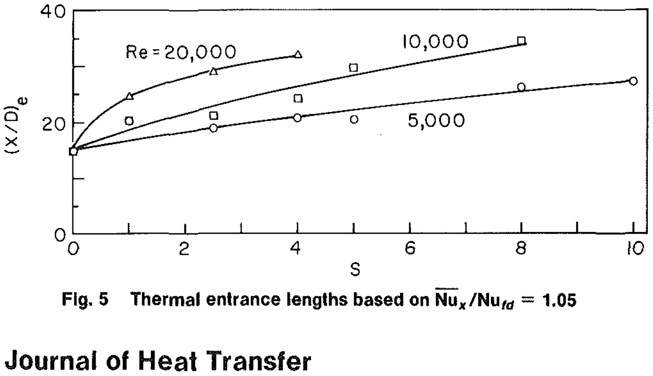

Fig. 5 Thermal entrance lengths based on $\overline{\mathrm{Nu}}_x/\mathrm{Nu}_{fd} = 1.05$

The figures pertain to Re = 5,000 and 20,000, respectively. Each figure contains several columns of graphs, with each column corresponding to a given value of S. The successive graphs in each column depict a succession of axial stations, starting with $x/D = 2$ at the top of the column and proceeding down along the column to larger x/D. In each graph, the angular distribution of the Nusselt number is plotted as a function of the coordinate θ, where $\theta = 0$ deg is at the top of the tube cross section and $\theta = 180$ deg is at the bottom. For reference purposes, it may be recalled that the fluid is withdrawn from the top of the cross section. The angular distribution at each axial station has been normalized by the circumferential average Nusselt number $\overline{\mathrm{Nu}}_x$ for that station.

The figures show that, in the main, the heat transfer coefficients in the upper part of the tube are higher than those in the lower part. This finding is consistent with the fact that the withdrawal of fluid causes a general displacement of the flow toward the upper part of the cross section. The circumferential variations are moderate, being at most on the order of ±20 percent for each case.

Although the circumferential variations are ultimately dissipated, they do not necessarily decrease monotonically with increasing x/D. For example, the variation in evidence at $x/D = 8$ for $S = 1$ is greater than that at $x/D = 2$, both for Re = 5,000 and 20,000. With increasing values of S, the maximum variations occur farther upstream, i.e., at the first or second measurement stations. An interesting feature of the results for large S is the reversal in the shape of the distribution curve at the third or fourth stations. This reversal is believed due to the effect of a strong circumferential flow from the top to the bottom of the cross section, which is driven by the large concentration of fluid

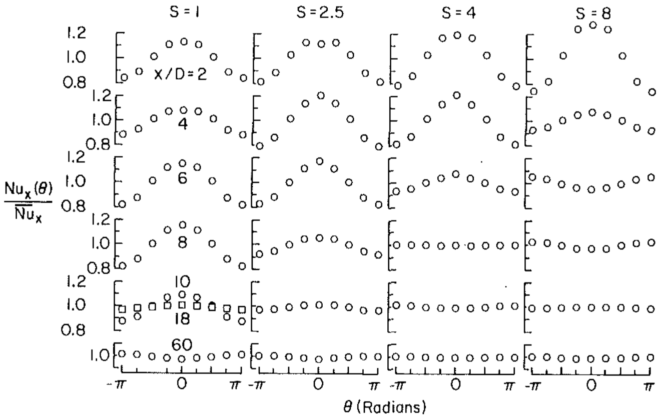

Fig. 6 Angular distributions of the Nusselt number, Re = 5,000

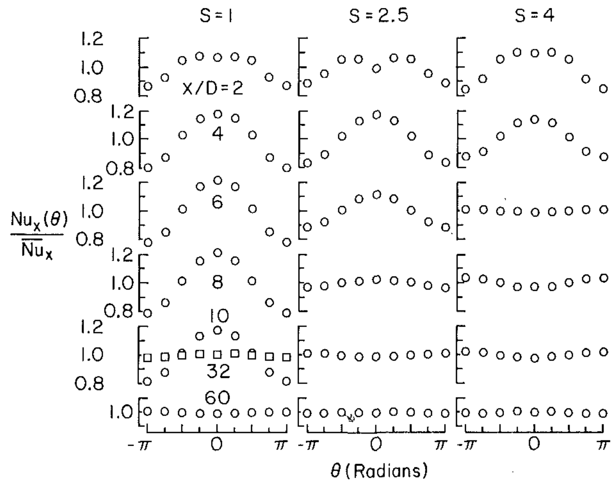

Fig. 7 Angular distributions of the Nusselt number, Re = 20,000

near the top that results from high rates of withdrawal.

For the most part, the circumferential variations are dissipated upstream of $x/D = 10$. Thus, the attainment of circumferential uniformity does not imply thermally developed flow. For $S = 1$, the circumferential variations are relatively long lived, as witnessed by the fact that substantial nonuniformities are still in evidence at $x/D = 10$. To provide information about downstream events for this case, an additional distribution curve has been plotted along with that for $x/D = 10$. This second distribution corresponds to the axial station at which circumferential uniformity first occurs.

The high degree of circumferential uniformity in evidence for $x/D = 60$ adds assurance that spurious factors such as unaccounted localized heat losses or wall thickness variations were not present.

Concluding Remarks

The experimental results have demonstrated that fluid withdrawal at a branch point in a pipe has a marked effect on the downstream heat transfer characteristics in the main line. The circumferential average Nusselt numbers $\overline{\mathrm{Nu}}_x$ in the thermal entrance region are much higher than those for a conventional axisymmetric flow having the same Reynolds number. The degree of augmentation at any fixed test-section Reynolds number is greater when the ratio of the withdrawn flow to the test section flow takes on higher values. If the flow split ratio is fixed, the axial distribution of $\overline{\mathrm{Nu}}_x/\mathrm{Nu}_{fd}$ is relatively insensitive to the Reynolds number. This suggests that the results for $\overline{\mathrm{Nu}}_x/\mathrm{Nu}_{fd}$ can be applied to Reynolds numbers that are higher than those for which the experiments were performed.

In the presence of fluid withdrawal, the thermal entrance lengths (based on $\overline{\mathrm{Nu}}_x/\mathrm{Nu}_{fd} = 1.05$) are in the 20 to 30 diameter range, with the higher values corresponding to larger flow splits and larger Reynolds numbers. These entrance lengths are substantially greater than the 8 to 10 diameters that typify conventional turbulent air flows in pipes.

The flow withdrawal process gave rise to circumferential variations of the heat transfer coefficient, with the higher values generally being on the same side of the tube from which fluid was withdrawn. The circumferential variations were moderate, on the order of ±20 percent, at most. For the most part, the variations were dissipated upstream of $x/D = 10$, except for a flow split of unity, where the nonuniformity persisted to $x/D = 20 - 30$, depending on the Reynolds number.

References

1 Kemink, R. G., "Heat Transfer in a Tube Downstream of a Withdrawal Branch," Thesis, Department of Mechanical Engineering, University of Minnesota, 1977.

2 Mills, A. F., "Experimental Investigation of Turbulent Heat Transfer in the Entrance Region of a Circular Conduit," *Journal of Mechanical Engineering Science*, Vol. 4, 1962, p. 63.

3 Hishida, M., "Turbulent Heat Transfer and Temperature Distribution in the Thermal Entrance Region of a Circular Pipe," *Bulletin of the JSME*, Vol. 10, 1967, p. 113.

4 Karlekar, B. V. and Desmond, R. M., *Engineering Heat Transfer*, West Publishing Co., St. Paul, 1977, p. 351.

5 Black, A. W., "The Effect of Circumferentially Varying Boundary Conditions on Turbulent Heat Transfer in a Tube," Ph.D. Thesis, Department of Mechanical Engineering, University of Minnesota, 1966.

S. V. Patankar
M. Ivanović
E. M. Sparrow

Department of Mechanical Engineering,
University of Minnesota,
Minneapolis, Minn. 55455

Analysis of Turbulent Flow and Heat Transfer in Internally Finned Tubes and Annuli

The fully developed turbulent flow and heat transfer characteristics for tubes and annuli with longitudinal internal fins were analyzed via a mixing length model. The model takes account of the proximity of both the fin surfaces and the tube wall as well as of the gradients in the radial and circumferential directions. Application was made to air flows, and a single adjustable constant in the model was fixed by comparisons with experimental data for the friction factor and the circumferential-average Nusselt number for internally finned tubes. The local heat transfer coefficients exhibited a substantial variation along the fin height, with the smallest value (essentially zero) at the base and the largest value at the tip. Lesser and more gradual variations were exhibited by the local heat transfer coefficients on the wall of the tube or annulus. In general, the fins were found to be as effective a heat transfer surface as the wall (per unit area). Average Nusselt numbers and friction factors are presented for both the tube and the annulus.

Introduction

The augmentation of the forced convection heat transfer performance of circular tubes by longitudinal internal fins has been investigated in several recent experiments [1–7]. When compared with unfinned tubes on a constant pumping power basis, the finned tubes exhibited substantially higher heat transfer coefficients [1, 8]. Such fins are also employed to improve the heat transfer characteristics of concentric annuli [9] (e.g., double pipe heat exchangers), and relevant experiments are summarized in [10]. Whereas the experimental work on tubes with longitudinal internal fins has been focused on turbulent flows, the published analyses [11, 12] have dealt exclusively with laminar flows. The internally finned annulus appears not yet to have been analyzed.

The present research was undertaken to analyze the turbulent flow and heat transfer characteristics of circular tubes and annuli with longitudinal internal fins. The analysis is based on the differential equations for momentum and energy conservation in the flowing fluid supplemented by a turbulence model having an adjustable constant. Attention is focused on the case of fully developed flow and heat transfer, with the thermal boundary condition being uniform heat input to the fluid per unit axial length. The conductance of the tube wall is assumed to be sufficiently high so that its temperature is circumferentially uniform in any cross section (the wall temperature varies axially, in step with the increase of the bulk temperature). As performed here, the analysis is primarily directed toward gas flows and, as a consequence, the variation of the temperature along the height of the fin can be neglected.

Schematic cross-sectional diagrams of the tube and annulus geometries to be analyzed are shown in Fig. 1, respectively at the left and at the right. The number of fins appearing in these figures is for pictorial purposes only; for the analysis, N equally spaced fins were considered. Furthermore, in accordance with the most recent experimental work, consideration was given to fins whose height does not span the entire flow cross section. Also, to simplify the analysis and to keep the number of parameters within reasonable limits, the fins were assumed to be thin. In the case of the annulus, heating was confined to the inner tube (i.e., to the finned tube), with the outer tube adiabatic.

Unlike conventional tube and annulus flows, where only radial variations of velocity and temperature occur in a given cross section,

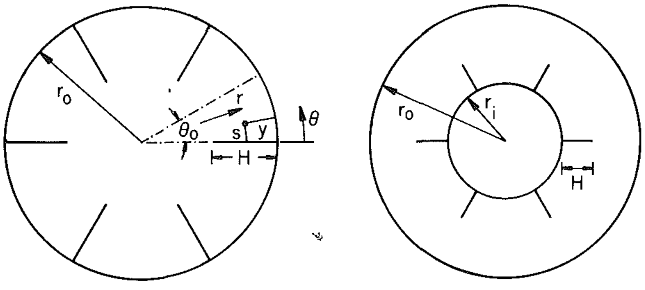

Fig. 1 Schematic cross-sectional diagrams of an internally finned tube and an internally finned annulus

---

Contributed by the Heat Transfer Division for publication in the JOURNAL OF HEAT TRANSFER. Manuscript received by the Heat Transfer Division February 13, 1978.

the flows being considered here experience circumferential variations as well as radial variations. The presence of the circumferential variations activates circumferential transport, both by turbulence as well as by molecular mechanisms. As a consequence, it is necessary to include the circumferential transport in the analysis and to employ an appropriate turbulence model. Another factor that was considered is the possibility that the turbulent transport at a given point in the flow is influenced both by the proximity of the tube wall and of the fin surface. In simpler situations, only the distance from one bounding wall need be considered. Various turbulence modeling schemes were examined, as will be described shortly. The model ultimately selected possesses the virtue of simplicity while providing results in good agreement with available experimental information.

Once the analytical model was established, it was used to obtain both average and local heat transfer results, as well as friction factors. The average Nusselt numbers and the friction factors are of direct relevance to design, whereas the local heat transfer results provide insights into the transport processes.

The local results are of special interest because they convey information that would be extremely difficult to obtain experimentally. This includes, in particular, the distribution of the heat loss along the height of the fin and the distribution of the tube wall heat loss around the circumference. Since the velocity varies along the fin height (i.e., in the radial direction), the local fin heat loss would be expected to reflect this variation. In particular, if the highest velocities were to occur in the neighborhood of the tip of the fin, the heat loss might be largest in that neighborhood. Such a finding, if encountered, would stand in contrast to the traditional fin model which assumes a uniform heat transfer coefficient and predicts a minimum heat loss at the tip. With regard to the tube wall heat loss, circumferential variations are also expected because the flow is highly constrained near the corner where the fin and tube meet and is less constrained away from the corner.

Aside from the aforementioned, results for two other quantities will be presented. One of these is the ratio of the fin heat transfer to the total heat transfer (fin plus tube). The other is the ratio of the mass flow in the inter-fin space to the total mass flow passing through the cross section. Perspective will be given to the mass flow ratio by comparing it with the corresponding mass ratio for a tube without internal fins. Such a comparison indicates the extent of the rearrangement of the flow field as the fluid seeks to avoid the relatively high frictional resistance in the inter-fin spaces.

In the presentation that follows, the work on the finned tube will be described first, encompassing the formulation and testing of the analytical model and the description and discussion of the results obtained by application of the model. This is followed by the annulus, for which further modeling is carried out as a prelude to the execution of the solutions and the presentation of results.

Internally Finned Tubes

The description of the analysis is facilitated by reference to the diagram of the internally finned tube pictured at the left of Fig. 1. Because of the evident symmetries, it is only necessary to analyze the flow and heat transfer processes in a pie-shaped section that spans half of the space between any two adjacent fins. The r, θ cylindrical coordinates are illustrated in the figure, and z is the axial coordinate normal to the plane of the page. Possible secondary flows are not considered because they are beyond the scope of the analytical model.

Conservation Equations and Boundary Conditions. For fully developed turbulent flow, the momentum equation appropriate to the present problem can be written as

$$\frac{1}{r}\frac{\partial}{\partial r}\left[r(\mu+\mu_t)\frac{\partial w}{\partial r}\right]+\frac{1}{r^2}\frac{\partial}{\partial \theta}\left[(\mu+\mu_t)\frac{\partial w}{\partial \theta}\right]=\frac{dp}{dz} \qquad (1)$$

in which μ and μ_t are, respectively, the molecular and turbulent viscosities. When the dimensionless variables

$$\eta = r/r_0,\ W = w/(r_0^2/\mu)(-dp/dz) \qquad (2)$$

are introduced, the momentum equation becomes

$$\frac{1}{\eta}\frac{\partial}{\partial \eta}\left[\eta(1+\mu_t/\mu)\frac{\partial W}{\partial \eta}\right]+\frac{1}{\eta^2}\frac{\partial}{\partial \theta}\left[(1+\mu_t/\mu)\frac{\partial W}{\partial \theta}\right]+1=0 \qquad (3)$$

With regard to the energy equation, the convection term can be evaluated for fully developed conditions and for uniform heating Q' per unit axial length. From an energy balance, the axial temperature gradient is given by

$$\partial T/\partial z = dT_b/dz = Q'/\rho c_p \bar{w}\pi r_0^2 \qquad (4)$$

where, consistent with the thin-fin assumption, the cross-sectional area for fluid flow is expressed as πr_0^2. Then, in dimensionless form, the energy equation is

$$-\frac{(W/\bar{W})}{\pi}=\frac{1}{\eta}\frac{\partial}{\partial \eta}\left[\eta(1+k_t/k)\frac{\partial \phi}{\partial \eta}\right]+\frac{1}{\eta^2}\frac{\partial}{\partial \theta}\left[(1+k_t/k)\frac{\partial \phi}{\partial \theta}\right] \qquad (5)$$

In this equation, ϕ is a dimensionless temperature

$$\phi = (T_w - T)/(Q'/k) \qquad (6)$$

and k and k_t are, respectively, the molecular and turbulent conductivities; T_w is the circumferentially uniform tube wall temperature

Nomenclature

A_f = surface area of fins
A_{ht} = heat transfer area of fins and tube
c_p = specific heat
DF = van Driest damping factor
D_h = hydraulic diameter
d = tube diameter
f = fanning friction factor, equation (23)
H = fin height
h = average heat transfer coefficient, $Q'/(T_w - T_b)A_{ht}$
h_f = local fin heat transfer coefficient, $q_f/(T_w - T_b)$
h_t = local tube-wall heat transfer coefficient, $q_t/(T_w - T_b)$
k = (molecular) thermal conductivity
k_t = turbulent thermal conductivity
L = Nikuradse-type mixing length
ℓ = mixing length
N = number of fins
Nu = average Nusselt number, hD_h/k
$\dot{m}$ = mass flow through entire cross section
$\dot{m}_H$ = mass flow in annulus between $y = 0$ and $y = H$
Pr = (molecular) Prandtl number
Pr_t = turbulent Prandtl number
p = pressure
Q' = heat transfer rate per unit axial length
Q'_f = fin heat transfer rate per unit axial length
q_f = local fin heat transfer
q_t = local tube-wall heat transfer
Re = Reynolds number, $\bar{w}D_h/\nu$
r = radial coordinate
r_i = inner radius of annulus
r_m = radius of maximum velocity
r_0 = tube radius; outer radius of annulus
s = circumferential distance, $r\theta$
s_0 = half-distance between fins, $r\theta_0$
T = temperature
T_b = bulk temperature
T_w = wall temperature
W = dimensionless velocity, equation (2)
$\bar{W}$ = mean value of W
w = velocity
$\bar{w}$ = mean velocity
y = coordinate measured normal to wall
z = axial coordinate
η = radial coordinate, r/r_0
θ = angular coordinate
θ_0 = half-angle between fins
μ = (molecular) viscosity
μ_t = turbulent viscosity
ν = kinematic viscosity
ρ = density
ϕ = dimensionless temperature, $(T_w - T)/(Q'/k)$
An overbar denotes an average value

at any arbitrary axial station in the thermally developed regime. It may be observed from equations (3) and (5) that both W and ϕ depend on the cross-sectional coordinates η and θ, but not on z.

To supplement the conservation equations (3) and (5), the boundary conditions and the turbulent transport coefficients μ_t and k_t have to be specified. For the velocity, the boundary conditions are that $W = 0$ on the solid surfaces and $\partial W/\partial\theta = 0$ on the symmetry lines. Since temperature variations have been assumed to be negligible both along the fin height and around the tube circumference, then $\phi = 0$ on the solid surfaces; on the symmetry lines, $\partial\phi/\partial\theta = 0$. The formulation of a model for the turbulent transport coefficients will be described in the next section.

Turbulence Model. A number of candidate turbulence models were examined prior to the formulation of the model finally adopted. One of those that was actually employed in exploratory computations was the k-ϵ model [13], where k is the turbulence kinetic energy and ϵ is its dissipation rate. The currently standard version of the k-ϵ equations cannot be employed in near-wall regions where, instead, the wall functions are used. From the exploratory computations, it was found that for certain parameter values, a substantial portion of the inter-fin space was, in effect, a near-wall region (i.e., $y^+ < \sim 15$). Since the available wall functions account for the influence of only a single wall, they are not suitable for the present problem, where the influences of both the tube wall and the fin surface are important. On this basis, further involvement with the k-ϵ model was discontinued.

The Buleev model [14] was carefully considered because it provides a means of evaluating the turbulent mixing length at any point in the flow, with account being taken of the influence of all the walls that bound the flow field. This capability is of importance in the present problem, since it is expected that the mixing length at any point in the inter-fin space would be affected both by the proximity of the tube wall and of the fin. The evaluation of Buleev's mixing length involves the determination of the lengths of rays which emanate in all directions from the point of interest and intersect the solid boundaries of the flow. In the present flow configuration (Fig. 1, left-hand diagram), the intersection pattern of such rays is very complex owing to the fact that the fins intercept certain rays and thereby "shadow" the tube surface. The complexity of the calculations, which would have had to be performed at a large number of points in the flow field, discouraged the use of the Buleev method. Equally dampening were the limitations of the method that were recently exposed by Quarmby [15].

The model adopted here, which is an algebraic model involving the mixing length, will now be described. Consider a typical point such as that shown in the figure. The point is situated at a distance y from the tube wall and a distance s ($= r\theta$) from the fin surface. The mixing length at the point is taken to be the resultant of two contributions. First, considering a pipe flow without fins, the mixing length at y is $\ell_p(y)$, where the subscript p refers to a pipe flow. Next, if the inter-fin space is likened to a parallel plate channel, the mixing length at s is $\ell_c(s)$, with c denoting channel.

In reality, the tube wall and fin surface simultaneously influence the mixing length at the point (y, s). Furthermore, the closer the point is to one of these surfaces, the greater should be the effect of that surface on the resultant mixing length. In considering a superposition of ℓ_p and ℓ_c that fulfills this requirement, it should be noted that $\ell_p(0) = \ell_c(0) = 0$. Therefore, a small value of ℓ associated with close proximity to one surface must overpower a large value of ℓ associated with remoteness of the other surfaces. Clearly, a suitable superposition should involve reciprocal values of ℓ_p and ℓ_c, and so we postulate that

$$\frac{1}{\ell} = \frac{1}{\ell_p} + \frac{1}{\ell_c} \tag{7}$$

where ℓ is the resultant mixing length. Equation (7) was employed to evaluate the mixing length at all points in the inter-fin space. At points in the open space between the fin tips and the tube centerline, i.e., for $y > H$, ℓ_c is presumed to have no influence, so that $\ell = \ell_p$.

The mixing lengths ℓ_p and ℓ_c were each represented as the product of a Nikuradse-type mixing length L and the van Driest damping factor DF, that is,

$$\ell_p = (DF)_p L_p,\ \ell_c = (DF)_c L_c \tag{8}$$

Nikuradse's work on turbulent pipe flow yielded [16]

$$L_p/r_0 = 0.14 - 0.08(1 - y/r_0)^2 - 0.06(1 - y/r_0)^4 \tag{9}$$

A mixing length representation analogous to equation (9) has not, to the authors' knowledge, been used to analyze turbulent flow in a parallel plate channel, although such a representation seems quite reasonable and could have been employed. For present purposes, it is convenient to propose a form for the channel mixing length L_c analogous to equation (9)

$$L_c/s_0 = a_1 - a_2(1 - s/s_0)^2 - a_3(1 - s/s_0)^4 \tag{10}$$

where s_0 is the half-width of the channel and a_1, a_2, and a_3 remain to be determined. In the present problem

$$s_0 = r\theta_0 \tag{11}$$

Two of the a's can be eliminated by employing the conditions that $L_c = 0$ at $s = 0$ and that the slope $\partial(L_c/s_0)/\partial(s/s_0)$ at $s = 0$ is equal to the Karman constant κ. These conditions give

$$a_2 = 2a_1 - \tfrac{1}{2}\kappa,\ a_3 = \tfrac{1}{2}\kappa - a_1 \tag{12}$$

With κ assigned its standard value of 0.4, it is seen that a_2 and a_3 can be eliminated from equation (10), leaving only a_1 to be determined.

Since the value of a_1 is not directly available, it was deemed advisable to treat it as an adjustable constant in the present analysis. In particular, as will be described in a coming section, it was used to assist in bringing together analytical and experimental results for the average Nusselt number and the friction factor for internally finned tubes. A value of $a_1 = 0.8$ was found to give the best agreement. With this, the L_c expression can be written as

$$L_c/s_0 = 0.8 - 1.4(1 - s/s_0)^2 + 0.6(1 - s/s_0)^4 \tag{13}$$

The van Driest damping factors appropriate to the pipe and channel mixing lengths are

$$(DF)_p = 1 - \exp(-y^+/A^+),\ (DF)_c = 1 - \exp(-s^+/A^+) \tag{14}$$

where

$$y^+ = y\sqrt{(\tau_w/\rho)}/\nu,\ s^+ = s\sqrt{(\tau_w/\rho)}/\nu \tag{15}$$

and $A^+ = 26$. The value of τ_w appearing in y^+ is the local shear stress on the pipe wall corresponding to the angular coordinate of the point (y, s) at which the mixing length is being calculated. Similarly, the τ_w in s^+ corresponds to the local shear on the fin surface.

When equations (9, 13, 14), and (15) are combined with (8), it is seen that the mixing lengths ℓ_p and ℓ_c are completely specified. With these, the resultant mixing length ℓ at any point (y, s) can be found from equation (7).

It now remains to evaluate the turbulent viscosity μ_t in terms of the mixing length and the local velocity derivatives. For flows in which there are significant velocity gradients in two coordinate directions, a commonly used representation for μ_t (specific to r, θ coordinates) is

$$\mu_t = \rho\ell^2[(\partial w/\partial r)^2 + (\partial w/r\partial\theta)^2]^{1/2} \tag{16}$$

This expression can be derived by the same reasoning as was used in [17, p. 78] to derive μ_t for flows in which there is one velocity gradient which is dominant.

By utilizing equation (16), the μ_t/μ ratio needed as input to the dimensionless momentum equation (3) can be evaluated. If the μ_t/μ expression is rephrased in terms of the W and η variables by writing $w = (W/\overline{W})\overline{w}$ and $y/r_0 = 1 - \eta$, the pipe Reynolds number

$$\mathrm{Re}_p = \overline{w}d/\nu \tag{17}$$

emerges as a parameter.

The turbulent conductivity k_t can be related to μ_t via the turbulent Prandtl number Pr_t

$$k_t = (\mu_t/\mathrm{Pr}_t)c_p \text{ or } k_t/k = (\mu_t/\mu)(\mathrm{Pr}/\mathrm{Pr}_t) \tag{18}$$

For pipe flows, a value of 0.9 for Pr_t is widely accepted and was used here. The molecular Prandtl number Pr was assigned a value of 0.7 for all of the present calculations.

Parameter Specification and Solution Method. An examination of the dimensionless governing equations and boundary conditions reveals the presence of four parameters: (a) Reynolds number, (b) Prandtl number, (c) half-angle θ_0 between adjacent fins (Fig. 1), (d) dimensionless fin height H/r_0. To facilitate comparisons with the recent literature, the Reynolds number to be used for parameterizing the results will be based on the hydraulic diameter, that is,

$$\mathrm{Re} = \bar{w}D_h/\nu,\ D_h = 4(\pi d^2/4)/(\pi d + 2NH) \tag{19}$$

The cross-sectional area appearing in the numerator of D_h reflects the thin-fin assumption, while N denotes the number of fins. The relationship between the Reynolds number Re of equation (19) and the pipe Reynolds number Re_p of equation (17) follows as

$$\mathrm{Re}_p/\mathrm{Re} = 1 + (N/\pi)(H/r_0) \tag{20}$$

For the computations, numerical values of Re were assigned in the range from 10^4 to 10^5.

As has already been noted, a Prandtl number of 0.7 was used in all the computations, which corresponds to air or other gases as the working fluid. The half-angle θ_0 is related to the number of fins N via $\theta_0 = \pi/N$, with N values between 6 and 18 used for the calculations. For H/r_0, values were used in the range from about 0.2 to 0.45. The ranges of Re, N, and H/r_0 were chosen to reflect available experimental data.

The solutions were obtained via finite differences, with the momentum equation being solved first and then used as input to the energy equation. Inasmuch as μ_t/μ depends on the velocity field and the wall shear stresses which appear in the damping factor, the momentum equation is nonlinear. This prompted an iterative solution in which μ_t/μ was evaluated from the velocity field of the prior iteration and then used as a known input to the current iteration. The solution of the energy equation does not require an iterative approach since k/k_t is determined (via equation (18)) when μ_t/μ is known from the velocity solution.

The finite difference grid was made up of 22 × 40 points, respectively in the circumferential and radial directions. The grid was deployed so that the points were finely spaced adjacent to the tube wall and the fin, with expanding step size in the direction away from the bounding surfaces. If i and j respectively denote the successive grid points in the circumferential and radial directions (with $i = 1$ and $j = 1$ corresponding to the wall-adjacent points), then the grid pattern was defined by $(s/s_0)_i \sim i^2$, $(y/r_0)_j \sim j^2$.

Model Testing; Average Coefficients and Friction Factors. Results for the average Nusselt number and for the friction factor will now be reported, and comparisons made with available information. To characterize the average heat transfer performance at any cross section in the fully developed regime, an average transfer coefficient and Nusselt number were evaluated from

$$h = Q'/(T_w - T_b)A_{ht},\ \mathrm{Nu} = hD_h/k \tag{21}$$

where the heat transfer area A_{ht} includes both the tube wall and the fin surface and is given by

$$A_{ht} = \pi d + 2NH \tag{22}$$

per unit axial length (note that Q' is also per unit axial length). The heat transfer coefficient defined by equation (21) averages the performance of the tube wall and the fins. For the friction factor, the Fanning definition was employed to facilitate comparisons

$$f = (-\,dp/dz)D_h/2\rho\bar{w}^2 \tag{23}$$

It is easily demonstrated that the Nusselt number is proportional to $1/\phi_b$ (ϕ_b = bulk value of the ϕ variable of equation (6)) and that f is related to $1/\bar{W}$.

As an initial (albeit partial) verification of the analytical model and of the computational procedure, results were obtained for fully developed turbulent flow and heat transfer in a tube without internal fins for Re between 10^4 and 10^5 and for Pr = 0.7. The Nusselt numbers and friction factors were respectively compared to those given by the correlations of Petukhov and of Filonenko [18], with respective agreement to within one and one-half and two percent.

Attention was next turned to possible comparisons with available experimental results for air flow in internally finned tubes. An examination of the literature showed that, unfortunately, the conditions of the tests were somewhat different from those of the analysis. The experiments were typically performed utilizing a double-pipe heat exchanger, with the internally finned tube surrounded by an annulus containing a flowing fluid other than air. For such a set-up, the heating (or cooling) of the air is not uniform along the length. In addition, since temperature measurements were confined to stations upstream and downstream of the test section, the reported heat transfer coefficients correspond to an axial average. Similarly, the measured friction factors also represent an axial average between stations upstream and downstream of the test section.

With the foregoing as background, the fully developed Nusselt numbers and friction factors predicted by the present analysis will be compared to the experimentally determined Nusselt numbers and friction factors of [1]. The experiments of [1] are the most recently reported air data and for this reason were chosen for the comparison.

The comparison is made in Fig. 2, where $\mathrm{Nu}/\mathrm{Pr}^{0.4}$ and f are plotted against Re, respectively in the left-hand and right-hand portions of the figure. The factor $\mathrm{Pr}^{0.4}$ dividing the Nusselt number was employed in [1] to generalize the results and has been retained in Fig. 2 for the same purpose. The solid lines in the figure represent the analytical predictions for the specific cases for which the data are identified in the inset.

It may be recalled that the analytical model contained a single adjustable constant, the coefficient a_1 in the circumferential mixing length distribution [10]. A succession of values were assigned to a_1, and that which give the best agreement between the analytical predictions and the experimental results was found to be about 0.8. The solid lines in Fig. 2 correspond to $a_1 = 0.8$. Considering the nature of the experiments as described in the foregoing and also noting the deviations between the test conditions and those of the analysis, the level of agreement is believed to be satisfactory. The greatest deviations between the analytical predictions and the data are seen to occur at high Reynolds numbers, but there is no ready explanation for this trend.

With regard to the results of Fig. 2, it is relevant to describe how the thin-fin analytical model was rationalized with the finite fin

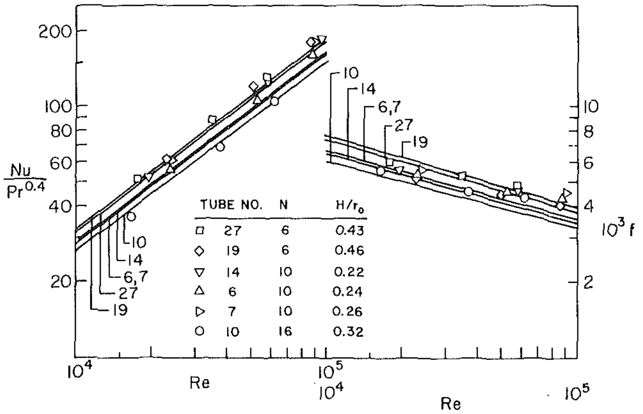

Fig. 2 Average Nusselt numbers and friction factors for internally finned tubes from the present analysis and from the experiments of [1]

thickness of the experiments. Let A_{flo} denote the actual flow cross section for a given experiment (i.e., taking account of the blockage caused by the fins). If this same flow cross section were to exist in a tube having very thin fins, then the diameter $\hat{d}$ of that tube would be equal to $2\sqrt{A_{\text{flo}}/\pi}$. Next, let the heat transfer surface (per unit length) in the tube used in the experiment be denoted by A_{ht}. For the same surface area, the height $\hat{H}$ of thin fins in a tube of diameter $\hat{d}$ would be obtained from

$$A_{ht} = \pi\hat{d} + 2N\hat{H} \text{ or } \hat{H} = [\tfrac{1}{2}A_{ht} - \sqrt{\pi A_{\text{flo}}}]/N \tag{24}$$

The $\hat{d}$ and $\hat{H}$ dimensions, defined above, were employed in specifying the parameter values for the analytical curves of Fig. 2.

Analytical predictions for the average Nusselt number and the friction factor corrsponding to parametric variations of Re, N, and H/r_0 were not generated because empirical correlations are available in [1]. Rather, attention will be focused on the presentation of local results and other information which would be extremely difficult to obtain experimentally.

Local Heat Transfer Coefficients. Since the temperature has been assumed to be uniform (and equal to T_w) along the fin height, local and average fin heat transfer coefficients may be defined as

$$h_f = q_f/(T_w - T_b),\ \bar{h}_f = \bar{q}_f/(T_w - T_b) \tag{25}$$

The variation of h_f along the height of the fin is presented in Fig. 3 for several representative cases, with $h_f/\bar{h}_f$ as ordinate and y/H as abscissa ($y/H = 0$ is at the fin base and $y/H = 1$ is at the tip). The two graphs respectively correspond to 6 fins and 18 fins, and in each graph results are given for dimensionless fin heights H/r_0 of 0.2 and 0.4 and for Reynolds numbers of 10^4 and 10^5.

From the figure, it is seen that for all cases, the heat transfer coefficient increases monotonically along the fin height, and the extent of the variation is substantial. In the neighborhood of the fin tip, the local coefficients are large (but finite) and in the range of 2–2½ times the average, while near the base they are virtually zero. These results stand in sharp contrast to the standard model used in fin analysis, where the heat transfer coefficient is assumed to be uniform.

The increase of h_f along the fin is entirely plausible and reflects the fact that the velocity of the fluid that washes the fin is very low in the neighborhood of the base and increases monotonically toward the tip. The h_f variations are smaller at higher Reynolds numbers because of the greater turbulent mixing and the resultant tendency toward more uniformity of the flow. Furthermore, the sensitivity of the $h_f/\bar{h}_f$ distributions to the number of fins is diminished at higher Reynolds numbers. The curves for the different fin heights are reasonably well correlated by the plotting parameters used in the figure.

It should also be noted that since the fin temperature is uniform along the height, it follows from equation (25) that $q_f/\bar{q}_f = h_f/\bar{h}_f$. Thus, in the present problem, not only does the heat transfer coefficient increase along the height, but the heat transfer itself increases. It is expected that this same behavior will prevail for fins characterized by moderate temperature variations, as is often the case for fins situated in air. This finding contradicts the prevailing notion that the fin heat transfer is necessarily greatest near the base and least near the tip.

Representative results for the local heat transfer coefficient along the tube wall are presented in Fig. 4 via a plot of $h_t/\bar{h}_t$ versus θ/θ_0, where

$$h_t = q_t/(T_w - T_b),\ \bar{h}_t = \bar{q}_t/(T_w - T_b) \tag{26}$$

The $\theta = 0$ position corresponds to the corner where the fin and tube intersect, while $\theta/\theta_0 = 1$ is midway between a pair of adjacent fins. Fig. 4 is structured in a similar manner to Fig. 3 and conveys results for the same cases.

The tube-wall heat transfer coefficient is virtually zero in the corner and increases monotonically along the circumference of the tube, attaining a maximum at the inter-fin mid-point. The extent of the h variation on the tube wall is not as great as that along the fin—the maximum value of $h_t/\bar{h}_t$ being about 1.2–1.3. In addition, the $h_f/\bar{h}_f$ and $h_t/\bar{h}_t$ distributions have rather different shapes. The h_f distributions tend to increase steeply along the entire fin height, while the h_t distributions exhibit a sharp rise in the corner and tend to level off thereafter. In general, it appears that the assumption of a uniform heat transfer coefficient is more tenable for the tube wall than for the fin. Furthermore, $h_t/\bar{h}_t$ is relatively insensitive to the variations of the parameters.

From the defining equations (26), it follows that $q_t/\bar{q}_t = h_t/\bar{h}_t$, so that Fig. 4 provides results for the local tube-wall heat transfer as well as for the transfer coefficient.

Heat Transfer and Mass Flow Ratios. It is of interest to inquire about the fraction of the heat load that is carried by the fins and the fraction that is carried by the tube, and Fig. 5 has been prepared in this connection. The figure compares the heat transfer (per unit length) Q'_f from the fins to the overall heat transfer Q' (fins plus tube). The Q'_f/Q' ratio is plotted as a function of the dimensionless fin height for parametric values of the Reynolds number (10^4 and 10^5) and of

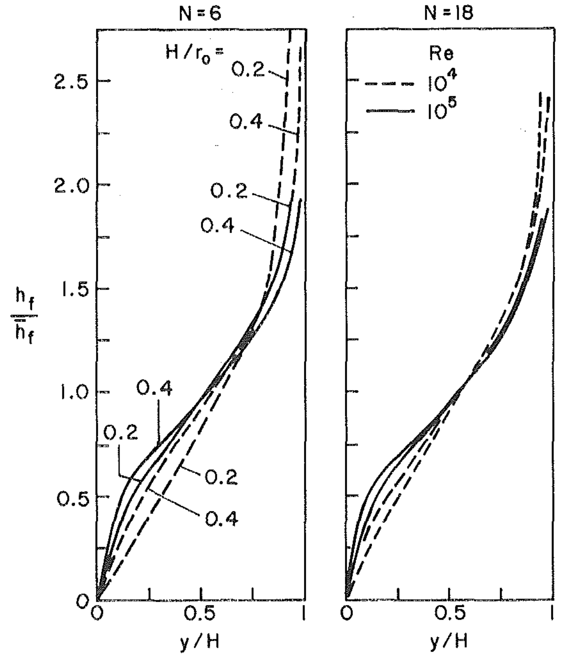

Fig. 3 Local heat transfer coefficients along the fin height for internally finned tubes

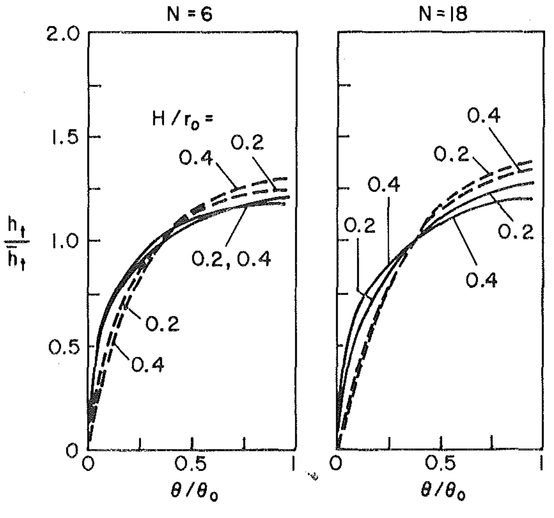

Fig. 4 Local heat transfer coefficients along the tube wall for internally finned tubes

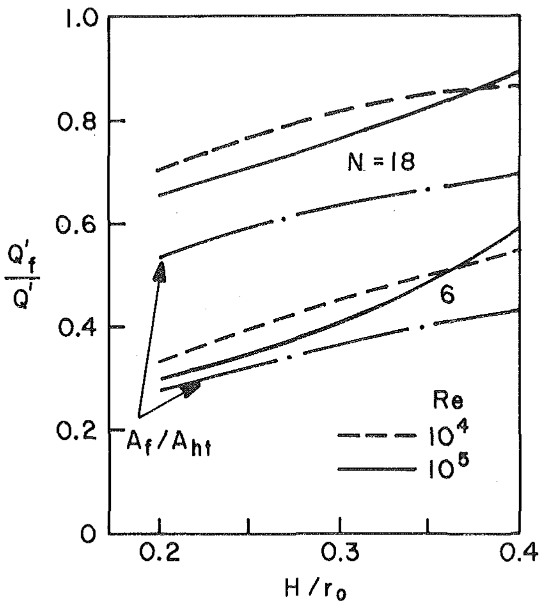

Fig. 5 Ratio of fin heat transfer to overall heat transfer for internally finned tubes

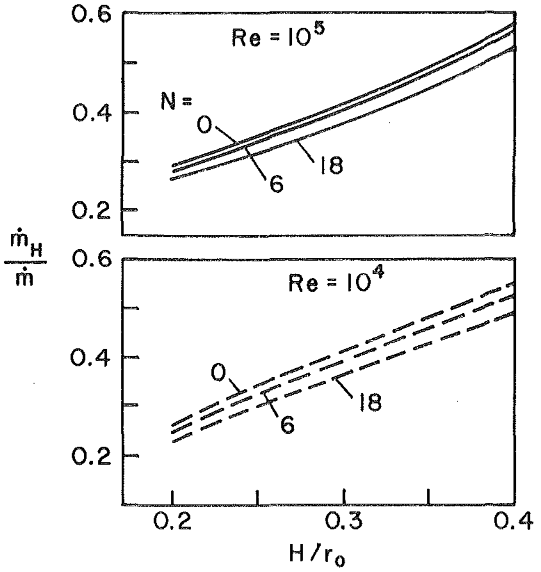

Fig. 6 Ratio of mass flow in annulus bounded by $y = 0$ and $y = H$ to total mass flow for internally finned tubes

the number of fins (6 and 18). Also given in the figure is the ratio of the fin surface area A_f to the total heat transfer area A_{ht}.

The curves show the expected increase of Q'_f/Q' with fin height and with the number of fins. What is less expected is that Q'_f/Q' exceeds the A_f/A_{ht} area ratio, signifying that the fins actually carry a larger fraction of the heat load than that which they would carry on purely area considerations. From this, it follows that on a unit area basis, the fins constitute a more effective heat transfer surface than the tube wall. This finding, which is the result of an analysis based on isothermal fins, should continue to hold for fins characterized by moderate temperature variations.

As a final result, the effect of the presence of the fins in bringing about a redistribution of the flow will be examined. Since the fluid passing through the inter-fin spaces experiences a greater resistance than that passing through the open area beyond the tips, a rearrangement, with more flow in the fin-free area, is to be expected.

Let $\dot{m}_H$ denote the mass flow passing through the annulus defined by $y = 0$ and $y = H$, while $\dot{m}$ is the mass flow in the entire cross section. The $\dot{m}_H/\dot{m}$ ratio is plotted in Fig. 6 as a function of H/r_0 for parametric values of the Reynolds number and of the number of fins. For purposes of reference, curves are shown for $N = 0$ (no fins) and, in fact, it is the displacement of the curves for $N \neq 0$ from that for $N = 0$ which signals the rearrangement of the flow. It is seen from the figure that as the number of fins increases, the fraction of the total flow that passes through the inter-face spaces decreases.[1] This rearrangement of the flow brings about the decreased heat transfer effectiveness of the tube wall that was evidenced by Fig. 5.

Internally Finned Annuli

The analysis of fully developed turbulent flow and heat transfer in an annulus with longitudinal internal fins will be carried out by utilizing the model that was developed for the internally finned tube. However, a modification is necessary because the mixing length L_p (equation (9)) for a pipe flow without fins does not apply for flow in an unfinned annulus. It is, therefore, appropriate to develop a mixing length representation to replace L_p.

The Model and its Verification. Consider a fully developed turbulent flow in an unfinned annulus with inner radius r_i and outer radius r_0. The velocity, which is zero at r_i, increases with increasing r, attains a maximum at $r = r_m$, and then decreases to zero at r_0. The radius of maximum velocity has been correlated in [19] as follows

$$\frac{r_m}{r_i} = \frac{1 + (r_0/r_i)^{0.657}}{1 + (r_i/r_0)^{0.343}} = \Omega \qquad (27)$$

We propose a mixing length representation consisting of Nikuradse-type expressions in the inner and outer annuli $r_i \leq r \leq r_m$ and $r_m \leq r \leq r_0$. For this purpose, let

$$y = r - r_i,\ y_m = r_m - r_i,\ y_0 = r_0 - r_i,\ y_{0m} = y_0 - y_m \qquad (28)$$

If the mixing lengths in the inner and outer annuli are respectively denoted by L_i and L_0, then

$$L_i/y_m = b_1 - b_2(1 - y/y_m)^2 - b_3(1 - y/y_m)^4 \qquad (29)$$

$$L_0/y_{0m} = c_1 - c_2(y - y_m)^2/y_{0m}{}^2 - c_3(y - y_m)^4/y_{0m}{}^4 \qquad (30)$$

The flow in the outer annulus is similar to a conventional pipe flow, except that the location of maximum velocity (and zero shear) is situated at a distance y_{0m} from the outer wall instead of at the pipe centerline. With this reasoning, the constants c_1, c_2, and c_3 should be equal to those for a pipe flow, i.e., $c_1 = 0.14$, $c_2 = 0.08$, $c_3 = 0.06$. To find the b's in the equation (29), the following three conditions are used: (a) $L_i = 0$ at $y = 0$, (b) $\partial L_i/\partial y = \kappa_i$ at $y = 0$, (c) $L_i = L_0$ at $y = y_m$. An expression for κ_i was derived in [20] as follows

$$\frac{\kappa_i}{\kappa} = \frac{(r_0/r_i) - \Omega}{\Omega - 1}\left[\frac{(r_0/r_i)^2 - \Omega^2}{(r_0/r_i)(\Omega^2 - 1)}\right]^{1/2} \qquad (31)$$

where κ is the Karman constant (= 0.4) and Ω is from equation (27). Thus, the b's depend upon r_0/r_i. For $r_i/r_0 = 0.5$, the application of conditions (a–c) yielded $b_1 = 0.14$, $b_2 = 0.045$, $b_3 = 0.095$.

The mixing length expressions (29) and (30) were respectively multiplied by a suitable damping factor to obtain a mixing length representation which replaces the ℓ_p used in the analysis of the internally finned pipe. Aside from this modification, all other features of the analytical model for the pipe-flow case were retained for the analysis of the annulus.

Since the foregoing model has not heretofore been employed for the unfinned annulus, it was deemed necessary to test it via comparisons with Nusselt number and friction factor information in the literature. The computations were performed for $r_i/r_0 = 0.5$, $\Pr_t = 0.9$, and $\Pr = 0.7$, with thermal boundary conditions of uniform heating at r_i and no heat transfer (adiabatic) at r_0. The results of these computations are presented in Fig. 7, where Nu and f are plotted against the Reynolds number (based on the hydraulic diameter). For

---

[1] This result is due solely to the greater resistance in the inter-fin space; blockage is not a factor since the fins are assumed to be negligibly thin.

the unfinned annulus, the hydraulic diameter D_h is equal to $2(r_0 - r_i)$ while $A_{ht} = 2\pi r_i$ for the assigned thermal boundary conditions.

The friction factors from the present analysis (solid lines) are compared with several sets of experimental data [21–26] and with analytical predictions based on other models [27–28]. The present results lie in the middle of the scatter band of the data and agree very well with the other analyses. With regard to heat transfer, the only available data are those of [19], with which the present predictions are in excellent agreement.

The comparisons presented in Fig. 7 lend confidence to the mixing length model (29) and (30). Attention will now be turned to the presentation of results for the internally finned annulus.

Results and Discussion. Owing to space limitations, results will be presented only for a single radius ratio $r_i/r_0 = 0.5$, with uniform heating per unit axial length at r_i and no heating at r_0. The fins are attached to the inner wall of the annulus as shown in the right-hand diagram of Fig. 1. Values of Pr and Pr_t were respectively assigned as 0.7 and 0.9 as before. The dimensionless fin height, expressed as $H/(r_0 - r_i)$, was given values of 0.2, 0.3, and 0.4. The definitions of Nu, f, and Re remain as before, but now

$$D_h = \frac{4\pi(r_0^2 - r_i^2)}{2\pi(r_0 + r_i) + 2NH}, \quad A_{ht} = 2\pi r_i + 2NH \qquad (32)$$

The friction factor and average Nusselt number results are presented in Fig. 8, which is subdivided into four panels. In three of the panels, results are given for 6, 12, and 18 fins, respectively. Although the dimensionless fin height $H/(r_0 - r_i)$ appears as a parameter, it has only a slight influence. In recognition of this, the results have been averaged over the three values of $H/(r_0 - r_i)$. The average curves are presented in the panel at the upper right, where results for the unfinned annulus ($N = 0$) are also included. These curves are parameterized by the number of fins. It is seen that the Nusselt number is somewhat more sensitive to N than is the friction factor, but neither is overly sensitive. In particular, the results for 6, 12, and 18 fins do not differ markedly, and it appears that the curves for $N = 18$ can be used for larger N, if desired. The results for the unfinned annulus provide an upper bound for those of the finned annulus.

Representative results for the local heat transfer coefficient on the fin are presented in Fig. 9, where $h_f/\bar{h}_f$ is plotted as a function of the dimensionless distance along the fin height. The variation of h_f is seen to be substantial, with the smallest values (essentially zero) at the base and the largest values ($h_f/\bar{h}_f \sim 2$) at the tip. For a given Reynolds number, both the shape and the extent of the variation are rather insensitive to the number of fins and to the dimensionless fin height. With increasing Reynolds number, the extent of the variation diminishes. The trends in evidence in Fig. 9 are identical to those of Fig. 3 for the internally finned pipe, and even the numerical values are more or less the same.

Local heat transfer coefficients on the heated wall of the annulus (i.e., at $r = r_i$) are plotted in Fig. 10 for several representative cases. As was also true for pipe flow (Fig. 4), the extent of the h variation along the tube wall is substantially smaller than that along the fins, and the shapes of the distribution curves are different. By overlaying the corresponding graphs in Figs. 4 and 10, it may be seen that the $h_t/\bar{h}_t$ curves for the pipe and the annulus are very nearly coincident. This result is somewhat unexpected, since the heated wall of the pipe is a concave boundary for the flow while the heated wall of the annulus is a convex boundary.

The fin heat load Q'_f is compared to the total heat load Q' (both per unit length) in Fig. 11. In addition to the curves for Q'_f/Q', the ratio of the fin area to the total heat transfer area is also plotted in the figure. For larger numbers of fins, $Q'_f/Q' > A_f/A_{ht}$, indicating that on a unit area basis, the fins are a more effective heat transfer surface than the tube wall. For fewer fins, the fin and tube surfaces are equally effective for smaller fin heights, with the fins being somewhat superior for larger heights. These characteristics are similar to those for pipe flow (Fig. 5).

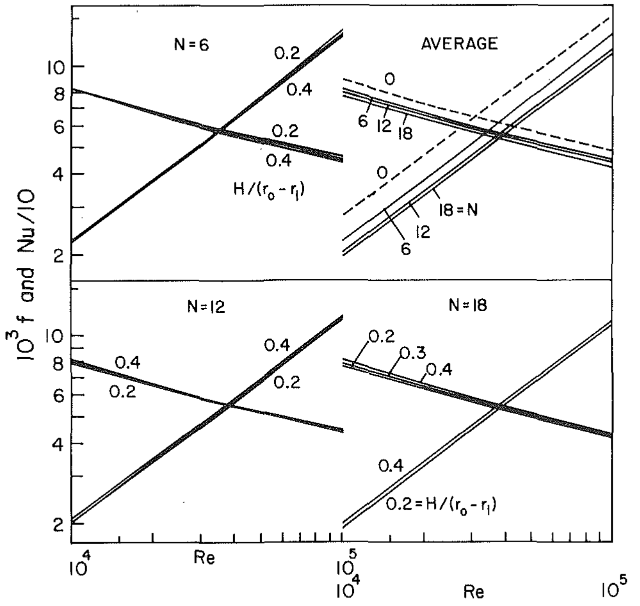

Fig. 8 Average Nusselt numbers and friction factors for internally finned annuli, $r_i/r_0 = 0.5$

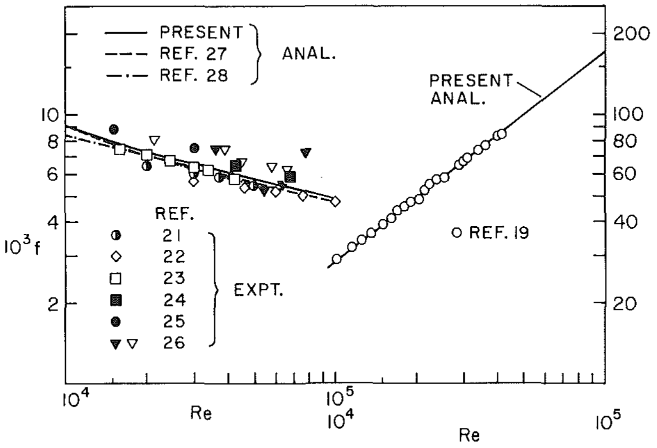

Fig. 7 Nusselt numbers and friction factors for unfinned annuli, $r_i/r_0 = 0.5$

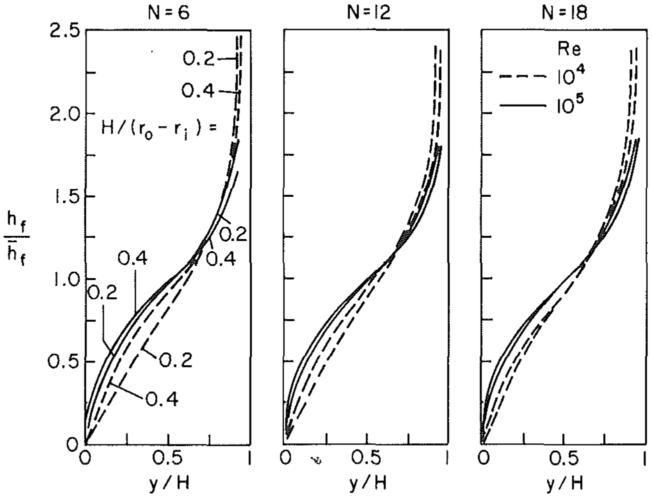

Fig. 9 Local heat transfer coefficients along the fin height for internally finned annuli, $r_i/r_0 = 0.5$

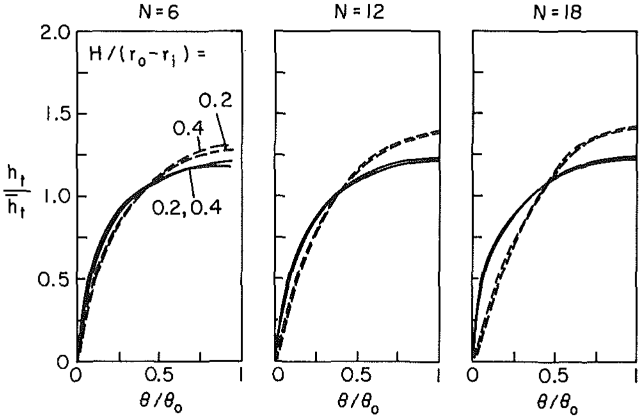

Fig. 10 Local heat transfer coefficients along the inner bounding wall (i.e., the heated wall) of internally finned annuli, $r_i/r_o = 0.5$

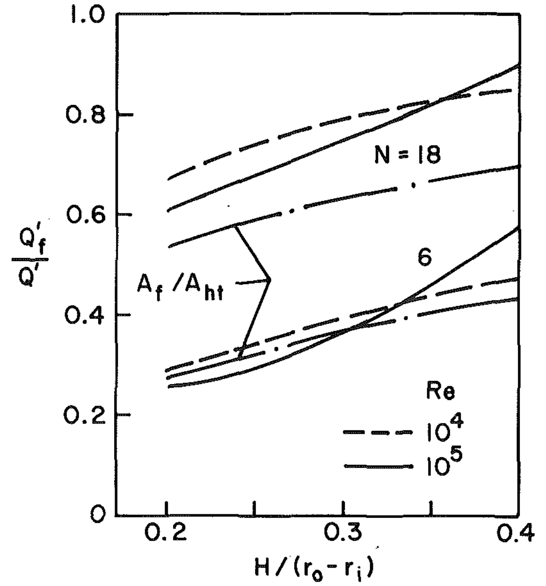

Fig. 11 Ratio of fin heat transfer to overall heat transfer for internally finned annuli, $r_i/r_o = 0.5$

The response of the flow distribution to the presence of the fins is illustrated in Fig. 12. In this figure, $\dot{m}_H$ is the mass flow passing through the annulus bounded by $y = 0$ and $y = H$, while $\dot{m}$ is the mass flow passing through the entire cross section. The decrease of $\dot{m}_H/\dot{m}$ as the number of fins increases indicates that more and more of the flow passes through the unfinned area in order to avoid the higher resistance in the inter-fin spaces.

Concluding Remarks

A mixing length model was formulated for analyzing fully developed turbulent flow and heat transfer in ducts in which there are significant variations of velocity and temperature in both cross sectional coordinates. An adjustable constant in the model was fixed by comparisons with friction factor and Nusselt number data for air-flow in internally finned tubes. The analytical results showed that the local fin heat transfer coefficient varied significantly along the fin height, with the smallest value (essentially zero) at the base and the largest value at the tip. Somewhat smaller variations were in evidence around the circumference of the tube wall. The fins were found to be a more effective transfer surface than the tube wall, on a unit area basis.

The model was extended to apply to an internally finned annulus. Consideration was given to an annulus whose inner bounding surface (the finned surface) is heated uniformly, while the outer boundary is adiabatic. Average Nusselt numbers and friction factors were evaluated for a range of Reynolds numbers, fin heights, and number of fins; the results were found to be quite insensitive both to fin height and to the number of fins. The local heat transfer coefficients exhibited trends similar to those for an internally finned pipe flow. The fins were found to be at least as effective a heat transfer surface as the heated wall of the annulus.

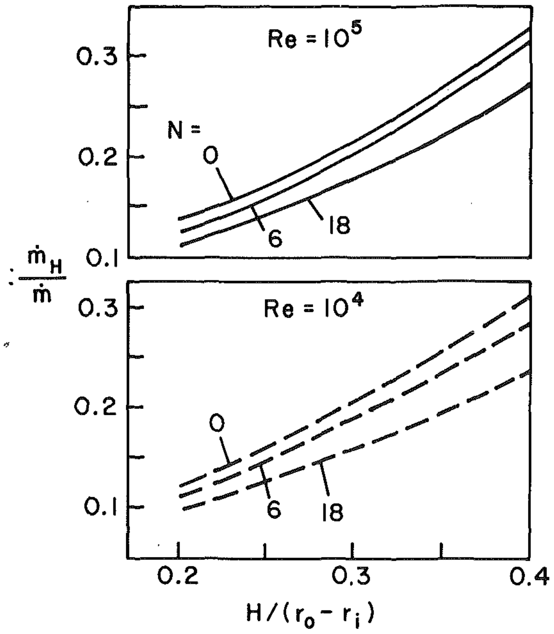

Fig. 12 Ratio of mass flow in annulus bounded by $y = 0$ and $y = H$ to total mass flow for internally finned annuli, $r_i/r_o = 0.5$

Before closing, mention may be made of the experiments of Stachiewicz [29] which dealt with turbulent heat transfer to air flowing in a longitudinally finned duct of square cross section. Comparisons between the present results and those of [29] were not undertaken because of differences in flow configuration and thermal boundary conditions and of the non-overlapping ranges of the fin height to inter-fin spacing ratio. Furthermore, the fins used in the experiments were composite structures consisting of a copper core covered with a nylon sheath; the latter introduces an additional thermal resistance not considered in the analysis.

Acknowledgment

This research was performed under the auspices of NSF Grant ENG-7518141.

References

1 Carnavos, T. C., "Cooling Air in Turbulent Flow with Internally Finned Tubes," AIChE Paper No. 4, 17th National Heat Transfer Conference, Aug. 1977.

2 Russell, J. R., and Carnavos, T. C., "An Experimental Study: Cooling Air in Turbulent Flow with Internally Finned Tubes," AIChE Paper No. 28, 16th National Heat Transfer Conference, Aug. 1976.

3 Watkinson, A. P., Miletti, D. L., and Kubanek, G. R., "Heat Transfer and Pressure Drop of Internally Finned Tubes in Laminar Oil Flow," ASME Paper No. 75-HT-41, 1975.

4 Watkinson, A. P., Miletti, D. L., and Kubanek, G. R., "Heat Transfer and Pressure Drop of Forge-Fin Tubes in Turbulent Air Flow," ASHRAE Paper No. 2347, ASHRAE Semi-Annual Meeting, 1975.

5 Watkinson, A. P., Miletti, D. L., and Tarassoff, P., "Turbulent Heat Transfer and Pressure Drop in Internally Finned Tubes," *AIChE Symposium Series*, Vol. 69, No. 131, 1973, pp. 94–103.

6 Bergles, A. E., Brown, Jr., G. S., and Snider, W. D., "Heat Transfer Performance of Internally Finned Tubes," ASME Paper No. 71-HT-31, 1971.

7 Hilding, W. E., and Coogan, Jr., C. H., "Heat Transfer and Pressure Loss Measurements in Internally Finned Tubes," Symposium on Air-Cooled Heat Exchangers, ASME, New York, 1964, pp. 57–85.

8 Bergles, A. E., "Survey and Evaluation of Techniques to Augment Convective Heat and Mass Transfer," *Progress in Heat and Mass Transfer*, Vol. 1, Pergamon Press, Oxford, 1969, pp. 331–424.

9 Kern, D. Q., and Kraus, A. D., *Extended Surface Heat Transfer,*

McGraw-Hill, New York, 1972, pp. 460–462.

10 Knudsen, J. G., and Katz, D. L., *Fluid Dynamics and Heat Transfer,* McGraw-Hill, New York, 1958, pp. 404–405.

11 Hu, H. M., and Chang, Y. P., "Optimization of Finned Tubes for Heat Transfer in Laminar Flow," ASME JOURNAL OF HEAT TRANSFER, Vol. 95, 1973, pp. 332–338.

12 Masliyah, J. H., and Nandakumar, "Heat Transfer in Internally Finned Tubes," ASME JOURNAL OF HEAT TRANSFER, Vol. 98, 1976, pp. 257–261.

13 Launder, B. E., and Spalding, D. B., "The Numerical Computation of Turbulent Flows," *Computer Methods in Applied Mechanics and Engineering,* Vol. 3, 1974, pp. 269–289.

14 Buleev, N. I., "Theoretical Model of the Mechanism of Turbulent Exchange in Fluid Flow," AERE Translation 957, 1963.

15 Quarmby, A., "An Evaluation of Buleev's Model of Turbulent Exchange," *International Journal of Heat and Mass Transfer,* Vol. 19, 1976, pp. 1319–1327.

16 Schlichting, H., *Boundary Layer Theory,* Sixth Edition, McGraw-Hill, New York, 1968, p. 568.

17 Launder, B. E., and Spalding, D. B., *Mathematical Models of Turbulence,* Academic Press, London, 1972.

18 Petukhov, B. S., Kurganov, V. A., and Gladuntsov, A. I., "Heat Transfer in Turbulent Pipe Flow of Gases with Variable Properties," *Heat Transfer—Soviet Research,* Vol. 5, No. 4, 1973, pp. 109–116.

19 Kays, W. M., and Leung, E. Y., "Heat Transfer in Annular Passages," *International Journal of Heat and Mass Transfer,* Vol. 6, 1963, pp. 537–557.

20 Roberts, A., "A Comment on the Turbulent Flow Velocity Profile in a Concentric Annulus," *International Journal of Heat and Mass Transfer,* Vol. 10, 1967, pp. 709–712.

21 Jonsson, V. K., "Experimental Studies of Turbulent Flow Phenomena in Eccentric Annuli," Ph.D. Thesis, University of Minnesota, 1965.

22 Brighton, J. A., and Jones, J. B., "Fully Developed Turbulent Flow in Annuli," *Journal of Basic Engineering,* Vol. 86, 1964, pp. 835–844.

23 Olson, R. M., and Sparrow, E. M., "Measurements of Turbulent Flow Development in Tubes and Annuli with Square or Rounded Entrance," *AIChE Journal,* Vol. 9, 1963, pp. 766–770.

24 Judd, R. L., and Wade, J. H. T., "Forced Convection Heat Transfer in Eccentric Annular Passages," *Proceedings of the Heat Transfer and Fluid Mechanics Institute,* 1963, pp. 272–288.

25 Rothfus, R. R., "Isothermal Skin Friction in Flow through Annular Sections," *Industrial and Engineering Chemistry,* Vol. 45, 1955, pp. 913–918.

26 Atherton, D. H., "Fluid Flow in Pipes of Annular Cross Section," *Trans ASME,* Vol. 48, 1926, pp. 145–175.

27 Wilson, N. W., and Medwell, J. O., "An Analysis of Heat Transfer for Fully Developed Turbulent Flow in Concentric Annuli," ASME JOURNAL OF HEAT TRANSFER, Vol. 90, 1968, pp. 43–50.

28 Quarmby, A., "An Analysis of Turbulent Flow in Concentric Annuli," *Applied Scientific Research,* Vol. A19, 1968, pp. 250–273.

29 Stachiewicz, J. W., "Effect of Variation of Local Film Coefficients on Fin Performance," ASME JOURNAL OF HEAT TRANSFER, Vol. 91, 1969, pp. 21–26.

I. D. R. Grant
D. Chisholm

National Engineering Laboratory,
East Kilbride,
Glasgow, Scotland

Two-Phase Flow on the Shell-Side of a Segmentally Baffled Shell-and-Tube Heat Exchanger

This paper reviews work carried out at the National Engineering Laboratory, UK., related to pressure drop flow patterns and phase distribution on the shell-side of segmentally baffled shell-and-tube heat exchangers. The experimental work reported was carried out using air/water mixtures in model exchangers of rectangular cross section with tube nests containing approximately 40 tubes. Data were obtained on crossflow pressure drop and on the pressure drop attributable to the windows. In certain configurations the void fraction and flow pattern maps were obtained. The geometric conditions examined related to configurations appropriate to operation as condensers and boilers. Correlations for pressure drop and void fraction were developed and flow pattern maps obtained.

Introduction

The shell-side of a segmentally baffled shell-and-tube heat exchanger is frequently used to evaporate or condense process fluids. The accurate prediction of pressure drop with two-phase flow across a tube bundle is essential to good design.

The work reported is part of an investigation undertaken at the National Engineering Laboratory, United Kingdom. A seven-tube model heat exchanger [1] was first used with air/water mixtures. The data in this paper were obtained in a 39 tube model [2, 3] with the same mixture. Work is currently in progress with larger units.

Experimental Heat Exchanger

The experimental data in this paper were obtained from the model shown in Fig. 1. It has a rectangular shell made in acrylic measuring 483 mm long by 302 mm high by 130 mm wide. The shell contains 39 tubes of 19 mm outside diameter arranged on an equilateral triangular layout of 1.25 pitch/tube diameter ratio. Half-tubes located on the walls prevent bypassing. Three segmental baffles give four passes on the shell-side.

Pressure tapping points are located between the baffles and level with the baffle cut-edges. The overall pressure drop is thus divided into the crossflow zone pressure drop (in the region of the baffle overlap) and the window zone pressure drop (around the baffle).

Flow Patterns

Two types of mixer were used upstream of the model to generate air/water mixtures. In the first, at high water flowrates, compressed air was injected into the water through a porous tube and in the second, at low water flowrates, water was sprayed into the air through a nozzle.

The flow patterns in the crossflow zones of the model are shown in Fig. 2. These were obtained by visual observation through the transparent end tube plates, which also showed that the patterns were maintained throughout the model. The patterns are as follows.

1 Spray flow occurring at high mass flow qualities with liquid carried along by the gas as a spray.

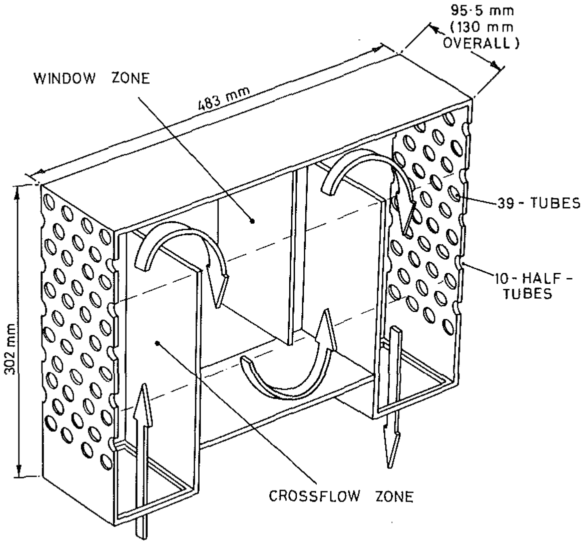

Fig. 1 Experimental heat exchanger

Contributed by the Heat Transfer Division and presented at the Winter Annual Meeting, Atlanta, Georgia, Nov. 27–Dec. 2, 1977, of THE AMERICAN SOCIETY OF MECHANICAL ENGINEERS. Revised manuscript received by the Heat Transfer Division February 17, 1977. Paper No. 77-WA/HT-22.

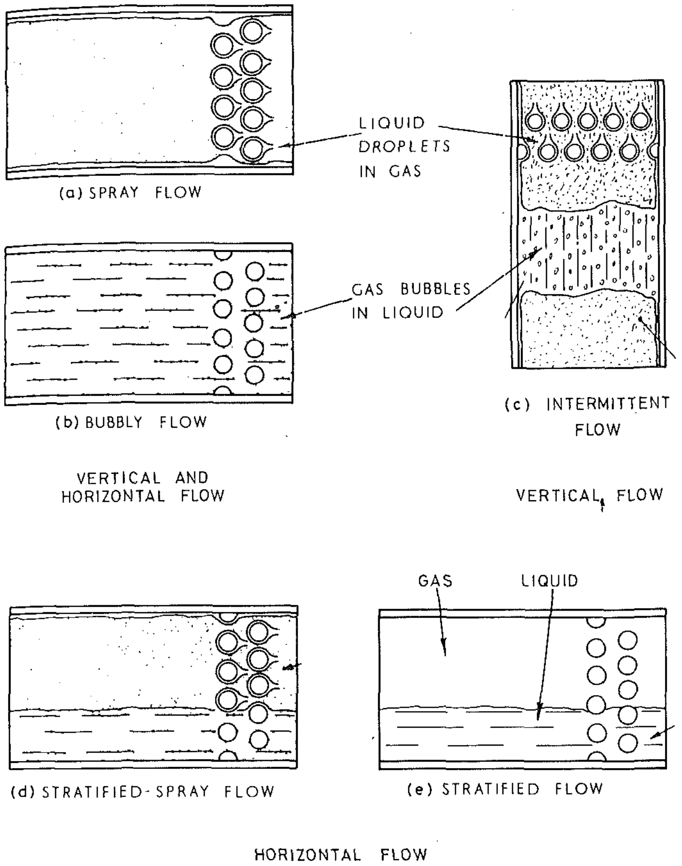

Fig. 2 Shell-side two-phase flow patterns

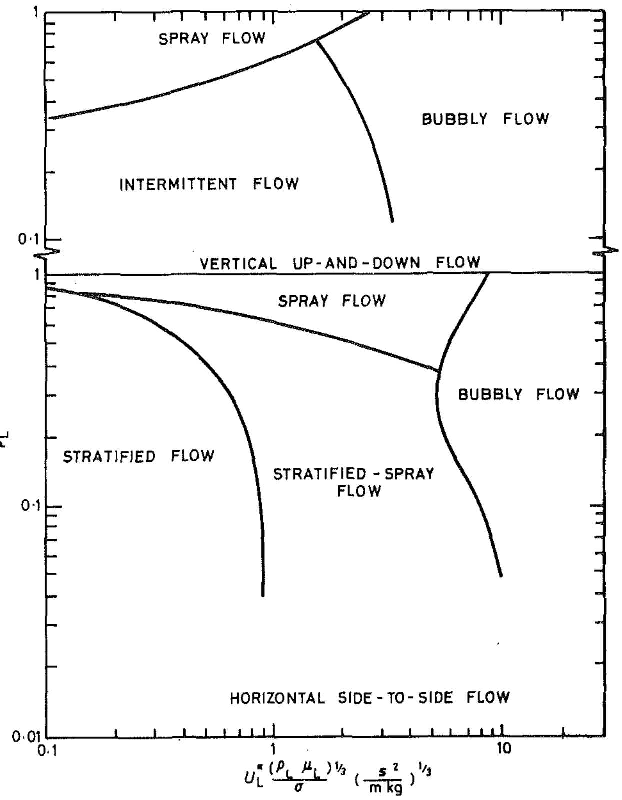

Fig. 3 Shell-side flow pattern maps

2 Bubbly flow occurring at low mass flow qualities with the gas distributed as discrete bubbles in the liquid.

3 Intermittent flow where intermittent slugs of liquid are propelled cyclically through the model by the gas.

4 Stratified-spray flow where the liquid and gas are tending to separate with liquid flowing along the bottom of the model. The gas-phase is entrained as bubbles in the liquid layer and liquid droplets are carried along by the gas as a spray.

5 Stratified flow where the liquid and gas are completely separated.

Spray and bubbly flow occurred with the model of Fig. 1 orientated for either vertical up-and-down flow or horizontal side-to-side flow. Intermittent flow only occurred with vertical up-and-down flow and stratified-spray and stratified flow with horizontal side-to-side flow.

Flow pattern maps were constructed for both vertical and horizontal flow [4, 5] as shown in Fig. 3. The parameters of these maps are those of Baker [6], modified according to Bell, Taborek, and Fenoglio [7]. The map is simply a plot of superficial gas velocity against superficial liquid velocity with physical property terms attached. Superficial is used in the sense that the total flow area and not the actual phase flow area is used to calculate the phase velocity. The flow area referred to is the minimum cross-sectional area for flow through the tube bank.

Equation Used

An equation, which is easy to use, has been developed by Chisholm [8] for predicting pressure drop with two-phase flow in smooth tubes. The equation is

$$\frac{\Delta P_{TP}}{\Delta P_{L0}} = 1 + (\Gamma^2 - 1)\{Bx^{(2-n)/2}(1 - x)^{(2-n)/2} + x^{2-n}\} \quad (1)$$

where n is the Blasius exponent and x the mass flow quality. ΔP_{L0} is the pressure drop for the total mass flowing as liquid and Γ a physical property coefficient defined by

$$\Gamma = \left(\frac{\Delta P_{G0}}{\Delta P_{L0}}\right)^{1/2} \quad (2)$$

where ΔP_{G0} is the pressure drop for the total mass flowing as gas. While no satisfactory general theoretical basis for the coefficient, B, exists a number of situations relevant to crossflow do give theoretical solutions. Homogeneous theory with the Blasius exponent $n = 0$

Nomenclature

A = coefficient in Blasius type equation (equation (12))
B = coefficient in equation (1)
f = crossflow friction factor
K = velocity ratio (= U_G/U_L)
n = index of Reynolds number in Blasius type equation (equation (12))
ΔP_{G0} = pressure drop due to friction if total mixture flows as gas, N/m^2
ΔP_{L0} = pressure drop due to friction if total mixture flows as liquid, N/m^2
ΔP_{TP} = pressure drop during two-phase flow, N/m^2
Re = crossflow Reynolds number
U_G = velocity of gas, m/s
U_G* = superficial velocity of gas, m/s
U_L = velocity of liquid, m/s
U_L* = superficial velocity of liquid, m/s
x = mass flow quality
α = gas volume fraction
Γ = physical property coefficient defined by equation (2)
μ_G = dynamic viscosity of gas, N s/m^2
μ_L = dynamic viscosity of liquid, N s/m^2
ρ_G = density of gas, kg/m^3
ρ_{HOM} = homogeneous density of mixture, kg/m^3
ρ_L = density of liquid, kg/m^3
σ = surface tension, N/m
ψ = parameter defined by equation (9)

corresponds to $B = 1.0$. Flow at changes of section, where the phase velocity ratio remains constant along the flow path, gives [9] (a separated flow model is used)

$$B = \left(\frac{1}{K}\frac{\rho_L}{\rho_G} + K - 2\right) \Big/ (\rho_L/\rho_G - 1) \tag{3}$$

where

$$K = \frac{U_G}{U_L}. \tag{4}$$

In that case $n = 0$ and

$$\Gamma^2 = \frac{\rho_L}{\rho_G} \tag{5}$$

The zero interface shear model [10] approximates [11] to

$$B = \frac{2^{2-n} - 2}{\Gamma + 1} \tag{6}$$

with an associated velocity ratio

$$K = \left(\frac{\mu_L}{\mu_G}\right)^{n/(2-n)} \left(\frac{\rho_L}{\rho_G}\right)^{(1-n)/(2-n)} \tag{7}$$

Lockhart and Martinelli's [12] empirical curve for the two-phase multiplier can be approximated [8, 13] by

$$B = \frac{21\Gamma - 2^{2-n} + 2}{\Gamma^2 - 1} \doteq \frac{21}{\Gamma}. \tag{8}$$

Much of the data used in deriving the empirical curve corresponded to a Γ value of about twenty, giving a B value of the order of unity.

For convenience ψ is used to represent the group.

$$\psi = \frac{\dfrac{\Delta P_{TP}}{\Delta P_{LO}} - 1}{\Gamma^2 - 1} = \frac{\dfrac{\Delta P_{TP}}{\Delta P_{GO}} - \dfrac{1}{\Gamma^2}}{1 - \dfrac{1}{\Gamma^2}}. \tag{9}$$

Equation (1) can then be written

$$\psi = Bx^{(2-n)/2}(1 - x)^{2-n)/2} + x^{2-n}. \tag{10}$$

It is also relevant to note from equations (9) and (10) that where $\Delta P_{TP}/\Delta P_{GO} \gg 1/\Gamma^2$ and $1 \gg 1/\Gamma^2$ then

$$\frac{\Delta P_{TP}}{\Delta P_{GO}} = Bx^{(2-n)/2}(1 - x)^{(2-n)/2} + x^{2-n}. \tag{11}$$

This can sometimes be the most convenient form in which to use the equations, particularly for condensers.

Crossflow Zone Pressure Drop

Pressure drop was measured initially with single-phase flow in the model [4, 5] to obtain crossflow and window zone single-phase data. Friction factors for the crossflow zones were fitted using a Blasius type equation

$$f = \frac{A}{\text{Re}^n}. \tag{12}$$

The crossflow friction factors for this model tend to lie below accepted values for ideal bundles [4].

In the analysis of the two-phase pressure drop measured in the crossflow zones of the model heat exchanger with vertical up-and-down flow, the pressure drops in adjacent zones were combined. This gave the following advantages.

1 Mass velocity effects (change in pressure drop ratio with mass velocity at a given mass flow quality) which are opposite in direction for up-flow and down-flow, tend to be eliminated.

2 The combined pressure drop does not have to be corrected for gravitational effects (reliable methods are not readily available for predicting the gas volume fraction for vertical two-phase flow in tube bundles).

3 A single prediction for crossflow zone pressure drop can be used.

The combined pressure drop data for adjacent crossflow zones of the model are shown in Fig. 4. The single-phase pressure drops ΔP_{GO} and ΔP_{LO} in equation (9) were calculated using the experimental Blasius coefficient A and exponent n for the combined zones ($A = 2.70$ and $n = 0.37$ in equation (12)). The data shown departing from the main trend are for intermittent flow conditions. The fit between equation (10) and the main data in Fig. 4 is obtained with $B = 1.0$. A value of 0.37 was used for n. The physical properties of air and water used in equation (10) were evaluated for a pressure of 10^5 N/m^2 and a temperature of 20°C. Data above a mass flow quality of 0.5 are replotted to a base of $(1 - x)$ to allow a clearer comparison with prediction.

A considerable spread in the crossflow zone pressure drop data was observed with horizontal side-to-side flow in the model. The spread is due to the difference in the type of flow pattern occurring with horizontal flow, that is the data for stratified and stratified-spray flow lie well below the data for spray and bubbly flow; this is shown in Fig. 5. The single-phase pressure drops in equation (9) were calculated as before using the experimental Blasius coefficient A and exponent n ($A = 7.24$ and $n = 0.46$ in equation (12)). Open symbols are used to plot spray and bubbly flow and solid symbols to plot stratified and stratified-spray flow.

Two values of B are used to fit equation (10) to the data in Fig. 5. The first, 0.75, fits the data for spray and bubbly flow and the second, 0.25, fits the data for stratified and stratified-spray flow. A value of 0.46 was used for n the Blasius exponent in both cases.

The fit by Diehl and Unruh (14) to their data for pure horizontal crossflow in a rotated square tube arrangement is also shown in Fig. 5. Their tests ranged from spray flow at high qualities to stratified flow at low qualities but did not include bubbly-type flow. The Diehl and Unruh curve is in good agreement with the crossflow data of this report for spray and stratified flows. Above a quality of 0.6 equation (10) will predict the Diehl and Unruh curve using

$$B = 0.75 + 3.5x^{10} \tag{13}$$

to within two percent.

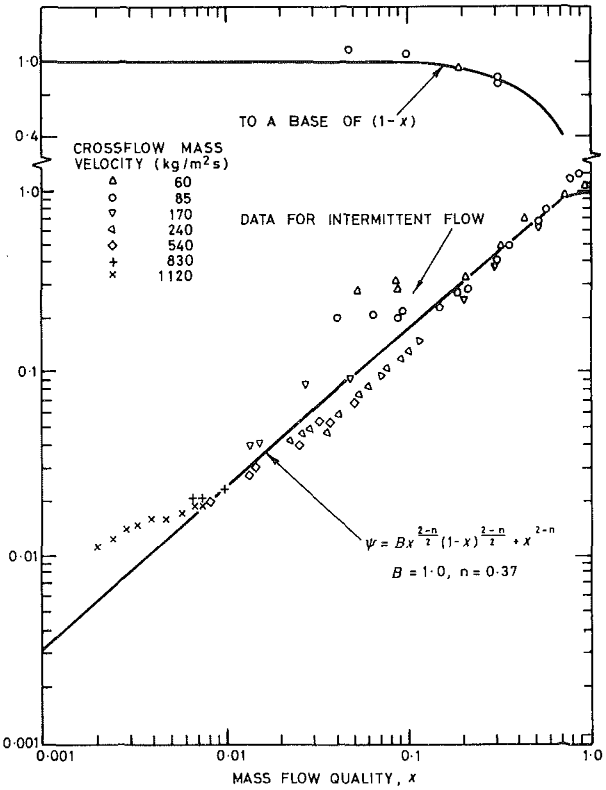

Fig. 4 **Two-phase pressure drop in crossflow zone (vertical up-and-down flow)**

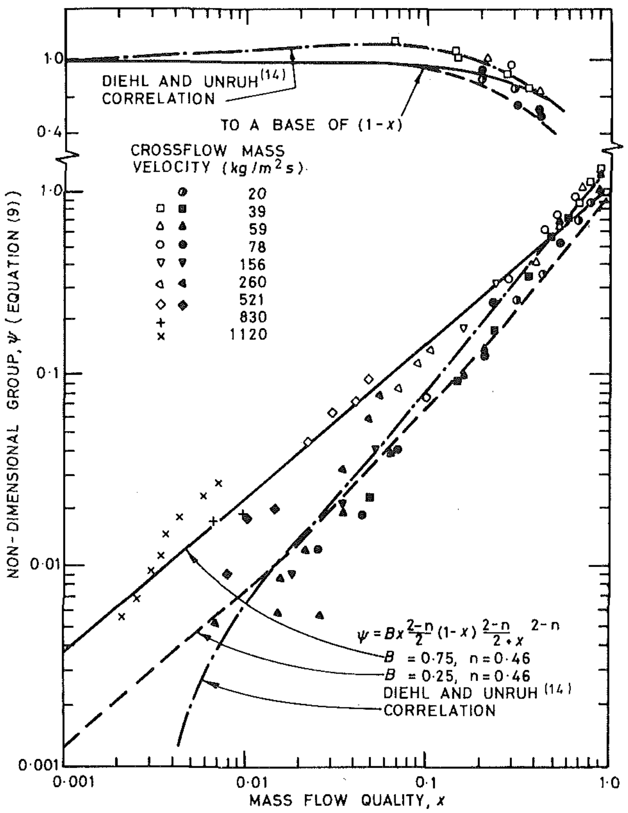

Fig. 5 Two-phase pressure drop in crossflow zone (horizontal side-to-side flow) open symbols for spray and bubbly flow, solid symbols for stratified and stratified-spray flow

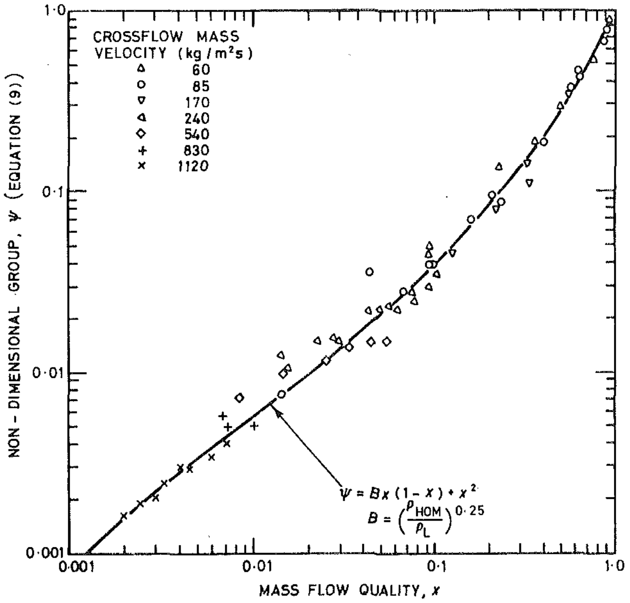

Fig. 6 Two-phase pressure drop in window zone (vertical up-and-down flow)

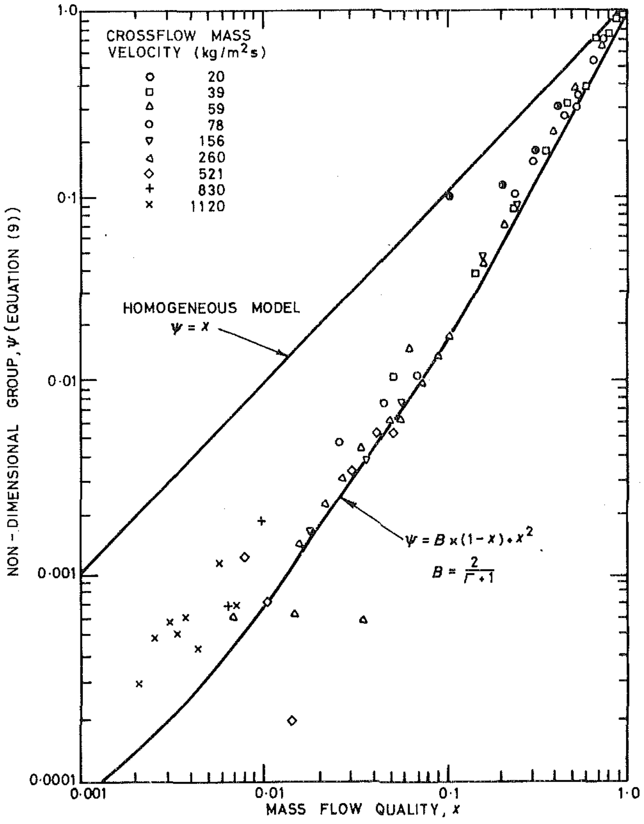

Fig. 7 Two-phase pressure drop in window zone (horizontal side-to-side flow)

It remains to be seen whether B for crossflow is a constant or a function of Γ the fluid physical properties. Chisholm (8) has shown that B is a function both of Γ and mass velocity for flow in tubes. No significant mass velocity effects were noticed in these studies and this agrees with the work of Diehl and Unruh (14) for horizontal crossflow.

Window Zone Pressure Drop

The window zone single-phase pressure drop was expressed as the number of velocity heads lost based on the geometric mean velocity in the window. The measured coefficients were independent of Reynolds number, that is $n = 0$ in equation (12). Equation (10) becomes

$$\psi = Bx(1 - x) + x^2. \qquad (14)$$

A prediction for a window zone based on the homogeneous flow model corresponds with $B = 1$ in equation (14); that is

$$\psi = x. \qquad (15)$$

This simple result is one advantage of using equation (1).

The experimental two-phase data for the window zones with vertical up-and-down flow are shown in Fig. 6. The single-phase pressure drops ΔP_{G0} and ΔP_{L0} in equation (9) were calculated using 1.88 velocity heads (the experimental loss). The data are well represented by equation (14) with

$$B = \left(\frac{\rho_{HOM}}{\rho_L}\right)^{0.25}. \qquad (16)$$

This form of equation was suggested by the form of correlation obtained by Chisholm and Rooney [15] for two-phase flow through orifices.

The data for the window zones with horizontal flow are shown in Fig. 7. The single-phase pressure drops in equation (9) were calculated using the experimental velocity head loss of 2.34. Although a detailed study of the flow patterns in the window zones was not possible, it was evident that stratified flow prevailed for most of the test conditions. From equation (6) with $n = 0$

$$B = \frac{2}{\Gamma + 1}. \qquad (17)$$

From Fig. 7 it is apparent that equation (14) with this value of B

is in good agreement with experiment. For air and water at 10^5 N/m^2 and 20°C, $\Gamma = 29$ and B is thus 0.067.

Tube Row Submergence

The performance of a condenser is reduced when part of the tube bundle is submerged in condensate owing to the reduced heat transfer on these tubes.

In a separate set of tests with stratified flow only the liquid levels along the first and last crossflow zones of the model were measured for three different flowrates. The free volume above these levels was integrated along the crossflow zone and converted into a mean liquid volume fraction as shown in Fig. 8.

The liquid fraction can be evaluated from

$$1-\alpha = \frac{1}{1+\dfrac{x\rho_L}{K(1-x)\rho_G}}. \qquad (18)$$

The velocity ratio K by the zero interface shear model is given by equation (7), and the curve corresponding to equations (7) and (18) is shown in Fig. 8. Surprisingly while these equations give good agreement at lower flow qualities, they underestimate the data at higher flow qualities.

Fig. 8 also shows the deduced velocity ratios. Values as high as 100 were obtained compared with theoretical values of 35. This aspect of the work is receiving further attention as part of the research programme of the Heat Transfer and Fluid Flow Service operated by the National Engineering Laboratory and AERE, Harwell, UK.

Conclusions

Equations are presented for calculating the shell-side pressure drop for segmentally baffled shell-and-tube heat exchangers with two-phase flow. The equations have been developed from experimental work where the heat exchanger models did not have manufacturing clearances.

The pressure drops were correlated using the equation

$$\frac{\Delta P_{TP}}{\Delta P_{LO}} = 1 + (\Gamma^2 - 1)\{Bx^{(2-n)/2}(1-x)^{(2-n)/2} + x^{2-n}\}.$$

In crossflow the following approximate values of B are given by experimental data:

vertical up-and-down spray and bubbly flow	$B = 1.0$
horizontal side-to-side spray and bubbly flow	$B = 0.75$
horizontal side-to-side stratified and stratified-spray flow	$B = 0.25.$

For the windows, where $n = 0$:

vertical up-and-down flow $B = \left(\dfrac{\rho_L}{\rho_{HOM}}\right)^{0.25}$

horizontal side-to-side flow $B = \dfrac{2}{\Gamma + 1}$

Acknowledgment

This paper is presented by permission of the Director, National Engineering Laboratory, Department of Industry. It is British Crown copyright reserved.

References

1 Sutherland, L. A., Murray, I., "Pressure Drop and Heat Transfer on the Shell-side of a Model Heat Exchanger with Two-Phase Flow," NEL Report No. 395, 1969, National Engineering Laboratory, East Kilbride, Glasgow.

2 Grant, I. D. R., "Two-Phase Flow on the Shell-side of Shell-and-Tube Heat Exchangers," *Heat and Fluid Flow in Steam and Gas Turbine Plant*, Conf., Pub. No. 3, Instn Mech. Engrs, London, 1973, pp 224–251.

3 Grant, I. D. R., "Flow and Pressure Drop with Single-phase and Two-phase Flow on the Shell-side of Segmentally Baffled Shell-and-tube Heat Exchangers," *Advances in Thermal and Mechanical Design of Shell-and-tube Heat Exchangers*, Report of a meeting at NEL, 28 November, 1975, NEL Report No. 950, 1975, National Engineering Laboratory, East Kilbride, Glasgow.

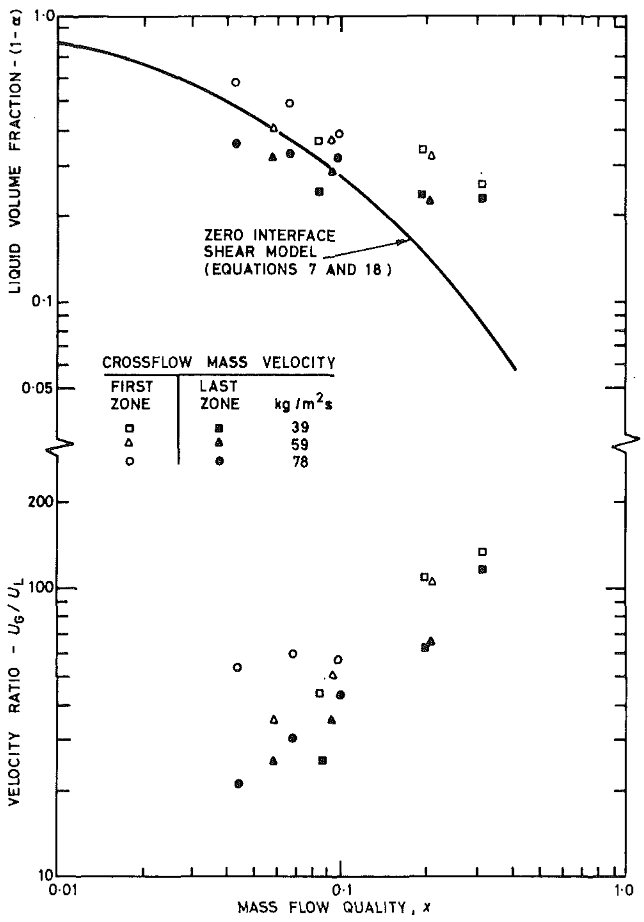

Fig. 8 Liquid fraction and velocity ratio for stratified flow

4 Grant, I. D. R., and Murray, I., "Pressure Drop on the Shell-Side of a Segmentally Baffled Shell-and-Tube Heat Exchanger with Vertical Two-phase Flow," NEL Report No. 500, 1972, National Engineering Laboratory, East Kilbride, Glasgow.

5 Grant, I. D. R., Murray, I., "Pressure Drop on the Shell-Side of a Segmentally Baffled Shell-and-Tube Heat Exchanger with Horizontal Two-phase Flow," NEL Report No. 560, 1974, National Engineering Laboratory, East Kilbride, Glasgow.

6 Baker, O., "Simultaneous Flow of Oil and Gas," *Oil Gas Journal.*, Vol. 53, No. 12, 1954, pp. 185–190.

7 Bell, K. J., Taborek, J., Fenoglio, F., "Interpretation of Horizontal In-tube Condensation Heat Transfer Correlations with a Two-phase Flow Regime Map," *Chem. Engng. Prog. Symp. Ser.*, Vol. 66, No. 102, 1970, pp 150–165.

8 Chisholm, D., "Pressure Gradients due to Friction during the Flow of Evaporating Two-phase Mixtures in Smooth Tubes and Channels," *Int. Journal Heat Mass Transfer*, Vol. 16, 1973, pp 347–358.

9 Chisholm, D., "Prediction of Pressure Drop at Pipe Fittings during Two-phase Flow," *Proc. 13th Int. Inst. Refrigeration Cong. Washington, D. C.*, 27 Aug.–3 Sept., Vol. 2, pp 781–789.

10 Gloyer, W., "Thermal Design of Mixed Vapour Condensers," *Hydrocarbon Process*, Vol. 49, No. 6, 1970, pp 103–108.

11 Chisholm, D., Discussion of paper "A Theoretical Solution of the Lockhart and Martinelli Flow Model for Calculating Two-phase Pressure Drop and Hold-up," by T. Johannessen, *Int. Journal Heat Mass Transfer*, Vol. 16, 1973, pp 225–226.

12 Lockhart, R. W., and Martinelli, R. C., "Proposed Correlation of Data for Isothermal Two-phase Two-component Flow in Pipes," *Chem. Engng. Prog.* Vol. 45, No. 1, 1949, pp 39–48.

13 Chisholm, D., and Laird, A. D. K., "Two-phase Flow in Rough Tubes," Trans. ASME, Vol. 80, No. 2, 1958, pp 276–286.

14 Diehl, J. E., Unruh, C. H., "Two-phase Pressure Drop for Horizontal Crossflow through Tube Banks," ASME Paper No. 58-HT-20, New York, N.Y., 1958.

15 Chisholm, D., and Rooney, D. H., "Pressure Drop during Steam/Water Flow through Orifices," *Journal Mech. Engng Sci.*, Vol. 16, No. 5, 1974, pp. 353–355.

D. M. Snider
Idaho National Engineering Laboratory,
EG&G Idaho, Inc.,
Idaho Falls, Idaho

The Thermal-Hydraulic Phenomena Resulting in Early Critical Heat Flux and Rewet in the Semiscale Core

Analysis was performed to determine the thermal-hydraulic behavior in the electrically heated core simulator of the Semiscale Mod-1 system during the early stage of a simulated LOCA initiated by a large cold leg break. The calculated incore hydraulic behavior was used to obtain a better understanding of early CHF (480 to 700 ms after rupture) and the occurrence of rewet in some locations after CHF. Analysis indicated that shortly after rupture the flow in the upper core stagnated for 600 ms, and the core rapidly voided of coolant. In the center and lower regions of the core, the calculated fluid qualities were between 30 and 70 percent at the time of measured CHF. The high fluid qualities in the flow channels about the heater rods indicated that the mechanism of CHF was dryout of the heater rod surfaces. Critical heat flux did not happen at the location of instantaneous flow stagnation associated with the flow reversal; nor did CHF occur in the region of the prolonged flow stagnation. At about 700 ms after rupture the core flow completely reversed direction, and the influx of coolant from above the heated core was responsible for the measured rewets.

Introduction

If a large rupture were to occur in an inlet (cold leg) pipe of a pressurized water reactor (PWR) vessel, the loss of coolant would produce a rapid decrease in pressure, the core coolant would reverse flow direction, and eventually the core would experience a critical heat flux (CHF) (loss of heat transfer leading to a rapid increase in fuel rod surface temperature). In such a postulated accident, the nuclear energy generation rate would decrease with the loss of the water moderator, but without a sufficient cooling period before CHF to reduce the stored thermal energy in the fuel rods and without effective emergency core cooling the cladding temperatures could rise to levels which could cause cladding melting or structural failure. In order to better understand the thermal-hydraulic behavior and mechanism leading to CHF in a PWR and to provide more information to better calculate the time of CHF in a PWR, results from a Semiscale Mod-1 experimental test were analyzed. Semiscale is a small non-nuclear system modeling a PWR for the purpose of providing data for evaluating system and core behavior during simulated loss-of-coolant accidents (LOCAs). Experimental and analytical results for the thermal-hydraulic behavior and CHF in the core during a simulated large cold leg pipe break are presented in this paper.

Prior experimental studies have been undertaken to understand the behavior which may occur in a core from a large cold leg pipe rupture. Leung [1] observed blowdown (loss of coolant resulting in depressurization) of Freon-11 in an internally heated annulus. He found that during blowdown with reverse flow the heated section quickly voided after the flow reversed direction and CHF was observed to occur at high void fraction. A critical heat flux did not happen at the time of instantaneous flow stagnation when the coolant reversed direction. Smith, Price, and Griffith [2], studying flow reversals of Freon-113 in a heated tube at constant pressure, also observed that CHF did not occur at the first reduction of flow to zero. The experiments by Smith did not product flow stagnation for an extended time within the tube, but Smith hypothesized that the possible occurrence of a stagnation for an extended time in a PWR would produce the worst conditions leading to CHF.

The Semiscale Mod-1 experiments, unlike those of Leung or Smith, were conducted with an electrically heated 40-rod bundle core with water as the coolant and simulated a pipe rupture from nominal PWR operating pressure and temperature. The purpose of the Semiscale non-nuclear thermal-hydraulic experiments is to provide experimental data that can be applied to the development and verification of analytical models describing LOCA phenomena in water cooled nuclear power plants. In the Semiscale tests with a double offset shear cold leg pipe rupture, a critical heat flux was observed to occur in the center and lower parts of the core within 700 ms after rupture and as early as 480 ms [3]. In some cases those rods which experienced CHF were rewet within 1.5 s after rupture.

Contributed by the Heat Transfer Division for publication in the JOURNAL OF HEAT TRANSFER. Manuscript received by the Heat Transfer Division March 3, 1978.

The purpose of this study is to improve the understanding of the core thermal-hydraulic phenomena during a simulated large cold leg pipe break using Semiscale as the tool, and to determine the conditions related to the occurrence of early CHF and rewet. To this end, the internal core hydraulic equations were solved using boundary conditions derived from measured data and the core energy transfer rate calculated from measured heater rod temperature data. Details of the results of these calculations and how they relate to measured CHF data are presented.

Semiscale Experimental System and Operating Procedure

The Semiscale Mod-1 experimental apparatus shown in Fig. 1 is a small scale model of a four-loop pressurized water reactor. The Semiscale system, which has a liquid volume of approximately 0.22 m^3, consists of a pressure vessel and internals, an intact loop consisting of a pressurizer, steam generator, and coolant pump, and a broken loop with hydraulic resistances that simulate an inactive steam generator and a locked rotor pump. The intact loop of the Semiscale system models three loops of a typical four-loop PWR. The broken loop simulates the fourth PWR loop. Simulated pipe ruptures are performed by blowing out rupture disks in the broken loop piping. A detailed description of the system configuration can be found in [4].

The Mod-1 core in the Semiscale system consists of 40 electrically heated rods of typical PWR fuel rod diameter (1.072 cm). Four Chromel-Alumel thermocouples swaged between an inner and outer cladding (Fig. 2) provide rod cladding temperature measurements at different axial locations along the 168 cm heated length of the heater rods. The overall length of the rod is about 526 cm and the bottom of the 168 cm heated section is about 363 cm below the vessel cold leg centerline. The rods extend from the bottom of the heated section to the vessel upper plenum, pass out through the vessel upper head, and are held in place by ten evenly spaced grid spacers. The axial power distribution has a half cosine shape with a center axial power factor of 1.58. The core minimizes the influence of nonheated boundaries surrounding the heated core rod bundle. A thermal insulator was located between the heated core bundle and the core shroud. The thermal insulator serves to reduce heat transfer to the downcomer during steady state conditions and reduces the transfer of stored heat from the core barrel to the coolant during the transient. The distance between the heater rods at the periphery of the rod bundle and the core shroud is half the distance between heater rods, which gives close to the same mass flux about all the heated rods.

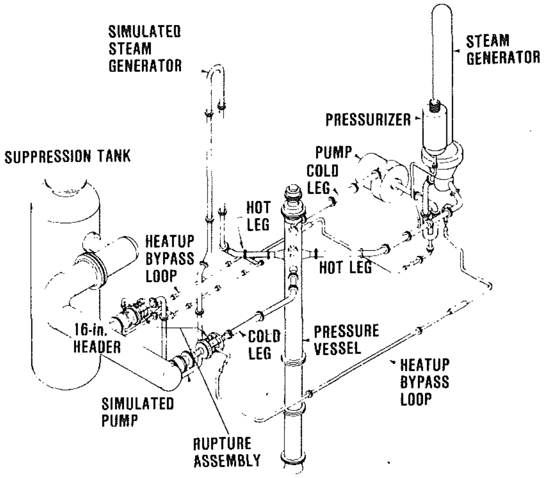

Fig. 1 Semiscale Mod-1 system cold leg break configuration isometric

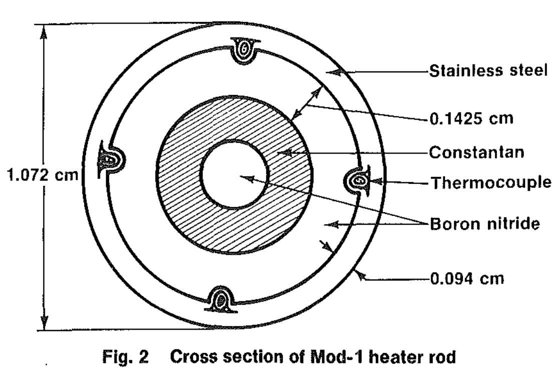

Fig. 2 Cross section of Mod-1 heater rod

Fluid density, flow, pressure, and temperature measurements were made at the core inlet and in the intact and broken loop hot leg piping adjacent to the vessel upper plenum. Fluid temperatures were measured at every other grid spacer in the heated core. Fluid density measurements were obtained from a gamma attenuation device. The flow measurements were obtained from both a turbine flowmeter (which measured volumetric flow rate) and a drag disk flowmeter (which measured momentum flux) used in conjunction with the fluid density measurement. Fluid temperature was measured using Chromel-Alumel thermocouples and platinum resistance temperature detectors. A strain gage diaphragm transducer connected between the upper and lower plenums by water-filled lines was used to measure the upper to lower plenum differential pressure. A Hall-effect multiplier device measured total core power, a digital voltmeter measured core voltage, and a shunt circuit provided core current.

Experimental data from Test S-02-9 [5] were used for this analysis. Test S-02-9 was a simulated double offset shear cold leg break test, and the experimental results during the early period of blowdown in this test were similar to results from other Semiscale tests with large cold leg breaks [6]. This test had a flat radial power profile (some Semiscale tests had a center-peaked radial power profile) which could be better modeled by the single channel hydraulic solution. Conditions prior to rupture were a core power of 1.56 MW, a core inlet temperature of 557 K, a core temperature rise of 38 K, a system pressure of 15.5 MPa, and a peak power density of 38.9 kW/m. For this test the core contained two failed heater rods, 37 powered heater rods, and one liquid level probe.

In preparation for Test S-02-9, the system was filled with treated demineralized water and vented to assure a liquid full system. The system was heated to initial conditions and held for 10 to 20 min in order to establish system equilibrium. The rupture assemblies were then actuated to produce a simulated double-ended pipe break. Digitized data were recorded at approximately 17 ms intervals.

Core Hydraulic Calculation

The core hydraulics were solved using the computer program COBRA-IV-I [7].[1] COBRA-IV-I solved the governing conservation equations for mass, momentum, and energy using homogeneous flow theory and thermal-equilibrium conditions. The COBRA-IV-I computer program was designed for multichannel core calculations with lateral energy and momentum transfer between subchannels. The Semiscale core was modeled as a single channel extending from the core barrel inlet to the upper plenum as illustrated in Fig. 3. The single channel COBRA-IV-I calculation was used for the radially flat power profile test as a prelude to multichannel analysis of tests with radial peaking power. The model contained 35 volumes with each volume having an axial height of 12.7 cm. The flow area contraction, which existed between the core barrel inlet and the start of the heated core, and the expansion at the top of the heated core where the core shroud terminated were included within the model. The wall component of the surface stress tension used in the conservation of momentum equation was modeled by a Blasius type empirical friction factor

---

[1] Code configuration control number H00062IB, Idaho National Engineering Laboratory.

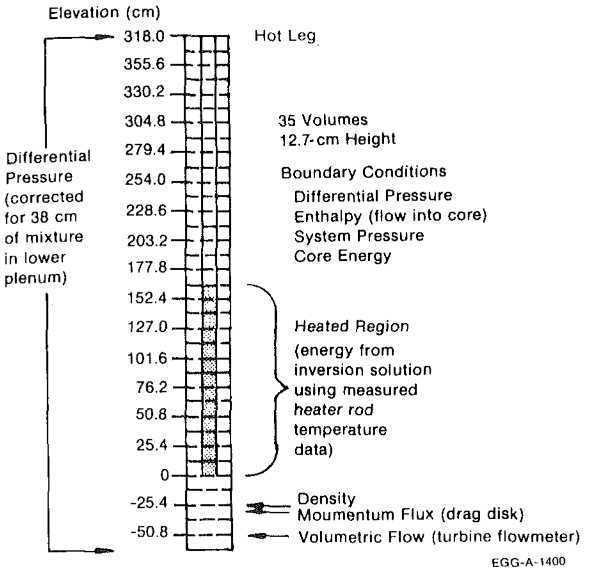

Fig. 3 COBRA-IV-I single-channel model for the Semiscale Mod-1 core

equation. A homogeneous two-phase multiplier was used to account for the increased pressure loss when the homogeneous quality was between zero and unity. The grid spacers, the mixer plate in the core barrel inlet housing, and the drag disk and turbine flowmeter flow resistances were included in the model as constant resistance factors determined from single-phase fluid experimental data.

The boundary conditions in the hydraulic calculation included:

a) System pressure

b) Enthalpy at the core bottom or top when flow was into the core

c) Differential pressure between core bottom and top

d) Heat transfer rate between core and coolant.

These boundary conditions were calculated from measured data. Enthalpy at the core bottom was determined from the measured fluid density and system pressure. Enthalpy at the core top was determined from system pressure and fluid densities measured next to the vessel in the intact and broken loop hot legs. The differential pressure between the upper plenum to the lower plenum was corrected for a 38 cm head of mixture which existed between the pressure measurement tap in the lower plenum and the core barrel inlet. The specified energy transfer from the core heater rods to the coolant was obtained from an inverse heat conduction solution (INVERT)[2] using measured heater rod temperature data.

COBRA-IV-I provides the option to use an implicit or explicit scheme for solution of the applicable conservation equations. The explicit scheme was designed for fast transient analysis. For this study, the implicit method of solution was used to obtain steady state conditions and the explicit method was used for the transient solution. The calculated variables were entered on magnetic tape at 20 ms intervals. Results presented are taken from data on the tape and, therefore, are limited to a 20 ms calculation resolution.

In this study, the single-channel model provided radially integrated variables in the core. Although subsequent multichannel analysis has shown that some radial redistribution of coolant occurs during both the steady state and the transient phases from variations in the fluid surface shear stresses and nonheated surfaces, the calculated variables from the multichannel calculations are not much different than those from the single-channel calculation. Therefore, the discussion and conclusions drawn from the single-channel study are consistent with those from a multichannel solution.

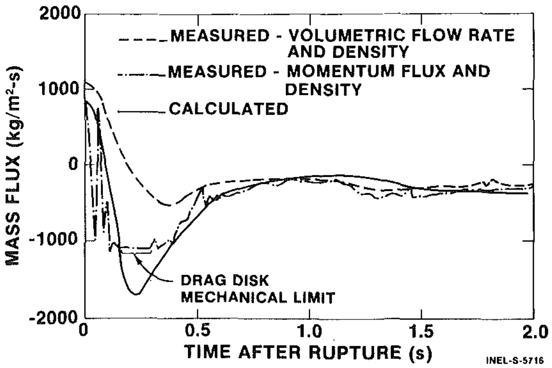

Fig. 4 Comparison of calculated mass flux with measured data at the core inlet

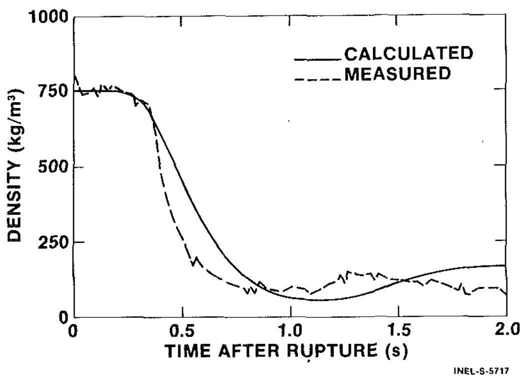

Fig. 5 Comparison of calculated density with measured data at the core inlet

Comparison of Calculations with Experiment Data

Comparisons between calculations and experiment data are presented in Figs. 4 and 5. Because of the complex Semiscale Mod-1 vessel and core geometry neither incore flow variables nor variables to define thermodynamic state were measured. Hence the calculated variables could only be compared with data measured in the core barrel inlet near the bottom of the core. Fig. 4 shows the calculated mass flux compared with the measured flux at the elevation of the momentum flux (drag disk) measurement. The measured mass fluxes shown were obtained from both the momentum flux and volumetric flow (turbine flowmeter) combined with the measured density. Between 100 and 300 ms after rupture, the drag disk reached its mechanical limit, and during this period no data were available for comparison with the calculation. The turbine flowmeter had a slower response time than the drag disk and did not measure the fast flow reversal accurately. Beyond 800 ms after rupture, however, the turbine flowmeter provided data which compared well with those from the drag disk and with the calculated mass flux. Fig. 5 compares the calculated and measured fluid densities. The density was also calculated well by COBRA-IV-I.

The good agreement between the COBRA-IV-I calculations and the experiment data lends confidence that COBRA-IV-I calculated the behavior correctly in the interior of the Semiscale Mod-1 core.

Results and Discussion

In experiments at nearly steady-state conditions, the critical heat flux has been found to be strongly related to fluid quality and to a lesser extent dependent on mass flux [8]. The influence of the quality and mass flux on critical heat flux during blowdown in which a flow reversal occurs is discussed. The COBRA-IV-I calculated results were used to provide the hydraulic variables associated with CHF and rewet. At times shortly after initiation of rupture the low flow resistance path to the cold leg break produced a fast flow reversal at the

---

[2] Code configuration control number H000861B, Idaho National Engineering Laboratory.

bottom of the core (Fig. 4). The flow reversal was calculated to extend above the center of the core heated region where a flow stagnation occurred, as shown in Fig. 6. The axial flow rates shown in Fig. 6 indicate that the flow stagnation occurred close to the 89-cm elevation.[3] About 700 ms after rupture the fluid above the stagnation region reversed direction, and coolant flowed from the upper plenum down through the core.

The center and lower core regions rapidly voided during the first 800 ms, whereas the upper core did not empty to as great an extent. This voiding rate is characterized in Fig. 7, which gives the calculated qualities at various axial elevations. Examination of these curves reveals that within 500 ms the quality increased from zero to about 90 percent in the central and lower regions of the core. Three major factors contributed to the fast rate of voiding in the center and lower parts of the core. First, the flow stagnation located within the core caused the core to empty from both ends. Second, coolant that was heated initially as it flowed up the core was reheated as it reversed direction and passed back down through the central and bottom regions of the core. The reheating process increased the mixture specific volume, which increased the rate of expulsion of coolant from the core. Third, the system pressure rapidly decreased as the system changed from a subcooled to a saturated state (subcooled blowdown). The pressure decrease (from 15.5 to 11 MPa within 50 ms) produced an increase in core to coolant heat transfer rate as shown in Fig. 8. With the drop in system pressure, the difference between the pressure of the water vapor at the heater rod surface and the pressure of the bulk fluid increased, which enhanced nucleate boiling. The result was that after rupture and up to the time of CHF, the core heat flux was larger (by as much as 45 percent) than the heat flux level prior to rupture (Fig. 7).

The increase in heat transfer caused by the subcooled depressurization is an important point to consider for those experimentally or analytically attempting to study core behavior during the early part of a LOCA. If during an experimental study, subcooled blowdown is not simulated, the energy transferred from the core to the coolant will be low. For the high power region of the Semiscale Mod-1 core, 12 to 15 percent more heat was transferred to the coolant prior to CHF than could have been added at the initial operating level. Smith, Price, and Griffith [2] in their calculations for the time to void a PWR fuel assembly of coolant performed analysis at constant pressure and, therefore, did not consider the addition of heat from enhanced nucleate boiling caused by subcooled blowdown. Their estimated times for voiding a PWR fuel assembly would presumably be shorter with the additional energy.

The upper part of the core, from the time of rupture until CHF, did not experience the fast rate of emptying or reach as high a void fraction level as did the center and lower parts of the core (Fig. 7). This upper region maintained more coolant partly because the fluid did not reheat after a reversal of flow direction. Also, for the half cosine axial distribution of power, the heat generation rate was lower in the upper core compared with that in the central core region, and less energy was transferred from core to coolant. This lower energy transfer rate did not produce as rapid an expulsion rate of coolant from the upper core as occurred for the central section of the core.

Fig. 9 shows the calculated quality compared with the mean heat flux at the core peak power zone. The axial peak power region was located at about the center of the core (53 to 79 cm) and the thermal-hydraulic behavior at this level was typical of both center and lower parts of the core where CHF predominantly happened. The mean heat flux was determined using 22 flux values calculated from measured heater rod temperature data in the peak power zone and the inverse conduction solution. Curves representing one standard deviation above and below the mean heat flux are also shown in Fig. 9. The variation about the mean heat flux up to the time of CHF (450 to 630 ms) was small, but became larger after CHF because of the

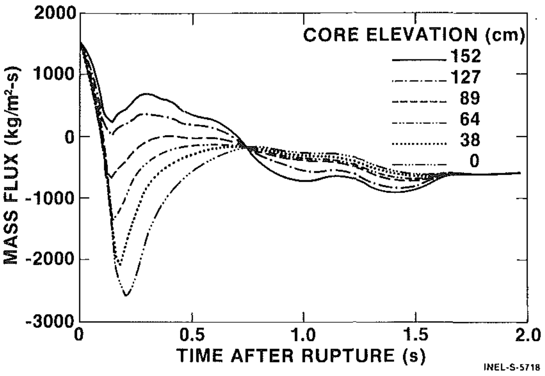

Fig. 6 Calculated mass flux at axial core elevations above bottom of heated core

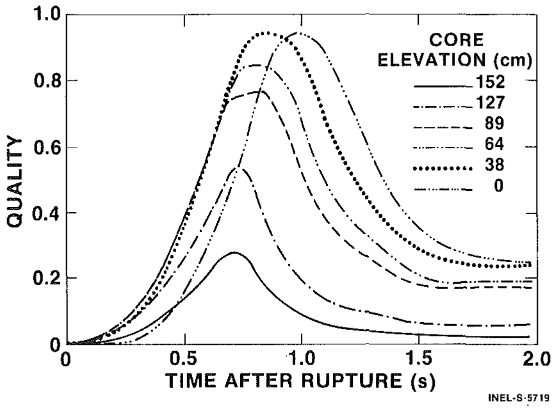

Fig. 7 Calculated quality at axial core elevations above bottom of heated core

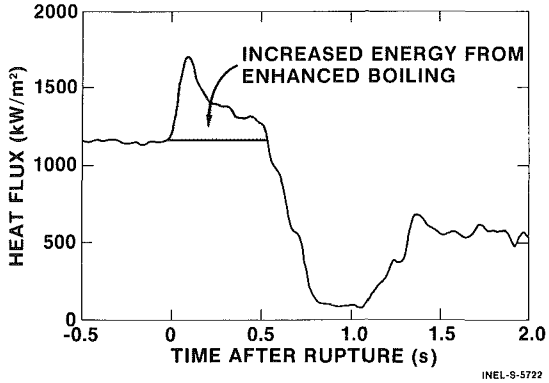

Fig. 8 Average heat flux from measured data at the core peak power zone (53 to 79 cm elevation)

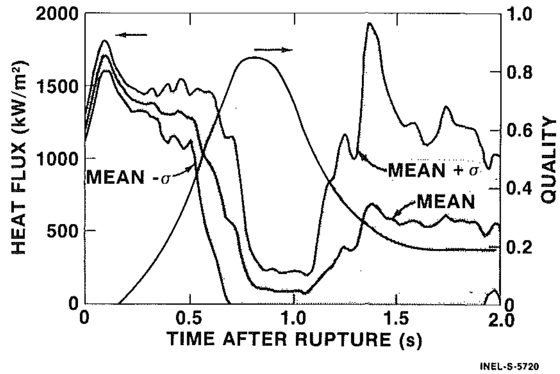

Fig. 9 Comparison of calculated quality with the average heat flux from measured data at the core peak power zone (53 to 79 cm elevation)

---

[3] Elevations are distances above the bottom of the heated core.

occurrence of some rewetting. Fig. 9 shows that the heat flux rapidly decreased during the time of rising quality (500 to 650 ms). This decrease in heat flux was indicative of CHF. The rate of change of the quality curve is steep, and the quality ranges from 30 to 65 percent during the 150 ms period in which the critical heat fluxes occurred. The range in quality corresponds to an 80 to 96 percent void fraction which suggests that the critical heat flux resulted from dryout at the rod surface as opposed to a steam film forming between the rod and a low quality mixture.

The mass flux has been found to be an important variable influencing CHF under quasi-steady test conditions; however, this analysis indicated the mass flux was not the principal independent variable influencing early CHF in this Semiscale Mod-1 experiment. Fig. 10 compares the mass flux and the mean heat flux at the peak power zone. CHF did not occur at the instantaneous stagnation associated with the flow reversal. This observation is consistent with other studies [1, 2]. The relative unimportance of mass flow rate on CHF is seen to be especially true in the upper section of core where the analysis showed a prolonged (600 ms) flow stagnation (Fig. 6). The lack of mixing and reduced convection did not lead to a CHF as might be expected, indicating the low flow rates or prolonged stagnation does not necessarily produce early CHF in the Semiscale Mod-1 system.

From examining the calculated incore hydraulics and heat flux, a descriptive account of the behavior leading to CHF during the blowdown transient can be formulated. As the coolant changed from subcooled to saturated state (about 100 ms after the pipe rupture), the high mass flux would have produced a turbulent bubble flow regime. Bubbly flow was visually observed by Leung during the initial stage of blowdown. As the core rapidly emptied from 100 to 600 ms, the void fraction approached unity which would have given some entrained liquid in the center of the almost voided flow channels while leaving a liquid film at the wall. As the void fraction increased and deentrainment to the liquid film decreased, the liquid film rapidly dried out. The rate at which the film dried out can be estimated by considering all the liquid in the core to be located at the heater rod walls, and no entrainment to the liquid film. For a film thickness of 0.05 cm which corresponds to a thermodynamic equilibrium quality of about 30 percent, the time to vaporize the film with a rod surface heat flux of 1.04 MW/m^2 would be about 48 ms. This illustrates the rapid rate at which dryout would happen as the core emptied and deentrainment ceased.

In the Semiscale core during Test S-02-9 and other cold leg break tests, core locations which experienced CHF often were rewet shortly after the CHF [3]. In most cases the rewet shortly after CHF was only temporary, and another CHF occurred. The effect of the rewet at an axial peak power location was to reduce the maximum rod surface temperture by 55 to 83 K below that of a similar rod at the peak power location which did not rewet. The rewet behavior depends strongly on surface temperature and the amount of coolant for rewetting the surface [9]. Analysis indicated that the rewets resulted from the influx of a lower enthalpy mixture into the heated core after complete flow reversal. The quality gradient increased in the downward direction (Fig. 7) after 1 s. The heater rod surface temperatures, on the other hand, peaked in the core center (because of the half cosine shaped power profile) and decreased above and below the center after CHF occurred. The resulting reestablishment of high cooling rate after CHF happened where the quality and rod surface temperatures were sufficiently low to allow rewets. Above the core center the quality was low (Fig. 7) as were the rod surface temperatures after CHF, and this combination of quality and surface temperature led to the measured rewets. The center of the core had both higher quality and higher rod surface temperatures after CHF (temperatures reached 760 K prior to the time of rewet) than did the upper region of the core. The increased quality and temperature led to only some rods rewetting. In the lower part of the core the quality increased from that of the center regions, but the surface temperatures after CHF were lower. The combination of surface temperatures and quality led to a similar rewet behavior observed in the core center; some rods rewet whereas others did not rewet.

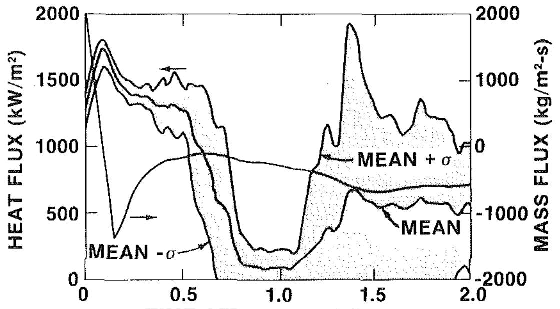

Fig. 10 Comparison of calculated mass flux with the average heat flux from measured data at the core peak power zone (53 to 79 cm elevation)

Conclusion

The calculated thermal-hydraulic behavior and experimental data provided a better understanding of the core phenomena and the conditions leading to the early CHF and rewet during blowdown produced by a large cold leg pipe rupture. On the basis of results obtained in this study, specific conclusions can be drawn:

a) After rupture, flow stagnation occurs in the upper section of core and lasts until about 700 ms after rupture.

b) During the flow stagnation time period, the center and lower core empty rapidly. The fast rate of voiding is produced by the core emptying from both ends, a reheating of coolant after flow reversal, and an increased heat flux produced by enhanced boiling from the rapid subcooled depressurization.

c) Voiding of flow channels about the heater rods in the center and lower core leads to a dryout of the heater rod surfaces.

d) Critical heat flux does not happen at the instantaneous flow stagnation associated with the flow reversal, nor does CHF occur in the region of the prolonged flow stagnation.

e) The observed rewetting of some rods which experienced CHF is produced by an influx of coolant into the top of the heated core after complete flow reversal (after 700 ms).

References

1 Leung, J. C., "Occurrence of Critical Heat Flux During Blowdown with Flow Reversal," M.S. Thesis, Northwestern University, April 1976.

2 Smith, R. A., Price, F. A., and Griffith, P., "Analysis of Critical Heat Flux in Flow Reversal Transients," ASME JOURNAL OF HEAT TRANSFER, Vol. 98, No. 2, May 1976, pp. 152–158.

3 Larson, T. K., "Core Thermal Response During Semiscale Mod-1 Blowdown Heat Transfer Tests," ANCR-NUREG-1285, June 1976.

4 Feldman, E. M., and Olson, D. J., "Semiscale Mod-1 Program and System Description for the Blowdown Heat Transfer Test (Test Series 2)," ANCR-1230, Aug. 1975.

5 Crapo, H. S., Jensen, M. F., and Sackett, K. E., Experiment Data Report for Semiscale Mod-1 Tests S-02-9 and S-02-9A (Blowdown Heat Transfer Tests)," ANCR-1236, Jan. 1976.

6 Cozzuol, J. M., "Thermal-Hydraulic Analysis of the Semiscale Mod-1 Blowdown Heat Transfer Test Series," ANCR-NUREG-1287, June 1976.

7 Wheeler, C. L., et al., COBRA-IV-I, "An Interim Version of COBRA for Thermal-Hydraulic Analysis of Rod Bundle Nuclear Fuel Elements and Cores," BNWL-1962, March 1976.

8 Tong, L. S., "Boiling Crisis and Critical Heat Flux, "TID-25887, 1972.

9 Collier, J. G., Convective Boiling and Condensation, McGraw-Hill, New York, 1972.

S. S. Sadhal[1]
Graduate Student.

M. S. Plesset
Professor.
Fellow ASME

Division of Engineering and Applied Science,
Department of Engineering Science,
California Institute of Technology,
Pasadena, Calif. 91125

Effect of Solid Properties and Contact Angle in Dropwise Condensation and Evaporation

For droplets condensing on or evaporating from a solid surface, the effects of the solid material properties and the droplet contact angle are analyzed by solving the steady heat-conduction equation for a geometry consisting of a spherical segment droplet on a semi-infinite solid. In obtaining the solution it is assumed that heat is transported to or from the solid only through the droplet and that there is perfect thermal contact at the solid-liquid interface. With suitable boundary conditions at the liquid-vapor interface some exact and approximate solutions are found and then used to obtain the overall heat flow through the droplet.

1 Introduction

In view of the large heat fluxes observed in dropwise condensation, this subject has received a considerable amount of attention. Although the analysis and the physical fundamentals of the reverse process, dropwise evaporation, are similar in many respects, most of the effort has been concentrated on the condensation problem. Due to the complexity of these heat-and-mass transfer processes, an exact analysis is virtually impracticable. However, several models have been proposed to approximate the condensation process but oversimplifications invalidate some of these. For example, Fatica and Katz [1], Sugawara and Michiyoshi [2], and Nijaguna [3] have considered steady heat conduction in a single droplet with a discontinuity in the temperature along the edge. The discrepancy due to this discontinuity was recognized by Ahrendts [4], Hurst and Olson [5] and Umur and Griffith [6] and it was later shown [7] that such a model is inadmissible because it predicts an infinite amount of heat flow across the droplet. Other models [4, 6, 7] are incomplete in the sense that the condenser material properties could not be considered and their validity is, therefore, restricted to cases in which the thermal resistance between the droplet and the vapor is dominant. However, there has been some interest in understanding the effect of the condenser material properties, and in one of the first analyses Mikic [8] suggested that the effect was due to large droplets behaving as inactive areas constricting the heat flow. Recently, this idea was further pursued by Hannemann and Mikic [9] with some modifications of the original model. Earlier, Hurst and Olson [5] considered the condenser material properties by numerically solving the heat equation for a hemispherical droplet on a flat disk-shaped condenser.

In the present study both evaporation and condensation of droplets are analyzed and the effect of the condenser (evaporator) material is dealt with by solving the steady heat conduction equation for a geometry consisting of a droplet in the form of a spherical segment on a semi-infinite solid (see Fig. 1). This model assumes that the influence on a droplet due to surrounding droplets is negligible. The results of this analysis show that for a liquid like water condensing on (evaporating from) a metallic solid the temperature within the solid approaches the far-field value rapidly with distance from the edge of the droplet. Therefore, it is quite reasonable to assume that the range of influence of a droplet is restricted to a distance which is of the order of the droplet size and droplets so distributed may be regarded as isolated. However, a large droplet near several very small ones has a strong influence on them, and the present analysis is not valid for such cases. The model also restricts the validity of the results to systems having condensers (evaporators) more than a few droplet radii thick. Thin solid sheets such as foils are excluded. For the droplets of interest (less than one mm diameter) the assumed droplet shape is quite

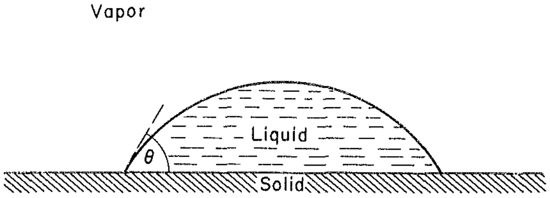

Fig. 1 Physical model for the analysis

---

[1] Present address: Department of Mechanical Engineering, and Applied Mechanics, University of Pennsylvania, Philadelphia, PA 19104

Contributed by the Heat Transfer Division for publication in the JOURNAL OF HEAT TRANSFER. Manuscript received by the Heat Transfer Division April 10, 1978.

reasonable because the effect of gravity is much weaker than that of surface tension. Also for such droplets the viscous forces dominate over gravity, and free convection can be neglected (the Grashof number is less than ten for water). One need not consider the transient effects in the heat conduction because the condensation or evaporation appears to be much slower than diffusion. That is, the time it takes for the droplet size to change by an amount comparable with the original size is much longer than the time it takes for the latent heat to diffuse into or out of the droplet. In solving the steady condensation problem, the transfer of latent heat into the liquid droplet due to the vapor flow is approximated by a mixed boundary condition involving a heat-transfer coefficent, h, which is calculated by using Plesset's formula [10, 11] for vapor flow onto a liquid sphere. By using such a boundary condition we match the heat fluxes on each side of the liquid-vapor interface. The vapor with a far-field temperature T_v deposits a heat flux $h(T_v - T_s)$ onto the cooler liquid surface having a temperature distribution T_s. This flux is equated with the heat flux conducted into the droplet. For an evaporating droplet, it follows from Plesset's results [10] that the temperature of the liquid-vapor interface can be taken equal to the far-field vapor temperature T_v. The solid-vapor interface for both cases is taken to be insulated because the thermal conductivity of the vapor is much smaller than that of the solid. This condition is not only realistic but also necessary to obtain a nontrivial bounded solution for the temperature. Along the solid-liquid interface perfect thermal contact is assumed and therefore the temperature and the heat flux are required to be continuous. At large distances into the solid the temperature is taken to be a constant, T_0. For this model, exact solutions are found for an evaporating droplet ($T_0 > T_v$). For the case of a condensing droplet ($T_0 < T_v$) exact solutions are found for some special values of h and approximate solutions for other values of h. These solutions are then used to obtain expressions for the overall heat flow Q across the droplet, the rate of change of the droplet size, and the lifetime for an evaporating droplet.

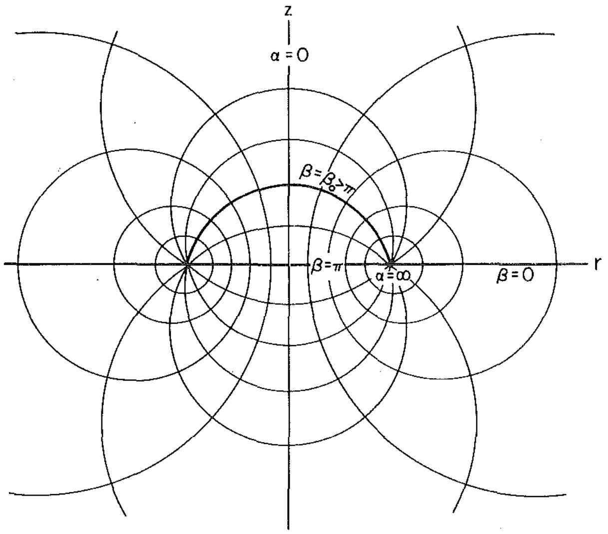

Fig. 2 Toroidal coordinate system

2 Mathematical Formulation

For the model described in Section 1, the temperature distribution is given by

$$\nabla^2 T_i^* = 0 \quad \text{in} \quad D_i, \quad i = 1, 2 \tag{1}$$

where T_1^* and T_2^* are the temperature distributions in the droplet and the solid respectively and D_1 and D_2 are the corresponding spatial regions. The boundary conditions discussed may be stated as

$$-k_1 \frac{\partial T_1^*}{\partial n}\bigg|_{\partial D_{1v}} = h[T_1^* - T_v]_{\partial D_{1v}}, \quad \text{for} \quad T_0 < T_v, \tag{2}$$

or

$$T_1^*|_{\partial D_{1v}} = T_v, \text{ for } T_v < T_0, \tag{2'}$$

$$T_1^*|_{\partial D_{12}} = T_2^*|_{\partial D_{21}}, \tag{3}$$

$$-k_1 \frac{\partial T_1^*}{\partial n}\bigg|_{\partial D_{12}} = k_2 \frac{\partial T_2^*}{\partial n}\bigg|_{\partial D_{21}}, \tag{4}$$

$$\frac{\partial T_2^*}{\partial n}\bigg|_{\partial D_{2v}} = 0, \tag{5}$$

and

$$T_2^*|_{\text{great depth}} = T_0, \tag{6}$$

where $\partial/\partial n$ is the outward normal derivative, ∂D_{1v} is the liquid-vapor interface, ∂D_{12} and ∂D_{21} are identically the solid-liquid interface, ∂D_{2v} is the solid-vapor interface, k_1 and k_2 are the thermal conductivities of the liquid and the solid, respectively, h is the liquid-vapor heat-transfer coefficient, T_v is the vapor temperature, and T_0 is the temperature of the solid at large distances from the droplet. To satisfy this set of equations (1–6), one resorts to a toroidal coordinate system involving the transformation [12]

$$z + ir = i\rho \coth[(\alpha + i\beta)/2], \tag{7}$$

where z and r are the coordinates for cylindrical geometry, ρ is the droplet radius, and α and β are the transformed coordinates (see Fig. 2). After transforming the set of equations to the (α, β) coordinate system, we obtain temperature distributions and heat flows for con-

Nomenclature

Bi = $h\rho/k_1$ = Biot number
D_1 = spatial region of droplet
D_2 = spatial region of semi-infinite solid
$\partial D_{12} = \partial D_{21}$ = solid-liquid interface
∂D_{1v} = liquid-vapor interface
∂D_{2v} = solid-vapor interface
$f(\tau)$ = correction factor
$g(\theta, \text{Bi})$ = correction function
h = heat-transfer coefficient
k_1 = thermal conductivity of liquid
k_2 = thermal conductivity of solid
Nu = $Q/[k_1\rho|T_0 - T_v|]$ = Nusselt number
$p^e(T)$ = equilibrium vapor pressure at temperature T
$P_{-1/2+i\tau}(x)$ = Legendre function of complex degree
q = heat flux
Q = overall heat flow
R = universal gas constant/molecular weight of vapor
T_1^* = temperature distribution in liquid
T_2^* = temperature distribution in solid
T_{if}^* = temperature distribution of solid-liquid interface
T_c^* = temperature at center of solid-liquid interface
T_v = vapor temperature
T_0 = temperature at large distance into solid
$T_1 = (T_1^* - T_0)/(T_v - T_0)$ = dimensionless temperature distribution in liquid
$T_2 = (T_2^* - T_0)/(T_v - T_0)$ = dimensionless temperature distribution in solid
$T_{if} = (T_{if}^* - T_0)/(T_v - T_0)$ = dimensionless temperature distribution of solid-liquid interface
$T_c = (T_c^* - T_0)/T_v - T_0)$ = dimensionless temperature of center of solid-liquid interface
t = time
t_0 = lifetime of an evaporating droplet
V = volume of droplet
α = spatial coordinate
β = spatial coordinate
$\beta_0 = \theta + \pi$
γ = accommodation coefficient
$\epsilon = k_1/k_2$
θ = contact angle
λ = latent heat of vaporization
ρ = base radius of droplet
ρ_0 = initial radius of evaporating droplet
ρ_ℓ = density of liquid
$\rho^e(T)$ = equilibrium vapor density at temperature T

densing and evaporating droplets. The details of the solution are presented in the Appendixes.

3 An Exact Solution for an Evaporating Droplet

For the case $T_\upsilon < T_0$ we find the temperature distributions given in nondimensional form as follows:

$$T_1 = \frac{T_1{}^* - T_0}{T_\upsilon - T_0} = (2\cosh\alpha - 2\cos\beta)^{1/2}$$
$$\times \int_0^\infty \frac{\epsilon \sinh(\beta_0 - \beta)\tau + [\tanh\pi\tau \tanh(\beta_0 - \pi)\tau + \epsilon]\cosh(\beta_0 - \pi)\tau \sinh(\beta - \pi)\tau}{[\tanh\pi\tau\tanh(\beta_0 - \pi)\tau + \epsilon]\cosh\pi\tau\sinh(\beta_0 - \pi)\tau} P_{1/2+i\tau}(\cosh\alpha)d\tau, \quad (8)$$

and

$$T_2 = \frac{T_2{}^* - T_0}{T_\upsilon - T_0} = (2\cosh\alpha - 2\cos\beta)^{1/2}$$
$$\times \int_0^\infty \frac{\epsilon\,\mathrm{sech}^2\,\pi\tau\cosh\beta\tau}{[\tanh\pi\tau\tanh(\beta_0 - \pi)\tau + \epsilon]} P_{-1/2+i\tau}(\cosh\alpha)d\tau, \quad (9)$$

where $P_{-1/2+i\tau}(\cosh\alpha)$ is the Legendre function of complex degree and $\epsilon = k_1/k_2$. As shown in Fig. 2, $\beta = \beta_0$ corresponds to the liquid-vapor interface, $\beta = \pi$ to the solid-liquid interface and $\beta = 0$ to the solid-vapor interface. The overall heat flow Q across the droplet is calculated by finding the heat flux across the solid-liquid interface and integrating over it. In dimensionless form it is given by the Nusselt number, Nu, as

$$\mathrm{Nu} = \frac{Q}{k_1\rho(T_0 - T_\upsilon)} = 4\pi\int_0^\infty \frac{\mathrm{sech}^2\,\pi\tau}{[\tanh\pi\tau\tanh\theta\tau + \epsilon]}d\tau, \quad (10)$$

where $\theta = (\beta_0 - \pi)$ is the contact angle (see Fig. 1). It is appropriate to mention here that Q is independent of the surface across which it is calculated as long as all the heat flow lines pass through it. Therefore, a suitable heat flow calculation, even within the solid, would yield the same result as (10).

It appears that an exact expression for the integral in (10) is not known and therefore, we have evaluated it numerically, and the results are presented in Fig. 3.

For most liquid droplets evaporating from metallic solids $\epsilon \sim 0.01$ and for such cases most of the contribution to the integral takes place near $\tau = 0$. It would therefore be a good approximation to replace $\tanh \theta\tau$ in the denominator by $(\theta/\pi)\tanh\pi\tau$. By the further substitution $x = \tanh\pi\tau$, the integral takes the form

$$\mathrm{Nu} \simeq \frac{4\pi}{\theta}\int_0^1 \frac{dx}{\left[x^2 + \frac{\pi\epsilon}{\theta}\right]} = 4\left(\frac{\pi}{\theta\epsilon}\right)^{1/2}\tan^{-1}\left[\left(\frac{\theta}{\pi\epsilon}\right)^{1/2}\right], \quad (11)$$

which for $\theta \gg 0$ can be further approximated as

$$\mathrm{Nu} \simeq \frac{2\pi^{3/2}}{(\theta\epsilon)^{1/2}}, \quad (12)$$

or

$$Q \simeq \frac{2\pi^{3/2}}{\theta^{1/2}}(k_1k_2)^{1/2}\rho(T_0 - T_\upsilon). \quad (13)$$

Equation (11) is exact for $\theta = 0$ and $\theta = \pi$, and agrees with (10) to within 20 percent for other contact angles when $\epsilon \leqslant 0.01$.

The solid-liquid interface temperature distribution may be obtained by letting $\beta = \pi$ in (8) or (9). Calculations for a hemisphere (see Appendix B) show that the temperature at the edge is T_υ. At the center (polar point) of the liquid-vapor interface the temperature $T_c{}^*$ is given by

$$T_c = \frac{T_0 - T_c{}^*}{T_0 - T_\upsilon} = 2\epsilon\left(\frac{1+\epsilon}{2\epsilon + \epsilon^2}\right)^{1/2}\left[1 - \frac{1}{\pi}\cos^{-1}\left(\frac{1}{1+\epsilon}\right)\right], \quad (14)$$

which may be approximated by $T_c \simeq (2\epsilon)^{1/2}$. The calculations also show that the base temperature varies from a value close to T_0 at the center to T_υ at the edge, and it is clearly not uniform.

From the heat flow results, the rate of dimunition in the droplet size can be calculated and used to find the time it takes to vanish. The rate of change of volume V is given by [7]

$$\frac{dV}{dt} = \pi\rho^2\frac{(1 - \cos\theta)^2(2 + \cos\theta)}{\sin^3\theta}\frac{d\rho}{dt} \quad (15)$$

and the volume evaporation rate of the liquid is $Q/(\lambda\rho_\ell)$, where λ is the latent heat of vaporization and ρ_ℓ is the density of the liquid. Therefore, the rate of change of the droplet base radius is obtained as

$$\frac{d\rho}{dt} = -\frac{k_1(T_0 - T_\upsilon)\mathrm{Nu}}{\rho\lambda\rho_\ell\pi}\frac{\sin^3\theta}{(1 - \cos\theta)^2(2 + \cos\theta)} \quad (16)$$

which upon integration leads to

$$\rho = \rho_0\left[1 - \frac{2k_1(T_0 - T_\upsilon)\mathrm{Nu}}{\pi\lambda\rho_\ell\rho_0{}^2}\frac{\sin^3\theta}{(1 - \cos\theta)^2(2 + \cos\theta)}t\right]^{1/2}, \quad (17)$$

where ρ_0 is the initial radius It is not difficult to see that the droplet takes a time

$$t_0 = \frac{\pi\lambda\rho_\ell\rho_0{}^2(1 - \cos\theta)^2(2 + \cos\theta)}{2k_1(T_0 - T_\upsilon)\sin^3\theta\,\mathrm{Nu}} \quad (18)$$

to vanish.

Similar calculations can be carried out for a condensing droplet but it turns out that the expression for Nu is much more complicated and involves the droplet radius ρ. The details are discussed in the next section.

4 An Approximate Solution for a Condensing Droplet

For a condensing droplet the boundary condition (2) cannot be satisfied exactly and, therefore, an approximate solution is obtained (see Appendix A). From this solution we obtain the overall heat flow Q given by the Nusselt number as

$$\mathrm{Nu} = \frac{Q}{k_1\rho(T_\upsilon - T_0)}$$
$$\simeq 4\pi\int_0^\infty \frac{\mathrm{sech}^2\,\pi\tau}{\tanh\pi\tau\tanh\theta\tau + \epsilon + \dfrac{\sin\theta}{2\,\mathrm{Bi}}\dfrac{\tanh\pi\tau\tanh\theta\tau}{\sinh^2\theta\tau}} \quad (19)$$

where $\mathrm{Bi} = h\rho/k_1$ is the Biot number. Since this result is approximate, it is tested for accuracy against some known exact results. For the case $\mathrm{Bi} \rightarrow \infty$ (i.e., $h \rightarrow \infty$) equation (2) becomes

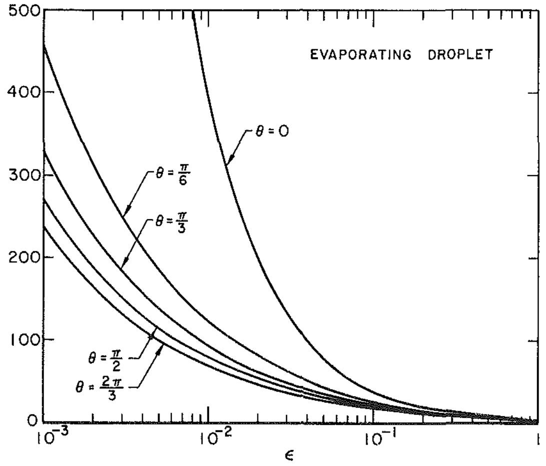

Fig. 3 Variation of evaporating droplet Nusselt number with conductivities ratio $\epsilon = k_1/k_2$ for different contact angles

$$T_1^*|_{\partial D_{1v}} = T_v \tag{20}$$

which is the same as (2′). Therefore, the expression for Nu should be the same as (10) and that indeed is the case when $\mathrm{Bi} \rightarrow \infty$ in (19). Also, for the case $\mathrm{Bi} = 1/2 \sin\theta$ we have obtained an exact solution which when compared with (19) shows exact agreement.

Further comparisons of (19) can be made with a set of results available from a previous analysis [7] in which a solution was obtained by assuming the droplet base temperature to be uniform at T_0. This solution corresponds to the case $\epsilon = 0$ in the present analysis, and again (19) is in exact agreement when we go to the trivial case $\theta = 0$; i.e.,

$$\mathrm{Nu}|_{\theta=0,\epsilon=0} = \pi \mathrm{Bi}. \tag{21}$$

However, for θ near $\pi/2$, Nu in (19) behaves like $\mathrm{Bi}^{1/2}$ for large Bi while numerical calculations from [7] show that $\mathrm{Nu} \sim \ell n\, \mathrm{Bi}$. The latter behavior is known to be exact for $\theta = \pi/2$ and therefore (19) does not hold for large Bi when $\epsilon = 0$.

To make use of the information available from both the exact solution for $\epsilon = 0$ and the exact solution for $\mathrm{Bi} = 1/2 \sin\theta$, a correction function $g(\theta, \mathrm{Bi})$ is added to the factor $\sin\theta/(2\,\mathrm{Bi})$ in (19) so that Nu may be written as

$$\mathrm{Nu} \simeq 4\pi \int_0^\infty \times \frac{\mathrm{sech}^2\, \pi\tau d\tau}{\tanh \pi\tau \tanh \theta\tau + \epsilon + \left[\dfrac{\sin\theta}{2\mathrm{Bi}} + g(\theta, \mathrm{Bi})\right] \dfrac{\tanh \pi\tau \tanh \theta\tau}{\sinh^2 \theta\tau}}. \tag{22}$$

The correction function $g(\theta, \mathrm{Bi})$ is chosen so that for $\epsilon = 0$, (22) yields approximately the same results as those obtained in [7] and so that at the same time the other exact solutions remain unaffected. Since logarithmic behavior in Bi is required and without $g(\theta, \mathrm{Bi})$ (22) would behave like $\mathrm{Bi}^{1/2}$, it is appropriate to choose $g(\theta, \mathrm{Bi}) \sim (\ell n\, \mathrm{Bi})^{-2}$. Furthermore, $g(\theta, \mathrm{Bi})$ is required to be zero when $\mathrm{Bi} = 1/2 \sin\theta$ and when θ and ϵ are both zero because at these values (19) is exact. After a few trials, a suitable expression for the correction function is found to be

$$g(\theta, \mathrm{Bi}) = 1.8 \sin^3\theta \left(1 - \frac{\sin\theta}{2\,\mathrm{Bi}}\right)^{14} \times \left(1 - \frac{1}{2\,\mathrm{Bi}}\right) \left[\ell n \left(\frac{\sin\theta}{2\,\mathrm{Bi}}\right)\right]^{-2}. \tag{23}$$

It is important to mention that since the results obtained in [7] were restricted to contact angles $0 \leqslant \theta \leqslant \pi/2$, the same condition must apply to (22).

Results from the numerical integration of (22) are presented in Fig. 4. It can be seen that for large values ϵ the dependence of Nu on ϵ is quite strong but, depending on the value of Bi, it gets weaker as ϵ becomes smaller.

The droplet growth rate for this case also is given by (16) but since Nu is a complicated function of ρ, straightforward integration is not possible.

6 Calculation of the Liquid-Vapor Heat-Transfer Coefficient

There has been considerable interest in the problem of vapor flow to a liquid surface. The difficulty, generally, has been in including the effect of the bulk velocity of the vapor, and some authors [13, 14] have dealt with this problem by introducing correction factors. However, in Plesset's work [10] on the flow of vapor between parallel liquid surfaces, the bulk velocity for low Mach number was considered implicitly. This result was later extended by Plesset and Prosperetti [11] for vapor flow between spherical and cylindrical surfaces.

In particular, for flow from an inner sphere of radius R_v and temperature T_v to an outer spherical cavity boundary of radius R_s and temperature T_s, the bulk velocity u_s at the cavity is given [11] by

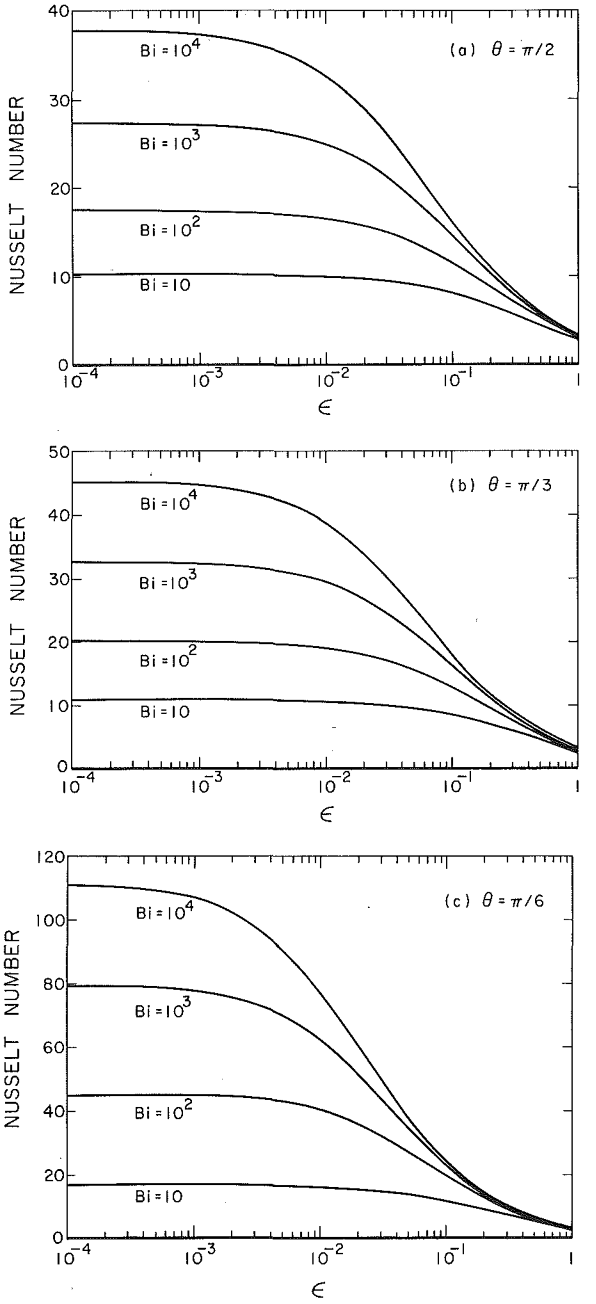

Fig. 4 Condensing droplet Nusselt number as a function of conductivities ratio $\epsilon = k_1/k_2$ for different Biot numbers: contact angles (a) $\pi/2$, (b) $\pi/3$ and (c) $\pi/6$

$$u_s = \gamma \left(\frac{RT_s}{2\pi}\right)^{1/2} \frac{p^e(T_v) - p^e(T_s)}{p^e(T_v) + \left(\dfrac{R_s}{R_v}\right)^2 \left(\dfrac{T_v}{T_s}\right)^{1/2} p^e(T_s)} \tag{24}$$

where γ is the accommodation coefficient, $p^e(T_v)$ and $p^e(T_s)$ are the equilibrium vapor pressures at temperatures T_v and T_s respectively, and R is the ratio of the universal gas constant to the molecular weight of the liquid and the vapor. This result can also be applied to vapor flowing from an outer cavity boundary of radius R_v and temperature T_v to an inner sphere of radius R_s and temperature T_s. For this case, in the limit $R_v \rightarrow \infty$, (24) takes the form

$$u_s = \gamma \left(\frac{RT_s}{2\pi}\right)^{1/2} \frac{p^e(T_v) - p^e(T_s)}{p^e(T_v)}, \tag{25}$$

from which the vapor flux J is evaluated to be

$$J = u_s \rho^e(T_s) = \gamma \frac{p^e(T_v) - p^e(T_s)}{(2\pi R T_s)^{1/2}} \tag{26}$$

where $\rho^e(T_s) = p^e(T_s)/(RT_s)$ is the equilibrium vapor density at temperature T_s.

From the Clausius-Clapeyron equation $p^e(T_v)$ and $p^e(T_s)$ can be related:

$$\frac{p^e(T_s)}{p^e(T_v)} = \exp\left[-\frac{\lambda}{RT_s}\left(1 - \frac{T_s}{T_v}\right)\right], \tag{27}$$

where λ is the latent heat of vaporization. For T_s very close to T_v, this may be further approximated by

$$p^e(T_s) \simeq p^e(T_v)\left[1 - \frac{\lambda}{RT_sT_v}(T_v - T_s)\right]. \tag{28}$$

Upon substitution of this approximation into (26), the heat flux $q = J\lambda$ is found to be

$$q = \gamma \frac{p^e(T_v)\lambda^2}{(2\pi)^{1/2} T_s{}^{3/2} T_v R^{3/2}} (T_v - T_s) \tag{29}$$

and by noting that $T_s{}^{3/2}\, T_v \simeq T_v{}^{5/2}$, the heat-transfer coefficient $h = q/(T_v - T_s)$ may be expressed as

$$h = \gamma \frac{p^e(T_v)\lambda^2}{(2\pi)^{1/2} R^{3/2} T_v{}^{5/2}}. \tag{30}$$

This is the result for vapor flowing onto a liquid sphere and due to symmetry it is also valid for a hemisphere. For the general case of vapor flowing onto an arbitrary spherical segment an expression for h is not available but may, nevertheless, be approximated by (30).

By taking $\gamma = 1$ as recommended by Nabavian and Bromley [14], numerical calculations for water at $T_v = 373$ K show that $h \simeq 7.7 \times 10^6$ Watts/(m^2 – K). The Biot number $\mathrm{Bi} = h\rho/k_1$ for droplets ranging in size from 10 μm to 1 mm varies from about 100 to 10,000.

7 Discussion

The results of the present study clearly illustrate the importance of the material properties of the solid and of the droplet contact angle for both evaporating and condensing droplets. For an evaporating droplet the liquid-vapor interface temperature is set at T_v. If the solid properties are ignored by setting the droplet base temperature to be $T_0 \neq T_v$, calculations show that the total heat flow Q would become unbounded, which is of course unrealistic. This behavior is made quite clear by equations (10–12) from which we see that if $k_2 \to \infty$ (i.e., $\epsilon \to 0$), then $\mathrm{Nu} \to \infty$. The overall behavior for $\theta \sim 1$ may be summed up by equation (13) which predicts Q as being proportional to $(k_1k_2)^{1/2}$. The dependence of Q on the contact angle is well described by (11).

For a condensing droplet, the analysis shows a strong dependence of Q on ϵ for $\ell n\, \mathrm{Bi} \sim 1/\epsilon^{1/2}$ or $\ell n\, \mathrm{Bi} > 1/\epsilon^{1/2}$. When $\ell n\, \mathrm{Bi} \gg 1/\epsilon^{1/2}$, the dependence of Q is dominated by ϵ and it approaches the value $Q \propto (k_1k_2)^{1/2}$ given by equations (10–13). Calculations for water condensing on metals show that Bi varies from about 100 to 10,000 while ϵ varies from about 0.001 to 0.01. Therefore, the importance of considering the condenser properties is evident, especially for large droplets and/or for small contact angles. Interestingly, the behavior $Q \propto (k_1k_2)^{1/2}$ agrees very well with the experimental results of Griffith and Lee [15]. This result differs from that of Nijaguna and Abdelmessih [16] who obtained $Q \propto k_2{}^{1/2}$ by considering the transient response of a thin film of liquid on a semi-infinite solid. Such behavior is to be expected because it is an intrinsic property of transient heat flows in all simple geometries. However, in the present analysis the proportionality of Q with $(k_1k_2)^{1/2}$ is the result of the edge effects of the droplet with the solid surface around it being insulated. Another important implication of the very large Biot numbers is that the solid-liquid interface temperature approaches high nonuniformity as in the case of an evaporating droplet. Therefore, it would be incorrect, under the circumstances described, to add the separate resistances of the droplet and the solid. In general, the criterion for the separability of resistances is the existence of an isotherm along the desired surface of separation. For small droplets, however, the Biot number may be small enough so that the overall resistance may be that of the droplet alone.

To obtain a more precise theoretical prediction, one can calculate the average heat flow across a given area by adding the individual flow rates across droplets for a known size distribution. Since the properties of the solid, the liquid, and the vapor are all considered simultaneously, such calculations would be a step closer to a more complete theory in the study of droplets.

Acknowledgments

One of us (S.S.S.) wishes to express his appreciation to the Natural Sciences and Engineering Research Council of Canada for a postgraduate scholarship. The study is a part of a program supported by the National Science Foundation under Grant No. ENG 75-22676.

References

1 Fatica, N., Katz, D. L. "Dropwise Condensation," *Chemical Engineering Progress*, Vol. 45, 1949, pp. 661–674.

2 Sugawara, S., Michiyoshi, I., "Dropwise Condensation," *Memoirs of Faculty of Engineering*, Kyoto University, Vol. 18 No. (2), 1956, pp. 84–111.

3 Nijaguna, B. T., "Drop Nusselt Number in Dropwise Condensation", *Applied Scientific Research*, Vol. 29, 1974, pp. 226–236.

4 Ahrendts, J., "Der Warmleitwiderstand eines Kondensattropfens," *Warme-und Stroffübertagung*," Vol. 5, 1972, pp. 239–244.

5 Hurst, C. J., Olson, D. R , "Conduction through Droplets during Dropwise Condensation," ASME JOURNAL OF HEAT TRANSFER, Vol. 95, 1973, pp. 12–20.

6 Umur, A., Griffith, P., "Mechanism of Dropwise Condensation," ASME JOURNAL OF HEAT TRANSFER, Vol. 87, 1965, pp. 275–282.

7 Sadhal, S. S., Martin, W. W., "Heat Transfer through Drop Condensate using Differential Inequalities," *International Journal of Heat and Mass Transfer*, Vol. 20, 1977, pp. 1401–1407.

8 Mikic, B., "On Mechanism of Dropwise Condensation," *International Journal of Heat and Mass Transfer*, Vol. 12, 1969, pp. 1311–1323.

9 Hannemann, R. J., Mikic, B. B., "An Analysis of the Effect of Surface Thermal Conductivity on the Rate of Heat Transfer in Dropwise Condensation," *International Journal of Heat and Mass Transfer*, Vol. 19, 1976, pp. 1299–1307.

10 Plesset, M. S., "Note on the Flow of Vapor Between Liquid Surfaces," *Journal of Chemical Physics*, Vol. 20, 1952, pp. 790–793.

11 Plesset, M. S., Prosperetti, A., "Flow of Vapor in a Liquid Enclosure," *Journal of Fluid Mechanics*, Vol. 78, 1976, pp. 433–444.

12 Lebedev, N. N., *Special Functions and Their Application*, Dover Publications, Inc., New York, N.Y., 1972.

13 Schrage, R. W., *A Theoretical Study of Interphase Mass Transfer*, Columbia University Press, New York, N.Y., 1953.

14 Nabavian, K., Bromley, L. A., "Condensation Coefficient of Water," *Chemical Engineering Science*, Vol. 18, 1963, pp. 651–660.

15 Griffith, P., Lee, M. S., "The Effect of Surface Thermal Properties and Finish on Dropwise Condensation," *International Journal of Heat and Mass Transfer*, Vol. 10, 1967, pp. 267–707.

16 Nijaguna, B. T., Abdelmessih, A. H., "Precoalescence Drop Growth Model for Dropwise Condensation," ASME 71-WA/HT-47, 1971.

APPENDIX A

Under the transformation (7), one finds that equation (1) takes the form

$$\frac{\partial}{\partial\alpha}\left[\frac{\sinh\alpha}{\cosh\alpha - \cos\beta}\frac{\partial T_i}{\partial\alpha}\right] + \frac{\partial}{\partial\beta}\left[\frac{\sinh\alpha}{\cosh\alpha - \cos\beta}\frac{\partial T_i}{\partial\beta}\right] = 0, \qquad i = 1, 2, \tag{A1}$$

where $T_i = (T_i{}^* - T_0)/(T_v - T_0)$. The variables cannot be separated directly for this equation. However, by making the transformation [12]

$$T_i = (2\cosh\alpha - 2\cos\beta)^{1/2} v_i, \qquad i = 1, 2 \tag{A2}$$

and by substituting into (A1), we find that the equation for v_i,

$$\frac{\partial^2 v_i}{\partial\alpha^2} + \frac{\partial^2 v_i}{\partial\beta^2} + \coth\alpha\frac{\partial v_i}{\partial\alpha} + \frac{1}{4}v_i = 0, \qquad i = 1, 2 \tag{A3}$$

can be separated. The boundary conditions (2–6) transform into

$$\left(1 + \frac{\sin\beta_0}{2\,\mathrm{Bi}}\right) v_1\bigg|_{\beta=\beta_0} + \frac{1}{2\,\mathrm{Bi}}(2\cosh\alpha - 2\cos\beta_0)\frac{\partial v_1}{\partial\beta}\bigg|_{\beta=\beta_0}$$

$$= \frac{1}{(2\cosh\alpha - 2\cos\beta_0)^{1/2}}, \quad \text{for} \quad T_0 < T_\upsilon, \quad (A4)$$

or

$$\upsilon_1\Big|_{\beta=\beta_0} = \frac{1}{(2\cosh\alpha - 2\cos\beta_0)^{1/2}}, \quad \text{for} \quad T_\upsilon < T_0, \quad (A4')$$

$$\upsilon_1\Big|_{\beta=\pi} = \upsilon_2\Big|_{\beta=\pi} \quad (A5)$$

$$\epsilon\frac{\partial\upsilon_1}{\partial\beta}\Big|_{\beta=\pi} = \frac{\partial\upsilon_2}{\partial\beta}\Big|_{\beta=\pi}, \quad (A6)$$

$$\frac{\partial\upsilon_2}{\partial\beta}\Big|_{\beta=0} = 0, \quad (A7)$$

and

$$\upsilon_2|_{\alpha,\beta\to 0} < \infty, \quad (A8)$$

where $\epsilon = k_1/k_2$, and $\mathrm{Bi} = h\rho/k_1$ is the Biot number. In the coordinate system used, $\beta = \beta_0$ corresponds to the liquid-vapor interface, $\beta = \pi$ to the solid-liquid interface, and $\beta = 0$ to the solid-vapor interface (see Fig. 2). At large distances from the droplet $\alpha, \beta \to 0$ and therefore, equation (6) is satisified because the factor $(2\cosh\alpha - 2\cos\beta)^{1/2}$ in ($A2$) goes to zero.

The solutions to ($A1$) take the form

$$\upsilon_1 = \int_0^\infty \frac{\Phi(\tau)\sinh(\beta_0-\beta)\tau + \Psi(\tau)\sinh(\beta-\pi)\tau}{\sinh(\beta_0-\pi)\tau} \times P_{-1/2+i\tau}(\cosh\alpha)d\tau \quad (A9)$$

and

$$\upsilon_2 = \int_0^\infty \frac{\Phi(\tau)\cosh\beta\tau}{\cosh\pi\tau} P_{-1/2+i\tau}(\cosh\alpha)d\tau \quad (A10)$$

where $P_{-1/2+i\tau}(\cosh\alpha)$ is the Legendre function of complex degree. These solutions satisfy the boundary conditions ($A5$, $A7$) and ($A8$). Upon satisfying ($A6$) we find that

$$\Psi(\tau) = \Phi(\tau)\left[\frac{1}{\epsilon}\tanh\pi\tau\sinh(\beta_0-\pi)\tau + \cosh(\beta_0-\pi)\tau\right]. \quad (A11)$$

Evaporating Droplet

For an evaporating droplet we need to satisfy ($A4'$) and we can do so exactly by writing its right side as

$$\frac{1}{(2\cosh\alpha - 2\cos\beta_0)^{1/2}}$$

$$= \int_0^\infty \frac{\cosh(\beta_0-\pi)\tau}{\cosh\pi\tau} P_{-1/2+i\tau}(\cosh\alpha)d\tau. \quad (A12)$$

By the substitution of ($A9$) into ($A4'$) and using the integral form for $(2\cosh\alpha - 2\cos\beta_0)^{-1/2}$ we determine $\Psi(\tau)$ as

$$\Psi(\tau) = \frac{\cosh(\beta_0-\pi)\tau}{\cosh\pi\tau} \quad (A13)$$

From ($A11$) it follows that

$$\Phi(\tau) = \frac{\epsilon}{[\tanh\pi\tau\tanh(\beta_0-\pi)\tau + \epsilon]\cosh\pi\tau}. \quad (A14)$$

The heat flux across the solid-liquid interface may now be written as

$$q(\alpha) = -k_2\left[\frac{\cosh\alpha - \cos\pi}{\rho}\right]\frac{\partial T_2{}^*}{\partial\beta}\Big|_{\beta=\pi}$$

$$= \frac{k_2}{2\rho}(T_0 - T_\upsilon)[2\cosh\alpha - 2\cos\pi]^{3/2}$$

$$\times \int_0^\infty \tau\tanh\pi\tau\Phi(\tau)P_{-1/2+i\tau}(\cosh\alpha)d\tau, \quad (A15)$$

and the overall heat flow Q is found to be

$$Q = \int_0^\infty 2\pi\left[\frac{\rho}{\cosh\alpha - \cos\pi}\right]^2 q(\alpha)\sinh\alpha d\alpha$$

$$= 4\pi k_1\rho(T_0 - T_\upsilon)\int_0^\infty \frac{\operatorname{sech}^2\pi\tau d\tau}{[\tanh\pi\tau\tanh\theta\tau + \epsilon]}, \quad (A16)$$

where $\theta = (\beta_0 - \pi)$.

Condensing Droplet

For a condensing droplet, instead of satisfying ($A4'$) one needs to satisfy ($A4$) in order to determine $\Phi(\tau)$ used in equations ($A9$–$A11$). However, an attempt to do so yields a double integral equation for $\Phi(\tau)$ with very complicated kernels. An explicit expression for $\Phi(\tau)$ can only be found for $\mathrm{Bi} = 1/2\sin\theta$ and $\mathrm{Bi} \to \infty$. Therefore, approximate solutions are sought and one such solution can be obtained by finding a suitable function $f(\tau)$ satisfying

$$\upsilon_1|_{\beta=\beta_0} = \int_0^\infty \Psi(\tau)P_{-1/2+i\tau}(\cosh\alpha)d\tau$$

$$= (2\cosh\alpha - 2\cos\beta_0)\int_0^\infty \Psi(\tau)f(\tau)P_{-1/2+i\tau}(\cosh\alpha)d\tau. \quad (A17)$$

Substitution of ($A11$) and ($A17$) into ($A4$) leads to

$$\int_0^\infty \left\{\left(1 + \frac{\sin\beta_0}{2\,\mathrm{Bi}}\right)f(\tau)\left[\frac{1}{\epsilon}\tanh\pi\tau\sinh(\beta_0-\pi)\tau + \cosh(\beta_0-\pi)\tau\right]\right.$$

$$\left. + \frac{1}{2\,\mathrm{Bi}}\tau\left[\frac{1}{\epsilon}\tanh\pi\tau + \tanh(\beta_0-\pi)\tau\right]\cosh(\beta_0-\pi)\tau\right\}\Phi(\tau)P_{-1/2+i\tau}(\cosh\alpha)d\tau$$

$$= \frac{1}{[2\cosh\alpha - 2\cos\beta_0]^{3/2}} = -\frac{1}{\sin\beta_0}\int_0^\infty \frac{\tau\sinh(\beta_0-\pi)\tau}{\cosh\pi\tau}P_{-1/2+i\tau}(\cosh\alpha)d\tau, \quad (A18)$$

and it is not difficult to see that

$$\Phi(\tau) = \frac{\operatorname{sech}\pi\tau}{\left(1 - \frac{\sin\theta}{2\,\mathrm{Bi}}\right)\frac{\sin\theta}{\tau\tanh\theta\tau}f(\tau)\left[\frac{1}{\epsilon}\tanh\pi\tau\tanh\theta\tau + 1\right] + \frac{\sin\theta}{2\,\mathrm{Bi}}\left[\frac{1}{\epsilon}\frac{\tanh\pi\tau}{\tanh\theta\tau} + 1\right]}, \quad (A19)$$

where $\theta = (\beta_0 - \pi)$ as before. Here $f(\tau)$ is still an unknown function and may be determined as an approximation by equating the total heat flow across the liquid-vapor interface with that across the solid-liquid interface.

The total heat flow Q across the liquid-vapor interface is given by the Nusselt number Nu:

$$\mathrm{Nu} = \frac{Q}{k_1\rho(T_v - T_0)} = \int_0^\infty \frac{8\pi\,\mathrm{Bi}}{[2\cosh\alpha + 2\cosh\theta]^2}[1 - T_1|_{\beta=\beta_0}]\sinh\alpha\, d\,\alpha$$
$$= 4\pi\int_0^\infty \frac{\left(\dfrac{f(\tau)\sin\theta}{\tau\tanh\theta\tau} - 1\right)\dfrac{2\,\mathrm{Bi}}{\sin\theta} + \left[\dfrac{\tanh\pi\tau}{\tanh\theta\tau} - \dfrac{f(\tau)\sin\theta}{\tau\coth\theta\pi\tau} + \epsilon\left(1 - \dfrac{f(\tau)\sin\theta}{\tau\tanh\theta\tau}\right)\right]\Big/[\tanh\pi\tau\tanh\theta\tau + \epsilon]}{\dfrac{\cosh\pi\tau\sinh\pi\tau}{\cosh\theta\tau\sinh\theta\tau}\left\{\left(1 - \dfrac{\sin\theta}{2\,\mathrm{Bi}}\right)\dfrac{f(\tau)\sin\theta}{\tau\tanh\theta\tau} + \dfrac{\sin\theta}{2\,\mathrm{Bi}}\left[\dfrac{\tanh\pi\tau}{\tanh\theta\tau} + \epsilon\right]\Big/[\tanh\pi\tau\tanh\theta\tau + \epsilon]\right\}}\, d\tau. \tag{A20}$$

If the heat flow calculation is carried out at the solid-liquid interface, the expression for the Nusselt number is

$$\mathrm{Nu} = \frac{4\pi}{\epsilon}\int_0^\infty (2\cosh\alpha + 2)\left.\frac{\partial T_2}{\partial\beta}\right|_{\beta=\pi}\frac{\sinh\alpha d\alpha}{(2\cosh\alpha + 2)^2}$$
$$= \frac{4\pi}{\epsilon}\int_0^\infty \frac{1}{(2\cosh\alpha + 2)^{1/2}}\int_0^\infty \tau\tanh\pi\tau\,\Phi(\tau)P_{-1/2+i\tau}(\cosh\alpha)d\tau\sinh\alpha d\alpha = \frac{4\pi}{\epsilon}\int_0^\infty \frac{\Phi(\tau)}{\cosh\pi\tau}d\tau, \tag{A21}$$

and by making use of (A19) the above expression becomes

$$\mathrm{Nu} = 4\pi\int_0^\infty \frac{\mathrm{sech}^2\,\pi\tau d\tau}{\left(1 - \dfrac{\sin\theta}{2\,\mathrm{Bi}}\right)\dfrac{f(\tau)\sin\theta}{\tau\tanh\theta\tau}[\tanh\pi\tau\tanh\theta\tau + \epsilon] + \dfrac{\sin\theta}{2\,\mathrm{Bi}}\left[\dfrac{\tanh\pi\tau}{\tanh\theta\tau} + \epsilon\right]}. \tag{A22}$$

If one requires that the integrands in (A20) and (A22) be identical, one obtains

$$f(\tau) = \frac{\tau\tanh\theta\tau}{\sin\theta}. \tag{A23}$$

It must be pointed out here that this expression for $f(\tau)$ is not necessarily exact. The above procedure for obtaining $f(\tau)$ is effectively equivalent to integrating the boundary condition (A4) and hence all the information cannot be obtained. Also, it is quite clear that to require the integrals in (A20) and (A22) to be equal, it is not necessary for the integrands to be identical. Therefore, it is appropriate to write, instead of (A23),

$$f(\tau) \simeq \frac{\tau\tanh\theta\tau}{\sin\theta}. \tag{A24}$$

By the substitution of (A24) into (A20) or (A22) we obtain an expression for Nu as given by (19).

APPENDIX B

The solid-liquid interface temperature distribution $T_{if}{}^*$ can be obtained from (8) or (9) as

$$T_{if} = \frac{T_0 - T_{if}{}^*}{T_0 - T_v} = (2\cosh\alpha + 2)^{1/2}$$
$$\times\int_0^\infty \frac{\epsilon\,\mathrm{sech}\,\pi\tau}{[\tanh\pi\tau\tanh\theta\tau + \epsilon]}P_{-1/2+i\tau}(\cosh\alpha)d\tau. \tag{B1}$$

For the special case of a hemispherical droplet, this expression becomes

$$T_{if} = 2\left(\frac{\epsilon}{1+\epsilon}\right)\cosh\frac{1}{2}\alpha\int_0^\infty \frac{P_{-1/2+i\tau}(\cosh\alpha)d\tau}{\left[\cosh\pi\tau - \dfrac{1}{1+\epsilon}\right]}. \tag{B2}$$

By using the integral representation for $\alpha > 0$ in (B2)

$$P_{-1/2+i\tau}(\cosh\alpha) = \frac{2}{\pi}\int_0^\alpha \frac{\cos\tau\phi}{(2\cosh\alpha - 2\cosh\phi)^{1/2}}d\phi, \tag{B3}$$

and integrating with respect to τ, we find that the expression for T_{if} reduces to

$$T_{if} = \frac{4}{\pi}\frac{\epsilon}{(2\epsilon + \epsilon^2)^{1/2}}\cosh\frac{1}{2}\alpha$$
$$\times\int_0^\alpha \frac{\sinh\left\{\left[1 - \dfrac{1}{\pi}\cos^{-1}\left(\dfrac{1}{1+\epsilon}\right)\right]\phi\right\}}{\sinh\phi[2\cosh\alpha - 2\cosh\phi]^{1/2}}d\phi. \tag{B4}$$

The temperature at the edge of the droplet is obtained (by letting $\alpha \to \infty$ in (B4)) to be T_v. By letting $\alpha \to 0$ in (B2), the temperature $T_c{}^*$ at the center of the base is found to be that given by (14).

F. J. Renk[1]
P. C. Wayner, Jr.

Department of Chemical and Environmental Engineering,
Rensselaer Polytechnic Institute,
Troy, N. Y. 12181

An Evaporating Ethanol Meniscus

Part I: Experimental Studies

The profile of an evaporating ethanol meniscus was measured as a function of the evaporative heat flux using interferometry. A measure of the evaporative heat flux was obtained using vapor deposited resistance thermometers. The meniscus profile was found to be stable and a function of the heat flux for the heat flux range of 0 – 1.36w/m of interline. These results were used in an analysis of capillary flow heat transfer in Part II.

Introduction

It is evident that evaporation and the resulting fluid flow in the vicinity of the triple interline (junction of solid-liquid-vapor) and the adjacent meniscus can control the change-of-phase heat transfer process occurring in various engineering devices such as heat pipes, boilers and grooved evaporators. It is likely that the study of heat transfer and fluid flow in a stationary evaporating meniscus will prove useful to understanding and improving these processes. However, limited experimental data are available for these regions because of the associated very small dimensions and the resulting very large gradients. The extended meniscus can be divided into three zones: (1) the immediate vicinity of the interline—the thin film region—where the thickness of the liquid can vary from a monolayer to approximately 5×10^{-8} m and where the fluid flow results from the pressure gradient produced in the liquid by the varying force of attraction between the liquid and solid (disjoining pressure), (2) the inner intrinsic meniscus region where the thickness range is approximately $(0.05 - 10) \times 10^{-6}$ m and where fluid flow resulting from very large pressure gradients due to curvature is possible, and (3) the outer intrinsic meniscus region where the thickness is greater than 10^{-5} m and where fluid flow resulting from small pressure gradients due to curvature is possible. Because of the large variation of the film thickness in the extended meniscus, it is currently necessary to study these regions independently. The objective of the experimental study described herein was to measure the inner intrinsic meniscus profile in the thickness range $(0.1 - 4) \times 10^{-6}$ m as a function of heat flux [1]. The optical technique of interferometry was used to obtain the meniscus profile and resistance thermometry was used to obtain the heat flux. The approximate location of the interline was also obtained. This experimental design was also used in a preliminary study which did not include an independent measurement of the heat flux and the interline location [2].

In Part II of this study [3], the measured heat flux was used in a model of the fluid flow field to obtain optimum agreement between the measured and predicted fringe locations. The resulting model equation was then used to obtain the curvature distribution, the heat flux distribution and the predicted interline location. The results of these coupled studies demonstrate that fluid flow in an evaporating meniscus results from a change in the meniscus profile which depends on the heat flux distribution. A previous experimental study of the outer meniscus region is in agreement with this conclusion [4].

Experimental Design and Procedure

A cross section of the test cell is presented in Fig. 1. A two-dimensional, horizontal meniscus was formed at the exit of the gap between the glass substrate (microscope slide) and the Teflon insert. The gap spacing was adjusted to 1.8×10^{-4} m and the liquid level was positioned at 6×10^{-3} m below the glass surface so that a stable, non-evaporating meniscus formed in which the pressure difference across the meniscus balanced the hydrostatic pressure drop at the start of a test run. The pressure was maintained slightly above atmospheric by adjusting the liquid storage levels. The glass substrate was cleaned in an ethanol vapor degreasing unit prior to installation in the test cell. Ethanol was also used as the test fluid because it wets glass very well. The dimensions of the glass substrate were 0.025 m $\times$ 0.076 m $\times$ 0.001 m.

Thin film nickel resistors—approximately 10^{-7} m thick, 1.27×10^{-4} m wide and 1.25×10^{-2} m long—with a resistance of approximately 500 ohms were vapor deposited on both sides of the glass substrate as shown in Fig. 2. Several of these on the upper surface were used to generate heat which was conducted through the glass to the meniscus region where evaporation occurred. The remainder were calibrated and used as resistance thermometers to measure the temperature distribution on the glass surface.[2] In addition, thermocouples were used to measure the temperature at various locations in the test cell. The substrate temperature distribution for four settings of the heater power input are presented in Fig. 3. The evaporating meniscus was stable during these tests and did not appear to vibrate. However, at significantly higher power settings a fluctuating meniscus was observed. The tests were conducted by first fixing the shape of the isothermal meniscus and then setting the power level so that evaporation occurred. The reported data represent the results of one continuous test run. No attempt was made to measure the maximum stable heat flux for the nonfluctuating case.

The test cell was mounted on a movable stage of a microscope so that the meniscus could be observed and photographed at 350X using monochromatic light with a wavelength of 5.89×10^{-7}m. Because of

---

[1] Present address: Westvaco Research Laboratory, Laurel, MD

Contributed by the Heat Transfer Division for publication in the JOURNAL OF HEAT TRANSFER. Manuscript received by the Heat Transfer Division March 27, 1978.

[2] A Keithley Model 520 nanowatt dissipation resistance bridge was used.

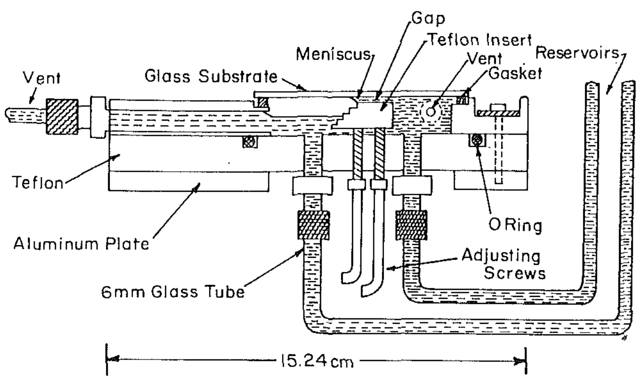

Fig. 1 Cross section of test cell (not drawn to scale)

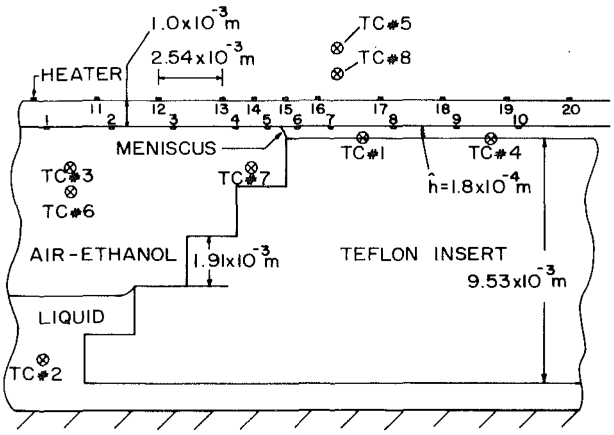

Fig. 2 Location of vapor deposited resistance thermometers

the significant difference between the refractive index of the glass, 1.5, and the ethanol liquid, 1.36, the interference patterns formed by the light waves reflected from the glass-liquid and liquid-vapor (ethanol-air mixture) boundaries were easily photographed for the various power settings. The photographic negatives were passed between a light source and a fiber optic probe connected to a photometer. The amount of transmitted light is an indication of the local film density. Using this densitometry method, the fringe locations were measured to an accuracy of approximately $\pm 10^{-7}$ m. The fringe number, No. 1 = first dark fringe, No. 2 = first light fringe, etc., is plotted versus the measured fringe location from the interline in Fig. 4 for the test runs. It is obvious that the fringes moved closer together as the heat flux was increased indicating a change in the meniscus shape due to evaporation.

In this experimental design, there is no change in the phase of lightwaves upon reflection at the boundaries because of the ever increasing refractive index. Therefore, the meniscus thickness profile, $h(x)$, can be related to the fringe location as follows:

$$\left.\begin{array}{l}\text{minimum}\\ \text{intensity}\end{array}\right\} h = \frac{(2L+1)\,\lambda\,(\cos\theta)}{2n_\ell\,(1+\cos\theta)}, \quad L = 0, 1, 2 \ldots \tag{1}$$

$$\left.\begin{array}{l}\text{maximum}\\ \text{intensity}\end{array}\right\} h = \frac{L\lambda\,(\cos\theta)}{n_\ell\,(1+\cos\theta)}, \quad L = 0, 1, 2 \ldots \tag{2}$$

where θ is the local meniscus slope. The meniscus thickness at the first fringe can be calculated using (1) if the slope is neglected:

$$h_1 = \lambda/4n_\ell \tag{3}$$

For an ethanol meniscus this gives a thickness of 1.08×10^{-7} m. Each succeeding fringe, minimum and maximum, represents a thickness increase of approximately this amount. Microscope slide roughness (Corning glass) was not examined explicitly. However, an evaluation of the uniformity of the fringes in the width and length direction did

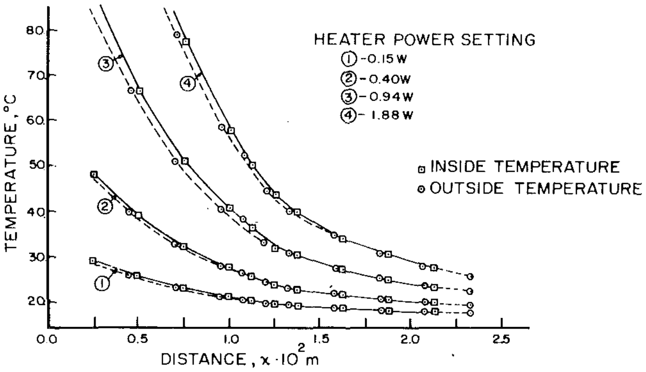

Fig. 3 Substrate temperature versus distance from heater

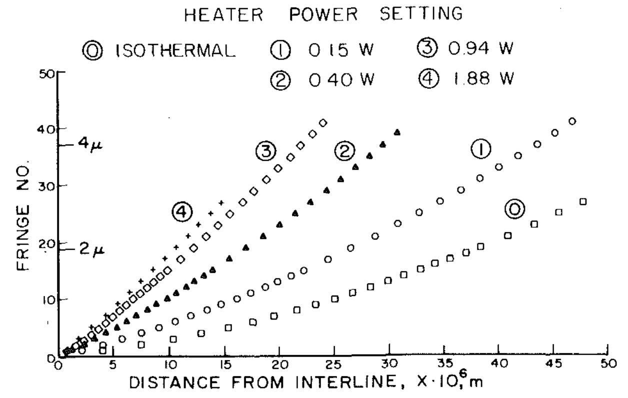

Fig. 4 Fringe number (No. 1 = first dark fringe, No. 2 = first light fringe, etc.) versus distance from interline, $X = x + |\hat{x}|$. (x = 0 at first fringe)

Nomenclature

H = latent heat of vaporization, $\mathrm{J \cdot kg^{-1}}$
k = thermal conductivity of substrate, $\mathrm{Jm^{-1}\,s^{-1}\,K^{-1}}$
N = fringe number, dimensionless
$\bar{Q}_e$ = nondimensional evaporative heat dissipation
Q^* = total evaporative heat dissipation per unit width, w – $\mathrm{m^{-1}}$
$\bar{\bar{Q}}$ = nondimensional heat flow rate conducted in substrate
$\bar{T}$ = temperature, °C
h = local meniscus thickness, m

k = thermal conductivity of glass substrate
n_ℓ = refractive index of liquid, dimensionless
$\dot{n}$ = local volumetric flow per unit width, $\mathrm{m^3 \cdot s^{-1} \cdot m^{-1}}$
$\dot{n}^*$ = total incoming volumetric flow per unit width, $\mathrm{m^3 \cdot s^{-1} \cdot m^{-1}}$
t = thickness of substrate, m
x = coordinate along meniscus, m
w = width of glass substrate
γ = defined in equations (5) and (6)

$\bar{\theta}$ = nondimensional temperature
$\bar{\bar{\theta}}$ = nondimensional temperature averaged over width and thickness
θ = meniscus angle, radians
λ = wavelength of light, m
ξ = nondimensional coordinate in x-direction
ρ_ℓ = liquid density, $\mathrm{kg \cdot m^{-3}}$

Superscripts

i = into meniscus region
j = out of meniscus region

not indicate the presence of a roughness effect. Although constructive interference occurs for small meniscus thicknesses, the location of the meniscus interline, if indeed a finite contact angle meniscus existed, was not sharply defined in our studies because of the relative intensities of the reflected light and the sensitivity of our equipment. Some information concerning the interline could be obtained but in most cases it was possible to determine only a right most bound for the interline location. That is, the point at which the presence of some liquid was detectable by observable interference. The measured value of this interline location is plotted versus the predicted value, from the model discussed in Part II, for the four power settings in Fig. 5. The interline location is given relative to the first fringe location which lies to the right of the interline. As expected, this distance decreased with an increase in the heat flux. In the nonevaporating case, a meniscus curvature of 1.6 × 10^{-1} m^{-1} was determined using interferometry versus an expected value of 2 × 10^{-3} m^{-1} based on hydrostatics. This difference is attributed primarily to insufficient accuracy in the measurement of the actual liquid level in the cell. This initial difference is not believed to effect the conclusions arrived at below because of the relatively large changes in meniscus shape on heating. Additional information concerning these experiments are available in [1].

Analysis of Temperature Data

The glass surface temperatures measured with the resistance thermometers are plotted in Fig. 3. Each measurement represents the surface temperature at a particular location averaged over one half of the width of the glass substrate (resistor length = 0.0125 m) and the width of the thin film resistor, 1 × 10^{-4} m. Using a two-dimensional analysis the substrate temperature was found to vary approximately 3 percent from its maximum value at the substrate centerline to its value at the edge of the resistance thermometer [1]. The precision of each temperature measurement was approximately ±0.1 °C. This was due to an uncertainty of ±0.05 ohms in measuring the resistance of the nickel thin films. Since we are concerned with heat flux rather than absolute temperature, the calibration error associated with the absolute temperature is of less importance. The temperature distribution, $\overline{T}(x)$, can be made nondimensional by defining

$$\xi = \frac{x}{w}; \quad \bar{\theta} = \frac{\overline{T} - T_\infty}{T_2 - T_\infty} \tag{4}$$

where T_∞ is the ambient temperature, $\overline{T}_2$ is the temperature measured by resistance thermometer No. 2 at that particular power input setting and w is the glass substrate width. As a result of this scaling, the data for all power input settings become nearly similar. In Fig. 6, the natural logarithm of the nondimensional temperature, ln $\bar{\theta}$, is plotted versus distance, ξ, for power setting No. 3, which is a typical case. Away from the evaporating meniscus region, the data indicate that the temperature can be assumed to be that of one-dimensional heat conduction in a thin slab with natural convection losses from the top surface. An analysis of conduction in the glass away from the meniscus region confirms this experimental result [1]. The data are well represented by the following equations

$$\bar{\bar{\theta}}^{(i)}(\xi) = \bar{\bar{\theta}}_0{}^{(i)} \exp(-\gamma^{(i)}\xi); \quad \xi < 0.3 \tag{5}$$

$$\bar{\bar{\theta}}^{(j)}(\xi) = \bar{\theta}_0{}^{(j)} \exp(-\gamma^{(j)}\xi); \quad \xi > 0.4 \tag{6}$$

where $\bar{\bar{\theta}}$ is the nondimensional temperature averaged over one half the substrate width and the thickness. The nondimensional heat flow rate, $\bar{\bar{Q}}(\xi) = -\gamma\bar{\bar{\theta}}$, can be obtained by differentiation of the one dimensional model equations (5) and (6). A measure of the heat removed by evaporation can be obtained by extending the one-dimensional model to the location of the meniscus interline. The line $\xi = 0.3$ corresponds to the location of resistance thermometer No. 4. The line $\xi = 0.4$ corresponds to the location of No. 6. Resistance thermometer No. 5 is located at $\xi = 0.36$. The temperature measured by sensor No. 5 is lowered by the proximity of the interline heat sink. Therefore, only the first four sensors were used to extrapolate the incoming heat flux to the meniscus interline. The heat flow rate out of the glass in the meniscus region which is predominately due to evaporation, $\overline{Q}_e$, is equal to the difference between the incoming and outgoing heat flow rates in the glass

$$\overline{Q}_e = \bar{\bar{Q}}^{(i)} - \bar{\bar{Q}}^{(j)} \qquad \xi = \begin{matrix}\text{meniscus}\\ \text{location}\end{matrix} \tag{7}$$

The actual evaporative heat loss from the glass due to evaporation per unit width can be calculated using

$$Q^* = \frac{kt}{w}(\overline{T}_2 - T_\infty)\overline{Q}_e \tag{8}$$

The above analysis demonstrates that the heat flux based on the interline length varied from zero to 1.36 w/m in our tests. This maximum level of heat flow can be averaged over the first 10^{-5} m to obtain an estimate of the average heat flux based on the area equal to 1.36 × 10^5 w/m^2. The results show that the ratio $Q_e/\bar{\bar{Q}}^{(i)}$ decreases from 0.31 to 0.22 as the power input setting is increased [1]. This indicates that substrate conduction limits the amount of heat delivered to the meniscus for evaporation. The incoming volumetric flow rate which must be evaporated per unit width to account for this heat flux can be calculated using

$$\dot{n}^* = Q^*/\rho_\ell H \tag{9}$$

where ρ_ℓ is the density of the liquid and H is the latent heat of vaporization. The results obtained for all power input settings are given in Table 1.

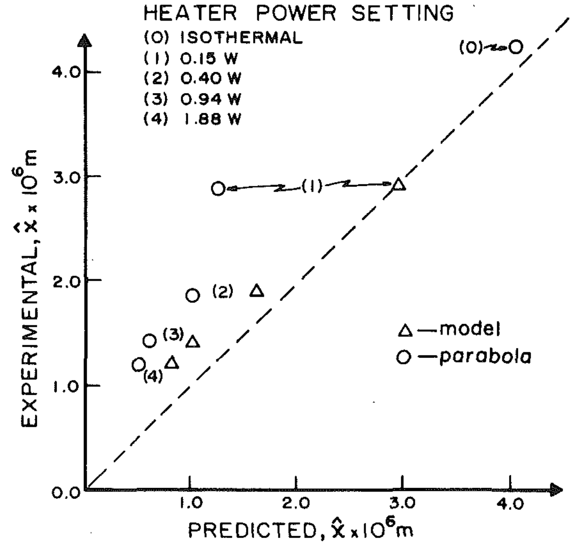

Fig. 5. Experimental versus predicted value of interline location relative to first fringe, $x = -\hat{x}$

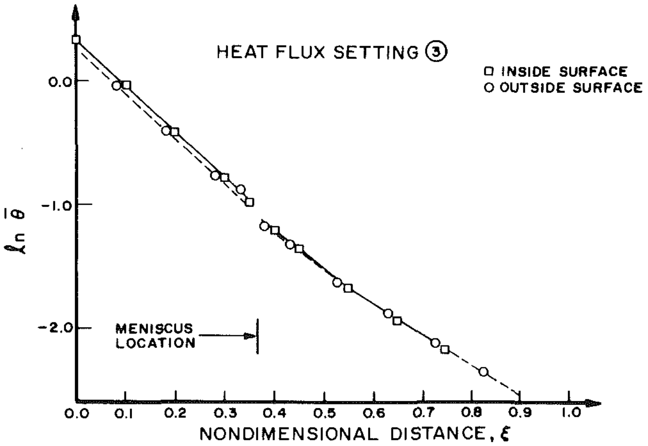

Fig. 6 Natural logarithm of the nondimensional temperature versus nondimensional distance from heater

Table 1

Heat Flux Setting	1	2	3	4
$\bar{\bar{\theta}}_0^{(i)}$	1.42	1.42	1.43	1.44
$\bar{\bar{\theta}}_0^{(j)}$ ($\xi = 0.4$)	0.31	0.31	0.30	0.29
$\gamma^{(i)}$	3.75	3.75	3.80	3.95
$\gamma^{(j)}$	2.72	2.96	3.10	3.20
ξ meniscus	0.360	0.362	0.365	0.368
$\bar{\bar{Q}}^{(i)}$ (ξ meniscus)	1.38	1.37	1.36	1.33
$\bar{\bar{Q}}^{(j)}$ (ξ meniscus)	0.94	1.03	1.04	1.03
$\bar{Q}_e$	0.44	0.34	0.32	0.30
$\bar{Q}_e/\bar{\bar{Q}}^{(i)}$ (ξ meniscus)	0.31	0.25	0.24	0.22
Q^* [w/m]	0.18	0.37	0.79	1.36
$\dot{n}^*$ [$m^3/m - s \times 10^{10}$]	2.60	5.35	12.74	20.48

The error in the determination of $\bar{Q}_e$ can be obtained from estimates of the error in determining the one dimensional heat flux into and away from the meniscus region. The relative error for the nondimensional heat flux can be calculated as

$$\frac{\Delta \bar{Q}}{\bar{Q}} = \frac{\Delta \gamma}{\gamma} + \frac{\Delta \theta_0}{\bar{\bar{\theta}}_0} \qquad (10)$$

The estimates for these quantities are $\Delta\gamma = \pm 0.025$ and $\Delta\bar{\bar{\theta}}_0 = \pm 0.05$. The uncertainty in determining the interline location is insignificant in this case. Using equation (10) for both the incoming and outgoing heat flux, an error estimate of 13 percent for the evaporative heat flux is obtained for the worst case.

Discussion and Conclusions

The experimental results presented above significantly increase the available data concerning the steady-state evaporating meniscus. In order to complete the study, a mathematical model is now needed to relate the observed change in the meniscus profile to the evaporative heat flux obtained from the temperature measurements. The model must relate the shape of the evaporating meniscus to the pressure gradient needed to supply the volumetric flow rate to maintain steady-state evaporation. The solution to this involved problem is discussed in Part II [3]. Briefly, we can say that the measured fringe locations for all heat flux settings were analyzed using the measured heat flux in a nonlinear parameter estimation technique. By assuming a mathematical model for the meniscus profile with adjustable parameters, the fringe location data were used to select those parameters which yielded the best agreement between the measured and predicted fringe location in the least squares sense. The results of this analysis demonstrated that a model which included fluid flow resulting from a curvature gradient represented the data better than a constant curvature model.

Using only the experimental results, we can state that:

1 the average evaporative heat flux in an evaporating meniscus has been measured for the range 0–1.36 w/m of interline using resistance thermometers vapor deposited on the galss substarte; and

2 the profile of an evaporating meniscus has been measured in the thickness range (0.1–4) × 10^{-6} m using the optical technique of interferometry.

These measurements lead to the conclusion that the evaporating meniscus profile is stable and that it is a function of the evaporative heat flux.

Acknowledgment

The financial support received through National Science Foundation Grants GK-43116 and ENG 76-01608 are gratefully acknowledged.

References

1 Renk, F. J., "Analytical and Experimental Investigation of an Evaporating Meniscus" Ph.D. Dissertation, Rensselaer Polytechnic Institute, Troy, N. Y., 1977.

2 Renk, F. and Wayner, P. C., Jr., "The Measurement of Fluid Flow and Heat Transfer in an Evaporating Meniscus," *Proceedings of the Fifth International Heat Transfer Conference,* Vol. 5, 1974, pp. 252–256.

3 Renk, F. and Wayner, P. C., Jr., "An Evaporating Ethanol Meniscus: Part II, Analytical Studies," ASME JOURNAL OF HEAT TRANSFER, Vol. 101, No. 1, 1979, pp. 59–62.

4 Preiss, G. and Wayner, P. C., Jr., "Evaporation from a Capillary Tube," ASME JOURNAL OF HEAT TRANSFER, May 1976, pp. 178–181.

F. J. Renk[1]
P. C. Wayner, Jr.
Department of Chemical and Environmental Engineering, Rensselaer Polytechnic Institute, Troy, N. Y. 12181

An Evaporating Ethanol Meniscus

Part II: Analytical Studies

A model of capillary flow heat transfer is used to analyze the data obtained in Part I. The results indicate that fluid flow resulting from a change in the meniscus profile replenishes the liquid evaporated in a stationary evaporating meniscus. Local evaporative heat fluxes can be very high near the interline region of a finite contact angle meniscus. Therefore, a small stationary evaporating meniscus can be used as a very effective local heat sink.

Introduction

The change in shape of a horizontal, two-dimensional evaporating ethanol meniscus has been experimentally determined as a function of heat flux [1, 2]. This was obtained by measuring the change in the location of naturally occurring interference fringes with heat input as discussed in Part I [2]. The evaporative heat dissipation in the vicinity of the meniscus interline was also obtained from the measured temperature distribution in the substrate. The incoming volumetric flow rate necessary to maintain a stationary, steady-state evaporating meniscus was calculated from this value. Herein, a mathematical model is used to relate the shape of the evaporating meniscus to the pressure gradient necessary to supply the required volumetric flow rate. The model represents the fluid flow distribution in a finite contact angle meniscus in which the pressure gradient is assumed to be solely due to capillarity, that is, a curvature gradient along the liquid-vapor interface. The model is then used to enhance our understanding of the evaporating meniscus by calculating the interline curvature, the heat flux distribution, the flow distribution, and local surface temperature difference. Nondimensional initial conditions are developed in the analysis which may be related to the burnout phenomena which occurs in many devices.

Fluid flow and heat transfer in an evaporating extended meniscus formed on a vertical flat plate with a constant surface temperature have been modelled by Potash and Wayner [3]. The extended meniscus consisted of both an intrinsic meniscus region (thickness greater than approximately 5×10^{-8} m and an adsorbed thin film region. It was demonstrated that capillary effects in the intrinsic meniscus region and disjoining pressure effects in the thin film region were sufficient to produce the necessary fluid flow for stable evaporation. The effect of thermocapillarity was shown to be small in a related study of evaporating thin films with thicknesses and curvatures of interest herein [4]. However, the quantitative limits where thermocapillarity can be neglected in these systems have not been established. The present analysis of experimental data supports the hypothesis that fluid flow results from a change in the evaporating meniscus profile.

Basic Equations

The coordinate system for the analysis of fluid flow in the vicinity of the interline of an evaporating meniscus is depicted in Fig. 1. The meniscus profile is denoted by $h(x)$, which gives the location of the liquid-vapor interface. The Navier-Stokes equations for steady, two-dimensional flow with constant properties can be solved by using the lubrication approximations (slight liquid film taper, body and inertial forces negligible). The liquid-vapor interface is considered to be shear free. In addition, no slip occurs at the liquid-solid boundary which is defined to be the zero streamline. The solution for the stream function under these conditions is

$$\Psi = \frac{-1}{6\mu}\frac{dP_\ell}{dx}(3y^2 h(x) - y^3) \tag{1}$$

The local volumetric flow can be obtained as

$$\dot{n}(x) = \int_0^{h(x)} u dy = \Psi(h) = \frac{-h^3(x)}{3\mu}\frac{dP_\ell}{dx} \tag{2}$$

The consistency of the above result can be demonstrated by showing that the evaporation rate $d\dot{n}(x)/dx$ is equal to the normal velocity component at the liquid-vapor interface. The normal velocity component is given by $(v \cos \theta - u \sin \theta)$, where $\tan \theta$ is equal to dh/dx.

The local liquid film pressure is related to the ambient pressure by the capillary equation

$$P_v - P_\ell(x) = \gamma_{\ell v} K(x) \tag{3}$$

where $K(x)$ is the local curvature of the liquid-vapor interface and $\gamma_{\ell v}$ is the surface tension. A change in curvature is then a mechanism

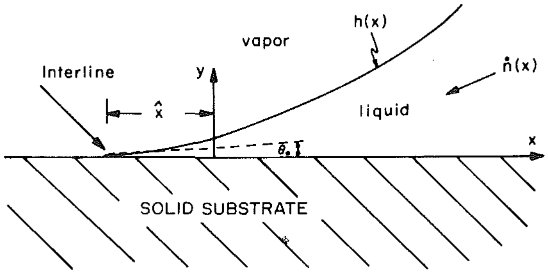

Fig. 1 Evaporating extended meniscus: film thickness at $x = 0$ is $h(0) = 1.08 \times 10^{-7}$ m; film thickness at $x = -\hat{x}$ is $h(-\hat{x}) = 0$

---

[1] Present address: Westvaco Research Laboratory, Laurel, MD

Contributed by the Heat Transfer Division for publication in the JOURNAL OF HEAT TRANSFER. Manuscript received by the Heat Transfer Division March 27, 1978.

for producing the pressure gradient for flow in the evaporating meniscus. Assuming constant surface tension along the interface (thermocapillary effects negligible), equation (3) can be differentiated as follows

$$-\frac{dP_\ell}{dx} = \gamma_{\ell v}\frac{d}{dx}\left[\frac{h''}{(1+h'^2)^{3/2}}\right] = \gamma_{\ell v}\left[h''' - \frac{3}{2}h'\,h''^2 + \ldots.\right] \tag{4}$$

It has been common practice to ignore all terms except for the first in the interline vicinity because of the small meniscus slope. The local mass flow rate can then be written solely as a function of the meniscus profile.

$$\Gamma = \frac{\rho_\ell \gamma_{\ell v} h^3(x)}{3\mu}\frac{d^3h}{dx^3} \tag{5}$$

In principle, using equation (5), the local mass flow rate could be obtained if the meniscus profile were measured exactly. However, the need to differentiate three times makes this difficult.

The local evaporation rate can be equated to the local heat conduction rate across the liquid film by introducing the latent heat of vaporization, H. The resulting equation is

$$-k_\ell\left[\frac{T_w(x) - T_{\ell v}(x)}{h(x)}\right] = \frac{\rho_\ell H \gamma_{\ell v}}{3\mu}\frac{d}{dx}\left(h^3\frac{d^3h}{dx^3}\right) \tag{6}$$

Convective heat transfer along the meniscus can be neglected for small Reynolds number as long as the Prandtl number is moderate. Equation (6) can be rearranged as follows

$$h\frac{d}{dx}\left(h^3\frac{d^3h}{dx^3}\right) = -3\Lambda\,[T_w(x) - T_{\ell v}(x)] \tag{7}$$

where $\Lambda = (\mu k_\ell/\rho_\ell H\gamma_{\ell v})$. The parameter Λ is a measure of the distortion of the meniscus profile due to evaporation for a given wall superheat. The value of Λ for ethanol is approximately 3.6 times higher than that for water when physical properties are evaluated at 20°C. This calculation demonstrates that ethanol is relatively sensitive to heat input compared to water and may explain why a dramatic change in meniscus shape was observed with heat input [2].

A Proposed Model

The energy balance described by equation (7) has introduced two additional unknowns—the solid substrate wall temperature ($T_w(x)$) and the liquid-vapor interfacial temperature ($T_{\ell v}(x)$). As an alternative, a comparable equation could be written using the temperature difference between the solid and the vapor. In the latter case, the wall temperature $T_w(x)$ is an unknown and the value of the liquid-vapor interfacial heat transfer coefficient is questionable for a polar liquid. To solve for these unknowns, one could invoke equations describing the heat transfer in the solid substrate and mass transfer away from the liquid-vapor interface. The evaporating meniscus shape would then be obtained by simultaneous solution of a coupled system of equations. However, there are difficulties associated with this approach. For example, Lorenz and Mikic [5] found it necessary to use a constant solid surface temperature and an arbitrary variation in the value of the interfacial heat transfer coefficient in their numerical evaluation of heat transfer in dropwise condensation. These assumptions are unacceptable in the current problem. The major difficulty at the present time is the lack of experimental data in the important film thickness range $\delta < 1.1 \times 10^{-7}$ m. This necessitates the use in this region of a microscopic model based on macroscopic data.

A practical alternative for obtaining the evaporating meniscus profile has been to assume some simple form of the temperature difference distribution in equation (7). This approach has been used in [6] wherein a power law temperature distribution has been shown to yield a power law solution for the meniscus profile. However, this solution predicts infinite curvature and pressure gradient at the interline and is valid only for zero contact angles. Another drawback to the general approach of specifying the temperature difference distribution is that there is no strong physical basis for a particular choice of the form of this driving function. Therefore we feel that a more suitable place to use physical reasoning with the current experimental data is in specifying the volumetric flow rate $\dot{n}(x)$. Two boundary conditions can be imposed on this function. The flow rate must be zero at the interline in order to satisfy mass conservation. Secondly, the flow rate must become asymptotic to a finite value with increasing meniscus thickness. It is proposed here that the following equation can be used to represent the volumetric flow rate in the evaporating meniscus.

$$\dot{n}(x) = -\dot{n}^*\left(\frac{h(x)}{h(x)+\delta^*}\right)^a;\ a > 0 \tag{8}$$

Equations (5) and (8) can be combined to give the following result

$$\frac{d^3h}{dx^3} = -\frac{3\mu\dot{n}^*}{\gamma_{\ell v}}\frac{h^{a-3}}{(h+\delta^*)^a} \tag{9}$$

For values of 'a' greater than 3, the value of the pressure gradient at the interline will be zero. For values of 'a' less than 3, it will be infinite. For 'a' equal to 3, the interline pressure gradient will be finite and the equation takes on the following form

$$(h+\delta^*)^3\frac{d^3h}{dx^3} = -\frac{3\mu\dot{n}^*}{\gamma_{\ell v}} \tag{10}$$

The experimental data on the temperature distribution gives the integral heat flow rate into the region of interest and, therefore, the incoming volumetric flow rate of the evaporating liquid, $\dot{n}^*$. The use of the incoming volumetric flow rate couples the microscopic fluid flow model to the macroscopic heat transfer measurement. According to the model, the change in meniscus profile is a measure of the heat flux distribution. The major heat transfer consequences of using this model are that it causes the evaporative heat flux distribution to start at zero at the interline, go through a maximum and become zero again at a large value of the meniscus thickness. This form for the heat flux distribution seems sensible. It also forces the volumetric flow rate to become zero at the interline. In the limit as the parameter δ^* approaches zero, the model reduces to the equation for constant volumetric flow rate. That is, the interline becomes a sink for evaporation. Therefore, the parameter δ^* is a measure of the region over which

Nomenclature

A = interline curvature, m^{-1}
G = nondimensional meniscus thickness
H = latent heat of vaporization, J·Kg^{-1}
K = meniscus curvature, m^{-1}
P_ℓ = liquid pressure, N·m^{-2}
P_v = vapor pressure N·m^{-2}
Q = local heat flux, ω/m^2
S_1, S_2 = nondimensional initial conditions
T_w = wall temperature, °C
$T_{\ell v}$ = liquid-vapor interfacial temperature, °C
h = meniscus thickness, m
k_ℓ = liquid thermal conductivity, J/m·s·K
$\dot{n}$ = local volumetric flow rate per unit width, m^2·s^{-1}
$\dot{n}^*$ = total incoming volumetric flow rate per unit width, m^2·s^{-1}
s = nondimensional x-coordinate
$\hat{s}$ = nondimensional interline location
u = velocity component in x-direction, m·s^{-1}
v = velocity component in y-direction, m·s^{-1}
x_0 = characteristic length, m
$-\hat{x}$ = interline location, m
Γ = mass flow rate, kg·m^{-1}·s^{-1}
$\gamma_{\ell v}$ = surface tension, N·m^{-1}
ρ_ℓ = liquid density, kg·m^{-3}
μ = absolute viscosity, N·s·m^{-2}
δ^* = parameter in model equation (8)
Λ = evaporating meniscus number, m·K^{-1}
Ψ = stream function, m^2·s^{-1}
θ = local meniscus angle, radians
θ_0 = contact angle, radians

evaporation occurs and of the size of the initial pressure gradient. The proposed model, therefore, contains the two parameters which describe the physical process—the incoming volumetric flow rate ($\dot{n}^*$) and an indication of the size of the evaporating region. The differential equation (10) is subject to three initial conditions,

$$h(-\hat{x}) = 0; h'(-\hat{x}) = \theta_0; h''(-\hat{x}) = A \qquad (11)$$

where $-\hat{x}$ is the location of the meniscus interline relative to the location of the first interference fringe. The thickness at this point which is chosen as the origin of the coordinate system is approximately 1.08 $\times 10^{-7}$ m.

No analytical solutions could be found for the proposed model equation. The model differential equation can be nondimensionalized in order to facilitate numerical solution by defining new variables,

$$G(s) = h(x)/\delta^*; s = x/x_0 \qquad (12)$$

where the meniscus characteristic length x_0 is chosen such that

$$\frac{3\mu\dot{n}^* x_0^3}{\gamma_{\ell v}\delta^{*4}} = 1 \qquad (13)$$

The model equation (10) and boundary conditions (11) become

$$\frac{d^3G}{ds^3} = \frac{-1}{(1+G)^3} \qquad (14)$$

$$\frac{d^2G}{ds^2}(-\hat{s}) = S_2; \frac{dG}{ds}(-\hat{s}) = S_1; G(-\hat{s}) = 0 \qquad (15)$$

The solution behavior of the nonlinear differential equation (14) is strongly dependent upon the initial conditions S_1 and S_2. For certain values, the solution behaves as a parabola for large values of the independent variable, that is the curvature approaches a constant value. For other values of the initial conditions, the solution behaves like a cubic polynomial with change of sign in the curvature. The solution is not monotonically increasing and is referred to here as unstable, since it cannot represent the shape of the steady state evaporating meniscus. The region of initial conditions which yield stable (monotonically increasing) solutions to the model differential equation (14) is depicted in Fig. 2. The boundary between stable and unstable solutions represent initial conditions for which the solution becomes asymptotic to a straight line. The pressure gradient for fluid flow results from the following changes at the meniscus interline given in Fig. (2): (1) the pressure near the interline is reduced by an increase in curvature near the interline as a result of an increase in evaporation rate, and (2) for a stable meniscus, an increase in the absolute magnitude of a negative curvature gradient must supplement the increase in interline curvature. The choice of the two nondimensional coefficients S_1 and S_2 is equivalent to picking a value of curvature gradient and curvature, S_2, at the interline. A decrease in contact angle is equivalent to an increase in the absolute magnitude of the curvature gradient at the interline. Obviously a high negative initial curvature gradient (low contact angle) must supplement a high positive initial curvature. Otherwise, negative curvature will result in the meniscus and the solution will be unstable.

Analysis of Meniscus Profile Data

The model differential equation (14) can be solved numerically with different values of the physical parameters until good agreement is obtained with the measured locations of the interference fringes [2]. The following parameters are estimated according to the method of Marquardt [7] to give optimum agreement in the least squares sense between predicted and measured fringe locations—the initial curvature, A, the parameter δ^*, and the interline location, $\hat{x}$. The evaporative heat dissipation obtained from the temperature data gives the appropriate volumetric flow rate, $\dot{n}^*$, for each heat flux level as given in Part I [2]. The contact angle, θ_0, is fixed at the value of 0.022 radians which was obtained by fitting a constant curvature model to the nonevaporating meniscus fringe data. It is assumed that the contact angle remained unchanged in the evaporating cases. An analysis of the effect of contact angle [1] justified this assumption.

In the nondimensional form of the model equation, the parameters to be estimated are S_1, S_2, and $\hat{s}$. The estimates of the initial conditions S_1 and S_2 obtained from the least squares fit to the interference fringe locations are plotted in Fig. 2 for all four heat flux levels. The values of the calculated physical parameters based on these estimates are given in Table 1. It should be noted that as the heat flux level is increased, the estimated values of the initial conditions approach the point given by S_1 equal to 0 and S_2 equal to 1 in Fig. 2. Although impossible to demonstrate at this time, we can suggest that this point is related to the burnout phenomenon which occurs in many devices when the evaporating meniscus can no longer pump the required flow rate to dissipate the heat flux. The model predicts a significant change in the interline location, $\hat{x}$, and the interline curvature, A, which are given in Table 1.

Discussion and Conclusions

The predicted interline location, $\hat{x}$, is plotted versus the measured interline location in Fig. 3. Although the predicted value of the dis-

Table 1 Estimates of physical parameters

Heat Flux Setting	1	2	3	4
Q^* w/m	0.18	0.37	0.79	1.36
$\dot{n}^*$ m^3/m-s $\times 10^{10}$	2.60	5.35	12.74	20.48
S_1	0.367	0.216	0.146	0.123
S_2	0.809	0.872	0.923	0.942
$\hat{x}$, m $\times 10^6$	2.99	1.61	0.92	0.80
δ^*, m $\times 10^6$	0.198	0.077	0.045	0.039
A/A_0	9.01	72.0	287.5	482.5

$A_0 = 1.63 \times 10^3 \text{m}^{-1}$ (curvature of nonevaporating meniscus)

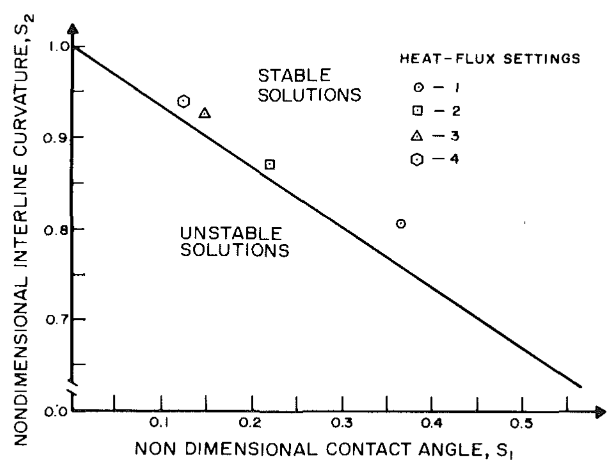

Fig. 2 Nondimensional interline curvature versus nondimensional contact angle

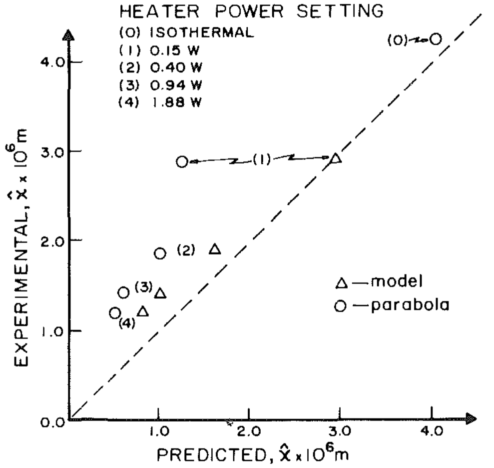

Fig. 3 Experimental versus predicted value of interline location relative to first fringe, $x = -\hat{x}$

tance is acceptable, it is found to be less than the measured value in three of the four cases. This difference cannot be accounted for by an estimate of the error in the volumetric flow rate nor by a different value of the meniscus contact angle. The difference is believed to result from thin film effects (disjoining pressure) in the region very near the interline which were neglected in the model. A model which neglects disjoining pressure effects would underestimate $\hat{x}$. A constant curvature model is not physically acceptable and, as shown in Fig. 3, does not represent the data well. Apparently, a more extensive model is needed which includes both capillarity and thin film forces and which provides for a smooth transition between these two regions of importance. The current model also demonstrates that an increase in heat flux causes a large increase in the curvature at, and near, the interline. The curvature gradient (pressure gradient) resulting from this profile change gives the necessary fluid flow for a stable meniscus.

Although many of the simplifying assumptions in the model do not hold for the thicker portion of the liquid film, it is interesting to note that the profile predicted by the model intercepts the edge of the Teflon block, with reasonable accuracy considering the distance, when extrapoled across the gap (within 5–7 percent for cases 1–3 and 15 percent for case 4). For heat flux setting number, case 4, the interline curvature is 7.85×10^5 m^{-1} whereas the curvature of the base of the meniscus in the gap is 5.13×10^3 m^{-1}. A 15 percent error in the base curvature could account for the error in case 4.

Using the parameters obtained from the meniscus profile data, the values of the volumetric flow rate, the average velocity, the heat flux and the temperature difference were calculated as a function of distance from the interline. These results are given in Figs. 4 and 5 for each heat flux level considered. It can be seen that significant evaporation occurs over a distance of less than 10^{-5} m. At the highest interline heat flow rate studied, 1.36 w/m, the analysis indicates that a heat flux of the order of 1.3×10^5 w/m^2 was present in the first 10^{-5} m of the stable evaporating ethanol meniscus. The local temperature difference between the liquid-vapor interface and substrate surface reaches a maximum rapidly and then decreases. The evaporative heat flux described by the model approaches zero asymptotically since the volumetric flow rate becomes a constant outside of the region of interest. These general characteristics appear reasonable. On the other hand, we expected that the maximum heat flux would occur closer to but not at the interline.

It should be pointed out that, since we are fitting a microscopic model to macroscopic data, the model is not presumed to be unique. In addition, due to the nature of the phenomena (large heat fluxes over extremely small distances in an ultra thin film with a very large curvature gradient) the model is susceptible to large error. We feel that data for the meniscus thickness region $\delta < 10^{-7}$ m are needed to develop a model further. This would naturally lead to the detail study of two-dimensional conduction in the interline region for comparison with the evaporative heat flux based on a model of viscous flow.

The above analysis of the data obtained in Part I [2] indicates that fluid flow resulting from a change in the meniscus profile replenishes the liquid evaporated in a stationary evaporating meniscus. As a result of this stable fluid flow field, a stationary evaporating meniscus can be used as an effective local heat sink.

Acknowledgment

The authors wish to acknowledge the support of the National Science Foundation Grants Nos. GK43116 and ENG 76-01608.

References

1 Renk, F. J., "Analytical and Experimental Investigation of an Evaporating Meniscus," Ph.D. Dissertation, Rensselaer Polytechnic Institute, Troy, N.Y. 1977.

2 Renk, F. J. and Wayner, P. C. Jr., "An Evaporating Ethanol Meniscus: Part I Experimental Studies," ASME JOURNAL OF HEAT TRANSFER, Vol. 101, No. 1, pp. 55–58.

3 Potash, M. L., Jr. and Wayner, P. C., Jr., "Evaporation from a Two Dimensional Extended Meniscus," *International Journal of Heat Transfer*, Vol. 15, 1972, pp. 1851–1863.

4 Potash, M. L., Jr. and Wayner, P. C., Jr., "Effect of Thermocapillarity on the Evaporating Mensicus," NTIS Accession No. PB 235737, Sept. 17, 1974.

5 Lorenz, J. J. and Mikic, B. B., "The Effect of Thermocapillary Flow on Heat Transfer in Dropwise Condensation" ASME JOURNAL OF HEAT TRANSFER, Vol. 92, No. 1, Feb. 1970, pp. 46–52.

6 Edwards, D. K., Balahrishnan, A., and Catton, I., "Power Law Solutions for Evaporation From a Finned Surface," ASME JOURNAL OF HEAT TRANSFER, Vol. 96, 1974, pp. 423–425.

7 Marquardt, D., "An Algorithm for the Least Squares Estimation of Nonlinear Parameters," *J. Soc. Indust. Appl. Math.*, Vol. 11, No. 2, June 1963, pp. 431–441.

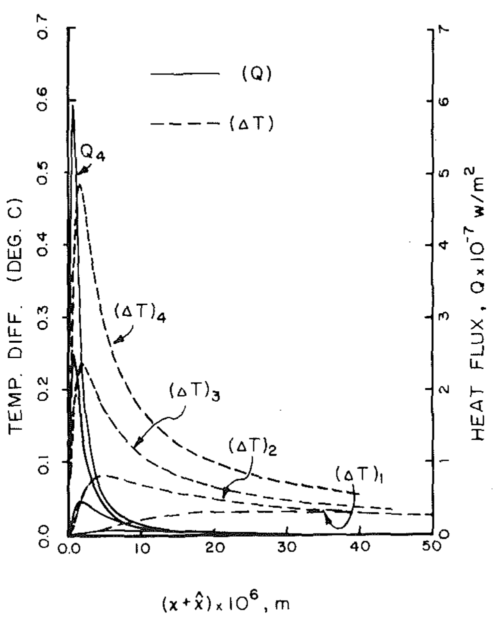

Fig. 4 **Temperature difference ($\Delta T = T_w - T_{lv}$) and local heat flux versus distance from the interline for the heat flux settings listed in Table 1**

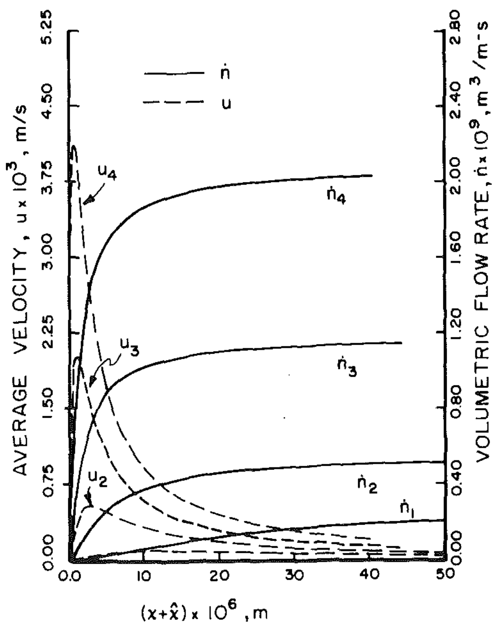

Fig. 5 **Average velocity and volumetric flow rate versus distance from the interline for the heat flux settings listed in Table 1**

K. J. Daniel
Systems Engineer.
General Electric Research Laboratory
Schenectady, New York 12301

N. M. Laurendeau
Assistant Professor of Mechanical Engineering.

F. P. Incropera
Professor of Mechanical Engineering.
Mem. ASME

Purdue University,
West Lafayette, Ind.

Prediction of Radiation Absorption and Scattering in Turbid Water Bodies

In this study four methods of solving the radiative transfer equation applied to shallow ponds have been compared. The methods include a simple version of Beer's law, a representative two-flux model, a six-flux model and the method of discrete ordinates. Calculations have been performed for a wide range of representative conditions typical to natural water. It was found that scattering was unimportant when the scattering albedo is small ($\omega \lesssim 0.5$) and the phase function is highly forward peaked. Consequently, even the simple Beer's law expression yielded accurate predictions. However, in general only the six-flux method provided a suitable compromise between accuracy and operational convenience for all the conditions considered. The two-flux method was found to be the least accurate primarily due to its inability to account for refraction.

Introduction

In recent years there has been considerable interest in the physical and biological properties of natural or man-made water bodies. This interest has been stimulated by the existing or anticipated use of water bodies in engineering applications such as power plant heat rejection, the treatment of wastewater and the intensive culture of edible aquatic organisms. Propagation of visible solar radiation through water bodies significantly affects their thermal structure and growth of photosynthetic organisms. In the interest of accurately predicting photosynthetic rates and/or thermal structure, there is a definite need for reliable methods of calculating the local volumetric rate of radiation absorption within the water [1–4].

A layer of water may be treated as a scattering-absorbing medium (Fig. 1). The incident solar radiation is comprised of diffuse and collimated components and experiences reflection and refraction at the air-water interface. Radiation absorption and scattering occur within the water, and reflection may occur at the bottom surface. The radiation field within the water is determined by the equation of transfer, which may be expressed as [5]

$$\mu \frac{dI_\lambda(\tau_\lambda, \mu, \phi)}{d\tau_\lambda} = -I_\lambda(\tau_\lambda, \mu, \phi) + \frac{\omega_\lambda}{4\pi} \int_0^{2\pi} \int_{-1}^{+1} p_\lambda(\mu', \phi' \rightarrow \mu, \phi) I_\lambda(\tau_\lambda, \mu', \phi') d\mu' d\phi' \quad (1)$$

where $\tau_\lambda \equiv \beta_\lambda z$ is the optical depth and $\omega_\lambda \equiv \sigma_\lambda/\beta_\lambda$ is the single-scattering albedo. Assuming that the water body is homogeneous, equation (1) may be solved for the monochromatic radiance I_λ as a function of position and direction subject to appropriate boundary conditions at the air-water interface and the bottom. The net radiant flux at any position may then be determined from the requirement that

$$F_\lambda(\tau_\lambda) = \int_0^{2\pi} \int_{-1}^{+1} I_\lambda(\tau_\lambda, \mu, \phi)\mu d\mu d\phi \quad (2)$$

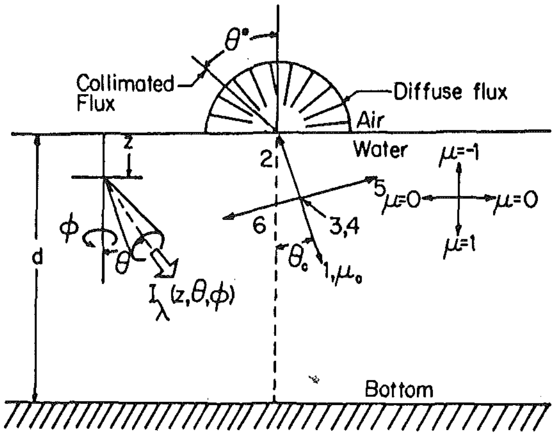

Fig. 1 Physical model and coordinate systems

Contributed by the Heat Transfer Division of THE AMERICAN SOCIETY OF MECHANICAL ENGINEERS and presented at the AIChE Heat Transfer Conference, Salt Lake City, Utah, August 15–17, 1977. Manuscript received by the Heat Transfer Division Ocotber 14, 1977. Paper No. 77-HT-47.

The net flux may in turn be used to determine a normalized form of the local volumetric radiation absorption rate, which is defined as

$$H_\lambda(\tau_\lambda) = -\frac{\partial}{\partial \tau_\lambda}\left[\frac{F_\lambda(\tau_\lambda)}{F_\lambda^*(0)}\right] \tag{3}$$

where $F_\lambda^*(0)$ is the irradiance on the air-water interface.

Past efforts to model solar radiation transfer within a body of water have generally been approximate, and little has been done to assess the relative merits and accuracy of different methods. Initial efforts neglected spectral effects and represented F and H in terms of one or more decaying exponentials [1, 6]. Moreover, such treatments typically ignore multiple scattering effects, as well as internal reflections off surface boundaries. Collectively, these assumptions can lead to significant error, particularly when used with shallow water layers [7, 8]. A variation of the Beer's law solution, which accounts for internal reflections and assumes that all scattered radiation propagates in the forward direction, has been used by Viskanta and Toor [8]. The method was termed forward scattering approximation. For the conditions for which it was initially tested, it provided good agreement with results obtained from more rigorous methods. Viskanta and Toor [7] have also used a variation of Beer's law that assumes all scattered radiation is lost from the radiation field. Consequently, this method ignores multiple scattering effects.

Extensive use has been made of two-flux models to determine the radiation field in scattering-absorbing media. One such model is based on the use of a two-point Gaussian quadrature [9–11]. A major shortcoming of this method is the assumption that the phase function can be accurately represented by the sum of the first two Legendre polynomials. Another related two-flux method [12–16] makes no such assumption and accounts more accurately for anisotropic scattering. However, neither of these methods can account for reflection and refraction effects of the air-water interface. In contrast Armaly [17] has used a two-flux model which accounts for a refractive index change at the upper surface of a semi-infinite medium. However, a major shortcoming of the method is its restriction to isotropic scattering.

A more detailed method is one which uses six discrete components to represent the angular distribution of scattered radiation [18]. However, little can be said about the method since it has not been used in any specific anisotropic scattering studies. Other, more rigorous methods have been reviewed, and one such technique, which is well suited for the problem at hand, is the method of discrete ordinates. It has been used to study the effect of Fresnel reflection at the boundaries of an anisotropically scattering medium [20] and to predict the radiation field in natural water bodies [8].

Although considerable attention has been devoted to the problem of radiative transfer in scattering-absorbing media, there has been no study which systematically compares different methods of solving the equation of transfer for realistic pond conditions. The purpose of this study has been to make such a comparison for four methods, which represent different levels of sophistication: a one-flux Beer's law method, a modified Hamaker two-flux method [12], the six-flux method [18], and the method of discrete ordinates. Although the discrete ordinate method is only one of several techniques for obtaining a high-order estimate of the radiation field [19], it is viewed here as a standard, to which the results of the simpler theories may be compared.

Solution Methods

The Beer's law solution used in this study represents the simplest possible approach to radiative transfer in a scattering-absorbing medium. Scattering is neglected, and it is assumed that there is no reflection off the pond bottom. In addition, the angular distribution of any diffuse contribution to the irradiance at the upper surface is neglected, and the total irradiance is represented by a single collimated beam. For these conditions equation (1) may be simplified to obtain the following result for the radiative flux $F_{c,\lambda}(\tau_\lambda)$ as a function of optical depth [21]:

$$F_{c,\lambda}(\tau_\lambda) = \frac{\mu_c^*}{\mu_c} t^*(\mu_c^*) F^*_{c,\lambda}(0) \exp\left[-(1-\omega_\lambda)\tau_\lambda/\mu_c\right] \tag{4}$$

where the term $[(1-\omega_\lambda)\tau_\lambda]$ is used for convenience in comparing the Beer's law result with the other methods. The variable F_c refers to the flux on a plane normal to the collimated beam, and the superscript * denotes conditions on the atmosphere side of the air-water interface. The transmissivity of this interface, $t^*(\mu_c^*)$, is determined from Fresnel's equation [5] and the cosines μ_c and μ_c^* are related through Snell's law. Note that for irradiation which is exclusively collimated and for zero bottom reflectance, the above solution is equivalent to the forward scattering approximation [7, 8].

Because it is able to account for anisotropic scattering, the Hamaker two-flux model [12] was selected for use in this study. However, the method was modified to separately account for collimated and diffuse components of the radiation field and to relate the scattering factors directly to the phase function. The method is outlined briefly in the following paragraphs, with details provided elsewhere [21].

The radiation field is divided into three components, which include a downward propagating collimated flux F_c and downward and upward propagating diffuse fluxes, F_+ and F_-. Note that the subscript λ has been deleted for convenience in the remainder of this paper. The variation of the collimated flux with optical depth may be obtained from equation (4) without the $(1-\omega_\lambda)$ term in the exponent, and expressions for the noncollimated fluxes may be found by integrating the equation of transfer over the bottom and top hemispheres. Assuming isotropic conditions in both directions and performing the integrations, the resulting expressions are

$$\frac{dF_+}{d\tau} = (-2 + f_s\omega)F_+ - b_s\omega F_- + \frac{\omega t^*(\mu_c^*) f_{s,c}}{2} F_c^*(0) \exp(-\tau/\mu_c) \tag{5}$$

$$\frac{dF_-}{d\tau} = (+2 - f_s\omega)F_- + b_s\omega F_+ + \frac{\omega t^*(\mu_c^*) b_{s,c}}{2} F_c^*(0) \exp(-\tau/\mu_c) \tag{6}$$

Nomenclature

b_s = backward scattering parameter for the two-flux method
d = pond depth, m
F = radiant flux, W/m^2-μm
f_s = forward scattering parameter for the two-flux method
H = normalized volumetric radiation absorption
I = radiance, W/m^2-sr-μm
N = number of Legendre polynominals used to fit the phase function
P_i = Legendre polynomial of order i
p = phase function
t = transmissivity of the air-water interface
z = vertical coordinate, m
β = extinction coefficient ($\beta = \kappa + \sigma$), 1/m
θ = declination angle, rad
κ = absorption coefficient, 1/m
μ = cos θ
ρ = surface reflectivity
σ = scattering coefficient, 1/m
τ = optical depth ($\tau = \beta z$)
ϕ = azimuth angle, rad
ω = scattering albedo ($\omega = \sigma/\beta$)
$\tilde{\omega}_i$ = weighting factor for the Legendre polynomials

Subscripts

c = collimated radiation
D = diffuse radiation
d = bottom ($z = d$) condition
0 = air-water interface condition
λ = monochromatic condition
1, 2, . . . , 6 directions of the six-flux method
+ = downward (positive z) direction
− = upward (negative z) direction

Superscripts

* = air side of air-water interface

where f_s, b_s, $f_{s,c}$ and $b_{s,c}$ are scattering factors for the diffuse field in the forward direction, the diffuse field in the backward direction, the collimated field in the forward direction and the collimated field in the backward direction, respectively. The scattering fractions are a result of expanding the phase function in a series of Legendre polynomials, $P_i(\mu)$, and employing the addition theorem of spherical harmonics. The resulting expressions for the scattering factors are

$$f_s \equiv \int_0^1 \int_0^1 \sum_{i=0}^{N} \tilde{\omega}_i P_i(\mu) P_i(\mu') d\mu' d\mu \tag{7}$$

$$b_s \equiv \int_0^1 \int_{-1}^0 \sum_{i=0}^{N} \tilde{\omega}_i P_i(\mu) P_i(\mu') d\mu' d\mu \tag{8}$$

$$f_{s,c} \equiv \int_0^1 \sum_{i=0}^{N} \tilde{\omega}_i P_i(\mu_c) P_i(\mu) d\mu \tag{9}$$

$$b_{s,c} \equiv \int_{-1}^0 \sum_{i=0}^{N} \tilde{\omega}_i P_i(\mu_c) P_i(\mu) d\mu \tag{10}$$

where $\tilde{\omega}_i$ is a weighting factor and N is the number of polynomials used to fit the phase function. These equations may be solved using standard techniques [21] with the following boundary conditions

$$\tau = 0: F_+(0) = -\rho_0 F_-(0) + t_D^* F_D^* \tag{13}$$

$$\tau = \tau_d: -F_-(\tau_d) = \mu_c \rho_d t^*(\mu_c^*) F_c^*(0) \exp(-\tau_d/\mu_c) + \rho_d F_+(\tau_d) \tag{14}$$

In equation (13) ρ_0 is the hemispherical reflectivity of the air-water interface to radiation incident from below and t_D^* is the transmittance of the interface to diffuse irradiation.

The six-flux method used in this study is identical to that reported by Chu and Churchill [18]. Briefly, differential equations are formulated for radiative fluxes propagating in six mutually perpendicular directions. As shown in Fig. 1, two of the directions (3, 4) are chosen to be parallel to the air-water interface, while two directions (1, 2) are taken along the collimated beam. If there is no collimated radiation, these directions are chosen to be those of the nadir and zenith. The boundary conditions of this study differ from those used by Chu and Churchill [18] and are summarized as follows

$$F_1(0) = [-\rho_0\mu_2 F_2(0) - \rho_0\mu_5 F_5(0) + t_D^* \pi I_D]\mu_1 + t^*(\mu_c^*) F_c^*(0) \tag{15}$$

$$F_6(0) = [-\rho_0\mu_2 F_2(0) - \rho_0\mu_5 F_5(0) + t_D^* \pi I_D^*]\mu_6 \tag{16}$$

$$-F_2(\tau_d) = [\rho_d\mu_1 F_1(\tau_d) + \rho_d\mu_6 F_6(\tau_d)]\mu_2 \tag{17}$$

$$-F_5(\tau_d) = [\rho_d\mu_1 F_1(\tau_d) + \rho_d\mu_6 F_6(\tau_d)]\mu_5 \tag{18}$$

where ρ_0 and ρ_d are the diffuse reflectivities of the upper and lower surfaces, respectively. As for the two-flux formulation, a major shortcoming of this method is the assumption that each of the fluxes is diffuse. This assumption is used to evaluate ρ_0 in equations (15) and (16).

The method of discrete ordinates has been used in other studies, and its development is adequately treated in the literature [8, 20, 21]. The radiation field is divided into a finite number of directions (ordinates), and an integrated radiance is assigned to each direction. In this study, 20 ordinates have been used and the boundary conditions have been formulated in the manner prescribed by Viskanta [8]. The method provides a suitable standard for evaluation of the other techniques.

For each of the four methods the local rate of radiation absorption may be evaluated from equation (3), and the results may be used as a basis for comparing the methods.

Results

The optical properties required for the calculations of this study include the single-scattering albedo and the scattering phase function. In natural waters these properties depend on the nature of the suspended particles. From measurements made in sea water [23, 24] and algal cultures [25], the albedo appears to vary from approximately 0.45–0.95. A constant value of 0.90 over the visible region of the spectrum is representative of dense algal cultures. The phase function is sharply peaked in the forward direction (Fig. 2) and is a weak function of wavelength [25]. Representation of the result for unicellular algae by a weighted sum of thrity Legendre polynomials has been used for the calculations of this study. The coefficients $\tilde{\omega}_i$ and the resulting scattering parameters are listed elsewhere [21]. The sharp decreases of the polynomial fit do not affect the results since they occur only where the absolute value of the phase function is small.

Additional parameters of interest include the declination angle of the collimated flux, μ_c, the bottom reflectivity, ρ_d, and the total optical depth, τ_d. Accounting for refraction at the air-water interface, an appropriate range for the declination angle is $0.661 \le \mu_c \le 1.0$. The refractive index of water was taken to be 1.333. In addition, suitable ranges for ρ_d and τ_d are 0.0–0.5 and 1.75–10, respectively. The approach adopted for the calculations involves selecting standard conditions for the parameters then systematically varying each parameter in order to span the conditions typically found in natural water. The standard values are $\omega = 0.75$, $\mu_c = 0.911$, $\rho_d = 0$ and $\tau_d = 10$. Note that calculations were performed for both pure diffuse irradiation and pure collimated irradiation, with the collimated case corresponding to $\mu_c = 0.911$ chosen as the standard condition.

The first comparison is for the standard conditions, and the results are shown in Fig. 3. It is evident that, relative to the discrete ordinate results, the two-flux method significantly overpredicts absorption in the upper region of the pond. This discrepancy is due to the assumption that any radiation scattered from the incident beam immediately becomes diffuse. This condition increases the effective path length, and hence absorption, of the radiation. Any increase in absorption for the upper layers must, of course, diminish the amount of radiation available for absorption in the lower regions. Conse-

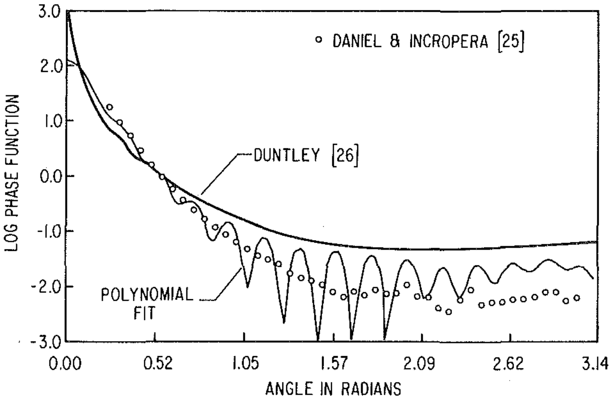

Fig. 2 Experimental phase function data for natural waters [26] and unicellular algae [25], with a polynomial curve fit

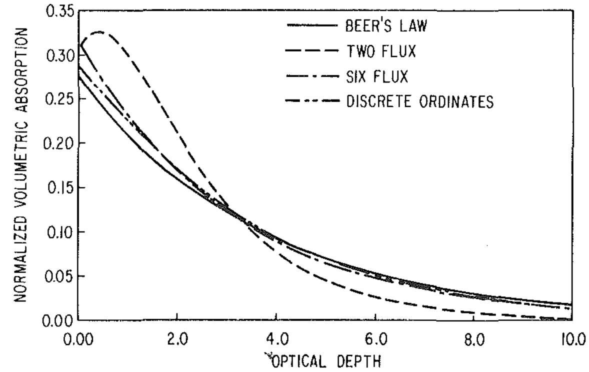

Fig. 3 Comparison of solutions to the equation of transfer for collimated irradiation with the standard conditions ($\omega = 0.75$, $\mu_c = 0.911$, $\rho_d = 0$, $\tau_d = 10$)

quently, the two-flux method underpredicts absorption in the lower regions. The same trend characterizes the six-flux method, but to a smaller degree. This increased accuracy is a direct consequence of resolving the radiation field into six, rather than two, discrete fluxes. The excellent agreement between the Beer's law solution and the discrete ordinate method is due to the fact that the phase function is highly forward peaked, in which case radiation must experience numerous scatterings before becoming appreciably diverged from the collimated beam. However, the discrete ordinate method does account for the small amount of scattering from the collimated beam and for this reason predicts absorption rates in the upper region which are larger than those obtained from Beer's law.

Fig. 4 shows the effect of varying the single scattering albedo. From this figure it is evident that for small values of $\omega \lesssim 0.5$, excellent agreement is obtained for all four methods. This result is due to the fact that, for collimated irradiation, all methods reduce to the Beer's law approximation as the albedo approaches zero. This convergence to Beer's law with decreasing ω becomes more pronounced if the phase function becomes increasingly more forward peaked. This trend is consistent with the observations of Viskanta and Toor [8], who found that the forward scattering approximation, which is identical to the Beer's law solution for the conditions employed in Fig. 4, provides accurate results for natural waters that have $\omega \lesssim 0.55$ and a phase function which is highly forward peaked. However, with increasing ω the differences between methods become more pronounced due to the increasing importance of scattering. For $\omega \gtrsim 0.8$ there appears to be considerable inaccuracy associated with the Beer's law (forward scattering approximation) and two-flux approximations, although reasonable accuracy may still be obtained from the six-flux method. The threshold value of ω for which significant discrepancies appear depends on the shape of the phase function. For phase functions which approach isotropic conditions, the threshold value would be much less than 0.8.

Fig. 5 shows the effect of incidence angle for the collimated radiation. For reasons provided earlier, the two-flux method overpredicts absorption in the upper layers of the water and underpredicts it in the lower layers. However, agreement between the methods improves with increasing incident angle. This trend is due to an increase in the pathlength of the collimated radiation per unit optical depth, causing more absorption to occur and hence reducing the significance of scattering. Note that the significant reduction in the magnitude of the absorption with increasing θ_c is due to a reduction in the transmissivity of the air-water interface.

The effect of diffuse irradiation is shown in Fig. 6, which was generated by using the standard conditions with totally diffuse irradiation at the upper surface. The significant discrepancy associated with the two-flux method is due to its inability to account for refraction at the air-water interface. That is, the two-flux method assumes that the radiation transmitted across this interface remains diffuse, when in fact it is concentrated into a cone within the critical angle for water. This concentration also contributes to the accuracy associated with Beer's law, which assumes all of the radiation in the water to be collimated at $\theta_c = 24.3$ deg (0.424 rad) or $\mu_c = 0.911$.

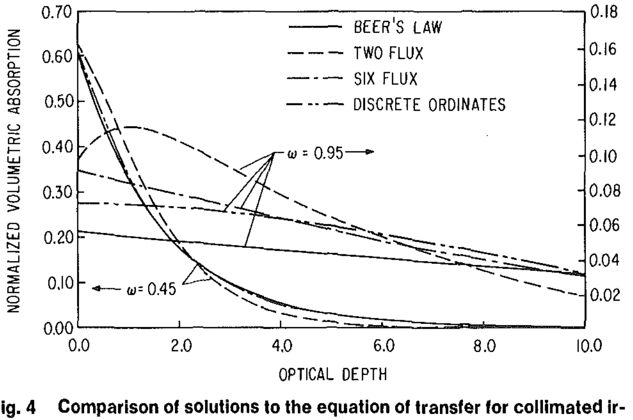

Fig. 4 Comparison of solutions to the equation of transfer for collimated irradiation with $\mu_c = 0.911$, $\rho_d = 0$, $\tau_d = 10$, and $\omega = 0.45$ or $\omega = 0.95$

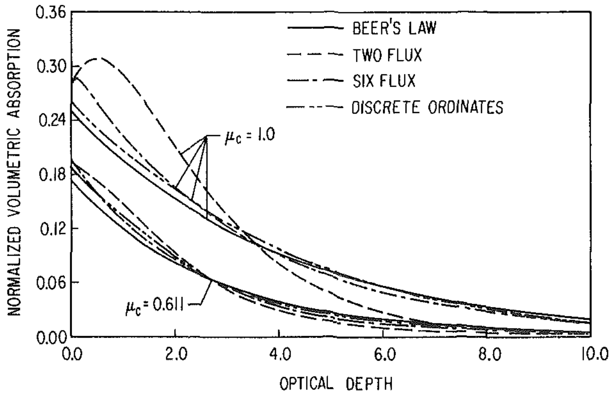

Fig. 5 Comparison of solutions to the equation of transfer for collimated irradiation with $\omega = 0.75$, $\rho_d = 0$, $\tau_d = 10$, and $\mu_c = 1.$, or $\mu_c = 0.611$

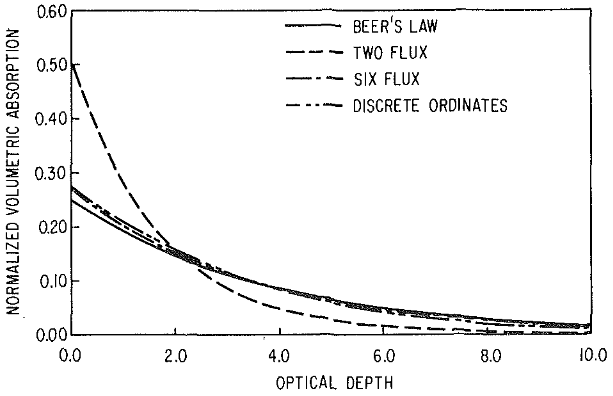

Fig. 6 Comparison of solutions to the equation of transfer for diffuse irradiation with $\omega = 0.75$, $\mu_c = 0.911$, $\rho_d = 0$, and $\tau_d = 10$

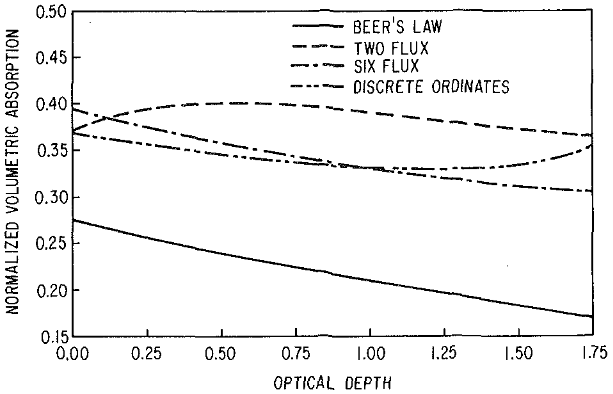

Fig. 7 Comparison of solutions to the equation of transfer for collimated irradiation with ω 0.75, $\mu_c = 0.911$, $\rho_d = 0.50$, and $\tau_d = 1.75$

For shallow ponds the reflectivity of the bottom, ρ_d, becomes important. Fig. 7 shows predictions for conditions in a shallow pond ($\tau_d = 1.75$) for a value of ρ_d equal to 0.50. Beer's law cannot be expected to yield an accurate result for these conditions since it does not account for radiation reflected from the bottom. The two-flux method again overpredicts absorption, due to the assumption that all of the scattered radiation is diffuse. Although there is still good agreement between the six-flux and discrete ordinate methods over a larger portion of the pond, the solutions diverge in the lower region. This effect results from the abrupt transition from a strongly collimated radiation field to a diffuse field, due to the assumption of diffuse reflection at the bottom. Since it includes a smaller number of discrete fluxes, the six-flux method cannot account for this change in directional distribution to the same extent as the discrete ordinate method.

Fig. 8 provides a comparison of the four solution methods for the standard conditions, except that isotropic scattering is now assumed. Although isotropic scattering would not be expected in a body of water, it is included in this study to compare solution methods for sharply contrasting conditions. For isotropic scattering a diffuse radiation field rapidly develops, in contrast to a radiation field which remains sharply peaked. The two-flux method now provides accurate results, since a diffuse field is tacitly assumed in its development. However, the Beer approximation now provides poor results due to its inability to account for the large backward scattering associated with diffuse radiation fields.

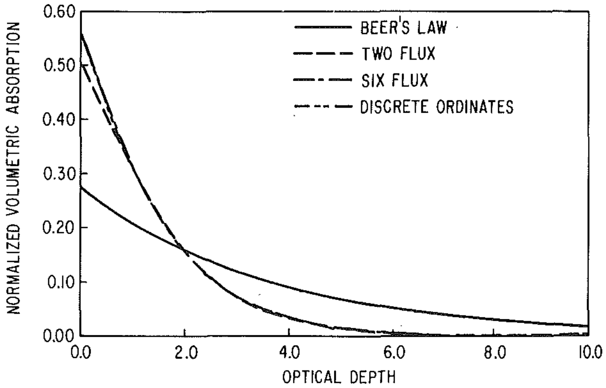

Fig. 8 Comparison of solutions to the equation of transfer for collimated irradiation with isotropic scattering ($\omega = 0.75$, $\mu_c = 0.911$, $\rho_d = 0$, and $\tau_d = 10$)

Summary

The purpose of this study has been to compare several methods of determining the radiation field for representative conditions in a body of water. The methods include a very simple form of Beer's law, a modified Hamaker two-flux model [12], a six-flux method [18] and the method of discrete ordinates. Comparisons were made on the basis of the local radiation absorption, and the discrete ordinate method was used as a standard for evaluating the remaining methods. The key conclusions are as follows:

1 The Beer's law solution provides good agreement with the method of discrete ordinates for most of the conditions considered. This agreement is due to the fact that the phase function is sharply peaked in the forward direction. However, the method does become inaccurate for shallow water layers with a large bottom reflectivity or systems with a large scattering albedo. Its use should, therefore, be restricted to situations for which $\omega \lesssim 0.8$, $\tau_d \gtrsim 2$ and $\rho_d \sim 0$. Moreover, the forward scattering method [8] should not be used for systems that have a large albedo, $\omega \gtrsim 0.8$.

2 Although the two-flux method used in this study is as rigorous as any such method which has been used to date, it provided poor agreement with the discrete ordinate method for virtually all of the conditions considered. Typically, the two-flux method overpredicts radiation absorption in the upper layers and underpredicts absorption in the lower region. Use of the method is only recommended for small values of $\omega \lesssim 0.50$ and large angles of incidence ($\theta_c^* \gtrsim 45$ deg) for collimated radiation.

3 Although also approximate in nature, the six-flux method provided accurate results for virtually the entire range of conditions considered in this study. Its use is recommended from the standpoint of accuracy and operational convenience.

Acknowledgments

Support of this work by the National Science Foundation under Grant No. ENG75-17370 is gratefully acknowledged.

References

1 Dake, J. M. K., Harleman, D. R. F., "Thermal Stratification in Lakes: Analytical and Laboratory Studies," *Water Resour. Res.*, Vol. 5, No. 2, 1969, pp. 488–495.

2 Snider, D. M., Viskanta, R., "Radiation Induced Thermal Stratification in Surface Layers of Stagnant Water," ASME JOURNAL OF HEAT TRANSFER, Vol. 97, No. 1, 1975, pp. 35–40.

3 Armaly, B. F., Lepper, S. P., "Diurnal Stratification of Deep Water Impoundments," ASME Paper 75-HT-35, AIChE-ASME Heat Transfer Conference, San Francisco, Aug. 1975.

4 Incropera, F. P., Thomas, J. F., "A Model for Solar Radiation Conversion to Algae in a Shallow Pond," *Solar Energy*, Vol. 20, No. 2, 1978, pp. 157–165.

5 Siegel, S., Howell, J. R., *Thermal Radiation Heat Transfer*, McGraw-Hill, Inc., New York, 1972.

6 Foster, T. D., "A Convective Model for the Diurnal Cycle in the Upper Ocean," *Journal Geophys. Res.*, Vol. 76, No. 3, 1971, pp. 666–675.

7 Viskanta, R., Toor, J. S., "Radiative Transfer in Waters," *Water Resour. Res.*, Vol. 8, No. 3, 1972, pp. 595–608.

8 Viskanta, R., Toor, J. S., "Effect of Multiple Scattering of Radiant Energy Transfer in Waters," *J. Geophys. Res.*, Vol. 78, No. 18, 1973, pp. 3538–3551.

9 Sagan, C., Pollack, J., "Anisotropic Nonconservative Scattering and the Clouds of Venus," *J. Geophys. Res.*, Vol. 72, No. 2, 1967, pp. 469–474.

10 Domoto, G., Wang, W., "Radiative Transfer in Homogeneous Non-Gray Gases with Nonisotropic Particle Scattering," ASME JOURNAL OF HEAT TRANSFER, Vol. 96, No. 2, 1974, pp. 385–390.

11 Wang W., Domoto, G., "The Radiative Effects of Aerosols in the Earth Atmosphere," *Journal Appl. Meteor.*, Vol. 5, No. 2, 1974, pp. 521–526.

12 Hamaker, H. C., "Radiation and Heat Conduction in Light Scattering Material," *Philips Res. Reports*, Vol. 2, 1947, pp. 55–67, 103–111, 112–125, 420.

13 Larkin, B. K., Churchill, S. W., "Heat Transfer by Radiation through Porous Insulations," *AIChE Journal*, Vol. 5, No. 2, 1959, pp. 467–473.

14 Chen, J. C., Churchill, S. W., "Radiant Heat Transfer in Packed Beds," *AIChE Journal*, Vol. 9, No. 1, 1963, pp. 35–41.

15 Bergquam, J. B., Seban, R. A., "Heat Transfer by Conduction and Radiation in Absorbing and Scattering Materials," ASME JOURNAL OF HEAT TRANSFER, Vol. 93, No. 1, 1971, pp. 236–241.

16 Sanders, C. F., Lenoir, J. M., "Radiative Transfer through a Cloud of Absorbing-Scattering Particles," *AIChE Journal*, Vol. 18, No. 1, 1972, pp. 155–160.

17 Armaly, B. F., Lam, T. T., "Influence of Refractive Index on Reflectance from a Semiinfinite Absorbing-Scattering Medium with Collimated Incident Radiation," *Int. J. Heat Mass Trans.*, Vol. 18, No. 4, 1975, pp. 893–899.

18 Chu, C. M., Churchill, S. W., "Numerical Solution of Problems in Multiple Scattering of Electromagnetic Radiation," *J. Phys. Chem.*, Vol. 59, No. 3, 1955, pp. 855–863.

19 Hansen, J. E., Travis, L. D., *Light Scattering in Planetary Atmospheres*, Goddard Institute for Space Studies, New York, 1974.

20 Hottel, H. C., Sarofim, A. F., Evans, L. B., Vasalos, I. A., "Radiative Transfer in Anisotropically Scattering Media: Allowance for Fresnel Reflection at the Boundaries," ASME JOURNAL OF HEAT TRANSFER, Vol. 90, No. 1, 1968, pp. 56–61.

21 Daniel, K. J., Incropera, F. P., "A Comparison of Methods for Predicting Radiation Absorption and Scattering in Algal Suspensions," TR ME-HTL-77-1, School of Mechanical Engineering, Purdue University, West Lafayette, Ind., 1977.

22 Korn, G. A., Korn, T. M., *Mathematical Handbook for Scientists and Engineers*, McGraw Hill Book Company, Inc., 1961, pp. 740.

23 Tyler, J. E., "A Survey of Experimental Hydrological Optics," *Journal Quant. Spectrosc. Rad. Trans.*, Vol. 8, No. 3, 1968, pp. 339–351.

24 Jerlov, N. G., *Marine Optics*, Elsevier Scientific Publishing Co., Amsterdam, 1976.

25 Daniel, K. J., Incropera, F. P., "Optical Property Measurements in Suspensions of Unicellular Algae," TR ME-HTL-77-4, School of Mechanical Engineering, Purdue University, West Lafayette, Ind., 1977.

26 Duntley, S. Q., "Light in the Sea," *Journal Opt. Soc. Am.*, Vol. 53, No. 1, 1963, pp. 214–220.

A. L. Crosbie
Thermal Radiative Transfer Group,
Department of Mechanical and
Aerospace Engineering,
University of Missouri-Rolla,
Rolla, Missouri 65401
Mem. ASME

Apparent Radiative Properties of an Isotropically Scattering Medium on a Diffuse Substrate[1]

The apparent directional and hemispherical radiative properties of a finite scattering medium bounded by a diffuse substrate are investigated. The isothermal medium emits, absorbs and isotropically scatters radiation. Specifically, the emittance and reflectance are determined. Using the principle of superposition, exact but simple equations are developed which express the apparent properties in terms of the properties of a medium not bounded by a substrate. Any arbitrary directional distribution of incident radiation can be handled. Integro-differential equations of the initial value type for the radiative properties are developed and solved. In general, when the substrate emittance is less than the emittance of a semi-infinite scattering medium, the scattering layer acts as a source and increases the apparent emittance. Conversely when the substrate emittance is greater, the scattering layer acts as a shield and decreases the apparent emittance.

Introduction

The apparent radiative properties of a semi-transparent medium are important in many heat transfer and remote sensing applications. These properties depend on the absorption and scattering properties of the medium, the angular distribution of the incident radiation, and the radiative properties of the bounding surfaces. Edwards and Bobco [1] and Crosbie [2, 3] used Chandrasekhar's X and Y- functions to study radiative properties of a finite, isothermal, isotropically scattering medium with a transparent substrate. The influence of substrate reflectance on the apparent properties of a scattering medium with a refractive index of unity has been investigated by Lii and Özisik [4] and Armaly and El-Baz [5, 6]. Using the normal-mode expansion technique, Lii and Özisik [4] calculated the hemispherical reflectance and transmittance for a medium with a nonemitting substrate with specular and diffuse reflection. These properties were also calculated using the P_1-approximation (Eddington approximation). Armaly and El-Baz [5, 6] used the exponential kernel approximation to analyze a diffuse substrate. The directional and hemispherical emittance, as well as the bidirectional, directional-hemispherical and hemispherical reflectance were calculated.

The objective of the present investigation is to express the apparent radiative properties for a medium of given optical thickness τ_0 backed by a diffuse substrate of arbitrary reflectance ρ_w in terms of the properties of a medium of thickness τ_0 backed by a transparent substrate. Since solutions to the latter situation are available, detailed multiple scattering calculations would not be necessary for each substrate reflectance. Thus, an engineer could readily evaluate the influence of substrate reflectance or the influence of an absorbing-scattering layer on the apparent radiative properties.

Formulation

The physical situation (see Fig. 1) consists of a finite planar layer bounded by a diffuse substrate. The layer emits, absorbs and scatters thermal radiation. The analysis is performed with the following assumptions: (1) one-dimensional geometry, (2) refractive index of unit, (3) isothermal medium and (4) isotropic scattering. The top of the layer is exposed to collimated radiation, $I^+(0, \mu, \phi) = I_0\delta(\mu - \mu_0)\delta(\phi - \phi_0)$, while the bottom is bounded by a diffusely emitting and reflecting substrate, $I^-(\tau_0) = R_w/\pi$.

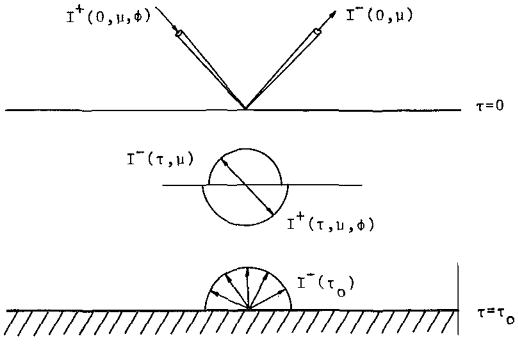

Fig. 1 Physical model

---

[1] This work was supported in part by the National Science Foundation through grant ENG 75-06237.

Contributed by the Heat Transfer Division for publication in the JOURNAL OF HEAT TRANSFER. Revised Manuscript received by the Heat Transfer Division July 6, 1978.

The intensity and flux distribution within the medium can be expressed in terms of the source function [7], i.e.,

$$I^+(\tau, \mu, \phi) = I_0\delta(\mu - \mu_0)\delta(\phi - \phi_0) \exp(-\tau/\mu) + \int_0^\tau S(\tau') \exp[-(\tau - \tau')/\mu]d\tau'/\mu \quad (1)$$

$$I^-(\tau, \mu) = (R_w/\pi) \exp[-(\tau_0 - \tau)/\mu] + \int_\tau^{\tau_0} S(\tau') \exp[-(\tau' - \tau)/\mu]d\tau'/\mu \quad (2)$$

$$\mathcal{F}^+(\tau) = I_0\mu_0 \exp(-\tau/\mu_0) + 2\pi \int_0^\tau S(\tau')E_2(\tau - \tau')d\tau' \quad (3)$$

$$\mathcal{F}^-(\tau) = 2R_wE_3(\tau_0 - \tau) + 2\pi \int_\tau^{\tau_0} S(\tau')E_2(\tau' - \tau)d\tau' \quad (4)$$

The source function is given by the following linear integral equation:

$$S(\tau) = (1 - \omega)I_b(T_m) + \frac{\omega}{4\pi} \int_0^{2\pi} \int_{-1}^{+1} I(\tau, \mu, \phi)d\mu d\phi$$

$$= (1 - \omega)I_b(T_m) + \frac{\omega}{4\pi} I_0 \exp(-\tau/\mu_0) + \frac{\omega}{2\pi} R_wE_2(\tau_0 - \tau) + \frac{\omega}{2} \int_0^{\tau_0} S(\tau')E_1(|\tau - \tau'|)d\tau' \quad (5)$$

Since integral equation (5) is linear, the principle of superposition can be applied to yield:

$$S(\tau) = (1 - \omega)I_b(T_m)\phi_s(\tau; \tau_0) + \omega(I_0/4\pi)J(\tau, \mu_0; \tau_0) + \omega(R_w/\pi)\phi_d(\tau; \tau_0) \quad (6)$$

where

$$\phi_s(\tau; \tau_0) = 1 + \frac{\omega}{2} \int_0^{\tau_0} \phi_s(\tau'; \tau_0)E_1(|\tau - \tau'|)d\tau' \quad (7)$$

$$J(\tau, \mu_0; \tau_0) = \exp(-\tau/\mu_0) + \frac{\omega}{2} \int_0^{\tau_0} J(\tau', \mu_0; \tau_0)E_1(|\tau - \tau'|)d\tau' \quad (8)$$

and

$$\phi_d(\tau; \tau_0) = \frac{1}{2} E_2(\tau_0 - \tau) + \frac{\omega}{2} \int_0^{\tau_0} \phi_d(\tau'; \tau_0)E_1(|\tau - \tau'|)d\tau' \quad (9)$$

This result can be confirmed by simply substituting equation (6) into equation (5). Physically, these universal functions $\phi_s(\tau; \tau_0)$, $J(\tau, \mu; \tau_0)$ and $\phi_d(\tau; \tau_0)$ represent the dimensionless source functions for a finite slab which is, isothermal, exposed to collimated radiation, and exposed to diffuse radiation, respectively. The functions ϕ_d and ϕ_s are simply related to J, i.e.,

$$\phi_s(\tau; \tau_0) = J(\tau, \infty; \tau_0) \quad (10)$$

$$\phi_d(\tau; \tau_0) = \frac{1}{2} \int_0^1 J(\tau_0 - \tau, \mu_0; \tau_0)d\mu_0 \quad (11)$$

Next, the radiosity must be determined. The flux leaving the diffuse substrate is given by

$$R_w = \epsilon_w\pi I_b(T_w) + \rho_w\mathcal{F}^+(\tau_0) \quad (12)$$

where ϵ_w, ρ_w are the hemispherical emittance and reflectance of the substrate, respectively. The flux incident on the substrate can be determined from equation (3). Substitution of the source function (6) into equation (3) yields:

$$\mathcal{F}^+(\tau) = 2\pi(1 - \omega)I_b(T_m)Q_s^+(\tau; \tau_0) + I_0\mu_0Q_c^+(\tau, \mu_0; \tau_0) + R_wQ_d^+(\tau; \tau_0) \quad (13)$$

$$Q_s^+(\tau;\tau_0) = \int_0^\tau \phi_s(\tau'; \tau_0)E_2(\tau - \tau')d\tau' \quad (14)$$

$$\mu_0Q_c^+(\tau, \mu_0; \tau_0) = \mu_0 \exp(-\tau/\mu_0) + \frac{\omega}{2} \int_0^\tau J(\tau', \mu_0; \tau_0)E_2(\tau - \tau')d\tau' \quad (15)$$

$$Q_d^+(\tau; \tau_0) = 2\omega \int_0^\tau \phi_d(\tau'; \tau_0)E_2(\tau - \tau')d\tau' \quad (16)$$

Evaluation of equation (13) at $\tau = \tau_0$ gives

$$\mathcal{F}^+(\tau_0) = \epsilon_m\pi I_b(T_m) + I_0\mu_0t_m(\mu_0) + R_w\rho_m \quad (17)$$

where

$$\epsilon_m = 2(1 - \omega)Q_s^+(\tau_0; \tau_0)$$

$$t_m(\mu_0) = Q_c^+(\tau_0, \mu_0; \tau_0)$$

$$\rho_m = Q_d^+(\tau_0; \tau_0) \quad (18)$$

Nomenclature

$E_n(\tau)$ = exponential integral, $\int_0^1 e^{-\tau/\mu} \mu^{n-2}d\mu$
$\mathcal{F}^+(\tau)$ = radiative flux in the positive τ-direction
$\mathcal{F}^-(\tau)$ = radiative flux in the negative τ-direction
$I^+(\tau, \mu, \phi)$ = radiant intensity in the positive τ-direction
$I^-(\tau, \mu, \phi)$ = radiant intensity in the negative τ-direction
$I_b(T)$ = Planck black body function
$I_i(\mu, \phi)$ = radiant intensity incident on the medium
$I_0\mu_0$ = incident radiant flux for the collimated case
I_1 = isotropic incident intensity
$J(\tau, \mu; \tau_0)$ = source function for collimated boundary condition, equation (8)
Q_s^+, Q_c^+, Q_d^+ = radiative flux, see equations (14, 15) and (16)
R_w = radiosity, radiative flux leaving substrate
$S(\tau)$ = source function, see equation (5)
T_m, T_w = temperature of medium and substrate, respectively
X, Y = Chandrasekhar's X and Y-functions
α_n, β_n = moments of X and Y-functions, equations (54) and (55)
$\delta(x)$ = Dirac delta function, $\int_a^b f(x)\delta(x - x_0)dx = f(x_0)$ for $a \leq x_0 \leq b$
$\epsilon(\mu)$, ϵ = directional emittance, hemispherical emittance
$\epsilon^*(\mu)$, ϵ^* = substrate emittances, see equations (77) and (74)
μ = cosine of the polar angle
μ_0, ϕ_0 = direction of the incident collimated radiation
$\rho(\mu, \mu_0)$ = bidirectional reflectance
$\rho(\mu)$, $t(\mu)$ = hemispherical-directional reflectance, transmittance
$\rho(\mu_0)$, $t(\mu_0)$ = directional-hemispherical reflectance, transmittance
ρ, t = hemispherical reflectance, transmittance
$\rho^* = 1 - \epsilon^*$
τ = optical depth, extinction coefficient times distance into medium
τ_0 = optical thickness, extinction coefficient times thickness of medium
ϕ = azimuthal angle
$\phi_d(\tau; \tau_0)$ = source function for diffuse case, equation (9)
$\phi_s(\tau; \tau_0)$ = source function for isothermal case, equation (7)
ω = single scattering albedo, ratio of scattering coefficient to the extinction coefficient

Subscripts

a = apparent properties
m = properties of medium without substrate
w = properties of the substrate
∞ = properties of a semi-infinite medium

Physically, ϵ_m and ρ_m represent the hemispherical emittance and reflectance, respectively for the medium itself. The quantity $t_m(\mu_0)$ is the directional-hemispherical transmittance of the medium. Utilization of equation (17) in (12) gives

$$R_w = \{\epsilon_w \pi I_b(T_w) + \rho_w[\epsilon_m \pi I_b(T_m) + \mu_0 I_0 t_m(\mu_0)]\}/(1 - \rho_w \rho_m) \quad (19)$$

The intensity leaving the medium is given by

$$I^-(0, \mu) = (R_w/\pi) \exp(-\tau_0/\mu) + \int_0^{\tau_0} S(\tau') \exp(-\tau'/\mu)(d\tau'/\mu) \quad (20)$$

or with the aid of equation (6)

$$I^-(0, \mu) = (1 - \omega) I_b(T_m) \int_0^{\tau_0} \phi_s(\tau'; \tau_0) \exp(-\tau'/\mu)(d\tau'/\mu) + \omega(I_0/4\pi) \int_0^{\tau_0} J(\tau', \mu_0; \tau_0) \exp(-\tau'/\mu)(d\tau'/\mu) + (R_w/\pi)\left[\exp(-\tau_0/\mu) + \omega \int_0^{\tau_0} \phi_d(\tau'; \tau_0) \times \exp(-\tau'/\mu)(d\tau'/\mu)\right] \quad (21)$$

This equation may be rewritten as

$$I^-(0, \mu) = \epsilon_m(\mu) I_b(T_m) + (I_0\mu_0/\pi)\rho_m(\mu, \mu_0) + (R_w/\pi) t_m(\mu) \quad (22)$$

where

$$\epsilon_m(\mu) = (1 - \omega) \int_0^{\tau_0} \phi_s(\tau'; \tau_0) \exp(-\tau'/\mu)(d\tau'/\mu) \quad (23)$$

$$\rho_{\mathrm{m}}(\mu, \mu_0) = \frac{\omega}{4} \int_0^{\tau_0} J(\tau', \mu_0; \tau_0) \exp(-\tau'/\mu) d\tau'/(\mu\mu_0) \quad (24)$$

$$t_m(\mu) = \exp(-\tau_0/\mu) + \omega \int_0^{\tau_0} \phi_d(\tau'; \tau_0) \exp(-\tau'/\mu)(d\tau'/\mu) \quad (25)$$

Physically, $\epsilon_m(\mu)$ is the directional emittance, $\rho_m(\mu, \mu_0)$ is the bidirectional reflectance and $t_m(\mu)$ is the hemispherical-directional transmittance for the medium without a substrate.

Substitution of equation (19) into (22) yields

$$I^-(0, \mu) = \epsilon_a(\mu) I_b(T_m) + \rho_a(\mu, \mu_0)(I_0\mu_0/\pi) \quad (26)$$

where the apparent directional properties are

$$\epsilon_a(\mu) = \epsilon_m(\mu) + \frac{\epsilon_w + \rho_w \epsilon_m}{1 - \rho_w \rho_m} t_m(\mu) \quad (27)$$

$$\rho_a(\mu, \mu_0) = \rho_m(\mu, \mu_0) + \frac{\rho_w t_m(\mu) t_m(\mu_0)}{1 - \rho_w \rho_m} \quad (28)$$

The flux leaving the medium can be written as

$$\mathcal{F}^-(0) = 2\pi \int_0^1 I^-(0, \mu)\mu d\mu = \epsilon_a \pi I_b(T_m) + \rho_a(\mu_0) I_0 \mu_0 \quad (29)$$

where the apparent hemispherical properties are

$$\epsilon_a = 2 \int_0^1 \epsilon_a(\mu)\mu d\mu = \epsilon_m + \frac{\epsilon_w + \rho_w \epsilon_m}{1 - \rho_w \rho_m} t_m \quad (30)$$

$$\rho_a(\mu_0) = 2 \int_0^1 \rho_a(\mu, \mu_0)\mu d\mu = \rho_m(\mu_0) + \frac{\rho_w t_m t_m(\mu_0)}{1 - \rho_w \rho_m} \quad (31)$$

The medium and the substrate have been assumed to be at the same temperature, i.e., $T_w = T_m$.

For an opaque substrate, $\rho_w + \epsilon_w = 1$, the apparent emittance decreases with an increase in substrate reflectance; while apparent reflectance increases. The behavior of the intensity and flux leaving the medium can be determined by looking at the derivatives with respect to ρ_w, i.e.

$$\frac{\partial I^-(0, \mu)}{\partial \rho_w} = t_m(\mu)[-t_m I_b(T_m) + (I_0\mu_0/\pi) t_m(\mu_0)]/(1 - \rho_w \rho_m)^2 \quad (32)$$

$$\frac{\partial \mathcal{F}^-(0)}{\partial \rho_w} = t_m[-t_m \pi I_b(T_m) + I_0 \mu_0 t_m(\mu_0)]/(1 - \rho_w \rho_m)^2$$

When $\pi t_m I_b(T_m) > I_0 \mu_0 t_m(\mu_0)$, the intensity and flux leaving the medium decreases as the substrate reflectance increases. When $\pi t_m I_b(T_m) < I_0 \mu_0 t_m(\mu_0)$, the opposite trend occurs.

For a nonemitting substrate $T_w \ll T_m$, the apparent emittances are

$$\epsilon_a(\mu) = \epsilon_m(\mu) + \frac{\rho_w \epsilon_m}{1 - \rho_w \rho_m} t_m(\mu) \quad (34)$$

$$\epsilon_a = \epsilon_m + \frac{\rho_w \epsilon_m}{1 - \rho_w \rho_m} t_m \quad (35)$$

The expressions for the apparent reflectances remain unchanged and the derivatives of the intensity and flux become

$$\frac{\partial I^-(0, \mu)}{\partial \rho_w} = t_m(\mu)[\epsilon_m I_b(T_m) + (I_0\mu_0/\pi) t_m(\mu_0)]/(1 - \rho_w \rho_m)^2 \quad (36)$$

$$\frac{\partial \mathcal{F}^-(0)}{\partial \rho_w} = t_m[\epsilon_m \pi I_b(T_m) + I_0 \mu_0 t_m(\mu_0)]/(1 - \rho_w \rho_m)^2 \quad (37)$$

Since these derivatives are always positive, the intensity and flux leaving the medium always increase with substrate reflectance.

An Arbitrary Directional Variation in Incident Radiation

With the expressions for the bidirectional reflectance and the directional emittance developed, any directional variation in the incident radiation can be easily handled. If the intensity incident on the medium is $I_i(\mu, \phi)$, the intensity and flux leaving the layer are

$$I^-(0, \mu) = \epsilon_a(\mu) I_b(T_m) + \frac{1}{\pi} \int_0^{2\pi} \int_0^1 I_i(\mu', \phi')\rho_a(\mu, \mu')\mu' d\mu' d\phi' \quad (38)$$

$$\mathcal{F}^-(0) = \epsilon_a \pi I_b(T_m) + \int_0^{2\pi} \int_0^1 I_i(\mu', \phi')\rho_a(\mu')\mu' d\mu' d\phi' \quad (39)$$

For an opaque substrate, the derivative with respect to ρ_w are

$$\frac{\partial I^-(0, \mu)}{\partial \rho_w} = t_m(\mu)\left[-t_m I_b(T_m) + \frac{1}{\pi} \int_0^{2\pi} \int_0^1 I_i(\mu', \phi') t_m(\mu')\mu' d\mu' d\phi'\right]/(1 - \rho_w \rho_m)^2 \quad (40)$$

$$\frac{\partial \mathcal{F}^-(0)}{\partial \rho_w} = t_m\left[-t_m \pi I_b(T_m) + \int_0^{2\pi} \int_0^1 I_i(\mu', \phi') t_m(\mu')\mu' d\mu' d\phi'\right]/(1 - \rho_w \rho_m)^2 \quad (41)$$

and for a nonemitting substrate

$$\frac{\partial I^-(0, \mu)}{\partial \rho_w} = t_m(\mu)\left[\epsilon_m I_b(T_m) + \frac{1}{\pi} \int_0^{2\pi} \int_0^1 I_i(\mu', \phi') t_m(\mu')\mu' d\mu' d\phi'\right]/(1 - \rho_w \rho_m)^2 \quad (42)$$

$$\frac{\partial \mathcal{F}^-(0)}{\partial \rho_w} = t_m\left[\epsilon_m \pi I_b(T_m) + \frac{1}{\pi} \int_0^{2\pi} \int_0^1 I_i(\mu', \phi') t_m(\mu')\mu' d\mu' d\phi'\right]/(1 - \rho_w \rho_m)^2 \quad (43)$$

Thus, the intensity and flux leaving the medium increase with substrate reflectance when the substrate is nonemitting or when $\int_0^{2\pi}\int_0^1 I_i(\mu', \phi') t_m(\mu')\mu' d\mu' d\phi' > t_m \pi I_b(T_m)$ for the opaque substrate.

For isotropic incident radiation, $I_i(\mu, \phi) = I_1$, the intensity and flux leaving the layer are

$$I^-(0, \mu) = \epsilon_a(\mu) I_b(T_m) + \rho_a(\mu) I_1 \quad (44)$$

$$\mathcal{F}^-(0) = \epsilon_a \pi I_b(T_m) + \rho_a \pi I_1 \qquad (45)$$

where the hemispherical reflectance is

$$\rho_a = 2\int_0^1 \rho_a(\mu)\mu d\mu = \rho_m + \frac{\rho_w t_m{}^2}{1 - \rho_w \rho_m} \qquad (46)$$

The intensity and flux leaving the medium increase with substrate reflectance when the substrate is nonemitting or when $I_1 > I_b(T_m)$.

Equations (27, 28, 30, 31), and (46) can be obtained by alternate methods including invariant embedding [8], finite-element embedding [9] and ray tracing [10].

Radiative Properties of a Finite Layer: exact solutions

The radiative properties of an isotropic scattering layer can be expressed exactly in terms of Chandrasekhar's X and Y-functions [2, 3]:

$$\rho_m(\mu, \mu_0) = \frac{\omega}{4}[X(\mu; \tau_0)X(\mu_0; \tau_0) - Y(\mu; \tau_0)Y(\mu_0; \tau_0)]/(\mu + \mu_0) \qquad (47)$$

$$\epsilon_m(\mu) = \left(1 - \frac{\omega}{2}\alpha_0 - \frac{\omega}{2}\beta_0\right)[X(\mu; \tau_0) - Y(\mu; \tau_0)] \qquad (48)$$

$$\rho_m(\mu) = 1 - \frac{\omega}{2}\beta_0 Y(\mu; \tau_0) - \left(1 - \frac{\omega}{2}\alpha_0\right) X(\mu; \tau_0) \qquad (49)$$

$$t_m(\mu) = \frac{\omega}{2}\beta_0 X(\mu; \tau_0) + \left(1 - \frac{\omega}{2}\alpha_0\right) Y(\mu; \tau_0) \qquad (50)$$

$$\epsilon_m = (2 - \omega\alpha_0 - \omega\beta_0)(\alpha_1 - \beta_1) \qquad (51)$$

$$\rho_m = 1 - \omega\beta_0\beta_1 - (2 - \omega\alpha_0)\alpha_1 \qquad (52)$$

$$t_m = \omega\beta_0\alpha_1 + (2 - \omega\alpha_0)\beta_1 \qquad (53)$$

where the moments are defined as

$$\alpha_n = \int_0^1 X(\mu; \tau_0)\mu^n d\mu \qquad (54)$$

$$\beta_n = \int_0^1 Y(\mu; \tau_0)\mu^n d\mu \qquad (55)$$

Note that $\rho_m(\mu) + t_m(\mu) + \epsilon_m(\mu) = 1$ and $\rho_m + t_m + \epsilon_m = 1$.

Extensive tables of Chandrasekhar's X and Y-functions are available [11–14]. However, their moments are not as extensively tabulated [11, 14]. The X and Y-functions can be easily calculated from the following coupled integro-differential equations [13]:

$$X' = Y\Phi \qquad (56)$$

$$Y' = -(Y/\mu) + X\Phi \qquad (57)$$

and

$$\Phi = \frac{\omega}{2}\int_0^1 Y(\mu'; \tau_0)d\mu'/\mu' = \frac{\omega}{2}\beta_{-1} \qquad (58)$$

with initial conditions, $\tau_0 = 0$, $X(\mu; 0) = Y(\mu; 0) = 1$. The prime indicates the derivative with respect to optical thickness, τ_0. The integral Φ is represented by a Gaussian quadrature of order N, and the resulting $2N$ ordinary differential equations can be easily solved by standard techniques. Multiplication of equations (56) and (57) by $\mu^n d\mu$ and integration from 0 to 1 yields the following equations for the moments:

$$\alpha_n' = \beta_n\Phi \qquad (59)$$

$$\beta_n' = -\beta_{n-1} + \alpha_n\Phi \qquad (60)$$

with initial conditions, $\tau_0 = 0$, $\alpha_n = \beta_n = 1/(n + 1)$.

Taking the derivative of $\rho_m(\mu, \mu_0)$, $\epsilon_m(\mu)$, $\rho_m(\mu)$ and $t_m(\mu)$ with respect to optical thickness and using equations (56, 57, 59) and (60) yields

$$\rho_m'(\mu, \mu_0) = \omega Y(\mu)Y(\mu_0)/(4\mu\mu_0) \qquad (61)$$

$$\epsilon_m'(\mu) = \left(1 - \frac{\omega}{2}\alpha_0 - \frac{\omega}{2}\beta_0\right)(Y/\mu) \qquad (62)$$

$$\rho_m'(\mu) = \frac{\omega}{2}\beta_0(Y/\mu) \qquad (63)$$

$$t_m'(\mu) = -\left(1 - \frac{\omega}{2}\alpha_0\right)(Y/\mu) \qquad (64)$$

with initial conditions, $\tau_0 = 0$, $\rho_m(\mu, \mu_0) = 0$, $\epsilon_m(\mu) = 0$, $\rho_m(\mu) = 0$ and $t_m(\mu) = 1$. Likewise,

$$\epsilon_m' = 2\left(1 - \frac{\omega}{2}\alpha_0 - \frac{\omega}{2}\beta_0\right)\beta_0 \qquad (65)$$

$$\rho_m' = \omega\beta_0{}^2 \qquad (66)$$

$$t_m' = -2\left(1 - \frac{\omega}{2}\alpha_0\right)\beta_0 \qquad (67)$$

with initial conditions, $\tau_0 = 0$, $\epsilon_m = \rho_m = 0$ and $t_m = 1$. In the process of obtaining these expressions, the following differential equation

$$\left(1 - \frac{\omega}{2}\alpha_0 - \frac{\omega}{2}\beta_0\right)' = \left(1 - \frac{\omega}{2}\alpha_0 - \frac{\omega}{2}\beta_0\right)\Phi \qquad (68)$$

with initial condition, $\tau_0 = 0$, $(1 - \omega/2\alpha_0 - \omega/2\beta_0) = (1 - \omega)$, was developed. Inspection of these equations reveals that the emittance and reflectance increase as the optical thickness is increased, while the transmittance decreases. This behavior agrees with what would be expected physically.

Using equations (56–60), the X and Y-functions and their moments are calculated for a large range of parameters. With these functions the radiative properties of the medium are determined from equations (47–53). The normal and hemispherical reflectance and transmittance are presented in Tables 1–4. The emittance can also be determined from the data presented in these tables since the sum of the emittance, reflectance and transmittance is equal to unity.

The influence of optical thickness and albedo on the ratio of hemispherical to normal reflectance is illustrated in Fig. 2. This ratio is always greater than unity and decreases with optical thickness. In addition, Fig. 2 shows that the ratio of hemispherical to normal emittance also decreases with optical thickness, being greater than unity for small τ_0 and less than unity for large τ_0.

Apparent Properties

The apparent hemispherical emittance of a medium with a nonemitting substrate is presented in Fig. 3. The values were calculated from equation (35) using Tables 2 and 4. The emittance increases with optical thickness and substrate reflectance. This behavior can be predicted from equation (35), i.e.

$$\frac{\partial\epsilon_a}{\partial\rho_w} = \epsilon_m t_m/(1 - \rho_w\rho_m)^2 \qquad (69)$$

$$\epsilon_a'|_{\tau_0=0} = 2(1 - \omega)(1 + \rho_w) \qquad (70)$$

Equation (70) was derived with the help of equation (65).

The apparent hemispherical emittance for a emitting opaque substrate is presented in Fig. 4. The emittances were calculated from equation (30) using Tables 2 and 4. The emittance decreases with substrate reflectance, i.e.

$$\frac{\partial\epsilon_a}{\partial\rho_w} = -t_m{}^2/(1 - \rho_w\rho_m)^2 \qquad (71)$$

and is always greater than the results for the nonemitting substrate. Equation (71) is obtained by taking the derivative of equation (30) with respect to ρ_w.

Inspection of Fig. 4 reveals that apparent hemispherical emittance increases with optical thickness when the substrate emittance is less than a certain value ϵ^*. The value of ϵ^* can be determined analytically by first taking the derivative of the apparent hemispherical emittance, equation (30) with respect to τ_0 and using the identity, $t_m' = -(\epsilon_m' + \rho_m')$, i.e.,

$$(1 - \rho_w\rho_m)^2\epsilon_a' = 2t_m(1 - \rho_w\rho_m)\rho_w\epsilon_m' - (\epsilon_w + \rho_w\epsilon_m)^2\rho_m' \qquad (72)$$

Table 1 Normal reflectance, $\rho_m(\mu = 1)$

τ_0	$\omega = 0.1$	$\omega = 0.5$	$\omega = 0.9$	$\omega = 0.95$	$\omega = 0.99$	$\omega = 1.00$
0.1	0.00406	0.02173	0.04210	0.04487	0.04712	0.04769
0.2	0.00695	0.03886	0.07937	0.08522	0.09004	0.09127
0.3	0.00909	0.05264	0.11261	0.12174	0.12937	0.13133
0.4	0.01072	0.06383	0.14235	0.15491	0.16554	0.16829
0.5	0.01196	0.07295	0.16904	0.18514	0.19892	0.20251
0.6	0.01291	0.08042	0.19303	0.21273	0.22980	0.23427
0.7	0.01365	0.08654	0.21461	0.23796	0.25844	0.26384
0.8	0.01423	0.09157	0.23406	0.26107	0.28505	0.29142
0.9	0.01469	0.09571	0.25159	0.28226	0.30982	0.31719
1.0	0.01504	0.09912	0.26741	0.30172	0.33292	0.34133
1.5	0.01596	0.10903	0.32623	0.37796	0.42792	0.44190
2.0	0.01625	0.11283	0.36165	0.42872	0.49749	0.51751
2.5	0.01634	0.11430	0.38299	0.46287	0.54969	0.57604
3.0	0.01637	0.11487	0.39582	0.48600	0.58961	0.62245
4.0	0.01639	0.11517	0.40814	0.51242	0.64505	0.69093
5.0	0.01639	0.11522	0.41254	0.52473	0.68008	0.73872
6.0	0.01639	0.11522	0.41410	0.53048	0.70298	0.77383
7.0	0.01639	0.11523	0.41465	0.53317	0.71831	0.80065
8.0	0.01639	0.11523	0.41484	0.53443	0.72875	0.82180
9.0	0.01639	0.11523	0.41491	0.53502	0.73594	0.83890
10.0	0.01639	0.11523	0.41493	0.53530	0.74093	0.85300

Table 2 Hemispherical reflectance, ρ_m

τ_0	$\omega = 0.1$	$\omega = 0.5$	$\omega = 0.9$	$\omega = 0.95$	$\omega = 0.99$	$\omega = 1.00$
0.1	0.00718	0.03843	0.07443	0.07931	0.08329	0.08430
0.2	0.01152	0.06432	0.13120	0.14085	0.14880	0.15082
0.3	0.01439	0.08306	0.17714	0.19143	0.20336	0.20642
0.4	0.01637	0.09705	0.21529	0.23412	0.25004	0.25415
0.5	0.01777	0.10768	0.24749	0.27076	0.29066	0.29583
0.6	0.01878	0.11585	0.27499	0.30258	0.32645	0.33270
0.7	0.01951	0.12220	0.29866	0.33046	0.35829	0.36562
0.8	0.02005	0.12717	0.31918	0.35507	0.38684	0.39526
0.9	0.02045	0.13108	0.33706	0.37691	0.41259	0.42212
1.0	0.02075	0.13417	0.35271	0.39640	0.43596	0.44659
1.5	0.02144	0.14236	0.40714	0.46807	0.52642	0.54268
2.0	0.02163	0.14509	0.43715	0.51213	0.58800	0.60994
2.5	0.02168	0.14603	0.45421	0.54031	0.63220	0.65983
3.0	0.02169	0.14636	0.46406	0.55876	0.66509	0.69836
4.0	0.02170	0.14652	0.47319	0.57926	0.70973	0.75403
5.0	0.02170	0.14654	0.47634	0.58859	0.73751	0.79234
6.0	0.02170	0.14654	0.47744	0.59290	0.75554	0.82033
7.0	0.02170	0.14654	0.47782	0.59491	0.76759	0.84166
8.0	0.02170	0.14654	0.47795	0.59585	0.77577	0.85847
9.0	0.02170	0.14654	0.47800	0.59628	0.78141	0.87205
10.0	0.02170	0.14654	0.47802	0.59649	0.78532	0.88325

Evaluation of this expression at $\tau_0 = 0$ yields

$$\epsilon_a'|_{\tau_0=0} = 4\rho_w - (1 + \rho_w)^2\omega \tag{73}$$

and setting this derivative equal to zero gives

$$\epsilon^* = 1 - \rho^* = 1 - [(2 - \omega) - 2(1 - \omega)^{1/2}]/\omega \tag{74}$$

A comparison of the hemispherical emittance for a semi-infinite medium ϵ_∞, [2], with ϵ^* reveals that ϵ^* is always slightly less than ϵ_∞ with a maximum difference of 0.0415 near $\omega = 0.9$. For substrate emittances greater than ϵ^*, the hemispherical emittance first decreases, reaches a minimum, and increases with optical thickness. The optical thickness at which the minimum occurs increases with ϵ_w. This behavior is not very pronounced and is difficult to see from Fig. 4.

To generalize, when $\epsilon_w > \epsilon_\infty$, the scattering medium acts as a shield and an increase in the optical thickness decreases the emittance. When $\epsilon_w < \epsilon_\infty$, the scattering medium acts as a source and an increase in optical thickness increases the emittance. For substrate emittance in the range $\epsilon^* < \epsilon_w < \epsilon_\infty$ the hemispherical emittance is very insensitive to changes in optical thickness. For example, the case of a substrate with an emittance of 0.50 and a medium with an albedo of 0.90 [$\epsilon^* = 0.48051$ and $\epsilon_\infty = 0.52198$], the maximum variation of the hemispherical emittance is only 4 percent when τ_0 is varied from zero to infinity.

The apparent directional emittance for the emitting opaque substrate case decreases with substrate reflectance. This behavior is predicted mathematically by taking the derivative of equation (27), i.e.,

$$\frac{\partial \epsilon_a(\mu)}{\partial \rho_w} = -t_m(\mu)t_m/((1 - \rho_w\rho_m)^2 \tag{75}$$

The variation of the apparent directional emittance with optical thickness can be determined by taking the derivative of equation (27), and evaluating it at $\tau_0 = 0$, i.e.,

$$\epsilon_a'(\mu)|_{\tau_0=0} = \left(2 + \frac{1}{\mu}\right)\rho_w - (\rho_w + 1)\left(\rho_w + \frac{1}{2\mu}\right)\omega, \tag{76}$$

Setting this derivative equal to zero gives the substrate emittance at which the slope of the directional emittance is zero, i.e.,

$$\epsilon^*(\mu) = 1 - \Big\{(2 - \omega)\left(1 + \frac{1}{2\mu}\right) - [(2 - \omega)^2 \Big((1 + \frac{1}{2\mu}\Big)^2 - (2\omega^2/\mu)]^{1/2}\Big\} \Big/ (2\omega) \tag{77}$$

The following limiting cases can easily be developed:

$$\epsilon^*(0) = (2 - 2\omega)/(2 - \omega) \tag{78a}$$

$$\epsilon^*\left(\frac{1}{2}\right) = \epsilon^* \tag{78b}$$

$$\epsilon^*(\mu) = \begin{cases} 1 - \dfrac{1}{2\mu} & \mu \geq \dfrac{1}{2} \\ 0 & \mu < \dfrac{1}{2} \end{cases} \quad \text{when } \omega = 1 \tag{78c}$$

Table 3 Normal transmittance, $t_m (\mu = 1)$

τ_0	$\omega = 0.1$	$\omega = 0.5$	$\omega = 0.9$	$\omega = 0.95$	$\omega = 0.99$	$\omega = 1.00$
0.1	0.90888	0.92647	0.94675	0.94950	0.95175	0.95231
0.2	0.82556	0.85697	0.89696	0.90274	0.90751	0.90873
0.3	0.74960	0.79182	0.85034	0.85928	0.86676	0.86867
0.4	0.68043	0.73095	0.80656	0.81873	0.82905	0.83171
0.5	0.61751	0.67423	0.76538	0.78081	0.79405	0.79749
0.6	0.56029	0.62147	0.72658	0.74524	0.76147	0.76573
0.7	0.50830	0.57249	0.68996	0.71181	0.73107	0.73616
0.8	0.46107	0.52706	0.65536	0.68033	0.70264	0.70858
0.9	0.41817	0.48499	0.62262	0.65063	0.67599	0.68281
1.0	0.37923	0.44606	0.59163	0.62257	0.65098	0.65867
1.5	0.23230	0.29177	0.45905	0.50274	0.54588	0.55810
2.0	0.14208	0.18932	0.35650	0.40931	0.46570	0.48249
2.5	0.08680	0.12212	0.27672	0.33504	0.40269	0.42396
3.0	0.05298	0.07841	0.21457	0.27523	0.35197	0.37755
4.0	0.01971	0.03199	0.12852	0.18692	0.27548	0.30907
5.0	0.007317	0.01292	0.07665	0.12749	0.22063	0.26128
6.0	0.002713	0.005179	0.04557	0.08712	0.17944	0.22617
7.0	0.001005	0.002064	0.02704	0.05958	0.14747	0.19935
8.0	3.721E-4	8.192E-4	0.01602	0.04076	0.12207	0.17820
9.0	1.247E-4	3.239E-4	0.009484	0.02789	0.10154	0.16110
10.0	5.092E-4	1.277E-4	0.005612	0.01908	0.08476	0.14700

Table 4 Hemispherical transmittance, t_m

τ_0	$\omega = 0.1$	$\omega = 0.5$	$\omega = 0.9$	$\omega = 0.95$	$\omega = 0.99$	$\omega = 1.00$
0.1	0.83965	0.87044	0.90595	0.91078	0.91471	0.91570
0.2	0.71489	0.76555	0.83015	0.83950	0.84722	0.84918
0.3	0.61330	0.67704	0.76572	0.77930	0.79067	0.79358
0.4	0.52894	0.60101	0.70960	0.72714	0.74201	0.74585
0.5	0.45801	0.53499	0.65992	0.68116	0.69942	0.70417
0.6	0.39787	0.47726	0.61545	0.64015	0.66166	0.66730
0.7	0.34655	0.42649	0.57530	0.60321	0.62786	0.63438
0.8	0.30253	0.38167	0.53879	0.56969	0.59736	0.60474
0.9	0.26462	0.34197	0.50541	0.53908	0.56966	0.57788
1.0	0.23185	0.30671	0.47475	0.51098	0.54435	0.55341
1.5	0.12211	0.18005	0.35235	0.39848	0.44430	0.45732
2.0	0.06586	0.10706	0.26558	0.31746	0.37335	0.39006
2.5	0.03610	0.06418	0.20187	0.25621	0.32000	0.34017
3.0	0.02002	0.03869	0.15417	0.20849	0.27822	0.30164
4.0	0.006321	0.01423	0.09056	0.14005	0.21663	0.24597
5.0	0.002046	0.005288	0.05342	0.09501	0.17315	0.20766
6.0	6.736E-4	0.001979	0.03156	0.06476	0.14071	0.17967
7.0	2.248E-4	7.442E-4	0.01865	0.04423	0.11561	0.15834
8.0	7.577E-5	2.809E-4	0.01103	0.03023	0.09568	0.14153
9.0	2.575E-5	1.063E-4	0.006521	0.02068	0.07959	0.12795
10.0	8.814E-6	4.034E-5	0.003856	0.01415	0.06643	0.11675

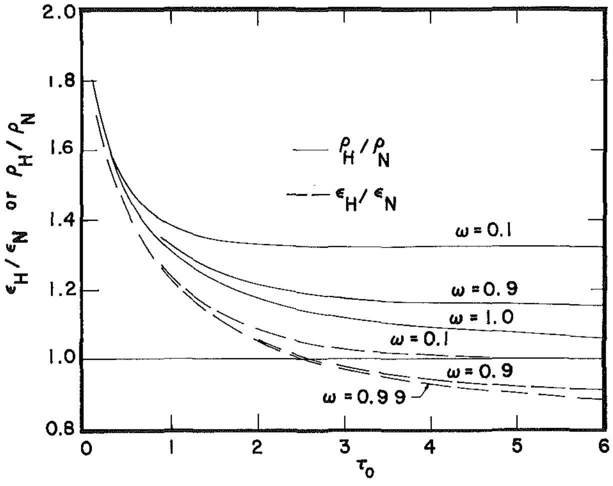

Fig. 2 Ratio of hemispherical to normal for reflectance and emittance

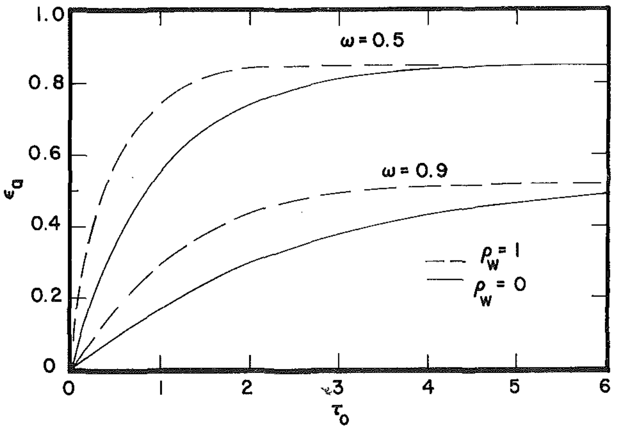

Fig. 3 Apparent emittance of a scattering medium with a nonemitting diffuse substrate

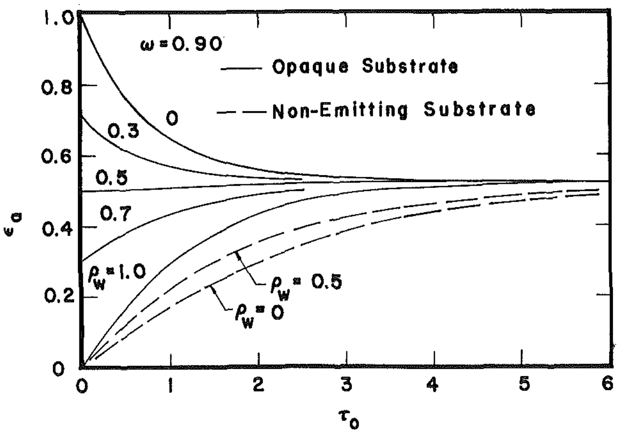

Fig. 4 Apparent hemispherical emittance for $\omega = 0.9$

Using the first two terms of a Taylor series expansions yields the small optical thickness behavior of the directional emittance

$$\epsilon_a(\mu) = \epsilon_w + \left[\left(2 + \frac{1}{\mu}\right) \rho_w - (\rho_w + 1) \left(\rho_w + \frac{1}{2\mu}\right) \omega \right] \tau_0 \quad (79)$$

Thus for small optical thicknesses, the apparent directional emittance decreases with τ_0 when substrate emittance is greater than $\epsilon^*(\mu)$ and increases when $\epsilon_w < \epsilon^*(\mu)$.

The behavior of the directional emittance, $\epsilon_a(\mu)$, with optical thickness can be predicted from the directional emittance of a semi-infinite medium, $\epsilon_\infty(\mu)$ [2]. This behavior is classified in Table 5. The optical thickness at which the maximum or minimum occurs increases as $|\epsilon^*(\mu) - \epsilon_w|$ is increased. The maximums or minimums are not very pronounced. A comparison of $\epsilon_\infty(\mu)$ with $\epsilon^*(\mu)$ reveals that $\epsilon_\infty{}^*(0) > \epsilon^*(0)$, $\epsilon_\infty(1) < \epsilon^*(1)$ and at some point $\mu \geq 1/2$, $\epsilon_\infty(\mu) = \epsilon^*(\mu)$. The difference between $\epsilon_\infty(\mu)$ and $\epsilon^*(\mu)$ decreases as ω becomes small. The largest difference occurs at $\mu = 1$ and $\omega = 1$.

As a generalization, when $\epsilon_w > \epsilon_\infty(\mu)$ the scattering medium acts as a shield and an increase in the optical thickness decreases the emittance. When $\epsilon_w < \epsilon_\infty(\mu)$ the scattering medium acts as a source and an increase in optical thickness increases the emittance. When $\epsilon_w \simeq \epsilon_\infty(\mu)$, the apparent directional emittance is a weak function of optical thickness. For example, the case of a substrate with an emittance of 0.60 and a medium with an albedo of 0.90 [$\epsilon^*(1) = 2/3$ and $\epsilon_\infty(1) = 0.58503$], the maximum variation of the apparent normal emittance is only four percent.

The behavior of the apparent reflectances follows from

$$\rho_a(\mu) + \epsilon_a(\mu) = 1 \quad (80)$$

$$\rho_a + \epsilon_a = 1 \quad (81)$$

These two identities can be found from equations (27, 30, 31) and (46). Physically, these identities arise because the medium-substrate is opaque. The behavior of the hemispherical reflectance is illustrated in Fig. 5.

To illustrate the utility of the results of this investigation, the following example is presented. In remote sensing of shallow bodies of water, one must determine the importance of the bottom on the reflected intensity. For solar illumination, emission can be neglected and the apparent bidirectional reflectance, given by equation (28), is the important property. The difference between the bidirectional reflectance for a black bottom and for a reflecting bottom is $\rho_w t_m(\mu) t_m(\mu_0)/(1 - \rho_w \rho_m)$. The maximum difference is $t_m{}^2(1)/(1 - \rho_m)[\mu = \mu_0 = 1$ and $\rho_w = 1]$. The investigation should also be useful in understanding the optical characteristics of ceramics and painted surfaces.

Table 5 Behavior of the directional emittance with optical thickness

Case I $\epsilon_\infty(\mu) > \epsilon^*(\mu)$	$\epsilon_w > \epsilon^*(\mu)$	emittance first decreases, reaches a minimum, and then increases with τ_0
	$\epsilon_w \leq \epsilon^*(\mu)$	emittance increases with τ_0
Case II $\epsilon_\infty(\mu) < \epsilon^*(\mu)$	$\epsilon_w \geq \epsilon^*(\mu)$	emittance decreases with τ_0
	$\epsilon_w < \epsilon^*(\mu)$	emittance first increases, reaches a maximum, and then decreases with τ_0

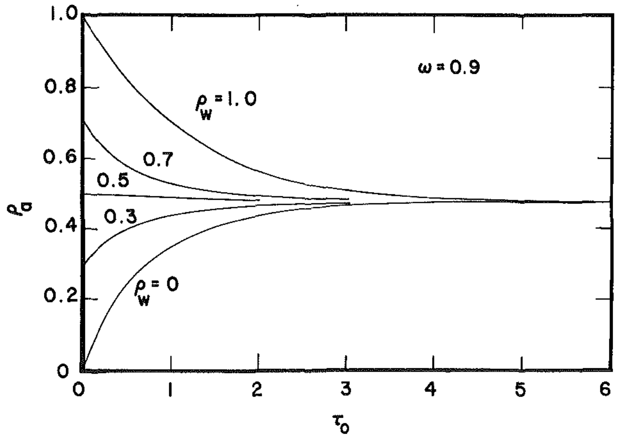

Fig. 5 Apparent hemispherical reflectance for $\omega = 0.9$ and isotropic incident intensity

Concluding Remarks

This study of the apparent radiative properties of an absorbing-isotropically scattering layer bounded by a diffuse substrate produced the following:

1 The apparent radiative properties have been expressed exactly and simply in terms of the properties of a medium not bounded by a substrate [see equations (27, 28, 30, 31) and (46)]. Any arbitrary directional distribution of incident radiation can be handled. This result increases the usefulness of the solutions for the medium not bounded by a substrate.

2 Differential equations of the initial value type (61–67) for the radiative properties of the scattering medium have been developed and solved.

3 The apparent emittance of medium bounded by a non-emitting substrate has been shown analytically to increase with optical thickness and substrate reflectance. For this situation the scattering layer always acts as a source.

4 The apparent emittance of a medium bounded by an emitting opaque substrate has been shown to increase with substrate emittance. However the apparent emittance decreases with optical thickness if the substrate emittance is greater than the emittance of a semi-infinite scattering medium. In this case the scattering layer acts as a shield.

References

1 Edwards, R. H., and Bobco, R. P., "Radiant Heat Transfer from Isothermal Dispersion with Isotropic Scattering," ASME JOURNAL OF HEAT TRANSFER, Vol. 89, No. 4, Nov., 1967, pp. 300–308.

2 Crosbie, A. L., "Emittance of an Isothermal, Isotropically Scattering Medium," *AIAA Journal*, Vol. 11, No. 8, Aug. 1973, pp. 1203–1205.

3 Crosbie, A. L., "Reflection Function for an Isotropically Scattering Finite Medium," *AIAA Journal*, Vol. 11, No. 10, Oct. 1973, pp. 1448–1450.

4 Lii, C. C., Özisik, M. N., "Hemispherical Reflectivity and Transmissivity of an Absorbing, Isotropically Scattering Slab with a Reflecting Boundary," *Int. Journal Heat Mass Transfer*, Vol. 16, No. 3, March 1973, pp. 685–690.

5 Armaly, B. F., and El-Baz, H. S., "Influence of Substrate Properties on the Apparent Emittance of an Isothermal Isotropically Scattering Medium," ASME JOURNAL OF HEAT TRANSFER, Vol. 99, No. 2, May 1977, pp. 208–211.

6 Armaly, B. F., and El-Baz, H. S., "Radiative Transfer through an Isotropically Scattering Finite Medium: Approximate Solution," *AIAA Journal*, Vol. 15, No. 8, Aug. 1977, pp. 1180–1185.

7 Viskanta, R., "Radiation Transfer and Interaction of Convection With Radiation Heat Transfer," *Advances in Heat Transfer,* Vol. 3, 1966, p. 175.

8 Sobolev, V. V., *A Treatise on Radiative Transfer,* D. Van Nostrand Co., Princeton, N. J., 1963.

9 Rogers, J. E., and Edwards, D. K., "Bidirectional Reflectance and transmittance of a Scattering-Absorbing Medium with a Rough Surface," *Progress in Astronautics and Aeronautics,* Vol. 49, 1976, pp. 3–24.

10 Heavens, O. S., *Optical Properties of This Solid Films,* Dover Publications, New York, N. Y., 1965.

11 Sobouti, Y., "Chandrasekhar's X-, Y- and Related Functions," *Astrophysical Journal Supplement Series,* Vol. 7, No. 72, Jan. 1963, pp. 411–560.

12 Carlstedt, J. L., and Mullikin, T. W., "Chandrasekhar's X- and Y-Functions," *Astrophysical Journal Supplement Series,* Vol. 12, No. 113, March 1966, pp. 499–585.

13 Bellman, R., Kagiwada, H., Kalaba, R., and Ueno, S., "Numerical Results for Chandrasekhar's X- and Y-Functions of Radiative Transfer," *Journal of Quantitative Spectroscopy and Radiative Transfer,* Vol. 6, No. 4, July/Aug., 1966, pp. 479–500.

14 Loskutov, V. M., "Calculation of Radiation Field in the Case of Monochromatic Isotropic Scattering II. Ambartsumyan's Functions $\phi(n, \tau_0)$ and $\psi(n, \tau_0)$ and their Moments," *Astrophysics,* Vol. 9, No. 3, July/Sept., 1973, pp. 205–210.

D. W. Amlin
Project Engineer.
Aeronautical Systems Div.,
Wright Patterson Air Force Base,
Ohio

S. A. Korpela
Associate Professor of Mechanical Engineering,
The Ohio State University,
Columbus, Ohio
Assoc. Mem. ASME

Influence of Thermal Radiation on the Temperature Distribution in a Semi-Transparent Solid

The importance of radiation on the temperature distribution in a semi-transparent solid is reported. The first-order differential approximation of radiation is combined with conduction analysis to investigate the temperature profiles in a plane slab and a rectangular region. The coupled nonlinear partial differential equations are solved numerically by either a standard implicit or an implicit alternating direction method. Results obtained for opaque boundaries are in good agreement with exact formulations found in the literature. An extension to partially transparent boundaries is made and results presented.

1 Introduction

The objective of this study is to determine the temperature distribution in a semi-transparent slab (an optical window in the present case) with one side exposed to high temperature (as a result of aerodynamic heating for example). Since it is known that in semi-transparent solids, heat transfer by thermal radiation may be as important as conduction [1, 2] when the temperatures are high, one needs to address the complexities which radiation introduces into the thermal analysis.

The complexity brought upon by the radiation is mathematical, for now instead of the linear partial differential equation of pure conduction, a partial integrodifferential equation, which is in addition nonlinear, must be solved. Because of the nonlinearity and possible two-dimensionality of the geometry, hope for finding an exact solution vanishes, and even a numerical treatment becomes cumbersome. Therefore, an approximate formulation (the differential formulation of radiative transfer) was resorted to in the present analysis and a numerical method (now more tractable than that required for the exact formulation) was used to solve the resulting equations. This approach was also thought to be sufficiently flexible to allow complexities such as would result from a three-dimensional geometry, irregular boundaries or convective boundary conditions to be easily implemented in practical applications.

The differential approximation has a long history in radiative transfer theory. It was first used in astrophysics by Milne [3] and Eddington [4], and later by Chandrasekhar [5] and Krook [6] for one-dimensional problems under conditions of radiative equilibrium. Its extension to two and three dimensions and a discussion of the appropriate boundary conditions to be used have been given in the context of neutron transport theory by Mark [7, 8] and Marshak [9]. In radiative gas dynamics it was used by Traugott [10] to resolve the structure of a radiating shock wave; by Cohen [11] and by Cheng [12] in some problems involving two-dimensional flows.

In these examples the radiating medium was assumed gray. By an analogy with neutron transport theory (see, for example, Davison [13], p. 350) Traugott [14] extended the differential approximation to nongray gases in a manner which yields the correct asymptotic limits when the gas is either optically thick or thin. This method of accounting for nongrayness is used in formulating the governing equations in the present study, although numerical results are presented only for a gray medium.

For a thorough discussion of heat transfer in semitransparent solids and an extensive list of references the reader is referred to the review article by Viskanta and Anderson [15].

2 Formulation and Solution

Consider a semi-transparent solid. Its temperature distribution is governed by the equation

$$\rho c \frac{\partial T}{\partial t} = k \frac{\partial^2 T}{\partial x_i \partial x_i} - \frac{\partial q_i{}^R}{\partial x_i} \tag{1}$$

in which T is the local value of the absolute temperature; t, the time; x_i, a position vector; ρ, the density of the material; c, its specific heat; and k, its thermal conductivity. The radiant heat flux is denoted by $q_i{}^R$.

Assuming for a moment that the medium is gray, the equation of transfer for the integrated (over all frequencies) radiation intensity I (in the direction of the unit vector ℓ_i and in the absence of scattering) is

---

Contributed by the Heat Transfer Division for publication in the JOURNAL OF HEAT TRANSFER. Manuscript received by the Heat Transfer Division February 21, 1978.

$$\frac{1}{c}\frac{\partial I}{\partial t} + \ell_i \frac{\partial I}{\partial x_i} = \alpha\left(\frac{n^2\sigma T^4}{\pi} - I\right) \tag{2}$$

where c is the speed of light; α, the gray absorption coefficient of the medium; σ, the Stefan-Boltzmann constant; and n, the index of refraction.

Defining next the first three moments of the intensity as (see, for example, Vincenti and Kruger [16], p. 491)

$$J = \int_0^{4\pi} I d\Omega \tag{3}$$

$$q_i^R = \int_0^{4\pi} \ell_i I d\Omega \tag{4}$$

$$\tau_{ij}^R = \frac{1}{c}\int_0^{4\pi} \ell_i \ell_j I d\Omega \tag{5}$$

in which J is the integrated mean intensity and τ_{ij}^R the radiative stress tensor, the first two moments of the equation of transfer (after the unsteady term has been neglected) can be written as

$$\frac{\partial q_i^R}{\partial x_i} = \alpha_p(4\sigma n^2 T^4 - J) \tag{6}$$

and

$$c\frac{\partial \tau_{ij}^R}{\partial x_j} + \alpha_R q_i^R = 0 \tag{7}$$

Following Traugott [14], the gray absorption coefficient has been replaced by the Planck mean absorption coefficient in the first equation and by the Rosseland mean in the second. These mean coefficients are defined by the equations

$$\alpha_p = \frac{\pi}{n^2\sigma T^4}\int_0^\infty \alpha_\nu B_\nu d\nu \qquad \frac{1}{\alpha_R} = \frac{\pi}{4n^2\sigma T^3}\int_0^\infty \frac{1}{\alpha_\nu}\frac{dB_\nu}{dT} d\nu \tag{8}$$

in which $B_\nu = (2h^3\nu^3/c^2)/[\exp(h\nu/kT) - 1]$ is the Planck function.

Invoking next the generalized Milne-Eddington approximation, the stress tensor can be related to J by

$$\tau_{ij}^R = \frac{1}{3c} J\delta_{ij} \tag{9}$$

where δ_{ij} is the Kronecker delta. Substituting this into equation (7) gives

$$\frac{\partial J}{\partial x_i} + 3\alpha_R q_i^R = 0. \tag{10}$$

Using equation (10), the energy equation can be written as

$$\rho c\frac{\partial T}{\partial t} = k\frac{\partial^2 T}{\partial x_i \partial x_i} + \frac{1}{3\alpha_R}\frac{\partial^2 J}{\partial x_i \partial x_i}. \tag{11}$$

The equation of transfer is replaced by

$$\frac{\partial^2 J}{\partial x_i \partial x_i} + 3\alpha_R\alpha_p(4n^2\sigma T^4 - J) = 0. \tag{12}$$

When conduction is present, the temperature jump (see, for example, Siegel and Howell [17] p. 500 or Goody [18] p. 54) disappears and at the opaque boundaries the radiative boundary condition becomes

$$\frac{\partial q_2^R}{\partial x_2} = \frac{\alpha_p}{\lambda} q_2^R. \tag{13}$$

In this equation q_2^R is the radiant heat flux in the positive x_2 direction and $1/\lambda = 4(1/\epsilon - 1/2)$, where ϵ is the total hemispherical emissivity of the boundary. In terms of J this becomes (see Arpaci and Gözüm [19])

$$\frac{\partial J}{\partial x_2} = 2\alpha_R\lambda(J - 4n^2\sigma T_w^4) \tag{14}$$

in which T_w is the boundary temperature.

The development of the radiative boundary condition at the partially transparent boundary is similar to that at opaque boundaries. Writing the mean intensity as

$$J = J^+ + J^-, \tag{15}$$

at the boundary in the x_2, x_3 plane equation (6) can be written as

$$\frac{\partial q_1^R}{\partial x_1} = \alpha_p[4\sigma n^2 T_w^4 - (J^+ + J^-)]. \tag{16}$$

Assuming that the intensities are hemispherically isotropic, the radiant heat flux, equation (4), at the wall becomes

$$2q_1^R = J^+ - J^-. \tag{17}$$

From equations (16) and (17)

$$J^+ = 2\sigma n^2 T_w^4 + q_1^R - \frac{1}{2\alpha_p}\frac{\partial q_1^R}{\partial x_1} \tag{18}$$

$$J^- = 2\sigma n^2 T_w^4 - q_1^R - \frac{1}{2\alpha_p}\frac{\partial q_1^R}{\partial x_1}. \tag{19}$$

Since the hemispherical intensity J^+ is made up of that portion of the radiation from an extended black body at temperature T_S which is transmitted across the boundary and the reflected part of J^-, we can also write

$$J^+ = 2(1-\rho)n^2\sigma T_s^4 + \rho J^- \tag{20}$$

where ρ is the hemispherical reflectivity of the boundary.

Using equations (17) and (18) to eliminate J^+ and J^- in equation (20) yields

$$2\sigma n^2(T_w^4 - T_s^4) + \left(\frac{1+\rho}{1-\rho}\right) q_1^R - \frac{1}{2\alpha_p}\frac{\partial q_1^R}{\partial x_1} = 0 \tag{21}$$

Nomenclature

A = aspect ratio
B_ν = Planck function
c = specific heat or speed of light
h = Planck's constant
I = integrated intensity
J = integrated mean intensity
J^+ = hemispherical integrated intensity
J^- = hemispherical integrated intensity
k = conductivity or Boltzmann constant
L = thickness of window
ℓ_i = unit vector
n = index of refraction
P_0 = Planck number, $\frac{\alpha_m k}{n^2\sigma T_0^3}$
q_i^R = radiative heat flux
T = temperature
T_1 = nondimensional inside temperature, T_i/T_0
T_2 = nondimensional temperature of the surroundings, T_s/T_0
T_i = inside temperature
T_s = temperature of surroundings
T_0 = reference temperature
T_w = wall temperature
t = time
x_i = position vector
x = position coordinate
y = position coordinate
α = gray absorption coefficient
α_P = Planck mean absorption coefficient
α_R = Rosseland mean absorption coefficient
α_m = geometric mean absorption coefficient, $(\alpha_P\alpha_R)^{1/2}$
δ_{ij} = Kronecker delta
ϵ = emissivity
ρ = density or surface reflectivity
$\lambda = [4(1/\epsilon - 1/2)]^{-1}$
ν = frequency of radiation
σ = Stefan-Boltzmann constant
Ω = solid angle
τ = optical thickness, $\alpha_m L$
τ_{ij} = radiative stress tensor
η = absorption coefficient ratio parameter, $(\alpha_P/\alpha_R)^{1/2}$

This can be written in terms of J by eliminating J^+ and J^- between equations (15), (17) and (18) and combining the result with (10) to give

$$\frac{\partial J}{\partial x_1} = \frac{3\alpha_R}{2}\left(\frac{1-\rho}{1+\rho}\right)(J - 4n^2\sigma T_s{}^4) \tag{22}$$

Introducing next the following scales—T_0 for temperature, L for lengths, $\rho c L^2/k$ for time, and $n^2\sigma T_0{}^4$ for the integrated mean intensity and calling $\alpha_m = (\alpha_P \alpha_R)^{1/2}$ the geometric mean absorption coefficient, $\eta = (\alpha_P/\alpha_R)^{1/2}$ the square root of the absorption coefficient ratio, $\tau = \alpha_m L$ the optical thickness, and $P_0 = \alpha_m k/n^2\sigma T_0{}^3$ the Planck number, the equations (11) and (12) can be written in the following nondimensional form (in x-y coordinates):

$$\frac{\partial T}{\partial t} = \frac{\partial^2 T}{\partial x^2} + \frac{\partial^2 T}{\partial y^2} + \frac{\eta}{3P_0}\left(\frac{\partial^2 J}{\partial x^2} + \frac{\partial^2 J}{\partial y^2}\right) \tag{23}$$

$$\frac{\partial^2 J}{\partial x^2} + \frac{\partial^2 J}{\partial y^2} = 3\tau^2(J - 4T^4). \tag{24}$$

No special symbols have been introduced for the nondimensional variables, for the presence of dimensionless parameters is sufficient for right interpretation.

The boundary conditions are made nondimensional in a similar manner. The conditions are given here for the case of a rectangular window (as shown in Fig. 1) with two opaque and two partially transparent boundaries. By taking the sides at $y = 0$ and $y = A$ ($A = H/L$ is the aspect ratio) to be opaque and at constant temperature, the radiative boundary conditions become

$$\frac{\partial J}{\partial y}(x, 0, t) = \frac{3\tau\lambda}{\eta}[J(x, 0, t) - 4T_1{}^4] \tag{25}$$

$$-\frac{\partial J}{\partial y}(x, A, t) = \frac{3\tau\lambda}{\eta}[J(x, A, t) - 4T_1{}^4] \tag{26}$$

The thermal boundary conditions remain

$$T(x, 0, t) = T(x, A, t) = T_1 \tag{27}$$

where $T_1 = T_i/T_0$.

The reference temperature up to now has been left unspecified. Letting it be equal to the outside surface temperature of the window, T_0, the boundary conditions at the partially transparent boundaries become

$$\frac{\partial J}{\partial x}(0, y, t) = \frac{3\tau}{2\eta}\left(\frac{1-\rho}{1+\rho}\right)[J(0, y, t) - 4T_2{}^4] \tag{28}$$

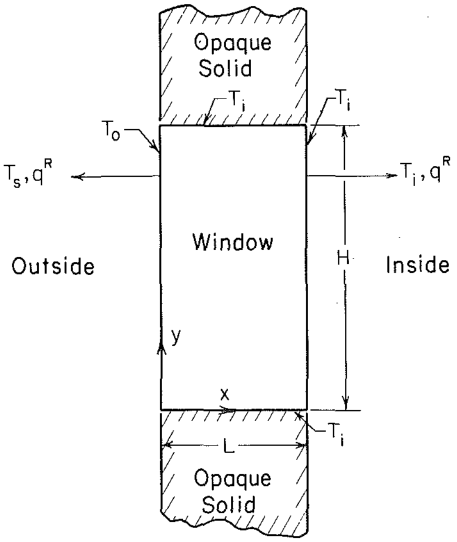

Fig. 1 **A rectangular window exchanging heat by radiation with surroundings at temperatures T_s and T_i**

$$-\frac{\partial J}{\partial x}(1, y, t) = \frac{3\tau}{2\eta}\left(\frac{1-\rho}{1+\rho}\right)[J(1, y, t) - 4T_1{}^4] \tag{29}$$

and

$$T(0, y, t) = 1 \quad T(1, y, t) = T_1, \tag{30}$$

where $T_2 = Ts/T_0$.

Finally, if the initial temperature of the window is T_i, the initial condition is given by

$$T(x, y, 0) = T_1. \tag{31}$$

The governing equations were solved numerically by finite difference methods. A standard implicit method (backward difference in time and central in space) was used for the one-dimensional cases and the implicit alternating direction algorithm for two-dimensional ones. It may be mentioned here that the freedom to choose a suitable algorithm from the large number devised for elliptic and parabolic equations is an important consequence of using the differential approximation.

3. Results

The first set of results obtained was for the much studied one-dimensional case of a gray semitransparent slab between two black walls. The corresponding numerical solution to the integrodifferential equation of the exact formulation has been worked out by Viskanta and Grosh [20]. Once the equations (23–31) are appropriately reduced and solved the temperature distributions shown in Fig. 2 are obtained. Three values of Planck number were considered for an optical thickness $\tau = 1.0$ and an inside to outside temperature ratio $T_1 = 0.1$. The differential approximation is seen to yield a set of curves which follow those of the exact formulation very closely. This has already been noted by Viskanta and Grosh for the values of Planck number $P_0 \geq 4$ (when conduction dominates). As one would expect the differential approximation deteriorates somewhat as radiation becomes the prominent energy transfer mode at low values of the Planck number. However, the shape of the temperature profiles is nevertheless quite faithfully predicted. Thus it appears that no essential physics is lost by treating the problem by the differential approximation.

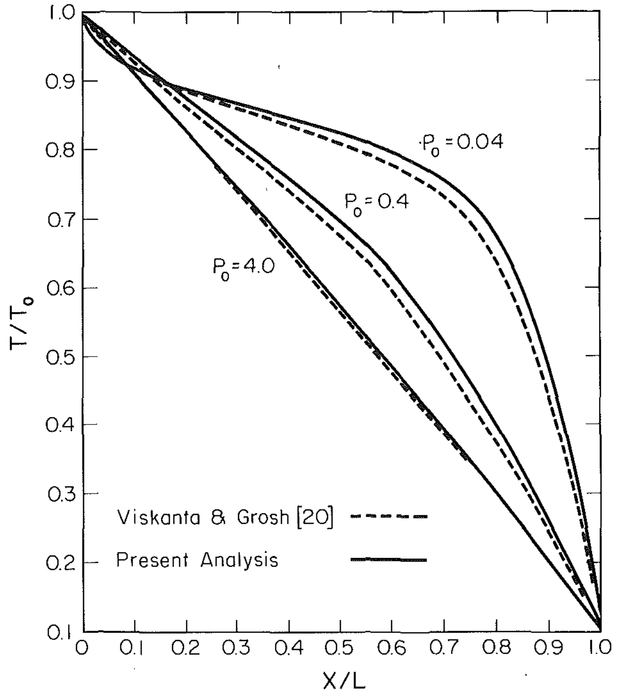

Fig. 2 **Temperature profiles for a slab by the differential approximation (τ = 1.0)**

Fig. 3 shows the influence of the optical thickness for a temperature ratio $T_1 = 0.5$. For $\tau = 0.1$ the value $P_0 = 0.04$ is sufficiently large for conduction to dominate whereas $P_0 = 4 \times 10^{-5}$ is small enough that radiation is the major factor. Indeed, in the latter case the temperature profile in the central region is identical to that obtained for pure radiation (not shown); only next to the boundaries (in the conduction boundary layers) is the diffusion of heat important. The conduction boundary layers must, of course, appear since a temperature jump is not allowed.

The influence of reduced boundary emissivity on the temperature profiles is shown in Fig. 4. The temperature gradient and thus also the conductive heat flux increases particularly near the hot boundary as the emissivity is lowered. This is because the lower surface emissivity reduces the radiative flux and since the sum of the conductive and radiative heat fluxes is constant, the conductive contribution must increase. Identical trends have already been obtained by Viskanta and Grosh [21] by numerical solution of the equations resulting from the exact formulation.

The calculations discussed above were carried out to check the accuracy of the differential approximation against some known solutions and to determine the range of parameters in which inaccuracies may be expected. This is important when the method is extended to cases which have not been considered by exact methods.

One such case is given in Fig. 5 in which the temperature distributions are shown for a slab which exchanges radiation through partially transparent boundaries with extended black surroundings, the nondimensional temperatures of which are T_1 and T_2. The reflectivity of the boundaries is $\rho = 0.2$, the surface temperature ratio $T_1 = 0.5$, and the optical thickness of the medium $\tau = 1.0$. The absorption coefficient ratio is taken to be unity in this and all the subsequent computations. This has the effect of making the medium gray. When the nondimensional temperature of the extended black body is unity the transparency of the boundaries is manifested only through the value of reflectivity, as a comparison of equation (28) with (25) shows. Thus the temperature distributions in the slab are the same as the corresponding (with same τ and P_0) ones in Fig. 3, except for the differences in the reflectivity. By lowering the nondimensional temperature of the surroundings to 0.8 and 0.1, the radiative cooling can be seen from Fig. 5 to become substantial, especially at $P_0 = 0.04$.

As was mentioned earlier, calculation of two-dimensional temperature fields was accomplished by utilizing the implicit alternating direction algorithm. These calculations were carried out for a medium surrounded by opaque black walls, three of which were at zero temperature and the fourth had a nondimensional temperature equal to unity. This corresponds to the situation worked out analytically by Modest [22] for pure radiation. The centerline temperature profiles from his study and those calculated here for $P_0 = 4 \times 10^{-5}$ are shown in Fig. 6. The curves follow one another closely except near the boundaries, owing again to the presence of conduction boundary layers. Thus for an optical thickness of order unity, the differential approximation appears to be adequate for determining the temperature distribution with a fair degree of accuracy.

The last case considered corresponds to a window with two opaque sides and two partially transparent ones. The temperature distribution in the window is governed by equations (23–31). The numerical solutions of the centerline temperature profiles are shown in Figs. 7 and 8. In the vertical profile the characteristic cooling of the midregion is again substantial in the low Planck number case. The horizontal profiles when compared with Fig. 5 look much the same as in the one-dimensional case except now the additional cooling for $T_2 = 1.0$ and 0.8 and heating for $T_2 = 0.1$, brought about by the top and bottom boundaries of the window, also show up.

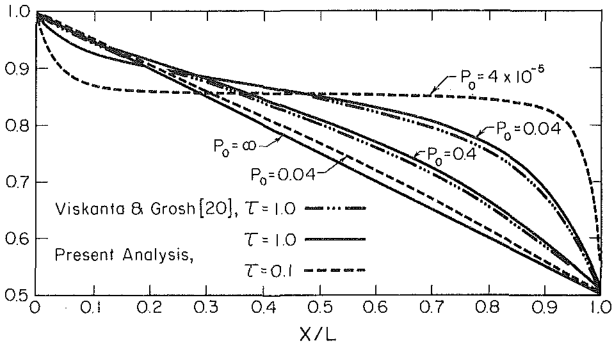

Fig. 3 Effect of Planck number and optical thickness on the temperature profiles in a slab

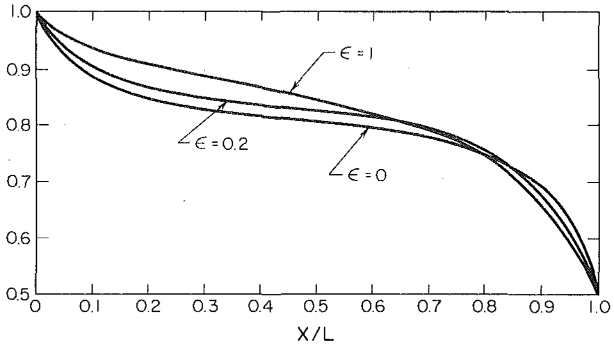

Fig. 4 Effect of surface emissivity on the temperature profiles in a slab ($P_0 = 0.08$, $\tau = 1.0$)

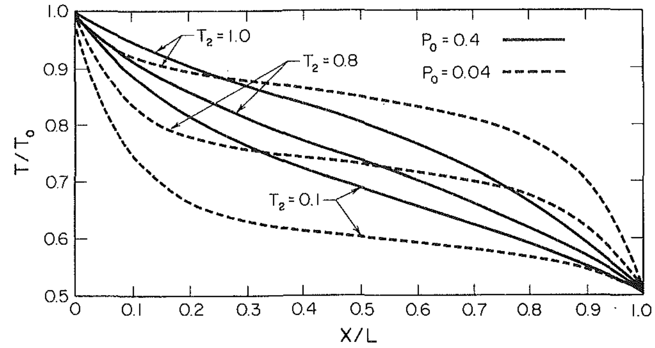

Fig. 5 The influence of the temperature of the surroundings on the temperature profiles in a slab ($\rho = 0.2$, $\tau = 1.0$)

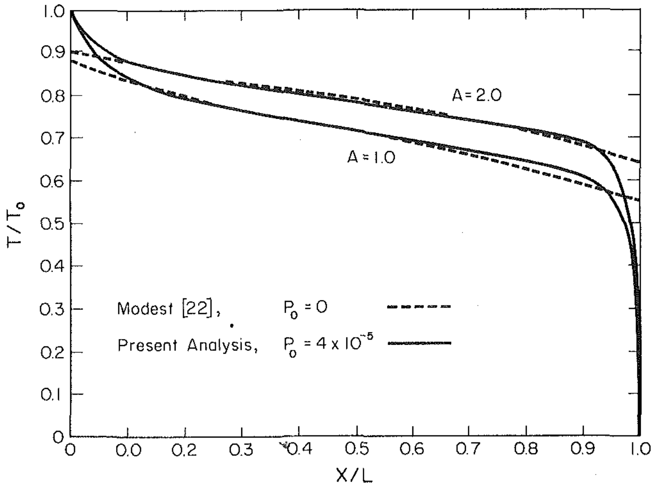

Fig. 6 Centerline temperature profiles for a rectangular window by the differential approximation ($\tau = 1.0$)

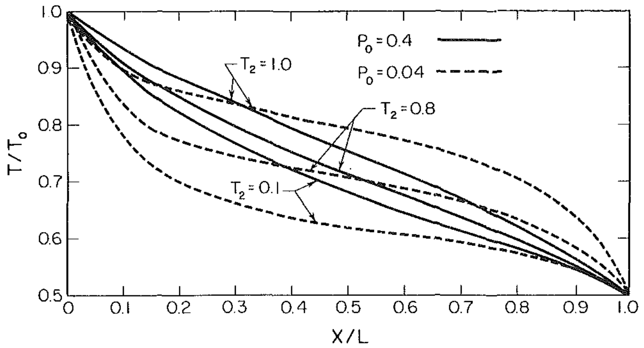

Fig. 7 The influence of the temperature of the surroundings on the centerline temperature profiles in a rectangular window ($A = 2.0$, $\rho = 0.2$, $\tau = 1.0$)

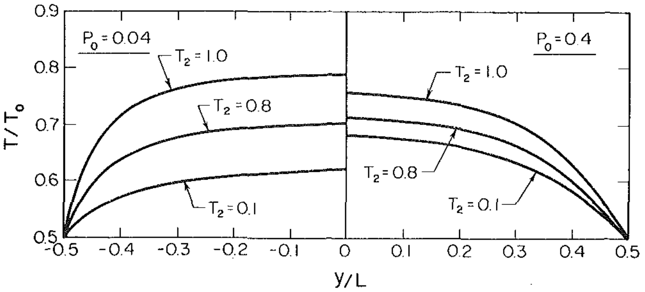

Fig. 8 The vertical temperature profiles in rectangular window ($A = 2.0$, $\rho = 0.2$, $\tau = 1.0$)

4 Summary and Conclusions

The first-order differential approximation has been used to study the interaction of conduction and radiation in a semi-transparent solid. For the parameter ranges investigated it provides a good agreement with the temperature profiles obtained by more exact methods. The effects of Planck number, boundary emissivity, surface reflectivity, external temperature and optical thickness were reported. These variables are important in the application (involving the determination of temperature profiles in an optical window) which promoted this study.

References

1 Gardon, R., "Calculation of Temperature Distributions in Glass Plates Undergoing Heat Treatment," *Journal of American Ceramic Society*, Vol. 41, 1958, pp. 200–209.

2 Gardon, R., "A Review of Radiant Heat Transfer in Glass," *Journal of American Ceramic Society*, Vol. 44, 1961, pp. 305–312.

3 Milne, E. A., "Thermodynamics of the Stars", *Handbuch Der Astrophysik*, Vol. 3, 1930, pp. 65–255.

4 Eddington, A., *The Internal Constitution of the Stars*, Dover, 1959.

5 Chandrasekhar, S., "Radiative Transfer," Dover, 1960.

6 Krook, M., "On the Solution of Equations of Transfer I," *Astrophys. Journal*, Vol. 10, 1964, pp. 253–259.

7 Mark, J. C., "The Spherical Harmonic Method I," National Research Council of Canada, Atomic Energy Report No. M797, 1945.

8 Mark, J. C., "The Spherical Harmonic Method II," National Research Council of Canada, Atomic Energy Report No. M797, 1945.

9 Marshak, R. E., "Note on the Spherical Harmonic Method as Applied to the Milne Problem for a Sphere," *Phys. Rev.*, Vol. 71, 1947, pp. 443–446.

10 Traugott, S. C., "A Differential Approximation for Radiative Transfer With Application to Normal Shock Structure," *Proc. 1953 Heat Transfer Fluid Mech. Inst.*, Stanford University Press, 1953 pp. 1–13.

11 Cohen, I. M., "Radiative Heat Flux Potential," *AIAA Journal*, Vol. 3, 1965, pp. 981–982.

12 Cheng, P., "Study of the Flow of a Radiating Gas by Differential Approximation," Ph.D. Dissertation, Stanford University, 1965.

13 Davison, B., "Neutron Transport Theory," Oxford, 1957.

14 Traugott, S. C., "Radiative Heat Flux Potential for a Nongray Gas," *AIAA Journal*, Vol. 4, 1966, pp. 541–542.

15 Viskanta, R. and Anderson, E. E., "Heat Transfer in Semitransparent Solids," in *Advances in Heat Transfer*, ed. J. P. Hartnett and T. Ervine, Jr., Vol. 11, 1975, pp. 317–439.

16 Vincenti, W. G. and Kruger, C. H., Jr., *Physical Gas Dynamics*, John Wiley, 1965.

17 Siegel, R. and Howell, J. R., *Thermal Radiation Heat Transfer*, McGraw-Hill, 1972.

18 Goody, R. M. *Atmospheric Radiation I. Theoretical Basis*, Oxford, 1964.

19 Arpaci, V. S. and Gözüm, D., "Thermal Stability of Radiating Fluids: The Benard Problem," *Physics of Fluids*, Vol. 16, 1973, pp. 581–588.

20 Viskanta, R. and Grosh, R. J., "Heat Transfer by Simultaneous Conduction and Radiation in an Absorbing Medium," *ASME Journal of Heat Transfer*, Vol. 84, 1962, pp. 63–72.

21 Viskanta, R. and Grosh, R. J., "Effect of Surface Emissivity on Heat Transfer by Simultaneous Conduction and Radiation," *International Journal of Heat and Mass Transfer*, Vol. 5, 1962, pp. 729–734.

22 Modest, M. F., "Radiative Equilibrium in a Rectangular Enclosure Bounded by Gray Walls," *Journal Quant, Spectrosc. Radiat. Transfer*, Vol. 15, 1975, pp. 445–461.

D. A. Nelson[1]

The Aerospace Corporation,
El Segundo, CA 90245

Band Radiation within Diffuse-Walled Enclosures

Part I: Exact Solutions for Simple Enclosures

Exact radiative transfer solutions for an isothermal medium confined within an isothermal enclosure are given for the planar, cylindrical and spherical configurations. The emphasis is upon band radiation and diffuse reflections. Specular reflections are also considered because solutions are easily obtained and are of interest for comparative purposes as well as intrinsic value.

Introduction

Many engineering applications of radiation heat transfer involve the assumption of an isothermal absorbing-emitting medium confined within a gray wall enclosure. Often it may be reasonable to assume the enclosure boundary is similarly isothermal. Examples might include a gas-turbine or rocket combustion chamber or perhaps a long, axially fired furnace.

If the medium is gray, the exact solution for such a simple problem can be expressed in terms of the isothermal exchange factor between the gas and the wall and may be found in Hottel and Sarofim [1]. Evaluation of the exchange factor, however, may present a considerable problem unless the medium is planar or spherical.

If the medium is nongray and characterized by band radiation, then exact solutions have been obtained only for some black wall enclosures [2] or the planar medium [3]. These, however, are merely formal, and no numerical examples have been given.

Although an enclosure of only two zones is simple, the solutions are not trivial, and much can be learned about the nature of nongray radiation from a gas that undergoes multiple reflections within the enclosure. This problem has been only briefly touched upon in the literature [1, p. 309; 3], and a complete quantitative account of the interesting phenomena encountered has been lacking.

In the present paper, then, an attempt is made to strengthen the qualitative expectations for multiply reflected band radiation through exact solutions for some simple two-zone enclosures. Aside from their intrinsic value, these will also provide standard solutions needed for later consideration of approximate methods for more complex enclosures.

Analysis

For the type of enclosure described above, the gray solution is well-known [1]. The spectral solution has an identical form and may be written

$$q_\nu = \epsilon Sg_\nu \frac{E_{\nu b}(T_g) - E_{\nu b}(T_w)}{1 - \rho S_\nu} \qquad (1)$$

The interpretation of this equation can be multifaceted. For the gray gas one simply suppresses the ν subscripts. If the walls are specular or diffuse, the distinction is contained in the exchange factors Sg_ν and S_ν. Only the elementary planar, cylindrical and spherical geometries will be considered here, for otherwise equation (1) would not be quite so simple.

Diffuse Reflections. The spectral exchange factors are given by [1, 4]

Slab:

$$Sg_\nu = 1 - 2E_3(\tau_{\nu h}) \qquad (2)$$

Sphere:

$$Sg_\nu = 1 - 2[1 - (1 + \tau_{\nu d})e^{-\tau_{\nu d}}]/\tau_{\nu d}^2 \qquad (3)$$

Cylinder:

$$Sg_\nu = \frac{4}{3}\tau_{\nu r}^2\{2[\tau_{\nu r}K_1(\tau_{\nu r})I_1(\tau_{\nu r}) + \tau_{\nu r}K_0(\tau_{\nu r})I_0(\tau_{\nu r}) - 1] + K_1(\tau_{\nu r})I_1(\tau_{\nu r})/\tau_{\nu r} + K_1(\tau_{\nu r})I_0(\tau_{\nu r}) - K_0(\tau_{\nu r})I_1(\tau_{\nu r})\} \qquad (4)$$

and since $S_\nu = 1 - Sg_\nu$, the gray solutions are immediately obtained by dropping the ν subscripts.

If band radiation is considered, then equation (1) must be integrated over wavenumber ν. It is assumed that the narrow-band approximation is valid so that

$$\int_0^\infty E_{\nu b} f(\nu) d\nu \approx \sum_{k=1}^{K} E_{kb} \int_{\Delta\nu_k} f(\nu) d\nu \qquad (5)$$

where K is the total number of absorption-emission bands and E_{kb} is the Planck function evaluated at the band wavenumber.

The spectral integration of equation (1) can only be effectively carried out by expanding $(1 - \rho S_\nu)^{-1}$ in its series representation. Following this procedure the flux for a single band can be written

$$q_k = \epsilon\omega_k Sg_k[E_{kb}(T_g) - E_{kb}(T_w)]M_k \qquad (6)$$

---

[1] Formerly at the Pennsylvania State University where the present work was largely carried out.

Contributed by the Heat Transfer Division for publication in the Journal of Heat Transfer. Manuscript received by the Heat Transfer Division August 11, 1977.

where

$$M_k = 1 + \sum_{n=1}^{\infty} \rho^n \prod_{m=1}^{n} S_k{}^{(m)} \tag{7}$$

is the multiple reflection coefficient, Sg_k is the band surface-gas exchange factor [2], and $S_k{}^{(m)}$ is the band transmissivity for radiation leaving the surface after having undergone m prior reflections. Unlike spectral or gray radiation, the band transmissivity depends upon the number of reflections as well as the geometry and optical parameters of the medium. The definition follows from the aforementioned spectral integration and is

$$S_k{}^{(m)} = \frac{1}{Sg_k \prod_{n=1}^{m-1} S_k{}^{(n)}} \int_{\Delta\nu_k} Sg_\nu [S_\nu]^m \frac{d\nu}{\omega_k} \tag{8}$$

If $m = 1$, the product factor in the denominator is unity.

For general band absorption characteristics, evaluation of equation (8) would be very difficult. However, the exponential band model for molecular gases [5] is widely accepted and for many situations allows the substitution $\tau_\nu = \tau_k \exp[-|\nu - \nu_k|/\omega_k]$ with $0 \leq |\nu - \nu_k| < \infty$. Using this relation and a transformation of variable, equation (8) can be expressed as

$$S_k{}^{(m)} = \frac{1}{Sg_k \prod_{n=1}^{m-1} S_k{}^{(n)}} \int_0^1 Sg_\nu(\tau_k\eta)[S_\nu(\tau_k\eta)]^m \frac{d\eta}{\eta} \tag{9}$$

Equation (9) can be evaluated in closed form for the planar medium only for $m = 1$ (Appendix). For the spherical geometry it may be evaluated for any m, but the labor is great even for $m = 2$ and becomes prohibitive for any larger value. It is not known if the integration can be carried out analytically for the cylinder, but it appears unlikely. Consequently, equation (9) is easiest to evaluate by numerical quadrature, while the closed form solutions may, where available, be used as a check. With care to allow for large τ_k and/or m, equation (9) can be quite satisfactorily evaluated by Gaussian quadrature with the integrand determined by any of equations (2–4).

Specular Reflections. When the reflections are specular, equation (1) is restricted not only to a specific wavenumber but to a specific direction as well. In that case, the gray solution is just as difficult as the nongray one, and it is convenient to treat them simultaneously.

As before, the denominator must be expanded in its series representation. The exchange factors are given now by

$$\pi Sg_\nu = 1 - e^{-\tau_{\nu t}};\ S_\nu = e^{-\tau_{\nu t}} \tag{10}$$

where $\tau_{\nu t}$ is the spectral optical depth for the line of sight path length, t, from one surface element to another. Using equation (10) and the series expansion, one finds that the n^{th} term is of the form

$$[e^{-n\tau_{\nu t}} - e^{-(n+1)\tau_{\nu t}}]/\pi \tag{11}$$

where $0 \leq n < \infty$.

Performing the spectral integration first, one makes use of the definition of dimensionless band absorption

$$A(\tau_{kt}) = \int_{\Delta\nu_k} (1 - e^{-\tau_{\nu t}}) \frac{d\nu}{\omega_k} \tag{12}$$

whereupon the n^{th} term may be expressed as

$$\omega_k\{A[(n+1)\tau_{kt}] - A[n\tau_{kt}]\}/\pi \tag{13}$$

The relation thus obtained is valid for any band absorption formulation. The gray and exponential bands are merely convenient special cases.

The flux dependence upon direction can be removed by integration over the entire hemispherical solid angle. The surface-gas direct exchange factor is defined by the integral

$$Sg_k = \frac{1}{\pi}\int_0^{2\pi}\int_0^1 A(\tau_{kt})\mu d\mu d\phi \tag{14}$$

The radiative flux for specularly reflecting surfaces can thus be expressed just as in equations (6) and (7) but the band transmissivities take on a different form given by

$$S_k{}^{(n)} = \frac{Sg[(n+1)\tau_k] - Sg[n\tau_k]}{Sg[n\tau_k] - Sg[(n-1)\tau_k]} \tag{15}$$

These transmissivities are rather more easily obtained than those for diffuse surfaces and have the advantage that arbitrary band absorption formulations may be easily employed, at least for the slab and the sphere. It is, therefore, of interest to compare specular and diffuse results. The length scale upon which τ_k is based depends upon the geometry and has, therefore, been suppressed in equation (15).

Results

Because solutions such as those presented herein can provide a standard of comparison for approximate procedures, rather extensive results have been obtained for both diffuse and specular enclosures for each of the elementary geometries. These are expressed in terms of the multiple reflection coefficient, given by equation (7), in Tables 1 and 2.

In Table 3 limited tabulations of band transmissivities are given. All results are based upon the overlapped-line, exponential band-model.

Discussion

Diffuse, multiple-reflection coefficients for planar, cylindrical and spherical geometries are presented in Table 1. The numerical values increase with increasing wall reflectivity simply because a greater fraction of the radiation survives a wall encounter. This increase tends to offset somewhat the decreased wall absorptivity and results in a slower rate of decrease of wall heat flux. For fixed reflectivity the results show a decreasing magnitude with increasing optical depth due to greater absorption within the gas. The minimum value of the multiple reflection coefficient is unity and occurs if $\rho \rightarrow 0$ for any τ. The maximum value is ϵ^{-1} which is approached as $\tau \rightarrow 0$ because the band transmissivities all approach unity. In the thin limit, then, the flux is independent of wall reflectivity for $\rho < 1$. In the optically thick limit $S_k{}^{(1)} \rightarrow 0$, although rather slowly, and the $S_k{}^{(N)}$ become constants (see Table 3). Thus, the multiple-reflection coefficients approach limits that depend upon ρ and are somewhat greater than unity.

Of particular interest is how the specular compare with the diffuse results. Direct comparison reveals that the largest differences occur at the smaller tabulated optical depths, at larger values of wall re-

Nomenclature

A = dimensionless band absorption
E = emissive power
E_n = exponential integral functions
I_n = modified Bessel functions, first kind
K_n = modified Bessel functions, second kind
M = multiple reflection coefficient
q = heat flux
S_ν = spectral transmission factor
$S_k{}^{(m)}$ = band transmission factor for m reflections
Sg = surface-gas exchange factor
ϵ = wall emissivity
ν = spectral wavenumber
ρ = wall reflectivity
τ = optical depth
ω_k = width parameter for band k

Subscripts

b = black body
d = diameter
g = gas
h = plate spacing for the slab geometry
k = band index, $1 \leq k \leq K$
r = radius
t = path length in given direction
w = wall
ν = spectral values

Table 1 Diffuse, multiple-reflection coefficients for an exponential band. P = planar, $\tau_h = \tau$; C = cylinder, $\tau_r = \tau$; S = sphere, $\tau_r = 3\tau/2$

τ	ρ = 0.2			0.5			0.8		
	P	C	S	P	C	S	P	C	S
0.1	1.224	1.223	1.222	1.846	1.838	1.837	3.804	3.760	3.751
0.2	1.204	1.201	1.200	1.743	1.728	1.724	3.247	3.178	3.162
0.5	1.164	1.158	1.156	1.561	1.536	1.529	2.507	2.424	2.402
1.	1.127	1.120	1.118	1.417	1.392	1.385	2.056	1.986	1.967
2.	1.093	1.088	1.087	1.300	1.282	1.278	1.740	1.693	1.682
5.	1.063	1.061	1.060	1.203	1.195	1.193	1.498	1.476	1.470
10.	1.050	1.049	1.049	1.162	1.157	1.155	1.396	1.382	1.378
20.	1.042	1.041	1.041	1.134	1.131	1.130	1.329	1.318	1.315
50.	1.034	1.033	1.033	1.110	1.107	1.106	1.268	1.261	1.259
100.	1.030	1.029	1.029	1.096	1.094	1.094	1.236	1.229	1.228
500.	1.023	1.023	1.023	1.075	1.073	1.073	1.184	1.179	1.178
1000.	1.021	1.021	1.021	1.068	1.067	1.067	1.168	1.164	1.163

Table 2 Specular, multiple-reflection coefficients for an exponential band. P = planar, $\tau_h = \tau$; C = cylinder, $\tau_r = \tau$; S = sphere, $\tau_r = 3\tau/2$.

τ	ρ = 0.2			0.5			0.8		
	P	C	S	P	C	S	P	C	S
0.1	1.211	1.217	1.219	1.790	1.814	1.821	3.580	3.649	3.673
0.2	1.190	1.194	1.196	1.686	1.698	1.703	3.068	3.078	3.084
0.5	1.151	1.150	1.149	1.517	1.508	1.505	2.399	2.354	2.343
1.	1.117	1.112	1.111	1.386	1.369	1.365	1.986	1.937	1.924
2.	1.086	1.082	1.081	1.279	1.265	1.262	1.693	1.659	1.651
5.	1.059	1.057	1.056	1.189	1.183	1.181	1.467	1.452	1.449
10.	1.047	1.045	1.045	1.150	1.147	1.146	1.371	1.362	1.360
20.	1.039	1.038	1.038	1.125	1.122	1.122	1.308	1.302	1.301
50.	1.032	1.031	1.031	1.102	1.100	1.100	1.251	1.247	1.247
100.	1.028	1.027	1.027	1.089	1.088	1.088	1.221	1.218	1.217
500.	1.022	1.021	1.021	1.070	1.069	1.069	1.172	1.170	1.170
1000.	1.020	1.020	1.019	1.064	1.063	1.063	1.157	1.156	1.155

Table 3 Band transmissivities for a diffuse-walled, cylindrical enclosure containing an isothermal medium with exponential bands

τ	$Sg_k S_k^{(1)}$	$S_k^{(2)}$	$S_k^{(5)}$	$S_k^{(10)}$	$S_k^{(20)}$	$S_k^{(30)}$	$S_k^{(35)}$
0.1	0.1710	0.9126	0.9211	0.9343	0.9549	0.9676	0.9719
0.2	0.2969	0.8452	0.8739	0.9119	0.9511	0.9671	0.9717
0.5	0.5176	0.7184	0.8235	0.9038	0.9509		
1.	0.6578	0.6291	0.8144	0.9037			
2.	0.7250	0.5821	0.8139				
5.	0.7462	0.5664					
10.	0.7491	0.5643					
20.	0.7498	0.5638					
∞	0.7500	0.5637	0.8139	0.9037	0.9509	0.9671	0.9717
∞ (specular)	0.6931	0.5850	0.8171	0.9046	0.9512	0.9672	0.9718

flectivity and for the planar medium. It is easy to verify that the results must be the same as $\tau \rightarrow 0$ and $\tau \rightarrow \infty$. The maximum absolute differences in the tabulated values occur for $\rho = 0.8$ and have the values 5.9, 3.1 and 2.5 percent for planar, cylindrical and spherical enclosures, respectively. At a reflectivity of 0.5 the maximum absolute differences reduce to 3.3, 1.8 and 1.6 percent. These are clearly of little consequence; thus, one could use to good approximation the more easily obtained specular solutions for these simple enclosures with diffuse walls. Edwards [3] made a similar but more restrictive observation some years ago.

Because of the simple structure of the specular solutions they have the advantage of being easily employed for planar or spherical enclosures using arbitrary band absorption formulations [2]; thus, one could investigate effects of different correlations as well as band line structure, both of which would cause considerable difficulty in a diffuse formulation. For a cylindrical enclosure a closed form solution for the surface-gas exchange factor is not known. However, it can be quite accurately approximated by that for the sphere by using a modified argument, as suggested by comparison of results in Tables 1 and 2.

Further insight into the problem of multiply reflected band radiation can be obtained through study of the band transmissivities given in Table 3. These are for the cylinder, but many asymptotic limits and general behavior are the same for the other geometries.

The band transmissivity for once reflected radiation is presented in a somewhat different fashion than those for higher reflections because it behaves differently. It, unlike the others, is a continuously decreasing function of optical depth but in product with Sg_k forms an increasing function with an asymptotic upper limit. For the slab and sphere this limit can be obtained from the results given in the Appendix; for the cylinder it is verified numerically. Two characteristics are immediately noticed; $S_k^{(N)}$ increases monotonically with N and decreases with τ to a lower limit for $N \geq 2$.

The decrease with increasing optical depth is intuitively expected. The asymptotic lower limit is a consequence of the form of the exponential band absorption equation for $\tau \rightarrow \infty$. The form involved herein is logarithmic, but similar behavior would occur for any power function due to a factoring property that eliminates a dependence on optical depth. This should be contrasted with results for a gray band where $S_k^{(N)} = 1 - Sg_k$, which decreases continuously with optical depth.

One should note as well that for a gray band the transmissivity is independent of the number of reflections, since the form of the spectral transmissivity applies to the band as a whole. In the case of nongray radiation the spectral distribution of reflected energy depends upon the number of reflections and, therefore, so too does the band transmissivity. Moreover, for bands with asymptotic wings, the transmissivity increases steadily with N because the significant remaining radiation is at spectral locations of weakening absorption. Asymptotically one must have $S_k^{(\infty)} \rightarrow 1$. Although results for $\tau < 0.1$ are not given here, calculations were carried out for τ as small as 10^{-4}. The results are consistent with all comments made herein and show further that as $\tau \rightarrow 0$ the band transmissivities become independent of N; a result to be expected on theoretical grounds.

Table 3 contains results applicable to specular reflections at large optical depth. These should be compared with the corresponding results for diffuse reflections. This shows that the maximum difference is in $S_k^{(1)}$ and is about 7.6 percent. Differences for larger values of N decrease rapidly and are uniformly smaller for smaller values of optical depth. Since it has already been shown that specular and diffuse predictions differ from one another in an amount that is less than the difference in $S_k^{(1)}$, an approximate procedure is suggested. In particular, the Appendix shows that $S_k^{(1)}$ can be exactly evaluated for an exponential band in the planar and spherical geometries, thus one could employ these results along with specular relations for $N > 1$ with clear expectation for errors significantly smaller than the difference between specular and diffuse solutions. This approximation would require no numerical integrations.

Concluding Remarks

For the simple two-zone enclosures considered herein, the method of series expansion of the spectral solutions followed by integration to allow for nongray absorption and emission is rather easily carried out. Although it is generally agreed that this is is a correct approach, it is not a sound one for real absorbing-emitting media confined within an enclosure of arbitrary geometry and consisting of the large number of surface and volume zones required for nonisothermal environments.

Part II of this paper considers the same problem treated herein from a rather different point of view, one which develops enclosure relations for band radiation and which has the potential for analysis of arbitrary enclosures using band absorption models, without the need for spectral solutions. The exact solutions provided here will be especially useful for evaluation of that approach and for comparative needs of further investigations.

References

1 Hottel, H. C. and Sarofim, A. F., *Radiative Transfer*, McGraw-Hill, New York, 1967.

2 Nelson, D. A., "Generalized Direct Exchange Factors for Isothermal Molecular Gases," *International Journal of Heat and Mass Transfer*, Vol. 20, 1977, p. 437.

3 Edwards, D. K., "Radiation Interchange in a Nongray Enclosure Containing an Isothermal Carbon-Dioxide-Nitrogen Gas Mixture," ASME JOURNAL OF HEAT TRANSFER, Vol. 84, 1962, p. 1.

4 Heaslet, M. A. and Warming, R. F., "Theoretical Predictions of Radiative Transfer in a Homogeneous Cylindrical Medium," *Journal Quant. Spectrosc. Radiat. Transfer,* Vol. 6, 1966, p. 751.

5 Edwards, D. K. and Menard, W. A., "Comparison of Models for Correlation of Total Band Absorption," *Applied Optics,* Vol. 3, 1964, p. 621.

APPENDIX

For $m = 1$ it is possible to evaluate equation (9) in closed form for both the planar and spherical geometries.

Using equation (2) with the argument indicated in equation (9), i.e., $\tau_k \eta$ replacing $\tau_{\nu h}$, one obtains for the planar medium

$$Sg_k S_k^{(1)} = 1 - e^{-\tau_k} E_2(\tau_k) - [1 - e^{-\tau_k}] E_1(\tau_k) - [1/2 - E_3(\tau_k)]^2 \tag{16}$$

where τ_k is based upon plate spacing, h.

Similarly, using equation (3) in equation (9) one finds for the sphere

$$\begin{aligned} Sg_k S_k^{(1)} = 3/4 - 1/\tau_k^2 + 1/\tau_k^4 + 2E_2(\tau_k)/\tau_k \\ + [4E_3(2\tau_k) + 2E_3(\tau_k)]/\tau_k^2 \\ + 8[E_4(2\tau_k) - E_4(\tau_k)]/\tau_k^3 + 4[E_5(2\tau_k) - 2E_5(\tau_k)]/\tau_k^4 \end{aligned} \tag{17}$$

where τ_k is based upon diameter, d.

These relations have optically thin limits of $2\tau_k$ and $2\tau_k/3$, respectively. In the optically thick limit each has the asymptotic value of 3/4. The latter has also been verified numerically to apply for the cylindrical geometry that has an optically thin limit of $2\tau_r$.

D. A. Nelson[1]

The Aerospace Corporation,
El Segundo, CA 90245

Band Radiation within Diffuse-Walled Enclosures

Part II: An Approximate Method Applied to Simple Enclosures

An asymptotically exact approximate method of analysis for band radiation has been applied to some simple enclosures. The principal feature of the method is direct utilization of band absorption formulations for absorbing-emitting media. The procedure is shown to be capable of arbitrarily high accuracy and to have very acceptable errors for low order approximations.

Introduction

The analysis of radiative transfer within enclosures containing an absorbing-emitting medium may assume any one of several different formulations.

The most common assumptions involve simple geometries and/or gray interactions over a part or the whole of the black-body spectrum. Typically, it has been found necessary to compromise one or more aspects of the analysis in order to fully accommodate others that are largely determined by needs or point of view.

One finds, for example, that studies which illuminate the essential physical features are confined almost wholly to the planar geometry. Those, however, which represent analysis of realistic engineering geometries often, if not always, employ physical models that obscure the fundamental interactions of radiation with the principal medium and its surroundings.

Few attempts have been made to formulate a general method that is capable of application to either type of problem. Yet, such a method would clearly unify the practical and theoretical methods of radiative transfer analysis and perhaps provide the greater insight essential to intuitive evaluation of problems whose full solution may be impractical.

Nongray radiative transfer within diffusely reflecting enclosures is, however, an uncommonly complex process and presents problems which must be carefully resolved. Consequently, the present paper is limited to rather simple systems in order to develop with some clarity the essential elements and the methods of resolving at least some obvious difficulties.

Of particular importance to the present investigation is the work of Hottel and Cohen [1], which provides the fundamental zonal formulation interpreted on a spectral basis, and that of Edwards [2] and Bevans and Dunkle [3], which provide the inspiration for development of band radiation analysis.

Analysis

Spectral Transfer Relations. For convenience and ease of presentation, the zone method developed by Hottel and Cohen [1] provides the necessary spectral relations. These are available elsewhere but are not expressed in the form desired here. The spectral radiative energy balance on a finite volume of isothermal medium gives, for the volumetric cooling rate,

$$V_iQ_{\nu i}{}^{*r} = 4\pi\rho_a\kappa_\nu V_iI_{\nu b}(T_i) - \sum_{j=1}^{N}(g_is_j)_\nu R_{\nu j} - \sum_{j=1}^{M}(g_ig_j)_\nu \pi I_{\nu b}(T_j)$$

$$= \sum_{j=1}^{N}(g_is_j)_\nu[\pi I_{\nu b}(T_i) - R_{\nu j}] + \sum_{j=1}^{M}(g_ig_j)_\nu \pi[I_{\nu b}(T_i) - I_{\nu b}(T_j)] \quad (1)$$

At a finite surface, similar considerations yield the spectral radiosity as

$$R_{\nu i} = \epsilon_i\pi I_{\nu b}(T_i) + \frac{\rho_i}{A_i}\left[\sum_{j=1}^{N}(s_is_j)_\nu R_{\nu j} + \sum_{j=1}^{M}(s_ig_j)_\nu \pi I_{\nu b}(T_j)\right] \quad (2)$$

where there are M gas zones and N surface zones.

The exchange-areas appearing above are most conveniently expressed in terms of the spectral absorptivity, $A_\nu(x) = 1 - \exp(-\rho_a\kappa_\nu x)$, as

$$(g_ig_j)_\nu = -\int_{V_i}\int_{V_j}\frac{d^2A_\nu(r_{ij})}{dr_{ij}^2}\frac{dV_jdV_i}{\pi r_{ij}^2} \quad (3)$$

---

[1] Formerly at the Pennsylvania State University where the present work was largely carried out.

Contributed by the Heat Transfer Division for publication in the JOURNAL OF HEAT TRANSFER. Manuscript received by the Heat Transfer Division August 11, 1977.

$$(g_is_j)_\nu = \int_{\tilde A_j}\int_{V_i} \frac{dA_\nu(r_{ij})}{dr_{ij}} \frac{\cos\theta_j dV_i d\tilde A_j}{\pi r_{ij}{}^2} \tag{4}$$

$$(s_is_j)_\nu = \tilde A_i F_{ij} - \int_{\tilde A_i}\int_{\tilde A_j} A_\nu(r_{ij}) \frac{\cos\theta_i \cos\theta_j d\tilde A_j d\tilde A_i}{\pi r_{ij}{}^2}$$

$$= \tilde A_i F_{ij} - (s_is_j)_\nu{}^* \tag{5}$$

Certain relations among exchange-areas are useful in algebraic manipulations and are

$$4\rho_a\kappa_\nu V_i = \sum_{j=1}^{M} (g_ig_j)_\nu + \sum_{j=1}^{N} (g_is_j)_\nu \tag{6}$$

$$\tilde A_i = \sum_{j=1}^{M} (g_js_i)_\nu + \sum_{j=1}^{N} (s_js_i)_\nu \tag{7}$$

In all the foregoing relations it has been assumed that the physical properties are constant. For analytical purposes this assumption is nearly always essential and only rarely serious. The spectral relations are fundamental but practically unusable because thousands of spectral calculations would normally be required for even adequate resolution of very simple nongray problems.

To overcome this difficulty, band models have been developed on both a quasi-spectral and total band foundation [4–8]. With few exceptions, however, it has not yet been clear just how these models can be used effectively for analysis of radiative transfer problems within diffuse walled enclosures. If the walls are black there is no difficulty, but if they are gray, the options are small in number and require special compromises. The Hottel [1, 9] method of using a "weighted sum of gray gases" is one such example and either does not use band models at all or only indirectly. Bevans, Dunkle and Edwards' [2, 3] method employs band models but is restricted in generality and uses gray band concepts requiring special care and interpretation for adaptation to real gases.

Thus, it appears that one should pursue other lines of reasoning with a particular view toward making a minimum of special assumptions.

Integrated Transfer Relations. It appears, at the present time, that the least restrictive method of nongray analysis is the narrow band approximation defined by assuming

$$\int_0^\infty I_{\nu b} f(\nu)d\nu \approx \sum_{k=1}^{K} I_{kb} \int_{\Delta\nu_k} f(\nu)d\nu \tag{8}$$

In this relation, $f(\nu)$ is generally a function of the spectral absorption or its derivatives, I_{kb} is the Planck intensity evaluated at the wavenumber of band k, K is the total number of absorption-emission bands, and $\Delta\nu_k$ implies an integral over a single band. Depending upon band model, the extent of $\Delta\nu_k$ may be either finite or infinite.

The narrow band assumption leads quite naturally to a formulation in terms of band absorption models [2–8]. In such a formulation two physical parameters play an essential role. These are the integrated band intensity defined by

$$\alpha_k = \int_{\Delta\nu_k} \kappa_\nu d\nu \tag{9}$$

and a band width parameter ω_k which can be interpreted in various ways but usually is an empirical coefficient [7]. With these the dimensionless total band absorption is defined by

$$A(\rho_k\alpha_k x/\omega_k) = \int_{\Delta\nu_k} A_\nu(x)d(\nu/\omega_k) \tag{10}$$

The spectrally integrated relation for the volumetric cooling rate obtained from equation (1) may now be expressed as

$$Q_i{}^{*r} = \sum_{k=1}^{K} 4\rho_k\alpha_k \left[E_{kb}(T_i) - \sum_{j=1}^{N} Gs_{kij}\tilde R_{kj}{}^{(i)} - \sum_{j=1}^{M} G_{kij}E_{kb}(T_j)\right]$$

$$= \sum_{k=1}^{K} 4\rho_k\alpha_k \left\{\sum_{j=1}^{M} G_{kij}[E_{kb}(T_i) - E_{kb}(T_j)]\right.$$

$$\left. + \sum_{j=1}^{N} Gs_{kij}[E_{kb}(T_i) - \tilde R_{kj}{}^{(i)}]\right\} \tag{11}$$

where the exchange factors are given by

$$G_{kij} = -\frac{\tau_{kij}}{4\xi_i}\int_{\xi_i}\int_{\xi_j} A''(\tau_{kij}x_{ij}) \frac{d\xi_j d\xi_i}{\pi x_{ij}{}^2} \tag{12}$$

$$Gs_{kij} = \frac{1}{4\xi_i}\int_{\sigma_j}\int_{\xi_i} A'(\tau_{kij}x_{ij}) \frac{\cos\theta_j d\xi_i d\sigma_j}{\pi x_{ij}{}^2} \tag{13}$$

where $\tau_{kij} = \rho_k\alpha_k z_{ij}/\omega_k$ is the interzone optical depth, z_{ij} is any convenient normalizing length but typically the centroid-to-centroid distance, $\xi = V/z^3$, $x = r/z$, $\sigma = \tilde A/z^2$, $A'(x) = dA(x)/dx$ and $A''(x) = d^2A(x)/dx^2$.

The band radiosity function $\tilde R_{kj}{}^{(i)}$ is defined by the relation

$$4\rho_k\alpha_k V_i Gs_{kij}\tilde R_{kj}{}^{(i)} = \int_{\Delta\nu_k} (g_is_j)_\nu R_{\nu j} d\nu \tag{14}$$

One should particularly note that the (i) superscript is essential for nongray bands and that a relation similar to equation (8) is inappropriate for approximate evaluation of the integral in equation (14), the reason being that $R_{\nu j}$ may vary rapidly over the sensible width of a band. This has been discussed by Edwards [2] and Hottel and Sarofim [9], and it is the central difficulty arising in nongray analysis of diffusely reflecting enclosures. Nevertheless, it was just such an approximation that was suggested by Bevans and Dunkle [3] at the expense of introducing a somewhat ambiguous effective-band-width. The ambiguity was partially resolved by Edwards [2, 7] through simple example and deductive generalization. A rather more general approach will be followed later in this paper.

The spectrally integrated relation obtained from equation (2) gives

Nomenclature

$A(x)$ = dimensionless band absorption
$A'(x) = dA(x)/dx$
$A''(x) = d^2A(x)/dx^2$
$\tilde A$ = area
E = emissive power
F = shape factor
G = gas-gas direct exchange factor
Gs = gas-surface direct exchange factor
(gg) = gas-gas direct exchange area
(gs) = gas-surface direct exchange area
H = surface irradiation
I = radiant intensity
$M^{(n)}$ = nth order multiple reflection coefficient
Q^{*r} = volumetric radiative cooling rate
q = heat flux
R = total surface radiosity
R_k = band radiosity, equation (18)
$\tilde R_k$ = band radiosity, equation (14)
r = distance between two points
Sa = surface direct exchange band absorption factor
Sg = surface-gas direct exchange factor
$\tilde S_k$ = band transmissivity for radiosity, $\tilde R_k$
(ss) = surface-surface direct transmission area
$(ss)^*$ = surface-surface direct absorption area
T = temperature
V = volume
x = dimensionless distance
z = normalizing length
α = integrated band intensity
ϵ = surface emissivity
θ = polar angle from surface normal
κ = mass absorption coefficient
ν = spectral wavenumber
ξ = dimensionless volume
ρ = surface reflectivity
ρ_a = absorbing gas density
ρ_k = absorbing gas density for band k
σ = dimensionless area
τ = optical depth
ω = band width parameter

Subscripts

b = blackbody
g = gas
i = zone index
j = zone index
k = band index
w = wall
ν = spectral value

the total surface radiosity as

$$R_i = \epsilon_i E_b(T_i) + \rho_i \sum_{j=1}^{N} \left[F_{ij}R_j - \sum_{k=1}^{K} \omega_k Sa_{kij} R_{kj}{}^{(i)} \right] + \rho_i \sum_{k=1}^{K} \sum_{j=1}^{M} \omega_k Sg_{kij} E_{kb}(T_j) \quad (15)$$

where

$$Sa_{kij} = \frac{1}{\sigma_i} \int_{\sigma_j} \int_{\sigma_i} A(\tau_{kij} x_{ij}) \frac{\cos\theta_i \cos\theta_j d\sigma_i d\sigma_j}{\pi x_{ij}{}^2} \quad (16)$$

$$Sg_{kij} = \frac{\tau_{kij}}{\sigma_i} \int_{\sigma_i} \int_{\xi_j} A'(\tau_{kij} x_{ij}) \frac{\cos\theta_i d\xi_j d\sigma_i}{\pi x_{ij}{}^2} \quad (17)$$

and by definition

$$\omega_k \tilde{A}_i Sa_{kij} R_{kj}{}^{(i)} = \int_{\Delta\nu_k} (s_i s_j)_\nu{}^* R_{\nu j} d\nu \quad (18)$$

The second term in brackets on the right-hand side of equation (15) accounts for band absorption of radiation traversing the enclosure between surfaces i and j, while the last accounts for direct surface irradiation due to gas emission. The other terms, aside from notational differences, are familiar ones for enclosures containing a nonabsorbing medium [10, 11].

There are some useful relations among the exchange factors, these being

$$\sum_{j=1}^{N} Gs_{kij} + \sum_{j=1}^{M} G_{kij} = 1 \quad (19)$$

$$\sum_{j=1}^{N} Sa_{kij} = \sum_{j=1}^{M} Sg_{kij} \quad (20)$$

and

$$\sigma_i Sg_{kij} = 4\tau_{kij} \xi_j Gs_{kji} \quad (21)$$

Once a solution of equation (15) has been obtained, the surface radiative flux can be found from

$$q_i = \frac{\epsilon_i}{\rho_i} [E_b(T_i) - R_i] \quad (22a)$$

or

$$q_i = \epsilon_i [E_b(T_i) - H_i] = R_i - H_i \quad (22b)$$

the latter generally being needed only when $\epsilon_i = 1$. H_i is the irradiation [10] and is given by the last three terms of equation (15) exclusive of ρ_i.

Obtaining solutions of either equations (11) or (15), however, requires relations for $\tilde{R}_{kj}{}^{(i)}$ and/or $R_{kj}{}^{(i)}$, a matter considered in the following section.

Band Radiosity Relations for a Simple Enclosure. The foregoing relations were obtained by a reasonably straightforward integration of the well-known spectral zone equations. The exchange factors which have arisen as a direct consequence of that integration are all familiar concepts involving, among them, direct interaction between two gas zones as expressed through G_{kij}, between a gas and a surface zone as expressed through Gs_{kij} or Sg_{kij}, and between a pair of surfaces and the intervening gas through the absorption factor Sa_{kij}.

The only novel feature found in either of the equations (11) or (15) is the express recognition that a band radiosity for nongray radiation cannot be related solely to the surface of its origin. It depends as well upon the destination, as expressed by the superscript (i), and upon the type of interaction in question, as expressed by the two distinct band radiosity functions $R_{kj}{}^{(i)}$ and $\tilde{R}_{kj}{}^{(i)}$. These factors lend a degree of complexity to a general formulation that might tend to impede rather than promote an appreciation of the basically simple concepts involved in the formulation of relations for the band radiosities. Moreover, the effectiveness of any formulation can only be established by comparison with exact solutions, and the latter are available only for fairly simple configurations [12].

This paper will, therefore, be restricted to rather detailed examination of simple enclosures. This will illustrate the fundamental concepts as well as the limitations and power of the approximate method.

The Two-Zone Enclosure. The simplest conceivable enclosure consists of a single isothermal gas zone surrounded completely by an isothermal surface zone.

For such a simple enclosure the foregoing relations may be used to show that equations (11) and (15) lead to identical results for q_i and that $R_{kj}{}^{(i)}$ and $\tilde{R}_{kj}{}^{(i)}$ are equivalent to one another.

The result for the flux into the surface may be obtained from equation (11) through use of equation (21)

$$q_{gi} = \sum_{k=1}^{K} \omega_k Sg_{kig} [E_{kb}(T_g) - \tilde{R}_{ki}{}^{(g)}] \quad (23)$$

where the subscripting has been retained not because it is needed but rather to illustrate the type of careful accounting required in more complex problems. Equivalent results for this problem can also be obtained through use of $Sg_{kig} = Sa_{kii}$ and/or $\tilde{R}_{ki}{}^{(g)} = R_{ki}{}^{(i)}$.

Through use of equation (21) the definition of $\tilde{R}_{ki}{}^{(g)}$ can be expressed from equation (14) as

$$Sg_{kig} \tilde{R}_{ki}{}^{(g)} = \int_{\Delta\nu_k} \frac{(gs_i)_\nu}{\tilde{A}_i} R_{\nu i} \frac{d\nu}{\omega_k} \quad (24)$$

Further, from equation (2) the spectral radiosity can be written

$$R_{\nu i} = \epsilon_i E_{\nu b}(T_i) + \frac{\rho_i}{\tilde{A}_i} [(s_i s_i)_\nu R_{\nu i} + (s_i g)_\nu E_{\nu b}(T_g)] \quad (25)$$

and through use of equation (7) can be simplified to

$$R_{\nu i} - E_{\nu b}(T_g) = \epsilon_i [E_{\nu b}(T_i) - E_{\nu b}(T_g)] + \frac{\rho_i}{\tilde{A}_i} (s_i s_i)_\nu [R_{\nu i} - E_{\nu b}(T_g)] \quad (26)$$

Now equation (24) clearly suggests how $\tilde{R}_{ki}{}^{(g)}$ can be obtained. Thus, one multiplies equation (26) by $(s_i g)_\nu d\nu/\tilde{A}_i \omega_k$ and integrates to obtain

$$\tilde{R}_{ki}{}^{(g)} - E_{kb}(T_g) = \epsilon_i [E_{kb}(T_i) - E_{kb}(T_g)] + \rho_i \tilde{S}_{kii}{}^{(g)} [\tilde{R}_{ki}{}^{(ig)} - E_{kb}(T_g)] \quad (27)$$

where

$$\tilde{S}_{kii}{}^{(g)} = \frac{1}{Sg_{kig}} \int_{\Delta\nu_k} \frac{(s_i g)_\nu}{\tilde{A}_i} \frac{(s_i s_i)_\nu}{\tilde{A}_i} \frac{d\nu}{\omega_k} \quad (28)$$

$$Sg_{kig} \tilde{S}_{kii}{}^{(g)} \tilde{R}_{ki}{}^{(ig)} = \int_{\Delta\nu_k} \frac{(s_i g)_\nu}{\tilde{A}_i} \frac{(s_i s_i)_\nu}{\tilde{A}_i} R_{\nu i} \frac{d\nu}{\omega_k} \quad (29)$$

The general pattern of the method is already clearly established. One may now easily obtain an equation for $\tilde{R}_{ki}{}^{(ig)}$ through multiplication of equation (26) by $(s_i g)_\nu (s_i s_i)_\nu d\nu/\tilde{A}_{(i)}{}^2 \omega_k$ and integration over $\Delta\nu_k$. For illustrative purposes the results are

$$\tilde{R}_{ki}{}^{(ig)} - E_{kb}(T_g) = \epsilon_i [E_{kb}(T_i) - E_{kb}(T_g)] + \rho_i \tilde{S}_{kii}{}^{(ig)} [\tilde{R}_{ki}{}^{(iig)} - E_{kb}(T_g)] \quad (30)$$

$$\tilde{S}_{kii}{}^{(ig)} = \frac{1}{Sg_{kig} \tilde{S}_{kii}{}^{(g)}} \int_{\Delta\nu_k} \frac{(s_i g)_\nu}{\tilde{A}_i} \left[\frac{(s_i s_i)_\nu}{\tilde{A}_i} \right]^2 \frac{d\nu}{\omega_k} \quad (31)$$

with an obvious definition of $\tilde{R}_{ki}{}^{(iig)}$.

Since, in general, each higher order equation generates another unknown band radiosity function, it might appear that little progress has been made. However, each higher order equation must be back substituted into the next lower order. When carried to completion this yields an infinite series solution for $\tilde{R}_{ki}{}^{(g)}$ that will converge for $\rho_i < 1$. The higher the order of $\tilde{R}_{ki}{}^{(i \cdots ig)}$, the less it contributes to the final result.

It is not difficult to show that the series solution so obtained yields a result for the flux that is identical to that obtained by following what is commonly believed to be the correct basic procedure for nongray analysis [7, 13]. That is, to solve equation (26) for the spectral radiosity, substitute the result into the relation for the spectral flux and subsequently perform the integration over wavenumber. The latter procedure, although easily carried out here [12], becomes impossibly cumbersome for more complex problems to the point of being essentially useless for either practical or theoretical purposes.

The series yielded by the present approach has far greater theoretical utility in more complex situations but is impractical for typical engineering problems. A more useful approximate procedure may be found by viewing relations such as equations (27) and/or (30) as a closure problem.

A Closure Approximation. The difficulty of equations (27) and/or (30), or any other higher order equation, is simply that there is no apparent relation between the band radiosity functions that appear on opposite sides of the equation. Thus, some approximation is clearly required.

It appears that the only obvious approximation, short of completely ignoring the higher order radiosity function, is to assume that one may put

$$\tilde{R}_{ki}{}^{(ii\ldots g)} \approx \tilde{R}_{ki}{}^{(i\ldots g)} \tag{32}$$

where the $(i\ldots g)$ indicates an arbitrary number of i indices between i and g. For a first order approximation one would thus employ equation (27) with $\tilde{R}_{ki}{}^{(ig)} \approx \tilde{R}_{ki}{}^{(g)}$, and to second order one would use $\tilde{R}_{ki}{}^{(iig)} \approx \tilde{R}_{ki}{}^{(ig)}$ in equation (30). When the shorthand superscript notation $(i\ldots ig) \rightarrow (N)$ is introduced wherein N represents the number of superscripts, the N^{th} order band radiosity approximation is written

$$\tilde{R}_k{}^{(N)} - E_{kb}(T_g) = \epsilon[E_{kb}(T_w) - E_{kb}(T_g)] + \rho\tilde{S}_k{}^{(N)}[\tilde{R}_k{}^{(N)} - E_{kb}(T_g)] \tag{33a}$$

with

$$\tilde{R}_k{}^{(N-1)} - E_{kb}(T_g) = \epsilon[E_{kb}(T_w) - E_{kb}(T_g)] + \rho\tilde{S}_k{}^{(N-1)}[\tilde{R}_k{}^{(N)} - E_{kb}(T_g)] \tag{33b}$$

for each lower order equation and where the redundant i subscripts have been dropped and T_w is the wall temperature. The solution of equation (33) is easy and thus

$$\tilde{R}_k{}^{(N)} - E_{kb}(T_g) = \frac{\epsilon[E_{kb}(T_w) - E_{kb}(T_g)]}{1 - \rho\tilde{S}_k{}^{(N)}} \tag{34}$$

If this is substituted into equation (33b), one finds

$$\tilde{R}_k{}^{(N-1)} - E_{kb}(T_g) = \epsilon[E_{kb}(T_w) - E_{kb}(T_g)]\left[1 + \rho\frac{\tilde{S}_k{}^{(N-1)}}{1 - \rho\tilde{S}_k{}^{(N)}}\right] \tag{35}$$

Similarly

$$\tilde{R}_k{}^{(N-2)} - E_{kb}(T_g) = \epsilon[E_{kb}(T_w) - E_{kb}(T_g)] \times\left[1 + \rho\tilde{S}_k{}^{(N-2)}\left\{1 + \rho\frac{\tilde{S}_k{}^{(N-1)}}{1 - \rho S_k{}^{(N)}}\right\}\right] \tag{36}$$

the form of which is exact as $N \rightarrow \infty$ [12].

The flux can be obtained from equation (23) and in the approximate form may be conveniently written

$$q = \epsilon \sum_{k=1}^{K} \omega_k Sg_k[E_{kb}(T_g) - E_{kb}(T_w)]M_k{}^{(N)} \tag{37}$$

where $M_k{}^{(N)}$ is the N^{th} order multiple reflection coefficient, which may be given by the inverse denominator of equation (34) or the last bracketed terms of equations (35) or (36). The solution is exact when $M_k{}^{(N)} = M_k{}^{(\infty)}$; this is thought to be an important consequence of the closure procedure.

Discussion

The method of analysis developed from the assumption of a closure condition has interesting theoretical properties, but perhaps of equal or greater importance is the evaluation of the effectiveness of low order approximations. If such approximations were to be acceptably accurate, theoretical studies would be relieved of unwarranted complexity and practical applications would be relieved of unnecessary inaccuracy.

In physical problems in which the basic transfer relations are well understood and widely accepted, the logical comparison is that between exact and approximate analytical solutions. In general, it is reasonable to obtain exact solutions only for the elementary planar, cylindrical, or spherical geometry. However, physical considerations lead one to suspect that of the many conceivable geometries, radiative transfer effects ought to be bounded in extremes by those of the slab and the sphere.

The exact solutions for the three elementary geometries have been considered in a companion paper [12]. The error in $M_k{}^{(N)}$ for first, second, and third order approximations is given in Tables 1 through 3 for the slab, cylinder and sphere, respectively. The magnitudes are

Table 1 The percent error in closure approximations from first to third order for the planar medium with an exponential band—$\tau_h = \tau$

	$\rho = 0.2$		0.5			0.8		
τ	ϵ_1	ϵ_2	ϵ_1	ϵ_2	ϵ_3	ϵ_1	ϵ_2	ϵ_3
0.1	-0.01	-0.00	-0.20	-0.09	-0.04	- 2.12	-1.57	-1.16
0.2	-0.04	-0.01	-0.55	-0.24	-0.10	- 4.72	-3.32	-2.33
0.5	-0.14	-0.02	-1.57	-0.57	-0.21	- 9.67	-6.07	-3.78
1.	-0.26	-0.03	-2.59	-0.77	-0.23	-13.0	-7.17	-3.94
2.	-0.36	-0.03	-3.32	-0.77	-0.19	-14.6	-6.88	-3.36
5.	-0.40	-0.02	-3.42	-0.60	-0.14	-14.1	-5.57	-2.62
10.	-0.37	-0.02	-3.17	-0.49	-0.11	-12.9	-4.75	-2.23
20.	-0.34	-0.02	-2.89	-0.42	-0.10	-11.7	-4.14	-1.95
50.	-0.30	-0.01	-2.54	-0.35	-0.08	-10.4	-3.54	-1.66
100.	-0.28	-0.01	-2.33	-0.31	-0.07	- 9.51	-3.19	-1.50
1000.	-0.21	-0.01	-1.79	-0.23	-0.05	- 7.40	-2.41	-1.13

Table 2 The percent error in closure approximations from first to third order for the cylindrical medium with an exponential band—$\tau_r = \tau$

	$\rho = 0.2$		0.5			0.8		
τ	ϵ_1	ϵ_2	ϵ_1	ϵ_2	ϵ_3	ϵ_1	ϵ_2	ϵ_3
0.1	-0.02	-0.00	-0.22	-0.10	-0.05	- 2.31	-1.71	-1.26
0.2	-0.05	-0.01	-0.63	-0.26	-0.11	- 5.18	-3.61	-2.51
0.5	-0.16	-0.02	-1.76	-0.62	-0.22	-10.4	-6.40	-3.91
1.	-0.28	-0.03	-2.77	-0.79	-0.23	-13.5	-7.26	-3.89
2.	-0.37	-0.03	-3.33	-0.76	-0.18	-14.5	-6.77	-3.27
5.	-0.38	-0.02	-3.30	-0.60	-0.13	-13.6	-5.54	-2.56
10.	-0.36	-0.02	-3.04	-0.50	-0.11	-12.5	-4.77	-2.19
20.	-0.33	-0.02	-2.77	-0.43	-0.09	-11.3	-4.17	-1.91
50.	-0.29	-0.01	-2.45	-0.36	-0.08	-10.0	-3.57	-1.64
100.	-0.27	-0.01	-2.24	-0.32	-0.07	- 9.20	-3.22	-1.48
1000.	-0.21	-0.01	-1.73	-0.23	-0.05	- 7.17	-2.43	-1.11

Table 3 The percent error in closure approximations from first to third order for the spherical medium with an exponential band—$\tau_r = 3\tau/2$

	$\rho = 0.2$		0.5			0.8		
τ	ϵ_1	ϵ_2	ϵ_1	ϵ_2	ϵ_3	ϵ_1	ϵ_2	ϵ_3
0.1	-0.02	-0.00	-0.23	-0.10	-0.05	- 2.35	-1.74	-1.28
0.2	-0.05	-0.01	-0.64	-0.27	-0.11	- 5.30	-3.68	-2.55
0.5	-0.17	-0.02	-1.81	-0.63	-0.22	-10.6	-6.49	-3.94
1.	-0.29	-0.03	-2.81	-0.80	-0.23	-13.6	-7.28	-3.88
2.	-0.37	-0.03	-3.33	-0.76	-0.18	-14.5	-6.75	-3.25
5.	-0.38	-0.02	-3.26	-0.60	-0.13	-13.5	-5.54	-2.55
10.	-0.35	-0.02	-3.00	-0.50	-0.11	-12.3	-4.77	-2.18
20.	-0.32	-0.02	-2.74	-0.43	-0.09	-11.2	-4.18	-1.90
50.	-0.29	-0.01	-2.42	-0.36	-0.08	- 9.93	-3.58	-1.63
100.	-0.26	-0.01	-2.21	-0.32	-0.07	- 9.11	-3.23	-1.47
1000.	-0.20	-0.01	-1.71	-0.24	-0.05	- 7.10	-2.44	-1.11

virtually identical for each of the geometries, which indicates that the method is not geometrically sensitive. The error in the first order approximation may at times be only tolerable for reflectivity as large as 0.8, but if the latter value is less than 0.5 the first order approximation is in excellent agreement with exact solutions. For the largest reflectivity value the second order approximation is quite acceptable, while that of third order is quite good. For reflectivities of 0.5 or less the error in second or third order approximation is entirely negligible.

It is interesting that the error, regardless of the order of approximation, is always negative. Thus, the approximate results are always less than the exact. For the simple enclosures considered here, it is easy to show that this is a property of the closure method. It is also intuitively clear that this should be the case for the following reason. For nongray radiation the initial attenuation will be greatest at those wavenumbers that correspond to greatest spectral absorption. The significant radiation that remains after one traversal of the medium will thus primarily consist of wavenumbers that are more weakly attenuated, therefore, a larger fraction of that remaining will survive a second traversal. The same may be said of radiation experiencing a larger number of traversals. In the case of molecular gas radiation, the band transmissivity, $\tilde{S}_k{}^{(N)}$, monotonically approaches one as $N \to \infty$ [12].

The effect of the closure approximation is to treat exactly the number of reflections corresponding to the order of the closure. Thus, first order accounts exactly for one reflection, second order accounts exactly for two and so on. Higher order reflections are treated approximately as follows: the first order closure approximates $\tilde{S}_k{}^{(N)}$ by $\tilde{S}_k{}^{(1)}$, the second order closure approximates $\tilde{S}_k{}^{(N)}$ by $\tilde{S}_k{}^{(2)}$ for $n > 2$, and third order uses $\tilde{S}_k{}^{(3)}$ for $\tilde{S}_k{}^{(N)}$ if $N > 3$. At any order the approximate transmissivities are always equal to or less than the true value, and thus the flux is always underpredicted but the exact value can be approached as closely as desired by higher order approximation. In this respect the closure method has an unexpected but clearly desirable property.

Concluding Remarks

An approximate method of analysis of band radiation within diffuse-walled enclosures has been developed through use of a closure method. Through application to simple enclosures it has been shown that the method will converge to the exact solution through a sequence of higher order approximations. The approximate solution of any order is always less than the exact one. An important finding is that the lowest order solution yields very acceptable results for any but the most extreme enclosure conditions. The errors seem to be insensitive to geometry as well.

The present development was motivated by a desire to link directly the important advances in the development of band models [4–8] with a method for diffuse-walled enclosure analysis. In doing so, an approach has been used that removes the difficulty of finding an appropriate band transmissivity for nongray radiation encountered in earlier work with a similar objective [2, 3]. It is hoped that the band transmissivity concept has been somewhat clarified in the process.

In papers to follow, the method will be developed further for more complex enclosures with attention to both useful engineering approximations and general enclosures of arbitrary geometry containing a nonisothermal, band radiating medium.

References

1 Hottel, H. C. and Cohen, E. S., "Radiant Heat Exchange in a Gas-Filled Enclosure: Allowance for Nonuniformity of Gas Temperature," *AIChE Journal*, Vol. 4, 1958, p. 3.

2 Edwards, D. K., "Radiation Interchange in a Nongray Enclosure Containing an Isothermal Carbon-Dioxide-Nitrogen Gas Mixture," ASME JOURNAL OF HEAT TRANSFER, Vol. 84, 1962, p. 1.

3 Bevans, J. T. and Dunkle, R. V., "Radiant Interchange within an Enclosure," ASME JOURNAL OF HEAT TRANSFER, Vol. 82, 1960, p. 1.

4 Ludwig, C. B., Malkmus, W., Reardon, J. E. and Thomson, J. A. L., *Handbook of Infrared Radiation from Combustion Gases,* NASA SP-3080, Scientific and Technical Information Office, Washington, D.C., 1973.

5 Edwards, D. K. and Balakrishnan, A., "Thermal Radiation by Combustion Gases," *International Journal of Heat and Mass Transfer,* Vol. 16, 1973, p. 25.

6 Tien, C. L., "Thermal Radiation Properties of Gases," *Advances in Heat Transfer,* Vol. 5, Academic Press, New York, 1968.

7 Edwards, D. K., "Molecular Gas Band Radiation," *Advances in Heat Transfer,* Vol. 12, Academic Press, New York, 1976.

8 Edwards, D. K. and Menard, W. A., "Comparison of Models for Correlation of Total Band Absorption," *Applied Optics,* Vol. 3, 1964, p. 621.

9 Hottel, H. C. and Sarofim, A. F., *Radiative Transfer,* McGraw-Hill, New York, 1967.

10 Sparrow, E. M. and Cess, R. D., *Radiation Heat Transfer,* Brooks/Cole, Belmont, Calif., 1966.

11 Ozisik, M. N., *Radiative Transfer,* John Wiley and Sons, New York, 1973.

12 Nelson, D. A., "Band Radiation within Diffuse-Walled Enclosures. Part I: Exact Solutions for Simple Enclosures," ASME JOURNAL OF HEAT TRANSFER, Vol. 101, 1979.

13 Eckert, E. R. G. and Drake, R. M., *Analysis of Heat and Mass Transfer,* McGraw-Hill, New York, 1972.

N. Seki
Professor.

M. Sugawara
Research Associate.

S. Fukusako
Associate Professor.
Hokkaido University
Sapporo 060 Japan

Back-Melting of a Horizontal Cloudy Ice Layer with Radiative Heating

This paper is concerned with the melting of a horizontal ice layer sticking to a substrate by using halogen lamps, which are comparatively short wave radiation sources. This radiation in the visible and infrared spectral range may be employed to remove ice from structures subject to atmospheric icing. It is concluded that the behavior of radiation transfer in a cloudy ice layer depends a great deal on the density of the cloudy ice including air bubbles which produce the scattering of radiation. Also the phenomenon of back-melting caused by radiant energy penetrating through the ice layer is observed. Moreover, it is shown that the melting rate of an ice layer can be predicted numerically by using the band model of extinction coefficient for cloudy ice assumed in this study.

Introduction

Radiative heating using solar energy or a tungsten lamp might be a useful method for melting or removing an ice layer sticking to a substrate. If a short wave beam including visible and near infrared radiation is employed, the back-melting of an ice layer by the radiative energy absorbed at the surface of the substrate facilitates the easy removal of the sticking ice layer from the substrate. However, the behavior of radiative transfer in a cloudy ice layer with air bubbles is significantly complicated because of scattering. Therefore, the evaluation of the extinction coefficient of cloudy ice is needed first to predict the radiative heat flux through the layer or the melting rate of the ice layer. Measurements of extinction coefficient have previously been made for antarctic plateau ice by Weller [1] and for river ice by Wendler [2]. However, in their studies, the spectral dependence of the extinction coefficient for cloudy ice was not fully given.

Recently, Sugawara, et al. [3] presented an experimental investigation of the melting of a horizontal ice layer by using an infrared lamp as a radiating heat source. They pointed out that the evaporation from the free surface and the free convection in the melt layer influenced the melting rate markedly. However, neither absorption nor scatter of radiant energy in the ice layer were considered in their study. Gilpin, et al. [4] discussed the internal absorption and scattering in the radiative heating of ice.

In this paper, a spectral band model of cloudy ice which enables radiative melting to be predicted is assumed from a consideration of both spectral extinction coefficient and transmission of total energy. Moreover, the effects of the temperature of the source of radiation, the density of the cloudy ice, and the thermal properties of the substrate on the melting rate of a horizontal cloudy ice layer sticking to the substrate are studied experimentally and analytically.

Absorption and Extinction Coefficient of Ice

Experimental Procedure. Measurements are made of the absorption coefficient of clear ice and extinction coefficient of cloudy ice by using a spectroscope of the type HITACHI-EPS-3T covering 0.2 μ to 2.6 μ in wavelength [5]. The spectroscope has a collimated double beam with a sectional area of 10 mm × 10 mm. The temperature of the test chamber, containing an ice sample, is kept at −3°C by circulating ethylene glycol coolant into a copper coil in order to prevent the ice sample from thawing during the run. Commercial ice is used as the clear ice sample, while the cloudy ice block is produced by rapidly freezing water aerated in advance at 0°C.

The extinction coefficient of various kinds of cloudy ice produced by controlling freezing rate is evaluated by measuring the radiant energy transmitted through the ice layer. However, it is difficult, in general, to accurately measure the total amount of energy emitted from the back surface of cloudy ice sample because of a strong scattering effect caused by air bubbles contained in the ice layer.

In the present study, the transmission of radiation through the ice layer, which is exposed to a total radiant energy emitted from a tungsten source, is measured by using the same instrument as shown in the literature [5]. The instrument is placed in a cold room to prevent the ice sample from thawing. The measurement of transmission are made for various ice samples having $h_i = 1 \sim 100$ mm in thickness.

Discussion. Fig. 1 shows the measured extinction coefficient k_ν for cloudy ice together with absorption coefficient a_ν for clear ice. For clear ice it can be seen that the absorption coefficient indicates a strong spectral dependence, and the wavelength at which the minimum absorption coefficient occurs is about 0.55 μ. For cloudy ice it can be seen that the measured k_ν in the range 0.3 μ (near visible) to 1.2 μ (near infrared) shows little dependence on wavelength. In this scattering region, the values are considerably higher than the absorption coefficient for clear ice without scattering. However, in the nonscattering region of $\nu > 1.2$ μ, the k_ν movements are nearly equal to the absorption coefficient a_ν due to little scattering (nonscattering).

The transmission of total energy through a cloudy or clear ice layer is shown in Fig. 2, which is used to derive a band model of extinction coefficient proposed in the present study. The transmission A, which is the ratio of transmitted energy to incident energy, increases with increasing temperature of radiating source T_b and with increasing density of ρ_i. A precipitous decrease of A with increasing ice thickness

---

Contributed by the Heat Transfer Division for publication in the JOURNAL OF HEAT TRANSFER. Manuscript received by the Heat Transfer Division February 6, 1978.

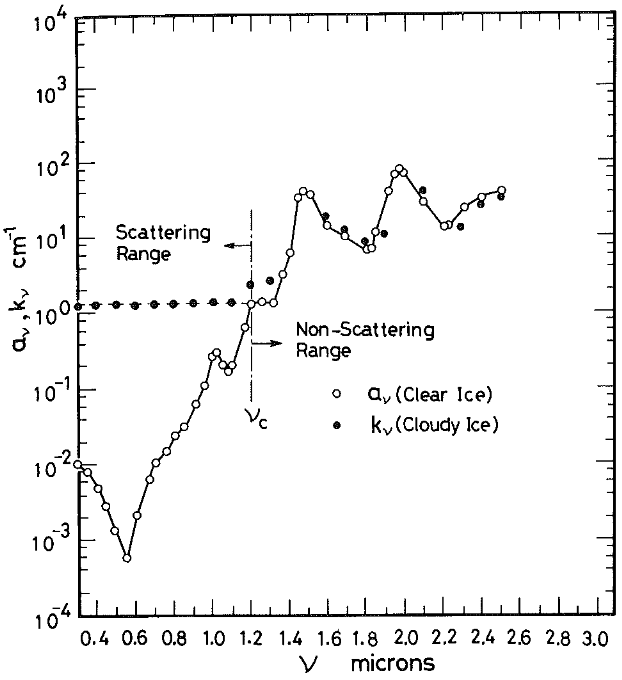

Fig. 1 Absorption and extinction coefficient: a_ν, k_ν

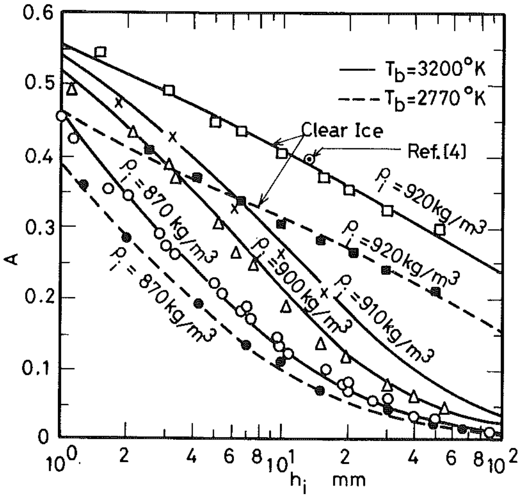

Fig. 2 Transmission, *A*

h_i takes place in the range of thin thickness of ice. Further increase in h_i causes a slow decrease in the transmission. The present experimental results of A for clear ice coincide well with the data measured by Gilpin, et al. [4]. The extinction coefficient for ρ_i = 870 kg/m^3 in the range of $h_i > 20$ mm is about 0.3 cm^{-1}, which is similar to 0.22 cm^{-1} for river ice obtained by Wendler [2]. Solid and dotted lines in Fig. 2 show the predictions of A based on the present band model, respectively. In Fig. 1, if the wavelength at the crossing of k_ν line and a_ν curve is defined as the critical wavelength, ν_c, the extinction coefficient may be described as following.

$$k_\nu = a_\nu \ldots \nu > \nu_c \tag{1}$$

On the other hand, in the scattering range the extinction coefficient with scattering k_s which is dependent on ice thickness may be assumed

$$k_s = k_0/(1 + Co.h_i{}^n) \ldots \nu < \nu_c \tag{2}$$

The energy emitted from the back surface of ice layer q_{rh} and the transmission A are described as

$$q_{rh} = \epsilon \int_0^{\nu_c} E_{b\nu}.\exp\{-k_s.h_i\}d\nu + \epsilon \int_{\nu_c}^{\infty} E_{b\nu}.\exp\{-k_\nu.h_i\}d\nu \tag{3}$$

$$A = q_{rh}/q_{r0} \tag{4}$$

where

$$\epsilon = q_{r0}/\sigma T_b{}^4$$

The extinction coefficient k_0 for $h_i \to 0$ is constant in the scattering region. Moreover, k_0 and Co depend mainly on ρ_i as shown in Fig. 3 which illustrates the results estimated from the present experiments of transmission demonstrated in Fig. 2. The optimum value of index number, n, in equation (2) is evaluated as 0.9.

Melting Behavior

Experimental Apparatus. Fig. 4 shows a schematic diagram of the low temperature room in which the test sample is to be melted under a prescribed environmental temperature below 0°C. The inside

Nomenclature

a_ν = monochromatic absorption coefficient of clear ice and water
A = transmission, defined in equation (4)
Co = constant
$E_{b\nu}$ = monochromatic emissive power of blackbody
h_D = mass transfer coefficient
h_i = thickness of ice layer
h_{in} = initial thickness of ice layer
h_m = thickness of substrate
k_0 = extinction coefficient for $h_i \to 0$
k_s = extinction coefficient with scattering (equation (2))
k_ν = monochromatic extinction coefficient
L_i = latent heat of melting
L_w = latent heat of evaporation or condensation
n = index number, defined in equation (2)
q_{r0} = radiant heat flux impinging on ice or free surface
q_{h_i} = heat flux absorbed at the surface of substrate
$q_{r1}\{y\}$ = radiative heat flux in upper melt layer
$q_{r2}\{y\}$ = radiative heat flux in lower melt layer
$q_{ri}\{y\}$ = radiative heat flux in ice layer
S_1 = thickness of upper melt layer
S_2 = thickness of lower melt layer
S'_2 = distance from free surface to bottom surface of ice layer
T = temperature
T_b = temperature of blackbody
T_i = temperature in an ice layer
T_{in} = initial temperature distribution in ice layer
T_{w1} = temperature in upper melt layer
T_{w2} = temperature in lower melt layer
T_∞ = environmental temperature
T_1 = temperature of the air-water or air-ice interface
T_2 = temperature of the substrate surface
T_3 = temperature of the back side surface of substrate
t = time
W_1 = saturated vapor concentration at free surface
W_∞ = vapor concentration at the environment
y = depth from free or ice surface
α = heat transfer coefficient
ϵ = ratio of q_{r0} to $\sigma T^4{}_b$ (= total emissivity of source)
κ_i = thermal diffusivity of ice
κ_w = thermal diffusivity of water
κ_m = thermal diffusivity of substrate
λ_i = thermal conductivity of ice
λ_w = thermal conductivity of water
λ_m = thermal conductivity of substrate
ν = wavelength
ν_c = critical wavelength
ρ_{av} = density of air-vapor mixture
ρ_i = density of ice
σ = Stefan-Boltzmann constant

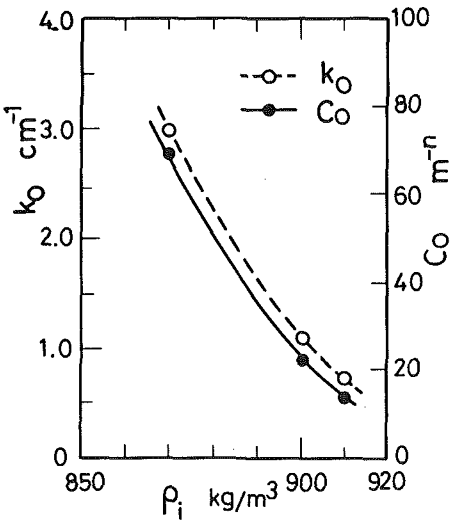

Fig. 3 Value of *Co*, k_0 versus density of ice

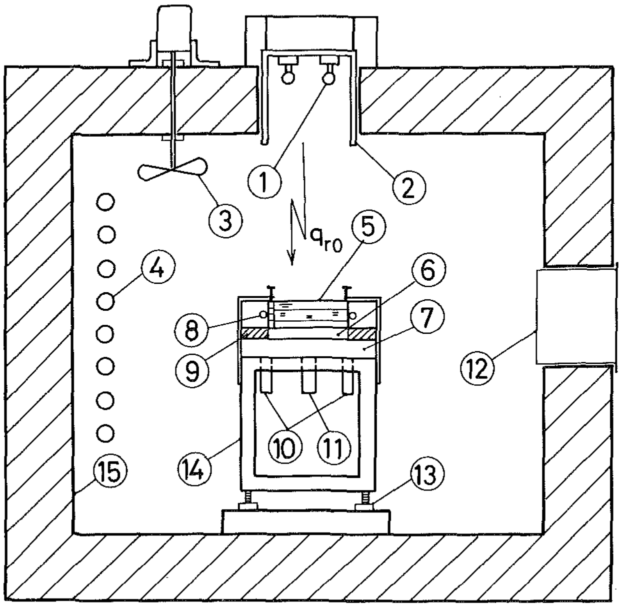

① halogen lamp ② aluminum case ③ fan ④ cooling pipe ⑤ vessel for melting ice layer ⑥ substrate ⑦ cooling box ⑧ vinyl tube to circulate coolant ⑨ insulation material ⑩ inlet of coolant ⑪ exit of coolant ⑫ visualizing window ⑬ ajusting screw ⑭ stand ⑮ low temperature room

Fig. 4 Experimental apparatus

dimension of the room is 0.7 m × 0.7 m × 0.6 m, and the room is automatically kept at the desired temperature. A window to observe the melting phenomena as well as to measure the melting rate is installed at one side wall of the room. The temperature at the back surface of the substrate is kept constant lower than 0°C by using a copper-made cooling box in which ethylene glycol coolant is circulated, as will be seen in the figure.

Short wave radiation is obtained by using halogen lamps with tungsten filament, which are arranged above the test section. The temperature of the radiating source is 3200 K at 100 volts and is varied to a desired value by adjusting a stabilized power source.

Radiant heat flux onto the surface of the melt layer or ice layer, q_{r0}, is evaluated from the measured value of the temperature rise of a water film about 1.5 mm in thickness. The water film is contained in a rectangular container made of 0.5 mm thick plastic plates with a bottom surface of 80 mm × 80 mm, painted black. The q_{r0} value was estimated from the following relation: $q_{r0} = (G_w.c_w + G_v.c_v)/F.(dT/dt)$ where G_w is the weight of water, G_v is the weight of container, c_w is the specific heat of water, c_v is the specific heat of container, F is the surface area of container, T is the temperature, and t is time. This measurement can be performed within a very short period of time (about 5 ~ 10 s); therefore, a negligible inherent heat loss could be fully expected.

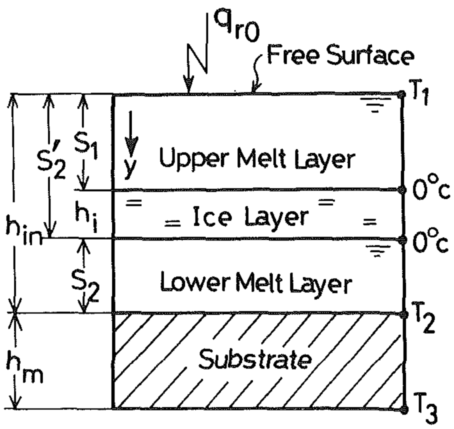

Fig. 5 Schematic diagram of the physical problem

The test vessel used for melting the ice layer is made of 4mm thick lucite plates with a surface area of 98 mm × 98 mm, and the bottom plate of the vessel is 1 mm thick copper plate whose surface is painted black so as to absorb the energy transmitted through the ice or liquid layer. In order to prevent the ice layer from detaching or floating upward due to melting from the side walls of the test vessel, the temperature of the walls is kept at 0°C by circulating temperature-controlled ethylene glycol coolant through a vinyl tube 3 mm ID around the walls. Therefore, one-dimensional heat flow in the ice layer could fully be expected during each run.

The surface temperature of the melt layer is measured by using a copper-constantan thermocouple of 50 μ in diameter which is soldered on a copper foil (20 μ, 2 mm × 2 mm) having negligible small heat capacity compared with that of the melt layer. The foil is floating on the surface of the melt layer. The junction of the thermocouple is soldered on one side of the foil. The other side of the foil is well polished by buffing in order to reflect the direct radiation. Therefore, the present measurement of the surface temperature may be taken to be correct.

The one-dimensional depth of upper and lower liquid melt layers is measured by taking a photograph of the ice-water system obtained.

To minimize the local temperature difference in the low temperature room, an electric fan is used. Therefore, the heat transfer coefficient, α, on the surface of the upper melt layer or ice layer is determined experimentally by measuring heat flux from an electric heater in the form of a thin carbon plate placed on an insulation material.

Analysis. Fig. 5 shows the present analytical model. Consider the ice layer having such a large extent as the heat is transfered one-dimensionally after radiant energy impinges on the surface of the ice layer. The temperatures of the ice layer and the melt layer are assumed to vary only in a vertical direction in the present study.

Radiative heat transfer in cloudy ice is discussed by Gilpin, et al. [4], who refer to the effect of anisotropic scattering. The main purpose of the present analysis is to predict the melting of cloudy ice when the thickness of the upper melt layer without scattering increases gradually with time. Therefore, in order to simplify the present analysis, the following assumptions are adopted.

Both the volumetric emission of radiation in the ice or water layer are neglected as small. Moreover, since the depth of melt layer with no scattering becomes large during melting period, while the ice layer becomes gradually thin, the back-scattered radiation may be assumed to be negligible in the present study.

The index of refraction for water is about 1.3. Therefore, the reflection of incident energy at the air-water interface is neglected as a small value of about 2 ~ 3 percent. Moreover, the radiating heat source (halogen lamp) is assumed to be a blackbody.

In this study, radiation and conduction could be treated analytically as dependent since the absorbed energy in ice or melt layer is to be transmitted by only the mechanism of conduction. Therefore, the basic equation of heat transmission in the melt layers, ice layer and substrate could be described as follows

$$\frac{\partial T_{w1}}{\partial t} = \kappa_w \frac{\partial^2 T_{w1}}{\partial y^2} - \frac{\kappa_w}{\lambda_w} \frac{\partial q_{r1}\{y\}}{\partial y} \ldots 0 < y < S_1 \tag{5}$$

$$\frac{\partial T_i}{\partial t} = \kappa_i \frac{\partial^2 T_i}{\partial y^2} - \frac{\kappa_i}{\lambda_i} \frac{\partial q_{ri}\{y\}}{\partial y} \ldots S_1 < y < S'_2,\ T_i \leqq 0°C \tag{6}$$

$$\frac{\partial T_{w2}}{\partial t} = \kappa_w \frac{\partial^2 T_{w2}}{\partial y^2} - \frac{\kappa_w}{\lambda_w} \frac{\partial q_{r2}\{y\}}{\partial y} \ldots S'_2 < y < h_{in} \tag{7}$$

$$\frac{\partial T_m}{\partial t} = \kappa_m \frac{\partial^2 T_m}{\partial y^2} \ldots h_{in} < y < h_{in} + h_m \tag{8}$$

where

$$q_{r1}\{y\} = \frac{0.165^2}{(0.165 + y)^2} \epsilon \int_0^\infty E_{b\nu}.\exp\{-a_\nu y\} d\nu \tag{9}$$

$$q_{ri}\{y\} = \frac{0.165^2}{(0.165 + y)^2} \left[\epsilon \int_0^{\nu_c} E_{b\nu}.\exp\{-a_\nu S_1 - k_s(y - S_1)\} d\nu + \epsilon \int_{\nu_e}^\infty E_{b\nu}.\exp\{-k_\nu y\} d\nu \right] \tag{10}$$

$$q_{r2}\{y\} = \frac{0.165^2}{(0.165 + y)^2} \left[\epsilon \int_0^{\nu_c} \mathrm{E}_{b\nu}.\exp\{-a_\nu (S_1 + y - S'_2) - k_s(S'_2 - S_1)\} d\nu + \epsilon \int_{\nu_c}^\infty E_{b\nu}.\exp\{-k_\nu y\} d\nu \right] \tag{11}$$

$[0.165^2/(0.165 + y)^2]$ included in the equations above is the correction factor as shown in Fig. 6 which expresses the experimental results of the decrease of radiation intensity with increasing distance from the radiating source. However, when one evaluates the absorbed energy in ice or melt layer using equations (5–7), the correction factor in equations (9–11) should be treated as constant, since heat absorption is to be independent of correction factor. The second term on the right-hand side of equations (5–7) represents the radiant energy absorbed in the media. The temperature in the ice layer is assumed as $T_i \leqq 0°C$. When the temperature of the ice layer has reached 0°C, the absorption of radiative energy in the layer causes internal melting [6].

The heat is dissipated by convection, evaporation or condensation from the surface of the upper melt layer or ice layer. Therefore the energy balance at the surface ($y = 0$) is expressed as following.

$$\lambda_{wi} \frac{\partial T_{wi}}{\partial y} = \alpha (T_1 - T_\infty) + h_D L_w \rho_{av} (W_1 - W_\infty) \tag{12}$$

where $\lambda_{wi} = \lambda_w$ or λ_i, $T_{wi} = T_{w1}$ or T_i, and α is heat transfer coefficient which does not include the effect of thermal radiation. The second term on the right-hand side of equation (12) represents the heat flux caused by evaporation or condensation. Mass transfer coefficient h_D is evaluated by using the well-known analogy between heat and mass transfer, assuming that the Lewis number is unity [9].

Since the effect of the difference in the total radiative energy transmitted on both sides of the interface of ice layer is included in the energy equations (5, 6, 7) implicitly, boundary conditions at the two ice-water interfaces as $y = S$ ($=S_1$ or S'_2) are expressed as follows, when the reflection of both sides is neglected.

$$-\lambda_w \frac{\partial T_w}{\partial y} + \lambda_i \frac{\partial T_i}{\partial y} = L_i \rho_i \frac{dS}{dt} \tag{13}$$

$$T_{w1},\ T_{w2} \text{ and } T_i = 0°C \tag{14}$$

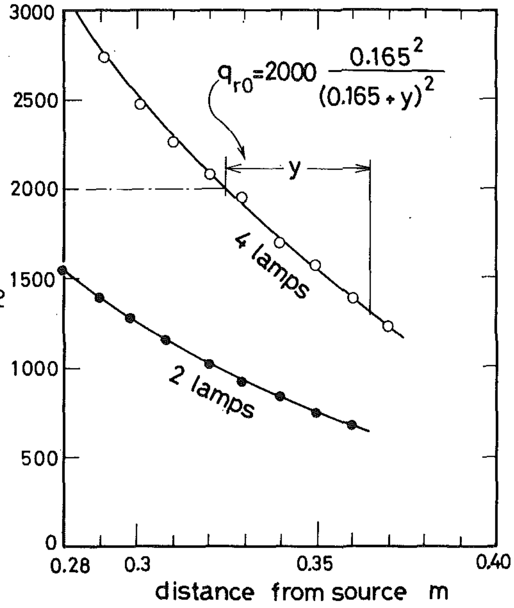

Fig. 6 Extinction of incident energy q_{r0}

where

$$T_w = T_{w1} \text{ or } T_{w2}$$

The boundary condition at the surface of the black substrate ($y = h_{in}$) is described as

$$-\lambda_{wi} \frac{\partial T_{wi}}{\partial y} + \lambda_m \frac{\partial T_m}{\partial y} = -q_{r2}\{h_{in}\} \tag{15}$$

where

$$T_{wi} = T_{w2} \text{ or } T_i$$

However, $q_{r2}\{h_{in}\}$ in equation (15) may be described as following in accordance with the range of wavelength, since it should be noted that the region $y = 0 \sim S_1$ is assumed as a non-scattering region for the wavelength $0 \sim \nu_c$ in the present study.

$$q_{r2}\{h_{in}\} = q_{h_i} = \frac{0.165^2}{(0.165 + S_1)^2} \times \epsilon \int_0^{\nu_c} \mathrm{E}_{b\nu}.\exp\{-a_\nu (S_1 + h_{in} - S'_2) - k_s (S'_2 - S_1)\} d\nu + \frac{0.165^2}{(0.165 + h_{in})^2} \epsilon \int_{\nu_c}^\infty E_{b\nu}.\exp\{-k_\nu h_{in}\} d\nu \tag{16}$$

The temperature at the back surface of the substrate ($y = h_{in} + h_m$) is maintained at constant below 0°C, that is

$$T_m = T_3 \tag{17}$$

The initial temperature distribution in the ice layer is assumed to be uniform as T_{in}.

Since the boundary condition is nonlinear and the absorbing rate of radiant energy has not a simple expression, a closed form analytical solution is very cumbersome in general. Therefore, numerical predictions for both melting rate of ice and unsteady temperature distributions in a prescribed system are carried out by using an implicit finite-difference method developed by Murray, et al. [7]. A uniform grid size as $\Delta y = 0.5$ mm is adopted in a depth direction.

For the boundary condition at the free surface, it is necessary to consider the effect of radiant energy absorbed near the free surface. Therefore, in this paper, the energy absorbed at the surface ($y = 0$) is assumed to be absorbed in half a mesh of the first finite-difference node from the standpoint of numerical calculation.

Under the initial conditions of $S_1 = 0$, $S'_2 = h_{in}$, $T_i\{y, t = 0\}$, it is impossible to start the calculation by the finite-difference method adopted. Therefore, very thin upper and lower melt layers are assumed to be melted prior to the numerical computation, whose advance is estimated by solving the ordinary differential equation of heat conduction for liquid phase with negligible heat capacity [8].

Results and Discussions

Radiative melting behavior obtained from the present experiments and the predicted results are shown in Figs. 7–10.

Fig. 7 shows the effect of the temperature of the radiating heat source, T_b, on the amount of both upper and lower melting under the condition that the ice layer was stuck to an insulation material with black surface; the density of the cloudy ice used is 870 kg/m^3. The results for clear ice are obtained under the conditions of q_{r0} = 2300 kcal/m^2 h, h_{in} = 40 mm. The heat transfer coefficient in the free surface, α, is 11 kcal/m^2 h°C. In this figure, the back-melting phenomenon from the lower melt layer which is caused by the absorption of a short wave radiation transmitted through the water or ice layer at the surface of the substrates is clearly recognizable. The ratio of the amount of back-melting to that of upper-melting, S_2/S_1, is increased with increasing T_b in spite of the same value of the incident energy q_{r0}. The amount of back-melting for cloudy ice, S_2, indicates the same trend as the present predictions, while the amount of upper-melting S_1 is markedly larger than the predictions. This melting behavior may mainly be attributed to the reason that a slice of ice is apt to remove from the ice-water interface due to the weakness of the ice structure including a great amount of air bubbles. Another likely reason for this behavior is the neglected backward scattering. Moreover, it can be seen that the rate of back-melting increases gradually with time since the q_{h_i} in equation (16) increases with decreasing thickness of cloudy ice layer during the melting process. On the other hand, the predictions of both S_1 and S_2 for clear ice layer are in good agreement with the experimental results.

The effect of the density of ice on the melting rate is shown in Fig. 8. From the results, it might be inferred that the amount of upper-melting, S_1, is influenced little by the density of ice because of neglected backward scattering, while the amount of lower-melting, S_2, has a strong density dependence due to the scattering effect, as can be seen in Fig. 2.

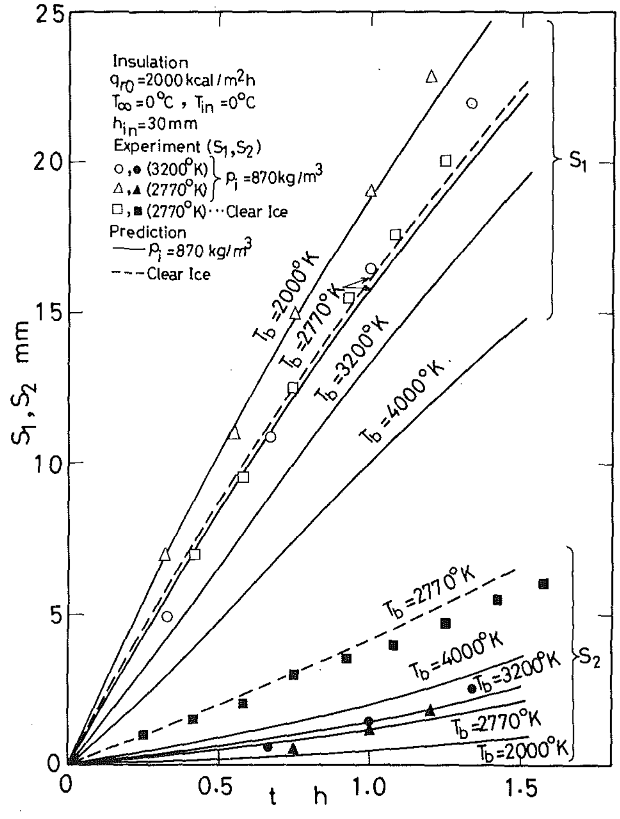

Fig. 7 Effect of T_b on melting of ice layer

The aforementioned results for radiative melting were obtained for an insulated substrate to which the ice was stuck. However, from the practical standpoint of removing the ice layer from structures subject to atmospheric icing, it is useful to examine the back-melting behavior of ice sticking to a substrate which is initially kept at a temperature below 0°C. Predicted results of S_1 and S_2 subject to the aforementioned thermal condition of the substrate are indicated in Fig. 9. The substrates adopted in this study are steel (λ_m = 46 kcal/m h °C, κ_m = 0.0534 m^2/h), wood (λ_m = 0.091 kcal/m h °C, κ_m = 0.0004 m^2/h) and insulation material. As shown in this figure, these substrates exert little influence on the upper-melting rate during a short melting period. However, as the melting advances, the effect of the thermal properties of substrate on the melting rate becomes gradually distinct with time. On the other hand, it is clear that the substrate

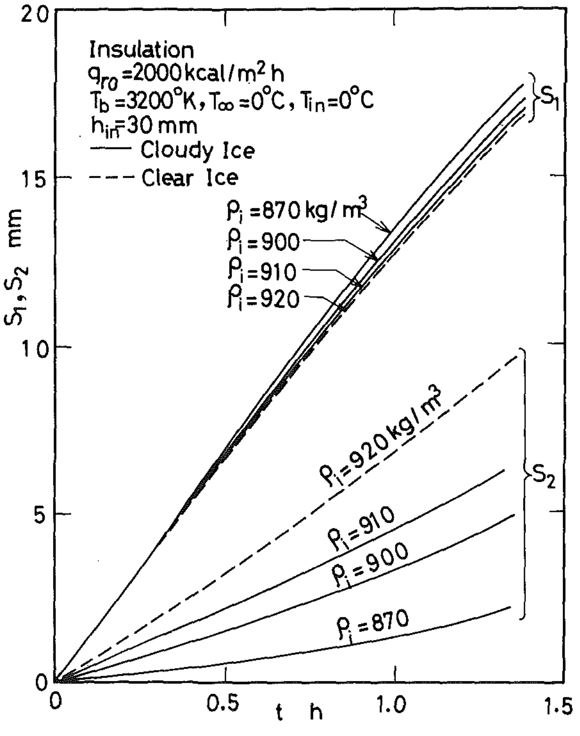

Fig. 8 Effect of ρ_i on melting of ice layer

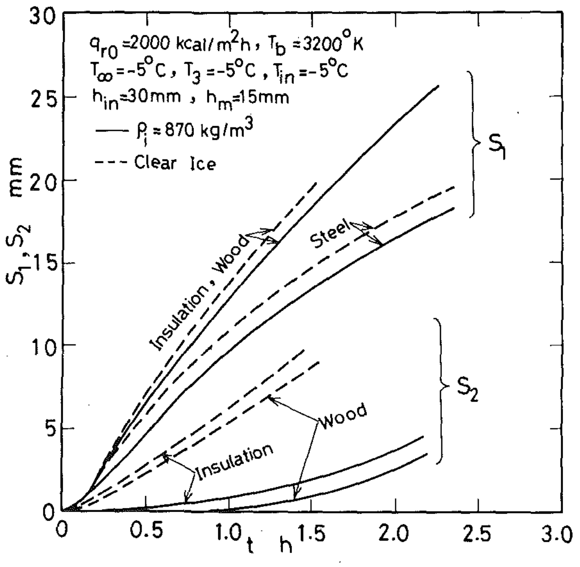

Fig. 9 Effect of substrate on melting of ice layer

exerts a marked influence in the back-melting rate.

Fig. 10 shows the predicted results for the time dependent temperature distribution of the ice layer, T_i, substrate, T_m, and liquid melt layers, T_{w1}, T_{w2}, together with the experimental results. The thermal conductivity λ_m and the thermal diffusivity κ_m of the substrate are 0.2 kcal/m h °C and 0.0004 m^2/h, respectively. In this figure it can be seen that the energy absorbed in the ice layer raises the temperature of ice layer to the melting point (0°C) in a short melting period. In particular, the temperature rise at the ice-substrate interface is characteristic of that which radiative heating provides. Upper melting occurs as the temperature of the free surface, T_1, reaches 0°C at about $t = 0.032$ h for cloudy ice. The temperature distribution of the ice layer at about $t = 1.0$ h is uniform at 0°C. Thereafter, additional energy absorbed in the ice layer produces internal melting [4, 6]. On the other hand, a great amount of back-melting is observed for the clear ice layer because of the large heat flux absorbed in the substrate after penetrating through the layer with little scattering effect. It should be noticed in Fig. 10 that the present numerical analysis for radiative heating predicts the reversal of temperature gradient near the free surface during the melting process well. Such a temperature distribution appears especially under the combined condition of high temperature, T_b, and large heat loss dissipated from the free surface by convective heat transfer and evaporation.

Conclusions

To examine the feasibility of removing an ice layer from a structure, short wavelength radiation obtained from halogen lamps was utilized as a heating source. The measurements were carried out to obtain the spectral dependence of the absorption and extinction coefficients of the ice layer. Based on the above experiments, a band model of extinction coefficient was assumed in order to analytically predict the melting rate of ice layers having various densities. In the results, a characteristic back-melting phenomenon was observed clearly. The numerical predictions of a radiative melting of an ice layer under the various melting conditions were in good agreement with the experimental results in general.

Summing up the results in this study, the following conclusions can be drawn:

1 The present band model of extinction coefficient for cloudy ice is useful in predicting the radiative heat transfer in an ice layer and its melting behavior.

2 The ratio of the amount of back-melting to that of upper-melting, S_2/S_1, is increased with increasing T_b at constant incident energy, q_{r0}.

3 The amount of the upper melting, S_1, is influenced little by the density of ice. However, the amount of the back-melting, S_2, depends markedly on it.

4 The substrate to which the ice layer is stuck exerts a marked influence on both the rate of back-melting and the rate of upper melting.

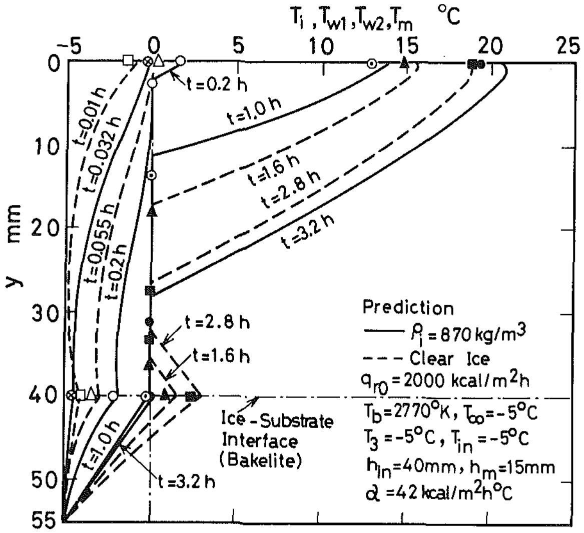

Fig. 10 Temperature distributions. data points: for cloudy ice ⊗ $t = 0.032$ *h*, ○ $t = 0.2$ *h*, ⊙ $t = 1.0$ *h*, ● $t = 3.2$ *h* for clear ice □ $t = 0.01$ *h*, △ $t = 0.055$ *h*, ▲ $t = 1.6$ *h*, ■ $t = 2.8$ *h*

References

1 Weller, G. E., "The Heat Budget and Heat Transfer Processes in Antarctic Plateau Ice and Sea Ice," *Anare Scientific Reports,* Series A(IV) Glaciology, Publication No. 102, 1968.

2 Wendler, G., "Some Measurement of the Extinction Coefficients of River Ice," *Polarforschung,* Organ der Deutschen Gesellschaft für Polarforschung, VI, 39, 1969, pp. 253–256.

3 Sugawara, M., Fukusako, S., and Seki, N., "Experimental Study of the Melting of a Horizontal Ice Layer," *Bulletin of the JSME,* Vol. 18, 1975. pp. 714–721

4 Gilpin, R. R., Robertson, R. B., and Singh, B., "Radiative Heating in Ice," ASME JOURNAL OF HEAT TRANSFER, Vol. 99, 1977, pp. 227–232.

5 Seki, N., Sugawara, M., and Fukusako, S., "Back-Melting of a Horizontal Ice Layer Sticking to the Substrate," *Preprint for JSME Meeting of Heat Engng.,* Paper No. 770-16, pp. 132–134.

6 Maeno, N., "Observation of Internal and Surface Melting of Ice," *Low Temperature Science,* Series A28, 1970, pp. 23–31.

7 Murray, W. D., and Landis, F., "Numerical and Machine Solution of Transient Heat-Conduction Problem Involving Melting or Freezing," ASME JOURNAL OF HEAT TRANSFER, Vol. 81, 1959, pp. 106–112.

8 Eckert, E. R., and Drake, R. M., *Analysis of Heat and Mass Transfer,* McGraw-Hill, 1972, pp. 223–224.

9 Katto Yoshiro, *Introduction to Heat Transfer,* Yokendo Book Co., 1974, p. 279.

M. M. Yan
P. N. S. Huang
Assoc. Mem. ASME

Department of Aeronautical Engineering
Chung Cheng Institute of Technology
P.O. Box 8243-11, Ta-Hsi, Tao-Yuan
Taiwan, Republic of China

Perturbation Solutions to Phase Change Problem Subject to Convection and Radiation

Perturbation solutions are obtained for one-dimensional phase change problem in a finite region subject to convective and radiative boundary condition at the fixed boundary. The radiative term is first approximated by Taylor's series expansion, then the perturbation technique is used. Analytical expressions for total solidification time and the rate of solidification as well as the temperature distributions are obtained. Close agreement is observed between the present analysis and that of an early work.

Introduction

The heat conduction problems involving change of phase are of great practical importance. They are encountered in application such as the missile re-entry, solidification of metals, freezing food and ice formation. However, due to the nonlinear boundary condition at solid-liquid interface, exact analytical solutions are limited to a few simple cases [1]. Therefore, approximate method of solution must be employed. The variational method developed by Biot [2–4] and the integral method by Goodman [5] are the most popular techniques. Both methods have been applied by many investigators for different types of boundary conditions [6–14]. Recently, Chung and Yeh [15] used the variational method and the heat balance integral technique in solving the phase change problem subject to radiation and convection. Pedroso and Domoto [16, 17] successfully adopted the perturbation method in solving the solidification problem with planar and spherical geometries.

In the present investigation, regular perturbation technique is extended to the phase change problem arising from aerodynamic and radiative cooling or heating. Both the temperature distributions and the location of the interface are to be determined and expressed in analytical forms. Comparison is made between the present analysis and that of an early work [15] using the variational method and numerical integration.

Analysis

A homogeneous slab of thickness ℓ is situated at its fusion temperature, T_i, initially as shown in Fig. 1. At time $t = 0$, radiative and convective cooling (or heating) is applied at the face, $x = 0$, and phase change starts. Assuming that the thermal properties are constants and the newly formed phase is opaque to radiation. The one-dimensional heat conduction equation describing the system can be written in the following form

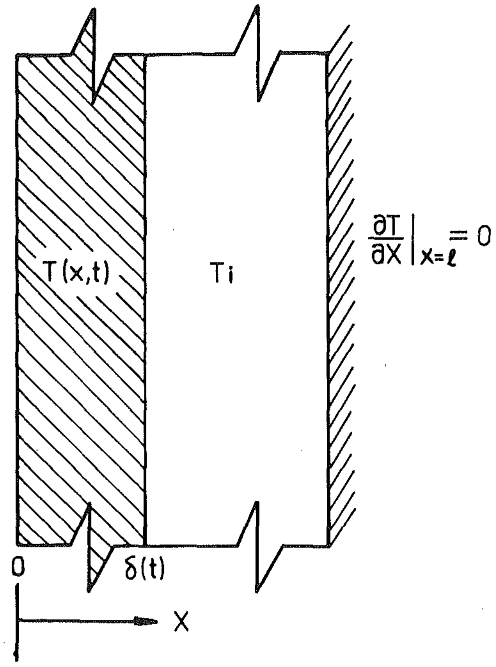

Fig. 1 Schematic representation of phase change problem

Contributed by the Heat Transfer Division and presented at the Winter Annual Meeting, Atlanta, Georgia, November 27–December 2, 1977 THE AMERICAN SOCIETY OF MECHANICAL ENGINEERS. Manuscript received by the Heat Transfer Division February 9, 1978. Paper No. 77-WA/HT-16.

$$\frac{\partial T}{\partial t} = \alpha \frac{\partial^2 T}{\partial x^2} \quad t > 0, \qquad 0 \le x \le \delta \tag{1}$$

$$T = T_i \qquad \text{at } x = \delta \tag{2}$$

$$k\left(\frac{\partial T}{\partial x}\right) = \sigma F(T^4 - T_e{}^4) + h(T - T_a) \qquad \text{at } x = 0 \tag{3}$$

$$k\left(\frac{\partial T}{\partial x}\right) = P\rho L \frac{d\delta}{dt} \qquad \text{at } x = \delta \tag{4}$$

$$\frac{\partial T}{\partial x} = 0 \qquad \text{at } x = \ell \tag{5}$$

$$T = T_i \qquad \text{at } t = 0 \tag{6}$$

where δ is the location of the interface between the solid and liquid. $P = 1$ and -1 represent the solidification case and melting case, respectively. F is overall radiation shape factor which is assumed to be constant. σ is the Stefan-Boltzmann constant and h is heat transfer coefficient. For simplicity, both the ambient temperature T_a and the environment temperature T_e are assumed to be equal in the present analysis. Equation (5) implies the finiteness of the liquid or solid region and guarantees the condition $T = T_i$ as $x \ge \delta(t)$.

The dimensionless quantities of physical parameter ϵ, temperature u, space coordinate $\bar{x}$, interface position, s, and time τ are defined as

$$\begin{aligned} \epsilon &= \frac{PC_p(T_i - T_a)}{L} \\ u &= \frac{PT}{T_i - T_a} \\ \bar{x} &= \frac{x}{\ell} \\ s &= \frac{\delta}{\ell} \\ \tau &= \frac{Pk(T_i - T_a)t}{\rho L \ell^2} \end{aligned} \tag{7}$$

The physical parameter ϵ is a qualitative measure of the ratio of sensible heat to latent heat, L. Let the dimensionless interface speed be

$$g = \frac{ds}{d\tau} \tag{8}$$

In the following analysis, an additional simplification will now be employed. For the first approximation, assume that the temperature difference are sufficiently small such that T^4 may be expressed as a linear function of temperature, thus

$$T^4 \approx 4T_a{}^3 T - 3T_a{}^4 \tag{9}$$

Substituting equations (7–9) into equations (1–6), changing variables $(t, x) \to (s, \bar{x})$ yields

$$\frac{\partial^2 u}{\partial \bar{x}^2} = \epsilon g \frac{\partial u}{\partial s} \tag{10}$$

$$u(s, \bar{x} = s) = u_i \tag{11}$$

$$\left.\frac{\partial u}{\partial \bar{x}}\right|_{\bar{x}=0} = B_0 R(u_s - u_a) \tag{12}$$

$$g = \frac{1}{P} \left.\frac{\partial u}{\partial \bar{x}}\right|_{\bar{x}=s} \tag{13}$$

$$\left.\frac{\partial u}{\partial \bar{x}}\right|_{\bar{x}=1} = 0 \tag{14}$$

$$u_s(0) = u_i \tag{15}$$

where B_0 is the Biot number and $R = 4Hua^3/B_0 + 1, H = \sigma FTi^3\ell/k$ $(1 - T_a/T_i)^3$. The solution to equation (10) can be written in general as

$$u = u(s, \bar{x}; \epsilon) \qquad g = g(s; \epsilon) \tag{16}$$

The perturbation series can be obtained by expanding u and g on ϵ in Taylor series about $\epsilon = 0$, thus

$$u(s, \bar{x}; \epsilon) = u_0(s, \bar{x}) + \epsilon u_1(s, \bar{x}) + \epsilon^2 u_2(s, \bar{x}) + \ldots$$

and

$$g(s; \epsilon) = g_0(s) + \epsilon g_1(s) + \epsilon^2 g_2(s) + \ldots \tag{17}$$

Substituting equation (17) into equations (10–15) and equating coefficients of like powers of ϵ yields

$$\begin{aligned} &\frac{\partial^2 u_j}{\partial \bar{x}^2} = \begin{cases} 0 & j = 0 \\ \sum_{k=1}^{j} g_{k-1} \frac{\partial u_{j-k}}{\partial s} & j \ge 1 \end{cases} \\ &u_j(s, \bar{x} = s) = \begin{cases} u_i & j = 0 \\ 0 & j \ge 1 \end{cases} \\ &\left.\frac{\partial u_j}{\partial \bar{x}}\right|_{\bar{x}=0} = \begin{cases} B_0 R(u0|_s - u_a) & j = 0 \\ B_0 R u_{j,s} & j \ge 1 \end{cases} \\ &g_j = \frac{1}{P} \left.\frac{\partial uj}{\partial \bar{x}}\right|_{\bar{x}=s} \qquad j \ge 0 \\ &\left.\frac{\partial u_j}{\partial \bar{x}}\right|_{\bar{x}=1} = 0 \qquad j \ge 0 \\ &u_{j,s}(0) = \begin{cases} u_i & j = 0 \\ 0 & j \ge 1 \end{cases} \end{aligned} \tag{18}$$

The zero-order solution to the linear system equation (18) is

Nomenclature

C_p = specific heat of material at constant pressure
F = over-all radiation shape factor
h = heat transfer coefficient
k = thermal conductivity
ℓ = thickness of the slab
L = latent heat
T = absolute temperature in solid or liquid
T_i = initial temperature
T_a = ambient temperature
T_e = environment temperature
T_s = surface temperature
t = time
x = dimensional space coordinate
α = thermal diffusivity of material, $k/\rho C_p$
σ = Stefan-Boltzmann constant
ρ = density
δ = position of solid-liquid interface
$B = L/C_p T_i$ for solidification
$= L/C_p T_a$ for melting
B_0 = Biot number, $h\ell/k$
g = normalized freezing or melting front speed, $ds/d\tau$
H' = radiation parameter for solidification, $\sigma F T_i{}^3 \ell/k$
= radiation parameter for melting, $\sigma F T_a{}^3 \ell/k$
$H = H'(1 - T_a/T_i)^3$ for solidification
$= H'(1 - T_i/T_a)^3$ for melting
P = 1 for solidification
= −1 for melting
s = normalized solidification or melting distance, δ/ℓ
$U_a = T_a/T_i$ for solidification
$= T_a/T_e$ for melting
u = normalized temperature, $PT/(T_i - T_a)$
$\bar{x}$ = normalized space coordinate, x/ℓ
τ = normalized time, $Pk(T_i - T_a)t/\rho L \ell^2$
$\tau' = \tau/\epsilon = \alpha t/\ell^2$
ϵ = perturbation parameter, $PC_p(T_i - T_a)/L$

$$
\begin{aligned}
u_0 &= \frac{DB_0R}{(1+B_0Rs)}\bar{x} + u_i - \frac{DB_0Rs}{(1+B_0Rs)} \\
g_0 &= \frac{1}{P}\frac{DB_0R}{(1+B_0Rs)} \qquad (19) \\
u_{0,s} &= u_i - \frac{DB_0Rs}{(1+B_0Rs)}
\end{aligned}
$$

where $D = u_i - u_a$.

The first-order solution is

$$u_1 = -\frac{g_0DB_0R}{(1+B_0Rs)^2}\left\{\frac{B_0R}{6}\bar{x}^3 + \frac{1}{2}\bar{x}^2 - \frac{(3+B_0Rs)s^2}{6(1+B_0Rs)}(B_0R\bar{x}+1)\right\}$$

$$
\begin{aligned}
g_1 &= \frac{1}{P}\frac{\partial u_1}{\partial \bar{x}}\bigg|_{\bar{x}=s} \\
&= -\frac{1}{P}\frac{g_0DB_0R}{3}\frac{s}{(1+B_0Rs)^3}(B_0{}^2R^2s^2 + 3B_0Rs + 3)
\end{aligned}
$$

$$u_{1,s} = \frac{g_0DB_0R}{(1+B_0Rs)^3}\left(\frac{B_0R}{6}s^3 + \frac{1}{2}s^2\right) \qquad (20)$$

The second-order solution is

$$
\begin{aligned}
u_2 = \frac{1}{P}\frac{g_0(DB_0R)^2}{(1+B_0Rs)^4}\bigg\{&\frac{(B_0R)^2}{40}\bar{x}^5 + \frac{B_0R}{8}\bar{x}^4 \\
&+ \frac{s(B_0{}^2R^2s^2 + 3B_0Rs + 12)}{6(1+B_0Rs)}\left(\frac{B_0R}{6}\bar{x}^3 + \frac{1}{2}\bar{x}^2\right) \\
&- \frac{s^3}{360(1+B_0Rs)^2}[19(B_0Rs)^3 + 114(B_0Rs)^2 \\
&+ 255B_0Rs + 360](B_0R\bar{x}+1)\bigg\}
\end{aligned}
$$

$$
\begin{aligned}
g_2 &= \frac{1}{P}\frac{\partial u_2}{\partial \bar{x}}\bigg|_{\bar{x}=s} \\
&= \frac{1}{P^2}\frac{g_0(DB_0R)^2s^2}{360(1+B_0Rs)^6}[56(B_0Rs)^4 + 336(B_0Rs)^3 \\
&\quad + 840(B_0Rs)^2 + 1080\,B_0Rs + 720] \\
u_{2,s} &= \frac{1}{P}\frac{g_0(DB_0R)^2s^3}{360(1+B_0Rs)^6}[19(B_0Rs)^3 + 114(B_0Rs)^2 \\
&\quad + 255\,B_0Rs + 360)] \qquad (21)
\end{aligned}
$$

The temperature distribution can be expressed as

$$u(s, \bar{x}; \epsilon) = u_0 + \epsilon u_1 + \epsilon^2 u_2 \qquad (22)$$

The surface temperature is

$$u(s, 0; \epsilon) = u_{0,s} + \epsilon u_{1,s} + \epsilon^2 u_{2,s} \qquad (23)$$

The speed of the moving boundary is

$$g(s, \bar{x}; \epsilon) = g_0\left(1 + \epsilon\frac{g_1}{g_0} + \epsilon^2\frac{g_2}{g_0}\right) \qquad (24)$$

Equation (24) can be inverted and integrated to give

$$
\begin{aligned}
\tau &= \int_0^s \frac{1}{g_0}\left\{1 - \epsilon\frac{g_1}{g_0} + \epsilon^2\left[\left(\frac{g_1}{g_0}\right)^2 - \frac{g_2}{g_0}\right]\right\}ds \\
&= \frac{P}{DB_0R}\left(\frac{B_0R}{2}s^2 + s\right) + \frac{\epsilon}{3}\left[\frac{s^2}{2} + \frac{s}{B_0R} - \frac{s}{B_0R(1+B_0Rs)}\right] \\
&\quad - \frac{\epsilon^2}{P}\frac{D}{360}\left\{8s^2 + \frac{16}{B_0R}s - \frac{1}{(B_0R)^2}\left[\frac{40}{(1+B_0Rs)^4}\right.\right. \\
&\quad \left.\left. - \frac{72}{(1+B_0Rs)^3} + \frac{40}{(1+B_0Rs)} - 8\right]\right\} \qquad (25)
\end{aligned}
$$

As expressed in equation (9), both equations (22) and (24) hold only for small temperature difference. In order to improve the accuracy and extending the present analysis to include moderate temperature difference, equation (9) has to be modified. This is accomplished by expanding T^4 in a Taylor series about T_a and including the second-order term

$$T^4 - T_a{}^4 \approx 4T_a{}^3(T - T_a) + 6T_a{}^2(T - T_a)^2 + \ldots \qquad (26)$$

Substituting equation (26) into equation (3) and following the similar procedures, solutions for u and s up to the first-order are obtained, thus

$$
\begin{aligned}
u &\approx u_0 + \epsilon u_1 \\
&= \frac{y_1 - y_2{}^{1/2}}{2Gs^2}\bar{x} + u_i - \frac{y_1 - y_2{}^{1/2}}{2Gs} + \frac{\epsilon}{P}\frac{y_1 - y_2{}^{1/2}}{2Gs^2} \\
&\quad \left\{\frac{y_2{}^{-1/2}(y_1+y_2) - (1+y_1)}{12G_s{}^3}\bar{x}^3 + \frac{1 - y_1y_2{}^{-1/2}}{4Gs^2}\bar{x}^2\right. \\
&\quad \left. - \frac{[(2-y_1) + (y_2 - 2y_1)y_2{}^{-1/2}]}{12Gy_2{}^{1/2}]}\left[\frac{(y_2{}^{1/2} - 1)}{s}\bar{x} + 1\right]\right\} \qquad (27)
\end{aligned}
$$

$$
\begin{aligned}
u_s &= u_{0,s} + \epsilon u_{1,s} \\
&= u_i - \frac{y_1 - y_2{}^{1/2}}{2Gs}\left\{1 + \frac{\epsilon}{P}\frac{(2-y_1) + y_2{}^{-1/2}(y_2 - 2y_1)}{12Gsy_2{}^{1/2}}\right\} \qquad (28)
\end{aligned}
$$

$$
\begin{aligned}
\tau &= \int_0^s \frac{1}{g_0}\left[1 - \epsilon\frac{g_1}{g_0}\right]ds \\
&= \frac{8GP}{b^2 - 4a}\left\{\frac{b}{4}s^2 + s + \frac{(2as+b)}{4a}\sqrt{y_2}\right. \\
&\quad \left. + \frac{\Delta}{8a}\frac{1}{\sqrt{a}}\ell\text{n}\left(\frac{2\sqrt{ay_2} + 2as + b}{2\sqrt{a} + b}\right) - \frac{b}{4a}\right\} + \frac{\epsilon}{3}\left\{\frac{s^2}{2}\right. \\
&\quad + \frac{1}{2a}\ell\text{n}y_2 + \frac{1}{a}(y_2{}^{1/2} - 1) + \frac{b}{2a}\frac{1}{\sqrt{a}}\ell\text{n}\left(\frac{2\sqrt{a} + b}{2\sqrt{ay_2} + 2as + b}\right) \\
&\quad \left. + \frac{b}{2a}\frac{1}{\sqrt{-\Delta}}\ell\text{n}\left(\frac{b - \sqrt{-\Delta}}{b + \sqrt{-\Delta}}\cdot\frac{b + 2as + \sqrt{-\Delta}}{b + 2as - \sqrt{-\Delta}}\right)\right\} \qquad (29a)
\end{aligned}
$$

for solidification case and

$$
\begin{aligned}
\tau &= \frac{8GP}{b^2 - 4a}\left\{\frac{b}{4}s^2 + s + \frac{(2as+b)}{4a}\sqrt{y_2}\right. \\
&\quad \left. + \frac{\Delta}{8a\sqrt{a}}\left(\sinh^{-1}\frac{2as+b}{\sqrt{\Delta}} - \sinh^{-1}\frac{b}{\sqrt{\Delta}}\right) - \frac{b}{4a}\right\} \\
&\quad + \frac{\epsilon}{3}\left\{\frac{s^2}{2} + \frac{1}{2a}\ell\text{n}y_2 + \frac{1}{a}y_2{}^{1/2}\right. \\
&\quad - \frac{b}{2a}\frac{2}{\sqrt{\Delta}}\left(\tan^{-1}\frac{2as+b}{\sqrt{\Delta}} - \tan^{-1}\frac{b}{\sqrt{\Delta}}\right) \\
&\quad \left. - \frac{b}{2a}\frac{1}{\sqrt{a}}\left(\sinh^{-1}\frac{2as+b}{\sqrt{\Delta}} - \sinh^{-1}\frac{b}{\sqrt{\Delta}}\right) - \frac{1}{a}\right\} \qquad (29b)
\end{aligned}
$$

for melting case, where

$$r = 4u_a{}^3 + 12u_a{}^2D + \frac{B_0}{H}$$

$$G = 6Hu_a{}^2$$

$$a = H^2r^2 - 4HDGr + 4D^2G^2$$

$$b = 2rH$$

$$y_1 = \frac{b}{2}s + 1$$

$$y_2 = as^2 + bs + 1$$

$$\Delta = 4a - b^2$$

The above analysis shows that the complicated phase change problem involving radiative and convective cooling (or heating) can be solved by using the perturbation method. Different approximate procedures are taken in treating the radiative term. The temperature distributions as well as the interface position and the surface temperature variations can be expressed in analytical forms. Evaluation of these quantities are straight forward and much simpler as compared to other approaches involving numerical integration.

Results and Discussion

In this section, comparison between the present study and the existing solutions on solidification are presented. At small temperature difference, $U_a = 0.75$. Fig. 2 shows the variation of freezing front with time for different values of the perturbation parameter, ϵ. Both the radiation parameter and Biot's number are taken as unity. For small values of ϵ, the modified perturbation solution, equation (29*a*), coincides with the result from the variational method utilizing numerical integration [15]. Even at the limiting situation when ϵ equals to unity, the difference is still small. The solidification rate can be easily evaluated from the slope of the curves. The total solidification time can also be found in Fig. 2 at s equals to unity. As compared to the numerical integration involved in the variational method, the present analysis requires much less computer time in evaluating the freezing front location. To simulated a phase change problem, the perturbation method usually requires only one tenth of the computational time as compared to the variational method. Fig. 3 shows that the surface temperature gradually decreases from unity as time increases. The difference between the present analysis and the variational method increases slightly with ϵ. At moderate temperature difference, $U_a = 0.50$, Fig. 4 shows close agreement between equation (29*a*) and the results from the variational method. However, apparent difference is observed when equation (25) is used. This is due to the limitation on linearization of the radiation term, equation (9). Fig. 5 shows that for moderate ϵ the difference between these two methods gradually decreases at later stage of the solidification process. As compared to other numerical results, Fig. 6 shows that equation (29*a*) is still applicable even at relatively large temperature difference, $U_a = 0.25$. It also indicates that apparent improvement in accuracy is achieved by including terms up to the quadratic one in series expansion of the radiative term (equation (29*a*) versus equation (25)). However, the problem will become too complicated to handle analytically if higher order terms in the series are included. At $U_a = 0.25$, Fig. 7 shows that the surface temperature difference between the present analysis and the numerical results of [15] is about ten percent.

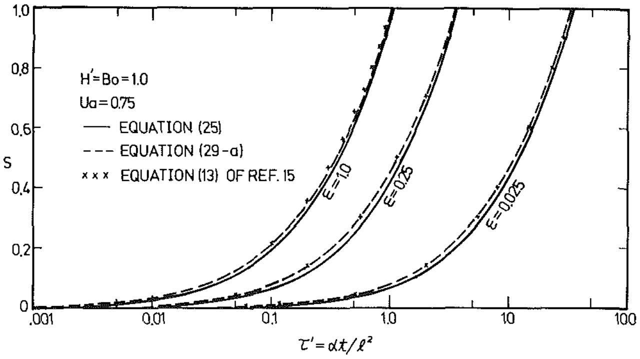

Fig. 2 Normalized interface position versus time

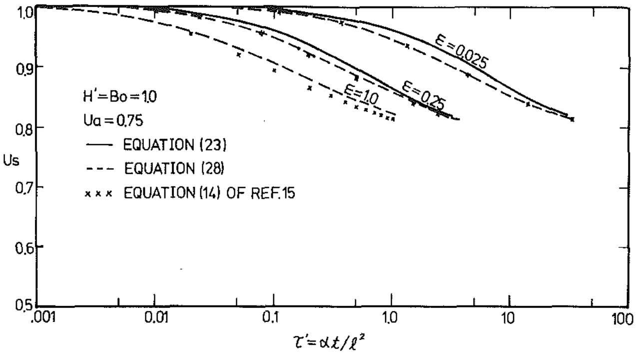

Fig. 3 Normalized surface temperature versus time

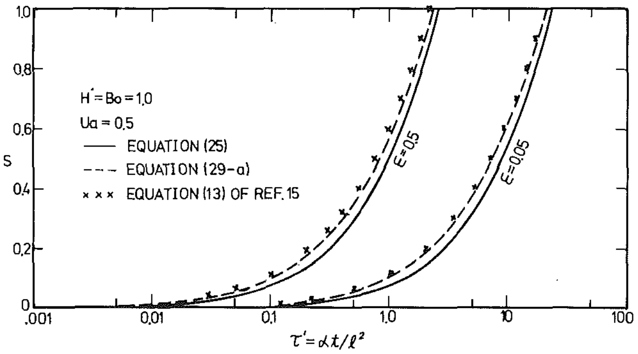

Fig. 4 Normalized interface position versus time

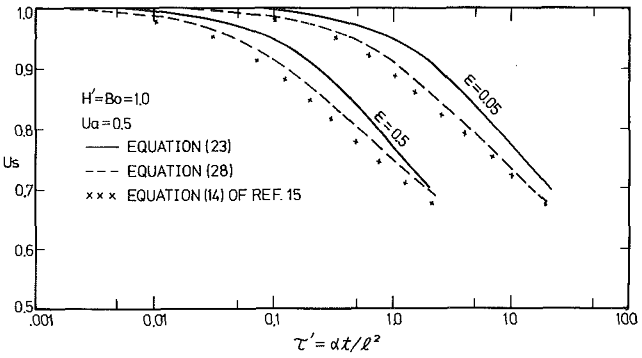

Fig. 5 Normalized surface temperature versus time

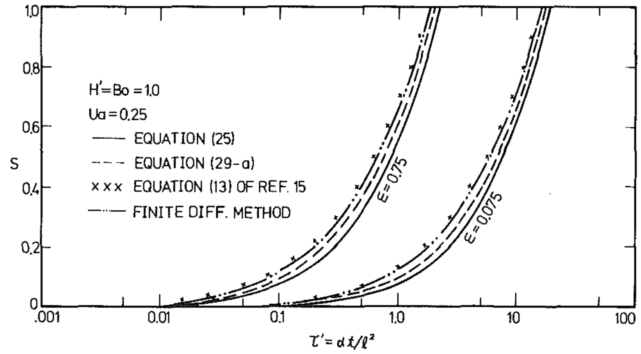

Fig. 6 Normalized interface position versus time

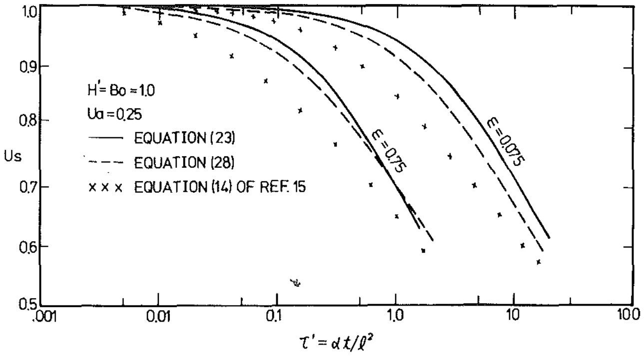

Fig. 7 Normalized surface temperature versus time

Conclusion

Approximate analytical solutions for the phase change problem involving radiative and convective boundary condition are presented. Both the temperature distributions and the interface position are obtained by approximating the radiation term with a Taylor series expansion. Perturbation method is then used in solving the one-dimensional heat conduction problem. For small and moderate temperature differences, close agreement is observed between the present analysis and the existing numerical solutions while a considerable saving in computer time is achieved by the perturbation method. At relatively large temperature difference results show that perturbation method is still applicable for practical purpose. When initial temperature differs from the fusion temperature, the problem becomes much more complicated as compared to the present one. The possibility of extending the perturbation technique to include that case is now under investigation.

References

1 Carslaw, H. S., and Jaeger, J. C., *Conduction of Heat in Solids,* 2nd ed., Clarendon Press, Oxford, 1959.

2 Biot, M. A., "New Methods in Heat Flow Analysis with Application to Flight Structures," *Journal of the Aeronautical Sciences,* Vol. 24, Dec. 1957, pp. 857–873.

3 Biot, M. A., "Further Developments of New Methods in Heat Flow Analysis," *Journal of the Aerospace Sciences,* Vol. 26, June 1959, pp. 367–381.

4 Biot, M. A., *Variational Principle in Heat Transfer,* Clarendon Press, Oxford, 1970.

5 Goodman, T. R., "The Heat-Balance Integral and Its Application to Problems Involving a Change of Phase," Trans ASME, Vol. 80, Feb. 1958, pp. 335–342.

6 Lardner, T. J., "Approximate Solutions to Phase-Change Problems," *AIAA Journal,* Vol. 5, Nov. 1967, pp. 2079–2080.

7 Biot, M. A., and Daughaday, H., "Variational Analysis of Ablation," *Journal of the Aerospace Science,* Vol. 29, Feb. 1962, pp. 227–229.

8 Biot, M. A., and Agrawal, H. C., "Variational Analysis of Ablation for Variable Properties," ASME JOURNAL OF HEAT TRANSFER, Vol. 86, Aug. 1964, pp. 437–442.

9 Prasad, A., and Agrawal, H. C., "Biot's Variational Principle for Aerodynamic Ablation of Melting Solids," *AIAA Journal,* Vol. 12, Feb. 1974, pp. 250–252.

10 Prasad, A., and Agrawal, H. C., "Biot's Variational Principle for a Stefan Problem," *AIAA Journal,* Vol. 10, March 1972, pp. 325–327.

11 Goodman, T. R., and Shea, J. J., "The Melting of Finite Slabs," *Journal of Applied Mechanics,* Vol. 82, 1960, pp. 16–24.

12 Cho, S. H., and Sunderland, J. E., "Approximate Solution for Rate of Sublimation—Dehydration of Foods," *Transactions of the ASAE,* Vol. 13, 1970, pp. 559–561.

13 Tien, R. H., and Geiger, G. E., "A Heat-Transfer Analysis of the Solidification of a Binary Eutectic System," ASME JOURNAL OF HEAT TRANSFER, Vol. 89, 1967, pp. 230–233.

14 Imber, M., and Huang, P. N. S., "Phase Change in a Semi-infinite Solid with Temperature Dependent Thermal Properties," *International Journal of Heat and Mass Transfer,* Vol. 16, Oct. 1973, pp. 1951–1954.

15 Chung, B. T. F., and Yeh, L. T., "Solidification and Melting of Materials Subject to Convection and Radiation," *Journal of Spacecraft,* Vol. 12, No. 6, 1975, pp. 329–333.

16 Pedroso, R. I., and Domoto, G. A., "Perturbation Solution for Spherical Solidification of Saturated Liquids, "ASME JOURNAL OF HEAT TRANSFER, Vol. 95, 1973, pp. 42–46.

17 Pedroso, R. I., and Domoto, G. A., "Exact Solution by Perturbation Method for Planar Solidification of a Saturated Liquid with Convection at the Wall," *International Journal of Heat and Mass Transfer,* Vol. 16, 1973, pp. 1816–1819.

18 Yan, M. M., "Perturbation Solutions to Phase Change Problem Subject to Radiation and Convection," M.S. Thesis, Chung Cheng Institute of Technology, Taiwan, Republic of China, 1976.

J. A. Wiebelt
Professor.

J. B. Henderson
Research Associate.

School of Mechanical Engineering,
Oklahoma State University,
Stillwater, Okla.

Selected Ordinates for Total Solar Radiant Property Evaluation from Spectral Data

Total radiant properties of materials at the earth's surface are a function of the condition and type of atmosphere traversed by the sun's energy. Therefore, the solar irradiation at the earth's surface has been reexamined using the latest atmospheric data. Based on these calculations a new and expanded set of selected ordinates was calculated. These ordinates are used to evaluate the total solar transmittance, or other properties, for a wide variety of atmospheric conditions, from the spectral data.

Introduction

The evaluation of the absorptance or transmittance of solar collector glazing materials requires a knowledge of the spectral characteristics of the solar irradiation (insolation). Since this is normally at the earth's surface, the insolation must be evaluated after the sun's rays have passed through varying amounts and types of atmosphere. Since the paper by Olson [1] was written, the characteristics of the insolation outside the earth's atmosphere has been refined by Thekaekara [2]. A large and expanding data base on absorption and scattering coefficients for the atmosphere has been and is being collected by the Air Force-Cambridge Research Laboratories [3]. With these new data available, a new and expanded set of selected ordinates for use in evaluating transmittance was prepared.

Selected Ordinate Procedure

The normal method of evaluating the total transmittance for material from spectral transmittance property data is shown in equation (1).

$$\tau = \frac{\int_{\lambda_1}^{\lambda_2} G_\lambda \, \tau_\lambda d\lambda}{\int_{\lambda_1}^{\lambda_2} G_\lambda d\lambda} \tag{1}$$

where G_λ is the spectral solar irradiation, τ_λ is the spectral transmittance, λ_1 is the shortest wavelength of the solar irradiation, λ_2 is the longest wavelength of the solar irradiation.

If equation (1) were to be evaluated rigorously, the continuous values of the spectral solar irradiation and material spectral transmittance would be required. This is normally not available so the evaluation is made by the approximation of equation (2).

$$\tau = \frac{\sum_{i=1}^{N} G_{\Delta\lambda_i} \, \tau_{\Delta\lambda_i} \, \Delta\lambda_i}{\sum_{i=1}^{N} G_{\Delta\lambda_i} \, \Delta\lambda_i} \tag{2}$$

where $G_{\Delta\lambda_i}$ is the average value of the spectral solar irradiation in the wavelength interval λ to $\lambda + \Delta\lambda_i$, $\tau_{\Delta\lambda_i}$ is the average transmittance in this wavelength interval.

Evaluation of equation (2) is much simpler if the wavelength intervals are properly chosen. In the selected ordinates method [1] the intervals are chosen such that $(G_{\Delta\lambda_i} \, \Delta\lambda_i)$ values are all equal, i.e., $G_{\Delta\lambda_1} \, \Delta\lambda_1 = G_{\Delta\lambda_2} \, \Delta\lambda_2 = \cdots = G_{\Delta\lambda_n} \, \Delta\lambda_n$. If this is done, equation (2) becomes,

$$\tau = \frac{\sum_{i=1}^{N} \tau_{\Delta\lambda_i}}{N} \tag{3}$$

Thus, if $\tau_{\Delta\lambda_i}$ is assumed to be the average value of the spectral transmittance in the wavelength interval $\Delta_{\lambda i}$, the transmittance is easily determined.

Method. Solar collector evaluations require the solar transmittance for the entire day. This implies the need for insolation at the collector location for zenith angles from 0 to 90 deg with varying types of atmosphere. Insolation outside of the atmosphere has been reevaluated in recent years resulting in some changes in the spectral distribution [2]. The NASA standard solar spectral insolation curve for the solar insolation outside of the earth's atmosphere was used in this work. The detailed structure presented by Thekaekara [2], which integrates to a solar constant value of 1353 W/m^2, was used.

To determine the insolation after passing through the atmosphere, the work of Selby, et al. [4] as presented in a computer program

---

Contributed by the Heat Transfer Division for publication in the JOURNAL OF HEAT TRANSFER. Manuscript received by the Heat Transfer Division June 29, 1978.

Table 1 20 equal energy bands—U.S. Standard atmosphere rural aerosol model

Visibility (Km)	Elevation above sea level (Km)	Energy band number	Zenith Angle of Sun					
			0^{o}		60^{o}		75^{o}	
			Abscissa Range μm	Abscissa Midpoint μm	Abscissa Range μm	Abscissa Midpoint μm	Abscissa Range μm	Abscissa Midpoint μm
23	0	1	0.300-0.409	0.374	0.300-0.438	0.405	0.300-0.480	0.446
		2	0.409-0.453	0.432	0.438-0.482	0.461	0.480-0.535	0.508
		3	0.453-0.487	0.470	0.482-0.522	0.502	0.535-0.585	0.561
		4	0.487-0.522	0.504	0.522-0.561	0.541	0.585-0.631	0.609
		5	0.522-0.558	0.540	0.561-0.601	0.582	0.631-0.671	0.653
		6	0.558-0.594	0.577	0.601-0.639	0.620	0.671-0.711	0.691
		7	0.594-0.632	0.612	0.639-0.677	0.658	0.711-0.753	0.733
		8	0.632-0.670	0.651	0.677-0.716	0.695	0.753-0.797	0.777
		9	0.670-0.710	0.689	0.716-0.759	0.736	0.797-0.839	0.816
		10	0.710-0.752	0.732	0.759-0.805	0.783	0.839-0.880	0.862
		11	0.752-0.802	0.778	0.805-0.853	0.829	0.880-0.940	0.905
		12	0.802-0.854	0.827	0.853-0.902	0.877	0.940-1.010	0.983
		13	0.854-0.909	0.881	0.902-0.982	0.932	1.010-1.058	1.031
		14	0.909-0.994	0.954	0.982-1.041	1.012	1.058-1.115	1.087
		15	0.994-1.063	1.025	1.041-1.108	1.071	1.115-1.219	1.183
		16	1.063-1.173	1.103	1.108-1.217	1.178	1.219-1.290	1.251
		17	1.173-1.277	1.220	1.217-1.321	1.264	1.290-1.562	1.494
		18	1.277-1.564	1.451	1.321-1.617	1.535	1.562-1.682	1.613
		19	1.564-1.948	1.662	1.617-2.041	1.695	1.682-2.142	1.765
		20	1.948-5.000	2.283	2.041-5.000	2.288	2.142-5.000	2.323
23	1.5	1	0.300-0.402	0.366	0.300-0.421	0.389	0.300-0.453	0.420
		2	0.402-0.444	0.424	0.421-0.465	0.446	0.453-0.499	0.477
		3	0.444-0.478	0.461	0.465-0.501	0.483	0.499-0.541	0.520
		4	0.478-0.510	0.494	0.501-0.537	0.519	0.541-0.583	0.562
		5	0.510-0.546	0.528	0.537-0.574	0.556	0.583-0.624	0.603
		6	0.546-0.582	0.563	0.574-0.611	0.592	0.624-0.662	0.644
		7	0.582-0.618	0.600	0.611-0.650	0.631	0.662-0.701	0.682
		8	0.618-0.656	0.637	0.650-0.688	0.669	0.701-0.740	0.720
		9	0.656-0.697	0.676	0.688-0.728	0.708	0.740-0.784	0.761
		10	0.697-0.740	0.718	0.728-0.776	0.750	0.784-0.829	0.806
		11	0.740-0.791	0.767	0.776-0.821	0.798	0.829-0.873	0.851
		12	0.791-0.842	0.815	0.821-0.874	0.846	0.873-0.925	0.897
		13	0.842-0.900	0.870	0.874-0.929	0.900	0.925-1.002	0.972
		14	0.900-0.980	0.936	0.929-1.009	0.978	1.002-1.058	1.027
		15	0.980-1.055	1.016	1.009-1.079	1.043	1.058-1.142	1.092
		16	1.055-1.159	1.096	1.079-1.190	1.126	1.142-1.232	1.196
		17	1.159-1.275	1.211	1.190-1.289	1.235	1.232-1.345	1.281
		18	1.275-1.549	1.371	1.289-1.581	1.486	1.345-1.627	1.552
		19	1.549-1.892	1.656	1.581-1.990	1.673	1.627-2.059	1.708
		20	1.892-5.000	2.291	1.990-5.000	2.292	2.059-5.000	2.299
5	0	1	0.300-0.434	0.399	0.300-0.489	0.448	0.300-0.606	0.540
		2	0.434-0.483	0.461	0.489-0.555	0.523	0.606-0.689	0.652
		3	0.483-0.527	0.505	0.555-0.612	0.583	0.689-0.755	0.723
		4	0.527-0.571	0.549	0.612-0.662	0.638	0.755-0.813	0.789
		5	0.571-0.611	0.592	0.662-0.708	0.684	0.813-0.868	0.842
		6	0.611-0.653	0.632	0.708-0.753	0.732	0.868-0.918	0.890
		7	0.653-0.695	0.675	0.753-0.803	0.781	0.918-0.994	0.970
		8	0.695-0.738	0.716	0.803-0.852	0.827	0.994-1.041	1.017
		9	0.738-0.785	0.761	0.852-0.897	0.874	1.041-1.086	1.063
		10	0.785-0.834	0.810	0.897-0.970	0.923	1.086-1.172	1.110
		11	0.834-0.884	0.860	0.970-1.022	0.998	1.172-1.223	1.196
		12	0.884-0.952	0.911	1.022-1.075	1.047	1.223-1.276	1.253
		13	0.952-1.017	0.987	1.075-1.163	1.099	1.276-1.498	1.306
		14	1.017-1.081	1.050	1.163-1.226	1.194	1.498-1.571	1.534
		15	1.081-1.179	1.119	1.226-1.301	1.259	1.571-1.637	1.598
		16	1.179-1.271	1.224	1.301-1.547	1.480	1.637-1.701	1.669
		17	1.271-1.522	1.324	1.547-1.647	1.595	1.701-2.017	1.752
		18	1.522-1.668	1.587	1.647-1.782	1.702	2.017-2.190	2.113
		19	1.668-2.143	1.771	1.782-2.261	2.112	2.190-2.350	2.270
		20	2.143-5.000	2.375	2.261-5.000	2.458	2.350-5.000	3.527

Table 2 20 equal energy bands—U.S. Standard atmosphere urban aerosol model

Visibility (Km)	Elevation above sea level (Km)	Energy band number	Zenith Angle of Sun					
			0°		60°		75°	
			Abscissa Range μm	Abscissa Midpoint μm	Abscissa Range μm	Abscissa Midpoint μm	Abscissa Range μm	Abscissa Midpoint μm
23	0	1	0.300-0.408	0.372	0.300-0.434	0.402	0.300-0.475	0.441
		2	0.408-0.451	0.431	0.434-0.479	0.458	0.475-0.528	0.502
		3	0.451-0.485	0.469	0.479-0.517	0.498	0.528-0.576	0.552
		4	0.485-0.520	0.502	0.517-0.557	0.537	0.576-0.622	0.599
		5	0.520-0.555	0.537	0.557-0.595	0.576	0.622-0.663	0.642
		6	0.555-0.592	0.573	0.595-0.633	0.614	0.663-0.700	0.681
		7	0.592-0.628	0.609	0.633-0.670	0.652	0.700-0.743	0.721
		8	0.628-0.667	0.646	0.670-0.710	0.690	0.743-0.787	0.766
		9	0.667-0.706	0.685	0.710-0.752	0.730	0.787-0.828	0.806
		10	0.706-0.749	0.728	0.752-0.799	0.775	0.828-0.872	0.851
		11	0.749-0.798	0.774	0.799-0.845	0.820	0.872-0.920	0.894
		12	0.798-0.849	0.823	0.845-0.894	0.869	0.920-1.000	0.972
		13	0.849-0.907	0.876	0.894-0.975	0.923	1.000-1.050	1.024
		14	0.907-0.987	0.947	0.975-1.035	1.003	1.050-1.102	1.073
		15	0.987-1.058	1.021	1.035-1.101	1.064	1.102-1.205	1.171
		16	1.058-1.167	1.098	1.101-1.212	1.170	1.205-1.280	1.242
		17	1.167-1.275	1.218	1.212-1.310	1.258	1.280-1.552	1.346
		18	1.275-1.559	1.417	1.310-1.603	1.532	1.552-1.667	1.603
		19	1.559-1.816	1.666	1.603-2.049	1.689	1.667-2.131	1.750
		20	1.816-5.000	2.265	2.049-5.000	2.292	2.131-5.000	2.305
23	1.5	1	0.300-0.400	0.365	0.300-0.420	0.388	0.300-0.451	0.418
		2	0.400-0.444	0.422	0.420-0.464	0.444	0.451-0.496	0.475
		3	0.444-0.476	0.460	0.464-0.499	0.481	0.496-0.537	0.517
		4	0.476-0.509	0.493	0.499-0.534	0.517	0.537-0.579	0.559
		5	0.509-0.544	0.527	0.534-0.572	0.554	0.579-0.619	0.599
		6	0.544-0.581	0.562	0.572-0.610	0.591	0.619-0.658	0.639
		7	0.581-0.617	0.599	0.610-0.648	0.627	0.658-0.696	0.677
		8	0.617-0.655	0.636	0.648-0.686	0.666	0.696-0.736	0.715
		9	0.655-0.695	0.676	0.686-0.725	0.705	0.736-0.779	0.754
		10	0.695-0.739	0.716	0.725-0.772	0.747	0.779-0.824	0.801
		11	0.739-0.788	0.763	0.772-0.820	0.794	0.824-0.869	0.845
		12	0.788-0.841	0.814	0.820-0.868	0.844	0.869-0.921	0.892
		13	0.841-0.898	0.869	0.868-0.927	0.897	0.921-0.995	0.964
		14	0.898-0.975	0.932	0.927-1.004	0.974	0.995-1.055	1.024
		15	0.975-1.052	1.014	1.004-1.077	1.037	1.055-1.130	1.082
		16	1.052-1.156	1.093	1.077-1.182	1.118	1.130-1.231	1.190
		17	1.156-1.270	1.213	1.182-1.286	1.232	1.231-1.334	1.273
		18	1.270-1.551	1.349	1.286-1.575	1.477	1.334-1.621	1.547
		19	1.551-1.834	1.658	1.575-1.981	1.676	1.621-2.050	1.701
		20	1.834-5.000	2.292	1.981-5.000	2.273	2.050-5.000	2.302
5	0	1	0.300-0.427	0.392	0.300-0.477	0.439	0.300-0.580	0.519
		2	0.427-0.477	0.454	0.477-0.538	0.509	0.580-0.666	0.628
		3	0.477-0.519	0.497	0.538-0.593	0.567	0.666-0.728	0.696
		4	0.519-0.560	0.539	0.593-0.643	0.619	0.728-0.790	0.757
		5	0.560-0.601	0.581	0.643-0.689	0.666	0.790-0.842	0.815
		6	0.601-0.642	0.621	0.689-0.735	0.710	0.842-0.891	0.865
		7	0.642-0.682	0.663	0.735-0.783	0.757	0.891-0.967	0.919
		8	0.682-0.725	0.704	0.783-0.829	0.806	0.967-1.017	0.995
		9	0.725-0.773	0.748	0.829-0.876	0.854	1.017-1.062	1.040
		10	0.773-0.820	0.797	0.876-0.928	0.902	1.062-1.113	1.085
		11	0.820-0.872	0.847	0.928-1.003	0.975	1.113-1.204	1.174
		12	0.872-0.929	0.899	1.003-1.057	1.027	1.204-1.254	1.231
		13	0.929-1.005	0.974	1.057-1.112	1.084	1.254-1.320	1.283
		14	1.005-1.070	1.037	1.112-1.209	1.174	1.320-1.551	1.519
		15	1.070-1.166	1.106	1.209-1.279	1.246	1.551-1.623	1.587
		16	1.166-1.258	1.213	1.279-1.527	1.331	1.623-1.693	1.652
		17	1.258-1.510	1.312	1.527-1.630	1.573	1.693-1.979	1.731
		18	1.510-1.657	1.580	1.630-1.761	1.693	1.979-2.177	2.107
		19	1.657-2.135	1.757	1.761-2.248	2.108	2.177-2.367	2.271
		20	2.135-5.000	2.380	2.248-5.000	2.459	2.367-5.000	3.596

Table 3 20 equal energy bands—tropical atmosphere rural aerosol model

Visibility (Km)	Elevation above sea level (Km)	Energy band number	Zenith Angle of Sun					
			0°		60°		75°	
			Abscissa Range µm	Abscissa Midpoint µm	Abscissa Range µm	Abscissa Midpoint µm	Abscissa Range µm	Abscissa Midpoint µm
23	0	1	0.300-0.407	0.371	0.300-0.434	0.403	0.300-0.476	0.443
		2	0.407-0.450	0.429	0.434-0.479	0.459	0.476-0.529	0.504
		3	0.450-0.483	0.466	0.479-0.516	0.498	0.529-0.575	0.552
		4	0.483-0.516	0.500	0.516-0.554	0.535	0.575-0.617	0.596
		5	0.516-0.550	0.533	0.554-0.591	0.572	0.617-0.657	0.638
		6	0.550-0.586	0.568	0.591-0.627	0.609	0.657-0.693	0.674
		7	0.586-0.621	0.603	0.627-0.663	0.645	0.693-0.734	0.710
		8	0.621-0.657	0.638	0.663-0.699	0.681	0.734-0.775	0.752
		9	0.657-0.694	0.675	0.699-0.740	0.718	0.775-0.813	0.794
		10	0.694-0.737	0.714	0.740-0.785	0.759	0.813-0.858	0.840
		11	0.737-0.783	0.756	0.785-0.831	0.804	0.858-0.902	0.877
		12	0.783-0.833	0.806	0.831-0.874	0.852	0.902-0.994	0.940
		13	0.833-0.884	0.859	0.874-0.940	0.899	0.994-1.039	1.015
		14	0.884-0.969	0.915	0.940-1.019	0.990	1.039-1.089	1.063
		15	0.969-1.038	1.005	1.019-1.078	1.050	1.089-1.199	1.154
		16	1.038-1.118	1.074	1.078-1.199	1.117	1.199-1.260	1.226
		17	1.118-1.244	1.199	1.199-1.285	1.235	1.260-1.543	1.301
		18	1.244-1.547	1.303	1.285-1.591	1.518	1.543-1.646	1.588
		19	1.547-1.749	1.638	1.591-1.791	1.672	1.646-2.099	1.715
		20	1.749-5.000	2.217	1.791-5.000	2.240	2.099-5.000	2.253
23	1.5	1	0.300-0.400	0.364	0.300-0.420	0.388	0.300-0.451	0.419
		2	0.400-0.442	0.421	0.420-0.463	0.444	0.451-0.496	0.474
		3	0.442-0.475	0.459	0.463-0.497	0.480	0.496-0.536	0.516
		4	0.475-0.507	0.490	0.497-0.532	0.515	0.536-0.576	0.556
		5	0.507-0.541	0.523	0.532-0.568	0.550	0.576-0.613	0.594
		6	0.541-0.575	0.557	0.568-0.602	0.585	0.613-0.649	0.632
		7	0.575-0.610	0.592	0.602-0.639	0.620	0.649-0.685	0.668
		8	0.610-0.646	0.627	0.639-0.675	0.658	0.685-0.723	0.704
		9	0.646-0.684	0.665	0.675-0.714	0.694	0.723-0.766	0.743
		10	0.684-0.726	0.705	0.714-0.756	0.734	0.766-0.808	0.787
		11	0.726-0.775	0.749	0.756-0.801	0.781	0.808-0.852	0.830
		12	0.775-0.822	0.798	0.801-0.853	0.827	0.852-0.896	0.876
		13	0.822-0.877	0.851	0.853-0.905	0.876	0.896-0.984	0.927
		14	0.877-0.956	0.911	0.905-0.991	0.946	0.984-1.039	1.008
		15	0.956-1.029	0.995	0.991-1.056	1.021	1.039-1.098	1.068
		16	1.029-1.112	1.069	1.056-1.164	1.089	1.098-1.212	1.172
		17	1.112-1.241	1.189	1.164-1.260	1.212	1.212-1.296	1.251
		18	1.241-1.532	1.308	1.260-1.553	1.328	1.296-1.599	1.532
		19	1.532-1.765	1.630	1.553-1.771	1.646	1.599-1.999	1.682
		20	1.765-5.000	2.240	1.771-5.000	2.241	1.999-5.000	2.246
5	0	1	0.300-0.431	0.396	0.300-0.484	0.445	0.300-0.593	0.533
		2	0.431-0.479	0.457	0.484-0.546	0.517	0.593-0.673	0.638
		3	0.479-0.521	0.500	0.546-0.600	0.575	0.673-0.738	0.705
		4	0.521-0.562	0.541	0.600-0.647	0.624	0.738-0.794	0.770
		5	0.562-0.602	0.583	0.647-0.691	0.670	0.794-0.848	0.822
		6	0.602-0.640	0.622	0.691-0.737	0.713	0.848-0.892	0.871
		7	0.640-0.679	0.661	0.737-0.783	0.759	0.892-0.984	0.921
		8	0.679-0.721	0.700	0.783-0.828	0.805	0.984-1.026	1.005
		9	0.721-0.767	0.744	0.828-0.871	0.851	1.026-1.068	1.044
		10	0.767-0.810	0.789	0.871-0.924	0.893	1.068-1.110	1.089
		11	0.810-0.861	0.839	0.924-1.002	0.977	1.110-1.207	1.184
		12	0.861-0.913	0.886	1.002-1.052	1.028	1.207-1.250	1.231
		13	0.913-0.997	0.964	1.052-1.103	1.077	1.250-1.306	1.276
		14	0.997-1.056	1.025	1.103-1.207	1.176	1.306-1.557	1.529
		15	1.056-1.150	1.088	1.207-1.271	1.236	1.557-1.608	1.578
		16	1.150-1.238	1.202	1.271-1.526	1.306	1.608-1.676	1.641
		17	1.238-1.495	1.288	1.526-1.619	1.577	1.676-1.766	1.709
		18	1.495-1.642	1.571	1.619-1.741	1.676	1.766-2.138	2.069
		19	1.642-2.099	1.727	1.741-2.212	2.071	2.138-2.303	2.214
		20	2.099-5.000	2.313	2.212-5.000	2.349	2.303-5.000	2.452

Table 4 20 equal energy bands—sub-Arctic summer atmosphere rural aerosol model

Visibility (Km)	Elevation above sea level (Km)	Energy band number	Zenith Angle of Sun					
			0^o		60^o		75^o	
			Abscissa Range µm	Abscissa Midpoint µm	Abscissa Range µm	Abscissa Midpoint µm	Abscissa Range µm	Abscissa Midpoint µm
23	0	1	0.300-0.408	0.373	0.300-0.437	0.405	0.300-0.478	0.444
		2	0.408-0.452	0.431	0.437-0.480	0.460	0.478-0.533	0.506
		3	0.452-0.486	0.469	0.480-0.520	0.500	0.533-0.582	0.558
		4	0.486-0.520	0.503	0.520-0.559	0.539	0.582-0.627	0.605
		5	0.520-0.555	0.537	0.559-0.597	0.578	0.627-0.667	0.647
		6	0.555-0.591	0.574	0.597-0.635	0.616	0.667-0.706	0.686
		7	0.591-0.628	0.609	0.635-0.672	0.654	0.706-0.747	0.726
		8	0.628-0.665	0.646	0.672-0.711	0.691	0.747-0.789	0.771
		9	0.665-0.705	0.684	0.711-0.753	0.731	0.789-0.832	0.810
		10	0.705-0.748	0.725	0.753-0.796	0.777	0.832-0.873	0.854
		11	0.748-0.796	0.774	0.796-0.846	0.820	0.873-0.924	0.895
		12	0.796-0.847	0.820	0.846-0.892	0.867	0.924-1.003	0.978
		13	0.847-0.902	0.874	0.892-0.974	0.922	1.003-1.052	1.025
		14	0.902-0.985	0.939	0.974-1.031	1.002	1.052-1.106	1.076
		15	0.985-1.054	1.020	1.031-1.099	1.062	1.106-1.208	1.178
		16	1.054-1.161	1.094	1.099-1.213	1.170	1.208-1.280	1.247
		17	1.161-1.263	1.212	1.213-1.303	1.255	1.280-1.549	1.455
		18	1.263-1.562	1.340	1.303-1.606	1.532	1.549-1.670	1.612
		19	1.562-1.792	1.651	1.606-2.028	1.684	1.670-2.122	1.745
		20	1.792-5.000	2.262	2.028-5.000	2.267	2.122-5.000	2.302
23	1.5	1	0.300-0.401	0.365	0.300-0.421	0.389	0.300-0.452	0.419
		2	0.401-0.444	0.422	0.421-0.464	0.445	0.452-0.497	0.475
		3	0.444-0.476	0.460	0.464-0.499	0.481	0.497-0.538	0.518
		4	0.476-0.509	0.492	0.499-0.535	0.517	0.538-0.580	0.560
		5	0.509-0.543	0.526	0.535-0.572	0.554	0.580-0.621	0.601
		6	0.543-0.579	0.561	0.572-0.609	0.590	0.621-0.660	0.640
		7	0.579-0.615	0.597	0.609-0.647	0.628	0.660-0.696	0.677
		8	0.615-0.653	0.634	0.647-0.683	0.666	0.696-0.736	0.715
		9	0.653-0.693	0.672	0.683-0.725	0.702	0.736-0.780	0.755
		10	0.693-0.736	0.714	0.725-0.770	0.744	0.780-0.822	0.800
		11	0.736-0.784	0.758	0.770-0.815	0.792	0.822-0.865	0.844
		12	0.784-0.835	0.808	0.815-0.866	0.842	0.865-0.917	0.889
		13	0.835-0.892	0.862	0.866-0.922	0.893	0.917-0.996	0.962
		14	0.892-0.972	0.925	0.922-1.004	0.970	0.996-1.048	1.021
		15	0.972-1.045	1.007	1.004-1.069	1.033	1.048-1.114	1.081
		16	1.045-1.146	1.086	1.069-1.182	1.107	1.114-1.228	1.186
		17	1.146-1.261	1.203	1.182-1.281	1.227	1.228-1.323	1.272
		18	1.261-1.547	1.330	1.281-1.570	1.465	1.323-1.614	1.539
		19	1.547-1.787	1.645	1.570-1.816	1.662	1.614-2.044	1.697
		20	1.787-5.000	2.269	1.816-5.000	2.271	2.044-5.000	2.278
5	0	1	0.300-0.433	0.398	0.300-0.487	0.447	0.300-0.601	0.537
		2	0.433-0.482	0.459	0.487-0.552	0.520	0.601-0.686	0.648
		3	0.482-0.525	0.503	0.552-0.607	0.580	0.686-0.749	0.717
		4	0.525-0.567	0.546	0.607-0.656	0.632	0.749-0.807	0.782
		5	0.567-0.609	0.588	0.656-0.701	0.680	0.807-0.862	0.837
		6	0.609-0.649	0.630	0.701-0.748	0.725	0.862-0.910	0.885
		7	0.649-0.690	0.670	0.748-0.795	0.775	0.910-0.991	0.961
		8	0.690-0.732	0.711	0.795-0.844	0.819	0.991-1.033	1.013
		9	0.732-0.779	0.755	0.844-0.887	0.866	1.033-1.079	1.055
		10	0.779-0.827	0.801	0.887-0.959	0.913	1.079-1.168	1.099
		11	0.827-0.876	0.853	0.959-1.016	0.992	1.168-1.218	1.191
		12	0.876-0.935	0.904	1.016-1.065	1.042	1.218-1.272	1.242
		13	0.935-1.008	0.978	1.065-1.144	1.089	1.272-1.481	1.298
		14	1.008-1.071	1.041	1.144-1.222	1.190	1.481-1.567	1.538
		15	1.071-1.171	1.108	1.222-1.286	1.250	1.567-1.624	1.595
		16	1.171-1.257	1.215	1.286-1.543	1.448	1.624-1.689	1.656
		17	1.257-1.511	1.306	1.543-1.635	1.583	1.689-1.988	1.742
		18	1.511-1.656	1.586	1.635-1.761	1.690	1.988-2.167	2.109
		19	1.656-2.123	1.749	1.761-2.239	2.109	2.167-2.331	2.245
		20	2.123-5.000	2.357	2.239-5.000	2.405	2.331-5.000	3.517

(LOWTRAN-3B) was used. Several atmosphere types are modeled in the Lowtran Computer Program. These are the 1962 Standard Atmosphere and five other climate types. Different visibilities, station elevations, air mass values and aerosol models may be considered with the program. In the use of the program the spectral detail of the atmosphere is represented by using 1568 wavelength intervals. Since the solar spectral irradiation tabulation of Thekaekara [2] has only 152 ordinate values in the wavelength range of interest, (0.3 to 5 μm) the ordinate values were linearly interpolated between the tabulated values.

The aerosol models available are "rural," "urban," "maritime," and "tropospheric." In this work the rural and urban aerosol models were used as being most representative of continental areas. These models are for the lower two kilometers of the atmosphere and consist of a specified aerosol size distribution which agreed with experimental data [7]. From the measurements the rural model was taken to consist of 70 percent water soluble material (ammonium and calcium sulfate and also organic compounds) and 30 percent dust like aerosols. The optical/IR properties of the aerosols was also taken to match measured values [7]. For the urban model the aerosol size distribution was taken to be the same as the rural model but the material was assumed to be 35 percent sootlike material and 65 percent rural mixture material. Once again the refractive index of the soot was based on experimental data.

In the troposphere above the two kilometer altitude the aerosol model was a general tropospheric model which was described as an extremely clear condition consisting of the rural model without the large particle component [7].

Results. Equal energy bands, i.e., ($G_{\Delta\lambda_i}\, \Delta\lambda_i$), were calculated for twenty bands. These energy bands are delimited by a beginning and ending wavelength. Another wavelength of interest is the wavelength in each band which divides the total band energy into two parts. Values for these wavelengths are tabulated for several atmospheres, zenith angles, visibilities, and elevations in Tables 1–4.

If additional spectral detail is required for the two extremes of the wavelength range, Table 5 may be used. The first and last energy bands for the U.S. Standard atmosphere, rural aerosol, 23 km visibility and U.S. Standard atmosphere, urban aerosol, 5 km visibility were divided into five separate equal energy subdivisions [8]. Using the average value of the spectral property as delimited by the five subdivisions for the first and last band results in additional spectral detail in these bands.

In order to compare the results of this work to Olson's [1], the values of the wavelength intervals for equal solar band energy outside the earth's atmosphere are presented in Table 6.

Finally, Table 7 presents the atmospheric total solar transmittance of several atmospheric models, visibilities, elevations and zenith angles which were calculated to compare the procedures used in the results obtained by Hottel [5].

Discussion of Results

The quality of the results obtained depends on the application of data which is continually being refined. For example, the atmospheric transmission model used in this work was included in the computer program LOWTRAN-3B while the work presented by Hottel [5] used LOWTRAN-2. This change has caused small changes in the transmittance values as shown in Table 7. Changes in LOWTRAN in model 2 and model 3B were primarily in the model for aerosols or haze in the atmosphere. For this reason, the most noticeable changes occurred when visibilities were less. If the visibility is 23 km at 1.5 km elevation, aerosols are not as important and the two procedures result in very nearly the same transmittance values.

Comparison of the results in Table 6 with the values presented by Olson [1] are not as close as the previous comparison. It was assumed that this is not only due to the change in the solar spectral irradiation data but also due to the use of a different initial and final wavelength for the solar spectrum. In this work the solar spectrum was considered to be in the wavelength range 0.2 to 5.0 μm outside the earth's atmosphere and 0.3 to 5.0 μm inside the atmosphere. Initial and final selected ordinates are changed by the choice of these ranges.

Table 5 5 band subdivision of energy bands 1 and 20—U.S. Standard atmosphere

			Zenith Angle of Sun					
			0°		60°		75°	
Visibility (Km)	Elevation above sea level (Km)	Energy band number	Abscissa Range μm	Abscissa Midpoint μm	Abscissa Range μm	Abscissa Midpoint μm	Abscissa Range μm	Abscissa Midpoint μm
			Rural Aerosol Model					
		1-1	0.300-0.344	0.332	0.300-0.369	0.350	0.300-0.411	0.390
		1-2	0.344-0.365	0.355	0.369-0.396	0.383	0.411-0.436	0.423
		1-3	0.365-0.382	0.374	0.396-0.412	0.405	0.436-0.454	0.446
		1-4	0.382-0.398	0.390	0.412-0.425	0.419	0.454-0.468	0.461
23	0	1-5	0.398-0.409	0.404	0.425-0.438	0.431	0.468-0.480	0.474
		20-1	1.948-2.094	2.033	2.041-2.139	2.093	2.142-2.207	2.166
		20-1	2.094-2.204	2.149	2.139-2.236	2.187	2.207-2.277	2.251
		20-3	2.204-2.342	2.283	2.236-2.338	2.288	2.277-2.363	2.323
		20-4	2.342-3.336	2.428	2.338-3.468	2.436	2.363-3.568	2.442
		20-5	3.336-5.000	3.812	3.468-5.000	3.791	3.568-5.000	3.821
			Urban Aerosol Model					
		1-1	0.300-0.355	0.339	0.300-0.400	0.375	0.300-0.467	0.440
		1-2	0.355-0.381	0.369	0.400-0.427	0.415	0.467-0.504	0.486
		1-3	0.381-0.402	0.392	0.427-0.447	0.439	0.504-0.533	0.519
		1-4	0.402-0.416	0.409	0.447-0.463	0.455	0.533-0.558	0.546
5	0	1-5	0.416-0.427	0.421	0.463-0.477	0.470	0.558-0.580	0.569
		20-1	2.135-2.218	2.168	2.248-2.310	2.279	2.367-2.437	2.385
		20-2	2.218-2.306	2.272	2.310-2.384	2.339	2.437-3.470	3.013
		20-3	2.306-2.440	2.380	2.384-3.249	2.459	3.470-3.695	3.596
		20-4	2.440-3.612	3.187	3.249-3.772	3.594	3.695-3.923	3.805
		20-5	3.612-5.000	3.913	3.772-5.000	4.025	3.923-5.000	4.090

Table 6 20 equal energy bands outside atmosphere (Theakakara data [2])

Energy Band No.	Abscissa Range (μm)	Abscissa Midpoint (μm)
1	0.200 - 0.356	0.324
2	0.356 - 0.410	0.386
3	0.410 - 0.449	0.430
4	0.449 - 0.482	0.465
5	0.482 - 0.516	0.499
6	0.516 - 0.554	0.535
7	0.554 - 0.593	0.573
8	0.593 - 0.635	0.614
9	0.635 - 0.680	0.657
10	0.680 - 0.729	0.704
11	0.729 - 0.785	0.756
12	0.785 - 0.847	0.815
13	0.847 - 0.920	0.883
14	0.920 - 1.003	0.960
15	1.003 - 1.105	1.051
16	1.105 - 1.235	1.166
17	1.235 - 1.411	1.316
18	1.411 - 1.655	1.521
19	1.655 - 2.153	1.841
20	2.153 - 5.000	2.705

Table 7 Total atmospheric transmittance—rural aerosol model

				Climate Models					
Aerosol Model	Visibility Km	Elevation Km	Zenith Angle	U.S. Standard	Tropical	Mid-Latitude Summer	Mid-Latitude Winter	Subarctic Summer	Subarctic Winter
Rural	23	0	0	0.6413* 0.6484	0.6194* 0.6248	0.6260* 0.6319	0.6503* 0.6580	0.6335* 0.640	— 0.6713
			60	0.4764* 0.4931	0.4563* 0.4709	0.4618* 0.4773	0.4839* 0.5020	0.4687* 0.4850	— 0.5146
			75	0.2973* 0.3241	0.2814* 0.3055	0.2857* 0.3105	0.3036* 0.3320	0.2913* 0.3170	— 0.3429
	23	1.5	0	0.7465* 0.7464	— 0.7253	— 0.7324	— 0.7550	— 0.7381	— 0.7661
			60	0.6232* 0.6291	— 0.6082	— 0.6150	— 0.6380	— 0.6204	— 0.6483
			75	0.4704* 0.4847	— 0.4651	— 0.4711	— 0.4930	— 0.4765	— 0.5032
	5	0	0	0.4077* 0.4358	— 0.4163	0.3964* 0.4223	— 0.4440	0.4016* 0.4288	— 0.4553
			60	0.2059* 0.2433	— 0.2282	0.1976* 0.2328	— 0.2490	0.2016* 0.2380	— 0.2588
			75	0.0708* 0.1041	— 0.0949	0.0669* 0.0976	— 0.1080	0.0688* 0.1008	— 0.1141

* Values from H.C. Hottel [5]

An indication of the effect of the use of this new set of selected ordinates was determined by evaluating the solar transmittance of a commercially available solar collector glazing material. This material was the commercial material "Filon" which is reinforced fiberglass plastic panels with a "Tedlar" coating. Spectral transmittance data for the material (available from the manufacturer) was used to determine the total solar transmittance. This value was obtained using the method of selected ordinates, Olson's [1] method, the method of weighted ordinates indicated by ASTM [6], and by the method of selected ordinates using the data of this work. The results obtained were:

1 Olson's selected ordinates — $\tau_s = 0.817$
2 ASTM weighted ordinates — $\tau_s = 0.835$
3 Present Work—U.S. Standard 23 km visibility—rural aerosol— 0 deg zenith angle — $\tau_s = 0.784$
4 Present work—U.S. Standard—23 km visibility—rural aerosol— 75 deg zenith angle — $\tau_s = 0.785$
5 Present work—U.S. Standard—5 km visibility—urban aerosol— 0 deg zenith angle — $\tau_s = 0.788$
6 Present work—U.S. Standard—5 km visibility—urban aerosol— 75 deg zenith angle — $\tau_s = 0.760$

Although these differences are quite small, it is obviously possible to change the expected performance of solar collectors significantly with these data.

Conclusions

If the solar transmittance, absorptance, or reflectance of any material must be determined from spectral data, the insolation at the location of interest must be considered. The method of selected ordinates presented herein will allow relatively rapid determination of the values with improved accuracy in the insolation data.

References

1 Olson, O. H., "Selected Ordinates for Solar Absorptivity Calculations," *Applied Optics,* Vol. 2, 1963.

2 Thekaekara, M. P., "Solar Energy Outside the Earth's Atmosphere," *Solar Energy,* Vol. 14, 1973.

3 Selby, J. E. A. and R. A. McClatchey, "Atmospheric Transmittance from 0.25 to 28.5 μm: Computer Code LOWTRAN-2. Air Force Cambridge Research Laboratories, -AFCRL-72-0745, Environmental Research Paper No. 427, 1972.

4 Selby, J. E. A., E. P. Shettle, and R. A. McClatchey, "Atmospheric Transmittance from 0.25 to 28.5 μm: Supplement LOWTRAN-3B (1976), Air Force Geophysics Laboratory, AFGL-TR-76-0258, 1976.

5 Hottel, H. C., "A Simple Model for Estimating the Transmittance of Direct Solar Radiation through Clear Atmospheres," *Solar Energy,* Vol. 18, 1976.

6 "Standard Test Methods for Solar Energy Transmittance and Reflectance (Terrestial) of Sheet Materials," ASTM E424-71, 1973.

7 Shettle, E. P. and Fenn, R. W., 1976, "Models of the Atmospheric Aerosols and Their Optical Properties," AGARD Conference Proceedings No. 183, *Optical Propagation in the Atmosphere,* presented at the Electromagnetic Wave Propagation Panel Sympasium, Lyngby, Denmark, 27–31 October 1975, (Available from NTIS Acc. No. N76-29817). pp. 2.1–2.16.

8 Edwards, D. K., Private Communication, Aug. 11, 1978.

A. C. Ratzel
Mem. ASME
C. E. Hickox
Mem. ASME
D. K. Gartling
Mem. ASME

Fluid Mechanics and Heat Transfer Division,
Sandia Laboratories,
Albuquerque, N. M. 87185

Techniques for Reducing Thermal Conduction and Natural Convection Heat Losses in Annular Receiver Geometries[1]

Analytical and experimental work has been undertaken to analyze thermal conduction and natural convection heat losses in annular receiver geometries. Techniques studied for reducing conduction heat loss include evacuation of the annulus gas, oversizing of the annular space while maintaining slight vacuum levels, and use of gases other than air in the annular space. For the geometry considered, total heat loss reductions of 10 percent to 50 percent may be obtained depending on the means by which the conduction heat loss is limited. In addition, natural convection studies considering the effects of nonuniform temperature distributions and eccentric cylinders are discussed. The numerical analysis performed indicates that highly nonuniform temperature distributions are required to appreciably affect the natural convection process between concentric cylinders and that rather large eccentricities cause only a slight increase in natural convection heat transfer.

1 Introduction

An effective device for the collection of solar energy which has received widespread attention is the so-called parabolic-cylindrical solar collector. In this device a circular receiver tube, with a suitable selective coating, is enclosed by a concentric glass envelope and situated along the focal line of a parabolic trough reflector. The heat transfer processes which occur in the annular space between the receiver tube and the glass envelope are important in determining the overall heat loss from the receiver tube. In typical high-temperature receiver tube designs, the rate of energy loss by combined thermal conduction and natural convection is of the same order of magnitude as that due to thermal radiation, and can amount to approximately 6 percent of the total rate at which energy is absorbed by the solar collector. The elimination of conduction and natural convection losses can significantly improve the performance of a large collector field.

In this paper, several techniques useful for the reduction of energy loss by thermal conduction and natural convection are considered. The receiver configuration chosen for study is typical of those used in the Midtemperature Solar Systems Test Facility at Sandia Laboratories. The receiver tube has a "black chrome" selective coating and is 2.54 cm in outside diameter. The inside diameter of the glass envelope is approximately 4.4 cm. Typical operating temperatures of the receiver tube and glass envelope are approximately 583 K and 333 K, respectively.

2 Heat Loss in an Annulus

In order to improve the overall efficiency of receiver designs, investigations into reducing the heat transfer through the annular space separating the glass and receiver tube have been undertaken. Of the three modes of heat transfer, the most significant heat loss savings can be accomplished by limiting conduction losses. Convection losses are negligible, so long as the annular space is properly sized. Radiation losses on the other hand, being primarily fixed by the receiver tube selective surface properties, are more difficult to reduce. Electroplating techniques have been optimized to provide high solar absorptivity (≥ 0.95) with thermal emissivities ranging between 0.20 and 0.30 for temperatures around 590 K. In order to reduce radiative heat loss significantly, thermal emissivities below 0.15 are required. Such reductions do not appear possible without an accompanying reduction in solar absorptivity. Several techniques for limiting the heat transfer rate in an annulus are considered in the remainder of this section.

---

[1] This work was supported by the United States Department of Energy.

Contributed by the Heat Transfer Division and presented at The Winter Annual Meeting, Atlanta, Georgia, November 27–December 2, 1977 of THE AMERICAN SOCIETY OF MECHANICAL ENGINEERS. Revised manuscript received by The Heat Transfer Division May 8, 1978.

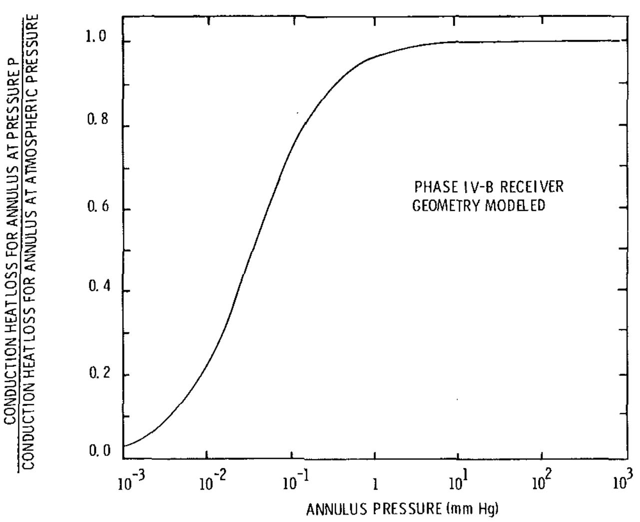

Fig. 1 Effects of pressure on conduction heat loss through an annular space (T_i = 589 K, T_0 = 366 K)

2.1 Effect of Vacuum. A review of the literature on vacuum technology indicates that the thermal conductivity of a gas is a function of the mean free path of the gas molecules [1–3]. An expression relating the mean free path of a gas to the enclosure pressure and gas temperature is given by

$$\lambda = 2.331(10^{-20})T/P\delta^2 \tag{1}$$

where T, P, and δ are given in deg K, mm Hg, and cm, respectively. For a given gas, the relative magnitudes of the molecular mean free path and the annulus gap determines the effective heat transfer coefficient for thermal conduction. This is shown in Fig. 1, which compares the conduction heat loss for a given annulus pressure to the conduction heat loss calculated for air at atmospheric pressure. Fig. 1 was generated using dimensional data and expected operating temperatures for a Sandia Laboratories' test receiver. The governing equation for the effective heat transfer coefficient for the annular space [1] is

$$H = \frac{K}{r_i \ln(r_o/r_i) + b\lambda(r_i/r_o + 1)} \tag{2}$$

where

$$b = \frac{2-a}{a}\left[\frac{9\gamma - 5}{2(\gamma + 1)}\right]$$

The reduction of receiver tube heat loss by evacuation has been modeled analytically and verified experimentally. Energy balances were made on the receiver tube and glass surfaces and were incorporated in a computer analysis [4] which could (1) predict the resultant receiver assembly temperatures for known heat inputs, or (2) predict the receiver assembly heat loss for a fixed receiver tube temperature. The analysis assumed steady state conditions and utilized standard correlations for the effects of pressure, wind, geometry, and temperature on the conduction and convection terms.

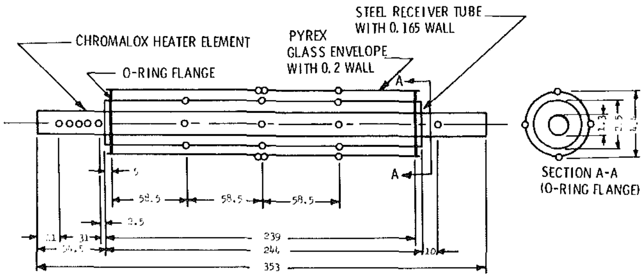

ALL DIMENSIONS ARE IN CENTIMETERS

○ THERMOCOUPLE LOCATION

CHROMALOX AND PYREX ARE REGISTERED BRAND NAMES.

Fig. 2 Schematic of thermocouple locations on the Phase IV-B receiver

The Sandia Laboratories Phase IV-B receiver assembly design was used for experimental verification. Heat input was provided by a Chromalox® heater element centered inside the receiver tube. Power supplied to the receiver assembly was monitored using a standard resistor and voltmeter. Input power was determined by measuring the voltage drop across the resistance heater and was maintained to within ±1.0 W during testing. Receiver assembly temperatures were monitored using 25 chromel-alumel thermocouples. Locations of these thermocouples as well as dimensional data on the Phase IV-B test assembly are shown in Fig. 2.

Annulus vacuums were monitored using a Pirani (thermocouple) Gauge for pressures below 1.0 mm Hg and a Wallace and Tiernan Pressure Gauge and Manometer for the higher pressures. All vacuums were maintained with a CEC Sampling Probe and Sargent-Welch single-stage vacuum pump.

Initial experimental work involved maintaining a fixed receiver assembly heat loss while varying the annulus pressure. Variations in receiver tube coating properties necessitated bracketing the experimental data with analytical results calculated for receiver tube emissivities of 0.2 and 0.3 at 589 K. The receiver tube temperature, as expected from the results of Fig. 1, is seen to be independent of annulus vacuum for pressures above 1 mm Hg in Fig. 3. This is also shown in Fig. 4 which provides heat loss data as a function of annulus pressure. Significant heat loss reductions of nearly 50 percent are seen to result if vacuums below 0.01 mm Hg can be maintained. Similar work has been reported by Ortabasi [5] for a tubular flat-plate collector. Differences in geometry between the two designs result in considerably different vacuum requirements for significant conduction heat loss reduction.

If required, the effect of wind on heat loss can be assessed through use of standard correlations [6] for flow normal to a heated horizontal cylinder. As one might expect, wind effects are found to be minimal

Nomenclature

a = accommodation coefficient
g = acceleration of gravity
H = effective heat transfer coefficient
K = thermal conductivity at standard conditions
K_{ef} = effective thermal conductivity
L = length of receiver tube
l = gap size
N_{Ra} = Rayleigh number
P = pressure
Q = heat loss
r_i = outer radius of receiver tube
r_o = inner radius of glass envelope
T = temperature
T' = temperature perturbation
T_i = temperature of receiver tube
T_0 = temperature of glass envelope
T_m = mean temperature
$\Delta r = r_o - r_i$
ΔT = temperature difference between cylinders
V = wind velocity normal to the receiver assembly
α = thermal diffusivity
β = coefficient of volumetric thermal expansion
δ = molecular diameter
ϵ = eccentricity
ϵ_{ir} = thermal emissivity
γ = ratio of specific heats
θ = angular position
λ = mean free path
μ = dynamic viscosity
ρ = density

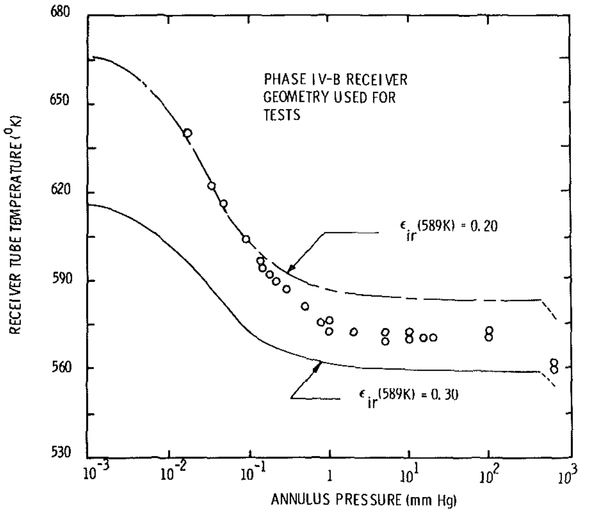

Fig. 3 Receiver tube temperature as a function of annulus pressure (Q = 182 W/m, V = 0 m/s)

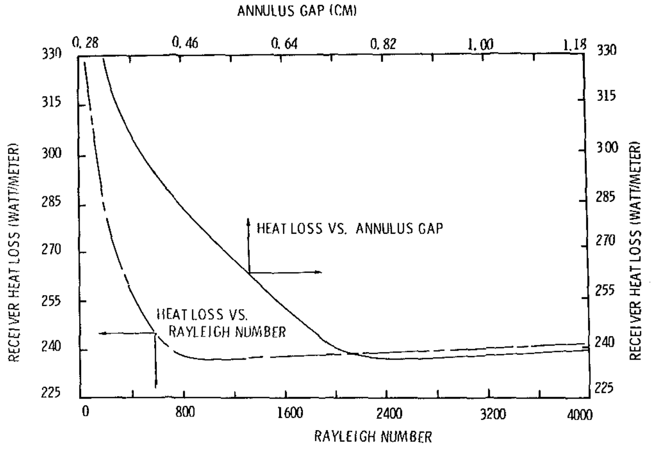

Fig. 5 Annular space sizing data for atmospheric pressure using a 2.54 cm receiver tube ($T_i \approx$ 589 K, ϵ_{ir} = 0.25, V = 2.24 m/s, P = 630 mm Hg)

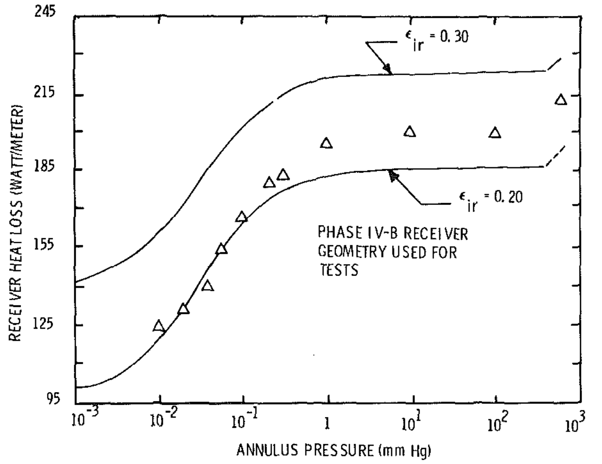

Fig. 4 Effects of pressure on receiver tube heat loss (T_i = 589 K, V = 0 m/s)

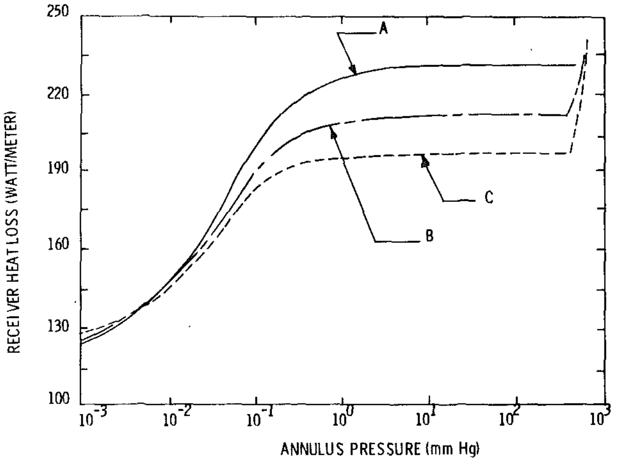

Fig. 6 Receiver annulus oversizing for reducing heat loss using a 2.54 cm receiver tube ($T_i \approx$ 589 K, ϵ_{ir} = 0.25, V = 2.24 m/s). Cases Modeled: A: Δr = 0.81 cm, N_{Ra} (P = 630 mm Hg) = 1000, B: Δr = 1.10 cm, N_{Ra} (P = 630 mm Hg) = 2600, C: Δr = 1.46 cm, N_{Ra} (P = 630 mm Hg) = 6400

for an evacuated annular receiver, since the energy loss is primarily by thermal radiation from the receiver tube.

2.2 Effect of Annulus Gap Sizing. Optimum sizing of the annular space for operation at atmospheric pressure requires that the energy transferred across the gap be by thermal conduction and radiation heat transfer. Incorrect sizing could result in enhanced convective energy transport which would increase the net heat loss. Work to be discussed in a later section concerning natural convection has indicated that the effects of natural convection will be negligible as long as the Rayleigh number is maintained below a value of 1000.

Experimental and analytical results shown in Figs. 3 and 4 indicate that the Phase IV-B receiver sizing has not been optimized since a loss reduction occurs when the annulus pressure is reduced below atmospheric pressure. By decreasing the pressure, the Rayleigh number is reduced below 1000 through lowering the annulus gas density. Based on these trends, the computer model was utilized to vary the gap spacing for a fixed receiver tube radius and temperature. From data presented in [7], the effective conduction coefficient used for a particular spacing was generated using the following correlation:

$$K_{ef} = K \text{ for } N_{\mathrm{Ra}} < 1000$$

$$K_{ef} = 0.1585 K N_{\mathrm{Ra}}{}^{0.2667} \quad \text{for} \quad N_{\mathrm{Ra}} > 1000 \tag{3}$$

where K_{ef} is the effective thermal conductivity, K is the actual thermal conductivity evaluated at the mean temperature, and N_{Ra} is the Rayleigh number defined by

$$N_{\mathrm{Ra}} = \rho g \beta l^3 \Delta T / \mu \alpha. \tag{4}$$

Fig. 5 shows that the heat loss is minimized for an annular space of 0.81 cm. (For the same test conditions, the Phase IV-B gap of 0.93 cm results in a Rayleigh number of 1550.) Despite the discrepancy in sizing, trends from Fig. 5 point out that oversizing the gap results in minimal increased heat loss compared to that obtained from reducing the gap size to maintain the Rayleigh number below 1000.

Further investigation into varying the annular space to reduce heat loss resulted in the data summarized in Fig. 6. By maintaining annulus pressures below 200–300 mm Hg and oversizing the gap, heat loss savings of between 15 and 30 W/m may be obtained over that lost by a receiver design sized to eliminate convection heat transfer at atmospheric pressure. Since the reduction of heat loss by 30 W/m for the "correctly" sized annular space necessitates using vacuums below 0.1 mm Hg, it can be noted that oversizing may allow for energy loss savings without requiring hard vacuum systems.

2.3 Effect of Gases other than Air. Utilization of gases other than air in the receiver annulus should reduce the conduction heat loss so long as (1) the gas thermal conductivity is less than that of air and (2) the effective Rayleigh number is similar to that of air for a given geometry. This is shown in Fig. 7 which compares the use of argon, air, and carbon dioxide in the annulus. Although carbon dioxide has a lower thermal conductivity than air (0.031 W/m-K compared to 0.048 W/m-K at 477 K), its other physical properties necessitate small gap spacings to minimize natural convection heat loss. The insulating effect of the lower thermal conductivity is thus lost because the conduction gap must be reduced.

For a given receiver tube operating temperature, heat loss savings of 25 to 30 W/m may be realized by replacing air with argon. Such savings are comparable to oversizing the annulus and maintaining a partial vacuum of 100–300 mm Hg. The advantage gained using argon gas to reduce the heat loss over the aforementioned technique is that, due to the similarity in sizing the gap for air or argon, a complete loss of argon and replacement with air will still minimize the heat loss. As can be seen from Fig. 6, an increase in heat loss will result in the event of loss of vacuum for the oversized geometry.

In summary, reduction of the conduction heat loss in the annular space can be accomplished through (1) evacuation, (2) oversizing the annular space while maintaining the Rayleigh number below 1000 (partial vacuum), and (3) use of gases with low thermal conductivities. Fig. 8 is provided to show the relative heat loss savings for each technique. Additional alternatives, such as charging the annular space with argon and evacuating and/or oversizing the gap are shown. Of the options, it appears that evacuation can best eliminate conduction heat loss. Problems, however, concerning the relative costs (including maintenance) of each heat loss reduction scheme must be considered in selecting the best option for the receiver assembly.

3 Natural Convection in an Annulus

In the previous section, the classical experimental result for natural convection heat transfer between horizontal, concentric, circular cylinders, as originally presented by Kraussold [7] was used in the analysis of the heat transfer process between the receiver tube and glass envelope. Many subsequent studies, dealing with the same topic, have been reported in the literature. Among the more notable are the experimental results of Liu, Mueller, and Landis [8], the experimental and theoretical studies of Kuehn and Goldstein [9], and Powe, Carley and Carruth [10], and the review by Buchberg, Catton, and Edwards [11].

Recently, Kuehn and Goldstein [12] have compiled a comprehensive review of the available experimental results for natural convection heat transfer between circular cylinders and proposed correlating equations using a conduction boundary-layer model. It is evident from this review that almost all the results available to date are, strictly speaking, valid only for horizontal, concentric, circular cylinders with uniform temperatures. Since the temperature distribution on a typical receiver tube is not uniform, it is important to determine the effect of this variation on the overall heat transfer process. Furthermore, it is also of importance to assess the effect of eccentricity since it is difficult to maintain precise alignment between the receiver tube and envelope due to deflections caused by gravity and differential thermal expansion.

Because of the scarcity of results for nonuniform temperature distributions and eccentric cylinders, a numerical analysis of the natural convection heat transfer process was performed in order to provide a better understanding of the effects of non-ideal situations [13]. Fundamental aspects of the analysis are outlined and the results discussed in the remainder of this section.

3.1 Numerical Method. At this point we wish to summarize the basic theory upon which the numerical analysis is based. The appropriate model is that of steady, planar, laminar thermal convection of a fluid due to nonuniformities of density in a gravitational field. In accordance with the usual Boussinesq approximation, density changes are neglected except insofar as they affect the body force term in the equations of motion. It is, of course, also assumed that the fluid is Newtonian. The partial differential equations which describe the heat transfer process are represented discretely through use of the Galerkin form of the finite element method, a technique which has been described in detail by several authors, e.g. Zienkiewicz [14], and will not be elaborated on here. The resulting methodology has been incorporated, by Gartling [15], into a user-oriented, finite element, computer program called NACHOS. This program makes use of an isoparametric mesh generator to allow complex boundaries to be modeled easily and accurately. The element library consists of an eight-node isoparametric quadrilateral and a six-node isoparametric triangle. Within each element, the velocity and temperature are approximated quadratically and the pressure approximated linearly. Fluid properties are allowed to vary with temperature.

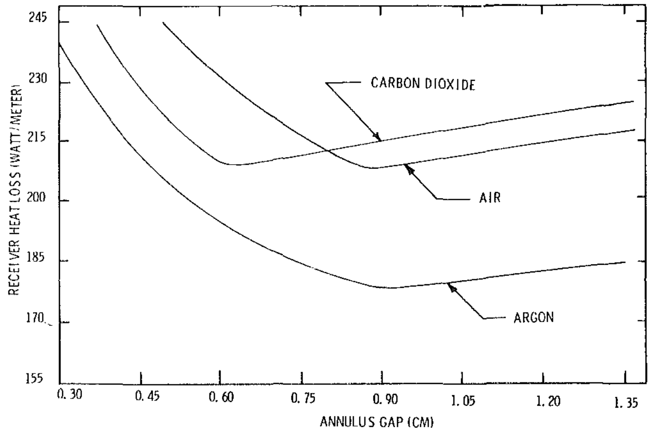

Fig. 7 Annulus sizing data for alternate gases using a 2.54 cm receiver tube (T_i = 589 K, ϵ_{ir} = 0.25, V = 0 m/s, P = 630 mm Hg).

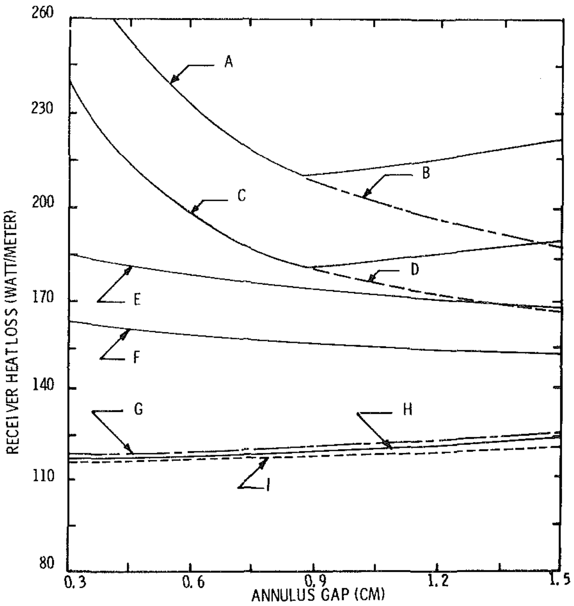

Fig. 8 Summary data on heat loss reduction techniques using a 2.54 cm receiver tube (T_i = 589 K, ϵ_{ir} = 0.25, V = 0 m/s) Cases Modeled: A: Air at 630 mm Hg, B: Air at 10 mm Hg, C: Argon at 630 mm Hg, D: Argon at 10 mm Hg, E: Air at 0.05 mm Hg, F: Argon at 0.05 mm Hg, G: Air at 0.001 mm Hg, H: Argon at 0.001 mm Hg, I: Radiation Heat Loss Only

3.2 Heat Transfer between Concentric Cylinders. In order to demonstrate that the results of the numerical analysis are compatible with existing experimental results, an initial series of calculations was performed for horizontal, concentric, circular cylinders with uniform temperatures. The temperatures of the inner and outer cylinders were held constant at 583°K and 333 K, respectively. These values were selected to correspond to the average operating conditions expected for the existing Sandia Laboratories' Midtemperature Solar Systems Test Facility collector field. The radius of the inner cylinder was held constant at 1.27 cm and the outer radius allowed to vary from 2.24 to 4.32 cm, producing radius ratios in the range 1.4 to 3.4. Rayleigh numbers ranging from approximately 300 to 97000 were thus obtained with the Rayleigh number defined in the usual way as given in equation (4).

Following the accepted standard, results of the analysis are presented in Fig. 9 as a plot of the heat loss ratio versus the Rayleigh number, where the heat loss ratio is defined to be the ratio of the energy loss per unit length due to conduction plus natural convection to that due to thermal conduction acting alone. In Fig. 9, the cross-hatched area indicates the region occupied by the experimental data as compiled by Kuehn and Goldstein [10]. Results obtained using equation (3) which was incorporated in the heat loss reduction section, are also shown. Typical streamlines and isotherms as computed for a Rayleigh number of approximately 12000 are shown in Fig. 10.

It is evident that, in general, there is rather good agreement between the computed and experimentally determined values of natural convection heat transfer rates. As expected, the heat loss is seen to initially deviate from that due to thermal conduction at a Rayleigh number of approximately 1000. The numerical method employed is apparently of sufficient accuracy to warrant its application to the study of the non-ideal situations described previously which have not, as yet, been extensively investigated.

3.3 Nonuniform Temperature Distribution. Two situations involving nonuniform temperature distributions on concentric, circular cylinders were selected for study. In both cases the temperature of the outer cylinder was held constant at 333 K and the temperature of the inner cylinder allowed to vary according to

$$T = T_m \pm T' \cos\theta \qquad (5)$$

where T_m is the mean temperature (583 K), T' is the perturbation to the mean, and θ is the angle measured from the bottom of the cylinder. A perturbation of 139 K was used in all calculations, yielding a total variation of 278 K around the inner cylinder. The two cases studied are distinguished by the choice of sign in equation (5), the positive sign corresponding to the occurrence of greatest temperature on the lower surface of the inner cylinder (Case A in Fig. 9) and vice versa (Case B). A variation of 278 K is far in excess of that encountered in conventional receiver tubes but, as will subsequently be shown, even this amount of nonuniformity has only a small effect on the natural convection process. In all calculations, the radius of the inner cylinder was held constant at 1.27 cm and the radius of the outer cylinder varied in order to vary the Rayleigh number. It should be noted that the average temperature upon which the Rayleigh number is based has the same value (458 K) as that associated with the uniform temperature case.

When the highest temperature occurred on the lower surface of the inner cylinder, the calculated results were virtually indistinguishable from those obtained with unifrom wall temperatures as plotted in Fig. 9. It should, however, be noted that the higher temperature on the lower surface produced flow patterns which, in some instances, differed significantly from that illustrated in Fig. 10. For Rayleigh numbers of approximately 12000 and greater, a two-cell flow pattern with one cell above the other and each spanning the entire gap between cylinders, was obtained. The altered flow pattern, however, produced no appreciable change in the overall heat transfer characteristics.

When the higher temperature occurred on the upper surface of the inner cylinder, the natural convection heat transfer rate was enhanced over that obtained with uniform temperatures, as shown in Fig. 9. Departure from the thermal conduction curve again occurs at a Rayleigh number of approximately 1000. Calculated streamlines and isotherms for a Rayleigh number of approximately 12000 are presented in Fig. 11.

From the results described in this section, it is evident that highly nonuniform temperature distributions are required in order to appreciably affect the natural convection process between concentric cylinders. Since the nonuniformity of temperature in typical receiver geometries is substantially less than that used in the current study,

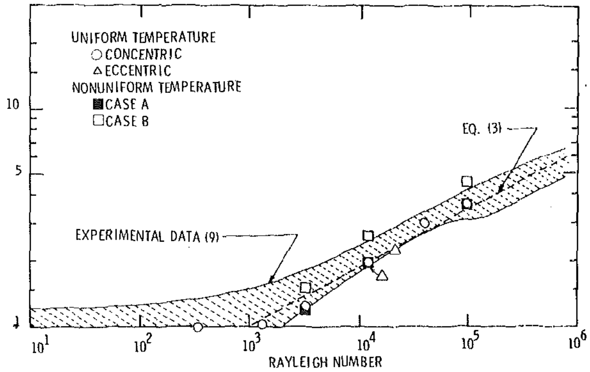

Fig. 9 Natural convection heat transfer in an annulus—comparison of computed and experimental results

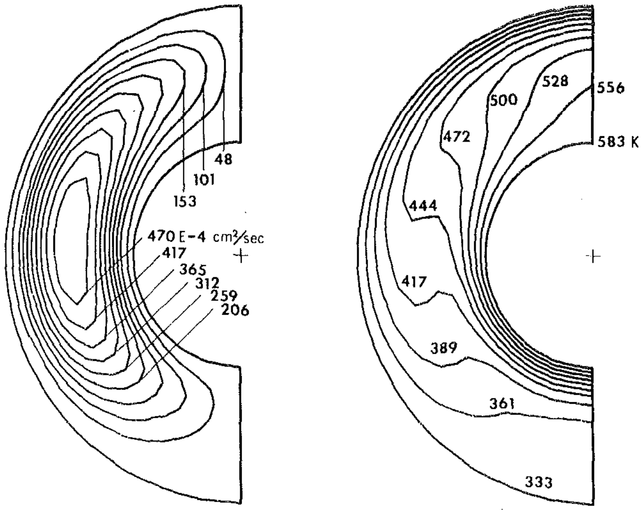

Fig. 10 Streamlines and isotherms for natural convection between concentric, circular cylinders—uniform temperature (T_i = 583 K, T_0 = 333 K, N_{Ra} = 12,142)

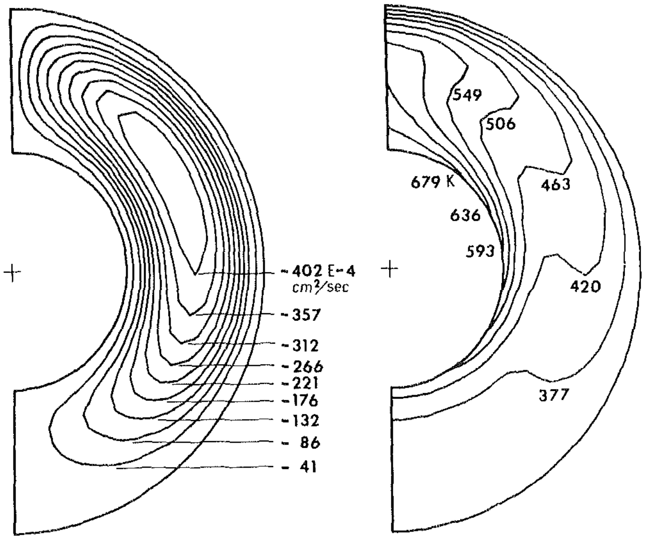

Fig. 11 Streamlines and isotherms for natural convection between concentric, circular cylinders—nonuniform temperature (444 K < T_i < 722 K, T_0 = 333 K, N_{Ra} = 12,142)

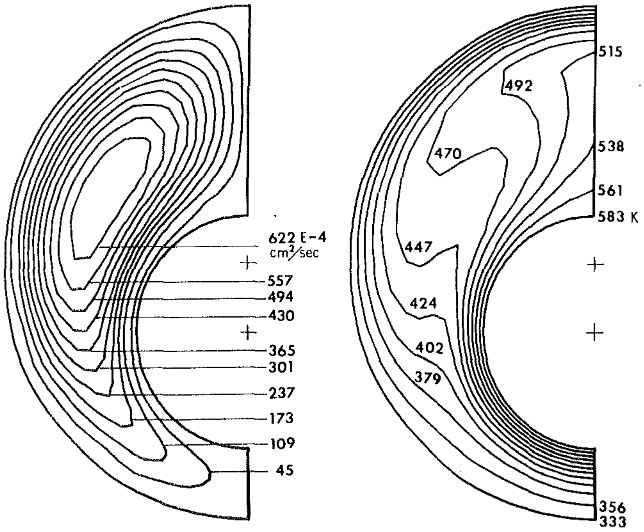

Fig. 12 **Streamlines and isotherms for natural convection between eccentric, circular cylinders—uniform temperature (T_i = 583 K, T_0 = 333 K, N_{Ra} = 12,142)**

it is anticipated that the effects of nonuniform temperature can be neglected in most instances.

3.4 **Eccentric Cylinders.** The geometry chosen for the study of eccentric cylinders consisted of inner and outer cylinders of radii 1.27 cm and 2.79 cm, with the inner cylinder displaced downward a distance equal to one-half the gap width, yielding an eccentricity of 0.76 cm. Each cylinder was held at a uniform temperature. Although other geometries could be analyzed without difficulty, the selection of the case chosen for study was influenced by certain practical considerations. First, a downward displacement of the inner cylinder enhances the convection process more than an upward displacement. Secondly, an eccentricity of one-half the gap width is greater than that encountered in practical receiver designs. Finally, it was convenient to maintain symmetry about a vertical plane in order to simplify the numerical computations.

For proper interpretation of subsequent results, it should be recalled that the heat loss by thermal conduction between eccentric, circular cylinders with uniform wall temperatures is given by [14]

$$Q/L = 2\pi K \Delta T / \ln(x + \sqrt{x^2 - 1}) \qquad (6)$$

where

$$x = (r_o{}^2 + r_i{}^2 - \epsilon^2)/2r_o r_i \qquad (7)$$

Equation (6) is used as the basis of comparison for the heat transfer results calculated for natural convection between eccentric cylinders.

The overall heat transfer results obtained for two different Rayleigh numbers are plotted in Fig. 9. Typical streamlines and isotherms are presented in Fig. 12. If the Rayleigh number is based on the mean gap size of 1.52 cm and the cylinders held constant at the values previously used in the analysis of concentric cylinders, a Rayleigh number of approximately 12000 results. For the remaining situation the temperature of the inner cylinder was increased and that of the outer cylinder decreased, by equal amounts, in order to produce a Rayleigh number of approximately 22000 while simultaneously maintaining the mean temperature constant at 458 K. This latter calculation was performed in order to tentatively assess the effect of Rayleigh number on the overall heat transfer process.

It is apparent from Fig. 9 that the results for eccentric cylinders coincide with those for concentric cylinders when the appropriate conduction solution is used as a reference and the Rayleigh number is based on the mean gap size. However, it should be noted that the overall heat transfer is slightly enhanced because of the increased effect of conduction for eccentric cylinders. For the variables used, the heat transferred by conduction is 14.75 percent greater for eccentric cylinders than for concentric cylinders.

4 Summary

It is well known that natural convection effects have a negligible influence on heat transfer in a uniformly heated annulus when the Rayleigh number, based on gap size, is less than approximately 1000. However, below this value, thermal conduction continues to be an important mode of heat transfer. The magnitude of this effect can be reduced if the pressure in the annulus is sufficiently reduced. Theoretical calculations showing the effects of a reduced annulus pressure were performed for a typical cylindrical solar collector and compared with measurements made on an electrically heated test section.

If it is not possible to maintain the pressure in the annulus low enough to effectively reduce conduction losses, then the energy loss for a uniformly heated annulus can be minimized by sizing the annulus so as to maintain a Rayleigh number near 1000 over the expected range of operating conditions. A numerical analysis was performed which demonstrated that highly nonuniform temperature distributions or large eccentricities are necessary to appreciably alter the above conclusion.

A reduction in energy loss by thermal conduction of from 10 to 20 percent can be effected by maintaining a moderately low pressure of, say, 50 mm Hg in the annulus and adjusting the gap size to correspond to the maximum allowable Rayleigh number (1000). Similar reductions in energy loss by thermal conduction were shown to be feasible through the use of gases other than air in the annulus.

References

1 Dushman, S., *Scientific Foundations of Vacuum Technique*, J. M. Lafferty, ed., John Wiley and Sons, New York, 1962.

2 *Handbook of Vacuum Physics, Volume 1: Gases and Vacua*, A. H. Beck, ed., Pergamon Press, London, 1966.

3 Holkeboer, D., Jones, D., Pagano, F., and Santeler, D., *Vacuum Engineering*, Boston Technical Publishers, Cambridge, 1967.

4 Ratzel, A. C., and Simpson, C. E., "Heat Loss Reduction Techniques for Annular Solar Receiver Designs," Sandia Laboratories Report SAND 78-1769, Sandia Laboratories, Albuquerque, NM, 1978.

5 Ortabasi, V., "Indoor Test Methods to Determine the Effect of Vacuum on the Performance of a Tubular Flat Plate Collector," ASME Paper 76-WA/SOL-24.

6 Chapman, A. J., *Heat Transfer*, Third Edition; Macmillan, New York, 1974, p. 351.

7 Kraussold, H., "Wärmeabgabe von Zylindrischen Flussigkeitsschichten bei natürlicher Konvektion," *Forsch Hft. Ver. Dt. Ing.*, Vol. 5, No. 4, 1934, pp 186–191.

8 Liu, C. Y., Mueller, W. K., and Landis, F., "Natural Convection Heat Transfer in Long Horizontal Cylindrical Annuli," *International Developments in Heat Transfer*, Part V, Paper No. 117, 1961, pp. 976–984.

9 Kuehn, T. H, and Goldstein, R. J., "An Experimental and Theoretical Study of Natural Convection in the Annulus Between Horizontal Concentric Cylinders," *J. Fluid Mech.*, Vol. 74, Pt. 4, 1976, pp. 695–719.

10 Powe, R. E., Carley, C. T., and Carruth, S. L., "A Numerical Solution for Natural Convection in Cylindrical Annuli," ASME JOURNAL OF HEAT TRANSFER, Vol. 93, 1971, pp. 210–220.

11 Buchberg, H., Catton, I., and Edwards, D. K., "Natural Convection in Enclosed Spaces: A Review of Application to Solar Energy Collection," ASME Paper No. 74-WA/HT-12, 1974.

12 Kuehn, T. H., and Goldstein, R. J., "Correlating Equations for Natural Convection Heat Transfer Between Horizontal Circular Cylinders," *Int. J. Heat Mass Transfer*, Vol. 19, 1976, pp. 1127–1134.

13 Hickox, C. E., and Gartling, D. K., "The Effects of Nonuniformities on Natural Convection in Annular Receiver Geometries," Sandia Laboratories Report SAND 77-1641, Sandia Laboratories, Albuquerque, NM, 1977.

14 Zienkiewicz, O. C., *The Finite Element Method in Engineering Science*, McGraw-Hill, New York, 1972.

15 Gartling, D. K., "Convective Heat Transfer by the Finite Element Method," *Comp. Meth. Appl. Mech. Eng.*, Vol. 12, 1977, pp. 365–382.

16 Carslaw, H. S., and Jaeger, J. C., *Conduction of Heat in Solids*, Oxford University Press, 1959, p. 449.

A. M. C. Chan
Graduate Student.

S. Banerjee
Professor.

Department of Engineering Physics,
McMaster University,
Hamilton, Ontario, L8S 4M1, Canada

Three-Dimensional Numerical Analysis of Transient Natural Convection in Rectangular Enclosures

A simple numerical technique of considerable practical utility for the solution of transient multidimensional natural convection problems is described. It is based on the solution of the conservation equations in primitive form. The technique can be extended to calculation of natural convection problems in porous media and in turbulent flows where the eddy viscosities and conductivities can be predicted. It has been applied to the solution of several two and three-dimensional natural convection problems. The solutions compare well with the numerical and experimental results published by other investigators.

Introduction

The analysis of multidimensional natural convection is of importance in many industrial and geophysical problems. For example, the motivation for the present work arose from a study of natural convection cooling of nuclear fuel in shipping flasks and in water filled storage bays. Cooling had to be analysed not only during routine operation of these facilities but also in postulated accidents. This led to a need for a transient multidimensional analysis.

Numerical techniques for the solution of laminar natural convection problems have been widely studied [1–6]. In most cases the stream function-vorticity form of the conservation equations were used. The use of "primitive" variables (velocity, pressure and temperature) in incompressible flow problems were reported by Harlow and Welch [7] and Hirt, et al. [8]. The technique was called the marker and cell (MAC) method. The possibility of using the technique in natural convection type problems was first suggested by Hirt and Cook [9].

In our present work, a simplified version of the MAC technique [10] was extended to study transient three dimensional natural convection flows in enclosures. The method was chosen for two reasons:

1 The technique uses the primitive variables, and boundary conditions for three-dimensional problems are much easier to handle for complex flow geometries than if the vorticity-stream function approach of Aziz and Hellums [3], and Ozoe, et al. [11] are used. We used the program for very complex geometries such as nuclear fuel shipping flasks and storage bays and this was an important factor in our choice.

2 The technique requires about the same amount of CPU time per node per time step for two and three-dimensional calculations (as discussed later). ADI and time-splitting techniques (Yanenko [12]) require progressively more CPU time per node per time step as the number of dimensions increases.

The MAC technique was used with "donor cell" differencing of the advective terms. It was recognized that this could be inaccurate for natural convection problems. This could be due to numerical diffusion (to which computation of natural convection flow fields would be expecially sensitive), and because the energy conservation equation is written in nonconservative form to decouple the velocity field calculation at each time step from the temperature field at that time step. Therefore, as a first step it was necessary to validate the method by comparing the results of our calculations on Nusselt numbers, isotherms and isovels with available two and three-dimensional experimental and numerical results. A secondary objective was to compare the results from a three-dimensional simulation of an experiment, with those of a two-dimensional simulation, in order to establish whether three-dimensional simulations were necessary.

We felt that the process of validation was necessary before the technique could be used to gain insight into three-dimensional flows and practical problems.

Mathematical Formulation

For natural convection flows with small density changes, the conservation equations may be simplified by the Boussinesq approximation [13]. The fluid density is considered constant except in buoyancy force terms that drive the natural convection. The equations for conservation of mass, momentum and energy may be written as:

$$\nabla \cdot \vec{v} = 0 \quad (1)$$

Contributed by the Heat Transfer Division for publication in the JOURNAL OF HEAT TRANSFER. Manuscript received by the Heat Transfer Division January 4, 1978.

$$\frac{D\vec{v}}{Dt} = -\frac{1}{\rho}\nabla P' - \beta \vec{g}\,(T - Te) + \nu \nabla^2 \vec{v} \qquad (2)$$

$$\frac{DT}{Dt} = \frac{k}{\rho Cp}\nabla^2 T + \frac{1}{\rho Cp}[Q + \phi] \qquad (3)$$

The initial conditions for temperature and velocity, and appropriate boundary conditions must be specified.

Numerical Technique

The conservation equations (1–3) are written in finite difference form for cells of the type shown in Fig. 1. The finite difference form of the equations used for our calculation used the donor cell or full upstream formulation for the advective terms to preserve the transportive property (Roache [14]). An example of the form of the finite difference equations in rectangular coordinates is shown below. Mass conservation equation:

$$\begin{aligned} D = {} & (U_{i+1/2,j,k}{}^{n+1} - U_{i-1/2,j,k}{}^{n+1})/(\Delta X)_{i,j,k} \\ & + (V_{i,j+1/2,k}{}^{n+1} - V_{i,j-1/2,k}{}^{n+1})/(\Delta y)_{i,j,k} \\ & + (W_{i,j,k+1/2}{}^{k+1} - W_{i,j,k-1/2}{}^{n+1})/(\Delta z)_{i,j,k} = 0 \qquad (4) \end{aligned}$$

Momentum equations:

Only the momentum equation in the y-direction is shown. The x and z-component are similar to the y-component.

$$\begin{aligned} V_{i,j+1/2,k}{}^{n+1} = {} & V_{i,j+1/2,k}{}^{n} + (\Delta t)[(P''_{i,j,k}{}^{n} \\ & - P''_{i,j+1,k}{}^{n})/(\Delta y)_{i,j+1/2,k} - FVX - FVY - FVZ + \frac{1}{2}\beta g \\ & \times (T_{i,j+1,k}{}^{n} + T_{i,j,k}{}^{n} - 2Te) + VISY] \qquad (5) \end{aligned}$$

where

$$\begin{aligned} FVX = {} & \left(U\frac{\partial V}{\partial X}\right)^{n}_{i,j+1/2,k} \\ = {} & \frac{1}{2}(V_{i+1,j+1/2,k}{}^{n} - V_{i,j+1/2,k}{}^{n})(U_{i,j+1/2,k}{}^{n} \\ & - |U_{i,j+1/2,k}{}^{n}|)/(\Delta X)_{i+1/2,j,k} + \frac{1}{2}(V_{i,j+1/2,k}{}^{n} - V_{i-1,j+1/2,k}{}^{n}) \\ & \times (U_{i,j+1/2,k}{}^{n} + |U_{i,j+1/2,k}{}^{n}|)/(\Delta x)_{i-1/2,j,k}) \end{aligned}$$

with

$$\begin{aligned} U_{i,j+1/2,k}{}^{n} = {} & \frac{1}{2}\left[\left(U_{i} - \frac{1}{2},_{j\mu} + U_{i}{}^{n} + \frac{1}{2},_{j,k}\right)(\Delta_{y})_{i,j+1,\mu}\right. \\ & \left. + \left(U_{i}{}^{n} - \frac{1}{2},_{j+1,k} + U_{i}{}^{n} + \frac{1}{2},_{j+1,\mu}\right)(\Delta y)_{i,j,k}\right]/((\Delta y)_{i,j,\mu} + (\Delta y)_{i,j+1,k}) \end{aligned}$$

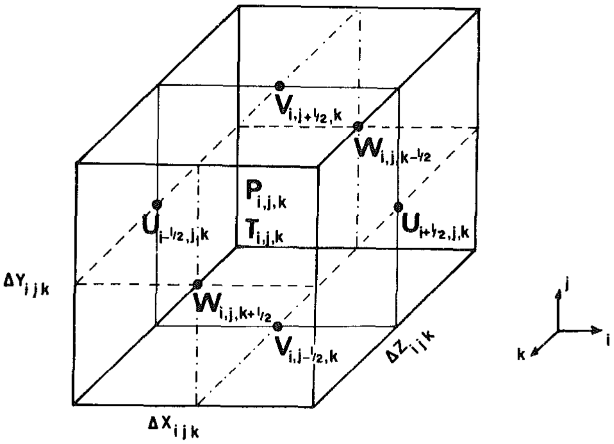

Fig. 1 Arrangement of finite difference variables in a typical cell

Expressions for FVY and FVZ are similar to FVX and are omitted.

$$\begin{aligned} VISY = {} & \nu\left(\frac{\partial^2 V}{\partial x^2} + \frac{\partial^2 V}{\partial y^2} + \frac{\partial^2 V}{\partial z^2}\right)^{n}_{i,j+1/2,k} \\ = {} & \nu\left[\left(\frac{V_{i+1,j+1/2,k} - V_{i,j+1/2,k}}{(\Delta X)_{i+1/2,j,k}} - \frac{V_{i,j+1/2,k} - V_{i-1,j+1/2,k}}{(\Delta X)_{i-1/2,j,k}}\right)\right/ \\ & \times (\Delta X)_{i,j,k}{}^{2} + \left(\frac{V_{i,j+3/2,k} - V_{i,j+1/2,k}}{(\Delta y)_{i,j+1,k}} - \frac{V_{i,j+1/2,k} - V_{i,j-1/2,k}}{(\Delta y)_{i,j,k}}\right)\Big/ \\ & \times (\Delta y)_{i,j+1/2,k}{}^{2} + \left(\frac{V_{i,j+1/2,k+1} - V_{i,j+1/2,k}}{(\Delta z)_{i,j,k+1/2}}\right. \\ & \left.\left. - \frac{V_{i,j+1/2,k} - V_{i,j+1/2,k-1}}{(\Delta z)_{i,j,k-1/2}}\right)\Big/(\Delta z)_{i,j,k}{}^{2}\right]^{n} \end{aligned}$$

Energy equation:

$$\begin{aligned} T_{i,j,k}{}^{n+1} = {} & T_{i,j,k}{}^{n} + (\Delta t)\,[-TUX - TVY - TWZ \\ & + k(TSX + TSY + TSZ)/\rho Cp + Q/\rho Cp] \qquad (6) \end{aligned}$$

Nomenclature

A = area
C = Courant number
C_p = specific heat of fluid
D = width of enclosure
g = gravitational acceleration
h = heat transfer coefficient
H = height of enclosure
k = thermal conductivity of fluid
L = width of enclosure
Nu = Nusselt number
P = pressure
P' = pressure fluctuation
$P'' = P'/\rho$
Pr = Prandtl number
Q = internal heat generation per unit volume
$\mathrm{Ra} = \dfrac{g\beta(T_H - T_C)H^3}{\nu\alpha}$ = Rayleigh number
t = time
T = temperature
T_e = reference temperature
u = velocity component in x-direction
$U = uH/\nu$ = dimensionless velocity component in x-direction
v; $\vec{v}$ = velocity component in y-direction, velocity vector
$V = vH/\nu$ = dimensionless velocity component in y-direction
w = velocity component in z-direction
$W = wH/\nu$ = dimensionless velocity component in z-direction
α = thermal diffusivity
β = volumetric coefficient of expansion of fluid
$\theta = \dfrac{T - T_C}{T_H - T_C}$ = dimensionless temperature
ν = kinematic viscosity
ρ = density of fluid
ϕ = frictional dissipation function
ϵ = convergence criterion
$\tau = t\nu/H^2$ = dimensionless time

Subscripts

C = cold surface
H = heated surface
i, j, k = denote quantities at computational cell centres
$i + 1/2$, $j + 1/2$, $k + 1/2$ = denote quantities at the right hand, upper and front cell faces respectively.
w = wall
s = spot

where

$$TUX = \left(U\frac{\partial T}{\partial X}\right)_{i,j,k}^{n} = [(U_{i+1/2,j,k} + U_{i-1/2,j,k} - |U_{i+1/2,j,k} + U_{i-1/2,j,k}|)\,(T_{i+1,j,k} - T_{i,j,k})/4(\Delta X)_{i+1/2,j,k} + (U_{i+1/2,j,k} + U_{i-1/2,j,k} + |U_{i,j+1/2,k} + U_{i-1/2,j,k}|) \times (T_{i,j,k} - T_{i-1,j,k})/4(\Delta x)_{i-1/2,j,k}]^{n}$$

$$TSX = \left(\frac{\partial^2 T}{\partial X^2}\right)_{i,j,k}^{n} = \left[\frac{T_{i+1,j,k} - T_{i,j,k}}{(\Delta X)_{i+1/2,j,k}} - \frac{T_{i,j,k} - T_{i-1,j,k}}{(\Delta X)_{i-1/2,j,k}}\right]^{n} \Big/ (\Delta X)_{i,j,k}$$

Expressions for TVY, TWZ, TSY and TSZ are omitted as they are similar to TUX and TSX.

The frictional dissipation function, ϕ may be easily included but is omitted in equation (6) because it is negligible for our problem. Furthermore, with slight restructuring of the finite difference forms, the viscosity and thermal conductivity at any time step can be made a function of the dependent variables and position in the previous time step allowing consideration of turbulent flows through "eddy" diffusivities. Though we have used the technique for turbulent flows, this aspect will not be discussed in the paper.

To impose the necessary boundary conditions, the fluid is considered to be surrounded by a single layer of fictitious cells in which the variables are specified. The specifications used in this paper are illustrated below for the left hand boundary.

1 Rigid, no slip wall cell:

$$U_{3/2,j,k} = 0,\ V_{1,j,k} = -V_{2,j,k},\ W_{1,j,k} = -W_{2,j,k}$$

2 Rigid, free slip wall cell:

$$U_{3/2,j,k} = 0,\ V_{1,j,k} = V_{2,j,k},\ W_{1,j,k} = W_{2,j,k}.$$

3 Adiabatic wall cell:

$$T_{1,j,k} = T_{2,j,k}$$

4 Isothermal, constant temperature wall cell:
The quadratic extrapolation technique was used,

$$T_{1,j,k} = AX_0^2 + BX_0 + C$$

Where A, B, and C are defined by the following set of equations:

$$T_{\text{boundary}} = AX_1^2 + BX_1 + C,$$

$$T_{2,j,k} = AX_2^2 + BX_2 + C,\ T_{3,j,k} = AX_3^2 + BX_3 + C.$$

To calculate velocities, pressures and temperatures at a new time step from the values at the previous time step, the following computational cycle is followed.

1 Compute estimates for the new velocity field from the momentum equations.

2 Adjust the new velocity field iteratively to satisfy the mass conservation equation (4) by changing the cell pressures. If the divergence, D, of a cell in equation (4) is negative, this corresponds to a net flow of mass into the cell, the cell pressure is then increased to eliminate the net inflow. Likewise, the cell pressure can be decreased to eliminate net outflow if D is positive. If the pressure of one cell is adjusted, then the adjacent cells are also affected. Therefore, the pressure adjustment must be done iteratively. The pressure change required to make D equal to zero is:

$$\delta P'' = \frac{D}{2\Delta t[(\Delta X)^{-2} + (\Delta Y)^{-2} + (\Delta Z)^{-2}]} \qquad (7)$$

The new pressure and velocity components after each iteration are given by:

$$P''_{i,j,k} = P''_{i,j,k} + \delta P'',$$

$$U_{i\pm 1/2,j,k} = U_{i\pm 1/2,j,k} \pm \Delta t\ \delta P''/\Delta X,$$

and similarly for V and W.

3 When the new velocity field has been converged, the new temperature field is calculated using the energy equation (6).

4 The velocity and pressure fields are then used as the starting values for the next time step cycle.

Numerical Stability and Computation Time

For our finite difference equations, stability is obtained provided the fluid is not permitted to cross more than one cell in one time step. Thus, the time increment must satisfy the usual courant number criterion for purely explicit schemes:

$$Cx = |U|\Delta t/\Delta X < 1.0,\ Cy = |V|\Delta t/\Delta y < 1.0,\ Cz = |W|\Delta t/\Delta z < 1.0$$

Also, when a nonzero value of kinematic viscosity is used, momentum must not diffuse more than one cell in one time step, this implies;

$$\nu\Delta t < \frac{1}{2}\frac{(\Delta X)^2(\Delta Y)^2(\Delta Z)^2}{(\Delta X)^2 + (\Delta Y)^2 + (\Delta Z)^2}$$

The problem computation time required per time increment depends in general, on (1) the number of cells, (2) the cell size, (3) the time step size, and (4) the convergence criterion (ϵ) set for the velocity field iteration to satisfy the continuity equation. The cell size and time step size are interrelated by stability conditions (Courant numbers). In general, we have found for transient calculations that, on the average, about 0.01 to 0.02 s CPU time is required per cell per time step with a convergence criterion of 10^{-3} on the McMaster University CDC 6400 computer. The higher values (~0.02 s) are required during rapid transients when more iterations are required to satisfy the convergence limit. CPU time can increase greatly if ϵ is reduced. For example, the average number of iterations increased by 4.7 and 7.3 times when ϵ was reduced from 10^{-1} to 10^{-3} and 10^{-4} respectively. No significant improvement in accuracy was achieved by setting ϵ smaller than 10^{-3} for the problems studied.

Two-Dimensional Calculations

The numerical technique was tested with regard to symmetry and numerical diffusion. Perfectly symmetric solutions for temperature and velocity fields were obtained where these results were to be expected from geometrical considerations.

The numerical diffusivity of the technique was studied by establishing a transient temperature gradient across a rectangular enclosure from top to bottom. Since the fluid was heated uniformly from the top, the computation should always result in a zero velocity field. Numerical inaccuracies resulting in a small velocity field can be fed back and affect computed temperature significantly. The numerical results obtained did not result in any fluid motion. When the numerical and analytical solutions were compared at different times, good agreement was obtained.

Numerical diffusion due to convection was also investigated. The thermal conductivity and volumetric coefficient of expansion were set equal to zero and a temperature spike was introduced into a constant velocity field. The movement and diffusion of the spike was then followed in time. The spike broadened due to "numerical diffusion" but the mean was found to travel with the correct veloicty. The broadening was reduced if the cell sizes and time steps were reduced. Higher harmonics did not develop and the technique appeared satisfactory provided convergence of the results were checked by reducing time step and cell size.

Isotherms and isovels were obtained for a two-dimensional rectangular enclosure with a horizontal temperature gradient. This was established by maintaining the left-hand wall of the enclosure at a constant, higher temperature (T_H) and the other side wall at a constant, lower temperature (T_C). The upper and lower walls were insulated. Calculations were made for Rayleigh numbers up to 1.5×10^5. A Prandtl number of 0.72 and an aspect ratio of 1.0 were used. The calculations were carried out with a 10×10 mesh, i.e., the cell size was $L/10 \times H/10$. Figs. 2(a) and 2(b) summarize the results obtained by plotting the temperature and vertical velocity profile at the enclosure mid-height. They were in excellent agreement with the computed results of other investigators—for example, DeVahl and Davis [15]

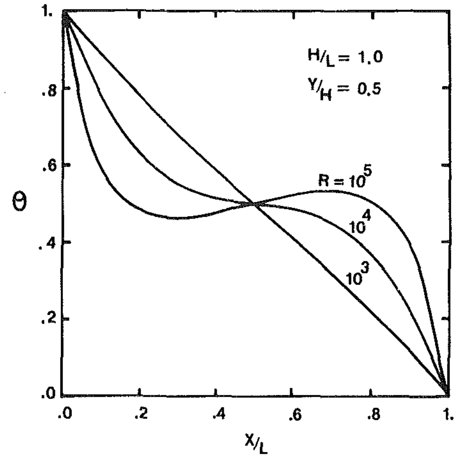

Fig. 2(*a*) Temperature profile at mid height of enclosure

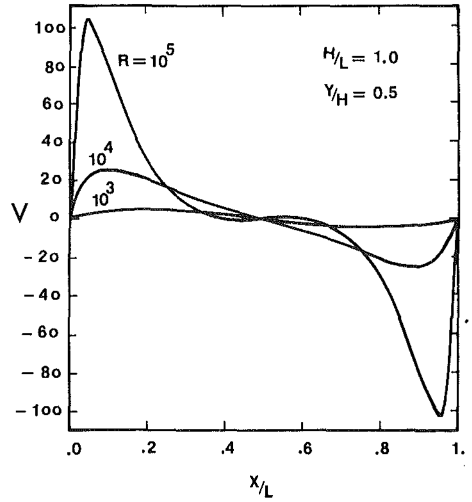

Fig. 2(*b*) Vertical velocity profile at mid height of enclosure

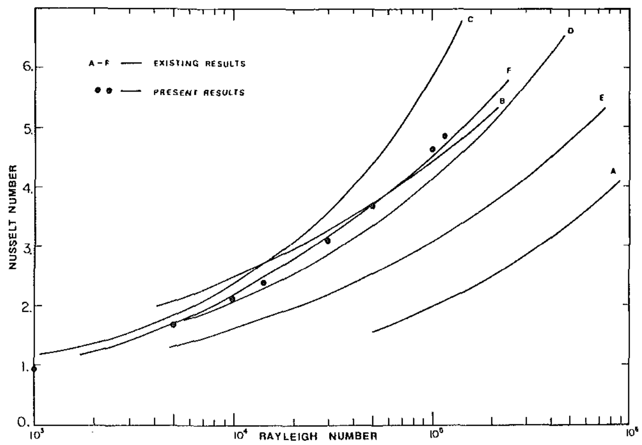

Fig. 3 Average Nusselt number versus Rayleight number A = Dropkin and Somerscales [18], B = Elder [19], C = DeVahl Davis [15], D = Eckert and Carlson [20], E = Landis and Yanowitz [21], F = MacGregor and Emery [16]

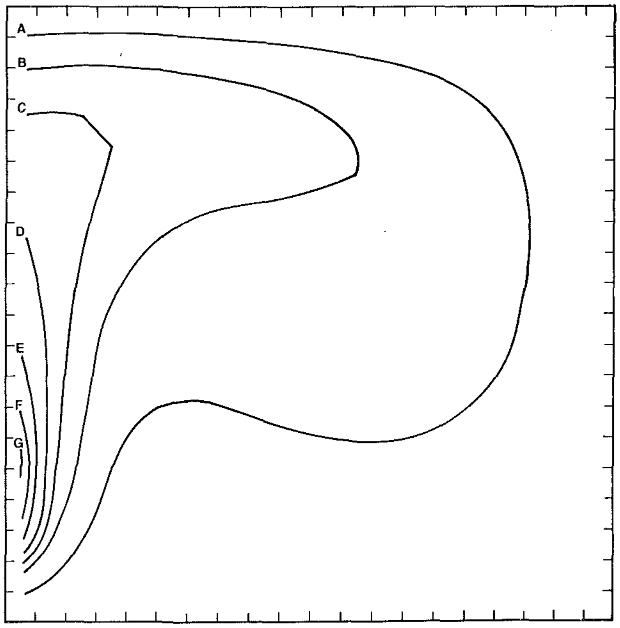

Fig. 4 Two-dimensional isotherms for a rectangular enclosure with a heated strip (Ra = 10^5, Pr = 0.72)

and MacGregor and Emery [16]. The average heat transfer coefficient and Nusselt number (defined below) were also computed for the different Rayleigh numbers

$$\overline{\mathrm{Nu}} = \frac{hH}{k} = \int_0^H \frac{\left(\frac{\partial T}{\partial X}\right)_{x=0} dy}{T_H - T_C} \tag{7}$$

Fig. 3 compares the average Nusselt numbers obtained with existing numerical and experimental results. It agrees very well with results in [B, C] and [F] in Fig. 3 which are numerically calculated values. The experimental curves, [A, D] and [E], generally lie below the computed curves. This is probably because the experimental curves are for aspect ratios of five or higher. Thus end region effects are less important than in the numerical curves which were computed for aspect ratios of unity.

The convergence of our solutions were investigated by using a finer mesh (20 × 20). The final results (Nusselt numbers, flow patterns and temperature distribution) were practically the same, indicating that the solution had converged for a 10 × 10 mesh.

To further test the capability of the present numerical technique to follow flow development in a more complicated system, comparisons were made with the results of Chu, et al. [6]. Their system was a two-dimensional square enclosure with a heating element in the form of an isothermal strip located in the otherwise insulated, vertical, left hand wall. The size of the heating element was $1/5$ of the enclosure height, H. The location of the heating element was defined by the ratio S/H, where S was the distance of the center of the heating element from the top of the enclosure. The other three walls were maintained at a constant, lower temperature. Calculations were made for Ra = 10^5, Pr = 0.72, S/H = 0.2 and 0.8. Results are in excellent agreement with those shown by Chu, et al. [6]. The temperature fields for the case S/H = 0.8 is shown in Fig. 4. Each isotherm is ten percent of the overall temperature difference. (Not all isotherms are shown because they become very crowded near the heating element).

From these studies, we concluded that the present technique worked well for two-dimensional natural convection problems in rectangular enclosures. Tests against three-dimensional experiments are now described.

Three-Dimensional Calculations

The system geometry used was similar to that of Torrance, et al. [17]. It was a rectangular enclosure with dimensions 305 mm × 152 mm × 152 mm ($L \times D \times H$). An isothermal, heated square was located at the center of the floor. The area of the square was 3.1416 cm^2. The right-hand vertical wall could be heated and the other walls (including the floor) were maintained at a constant, lower temperature. The main difference in geometry from that of Torrance et al was that they used a heated disk, which we simulated with a square of the same area. The results of several different cases are discussed below.

In the first case, the steady state solution was obtained with the temperature of the heated element 16°C above ambient and all the walls at ambient temperature. In the second case, the right-hand wall had a constant temperature 5°C above the other five walls which were kept at ambient temperature. The heated square was removed in this case. The velocity field obtained for the latter case is shown in Fig. 5(*a*). We also show the results of a two-dimensional calculation for this case in Fig. 5(*b*) for comparison. The results can be compared with the streak-line photographs presented by Torrance, et al. [17]. The three-dimensional calculations and experiments agree well for both cases. The flow patterns obtained are very close to Torrance's results.

The three-dimensional effect on the solutions can be seen when comparing the flow patterns from the three- and two-dimensional simulations. (Figs. 5(*a*) and 5(*b*)). It can be seen that the elongated vortex core found in the three-dimensional solution moves closer to the middle of the enclosure in the two-dimensional case. The isotherms show significant differences as well. The steady state average temperature of the fluid in the two-dimensional case is much higher than the three-dimensional case.

Therefore a two-dimensional simulation does not give good results for three-dimensional situations at least of this type.

The superimposed effect of a heated square and a heated right-hand wall is shown in the results of a three-dimensional calculation in Fig. 5(*c*). The heated square was 20°C and the heated wall was 5°C above ambient temperature. The other walls were kept at constant, ambient temperature. The flow pattern in this case, however, differs somewhat from Torrance's corresponding streak-line photograph. The effect of the heated square on the floor appears to be more pronounced. The reason for the difference is not clear. A probable explanation is that the experimental conditions were not simulated exactly in the numerical solution; for example, Torrance, et al. estimated that the conduction loss from the heated disk to the metal floor was more than 40 percent in their experiment. This would explain the more pronounced effect of the heated spot in the numerical calculations.

Convergence Tests

The nodalization used in all three cases shown was 15 × 7 × 7. "Uniform" mesh sizes were used except for the heated element cell in cases 1 and 3. The size of the heated element cell was $\sqrt{\pi}$ cm × $\sqrt{\pi}$ cm × H/7 cm. The velocity plots in Figs. 5(*a*) and 5(*c*) are solutions at the central plane in the *z*-direction.

Since only streak-line photographs were available in Torrance's experiment, no quantitative comparison with the numerical solutions could be made. The velocity plots (Fig. 5), obtained do not give a good indication of whether converged numerical solutions have been obtained. We felt that Nusselt numbers would be a more sensitive indicator of convergence than velocity or temperature plots because they depend on the derivatives of the temperature field at the wall. Therefore the effect of mesh spacing on Nusselt number was determined for cases 2 and 3.

The wall Nusselt number for a heated right hand wall is defined:

$$N_u{}^{w} = \frac{hH}{k} = \frac{\int_0^D \int_0^H \left(\frac{\partial T}{\partial X}\right)_{X=L} dydz}{D\Delta T_W} \qquad (8)$$

In case 2, numerical calculations were first done using uniform 11 × 7 × 7, 15 × 7 × 7 and 21 × 10 × 9 nodalization. As evident from Fig. 6, the Nusselt number increased substantially, even though there was no discernible effect on the velocity plots. We then decided to use a nonuniform mesh refined in the wall regions. The Nusselt numbers obtained were plotted against mesh size near the wall relative to the 11 × 7 × 7 mesh size.

The results, shown in Fig. 6, indicate that Nusselt numbers continued to increase as mesh spacing near the wall was decreased until the mesh spacing was about 1/10 of the value of the 11 × 7 × 7 uniform spacing. The velocity plots did not, however, change significantly. The Nusselt numbers were evidently much more sensitive to mesh spacing. Furthermore, it is clear that Nusselt numbers closer to the converged

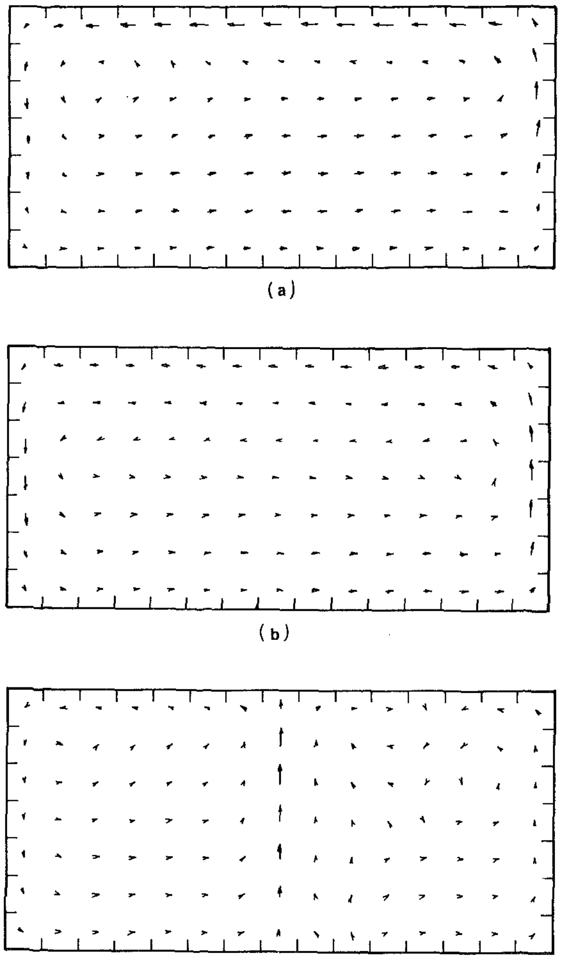

Fig. 5 a) Velocity plot for a three-dimensional rectangualr enclosure with heated right hand wall, b) velocity plot for a two-dimensional rectangular enclosure with heated right hand wall c) Velocity plot for a three-dimensional rectangular enclosure with heated right hand wall superimposed with a heated spot

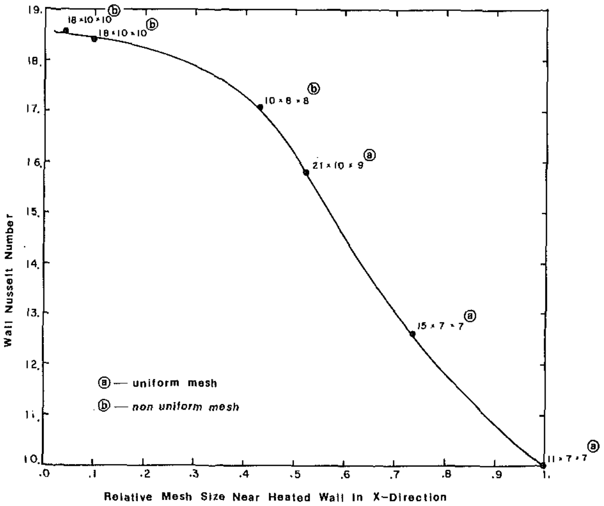

Fig. 6 Wall Nusselt number versus relative mesh size for a three-dimensional rectangular enclosure with heated right hand wall

value can be obtained using a smaller number of nonuniform meshes refined in the wall region, e.g., 10 × 8 × 8 or 18 × 10 × 10, than a larger number of uniform meshes (21 × 10 × 9).

Similar results were obtained in the third case. Again the wall and spot Nusselt numbers were found to be more sensitive to mesh spacing than velocity and temperature plots. The spot Nusselt number was defined as:

$$N_u{}^S = \frac{hH}{k} = \frac{H \iint_{\text{spot}} \left(\frac{\partial T}{\partial y}\right)_{y=0} dx\, dz}{A_S\, \Delta T_S} \qquad (9)$$

The calculated Nusselt numbers are shown in Fig. 7 against relative mesh size near the walls and heated spot taking the uniform 11 × 7 × 7 mesh spacing as reference. Again, Nusselt numbers closer to converged values were obtained with a smaller number of nonuniform meshes refined near the walls or spot, than with a large number of uniform meshes. Converged results appeared to be obtained with 18 × 10 × 10 nodes with a relative mesh spacing $\frac{1}{10}$ that of the uniform 11 × 7 × 7 nodes in the region of wall and spot. A 2 × 2 subdivision perpendicular to the plane of the heated spot appeared sufficient and a 4 × 2 subdivision did not affect the spot Nusselt number significantly.

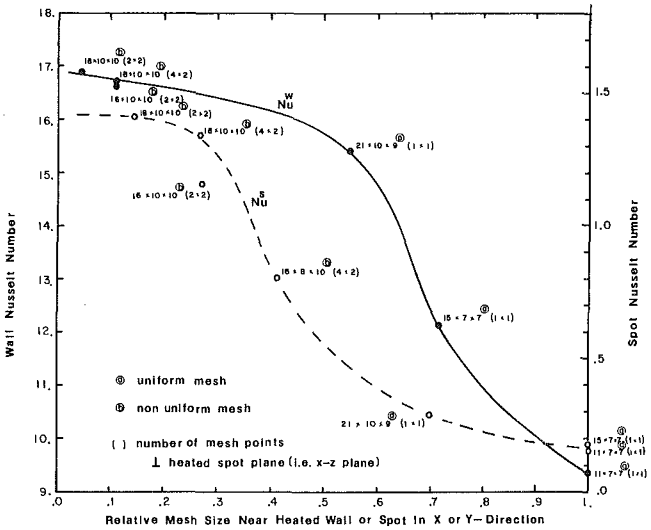

Fig. 7 Wall and spot Nusselt numbers versus relative mesh size for a three-dimensional rectangular enclosure with heated right hand wall and a center spot. The dotted line represents the spot Nusselt number.

From these studies, it appears that convergence can be obtained with a reasonable number of mesh points provided a non-uniform grid refined in the region of the walls or heated spots is used.

The CPU-time requirement for three-dimensional computation is of the same order as for two-dimensional cases per cell per time step. It ranges from 0.01 to 0.02 s per cell per time step. The higher value is required during rapid changes in the flow field as more iterations are required to satisfy the convergence criterion.

Conclusions

A numerical technique based on the marker and cell method has been applied to the computation of two and three-dimensional, transient, natural convection problems in rectangular enclosures. The technique appears to require 0.01 to 0.02 second CPU time per cell per time step on the McMaster University CDC 6400 computer for both two and three dimensional calculations.

The solutions obtained have been compared with a number of two-dimensional investigations and the three dimensional experiments of Torrance, et al. [17]. In the latter case, comparisons with flow patterns were made as only streak-line photographs are presented in [17]. The agreement was good.

The technique is easy to extend and has been used by us for three dimensional natural convection problems in porous media with internal heat generation and in turbulent flow problems using cell loss factors. The technique may also be used for turbulent natural convection problems with eddy viscosities and eddy conductivities (with minor modification to the finite difference equations), if these quantities can be expressed in terms of the dependent variables and position. Finally, the technique can be used in other coordinate system (such as cylindrical and spherical) again by simple modifications to the difference equations.

References

1 Fromm, J. E., "Numerical Solution of the Nonlinear Equations for a heated Fluid Layer," *Phys. of Fluid*, Vol. 8, No. 10, 1965, pp. 1757–1769.

2 Wilkes, J. O. and Churchill, S. W., "The Finite-Difference Computation of Natural Convection in a Rectangular Enclosure," *A.I.Ch.E. Journal*, Vol. 12, No. 1, 1966. pp. 161–166.

3 Aziz, K. and Hellums, J. D., "Numerical Solution of the Three Dimensional Equations of Motion for Laminar Natural Convection," *Phys. of Fluids*, Vol. 10, No. 2, 1976, pp. 314–324.

4 Torrance, K. E. and Rockett, J. A., "Numerical Study of Natural Convection in an Enclosure with Localized Heating from Below—Creeping Flow to the Onset of Laminar Instability," *J. Fluid Mech.*, Vol. 38, pt. 1, 1969, pp. 33–54.

5 Cabelli, A. and De Vahl Davis, G., "A Numerical Study of the Bernard Cell," *J. Fluid Mech.*, Vol. 45, pt. 4, 1971, pp. 805–829.

6 Chu, H. H. S., Churchill, S. W. and Patterson, C. V. S., "The Effects of Heater Size, Location Aspect Ratio, and Boundary Condition on Two-Dimensional, Laminar, Natural Convection in Rectangular Channel," ASME JOURNAL OF HEAT TRANSFER, 1976, pp. 194–201.

7 Harlow, F. H. and Welch, J. E., "Numerical Calculation of Time-Dependent Viscous Incompressible Flow of Fluid with Free Surface," *Phys. of Fluids* Vol. 8, No. 12, 1965, pp. 2182–2189.

8 Hirt, C. W., Nichols, B. D. and Romero, N. C., "SOLA—A Numerical Solution Algorithm for Transient Fluid Flow," LA-5852, Los Alamos, 1975.

9 Hirt, C. W. and Cook, J. L., "Calculating Three-Dimensional Flows Around Structures and Over Rough Terrain," *J. Comp. Phys.*, Vol. 10, 1972, pp. 324–340.

10 Harlow, F. H. and Amsden, A. A., "Numerical Calculation of Almost Incompressible Flow," *J. of Comp. Phys.*, Vol. 3, 1968, pp. 80–93.

11 Ozoe, H., Yamamoto, K., Churchill, S. W. and Sayama, H., "Three Dimensional, Numerical Analysis of Laminar Natural Convection in a Confined Fluid Heated From Below," ASME JOURNAL OF HEAT TRANSFER, May 1976, pp. 202–207.

12 Yanenko, *Method of Fractional Time Steps*, ed. M. Holt, Springer-Verlag, N.Y., 1971.

13 Calder, K. L., "In Clarification of the Equations of Shallow-Layer Thermal Convection for a Compressible Fluid based on the Boussinesq Approximation," *Quarterly J. of the Royal Meteorological Soc.*, Vol. 97, 1968, pp. 88–92.

14 Roache, P. J., *Computational Fluid Dynamics*, Hermosa Publishers, 1972.

15 De Vahl Davis, G., "Laminar Natural Convection in an Enclosed Rectangular Cavity," *Int. J. of Heat Mass Transfer*, Vol. 11, 1968, pp. 1675–1693.

16 MacGregor, R. K. and Emery, A. F., "Free Convection Through Vertical Plane Layer—Moderate and High Prandtl Number Fluids," ASME JOURNAL OF HEAT TRANSFER, Vol. 91, 1969, pp. 391–403.

17 Torrance, K. E., Orloff, L. and Rockett, J. A., "Experiments on Natural Convection in Enclosures with Localized Heating from Below," *J. of Fluid Mech.*, Vol. 36, pt. 1, 1969, pp. 21–31.

18 Dropkin, K. and Somerscales, E., "Heat Transfer by Natural Convection in Liquids Confined by Two Parallel Plates Which are inclined at various Angles With respect to the Horizontal," ASME JOURNAL OF HEAT TRANSFER, Vol. 87, 1965, pp. 77–84.

19 Elder, J. W., "Numerical Experiments with Free Convection in a Vertical Slot," *J. Fluid Mech.*, Vol. 24, 1966, pp. 823–843.

20 Eckert, E. R. G. and Carlson, W. O., "Natural Convection in an Air Layer Enclosed Between Two Vertical Plates with Different Temperatures," *Int. J. Heat Mass Transfer*, Vol. 2, 1961, pp. 106–120.

21 Landis, F. and Yanowitz, H., "Transient Natural Convection in a Narrow Vertical Cell," *Proceedings of the Fifth International Heat Transfer Conference*, Chicago, Aug. 1966, Vol. 2, pp. 139–151.

K. R. Randall
Research Assistant.
Mechanical Engineering Department

J. W. Mitchell
Professor.
Mechanical Engineering Department

M. M. El-Wakil
Professor.

Mechanical and Nuclear Engineering Departments
University of Wisconsin
Madison, Wisc.

Natural Convection Heat Transfer Characteristics of Flat Plate Enclosures

Heat transfer by natural convection in rectangular enclosures has been experimentally studied using interferometric techniques. The effects of Grashof number, tilt angle, and aspect ratio on both the local and average heat transfer coefficients have been determined. The Grashof number range tested was 4×10^3 *to* 3.1×10^5*, and the aspect ratio (ratio of enclosure length to plate spacing) varied between 9 and 36. The angles of tilt of the enclosure with respect to the horizontal were 45, 60, 75 and 90 deg. Correlations are developed for both local and average Nusselt number over the range of test variables. The effect of tilt angle is found to reduce the average heat transfer by about 18 percent from the value of 45 deg to that at 90 deg. No significant effect of aspect ratio over the range tested was found. A method for characterizing the flow regimes that is based on heat transfer mechanisms is proposed.*

Introduction

The free convection heat loss across inclined layers is of interest in many engineering systems, and, recently, to designers of flat plate solar collectors. Reduction of heat loss through cover plates increases collector efficiency and allows smaller collector areas to be used. While there have been many relevant studies of free convection heat transfer in enclosures [1–17], adequate correlations do not exist over a wide range of angles and aspect ratios.

The recent results and correlations of Hollands, et al. [8] for average heat transfer are generally accepted as representative of heat transfer in large aspect ratio enclosures for inclinations less than 70 deg, and agree well with the previous data. Raithby, et al. [11] present a correlation for 90 deg which has been theoretically derived and substantiated with data from other studies, and is postulated to apply for angles between 70 and 150 deg.

There is a general lack of agreement on the effect of aspect ratio on the average heat transfer coefficient. Eckert and Carlson [5], Emery and Chu [6], MacGregory and Emery [9] and Raithby, Hollands, and Unny [11] report a definite effect of aspect ratio for vertical enclosures. There is not agreement on the magnitude of the effect. Correlations of average Nusselt number with aspect ratio in the form

$$\overline{\mathrm{Nu}}_L = C\mathrm{Gr}_L{}^n A^m$$

yield values of the exponent m ranging from −0.1 [5] to −0.3 [9].

Batchelor [14] has theoretically determined that the effect of enclosure ends should extend along the heated surface for a distance approximately equal to the plate spacing. This implies that the effect of aspect ratio decreases as aspect ratio increases. Dropkin and Sommerscales [4] and DeGraaf and van Der Held [3] have found no effect of aspect ratio over all angles of inclination.

Although average heat transfer rates have been extensively studied, little information exists on the local variation of heat transfer coefficient along the heated surface. Eckert and Carlson [5] conducted a study of local coefficients for vertical enclosures and found several flow regimes. Correlations were developed for the local coefficients at each end of the enclosure.

In the present study, local values of the heat transfer coefficient along the hot plate are obtained using interferometric techniques. The range of inclination angles studied is 45 to 90 deg, and the aspect ratio is varied from 9 to 36. The local values are integrated over the plate length to determine average heat transfer coefficients.

Test Procedure

Fig. 1 is a two-dimensional schematic of the test facility. The lower heated plate is a 45.7 cm long by 10.2 cm wide copper plate and the upper plate, of the same size, is constructed of aluminum. The copper plate is electrically heated by a thin foil-type heater cemented to the backside and the aluminum plate is cooled by passing water through channels machined into its backside.

Surface temperature measurements are obtained from nine thermocouples penetrating each plate from the rear to the front face. Maximum temperature variations of less than 0.5°C over the surface of the cold plate and 1.5°C over the surface of the hot plate were observed at temperature differences up to 90°C. Each surface was polished and nickel plated to reduce radiation contributions to the total heat flow for energy balance purposes.

The small diameter of the interferometer light beam (3.6 cm) necessitated moving the test section relative to the light path in order to view the entire enclosure length. A rigid insulated channel consisting of bakelite sides with external styrofoam insulation was constructed and into which the test section tightly fit. Two optically flat glass windows were inserted into opposite sides of the channel so that the interferometer light beam passed through the air layer. The test apparatus could then slide past the windows so the air layer could be viewed through the interferometer in its whole extent while the bakelite channel provided lateral retaining walls for the air layer.

Contributed by the Heat Transfer Division for publication in the JOURNAL OF HEAT TRANSFER. Manuscript received by the Heat Transfer Division January 4, 1978.

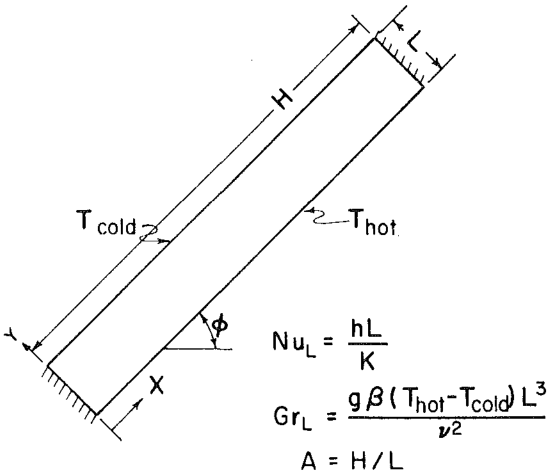

Fig. 1 Schematic of test facility showing nomenclature used for presenting results

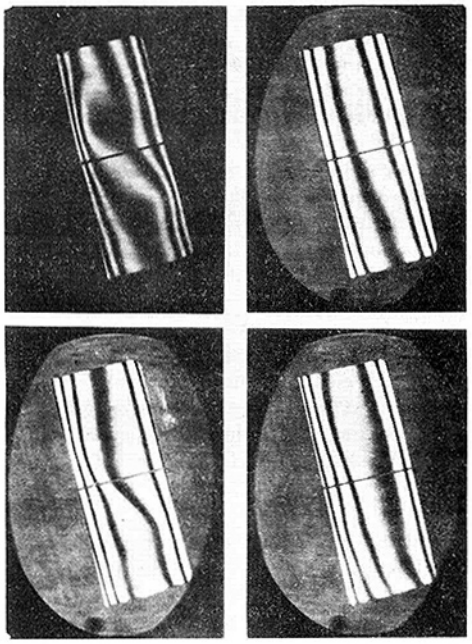

Fig. 2 Interferograms for four different times for Gr_L = 26000, 75 deg tilt angle

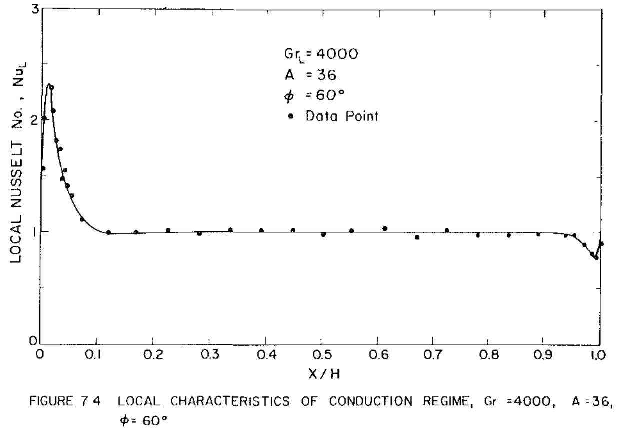

Fig. 3 Local heat transfer coefficient along the surface for the conduction regime

The aspect ratio of the enclosure was varied using interchangeable end spacers constructed of bakelite. The range of enclosure aspect ratios (H/L) was 9 to 36, and the width aspect ratio range (W/L) was 2.3 to 8. The temperature profile along the surface of the spacers was found to be very close to linear. This was determined by analysis of interferograms.

Fig. 2 presents interferograms typical of those obtained in this study. The dark and light contours are isotherms. Measurements of local temperature gradients were obtained from similar interferograms and used to determine the local heat transfer coefficients. The accuracy of the results is mainly dependent on the accuracy of measurements made on the interferograms. Based on the repeatability of readings, the accuracy of determining heat transfer coefficients from the pictures is ±5 percent.

The local Nusselt number is based upon the plate spacing, L, and the total temperature difference, $T_H - T_C$. It is calculated from the nondimensional temperature gradient at the hot surface which is then multipled by the ratio of the thermal conductivity evaluated at the surface temperature to that evaluated at the mean enclosure temperature

$$\mathrm{Nu}_L = \frac{hL}{k} = -\left[\frac{k_H}{k}\,\frac{\partial[(T-T_C)/(T_H-T_C)]}{\partial(y/L)}\right]_0 \qquad (1)$$

where k is evaluated at the mean temperature, $(T_H + T_C)/2$.

The average Nusselt number is found by numerically integrating the local values over the entire plate length

$$\overline{\mathrm{Nu}}_L = \frac{\bar{h}L}{k} = \frac{1}{H}\int_0^H \mathrm{Nu}_L dx \qquad (2)$$

The corresponding value of the Grashof number is based on properties also evaluated at the arithmetic mean temperature.

Local Heat Transfer Results

1 **Conduction Regime.** Heat transfer in the conduction regime is traditionally characterized by purely molecular conduction in the center of the enclosure. In this region, $\mathrm{Nu}_L = 1$. However it is known that there is convection in the end turn-around regions, and $\mathrm{Nu}_L \neq 1$ there. Analysis of interferograms for this regime shows that boundary layers develop on both surfaces and merge within a short distance. There is no net heat transport by convection in the boundary layers in the center section of the cavity.

Fig. 3 presents a typical profile for the local Nusselt number along the surface for the conduction regime. At the lower corner of the hot plate and the upper corner of the cold plate (labeled the starting

Nomenclature

g = acceleration due to gravity
$\mathrm{Gr}_L = g\beta(T_H - T_C)L^3/\nu^2$ Grashof number
$\mathrm{Gr}_x = g\beta(T_H - T_C)x^3/\nu^2$ Grashof number
h = local heat transfer coefficient
$\bar{h}$ = average heat transfer coefficient
H = plate length
k = thermal conductivity
L = plate spacing
$\overline{\mathrm{Nu}}_L = \bar{h}L/k$ average Nusselt number
$\mathrm{Nu}_L = hl/k$ local Nusselt number
$\mathrm{Nu}_x = hx/k$ local Nusselt number
$\mathrm{Pr} = \nu/\alpha$ Prandtl number
T = temperature
W = plate width
x = distance along plate from corner
y = distance normal to plate
α = thermal diffusivity
β = coefficient of volumetric expansion
ν = kinematic viscosity
ϕ = enclosure tilt angle from horizontal

Subscripts

C = cold plate
d = departure corner
H = hot plate
L = based on L
p = penetration
s = starting corner
x = based on x

corners by Eckert and Carlson [5]) the local heat transfer coefficient is larger than the average by a factor of at least two indicating a significant contribution by convection to the local heat transfer. In contrast, at the upper corner of the hot plate and lower corner of cold plate (labeled the departure corners), the heat transfer coefficient is lower.

The linear temperature profile along the end spacers of the test facility forces the local Nusselt number to approach unity at either end. This results in a maximum local Nusselt number near the starting corner and a minimum near the departure corner. This behavior generally occurs within 1.27 cm of the corners and has been neglected in obtaining local Nusselt number correlations for flow in the conduction and laminar boundary layer regimes.

The local heat transfer near the ends is a function only of the plate spacing and the local distance from the corner, and independent of the plate length. Eckert and Carlson [5] found for vertical orientations that the local Nusselt number in the starting corners could be correlated in terms of the distance from the corner by

$$\mathrm{Nu}_{x,s} = C_1 \mathrm{Gr}_x{}^n \tag{3}$$

The local heat transfer coefficient decreases until it reaches a point where the local Nusselt number, Nu_L, equals unity. This distance is called the penetration depth, x_p, and Eckert and Carlson present a detailed procedure for finding the penetration depth and the average heat transfer in the corner for vertical enclosures. The penetration depth is the distance it takes for the local value to reach the center value. The penetration depth and the average Nusselt number over the penetration distance are correlated as

$$x_{p,s}/L = C_2 Gr_L{}^m,\ \overline{\mathrm{Nu}}_{L,s} = C_3 \tag{4}$$

The present results are also correlated on this basis, and the coefficients as a function of tilt angle are given in Table 1. The results for 90 deg agree within 15 percent of those from [5].

In the departure corner, the local heat transfer is a function of both distance from the corner and plate spacing. Following the form developed by Eckert and Carlson for vertical enclosures, the present results can be represented as

$$x_{p,d}/L = C_2 \mathrm{Gr}_L{}^{0.75},\ \mathrm{Nu}_{x,d} = C_1 \mathrm{Gr}_x{}^n \mathrm{Gr}_L{}^{-0.55},\ \overline{\mathrm{Nu}}_{L,d} = C_3 \tag{5}$$

where x is the distance measured from the corner. The coefficients are given in Table 2 where the values for 90 deg agree within 15 percent of those from [5].

2 Laminar Boundary Layer Regime. For Grashof numbers beyond the critical value, the flow becomes unstable and buoyancy driven laminar boundary layers form on the hot and cold surfaces. For small Grashof numbers the thermal boundary layers build up in a manner similar to flow over vertical flat plates in an infinite medium. The boundary layers are relatively thick and merge together in the center of the cavity. An analysis of interferograms taken under these conditions shows that the major portion of the heat transfer from one plate to another occurs by convection in the boundary layers while in the center a small fraction is transferred by conduction across the flow.

Table 1 Coefficients for use in equations (3) and (4) for the starting corner, conduction regime

ϕ	C_1	n	C_2	m	C_3
90	0.31	0.21	0.048	0.54	1.62
75	0.30	0.21	0.043	0.54	1.62
60	0.30	0.21	0.043	0.54	1.62
45	0.26	0.21	0.031	0.54	1.62

Table 2 Coefficients for use in equations (5) for the departure corner, conduction regime

ϕ	C_2	n	C_1	C_3
90	0.0035	0.4	3.09	0.83
75	0.0051	0.4	2.85	0.83
60	0.0030	0.4	3.20	0.83
45	0.0027	0.4	3.27	0.83

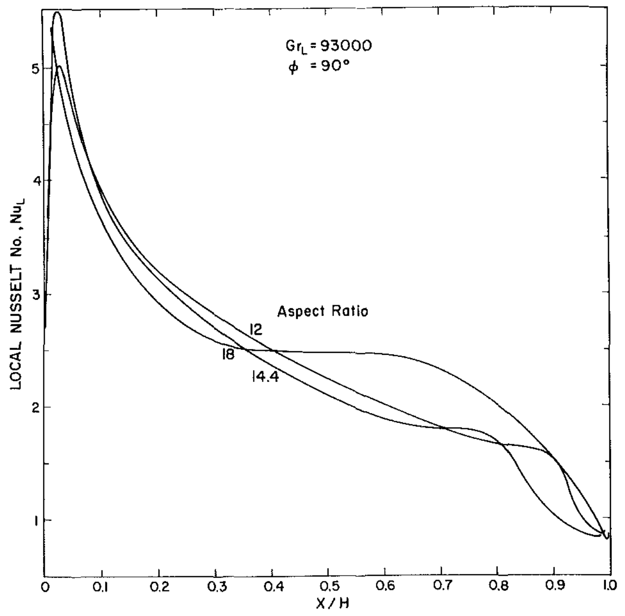

Fig. 4 Local heat transfer coefficient along the surface of a vertical enclosure for laminar boundary layer regime

Fig. 4 shows local heat transfer coefficients in the laminar boundary layer regime for three aspect ratios. At the lower aspect ratios, the local Nusselt number continuously decreases with distance along the plate. In this case the average heat transfer is not accurately reflected by the local values at the center of the enclosure. This is called the transition region of the laminar boundary layer regime.

At increased aspect ratio, or for higher Grashof numbers, the individual boundary layers on the hot and cold surfaces are separate. The region between the boundary layers is thoroughly mixed by eddy diffusion. The local Nusselt number is uniform in the center of the enclosure, and the average value equals the local value at the center. This is called the fully established region.

Continuous observation of the temperature profiles shows that the boundary layers are laminar. In the center of the cavity, continuous mixing occurs and eddies can be seen to randomly separate from the outer edges of the layers and disappear into the core. This results in large scale perturbations of the temperature profiles near the walls, and the profile across the cavity varies with time. Eckert and Carlson and DeGraaf and van der Held have also noted these fluctuations in the core and the low frequency fluctuations of the temperature profiles in the boundary layer.

Fig. 2 shows four interferograms taken at random intervals in the center of the enclosure for a tilt angle of 75 deg, a plate spacing of 1.9 cm, and a Grashof number of 26000. These show the large scale mixing and unsteadiness in the core. These fluctuations are too large to be classified as turbulent eddies and are probably due to local buoyancy effects.

An analysis of free convection under these eddying conditions require multiple pictures to obtain an average local Nusselt number. Pictures were taken at random, different times, and the average local value was obtained from averaging the individual values. The average local Nusselt profiles along the surface are essentially constant in the center section where the major eddy effects occur. Near the ends where the flow is developing, the local values do not fluctuate.

Fig. 5 shows a typical local Nusselt number profile. The data points are shown for a typical local Nusselt number profile. The data points are shown to demonstrate the large fluctuations of the local Nusselt number in the center. The constant value of the average Nusselt number in the center of the enclosure indicates that the average local wall heat flux is a constant. Therefore, there is no boundary layer growth or convection along the surface and the transport mechanism is eddy diffusion across the channel. The average value of local Nusselt number was consistently found to be nearly constant in the center of the enclosure for all angles of tilt, even though the instantaneous

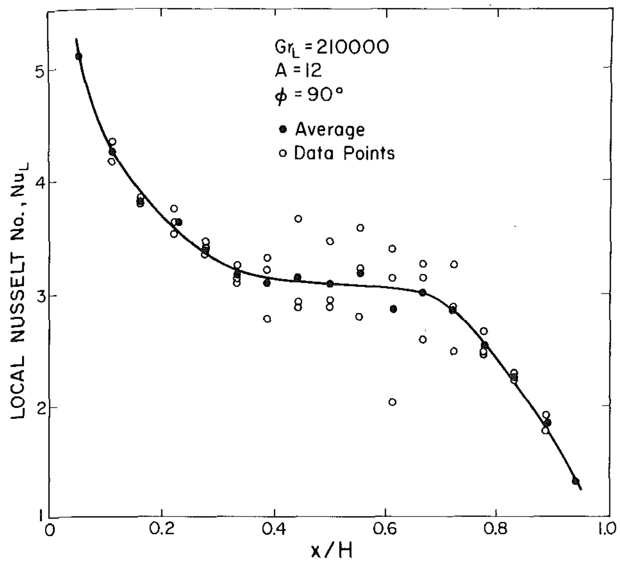

Fig. 5 Fluctuations of local heat transfer coefficient for vertical enclosure

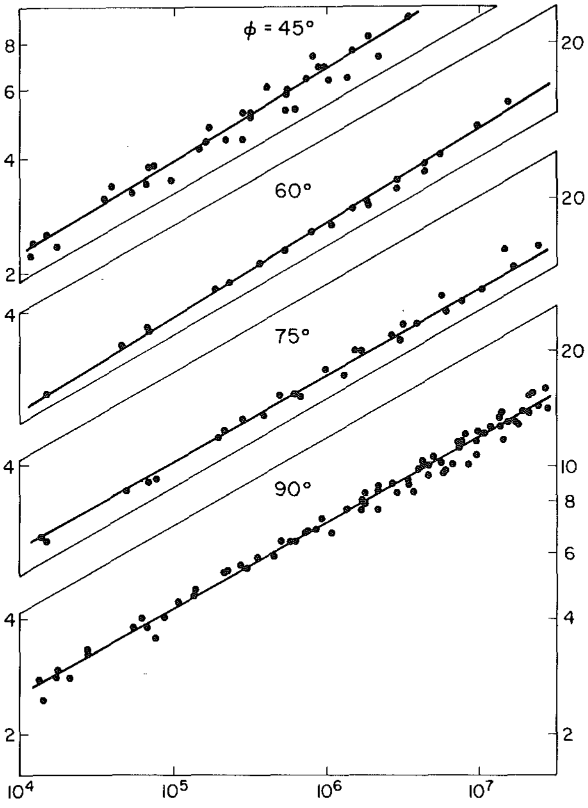

Fig. 6 Local heat transfer coefficients for starting corner, laminar boundary layer regime

Table 3 Coefficients for use in equation (3) for the starting corner, laminar boundary layer regime

φ	C_1	n
90	0.34	0.22
75	0.29	0.23
60	0.23	0.24
45	0.24	0.24

values fluctuated considerably.

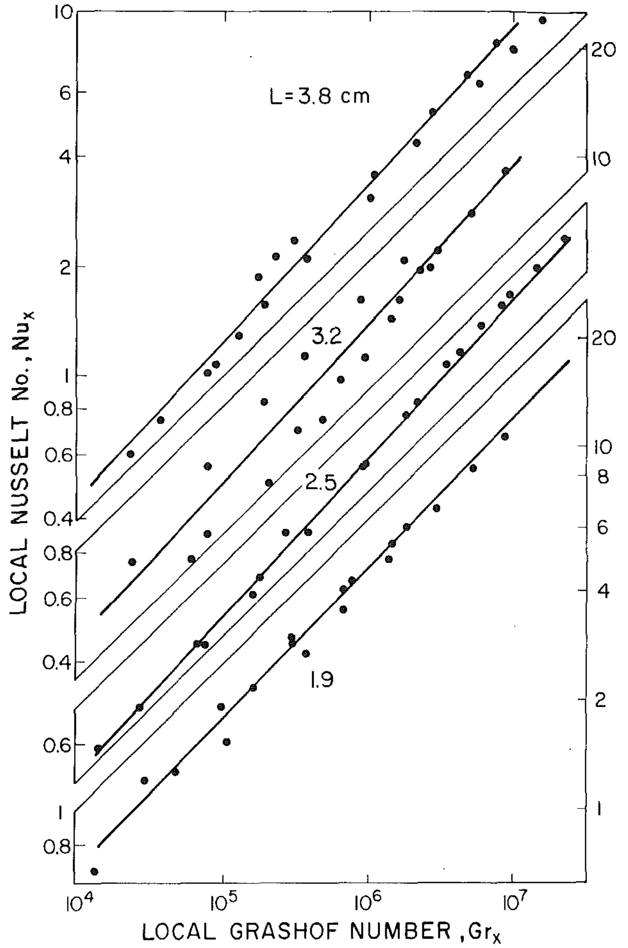

Fig. 7 Local heat transfer coefficients for departure corner, laminar boundary layer regime, φ = 90 deg

Table 4 Coefficients for use in equation (6) for the departure corner, laminar boundary layer regime

φ	L(cm)	C_1	φ	L(cm)	C_1
90	1.9	0.01	75	2.54	0.0096
	2.54	0.0084		3.81	0.0078
	3.14	0.0079			
	3.81	0.0077	60	2.54	0.011
				3.81	0.0092
			45	A11	0.014

The local Nusselt number in the starting corner can be correlated in the same manner as for the conduction regime. The characteristic distance is again the distance from the starting corner. The results are presented in Fig. 6 for tilt angles of 45, 60, 75 and 90 deg and aspect ratios of 9 to 24. Data for both the transition region and the region dominated by the eddy diffusion effect are included. A least squares fit of the data to equation (3) results in the constants given in Table 3 which fit the data to within ±5 percent.

Attempts to correlate the local variations of the heat-transfer coefficient at the departure end are complicated by the fact that there is an effect of plate spacing as well as tilt angle. All tests using the same plate spacing correlate regardless of Gr_L and the plate length, and a nondimensional quantity using the plate spacing could not be found. The results for tilt angles of 90 deg and four plate spacings are shown in Fig. 7. The variation with plate spacing is greatest for 90 deg, and the results for 45 deg for all spacings are the same.

The resulting correlation for a given plate spacing is:

$$Nu_{x,d} = C_1 Gr_x{}^n \qquad (6)$$

where C_1 is a function of plate spacing and angle as given in Table 4 for the different tests, and n equals 0.44 for all tests.

For tilt angles less than 90 deg the penetration depth in the starting and departure corners becomes progressively smaller as the angle is decreased. This is due to the increasing component of the buoyant force perpendicular to the wall which promotes faster development of the boundary layers. At angles of 45 deg and 60 deg the end effects occupy approximately the same area and play less of a role in the total heat transfer. For all runs at 45 and 60 deg the end effects failed to penetrate to the center of the enclosure for aspect ratios greater than 12. This suggests that the measurements of Hollands, et al. [8] in which the heat transfer is measured only in the center of the enclosure are valid over this range of tilt angles.

At angles near vertical the disturbance caused by the corners occupies a much larger portion of the enclosure and may in fact occupy the whole area. It is to be expected that significant effects of aspect ratio on the local heat transfer coefficient would be evident at these angles. As shown in Fig. 4, for the vertical orientation at a Grashof number of 93,000, a decrease in aspect ratio from 18 to 14.4 to 12 changes the flow regime from the fully established region to the transition region in the laminar boundary layer regime.

Average Heat Transfer Results

The average heat transfer coefficient, evaluated by integrating the local values over the plate length, is a function of Grashof Number and aspect ratio. The effect of the aspect ratio is determined by the penetration depth of the disturbances in the starting and departure corners. For very large enclosures, these disturbances each occupy a relatively small area and are separated by a region in which Nu_L is essentially constant. For small enclosure lengths, the disturbances occupy a proportionately larger area, and a length is reached where the entire enclosure is occupied by end effects. For a fixed plate spacing and Grashof number, the end effects occupy a smaller portion of the collector area as the angle from the vertical increases.

1 **Conduction Regime.** The average Nusselt number in the conduction regime can be directly computed because the Nusselt number in the center of the enclosure is unity provided that the end turnaround regions do not penetrate to the center section. The average heat transfer coefficient along the plate surface evaluated using equation (2) yields

$$\overline{\mathrm{Nu}}_L = 1 + (\overline{\mathrm{Nu}}_{L,s} - 1)(x_{p,s}/L)(L/H) + (\overline{\mathrm{Nu}}_{L,d} - 1)(x_{p,d}/L)(L/H) \tag{7}$$

Equations (4) and (5) can be substituted into (7) to determine the average heat transfer rate in the conduction regime.

Equation (7) demonstrates that although the local value in the center section is unity, the average value may be different from unity due to the end effect. For the experiments of Hollands, et al. [8], in which the heat transfer is measured only in the center five in. of the enclosure, $\overline{\mathrm{Nu}}_L$ would be found to be 1, while equations (4, 5) and (7) would yield values a few percent greater than unity. This demonstrates that if the enclosure is not sufficiently long the net heat transfer in the corners can contribute significantly to the total heat transfer.

2 **Laminar Boundary Layer Regime.** Heat transfer in the boundary layer regime is complicated by the fact that there are two distinct flow patterns. In the transition region the boundary layers join together and in the fully established region the boundary layers are separated by a mixed core. For the fully established regime, $\overline{\mathrm{Nu}}_L$ has been found to be equal to the local Nusselt number at the center section of the enclosure within the accuracy of the data.

For flow in the transition region Nu_L is a continuously decreasing function of distance from the starting corner. There is significant heat transfer by convective transport in the boundary layer and conductive transport across the center. There is also a significant aspect ratio effect on the local profile as evident in Fig. 4, but the integrated average Nusselt number does not vary significantly with aspect ratio for the range studied. For smaller aspect ratios, the local coefficient in the starting corner is higher than that at larger aspect ratios while in the departure corner, the reverse is true. The net effect is to bring the averages for different aspect ratios into close agreement (within four percent). An effect of aspect ratio of the magnitude suggested by [6] and [7] has not been noted.

Fig. 8 shows a comparison of the integrated local Nusselt numbers with correlations of previous investigations for tilt angles of 45 and 90 deg. The present results fall midway in the range of the reported correlations and there is general agreement within about 10 percent. There has been no aspect ratio effect determined from these studies.

An examination of the effect of tilt angle on the average Nusselt number shows a continuously decreasing function as the tilt angle increases beyond 45 deg. This is in contrast to the results of [1] where a definite minimum was noted at an angle of approximately 70 deg and to [11] and [12] which suggest that the results for the vertical cavity can be scaled to as low as 70 deg by $\mathrm{Gr}_L\ \mathrm{Pr} \sin \phi$, which results in an average Nusselt number which increases with angle. This difference can, in part, be attributed to differences in aspect ratio range. The experimental results of [1] are for aspect ratios in the range of 1 to 6. The suggestion made in [11] about scaling is based on the results from the theoretical two-dimensional analysis of [12], which concentrates on aspect ratios of 3 and 10. The present data are for aspect ratios of 9 to 36.

The experimental observation that $\overline{\mathrm{Nu}}_L$ decreases with tilt angle suggests the possibility of scaling the results of the 45 deg enclosure to larger angles. The data, correlated on a purely empirical basis, are shown in Fig. 9 and can be represented over the range of 45 deg to 90 deg by

$$\overline{\mathrm{Nu}}_L = 0.118[\mathrm{Gr}_L \mathrm{Pr} \cos^2 (\phi - 45)]^{0.29} \tag{8}$$

Equation (8) fits the data to within ±8 percent over the Grashof number range of 4×10^3 to 3.1×10^5, and aspect ratios of 9 to 36. Results obtained from this equation agree within 10 percent of [8] and [16] at tilt angles of 45 deg and 60 deg.

Previously, flow regimes for free convection were defined based on the temperature distribution across the core of the cavity [5]. In the "transition" regime the temperature profile is linear in the center, while in the "fully established" regime the temperature gradient is

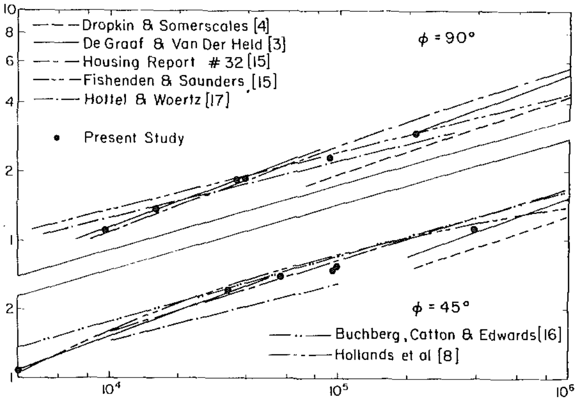

Fig. 8 Comparison of present average heat transfer results with those of previous investigators

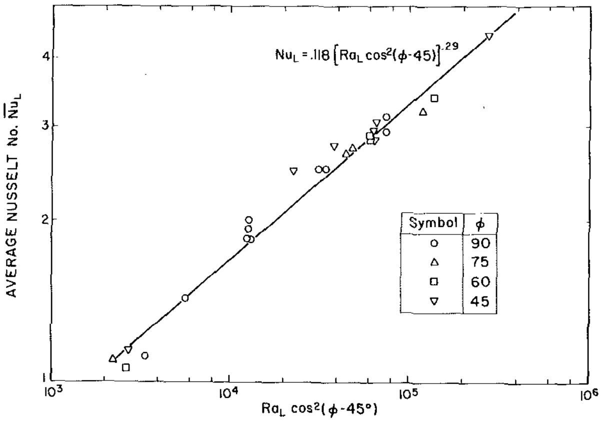

Fig. 9 Empirical correlation for present results for the range of tilt angles of 45 to 90

zero at the centerline. It appears more relevant from a heat transfer view to define the regimes based on the mechanisms and heat transfer behavior consistent with definitions for internal flow.

In the transition regime, the mechanisms are convection in the boundary layer and molecular conduction across the cavity in the core. The local heat transfer coefficient continuously decreases with distance along the surface. In the fully established regime, the boundary layers are fully established and heat is transferred by eddy mixing across the core. The heat transfer coefficient is uniform along the surface in the center of the enclosure.

Figs. 10 and 11 show the flow regimes on a plot of aspect ratio as a function of Grashof number for enclosure angles of 45 and 90 deg. The conduction limits are from [7] for 45 deg and [5, 7] and [13] for 90 deg. Data for the boundary between the transition and fully established regimes were generated from visual observations of the fringe patterns. At a fixed aspect ratio, the Grashof number was increased and the value at which the steady pattern for the transition regime changed to the unsteady motion of the fully established regime was observed. The boundary between the two regimes is not a well defined line as the change is not abrupt.

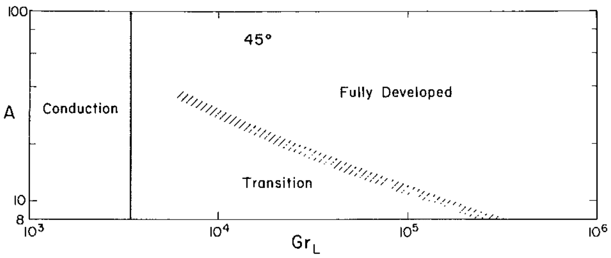

Fig. 10 Flow regimes for a tilt angle of 45 deg

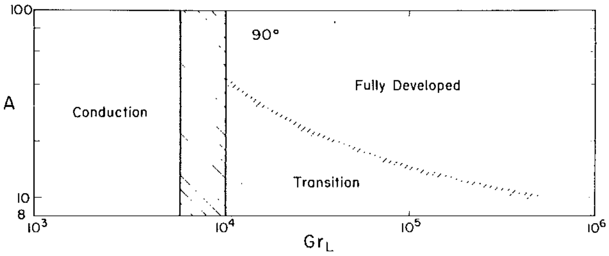

Fig. 11 Flow regimes for a tilt angle of 90 deg

Conclusions

The use of interferometry has proven a suitable and accurate means to evaluate the two-dimensional temperature fields, and therefore the local heat transfer coefficients in inclined flat plate enclosures. Correlations have been developed for the local as well as average natural convection heat transfer over a range of tilt angles from 45 to 90 deg. The following conclusions were drawn for this study.

1 A conduction regime exists for the range of $\mathrm{Gr}_L \mathrm{Pr} \cos \phi$ less than 1709 for tilt angles less than 72 deg, while above this angle the criterion is a nonanalytic function of angle [7]. In this regime the convective heat transport in the ends of the enclosure can be significant for low aspect ratio enclosures. Equation (7) can be used to evaluate the average Nusselt number. The average heat transfer remains relatively constant for tilt angles between 60 and 90 deg.

2 A laminar boundary layer regime exists for Gr numbers greater than the critical value. The flow in this regime can be characterized by two distinct regions: (a) the transition region where there is significant heat transfer across the center of the enclosure by conduction; (b) the fully developed region where the transport mechanism is eddy diffusion across the center of the enclosure.

3 In the transition region the local Nusselt number continuously decreases from the starting to departure corner and the average heat transfer is not equal to the local value at the center. The local correlations based upon the distance from the corners are not valid to the center of the enclosure.

4 In the fully developed region the flow is highly unsteady in the enclosure center, but the average local Nusselt number is uniform. The average heat transfer over the entire surface is equal to the local values in the center. The local correlations in the starting and departure corners can be extended until they meet the average.

5 The effect of aspect ratio on the average heat transfer in the laminar boundary layer regime is found to be negligible over the range studied. The effects of tilt angle and Grashof number can be adequately represented by the empirical correlation

$$\overline{\mathrm{Nu}}_L = 0.118[\mathrm{Gr}_L \mathrm{Pr} \cos^2 (\phi - 45)]^{0.29} \tag{8}$$

over the range of angles between 45 and 90 deg, Grashof number values of 4×10^3 to 3.1×10^5, and aspect ratios of 9 to 36.

Acknowledgments

The research on which this paper is based has been supported by the Energy Research and Development Agency under Contract No. E(11-1)-2971.

References

1 Arnold, J. N., I. Catton and D. K. Edwards, "Experimental Investigation of Natural Convection in Inclined Rectangular Regions of Differing Aspect Ratios," ASME JOURNAL OF HEAT TRANSFER, Vol. 98, 1976, pp. 67–71.

2 Catton, I., P. Ayyaswamy and R. M. Clever, "Natural Convection Flow in a Finite Rectangular Slot Arbitrarily Oriented with Respect to the Gravity Vector," *International Journal Heat Mass Transfer*, Vol. 17, 1974, pp. 173–184.

3 DeGraaf, J. and E. van Der Held, "The Relation Between the Heat Transfer and the Convection Phenomena in Enclosed Plane Air Layers," *Appl. Sci. Res.*, Section A, Vol. 3, 1952, pp. 393.

4 Dropkin, D. and E. Somerscales, "Heat Transfer by Natural Convection in Liquids Confined by Two Parallel Plates Which are Inclined at Various Angles with Respect to the Horizontal," ASME JOURNAL OF HEAT TRANSFER, Vol. 87, 1965, pp. 77–84.

5 Eckert, E. R. G. and W. O. Carlson, "Natural Convection in an Air Layer Enclosed Between Two Vertical Plates with Different Temperatures," *International Journal Heat Mass Transfer*, Vol. 2, 1961, pp. 106–120.

6 Emery, A. and N. C. Chu, "Heat Transfer Across Vertical Layers," ASME JOURNAL OF HEAT TRANSFER, Vol. 91, 1969, p. 391.

7 Hollands, K. G. T. and L. Konicek, "Experimental Study of the Stability of Differentially Heated Inclined Air Layers," *International Journal Heat Mass Transfer*, Vol. 16, 1973, pp. 1467–1476.

8 Hollands, K. G. T., T. E. Unny, G. Raithby and L. Konicek, "Free Convection Heat Transfer Across Inclined Air Layers," ASME JOURNAL OF HEAT TRANSFER, Vol. 98, 1976, pp. 189–193.

9 MacGregor, R. K. and A. F. Emery, "Free Convection Through Vertical Plane Layers-Moderate and High Prandtl Number Fluids," ASME JOURNAL OF HEAT TRANSFER, Trans. ASME, Vol. 91, 1969, p. 391.

10 Ozoe, H. and H. Sayama, "Natural Convection in an Inclined Square Channel," *International Journal Heat Mass Transfer*, Vol. 17, 1974, pp. 401–406.

11 Raithby, G. D., K. G. T. Hollands and T. E. Unny, "Free Convection Heat Transfer Across Fluid Layers of Large Aspect Ratio," ASME Paper 76-HT-37.

12 Ayyaswamy, P. and I. Catton, "The Boundary-Layer Regime for Natural Convection in a Differentially Heated, Tilted Rectangular Cavity," ASME JOURNAL OF HEAT TRANSFER, Vol. 95, 1973, pp. 543–545.

13 Dixon, M. and S. D. Probert, "Heat Transfer Regimes in Vertical, Plane-Walled, Air-Filled Cavities," *International Journal Heat and Mass Transfer, 18*:709–710, 1975.

14 Batchelor, G. K. "Heat Transfer by Free Convection Across a Closed Cavity Between Vertical Boundaries at Different Temperatures," *Quant. of Applied Math.*, Vol. 12, pp. 209–233, 1954.

15 Tabor, H., "Radiation, Convection and Conduction Coefficients in Solar Collectors," *Bull. Res. Council of Israel*, Vol. 6C, 1974.

16 Buchberg, H.; I. Catton, and D. R. Edwards, "Natural Convection in Enclosed Spaces: A Review of Application to Solar Energy Collection," *JNT 98*:2, May, 1976.

17 Hottel, H. C. and D. B. Woertz, "The Performance of Flat Plate Solar Heat Collectors," Trans. ASME, Vol. 64, 1942, pp. 91–104.

P. C. Jain
B. L. Lohar
Department of Mathematics
Indian Institute of Technology, Bombay
Powai, Bombay-400 076
India

Unsteady Mixed Convection Heat Transfer from a Horizontal Circular Cylinder

A numerical investigation of an unsteady mixed convection from a horizontal circular cylinder is presented. The coupled basic equations of motion and energy are solved for two cases 1) $Re = 100$, $Gr = 10^4$ and 2) $Re = 200$, $Gr = 5 \times 10^4$. The velocity field and the temperature field around the cylinder are exhibited by streamlines and isotherms at different times. The Strouhal number for the shedding of vortices in the wake of the cylinder is calculated. Figures have been drawn to show the variations of the local and the mean Nusselt numbers with time. The effects of the presence of free convection are discussed.

Introduction

In the area of hot wire anemometry, the ambient fluid current is so fast that, generally, the buoyancy effect can be neglected. But in the case of slow fluid flow this may not be the case and the cooling of wire may be affected by buoyancy forces. Hence, a study of the phenomena of heat transfer, when both natural and forced convection are important, seems to be of great interest.

Some studies on the dynamical behavior of the fluid flow past a circular cylinder at moderate Reynolds numbers have been reported in the literature [1, 2, 3]. The problem of forced convection from a horizontal circular cylinder has also been studied by several authors. Eckert and Soehngen [4] have presented an experimental study of the local heat transfer around a circular cylinder at Reynolds numbers 20–500, while Krall and Eckert [5] have reported experimental results for a wide range of Reynolds numbers 1–5000. Hieber and Gebhart [6] have examined the steady-state problem of forced convection by the method of matched asymptotic expansions at low Reynolds numbers. Krall and Eckert [5] have also presented the numerical results for the forced convection problem for Reynolds numbers 20–200 by taking two surface boundary conditions: 1) uniform wall temperature and 2) uniform heat flux. Jain and Goel [7] have studied the unsteady problem numerically for forced convection from a circular cylinder at moderate Reynolds numbers.

There are several papers reporting experimental results on the mixed convection from a horizontal circular cylinder. When the buoyancy forces and the fluid flow are in the same direction, Oosthuizen and Madan [8] suggested a correlation formula relating the heat transfer due to the forced convection to that due to the mixed convection. They [9] also studied the effect of a change in the direction of the forced flow on the heat transfer from the cylinder. Sharma and Sukhatme [10] have considered a forced flow at right angle to the buoyancy forces. Gebhart, et al. [11] considered the spectrum of processes from the forced, through mixed to natural convection from long horizontal wires. Sarma and Sukhatme [12] measured the heat transfer in cross-flow in forced convection and mixed convection by using a modified mixed convection parameter. Nayak and Sandborn [13] made an experimental study of heat transfer from small horizontal cylinders in directly opposed forced and free convection flow.

Some authors studied the steady-state problem of mixed convection by using approximate methods. Joshi and Sukhatme [14] used a coordinate perturbation technique for the case of assisting and opposed free and forced convection flows by neglecting the buoyancy force term in one of the basic equations. Sparrow and Lee [15] obtained a solution of the problem by expanding velocity and temperature terms in power series. Merkin [16] used a numerical technique for the heated and cooled cylinder by taking large Reynolds number and Grashof number.

Unsteady behavior of heat transfer in the case of mixed convection has not been reported in the literature. In the present paper, we consider the flow of a uniform stream over a horizontal circular cylinder which is held at a constant temperature T_w surrounded by fluid at temperature T_∞, with the fluid flowing in an upward vertical direction. It may be recalled that in the case of mixed convection, the momentum equation and the energy equation are coupled, contrary to the case of forced convection [7]. This feature introduces additional constraints on the numerical method for the solution of the problem. We have considered two cases by making the mixed convection parameter (Gr/Re^2) equal to 1 ($Re = 100$, $Gr = 10^4$) and 1.25 ($Re = 200$, $Gr = 5 \times 10^4$). We have made the Prandtl number Pr equal to 0.73.

Governing Equations and Boundary Conditions

We consider two-dimensional unsteady flow of an infinite stream of an incompressible viscous fluid past a horizontal circular cylinder. The incident stream is uniform and has the velocity U [17] and temperature T_∞. The cylinder has the uniform wall temperature $T_w > T_\infty$. Heating by viscous dissipation is neglected and ν, K, β are assumed to be constants throughout the fluid. The density is assumed

---

Contributed by the Heat Transfer Division for publication in the JOURNAL OF HEAT TRANSFER. Manuscript received by the Heat Transfer Division May 22, 1978.

to vary with temperature. The equations of motion in cylindrical polar coordinates in the nondimensional form, after applying Boussinesq's approximation [18], are given by

$$-\frac{\partial \zeta}{\partial t} + \frac{1}{r}\frac{\partial(\psi, \zeta)}{\partial(r, \theta)} = -\frac{2}{\mathrm{Re}}\nabla^2\zeta + 4\frac{\mathrm{Gr}}{\mathrm{Re}^2}\left\{\frac{\partial T}{\partial \theta}\sin\theta + \frac{1}{r}\frac{\partial T}{\partial \theta}\cos\theta\right\} \quad (1)$$

$$\zeta = -\nabla^2\psi \quad (2)$$

$$-\frac{\partial T}{\partial \mathrm{t}} + \frac{1}{r}\frac{\partial(\psi, T)}{\partial(r, \theta)} = -\frac{2}{\mathrm{Re\,Pr}}\nabla^2 T \quad (3)$$

where

$$\nabla^2 \equiv \frac{\partial^2}{\partial r^2} + \frac{1}{r}\frac{\partial}{\partial r} + \frac{1}{r^2}\frac{\partial^2}{\partial \theta^2},$$

$$u = \frac{1}{r}\frac{\partial \psi}{\partial \sigma}, \upsilon = -\frac{\partial \psi}{\partial r},$$

Reynolds number $\mathrm{Re} = \frac{2aU}{\nu}$,

Grashof number $\mathrm{Gr} = \frac{g\beta(T_w - T_\infty)a^3}{\nu^2}$,

Prandtl number $\mathrm{Pr} = \frac{\nu}{\alpha} = \frac{\mu c_p}{K}$.

Transforming the independent variable r by $\xi = \log r$ and the dependent variable ψ by the relation $\psi = r\sin\theta + \phi$, equations (1–3) take the form

$$-\frac{\partial \zeta}{\partial t} + e^{-2\xi}\frac{\partial(\phi, \zeta)}{\partial(\xi, \theta)} + e^{-\xi}\left\{\frac{\partial \zeta}{\partial \theta}\sin\theta - \frac{\partial \zeta}{\partial \xi}\cos\theta\right\}$$
$$= -\frac{2}{\mathrm{Re}}\Delta\zeta e^{-2\xi} + 4\frac{\mathrm{Gr}}{\mathrm{Re}^2}e^{-\xi}\left\{\frac{\partial T}{\partial \xi}\sin\theta + \frac{\partial T}{\partial \theta}\cos\theta\right\} \quad (4)$$

$$\zeta = -e^{-2\xi}\Delta\phi \quad (5)$$

$$-\frac{\partial T}{\partial t} + e^{-2\xi}\frac{\partial(\phi, T)}{\partial(\xi, \theta)} + e^{-\Xi}\left\{\frac{\partial T}{\partial \theta}\sin\theta - \frac{\partial T}{\partial \xi}\cos\theta\right\}$$
$$= -\frac{2}{\mathrm{Re\,Pr}}e^{-2\xi}\Delta T \quad (6)$$

where

$$\Delta \equiv \frac{\partial^2}{\partial \xi^2} + \frac{\partial^2}{\partial \theta^2}$$

The initial and boundary conditions are [7]

$$t \geq 0; \quad \text{on} \quad \xi = 0, \phi = \frac{\partial \phi}{\partial \xi} = -\sin\theta, T = 1 \quad (7)$$

$$\text{on} \quad \xi = \Sigma, \phi = \zeta = T = 0 \quad (8)$$

For computational work, we take a circular domain of radius $\exp(\Sigma)$ in the physical plane [17]. By taking $\Sigma = \pi$, $\exp(\pi) = 23.14069$ which is sufficiently large for assuming ψ and T to be very small on this boundary. Condition (8) has been derived by making use of this assumption.

Numerical Method

The region of computation is a rectangle in (ξ, θ)-plane [17]. It is discretized by a squared grid with mesh size $h(=\pi/60)$ in both ξ and θ-directions. The step size in time is denoted by Δt. After making some numerical experiments for the stability of the numerical scheme, Δt was fixed at 0.03 for Re = 100, Gr = 10^4 and 0.04 for Re = 200, Gr = 5×10^4.

We used the Alternating Direction Implicit scheme [19] to find numerical solutions of equations (4) and (6). Equation (5) is solved by the SOR scheme [20]. The wall vorticity is calculated by

$$\zeta_0 = -\left\{\frac{2(\phi_2 + \sin\theta)}{h^2} + \frac{2\sin\theta}{h} + \sin\theta\right\} \quad (9)$$

where the suffix 0 refers to a point on the surface and the suffix 2 refers to a point at distance h above the surface in the (ξ, θ)-plane.

In the following discussion, we shall refer only to the finite difference forms of equations (4, 5) and (6). The first and the second finite difference equations approximating (4) are labelled (4*a*) and (4*b*). Similarly, we denote the ADI finite difference equations approximating (6) by (6*a*) and (6*b*).

These equations are solved by the following procedure:

Step 1: At $t = 0$
1 Calculate ϕ at all the interior points from (5),
2 Compute ζ_0 from (9).

Step 2: At $t = \Delta t/2$
1 Calculate T from (6*a*),
2 Compute ζ from (4*a*).

Step 3: At $t = \Delta t$
1 Calculate T from (6*b*),
2 Calculate ζ from (4*b*),
3 Obtain ϕ from (5),

Nomenclature

a = radius of the cylinder
C_p = specific heat at constant pressure
D = diameter = $2a$
f = shedding frequency
g = acceleration due to gravity
h_ℓ = local coefficient of heat transfer
K = thermal conductivity
p = pressure
$\bar{r}$ = distance polar coordinate
$\bar{t}$ = time
$\bar{T}$ = ambient temperature
T_∞ = free stream temperature
T_w = constant wall temperature
U = free stream velocity
$\bar{u}$ = velocity component in $\bar{r}$-direction
$\bar{\upsilon}$ = velocity component in $\bar{\theta}$-direction
α = thermal diffusivity
β = thermal coefficient of expansion
ρ = fluid density
μ = viscosity
ν = Kinematic viscosity
$\bar{\theta}$ = angular coordinate
$\bar{\psi}$ = stream function
$\bar{\zeta}$ = vorticity

Nondimensional Quantities

C_D = total drag = $C_{D_p} + C_{D_f}$
C_{D_p} = drag due to pressure
C_{D_f} = drag due to friction
Gr = Grashof number = $\frac{g\beta(T_w - T_\infty)a^3}{\nu^2}$
h = mesh size
Nu = Nusselt number for mixed convection
Nu_m = mean Nusselt number for mixed convection
Nu_{for} = mean Nusselt number for forced convection
Pr = Prandtl number = ν/α
r = distance coordinate = $\frac{\bar{r}}{a}$
Re = Reynolds number = $\frac{2aU}{\nu}$
S = Strouhal number = $\frac{fD}{U}$
t = time = $\frac{\bar{t}U}{a}$
T = temperature = $\frac{\bar{T} - T_\infty}{T_w - T_\infty}$
u = velocity component = $\frac{\bar{u}}{U}$
υ = velocity component = $\frac{\bar{\upsilon}}{U}$
ζ = vorticity = $\frac{\bar{\zeta}a}{U}$
ζ_0 = vorticity on the surface of the cylinder
θ = angular coordinate
ψ = stream function = $\bar{\psi}/aU$
ϕ = perturbed stream function
Σ = length of rectangular domain
$\Delta = \frac{\partial^2}{\partial \xi^2} + \frac{\partial^2}{\partial \theta^2}$
ξ = logr (transformation)

4 Obtain ζ_0 from (9).

Then step 2 and step 3 are repeated for further use.

Nusselt Number, Pressure and Drag

The heat exchange between the cylinder and the fluid is measured by means of the local coefficient of the heat transfer h_ℓ. Once the temperature distribution around the cylinder becomes known, the local heat transfer coefficient can be evaluated by the following formula:

$$\mathrm{Nu}(\theta) = \frac{2h_\ell a}{K} = -2\left(\frac{\partial T}{\partial \xi}\right)_{\xi=0} \tag{10}$$

Then the mean Nusselt number is calculated by

$$\mathrm{Nu}_m = \frac{1}{2\pi}\int_0^{2\pi} \mathrm{Nu}(\theta) d\theta \tag{11}$$

The pressure on the surface of the cylinder $p(\theta)_{r=1}$ is calculated from

$$\left.\frac{\partial p}{\partial \theta}\right|_{\xi=0} = \frac{4}{\mathrm{Re}}\left.\frac{\partial \zeta}{\partial \xi}\right|_{\xi=0} - 8\frac{\mathrm{Gr}}{\mathrm{Re}^2}\sin\theta \tag{12}$$

Total drag is computed by the formula

$$C_D = C_{D_p} + C_{D_f} = -\frac{1}{2}\int_0^{2\pi} p\cos\theta\, d\theta - \frac{2}{\mathrm{Re}}\int_0^{2\pi} \zeta_0 \sin\theta\, d\theta \tag{13}$$

Results and Discussion

By using the numerical technique, the flow characteristics and the heat transfer are computed for two sets of values of the Reynolds number and Grashof number: (1) Re = 100, Gr = 10^4 and (2) Re = 200, Gr = 5×10^4.

Streamlines and Isotherms

Figs. 1(*a*), 1(*b*) and 1(*c*) illustrate the phenomena of vortex shedding and the pattern of streamlines at Re = 200, Gr = 5×10^4. In the early stage of the flow, a symmetrical pair of eddies in the wake is observed [17]. At $t = 2.8$, we have an S-shaped pattern of streamlines along with a longer eddy on the left and a smaller one on the right in the wake (Fig. 1(*a*)). The longer vortex loses strength, breaks down and starts diffusing into the main stream while the smaller one grows larger. This is depicted in Fig. 1(*b*) at $t = 5.2$. At $t = 6.4$, we find that the left vortex has grown fully and moved towards the central line (Fig. 1(*c*)). On performing further computations, we found the formation of a small vortex in the left region of the wake.

Fig. 2 shows the isotherm patterns at $t = 2.8$, 5.2 and 6.4 for Re = 200, Gr = 5×10^4. It is found that the asymmetry in the streamline pattern in the wake gives rise to an unsymmetrical isotherm pattern. As the process of the shedding of vortices sets in, a significant distortion in the symmetry of the isotherm pattern around the cylinder is observed. We find that this change in the pattern of the isotherms takes place only in the wake region.

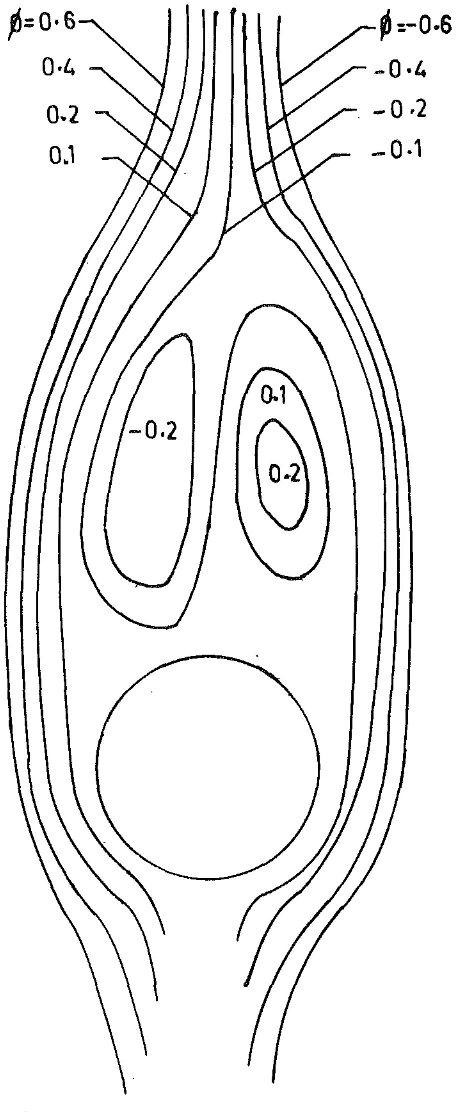

Fig. 1(*a*) Streamline pattern at time $t = 2.8$, Re = 200, Gr = 5×10^4

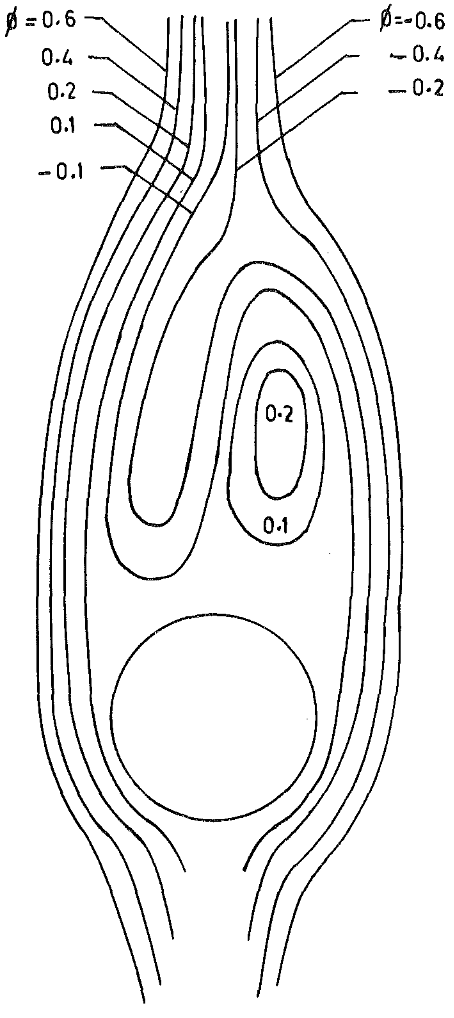

Fig. 1(*b*) Streamline pattern at time $t = 5.2$, Re = 200, Gr = 5×10^4

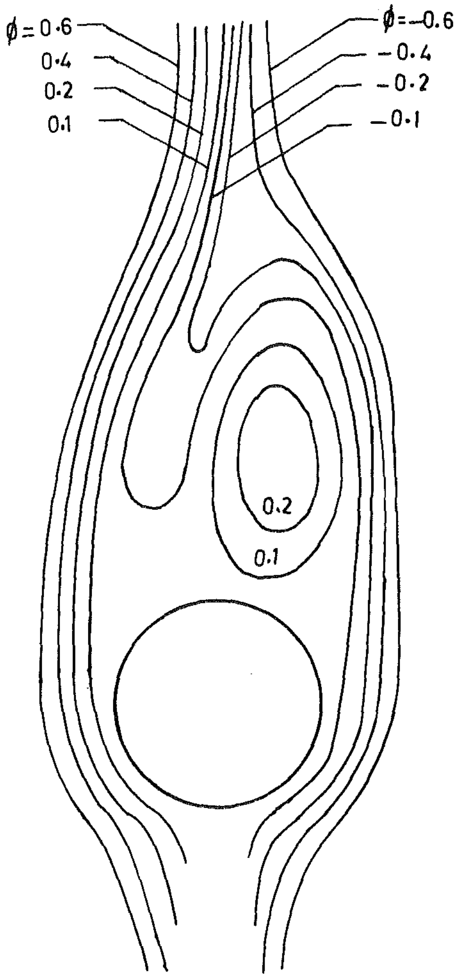

Fig. 1(*c*) Streamline pattern at time $t = 6.4$, Re = 200, Gr = 5×10^4

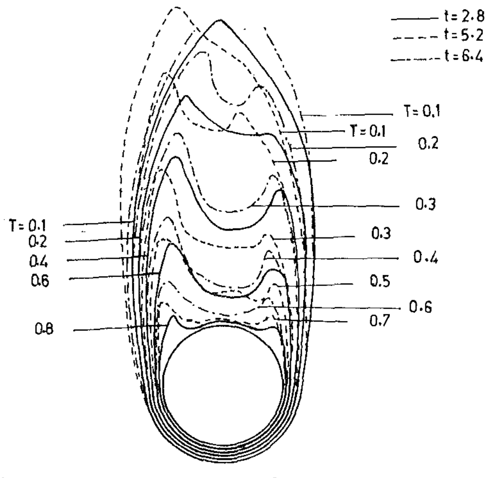

Fig. 2 Isotherm patterns at time $t = 2.8, 5.2$ and 6.4, Re = 200, Gr = 5×10^4

Strouhal Number

The Strouhal number is taken as $S = f.D/U$, where f is the shedding frequency on one side, D is the diameter of the cylinder and U is the characteristic velocity. Comparing the Strouhal numbers (0.15, at Re = 100, 0.17 at Re = 200) computed by Jain and Goel [3] with the present results (0.166 at Re = 100, Gr = 10^4 and 0.192 at Re = 200, Gr = 5×10^4), we find that the shedding of vortices is faster in the case of mixed convection.

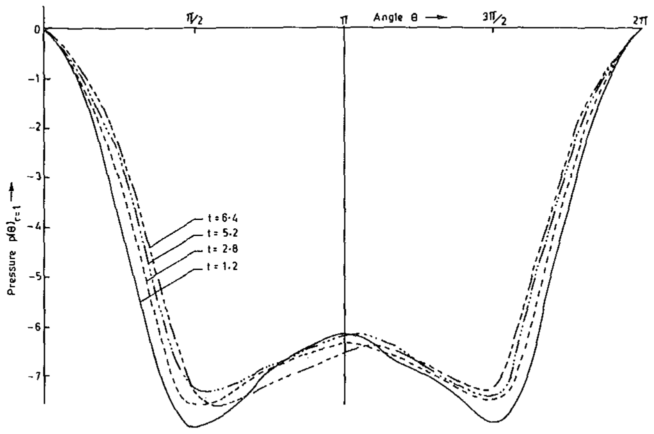

Fig. 3 Pressure distribution on the surface, Re = 200, Gr = 5×10^4

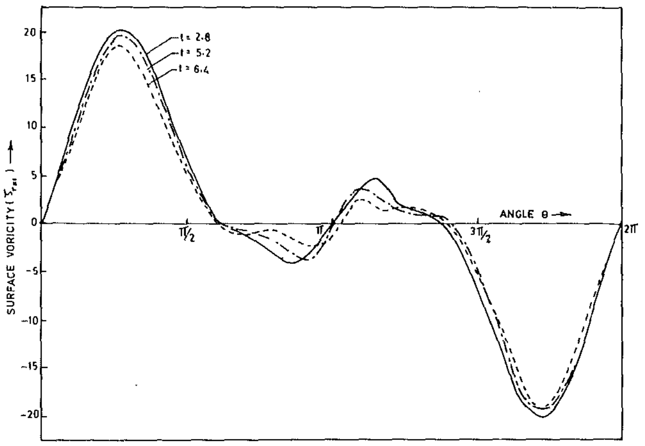

Fig. 4 Vorticity on the surface of the cylinder, Re = 200, Gr = 5×10^4

Pressure and Drag

The distribution of the pressure and the vorticity on the surface of the cylinder are shown in Figs. 3 and 4, respectively. We compare these results with those given by Jain and Goel [3]. It is found that the presence of the free convection gives rise to more surface vorticity (in magnitude). The maximum and minimum values of $\zeta_{r=1}$ are 18.524 and -19.254 ($t = 6.4$, Re = 200, Gr = 5×10^4) while the corresponding values obtained by Jain and Goel [3] are 16.6 and -15.6 ($t = 16.4$, Re = 200).

By examining the values of the pressure at the front and the rear stagnation points as computed by Jain and Goel [3] and our results, it is found that the presence of the free convection increases the pressure on the surface of the cylinder.

In Fig. 7, the variations of the total drag and the distribution of the mean Nusselt number with time are shown at Re = 100, Gr = 10^4 and Re = 200, Gr = 5×10^4. On comparing the values of C_D [3] with our results, it is found that the total drag increases due to the presence of the free convection. The curves for the drag and the mean Nusselt numbers have fluctuations which can be attributed to the oscillatory behavior of the flow for large t.

Heat Transfer

The distribution of the local Nusselt number for both cases at different times is presented in Figs. 5 and 6. The phenomenon is periodic in time and we have presented the computational results for the half cycle. The examination of these figures yields the following results: The maximum heat transfer occurs at the forward stagnation point while the minimum heat transfer takes place at a point in between

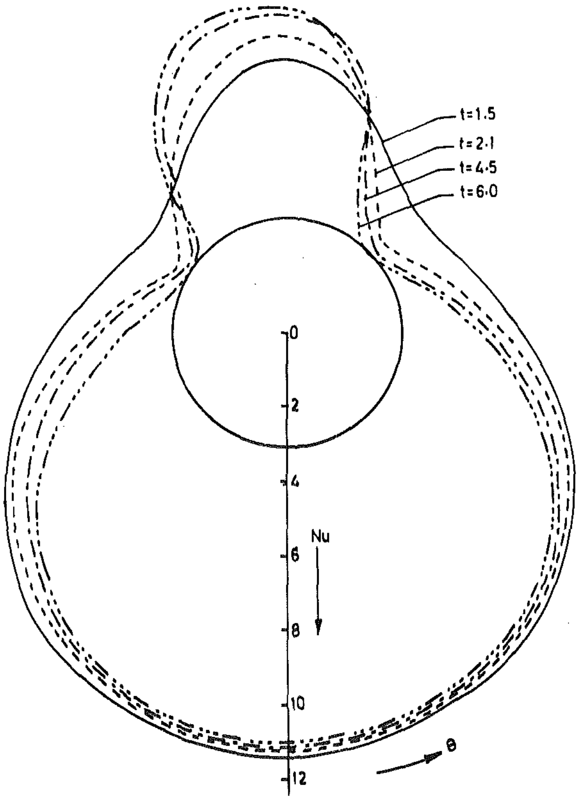

Fig. 5 Local Nusselt number, Re = 200, Gr = 5 × 10^4

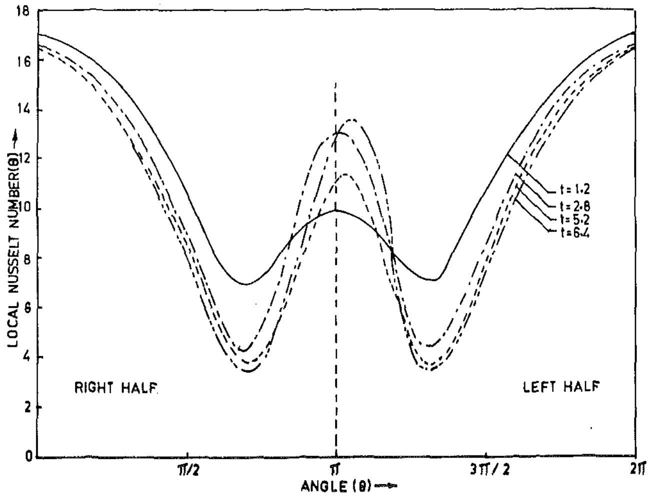

Fig. 6 Local Nusselt number, Re = 200 Gr = 5 × 10^4

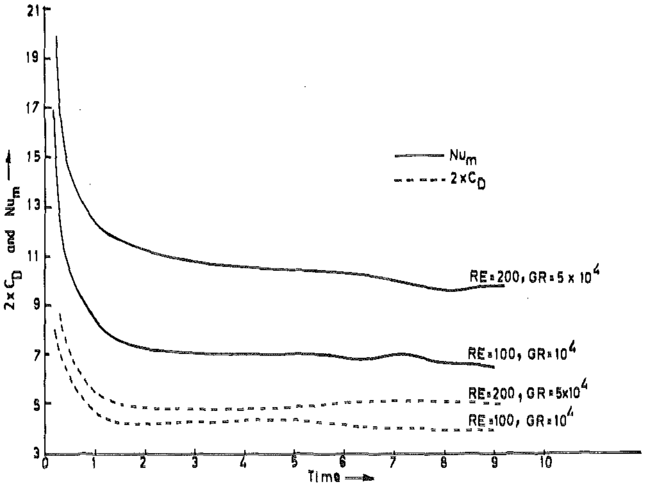

Fig. 7 Variation of mean Nusselt number and drag with time

Table 1 Variation of the angles of separation with time

	Re = 100		Re = 200	
	Right separation	Left separation	Right separation	Left separation
Forced convection Jain and Goel [7]	114°–120°	241°–246°	105°–111°	250°–255°
Mixed convection Our results	116°–122° (Gr = 10^4)	238°–244° (Gr = 10^4)	108°–113° (Gr = 5 × 10^4)	246°–253° (Gr = 5 × 10^4)

the rear stagnation point and the point of separation. In Table 1, it is seen that in the case of mixed convection, the separation of the boundary layer is delayed as the buoyancy forces accelerate the fluid motion in the layer and so reduce the deceleration of the fluid caused by the adverse pressure gradient. This result conforms with the results obtained by Merkin [16].

The distribution of the Nusselt number on the lower part of the cylinder up to the points of separation is found to be almost symmetric. The shedding of vortices gives rise to an asymmetry in the distribution of the Nusselt number in the wake region.

The Nusselt number distribution on the surface of the cylinder remains almost symmetrical except in the wake region where asymmetry is found. It is found that the distribution of the local Nusselt number is skewed towards the left side in the wake region, the skewness is more pronounced for Re = 200, Gr = 5 × 10^4 compared to the case of Re = 100, Gr = 10^4. A comparison of these figures with those for the forced convection (cf. Jain and Goel [7], Fig. 5), shows that mixed convection gives rise to more skewness in the distribution of the local Nusselt number. Thus, we find that the shedding process introduces more asymmetry in the heat transfer phenomena in the wake region for the mixed convection flow compared to the forced convection case [7]. A striking feature of the distribution of the local Nusselt number for the mixed convection is its fluctuations along the line of symmetry in the wake at Re = 200, Gr = 5 × 10^4. These fluctuations are absent at Re = 100, Gr = 10^4. The local Nusselt number in this region increases from t = 1.5 to the peak value at t = 6.0 for Re = 100, Gr = 10^4. For Re = 200, Gr = 5 × 10^4, it increases from t = 1.2 till t = 2.8 and then starts decreasing till t = 5.2. After that it again increases till t = 6.4. Thus the local Nusselt number in the wake region fluctuates with time along the line of symmetry at Re = 200, Gr = 5 × 10^4. For the forced convection [7], the local Nusselt number fluctuates along the line of symmetry for both Re = 100, 200. Hence, the presence of free convection gives rise to more asymmetry about the central line and reduces fluctuations along the central line in the distribution of the local Nusselt number in the wake region.

Oosthuizen and Madan [6] have derived an empirical formula for the heat transfer rate,

$$\frac{\mathrm{Nu}_m}{\mathrm{Nu}_{for}} = 1 + 0.18\left(\frac{\mathrm{Gr}}{\mathrm{Re}^2}\right) - 0.011\left(\frac{\mathrm{Gr}}{\mathrm{Re}^2}\right)^2 \qquad (14)$$

where Nu_m is the mean Nusselt number for mixed convection and Nu_{for} is the mean Nusselt number for forced convection. Using this formula and the values of Nu_{for}, we have calculated Nu_m; these values are compared with our computed values as presented in Table 2. It is found that our computed results are in good agreement with the correlated values derived from [14].

Table 2

	Nu_{for}		Nu_m from equation (14)	
Authors	Re = 100	Re = 200	Re = 100 Gr = 10^4	Re = 200 Gr = 5×10^4
Hilpert [21]	5.25866	7.26365	6.14737	8.77313
Eckert and Soehngen [4]	5.23	7.21822	6.11387	8.71826
Jain and Goel [7]	5.52	7.63	6.45288	9.21560
Our results	—	—	6.612 (computed)	9.594 (computed)

Acknowledgment

The authors wish to express their gratitude to the Department of Atomic Energy, Government of India, for their support in the preparation of this paper. The computational work was done on CDC 3600 and DEC-10 at Tata Institute of Fundamental Research, Bombay.

References

1 Thomas, D. C., Szewczyk, A. A., "Time Dependent Viscous Flow Over a Circular Cylinder," *Phys. Fluids*, Suppl. II, Vol. 12, 1969, pp. II-76–II-86.

2 Collins, W. M., Dennis, S. C. R., "Flow Past an Impulsively Started Circular Cylinder," *Journal of Fluid Mech.*, Vol. 60, 1973, pp. 105–127.

3 Jain, P. C., Goel, B. S., "Shedding of Vortices Behind a Circular Cylinder," *Computers and Fluids*, Vol. 4, 1976, pp. 137–142.

4 Eckert, E. R. G., Soehngen, E., "Distribution of Heat Transfer Coefficients Around Circular Cylinder in Cross Flow at Reynolds Numbers 20 to 500," Trans ASME, Vol. 74, 1952, pp. 343–347.

5 Krall, K. M., Eckert, E. R. G., "Heat Transfer to a Transverse Circular Cylinder at Low Reynolds Number Including Rarefaction Effects," Fourth International Heat Transfer Conference, Paris-Versailles, F.C. 7.5, 1970.

6 Hieber, C. A., Gebhart, B., "Low Reynolds Number Heat Transfer From a Circular Cylinder," *Journal of Fluid Mech.*, Vol. 32, 1968, pp. 21–28.

7 Jain, P. C., Goel, B. S., "A Numerical Study of Unsteady Laminar Forced Convection From a Circular Cylinder," ASME JOURNAL OF HEAT TRANSFER, Vol. 98, 1976, pp. 303–307.

8 Oosthuizen, P. H., Madan, S., "Combined Convective Heat Transfer From Horizontal Cylinder in Air," ASME JOURNAL OF HEAT TRANSFER, Vol. 92, 1970, pp. 194–196.

9 Oosthuizen, P. H., Madan, S., "The Effect of Flow Directions on Combined Convective Heat Transfer From Cylinders to Air," ASME JOURNAL OF HEAT TRANSFER, Vol. 93, 1971, pp. 240–242.

10 Sharma, G. K., Sukhatme, S. P., "Combined Free and Forced Convection Heat Transfer From a Heated Tube to a Transverse Air Stream," ASME JOURNAL OF HEAT TRANSFER, Vol. 91, 1969, pp. 457–459.

11 Gebhart, B., Audunson, T., Pera, L., "Forced Mixed and Natural Convection From Long Horizontal Wires, Experiments at Various Prandtl Numbers," Fourth International Heat Transfer Conference, Paris-Versailles, N.C. 3.2, 1970.

12 Sarma, T. S., Sukhatme, S. P., "Local Heat Transfer From a Horizontal Cylinder to Air in Cross Flow: Influence of Free Convection and Free Stream Turbulence," *International Journal of Heat and Mass Transfer*, Vol. 20, 1977, pp. 21–26.

13 Nayak, S. K., Sandborn, V. A., "Periodic Heat Transfer in Directly Opposed Free and Forced Convection Flow," *International Journal of Heat Mass Transfer*, Vol. 20, 1977, pp. 189–194.

14 Joshi, N. D., Sukhatme, S. P., "An Analysis of Combined Free and Forced Convection Heat Transfer From a Horizontal Circular Cylinder," ASME JOURNAL OF HEAT TRANSFER, Vol. 93, 1971, pp. 441–448.

15 Sparrow, E. M., Lee, L., "Analysis of Mixed Convection About a Horizontal Cylinder," *Int. J. Heat Mass Transfer*, Vol. 19, 1976, pp. 229–232.

16 Merkin, J. H., "Mixed Convection From a Horizontal Circular Cylinder," *Int. J. Heat Mass Transfer*, Vol. 20, 1977, pp. 73–77.

17 Jain, P. C., Rao, K. S., "Numerical Solution of Unsteady Viscous Incompressible Flow Past a Circular Cylinder," *Phys. Fluids*, Supp. II, Vol. 12, 1969, pp. II-57–II-64.

18 Gray, D. D., Giorgini, A., "The Validity of The Boussinesq Approximation for Liquids and Gases," *Int. J. Heat Mass Transfer*, Vol. 19, 1976, pp. 545–551.

19 Peaceman, D. W., Rachford Jr., H. H., "The Numerical Solution of Parabolic and Elliptic Differential Equations," *J. Soc. Indust. Appl. Math.*, Vol. 3, 1955, pp. 28–41.

20 Kawaguti, M., Jain, P., "Numerical Study of Flow Past a Circular Cylinder," *J. Phys. Soc. Japan*, Vol. 21, 1962, pp. 2055–2062.

21 Hilpert, R., *Forsch Gebiete Ingeneieurw*, Vol. 4, 1933, p. 215.

J. V. Beck
Department of Mechanical Engineering and
Division of Engineering Research,
Michigan State University,
East Lansing, Mich. 48823
Consultant,
Sandia Labs.
Albuquerque, N. M.

Effects of Multiple Sources in the Contact Conductance Theory

An analysis of regularly spaced disk sources on the surface of a semi-infinite body is given and related to steady-state contact conductance theory. It is shown that simple superposition utilizing the steady-state temperature distribution for a single typical disk source is not valid since a steady state does not exist for the temperature resulting for an infinite number of regularly spaced sources on the surface of a semi-infinite solid. A novel analysis is presented that treats the transient surface temperature in such a manner that a steady-state conductance is derived. The conductance results are compared with those obtained by Yovanovich who use a complementary analysis. The method of analysis can be applied to other disk spacings and to random distribution of contacts. Also considered is the case of contact radius being a uniformly-distributed random variable which yielded the results of increased contact resistance compared to that using the average contact radius.

Introduction

In the theory of analysis of contact conductances it is assumed that there are a large number of contacts which are regularly spaced. A basic building block in the analysis is the investigation of a single contact. This contact might be over a small circular area on the surface of a semi-infinite body where a constant heat flux is sometimes assumed. For a single contact a steady-state temperature distribution exists. When, however, an infinite number of regularly-spaced disk sources are introduced into the surface, a steady state does *not* exist for a semi-infinite body. This paper presents a study accounting for a transient effect when an infinite number of circular sources are used. In the usual analyses of the contact conductance, this effect is not considered. A random distribution of the contact radius is also investigated.

Analysis for Average Contact Temperature

The temperature at the *center* of a disk source due to the heating of that source *and* all others is to be found. After the analysis for the center temperature is completed, it is then extended to provide the average surface temperature at a source. The geometry being considered is shown in Fig. 1. The temperature at the center of a typical source labeled "starting disk source" is to be found. The disk sources each of radius R are arranged in a square pattern with a spacing distance δ.

Rather than attempting to directly superimpose the temperature rises on the center of the starting disk source for an *infinite* number of sources, the sources are considered in two groups: a) those in the region near the starting source and b) those away from the starting source. Thus this part of the analysis has two distinct components. For the region near the starting source the analysis is tractable since only a finite number of sources are included. For the region away from the starting source, the temperature rise at the center of the starting source due to the infinite number of equally spaced sources in this far region can be approximated by the temperature produced by uniform heating over the far region with a heat flux that is the average of that produced by the sources. For both regions the temperature distributions of interest are for very large times; for the near region this happens to be a steady-state solution but the far region does not have a steady solution. After the two components of the temperature added, the correct temperature is found by letting the near region become ever larger, approaching infinity in the limit.

The fact that an infinite number of regularly spaced sources on the surface of a semi-infinite body does not have a steady-state temperature solution is not obvious. Analyses of contact conductance have not included this aspect, in some cases because the investigators were not aware of it. For these reasons, before directly proceeding with the

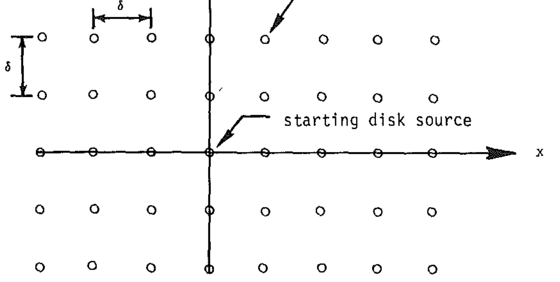

Fig. 1 An infinite array of disk sources on the surface of a semi-infinite body

---

Contributed by the Heat Transfer Division for publication in the JOURNAL OF HEAT TRANSFER. Manuscript received by the Heat Transfer Division May 8, 1978.

analyses, the nonexistence of a steady state is shown. The infinite array of sources shown in Fig. 1 can be imagined as being an infinite number of lines of sources. If a series of sources regularly spaced along a line does not produce a steady-state solution, then certainly no steady state temperature exists for the complete infinite array of sources shown in Fig. 1.

Yovanovich [1] has shown for a semi-infinite body that the steady surface temperature at a radial distance r measured from the center of a circular area having a heat flux q is

$$T(r,0) - T_\infty = \frac{2}{\pi}\frac{qR}{\lambda}\,\kappa\,\frac{E(\kappa) - (1-\kappa^2)\,K(\kappa)}{\kappa^2} \tag{1}$$

where $K(\kappa)$ and $E(\kappa)$ are the complete elliptic integrals of the first and second kind. The modulus κ is defined to be R/r and is less than one since here $r > R$ is assumed. The thermal conductivity is denoted λ and T_∞ is the temperature at a large distance from the source. For small values of κ, $T(r,0)$ can be approximated by

$$T(r,0) - T_\infty \approx \frac{qR^2}{2\lambda r}\left[1 + \frac{1}{8}\left(\frac{R}{r}\right)^2\right] \tag{2}$$

Hence for $R/r < 0.1$, $T(r,0)$ can be approximated with an error of less than 0.125 percent by

$$T(r,0) - T_\infty \approx \frac{qR^2}{2\lambda r} \tag{3}$$

The temperature at a point due to sources along a line at $r = \pm\delta, \pm 2\delta, \pm 3\delta, \ldots$ and $z = 0$ is

$$T = 2\sum_{i=1}^{\infty}\frac{qR^2}{2\lambda i\delta} + T_\infty \tag{4}$$

where $\delta > 10R$. This series is nonconvergent. Physically this means that there is no steady-state solution for a series of disk sources arranged along an infinite line. Since the geometry shown in Fig. 1 can be formed by an infinite number of lines, no steady-state solution exists for this distribution of sources on a semi-infinite body.

Consider next the temperature analysis for the near region. The steady temperature at the center of the starting source is to be found for the disk sources inside the square region bounded by $x = \pm(n + \tfrac{1}{2})\delta$ and $y = \pm(n + \tfrac{1}{2})\delta$ where n is a finite positive integer. For convenience temporarily assume that $\delta/R > 10$ so that (3) can be used for simplicity (and without loss of generality) let the temperature T_∞ be equal to zero. For the starting source the center temperature is exactly [1]

$$T_{\text{start. source}} = \frac{qR}{\lambda} \tag{5}$$

For the sources along the x and y axes and also on the diagonals passing through the starting source, the resulting temperature at the center of the starting source is

$$T_{x,y,\,\text{diag}} = \frac{qR}{\lambda}\frac{R}{\delta}(2+\sqrt{2})\sum_{i=1}^{n}\frac{1}{i} \tag{6}$$

When the temperature contributions due to all the near sources including those neither on the axes or diagonals are considered, the steady temperature (or equivalently, the very large time solution) at the center of the starting source is

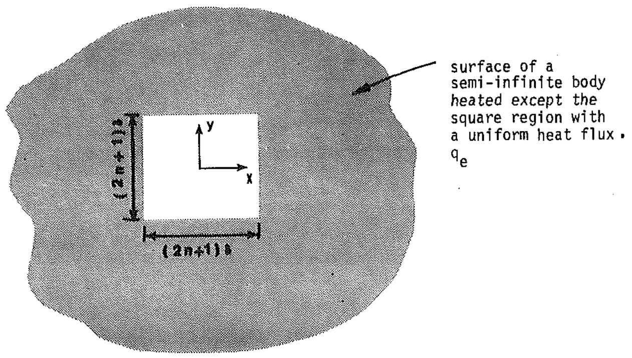

Fig. 2 **Region away from the starting source that is considered uniformly heated**

$$T_{\text{Near}} = \frac{qR}{\lambda}\left\{1 + \frac{R}{\delta}\left[(2+\sqrt{2})\sum_{i=1}^{n}\frac{1}{i} + 4\sum_{i=1}^{n-1}\sum_{j=i+1}^{n}(i^2+j^2)^{-1/2}\right]\right\} \tag{7}$$

For the far region the temperature of the center of the square insulated region shown in Fig 2 is needed. The outer region is heated with the average flux of q_e which is

$$q_e = \frac{\pi R^2}{\delta^2}q \tag{8}$$

with q being the flux over the disk regions in Fig. 1. The temperature can be found by the superposition of the surface temperature of a semi-infinite body heated over the entire surface,

$$T_{\text{s.i.}} = 2q_e\left[\frac{t}{\pi\lambda\rho c}\right]^{1/2} \tag{9}$$

(where ρ is density, c is specific heat and t is time) and the temperature due to the heat flux $-q_e$ over the square area which can be found in [1] to be

$$T_{sq} = \frac{-q_e[(2n+1)\delta]}{\lambda}\frac{2}{\pi}\ln\tan\frac{3\pi}{8} \tag{10}$$

which represents the temperature depression due to a square sink. Equation (9) is a solution that is valid for all times and (10) is valid only for very large times.

The temperature for large times at the center of the starting node is then the sum of those given by (7, 9) and (10) which is

$$T = \frac{qR}{\lambda}\left\{1 + \frac{R}{\delta}\left[(2+\sqrt{2})\sum_{i=1}^{n}\frac{1}{i} + 4\sum_{i=1}^{n-1}\sum_{j=i+1}^{n}(i^2+j^2)^{-1/2} + 2\left[\frac{\pi\lambda t}{\rho c\delta^2}\right]^{1/2} - 2(2n+1)\ln\tan(3\pi/8)\right]\right\} \tag{11}$$

Nomenclature

A = area
b = multiplying factor for δ or radius of cylinder in [3]
c = specific heat
$E(\kappa)$ = complete elliptic integral of the second kind
$K(\kappa)$ = complete elliptic integral of the first kind
L = depth in z-direction
q = uniform heat flux over a disk source
q_e = equivalent heat flux defined by equation (8)
Q = total heat flow
r = radial coordinate measured from center of starting source
R = radius of a disk source
$\mathbf{R}$ = contact resistance
t = time
T = temperature
T_∞ = temperature at a large distance from a single disk source
x = coordinate parallel to semi-infinite surface, (see Fig. 2)
y = coordinate parallel to semi-infinite surface
z = coordinate normal to semi-infinite surface
β_i = parameter value in equation (16)
δ = spacing distance between center of adjacent contacts
$\kappa = R/r$
λ = thermal conductivity
μ = mean value of R
ρ = density
σ = standard deviation
ψ = dimensionless contact resistance

Notice that in deriving (11), steady-state and transient solutions were not arbitrarily superimposed; instead, long time solutions for both the near and far regions were added together.

Thermal Constriction Analysis

A common definition of thermal constriction resistance is

$$\mathbf{R} = \frac{\overline{T} - T_\infty}{Q} \tag{12}$$

where $\overline{T}$ is the average temperature over a disk contact area, T_∞ is the temperature far from the heated surface and Q is the total heat flow rate for a large surface area A. This definition is not convenient for this analysis because the temperature difference in (12) changes with time. Instead a relation is used that comes from steady state analysis of composite systems [2],

$$Q = \frac{\overline{T} - T(z = L)}{\dfrac{T}{\lambda A} + \mathbf{R}} \tag{13}$$

where L is some finite z distance that is large compared with R. For a transient problem in a semi-infinite body the temperature difference $\overline{T} - T(z = L)$ approaches for sufficiently large times a constant value for finite L. For large times the temperature at $z = L$ is equal to the temperature of the heated surface for a uniform heat flux of q_e minus a temperature drop of q_eL/λ. (Note that $Q/A = \pi R^2q/\delta^2$.) Then $T(z = L)$ is equal to

$$T(z = L) = 2q_e \left\{\frac{t}{\lambda\rho c\pi}\right\}^{1/2} - \frac{q_eL}{\lambda} \tag{14}$$

Next introducing (14) with $A = \delta^2$ in (13) and solving for the dimensionless resistance ψ gives

$$\psi \equiv \lambda R\,\mathbf{R} = \frac{1}{\pi}\left\{1 + \frac{R}{\delta}\left[(2 + \sqrt{2}) \sum_{i=1}^{n} \frac{1}{i} + 4 \sum_{i=1}^{n-1} \sum_{j=i+1}^{n} (i^2 + j^2)^{-1/2} - (4n + 2) \ln \tan \frac{3\pi}{8}\right]\right\} \tag{15}$$

It is worth noting that the two summation terms in (15) and the subtracted term involving ln tan correspond to the difference of a) the temperature at the starting point due to uniformly distributed disk sources over the square region inside $x = \pm(n + ½)\delta$, $y = \pm(n + ½)\delta$ (omitting the starting source) and b) the temperature at the same point due to a uniform equivalent heat flux over the same square region.

Several things have to be done to (15). First the value of the term inside the brackets of (15) is needed as n becomes large. Calculated values are shown in Table 1. Notice that the value for $n = 1$ is only about four percent different from that for $n = 2000$. Nevertheless even for the largest n shown the value is slowly changing. Because of this slow change in the value, the converged value for $n \to \infty$ is estimated using the following approximation for the term in the brackets of (15).

$$[\quad] = \beta_1 + \beta_2 n^{-1} + \beta_3 n^{-2} \tag{16}$$

Various combinations of n are used to get the extrapolated value for $n \to \infty$, which is β_1 in (16). See Table 2. Notice that using $n = 10$, 25 and 50 gives a more accurate approximation for $n \to \infty$ than $n = 2000$ which involves about 1200 times as much computation since the calculations go up as n^2. It appears that the extrapolated value is −1.95013246. It is necessary to use double precision on the CDC 6600 (normally using about 15 significant digits) to obtain this answer. If single precision values are compared with those in Table 1 which gives double precision values, differences would be observed in the fifth decimal place for $n = 1200$ and in the fourth for $n = 2000$. This would cause the extrapolated values of Table 2 to change in the fourth decimal place while with double precision, differences are noted only in the eighth decimal place.

Another improvement in (15) is to use the average temperature at the starting source which is influenced by the distribution of temperature over the starting source itself as well as for all other sources. The major correction is to use the average temperature for the starting source itself; from [1] the average temperature is $8/3\pi$ times the right side of (5) and hence the unity value just inside the brace of (15) is replaced by $8/3\pi$.

Table 1 Value of terms in brackets of equation (15)

n	Value	n	Value
1	−1.87403	25	−1.945519
2	−1.90356	50	−1.947813
3	−1.916674	200	−1.949544675
4	−1.924045	800	−1.949985238
5	−1.928762	1000	−1.950014668
6	−1.932037	1200	−1.950034292
8	−1.936285	1500	−1.950053919
10	−1.938920	2000	−1.950073549

Table 2 Extrapolated values using equation (16)

Used n values	Extrapolated value
10, 25, 50	−1.950154
200, 800, 1000	−1.9501324599
800, 1000, 1200	−1.9501324588
1000, 1200, 1500	−1.9501324564
1000, 1500, 2000	−1.9501324600

Another improvement in (15) is to account for the average temperature effect from each other source. This is done for values of R/δ up to about 0.3. In addition, the effect of the sources being disks is included. For a single disk source located at $b\delta$ from the starting source the resulting average temperature over the starting disk is about

$$\overline{T} \approx \frac{qR^2}{2\lambda b\delta}\left[1 + \frac{1}{8}\left(\frac{R}{b\delta}\right)^2\right] \tag{17}$$

so that the correction is $(R/b\delta)^2/8$. For all the sources (except the starting one) this gives a correction of

$$⅛\left(\frac{R}{\delta}\right)^3\left[(2 + 2^{-1/2}) \sum_{i=1}^{n} i^{-3} + 4 \sum_{i=1}^{n-1} \sum_{j=i+1}^{n} (i^2 + j^2)^{-3/2}\right] \tag{18}$$

which for large n is $0.56460(R/\delta)^3$.

Finally putting all these corrections into (15) gives

$$\psi \approx \frac{1}{\pi}\left[\frac{8}{3\pi} - 1.95013246\frac{R}{\delta} + 0.56460\left(\frac{R}{\delta}\right)^3\right] \tag{19a}$$

$$= 0.270190 - 0.620746\frac{R}{\delta} + 0.17972\left(\frac{R}{\delta}\right)^3 \tag{19b}$$

The effect of the corrections is to reduce the constriction resistance with the reduction being about 23 percent for $R/\delta = 0.1$.

The R/δ dependence given by (19) is similar to that given in [3]. A plot of ψ divided by its value at $R/\delta = 0$ (widely separated contacts) is shown in Fig. 3. Also shown are values obtained by Yovanovich [3] for a semi-infinite, insulated cylinder of radius b with a disk source of radius R (with $R \leq b$) at $z = 0$. The dashed curve is for a plot with δ replaced by $2b$. The dot-dash curve is for equal relative areas in both cases which causes δ to be replaced by $b\sqrt{\pi}$. This latter way of plotting results is in excellent agreement for $R/\delta < 0.25$. In the Yovanovich solution hundreds of terms involving Bessel functions had to be evaluated for $R/\delta < 0.05$ and a linear relationship for ψ in terms of R/δ was *assumed*. The above derivation shows that this assumption is correct and an additional term is given in (19).

Another way to compare the present results with those of Yovanovich [3] is to use his tabulated values which are given as a function of ϵ, the radii ratio of the contact radius R to the outer radius b. Hence, R/δ in (19b) for equal relative areas can be replaced by $\epsilon/\sqrt{\pi}$. In Yovanovich's paper his ψ is four times the present one. Then using (19b) with the factor of four and also ϵ gives

$$\psi_B = 1.080759 - 1.40087\epsilon + .12910\epsilon^3 \tag{19c}$$

Table 3 gives ψ values using this expression and those from Yovanovich [3] which are denoted ψ_Y. For the large range of $\epsilon = 0$ to 0.4,

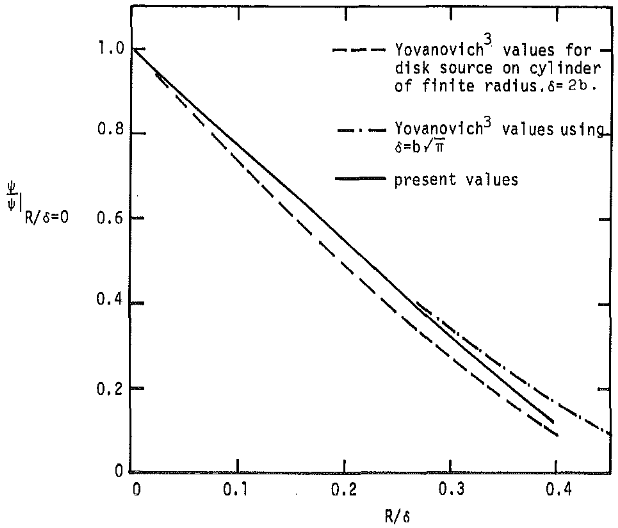

Fig. 3 Comparison of present values with Yovanovich values [3] for disk source on cylinder of finite radius

Table 3 Comparison of equation (19*c*) and Yovanovich [3] values for a cylinder with a single contact

ϵ	0.0	0.1	0.2	0.3	0.4	0.5
ψ_B	1.0808	0.9408	0.8016	0.6640	0.5287	0.3965
ψ_Y	(1.0808)	0.9397	0.8008	0.6649	0.5337	0.4092

there is less than ± one percent difference between the ψ values which shows remarkably good agreement. This result implies that the contact resistances for a long cylinder and a long square rod both heated over a small circular area at an end are nearly equal.

Further Cases

In addition to the square array of sources examined herein, others can be treated including a triangular spacing. Since, however, the results of Table 1 indicate that sources closest to the starting source have by far the greatest effect, it is probable that other source spacings will not change the results greatly, particularly if appropriate normalizing factors are chosen. This conclusion is also suggested by the comparison given in Fig. 3. In physical situations involving contact resistance, the actual points of contact are random in spatial distribution and in radius. The temperature effects are local for cases when $R/\delta < 0.1$ on the average; this can also be inferred from Table 1 and Fig. 3. The methods of this paper can be extended to cover random sources in a more definitive manner, however.

Many possible random cases can be investigated but only one is briefly considered. Let the same square array shown in Fig. 1 be present with a fixed spacing of δ but with each disk contact having a radius R which is a random variable. Consider the case of R having a uniform distribution between $R = r_1$ and r_2 and zero otherwise. This means that R can assume a value at any R between r_1 and r_2 with equal probability. For this case the mean (μ) and standard deviation (σ) of R are [4]

$$\mu = \frac{r_1 + r_2}{2}, \quad \sigma = \frac{r_2 - r_1}{\sqrt{12}} \tag{20}$$

The problem is to find the mean value of the contact resistance **R** for this uniform distribution; it is found by taking the expected value of **R**. Then using the expression ψ given by (19*b*) the expected value of **R** is

$$\mathbf{E}(\mathbf{R}) = \frac{1}{\lambda} \int_{r_1}^{r_2} \left[\frac{C_1}{R} - \frac{C_2}{\delta} + \frac{C_3 R^2}{\delta^3} \right] \frac{dR}{r_2 - r_1} \tag{21}$$

where the C_i values are the numerical constants in (19*b*); for example

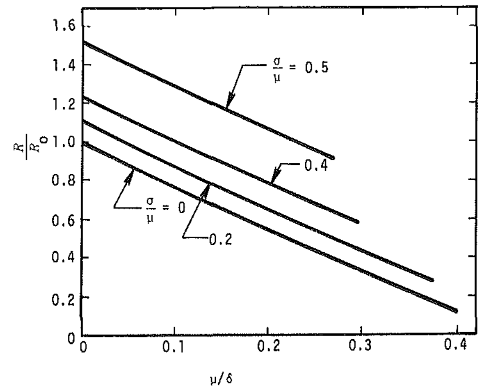

Fig. 4 Effect on contact resistance of uniform distribution of the contact radius

$C_1 = 0.27019$. Carrying out the integration, dividing by $\mathbf{R}_0$ defined by

$$\mathbf{R}_0 = C_1/\mu\lambda \tag{22}$$

and re-arranging gives

$$\frac{\mathbf{E}(\mathbf{R})}{\mathbf{R}_0} = \frac{\mu/\sigma}{2\sqrt{3}\,C_1} \left\{ C_1 \ln \frac{1 + \sqrt{3}\dfrac{\sigma}{\mu}}{1 - \sqrt{3}\dfrac{\sigma}{\mu}} - 2\sqrt{3}\, C_2 \frac{\sigma}{\mu}\frac{\mu}{\delta} + \frac{C_3}{3}\left(\frac{\mu}{\delta}\right)^3 \left[\left(1 + \sqrt{3}\frac{\sigma}{\mu}\right)^3 - \left(1 - \sqrt{3}\frac{\sigma}{\mu}\right)^3 \right] \right\} \tag{23}$$

This expression is a function of two dimensionless groups, σ/μ and μ/σ; the latter is similar to R/σ since μ is the expected value of R.

The ratio given by (23) is plotted in Fig. 4 as a function of μ/δ for values of σ/μ equal to 0, 0.2, 0.4 and 0.5. The zero curve is the same as the solid one of Fig. 3. (The curves have shortened lengths as σ/μ increases to avoid the possibility of the contact disks overlapping.) One observation is that random variation in the contact radius can lead to substantially increased values in the conduct resistance. The amount of increase is nearly independent of μ/δ for a given ratio of σ/μ. For example, for $\sigma/\mu = 0.5$ the increase is about $\mathbf{R}/\mathbf{R}_0 = 0.5$ for all μ/δ values shown. This causes the contact resistance to be much less sensitive to the radius to spacing ratio (μ/δ) than for invariable contact radius.

Summary and Conclusions

In the theory of contact conductances a single contact on the surface of a semi-infinite body has been frequently used as a building block for the case of real surfaces which have many contacting points. The implied assumption was that the results of the steady state analyses for a single contact could be directly superimposed. It is shown herein that this is not possible because a steady-state temperature distribution does not exist for the case of an infinite number of regularly distributed sources on the surface of a semi-infinite body. It is possible, however, to derive results for a steady state resistance. A method for accomplishing this is given in the paper and results are given. The method of solution for obtaining the dimensionless resistance involves investigating the contributions of sources to a typical source, called the starting source. In the analysis of sources placed in a square array over a semi-infinite surface, the resistance is shown to be sensitive mainly to those sources near the starting source. Hence, the distribution of sources could be quite arbitrary far from the starting source (provided the same average heat flow is applied) and yet produce the same resistance.

The analysis for an infinite number of sources placed in a square array on the surface of a semi-infinite solid also applies to the case of a square rod insulated on the sides and heated only over a circular area at the axis of one end. Yovanovich [3] investigated the similar geometry of a long cylinder insulated at all surfaces except over a circular region at the axis of one end. A comparison of the results shows that the dimensionless resistances are almost equivalent for a large range of the ratio of the heated radius divided by the cylinder radius.

At the contact of real surfaces, there are many randomly-placed contacting points. The present paper provides insights for two methods of analysis for randomly spaced contacts. First, randomly spaced contacts could be investigated using a Monte Carlo analysis. This paper shows that a random distribution of sources need be considered only near the starting source. Second, a method for investigating the effect of a single random variable such as the source radius is given. Use of the method in this case shows that the resistance is increased over the value that would be found using the average contact radius.

Acknowledgment

The support of the Division of Engineering Research of Michigan State University and the comments of Dr. C. R. St. Clair, Jr. are appreciated.

References

1 Yovanovich, M. M., "Thermal Constriction Resistance of Contacts on a Half-Space: Integral Formulation," *AIAA Progress in Astronautics and Aeronautics: Radiative Transfer and Thermal Control,* Vol. 49, ed. A. M. Smith, New York, 1976, pp. 397–418.

2 Holman, J. P., *Heat Transfer,* fourth ed., McGraw-Hill, New York, 1976, p. 25.

3 Yovanovich, M. M., "General Expressions for Circular Constriction Resistances for Arbitrary Flux Distribution," *AIAA Progress in Astronautics and Aeronautics: Radiative Transfer and Thermal Control,* Vol. 49, ed. A. M. Smith, New York, 1976, pp. 381–396.

4 Beck, J. V. and Arnold, K. J., *Parameter Estimation in Engineering and Science,* John Wiley and Sons, New York, 1977, p. 67.

L. Feijoo,
H. T. Davis
Department of Chemical Engineering
and Materials Science,
University of Minnesota,
Minneapolis, Minn. 55455

D. Ramkrishna
School of Chemical Engineering,
Purdue University,
West Lafayette, IN 47906

Heat Transfer in Composite Solids with Heat Generation

Steady-state heat transfer problems have been considered in a composite solid comprising two materials, one, a slab, which forms the bulk of the interior and the other, a plate, which forms a thin layer around the boundary. Through the use of appropriate Green's functions, it is shown that the boundary value problem can be converted into a Fredholm integral equation of the second kind. The integral operator in the integral equation is shown to be self-adjoint under an appropriate inner product. Solutions have been obtained for the integral equation by expansion in terms of eigenfunctions of the self-adjoint integral operator, from which the solution to the boundary value problem is constructed. Two problems have been considered, for the first of which the eigenvalues and eigenvectors of the self-adjoint operator were analytically obtained; for the second, the spectral decomposition was obtained numerically by expansion in a convenient basis set. Detailed numerical computations have been made for the second problem using various types of heat source functions. The calculations are relatively easy and inexpensive for the examples considered. These examples, we believe, are sufficiently diverse to constitute a rather stringent test of the numerical merits of the eigenvalue technique used.

1 Introduction

Heat transfer in composite materials is of considerable interest to engineers. Indeed, composite media are more often encountered in applications than homogeneous materials. Consequently, heat transfer problems arising therefrom have been the subject of active investigation. There is a diverse variety of such problems, some of which are amenable to solution by expansion in terms of eigenfunctions of associated Sturm-Liouville operators with suitable boundary conditions.

Essentially, the formulation of heat transfer problems in composite materials involves supplementing the differential equation of energy conservation, in which the thermal properties are regarded as possessing appropriate discontinuities at interfaces, with *boundary* and *interface* conditions. The interface conditions demand continuity of temperature and heat flux across the interface. Both the boundary and interface conditions participate in determining the eigenvalues and eigenfunctions of the associated Sturm-Liouville operator, which can be shown to be symmetric under suitable conditions.

In this paper, we will be concerned with composite solids comprising two materials, one of which forms the bulk of the interior and the other forms a "thin" layer around the boundary. A practical instance, where such a situation arises, is encountered with nuclear fuel rods, which consist of tubes tightly packed with fuel material. The problem, when viewed in proper perspective is amenable to very convenient methods of solution. We will limit ourselves to rectangular geometry, but extensions to other standard shapes represent trivial detail.

2 Heat Transfer Problem

We consider a rectangular slab, which has an internal heat source extending finitely in the x and y-directions (see Fig. 1), and bounded by a thin plate of another material on either sides. The heat source function is symmetric about the x-axis. Heat loss to the surroundings in the y-direction is assumed negligible for simplicity, although it can be accommodated without much additional complication. We allow for the existence of resistance to heat transfer at the interface through the use of a "gap conductance."

The energy generated in the slab is transported by conduction through the slab and plate materials at rates governed by the magnitudes of their conductivities. Conduction in the slab occurs both in the axial and transverse direction, whereas in the thin plate conduction is essentially in the axial direction. Clearly a high conductivity in the plate would provide for efficient removal of the generated heat.

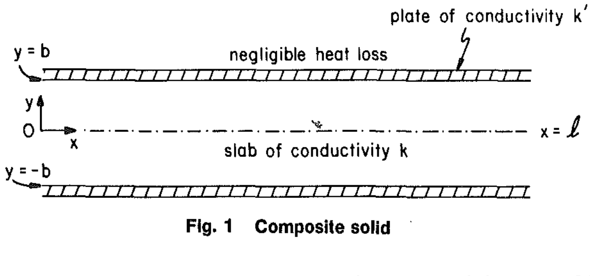

Fig. 1 Composite solid

Contributed by the Heat Transfer division for publication in the JOURNAL OF HEAT TRANSFER. Manuscript received by the Heat Transfer Division November 30, 1977.

Under steady-state conditions, the energy equation may be written as

$$\frac{\partial^2 T}{\partial x^2} + \frac{\partial^2 T}{\partial y^2} = -f(x, y) \tag{2.1}$$

where $f(x, y)$ is the heat source function divided by thermal conductivity, k, of the slab. From symmetry, we need to consider only the top half of the slab, the boundary condition at $y = 0$ being given by

$$y = 0, \quad \frac{\partial T}{\partial y} = 0 \tag{2.2}$$

Since the plate at $y = b$ is thin, we may neglect temperature variations in the y-direction within the plate. Thus the energy balance at $y = b$ is found to be

$$-k'A\frac{d^2t}{dx^2} = -kP\frac{\partial T}{\partial y}\bigg|_{y=b-0} = hP[T(x, b) - t(x)] \tag{2.3}$$

where $t(x)$ is the temperature of the plate, A is the cross-sectional area of the plate normal to axial heat flow and P is the perimeter denoting the surface area per unit length, normal to the y-axis at $y = b$.

We must now identify the boundary conditions with respect to x for both temperatures T and t, which may or may not be identical. Thus, for example, we may consider Problem I, in which, the boundary conditions at $x = 0$, and $x = \ell$ are identical for T and t, given by, say

$$x = 0, \qquad \frac{\partial T}{\partial x} = 0, \quad \frac{dt}{dx} = 0 \tag{2.4}$$

$$x = \ell, \qquad T = 0, \quad t = 0, \tag{2.5}$$

and Problem II, in which we assume that boundary condition (2.4) holds but (2.5) is replaced by the condition

$$x = \ell, \qquad \frac{\partial T}{\partial x} = 0, \quad t = 0 \tag{2.6}$$

Clearly in Problem II, the boundary conditions with respect to x are not identical for T and t.

For Problem I, the mathematical problem consists of the assembly of equations (2.1–2.5), while for Problem II, we have equations (2.1–2.4) and (2.6). Now Problem I may be solved analytically by methods similar to those presented elsewhere [1]. However these methods are not applicable to Problem II. In considering the solution of either Problem I or II, we proceed by recasting the problem in terms of suitably defined operators.

First, we define the Laplacian operator

$$\Delta \equiv -\left(\frac{\partial^2}{\partial x^2} + \frac{\partial^2}{\partial y^2}\right) \tag{2.7}$$

on functions $u(x, y)$, $(x, y) \in \Omega \equiv \{0 < x < \ell, 0 < y < b\}$, which belong to either of the following two *subspaces* of $\mathcal{L}_2(\Omega)$

$$D_I(\Delta) \equiv \Big\{\mathbf{u}: \Delta\mathbf{u} \in \mathcal{L}_2(\Omega): x = 0, \frac{\partial u}{\partial x} = 0; \quad x = \ell, u = 0; y = 0, \frac{\partial u}{\partial y} = 0; \quad y = b, \frac{\partial u}{\partial y} + \frac{h}{k}u = 0\Big\} \tag{2.8}$$

$$D_{II}(\Delta) \equiv \Big\{\mathbf{u}: \Delta\mathbf{u} \in \mathcal{L}_2(\Omega): x = 0, \frac{\partial u}{\partial x} = 0; \quad x = \ell, \frac{\partial u}{\partial x} = 0; y = 0, \frac{\partial u}{\partial y} = 0; \quad y = b, \frac{\partial u}{\partial y} + \frac{h}{k}u = 0\Big\} \tag{2.9}$$

where boldface letters have been used to represent functions as elements of a vector space. It is readily shown that, in either of domains $D_I(\Delta)$ and $D_{II}(\Delta)$, Δ is symmetric with respect to the inner product.

$$(\mathbf{u}, \mathbf{v}) = \int_\Omega u(x, y)v(x, y)dxdy \tag{2.10}$$

Note that the two domains arise from the two separate Problems I and II under consideration. In either case, there exists for Δ a *self-adjoint inverse operator* $\mathbf{G}$ *defined on* $\mathcal{L}_2(\Omega)$, *which can be shown to be a* Hilbert-Schmidt integral operator, i.e.,

$$\int_\Omega dxdy \int_\Omega d\xi d\eta\, G^2(x, y; \xi, \eta) < \infty \tag{2.11}$$

despite a singularity along $(x, y) = (\xi, \eta)$. Also, it is possible to determine $\mathbf{G}$ by Mercer's expansion, using the eigenfunctions and eigenvalues of $\mathbf{G}$, for each of the domains $D_I(\Delta)$ and $D_{II}(\Delta)$. In the present cases, we may even use a simpler expansion formula. Thus for $D_I(\Delta)$, we may write

$$G(x, y; \xi, \eta) = \frac{2}{\ell}\sum_{n=1}^{\infty} g_n(y, \eta) \sin \mu_n(\ell - x) \sin \mu_n(\ell - \xi) \tag{2.12}$$

where

$$g_n(y, \eta) = \begin{cases} \cosh \mu_n y\, \chi_n(\eta; \mu_n), & y < \eta \\ \cosh \mu_n \eta\, \chi_n(y; \mu_n), & y > \eta \end{cases} \tag{2.13}$$

where $\mu_n = \dfrac{(2n - 1)\pi}{2\ell}$ and

$$\chi_n(y; \mu_n) \equiv \frac{\frac{h}{k}\sinh \mu_n(b - y) + \mu_n \cosh \mu_n(b - y)}{\mu_n\left[\frac{h}{k}\cosh \mu_n b + \mu_n \sinh \mu_n b\right]} \tag{2.14}$$

Nomenclature

A = cross-sectional area of plate
b = half-thickness of slab
D = domain of differential operator
F = first term on the right hand side of equation (2.18)
f = heat source function
G = Green's function for the Laplacian operator
G_b = G evaluated at $y = b$, $\eta = b$
g = function defined by equation (2.28)
h = gap conductance, also function defined by equation (22)
k = thermal conductivity of slab
$\mathbf{K}$ = operator product $\mathbf{\Gamma}\,\mathbf{G}_b$
k' = thermal conductivity of plate
L = differential operator defined just above equation (2.21)
ℓ = length of slab
P = surface area at the periphery of slab per unit length
T = temperature of slab
t = temperature of plate
x, y = Cartesian coordinates
α = parameter in heat source function Case 4 in Table 1
β = parameter defined below equation (2.20)
Γ = Green's function for plate
Δ = Laplacian operator
χ_n = function defined by equation (2.14)
ϕ_n = n^{th} eigenvector of operator $\mathbf{G}_b$, equation (3.6) for Case 1, equation (3.9) for Case 2.
ψ_n = n^{th} eigenvector of operator $\mathbf{K}$
λ = parameter defined just above equation (2.29)
λ_n = n^{th} eigenvalue of $\mathbf{K}$
μ_n = equal to $\dfrac{(2n-1)\pi}{2\ell}$
ν_n = equal to $\dfrac{n\pi}{\ell}$
Ω = domain of Δ
δ_{ij} = Kronecker delta. equals unity if $i = j$ and zero if $i \neq j$
bold face symbol indicates a vector or an operator

For the domain $D_{II}(\Delta)$, we may replace (2.12) by

$$G(x, y; \xi, \eta) = \frac{1}{\ell} g_0(y, \eta) + \frac{2}{\ell} \sum_{n=1}^{\infty} g_n(y, \eta) \cos \nu_n x \cos \nu_n \xi \qquad (2.15)$$

where

$$g_0(y, \eta) = \begin{cases} \frac{k}{h} + (b - \eta) & y < \eta \\ \frac{k}{h} + (b - y) & y > \eta \end{cases} \qquad (2.16)$$

$$g_n(y, \eta) = \begin{cases} \cosh \nu_n y \; \chi_n(\eta; \nu_n) & y < \eta \\ \cosh \nu_n \eta \; \chi_n(y; \nu_n) & y > \eta \end{cases} \qquad (2.17)$$

where $\nu_n \equiv n\pi/\ell$ and $\chi_n(y; \nu_n)$ is given by (2.14) with μ_n replaced by ν_n. Both expressions (2.12) and (2.15) may be obtained by taking the inner product of equation (2.1) with the eigenfunctions of the operator $[-d^2/dx^2]$ on functions satisfying the boundary conditions with respect to x, and solving the resulting equation by the method of Green's functions. Since this method is standard procedure, no details are provided here.

It is now possible to express the temperature of the slab, $T(x, y)$ by the following formula (see for example Morse and Feshbach [2])

$$T(x, y) = \int_0^\ell d\xi \int_0^b d\eta G(x, y; \xi, \eta) f(\xi, \eta) + \frac{h}{k} \int_0^\ell d\xi t(\xi) G(x, b; \xi, b) \qquad (2.18)$$

which holds for both Problems I and II depending on whether G is given by (2.12) or (2.15). Thus the temperature at $y = b$ may be written as

$$T(x, b) = \int_0^\ell d\xi \int_0^b d\eta G(x, b; \xi, \eta) f(\xi, \eta) + \frac{h}{k} \int_0^\ell d\xi t(\xi) G(x, b; \xi, b) \qquad (2.19)$$

Equation (2.3) may be rewritten as

$$-\frac{d^2 t}{dx^2} + \beta^2 t = \beta^2 T(x, b) \qquad (2.20)$$

where $\beta^2 \equiv \frac{hP}{k'A}$.

We next define an operator $\mathbf{L} \equiv -\frac{d^2}{dx^2} + \beta^2$ with domain $D(\mathbf{L})$ defined by

$$D(\mathbf{L}) \equiv \{\phi : \mathbf{L}\phi \epsilon \mathcal{L}_2[0, \ell]; \phi'(0) = 0, \phi(\ell) = 0\} \qquad (2.21)$$

L is symmetric in $D(\mathbf{L})$ and has a *self-adjoint, completely continuous* inverse operator $\boldsymbol{\Gamma}$; which is easily determined to be

$$\Gamma(x, \xi) = \begin{cases} \dfrac{\cosh \beta x \sinh \beta(\ell - \xi)}{\beta \cosh \beta \ell} & x < \xi \\ \dfrac{\cosh \beta \xi \sinh \beta(\ell - x)}{\beta \cosh \beta \ell} & x > \xi \end{cases} \qquad (2.22)$$

It follows from (2.20), that

$$t(x) = \beta^2 \int_0^\ell \Gamma(x, \xi) T(\xi, b) d\xi \qquad (2.23)$$

Some notational brevity can be gained by denoting the integral operator, $G(x, b; \xi, b)$ in equation (2.19), which operates on elements of $\mathcal{L}_2[0, \ell]$, by $\mathbf{G}_b$, letting

$$h(x) \equiv \int_0^\ell d\xi \int_0^b d\eta \, G(x, b; \xi, \eta) f(\xi, \eta) \qquad (2.24)$$

and denoting $T(x, b)$ by $T_b(x)$. Thus equation (2.19) becomes

$$\mathbf{T}_b = \mathbf{h} + \frac{h}{k} \mathbf{G}_b \mathbf{t} \qquad (2.25)$$

where, we have used vector notation throughout. Similarly equation (2.23) may be written as

$$\mathbf{t} = \beta^2 \boldsymbol{\Gamma} \mathbf{T}_b \qquad (2.26)$$

which, on combining with equation (2.25), yields the following operator equation in **t**.

$$\mathbf{t} = \mathbf{g} + \frac{h\beta^2}{k} \boldsymbol{\Gamma} \mathbf{G}_b \mathbf{t} \qquad (2.27)$$

with $\mathbf{g} \equiv \beta^2 \boldsymbol{\Gamma} \mathbf{h}$ or

$$g(x) \equiv \beta^2 \int_0^\ell d\xi' \Gamma(x, \xi') \int_0^\ell d\xi \int_0^b d\eta \, G(\xi', b; \xi, \eta) f(\xi, \eta) \qquad (2.28)$$

By letting $\lambda \equiv \frac{h\beta^2}{k}$, equation (2.27) may be written as

$$\mathbf{t} = \mathbf{g} + \lambda \boldsymbol{\Gamma} \mathbf{G}_b \mathbf{t} \qquad (2.29)$$

Thus we have reduced the boundary value problems for Problems I and II to the solution of the integral equation (2.29).[1] The integral operator $\mathbf{G}_b$ for Problems I and II is given by

$$G_b(x, \xi) = \frac{2}{\ell} \sum_{n=1}^{\infty} \frac{\sin \mu_n(\ell - x) \sin \mu_n(\ell - \xi)}{\left[\frac{h}{k} + \mu_n \tanh \mu_n b\right]} \qquad \text{(Problem I)} \qquad (2.30)$$

$$G_b(x, \xi) = \frac{k}{h\ell} + \frac{2}{\ell} \sum_{n=1}^{\infty} \frac{\cos \nu_n x \cos \nu_n \xi}{\left[\frac{h}{k} + \nu_n \tanh \nu_n b\right]} \qquad \text{(Problem II)} \qquad (2.31)$$

At this stage, however, all we have accomplished is to obtain an integral formulation of the boundary value problems posed. When equation (2.29) is solved, it is possible to determine the solution of the boundary value problems completely. We next consider the solution of equation (2.29).

3 Method of Solution

As pointed out earlier, the solution of the boundary value problem is accomplished, if equation (2.29) is solved. If we denote $\mathbf{K} = \boldsymbol{\Gamma}\mathbf{G}_b$, then because $\boldsymbol{\Gamma}$ and $\mathbf{G}_b$ are both completely continuous operators **K** is also completely continuous. $\boldsymbol{\Gamma}$ and $\mathbf{G}_b$ are self-adjoint operators under the inner product

$$(\phi, \psi) \equiv \int_0^\ell \phi(\xi) \psi(\xi) d\xi \qquad (3.1)$$

We note that the eigenvalues of **K** are real and its eigenvectors span the Hilbert space $\mathcal{L}_2[0, \ell]$. We do not provide the proof here. However, it may be understood in analogy with the product of two symmetric matrices, which can be shown to have real eigenvalues and eigenvectors spanning the appropriate dimensional space.

An even more useful result may be established as follows. While the domain of **K** is $\mathcal{L}_2[0, \ell]$, its range is $D(\mathbf{L})$. Consider the subspace $D(\mathbf{L})$ and define a new inner product,

$$\langle \boldsymbol{\phi}, \boldsymbol{\psi} \rangle \equiv (\mathbf{L} \boldsymbol{\phi}, \boldsymbol{\psi}) \qquad \boldsymbol{\phi}, \boldsymbol{\psi} \in \mathbf{D}(\mathbf{L}) \qquad (3.2)$$

It is easily proved that (3.2) represents a valid inner product from the symmetry and positive-definiteness of **L**. The pair $\{D(\mathbf{L}), \langle \, , \, \rangle\}$ is then an inner product space (but not a Hilbert Space!) in which **K** is symmetric because for $\boldsymbol{\phi}, \boldsymbol{\psi} \in D(\mathbf{L})$

---

[1] See [3] for a general discussion of such reduction to integral equations of boundary value problems of the type considered here.

$$\langle \mathbf{K}\phi, \psi \rangle = (\mathbf{LK}\phi, \psi) = (\mathbf{L\Gamma G}_b\phi, \psi) = (\mathbf{G}_b\phi, \psi) = (\phi, \mathbf{G}_b\psi) = \langle \phi, \mathbf{K}\psi \rangle$$

This result is indeed useful because the eigenvectors of **K** would belong to **D**(**L**) and any two of them corresponding to distinct eigenvalues will be orthogonal with respect to the inner product (3.2). Thus if $\{\psi_j\}$ represent the eigenvectors of **K**, then

$$\langle \psi_j, \psi_k \rangle = \delta_{jk} \qquad (3.3)$$

and the solution of Equation (2.29), rewritten as

$$\mathbf{t} = \mathbf{g} + \lambda \mathbf{Kt} \qquad (3.4)$$

can be accomplished by expansion in terms of the eigenvectors of **K**. It is easily seen that

$$\mathbf{t} = \sum_{j=1}^{\infty} \frac{\langle \mathbf{g}, \psi_j \rangle}{(1 - \lambda\lambda_j)} \psi_j \qquad (3.5)$$

where $\{\lambda_j\}$ are the eigenvalues of **K**.

Substitution of the solution (3.5) into (2.18) yields the solution to the boundary value problems. Of course the eigenvalues and eigenvectors of **K** remain to be evaluated. We now consider Problems I and II separately.

Problem I. The eigenvalues and eigenvectors of **K** may be obtained readily in this case. Since the boundary conditions *w.r.t.x* for T and t are the same, it is readily shown that Γ and $\mathbf{G}_b$ have the same eigenfunctions ϕ, given by

$$\phi_n = \sqrt{\frac{2}{\ell}} \sin \mu_n(\ell - x) \qquad (3.6)$$

The eigenvalues, on the other hand, are of course different. Thus Γ and $\mathbf{G}_b$ have eigenvalues $\{(\beta^2 + \mu_n{}^2)^{-1}\}$ and $\{(h/k + \mu_n \coth \mu_n b)^{-1}\}$ respectively so that the eigenvalues $\{\lambda_n\}$ of **K** are given by

$$\lambda_n = \frac{1}{(\beta^2 + \mu_n{}^2)\left[\frac{h}{k} + \mu_n \tanh \mu_n b\right]} \qquad (3.7)$$

The solution for the temperature of the plate becomes

$$\mathbf{t} = \sum_{j=1}^{\infty} \frac{\langle \mathbf{g}, \psi j \rangle \psi_j}{1 - \lambda/\left[\left(\beta^2 + \mu_j{}^2\right)\left(\frac{h}{k} + \mu_j \tanh \mu_j b\right)\right]} \qquad (3.8)$$

where $\psi_j = \phi_j/\sqrt{\mu_j{}^2 + \beta^2}$

From equation (2.18), we can now determine the temperature of the slab everywhere. In the present case, it reduces to

$$T(x, y) = F(x, y) + \beta^2 \frac{h}{k} \sum_{n=1}^{\infty} \frac{(\boldsymbol{h}, \phi_n) \sqrt{\frac{2}{l}} \sin \mu_n (l - x)}{\left(\frac{h}{k} + \mu_n \tanh \mu_n b\right)(\mu_n{}^2 + \beta^2) - \lambda}$$

$$\left[1 - \frac{\lambda}{(\beta^2 + \mu_n{}^2)\left(\frac{h}{k} + \mu_n \coth \mu_n b\right)}\right]$$

where $F(x, y)$ is the first term on the right hand side of (2.18), which is known. We make no numerical calculations for this case from the analytical solution (3.14). Instead, we turn to the more difficult Problem II.

Problem II. This is much more difficult because there is no direct analytical handle on the eigenvalues and eigenvectors of **K**. We therefore resort to an approximation scheme, which consists in expanding, say $\psi \epsilon D(\mathbf{L})$ in terms of a finite number of eigenvectors $\{\phi_n\}$ of $\mathbf{G}_b$. Thus let

$$\psi \approx \sum_{j=1}^{N} C_j \phi_j; \; \phi_j = \sqrt{\frac{2 - \delta_{j0}}{\ell}} \cos \nu_j x \qquad (3.9)$$

To calculate the eigenvalues and eigenvectors of **K**, we demand that

$$\sum_{j=1}^{N} (\mathbf{K}\phi_j - \lambda\phi_j) C_j$$

be as close to zero as possible. One way to accomplish this is by orthogonalizing the residual with each member of the set $\{\phi_j\}_1{}^N$. Thus we have

$$\sum_{j=1}^{N} [(\mathbf{K}\phi_j, \phi_i) - \lambda] C_j = 0 \qquad (3.10)$$

The problem has now been reduced to one of determining the eigenvalues of the $(N \times N)$ matrix $K_{ij} = (\mathbf{K}\phi_j, \phi_i)$. The elements of the matrix K_{ij} are given in the Appendix.

The eigenvalues of the matrix **K** were determined for $N = 25$, 50, 75, and 100 and the results indicate satisfactory convergence. In fact, there is surprisingly good agreement between all the eigenvalues determined for given N and the corresponding eigenvalues determined for higher N. For example, $\lambda_1 = 0.25471$ for all four N's and $\lambda_{24} = 2.4544 \times 10^{-6}$ for $N = 25$ and 2.5034×10^{-6} for $N = 100$.

Calculations have been made for a variety of source functions $f(x, y)$. All the functions have been normalized to represent a constant total rate of heat generation to facilitate comparison of the temperature profiles for various choices of the source distribution. The source function has been expanded in terms of the set $\{\phi_n\}$ the eigenvectors of $\mathbf{G}_b$, using varying numbers of elements. Thus

$$\mathbf{f}(y) = \sum_{n=1}^{\infty} (\mathbf{f}(y), \phi_n)\, \phi_n \qquad (3.11)$$

where $\mathbf{f}(y) \equiv \{f(x, y)\}$ is regarded as an element of $\mathcal{L}_2\,[0, \ell]$ for each fixed value of y. The series (3.11) truncated at $n = M$ is used as the actual source function, so that by varying M a further variation in the source term can be introduced. Of course for sufficiently large values of M, the expansion will reproduce the source function $f(x, y)$. The choices of the source function have been summarized in Table 1.

Table 1 Source *functions* considered for Problem II

$$\boldsymbol{\phi_n(x) = \sqrt{(2 - \delta_{n0})/\ell} \cos \nu_n x}$$

Case 1

$$f(x, y) = \sum_{n=0}^{M} (\tilde{\mathbf{f}}(y), \phi_n)\, \phi_n(x), \; M = 99$$

where

$$\tilde{\mathbf{f}}(x, y) = \frac{e^{-4(x - \ell/2)^2/\ell^2}\, e^{-4y^2/b^2}}{\int_0^{\ell} e^{-4(x - 1/2)^2/\ell^2} dx \int_0^{b} e^{-4y^2/b^2} dy}$$

Case 2

$$f(x, y) = \frac{1}{b\ell^{1/2}} \sum_{n=0}^{M} \phi_n(x) \qquad \text{(independent of } y\text{).}$$

Case 2a $M = 2$; *Case 2b* $M = 99$

Case 3

$$f(x, y) = \frac{1}{b\ell^{1/2}} \sum_{n=0}^{M} \phi_n(x) \left[\delta_{no} + \tanh \frac{n\pi y}{\ell}\right]$$

$$\text{where } \delta_{no} = \begin{cases} 1 & n = 0 \\ 0 & n \neq 0 \end{cases}$$

Case 3a $M = 2$; *Case 3b* $M = 99$

Case 4

$$f(x, y) = \sum_{n=0}^{99} (\tilde{\mathbf{f}}, \phi_n)\, \phi_n(x)$$

$$\tilde{f}(x, y) = \frac{2}{b\ell}\left\{1 - \frac{1}{e^{-\alpha(x - \ell/2)/\ell} + 1}\right\}$$

Case 4a $\alpha = -400$; *Case 4b* $\alpha = 400$; *Case 4c* $\alpha = 0$

The source functions have been represented by contour maps in Figs. 2–3. For construction of these contour maps and for the calculations presented in what follows, $\ell = 1$, $b = 0.2$, $\beta\ell = 1$, $h\ell/k = 1$, and f is a unit source, i.e., $\int_0^{\ell} \int_0^{b} f dx dy = 1$.

The source function in the lower graph of Fig. 2 shows a high heating rate at the center of the slab that diminishes toward the edges. In the upper graph of Fig. 2 the source oscillates somewhat but eventually increases to large values towards the left end of the slab. Similarly the nature of the other sources may be interpreted easily from Fig. 3. A contour map of Case 3b is not given. This case is difficult to plot, but the contour map is similar to Case 2b shown in the lower graph of Fig. 3 in that the values of f are large near $x = 0$ and are relatively small elsewhere. Contours for Cases 4a, 4b and 4c are not given since these are simple. Cases 4a and 4b are almost step functions with $f = 10$ in half the slab and $f = 0$ in the other half ($f = 10$ in the half $x < 1/2$ for 4a and in the half $x > 1/2$ for 4b). For Case 4c, f is almost five throughout the slab.

The temperature profiles in the peripheral plate is plotted in Figs. 4–6. Since the left end is insulated, the temperature there is the maximum and decreases progressively towards the right end. This is true in all of the cases considered including cases 4a and 4b in Table 1. The special reference to these cases is because their choice was based on the belief that this may lead to some feedback of energy from the peripheral plate to the main slab in regions where the heat source vanished. The calculations did not reveal such effects possibly because they depend on suitable values of the parameters such as the ratio of thermal conductivities, the gap conductance, and the right end temperature.

The slab temperatures as obtained from equation (2.18) are presented as contour maps in Fig. 7 for Cases 1 and 2b. Although the plate temperatures showed no particularly interesting trends, the slab

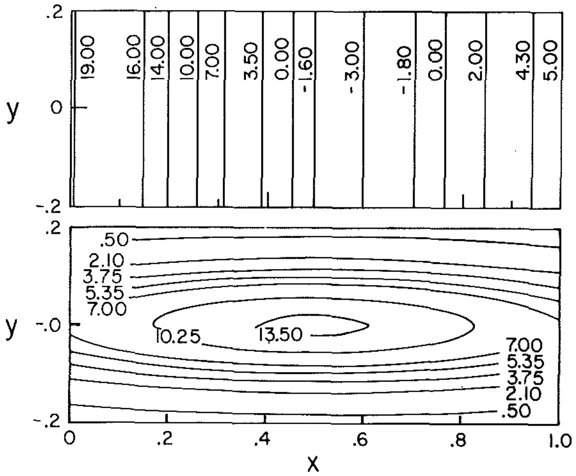

Fig. 2 Contour maps of source function. lower graph: Case 1, upper graph: Case 2a

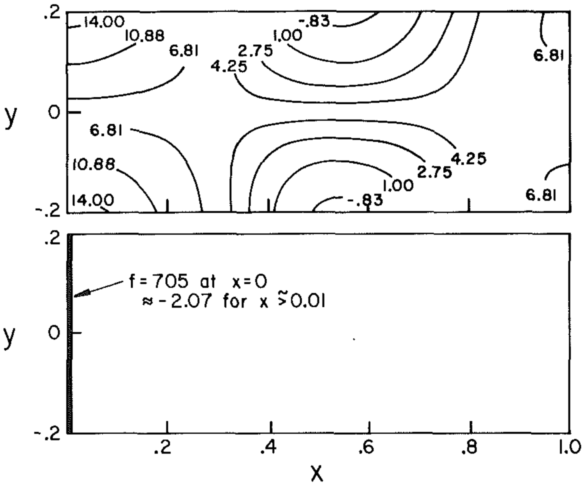

Fig. 3 Contour maps of source function. lower graph: Case 2b, upper graph: Case 3a

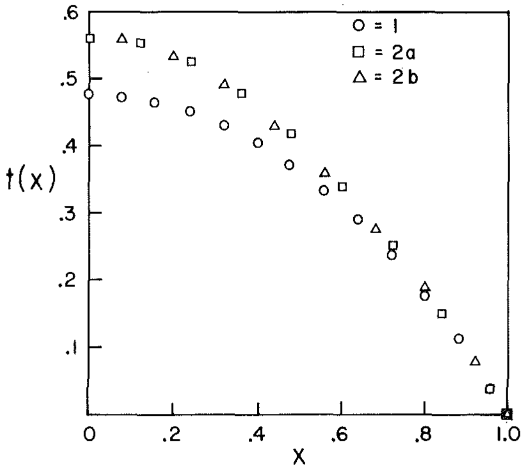

Fig. 4 Plate temperature profiles. Cases 1, 2a and 2b

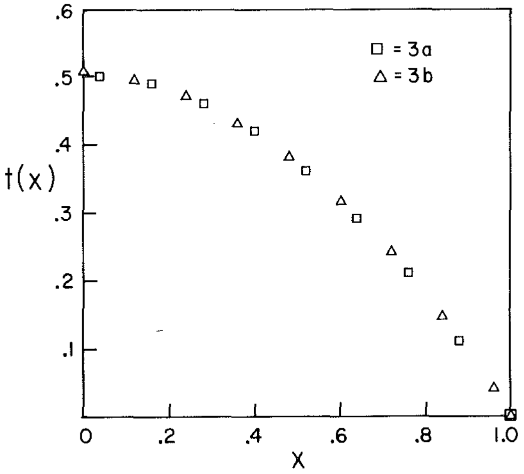

Fig. 5 Plate temperature profiles. Cases 3a and 3b

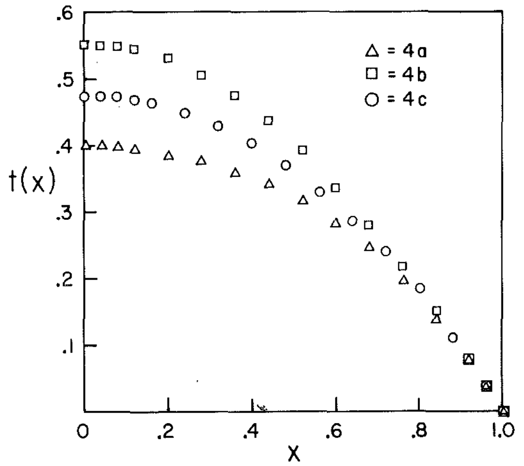

Fig. 6 Plate temperature profiles. Cases 4a, 4b and 4c

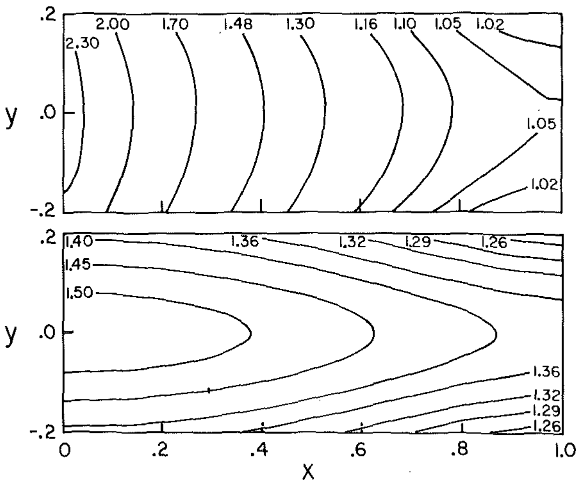

Fig. 7 Contour maps of slab temperature. lower graph: Case 1, upper graph: Case 2b.

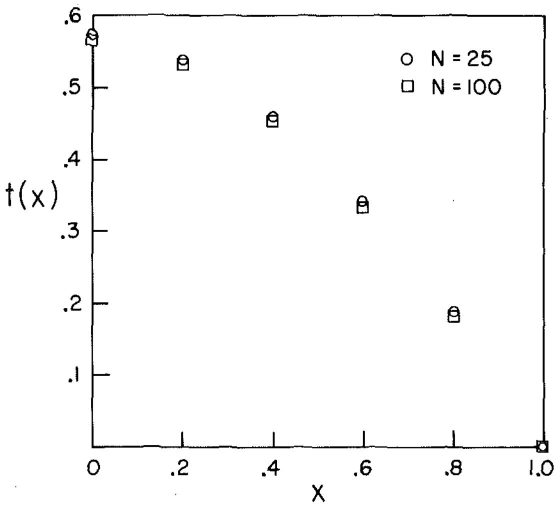

Fig. 8 Convergence and accuracy test of plate profile calculations, Case 2b

temperatures vary significantly. For example, in the lower graph of Fig. 7 the slab temperatures near the peripheral plate towards the left end are considerably less than those in the upper graph of Fig. 7 because in the former the heat source is peaked at the center of the slab and in the latter the heat source is concentrated at the left end, whereas the energy is removed more readily from the right end. The insensitivity of $t(x)$ to the detailed shape of the source $f(x, y)$ suggests that the special features of $T(x, y)$ arise from the first term on the rhs of equation (2.18). Since only a finite number of vectors from the basis set $\{\phi_n\}$ were used in obtaining the eigenvectors $\{\psi_n\}$ (see equation 3.9), it is of interest to check whether $t(x)$ does satisfy its boundary conditions at $x = 0$ and $x = \ell$. To demonstrate the accuracy and convergence of our calculations we present in Fig. 8 the identical plate temperature profiles (for case 2b) with $N = 25$ and 100; in Fig. 9 the value of $t(\ell)$ is plotted against $1/N$. Both Figs. 8 and 9 establish the accuracy and convergence of our procedure. They imply that the relatively small basis, $N = 25$, may be all that is required for many problems. Cases other than 2b yielded similar results.

Conclusions

The problem of steady-state two-dimensional heat transfer with heat generation in a slab with a thin peripheral plate has been solved by using Green's functions for the slab and the plate, which generates an integral equation for the plate temperature with an unsymmetric kernel. However when viewed as an operator **K** on $\mathcal{L}_2[0, \ell]$, the unsymmetric kernel is the product of two other self-adjoint operators Γ and G_b on $\mathcal{L}_2[0, \ell]$. We have used the interesting fact that **K** can be converted into a self-adjoint operator using the alternative inner product (3.2); the spectral decomposition of **K** (analytically as in Problem I and numerically as in Problem II) has then been used to construct the solution to the boundary value problem. The computations reported herein took about 3 min. on the Cyber 74 CDC computer of the University of Minnesota, a reasonable cost compared to finite difference or similar numerical techniques.

Acknowledgment

We are grateful to the National Science Foundation for financial support of the research presented herein.

References

1 Ramkrishna, D., and N. R. Amundson, *Chemical Engineering Science*, Vol. 29, pp. 1457–1464, 1974.

2 Morse, P. M. and Feshbach, H., *Methods of Theoretical Physics*, McGraw-Hill, New York, 1953, p. 807.

3 Ramkrishna, D. and N. R. Amundson, to appear in *Chemical Engineering Science*.

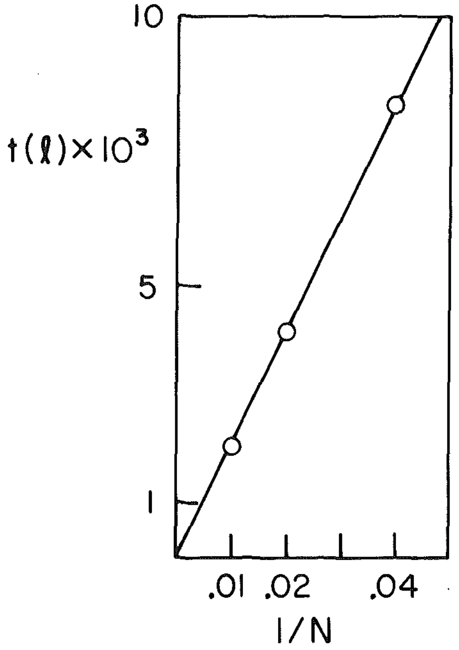

Fig. 9 Convergence test on boundary condition, $t(\ell) = 0$, of plate temperature, Case 2b

Appendix

Elements of Matrix K_{ij}

From the definition of K_{ij}

$$K_{ij} = (K\phi_i, \phi_j)$$

$$= \int_0^\ell \int_0^\ell \int_0^\ell \phi_j(x)\Gamma(x, \xi')G_b(\xi', \xi)\phi_i(\xi)dxd\xi d\xi', \qquad \text{(A1)}$$

we find

$$K_{ij} = \Gamma_{ij}\, \sigma_j$$

where

$$\sigma_j = \frac{1}{\dfrac{h}{k} + \nu_j \tanh(\nu_j b)} \qquad \nu_j \equiv \frac{j\pi}{\ell}$$

and

$$\Gamma_{ij} = \frac{1}{8}\frac{\tanh(\beta\ell)}{\beta\ell}\sqrt{(2-\delta_{i,0})(2-\delta_{j,0})}\,A_{ij}$$

where

$$i = j = 0$$

$$A_{ij} = \frac{8}{\beta^2}\left(\frac{\beta\ell}{\tanh(\beta\ell)} - 1\right)$$

$$i = j \neq 0$$

$$A_{ij} = \frac{4}{\nu_i{}^2+\beta^2}\left(\frac{\beta\ell}{\tanh(\beta\ell)} - \frac{2\beta^2}{(\nu_i{}^2+\beta^2)}\right)$$

$$i \neq j,\ i + j = \text{odd}$$

$$A_{ij} = \frac{8}{i^2-j^2}\left(\frac{i^2}{\nu_i{}^2+\beta^2} - \frac{j^2}{\nu_j{}^2+\beta^2}\right)$$

$$i \neq j \qquad i + j = \text{even}$$

$$A_{ij} = \frac{4}{\nu_i{}^2+\beta^2}\left\{\frac{\nu_i{}^2+\nu_i\nu_j-2\beta^2}{(\nu_i+\nu_j)^2+4\beta^2} + \frac{\nu_i{}^2-\nu_i\nu_j-2\beta^2}{(\nu_i-\nu_j)^2+4\beta^2}\right\}$$
$$+ \frac{4}{\nu_j{}^2+\beta^2}\left\{\frac{\nu_j{}^2+\nu_i\nu_j-2\beta^2}{(\nu_i+\nu_j)^2+4\beta^2} + \frac{\nu_j{}^2-\nu_i\nu_j-2\beta^2}{(\nu_i-\nu_j)^2+4\beta^2}\right\}$$

L. W. B. Browne
R. A. Antonia

Department of Mechanical Engineering,
University of Newcastle,
New South Wales, 2308,
Australia.

Calculation of a Turbulent Boundary Layer Downstream of a Step Change in Surface Temperature

Mean temperature and heat flux distributions in a thermal layer that develops within a momentum boundary layer subjected to a step change in surface temperature are calculated using two different methods. The method of Bradshaw and Unsworth, which uses the method of Bradshaw, Ferriss and Atwell to determine the mean velocity and Reynolds shear stress distributions and then assumes a constant turbulent Prandtl number for the heat flux calculation, yields heat flux distributions that are significantly different than the available experimental results at small distances from the step. Good agreement between calculations and experimental values is achieved when the distance x from the step is about 20 δ_0, where δ_0 is the boundary layer thickness at the step. To obtain good agreement with measurements of heat flux and mean temperature near the step, estimated distributions of turbulent viscosity and effective Prandtl number have been derived using an iterative updating procedure and the calculation method of Patankar and Spalding. These distributions are compared with those available in the literature. Calculated heat flux distributions show that the internal thermal layer is only likely to reach self-preserving conditions when x exceeds 40 δ_0.

Introduction

In the calculation of turbulent shear flows with heat transfer, first consideration is usually given to the calculation of the hydrodynamic field at least when small temperature differences exist across the flow. Once the velocity and shear stress fields are calculated, the heat transfer calculation can proceed, usually with a fairly low level closure assumption for the heat flux field. The effectiveness of different levels of partial differential equation models for the calculation of the velocity and stress fields has recently been reviewed by Reynolds [1] (also Reynolds and Cebeci [2]). Proposals at various levels of closure for models of heat and mass transport have been considered by Launder [3].

A calculation method that has had considerable success at calculating turbulent shear flows without heat transfer is that of Bradshaw, Ferriss and Atwell [4]. The Bradshaw, et al. method is, using Reynolds' [1] classification scheme, a one-equation model since, in addition to the momentum and continuity equations, the turbulent kinetic energy equation is used as the turbulence velocity scale equation. Bradshaw and Ferriss [5] introduced a heat transfer extension of the Bradshaw, et al. program. Bradshaw and Unsworth [6] replaced the one-equation model for $\overline{v\theta}$ by a zero-equation model in which the turbulent eddy-conductivity or turbulent Prandtl number is prescribed in a simple heat-transfer routine. Bradshaw and Unsworth's argument in 1974 that heat-transfer data are still not sufficiently plentiful or accurate to document a transport-equation approach effectively will hopefully become less valid in the near future. Encouraging signs are already evident in Launder's [3] review. A major attraction of the equation for θ (or $\overline{\theta^2}$) is that it does not contain a pressure fluctuation term. Further, all components of the destruction term for $\overline{\theta^2}$ can be measured thus eliminating the need to invoke local isotropy for small scale turbulence. The lack of attention paid to heat flux closure models may have been partly caused by requirements of engineering heat transfer applications since, as mentioned by Launder [3], a 15 percent error in the heat transfer coefficient may be tolerable while a similar error in estimating the skin friction coefficient is usually unacceptable.

A further calculation method that has been widely used is that of Patankar and Spalding [7]. This solves the continuity, momentum and energy equations using a finite difference method and integrating the equations in a forward-marching procedure. To integrate the equations, suitable boundary conditions are specified for the dependent variables. The equations are transformed using the von Mises transformation and then normalized so that the computing grid grows with the boundary layer. Details are contained in reference [7]. Various models for the shear stress and heat flux can readily be accommodated by the program.

In this paper, we examine how the computer programs of Bradshaw and Unsworth [6] (referred to hereafter as B-U) and of Patankar and

---

Contributed by the Heat Transfer Division for publication in the JOURNAL OF HEAT TRANSFER. Manuscript received by the Heat Transfer Division February 10, 1978.

Spalding [7] (referred to hereafter as P-S) behave for the calculation of mean temperature profiles and of heat flux fields downstream of a step change in the surface temperature. The P-S program used incorporates a different model for the shear stress and heat flux from that of reference [7]. The experimental work that is used to test the computations is that of Blom [8], Fulachier [9] and Perry and Hoffmann [10].

Reynolds, et al. [11] studied the temperature step problem because of its importance as a consequence of the linearity of the heat transfer equation. The problem is also of practical interest to both engineering and atmospheric situations.

Experimental Conditions

Four experimental configurations were chosen from the literature as test cases for the calculation methods. These configurations are shown in schematic form in Fig. 1, on which the approximate positions of the outer edge of the velocity and temperature boundary layers are shown to scale. The plates were all maintained at isothermal conditions downstream of the step, within the limits of experimental accuracy—generally ±0.2°C, and in all cases there was a small favorable pressure gradient in the direction of flow. Other relevant experimental conditions are summarized in Table 1 and full details are contained in the references. The temperature difference at the step is small enough for the temperature to be treated as a passive contaminant of the flow. Mean temperature and fluctuating temperature intensity profiles were measured in all cases but heat flux and Reynolds shear stress measurements were reported only by Blom [8] and Fulachier [9]. In Perry and Hoffmann's [10] experiments however, profiles were measured at values of x/δ_0 significantly larger than those considered in the other investigations.

It should be noted that turbulent heat flux distributions were reported by Johnson [14] downstream of a step change in surface temperature but there is doubt (e.g., Swenson [15]) as to the two-dimensionality of this flow and the results have been excluded from present considerations.

The B-U Calculation Method

In the B-U program, mean velocity and Reynolds shear stress distributions are first computed by the method of characteristics described in Bradshaw, Ferriss and Atwell [4]. Once these distributions are calculated, the mean temperature T and thermometric local heat flux $\overline{v\theta}$ profiles are obtained by solving the conservation equation (neglecting the molecular term)

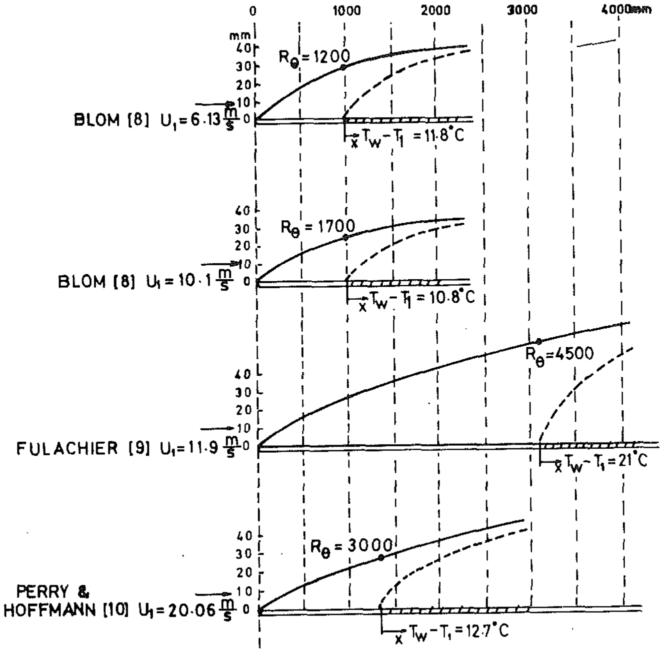

Fig. 1 Schematic layout of experimental arrangements. — Velocity boundary layer approximately to scale, - - - Temperature boundary layer approximately to scale

$$U\frac{\partial T}{\partial x} + V\frac{\partial T}{\partial y} + \frac{\partial \overline{v\theta}}{\partial y} = 0 \qquad (1)$$

with the assumption that the turbulent Prandtl number

$$\mathrm{Pr}_t = \frac{\overline{uv}/(\partial U/\partial y)}{\overline{v\theta}/(\partial T/\partial y)} \qquad (2)$$

is constant. The routine to obtain T and $\overline{v\theta}$ uses a fully implicit algorithm. The inner boundary condition on the temperature profile is given by

$$\frac{T_w - T}{T_\tau} = \frac{1}{\kappa_\theta}\ln\frac{yU_\tau}{\nu} + C_\theta \qquad (3)$$

where T_τ is the friction temperature, U_τ is the friction velocity, κ_θ a

Nomenclature

A^+ = van Driest constant, equation (11)
B-U = Bradshaw and Unsworth calculation method
c_f = friction coefficient defined by $\tau_w = c_f \cdot \rho U_1{}^2\, 1/2$
c_p = specific heat at constant pressure
C_θ = constant, equation (3)
k = thermal conductivity
ℓ = Prandtl mixing length
F = van Driest dampling factor, equation (11)
$\tilde{h}$ = stagnation enthalpy = $c_pT + 1/2U^2$
P = pressure
Pr = Prandtl number
P-S = Patankar and Spalding calculation method
q = total heat flux
Q = total heat flux (thermometric)
R_θ = Reynolds number based on the momentum thickness = $\delta_\theta \cdot U_1/\nu$
St = Stanton number = $Q_w/U_1(T_w - T_1)$
T = local mean temperature
T^+ = dimensionless temperature = $(T_w - T)/T_\tau$
T_τ = friction temperature = Q_w/U_τ
u = velocity fluctuation in the streamwise direction
$\overline{uv}$ = kinematic Reynolds shear stress
U = local mean velocity in streamwise direction
U_τ = friction velocity = $(\tau_w/\rho)^{1/2}$
v = velocity fluctuation normal to plate
$\overline{v\theta}$ = turbulent heat flux (thermometric)
v = mean velocity normal to plate
x = coordinate in streamwise direction or downstream distance from the step
X^+ = dimensionless distance downstream from the step = $\int_0^x U_\tau/\nu\, dx$
y = coordinate normal to plate or distance from plate
Y^+ = dimensionless distance from plate = yU_τ/ν
δ = velocity boundary layer thickness
δ_0 = velocity boundary layer thickness at the step
δ_i = enthalpy thickness = $\int_0^\infty U/U_1 \cdot (T - T_1)/(T_w - T_1)\, dy$
δ_θ = momentum thickness = $\int_0^\infty U/U_1 \cdot (U_1 - U)/U_1\, dy$
Δ_T = length scale, equation (15)
θ = temperature fluctuation
κ = von Karman constant
κ_θ = constant, equation (3)
μ = absolute viscosity
ν = kinematic viscosity
ρ = density
τ = shear stress
— = time average value, e.g., $\overline{v\theta}$

Subscripts

1 = free stream value
eff = effective value
t = turbulent value
w = value at the wall
0 = value at the position of the step

"universal" constant analogous to the von Karman constant κ and C_θ is an additive constant which is a function of the molecular Prandtl number. Values of κ_θ and C_θ used in the calculation method are 0.45 and 3.3 respectively. These values are in reasonable agreement with those shown in Table 1 and with the average values (in the case of air) inferred from the survey of Kader and Yaglom [16]. The large values of κ_θ and C_θ reported in Table 1 were obtained by Blom [8] at relatively small values of x/δ_0. It should be noted that in this region of the flow, the thermal layer is not in equilibrium and the budget of $\overline{\theta^2}$ measured by Antonia, et al. [12] shows that advection and diffusion terms are comparable with production and destruction terms in this region. Although a logarithmic mean temperature profile is established downstream of the step, κ_θ and C_θ do not appear to attain constant values before a distance of about 15 δ_0. The use of equation (3) is thus a defect in the B-U approach but the question of how far downstream of the step does one need to go before the B-U calculation is valid is still of interest.

The turbulent Prandtl number may be written as

$$\mathrm{Pr}_t = \frac{\kappa}{\kappa_\theta} \tag{4}$$

in the logarithmic (velocity or tempreature) region, with the assumption that the shear stress and heat flux are constant and equal to the wall flux values in this region. With $\kappa = 0.41$, Pr_t is set equal to 0.91 in the B-U program. This value is consistent with values in Table 1 and with the conclusion in the recent survey by Launder [3] that the "weight of experimental evidence seems to suggest that the near-wall value of Pr_t is a little above 0.9". The experimental trend of Pr_t in the outer part of the boundary layer is not yet clearly established. In view of unavoidable uncertainties in determining Pr_t the assumed constancy of Pr_t right across the layer is perhaps not unreasonable. Some encouragement may perhaps be derived from the fact that this assumption has yielded correct values for the Stanton number in boundary layer and pipe flows with uniformly heated boundaries. Further comments on Pr_t distributions are contained in the following section.

The distribution of other parameters (dissipation length scale, diffusion functions, etc.) that have been used in the program is as prescribed in Bradshaw, et al. [4].

The calculation method was started at the measurement station over the unheated plate immediately upstream of the step. Experimental mean velocity profiles were available at this station for all four cases considered. In the case of Blom [8] and Fulachier [9], starting Reynolds shear stress profiles were derived from measured profiles well downstream of the step by assuming similarity (the experimental wall shear stress was available at the starting station). In the case of Perry and Hoffmann [10], no shear stress profiles were reported and the starting distribution of τ was derived fromKlebanoff's [18] τ distribution in a self-preserving smooth wall boundary layer. The first mesh point in the B-U calculation is in the fully turbulent part of the flow (nominally outside the viscous sublayer). Mesh points are evenly spaced across the flow, 25 being used at the starting position and up to 45 at the end. The equations are not used in the sublayer, the boundary conditions for velocity and temperature at the surface being satisfied by matching the solutions to the logarithmic laws of the wall at the first mesh point.

The P-S Calculation Method

The momentum and energy equations used by the P-S program are

$$U\frac{\partial U}{\partial x} + V\frac{\partial U}{\partial y} = -\frac{1}{\rho}\frac{dP}{dx} + \frac{1}{\rho r}\frac{\partial}{\partial y}(r\tau) \tag{5}$$

and

$$U\frac{\partial \hbar}{\partial x} + V\frac{\partial \hbar}{\partial y} = \frac{1}{\rho}\frac{\partial}{\partial y}(-q + U\tau) \tag{6}$$

with $r = 1$ for cartesian coordinates and r = radius from axis of symmetry for polar coordinates.

Many different approaches have been used in the treatment of τ and q in these equations. Using Reynolds' [1] classification scheme the most popular approach has been to use a zero-equation model and define

$$\tau = \mu_{\text{eff}}\frac{\partial U}{\partial y},\ q = -k_{\text{eff}}\frac{\partial T}{\partial y} \tag{7}$$

where

$$\mu_{\text{eff}} = \mu + \mu_t,\ k_{\text{eff}} = k + k_t \tag{8}$$

and

$$k_t = \frac{\mu_t}{\mathrm{Pr}_t}C_p \tag{9}$$

the distributions of μ_t and Pr_t being assigned by a variety of methods. One approach, used by Patankar and Spalding [7], although it is not the method used in this paper, is the mixing length approach:

$$\mu_t = F\rho\ell^2\left|\frac{\partial U}{\partial y}\right| \tag{10}$$

where

$$F = \left[1 - \exp\left(-\frac{Y^+}{A^+}\right)\right]^2 \tag{11}$$

is the van Driest damping factor and the mixing length ℓ is given by

$$\ell = \begin{cases} C_1 y & \text{for } 0 < y \le C_2\delta \\ C_3\delta & \text{for } y > C_2\delta. \end{cases}$$

A^+, C_1, C_2 and C_3 are constants and Pr_t was assumed constant.

Wassel and Catton [19], using a slightly modified P-S procedure, used the same μ_t distribution with a Pr_t distribution given by

$$\mathrm{Pr}_t = \frac{C_1}{\mathrm{Pr}}\left(\frac{1 - \exp\left(-\dfrac{C_2}{\mu_t/\mu}\right)}{1 - \exp\left(-\dfrac{C_3}{\mathrm{Pr}\mu_t/\mu}\right)}\right) \tag{12}$$

where C_1, C_2 and C_3 are constants. The options available for Pr_t dis-

Table 1 Summary of conditions for experiments* and calculations

Experiment	U_1 (m/s)	δ_0 cm	R_δ‡	κ_θ	C_θ	κ/κ_θ	Pressure Gradient Conditions
Blom [8]	6.13	2.7	1.07×10^4	.47 – .58†	3.15 – 4.45†	.87 – .71	Favorable [small but constant] pressure gradient beyond 30 cm from the leading edge
Blom [8]	10.1	2.3	1.56×10^4	.42 – .52†	2.6 – 3.90†	.98 – .79	
Fulachier [9]	11.9	4.9	3.80×10^4	.44	3.13	.93	Small favorable pressure gradient
Perry and Hoffmann [10]	20.06	2.4	2.53×10^4	.47	3.8	.85	Favorable pressure gradient near the leading edge of plate

† There is a systematic decrease in κ_θ and C_θ with distance from the step.
‡ Reynolds number, based on boundary layer thickness at the start of the calculation of B-U.
* Note: All experiments used air.

tributions are daunting. In his review paper, Reynolds [20] examines more than thirty ways of modeling Pr_t.

In this paper the zero-equation model is used with the distribution of μ_t and Pr_t being determined by, as far as is known, a previously unreported technique. This consists of initially assuming a distribution of μ_t and $\mathrm{Pr}_{\mathrm{eff}}$, where $\mathrm{Pr}_{\mathrm{eff}} = \mu_{\mathrm{eff}}\, c_p/k_{\mathrm{eff}}$, and then updating the distributions until the results obtained agree, on the average, with the experimental results. The criterion of agreement was taken to be the closeness (visual judgment was used) of the calculated and experimental mean temperature and velocity profiles.

In order to obtain curves that gave good agreement with the velocity profiles it was necessary to pay particular attention to the distribution of μ_t/μ in the region $5 < Y^+ < 12$.

Since most investigators report Pr_t values, then, in order to compare these with the values used in the P-S program, it is necessary to determine the Pr_t distributions from the μ_t and $\mathrm{Pr}_{\mathrm{eff}}$ distributions. The relationship is given by

$$\mathrm{Pr}_t = \frac{\dfrac{\mu_t}{\mu}}{\dfrac{1 + \mu_t/\mu}{\mathrm{Pr}_{\mathrm{eff}}} - \dfrac{1}{\mathrm{Pr}}}. \tag{13}$$

Comparisons of Pr_t distributions used in the P-S program with those reported by Blom [8] and Wassel and Catton [19] are made in Fig. 2. There is certainly little agreement here although the general trends are similar for the Wassel and Catton values and those of the P-S calculations for $x/\delta_0 > 6$.

Trinité and Valentin [21] report distributions of a combination of μ_t and Pr_t for experimental conditions similar to those considered here, but with $U_1 = 29.8$ m/s and $T_w - T_1 \approx 40°\mathrm{C}$, although the R_θ values were not stated. These are shown in Fig. 3. The corresponding values used in the P-S calculations follow the same trend but there is no agreement in detail.

The P-S program allows up to 43 nodes but 21 were found to be adequate. These always span the boundary layer, i.e. the y spacings change although the Y^+ values are reasonably constant. Typical Y^+ values for the nodes near the wall are 0.05, 0.2, 1, 3, 7 and 12, while for nodes at the outer region typical Y^+ values are 550, 750, 1000, 1270, 1600 and 2000. The sublayer model of Patankar and Spalding [7] is used and any crudities it may contain are obviated by having a number of nodes in the laminar sublayer.

Results

The calculated and experimental values for wall heat flux are compared in Table 2. Where the experimenter has determined the heat flux by a number of different methods, the average value only has been shown in this table. Also shown are the values obtained using equation (11.20) of Kays [22].

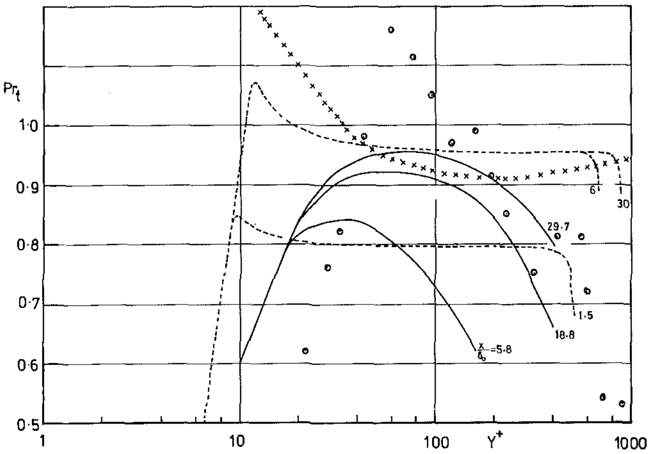

Fig. 2 Comparison between turbulent Prandtl numbers used in the P-S program and those of Blom [8] and Wassel and Catton [19]. - - -, P-S program; ⊙ Blom, $U_1 = 10.1$ m/s, $x/\delta_0 = 29.7$, from direct measurement of $\overline{uv}$ and $\overline{v\theta}$; — Blom, $U_1 = 10.1$ m/s, $\overline{uv}$ and $\overline{v\theta}$ determined by integrating the momentum and energy equations; xxx; Wassel and Catton for a fully heated plate

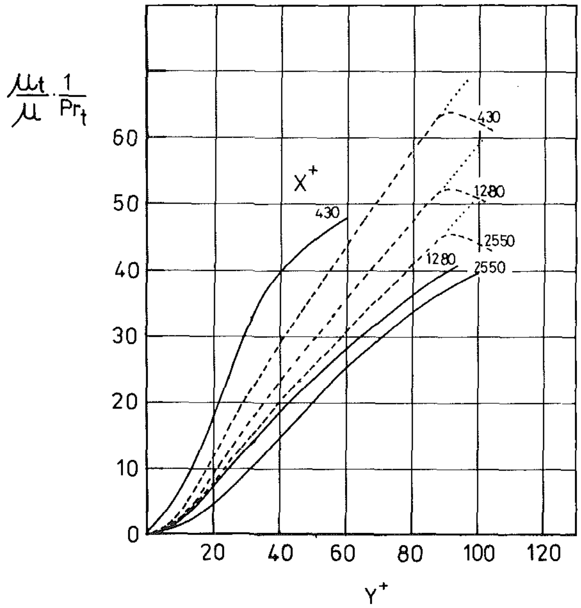

Fig. 3 Comparison between the turbulent viscosity and turbulent Prandtl numbers used in the P-S program with those of Trinité and Valentin [21], - - -, P-S program, $R_\theta = 1000$; . . . , P-S program, $R_\theta > 1000$; —, Trinité and Valentin

Table 2 Wall heat flux values

Reference	x/δ_0	Heat Flux – W/m^2 Expt'l Results	B-U Calcs.	P-S Calcs.	Kays [22] Eq. 11.20
Blom—low speed	1.2	418	355	424	329
	4.9	333	330	311	280
	8.6	310	309	285	261
	16.0	288	283	260	240
	25.3	273	265	243	224
Blom—high speed	1.4	550	491	550	448
	5.8	447	457	418	381
	10.1	416	433	386	355
	18.8	385	408	353	327
	29.7	362	390	331	306
Fulachier	1.0	1000	784	991	865
	3.1	850	737	795	762
	5.1	750	708	736	718
	7.1	690	687	702	693
	10.2	660	663	668	662
	13.1	640	642	644	643
	16.3	640	622	623	622
Perry and Hoffmann	7.3	795	736	723	732
	24.0	675	607	604	627
	40.7	625	545	550	583
	57.3	590	505	513	552

Comparisons between calculated mean temperature profiles and experimental results, in the form of T^+ versus Y^+, are shown in Fig. 4 for the Blom high speed case and Fig. 5 for the Fulachier and Perry and Hoffmann cases. For Fulachier, results at only one station were reported while results at a number of stations downstream from the step were reported by the other investigators.

Total heat flux distributions across the boundary layer, as determined by Fulachier and also by Blom, are shown together with the calculated values in Fig. 6.

The Fulachier turbulent heat flux distributions are shown in Fig. 7, which also shows the calculated distributions at different stations downstream from the step. For clarity, the P-S calculations have been omitted from this figure.

The calculated values of $\mathrm{St}/c_f/2$ as a function of distance down-

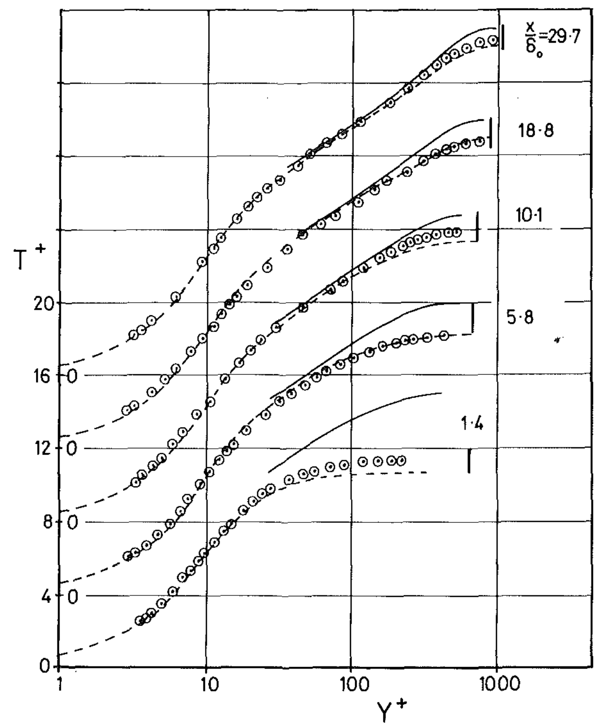

Fig. 4 Comparison between calculated mean temperature profiles and measurements of Blom [8] for U_1 = 10.1 m/s, ⊙, experiment; —, calculation (B-U); - - -, calculation (P-S); |, approximate location of limit of velocity boundary layer

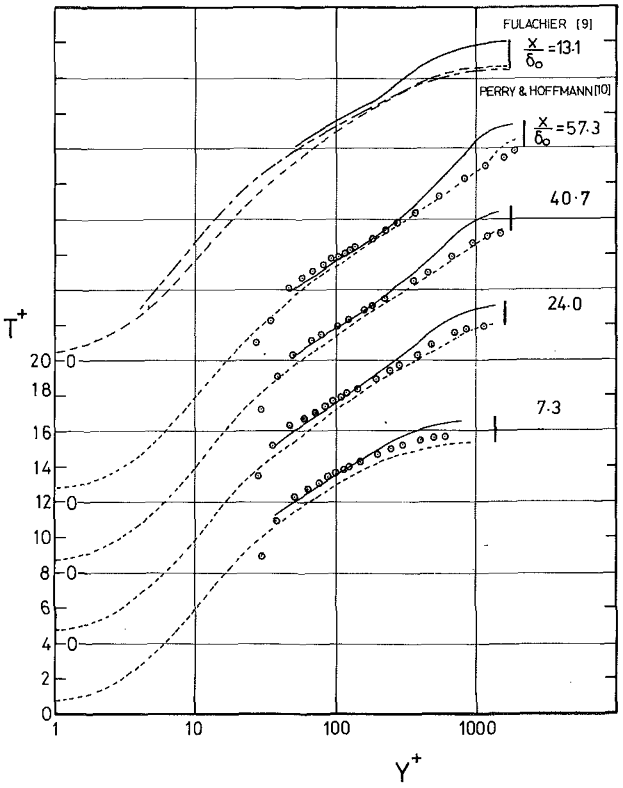

Fig. 5 Comparison between calculated mean temperature profiles and measurements of Perry and Hoffmann [10] and Fulachier [9], ⊙, experiment, Perry and Hoffmann; – – -, experiment (best fit curve), Fulachier; —, calculation, B-U; - - -, calculation, P-S; |, approximate location of limit of velocity boundary layer

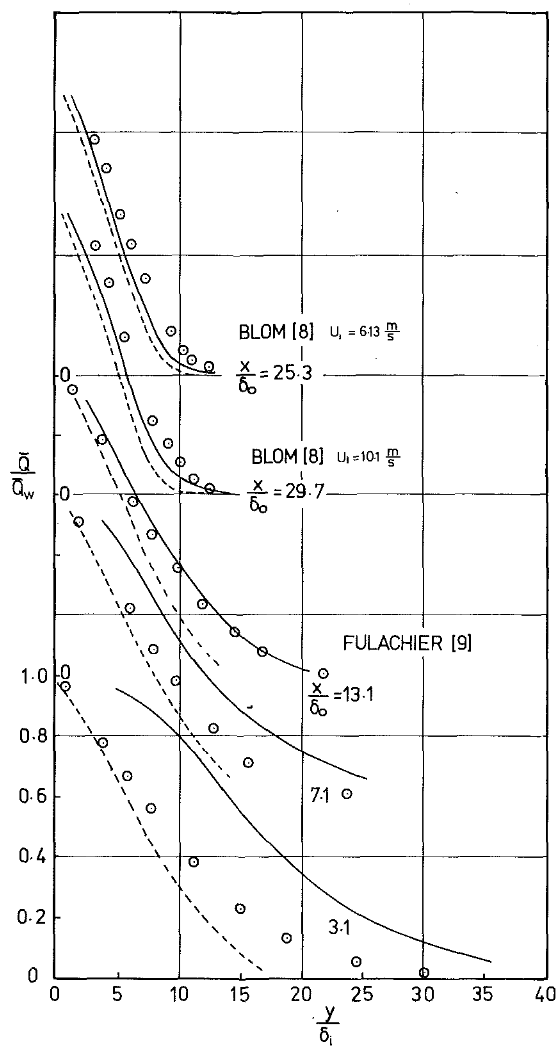

Fig. 6 Comparison between experimental heat flux distributions with present calculations: ⊙, experimental; —, B-U; - - - P-S

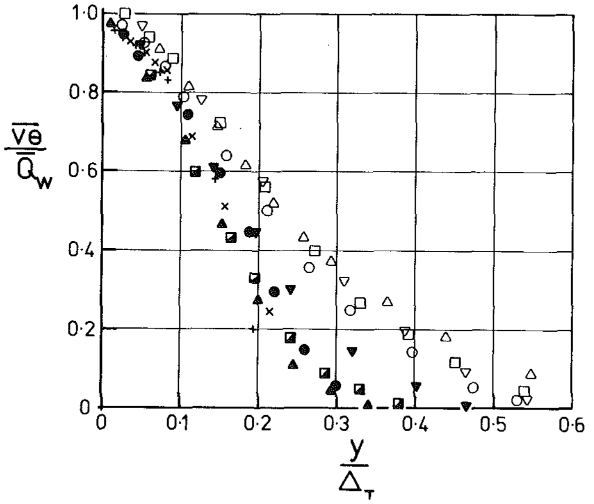

Fig. 7 Comparison between calculated heat flux distributions downstream of a step change in surface temperature and measurements in a self-preserving thermal layer—Measurements: ●, Fulachier [9] (smooth wall), R_θ = 4500; x, Pimenta, et al. [17] (rough wall), 4666; +, Pimenta, et al. [17] (rough wall), 13,343. Calculations (B-U): ▽, Blom, U_1 = 6.13 m/s x/δ_0 = 13.5, R_θ = 2069; □, Blom, U_1 = 10.1 m/s 13.1, 2283; ○, Fulachier, 17.3, 4914; △, Perry and Hoffmann, 7.5, 3280; ▼, Perry and Hoffmann, 24.0, 4124; □, Perry and Hoffmann, 42.6, 4909; ▲, Perry and Hoffmann, 59.3, 5555

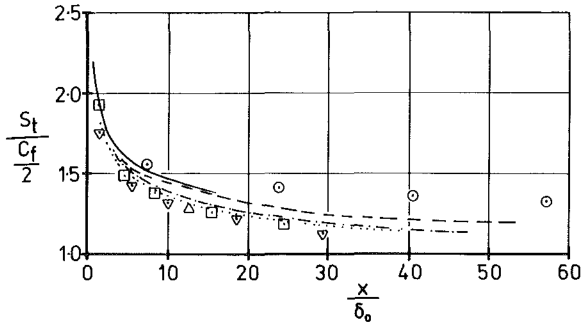

Fig. 8 Comparison between calculated Reynolds analogy factors and those of Blom [8], Fulachier [9] and Perry and Hoffmann [10]—Experimental: ⊡ Blom, U_1 = 6.13 m/s; △ Blom, U_1 = 10.1 m/s; ▵, Fulachier; ⊙ Perry and Hoffmann. P-S calculations: ··· Blom, U_1 = 6.13 m/s; - - - Blom, U_1 = 10.1 m/s; — Fulachier; - - - Perry and Hoffmann

stream from the step, together with the experimental values (only one in the case of Fulachier), are shown in Fig. 8. In this case, for clarity, the B-U calculations have been omitted.

Discussion of Results

The P-S temperature distributions in Fig. 4 are, as expected, in good agreement with the experimental results of Blom. The B-U method however yields consistently high values of T^+. The discrepancy is particularly large at small values of x while agreement with measurements is good at $x/\delta_0 = 38.6$, the furthest downstream station considered by Blom for $U_1 = 10.1$ m/s. The high values of the calculated T^+ are partly due to the low values of the calculated heat flux (Table 2). This flux is deduced from the logarithmic law (3) using the known value of T_w and the calculated mean temperature at the first mesh point. As noted earlier, both the logarithmic law and the assumption Pr_t = constant are not likely to be valid for small values of x and this is substantiated by the P-S calculations. It must be noted however that the Reynolds analogy factor $\mathrm{St}/c_f/2$, Fig. 8, remains as high as 1.30 at $x/\delta_0 = 20$, so that the use of the Reynolds analogy would lead to the wall heat flux being underestimated by 30%. Both calculation methods underestimate the values of heat flux given by Blom, Fig. 6.

The Fulachier temperature profile, Fig. 5, is reproduced by the P-S calculations in the outer part of the flow while there is some discrepancy closer to the wall. The B-U T^+ values are in reasonable agreement with the Fulachier curve. This is consistent with the agreement between the values of κ_θ and C_θ chosen in the program and the experimental values. Fulachier integrated an energy equation of the form

$$U\frac{\partial T}{\partial x} + V\frac{\partial T}{\partial y} = -\frac{\partial \overline{Q}}{\partial y} + \frac{\mu_{\mathrm{eff}}}{\rho c_p}\left(\frac{\partial U}{\partial y}\right)^2$$

across the boundary layer, neglecting the last term on the R.H.S., to obtain

$$\left(\frac{\overline{Q}}{\overline{Q}_w}\right)_y = 1 + \frac{1}{\overline{Q}_w}\left[T\cdot\frac{d}{dx}\int_0^y U\,dy - \frac{d}{dx}\int_0^y (UT)dy\right] \tag{14}$$

Using this equation and his experimental curves of $U(y)$ and $T(y)$ the heat flux distributions shown in Fig. 6 were obtained. The P-S calculations give $\overline{Q}$ values consistently lower than the Fulachier results while the B-U calculations are in excellent agreement for $x/\delta_0 > 12$. The B-U values are in poor agreement close to the step and part of this discrepancy must be due to the low values of $\overline{Q}_w$ indicated in Table 2. Unfortunately, the last experimental station of Fulachier is at $x/\delta_0 \approx 16$ so that comparisons with a more fully developed thermal boundary layer were not possible.

Good agreement was again achieved between the Perry and Hoffmann temperature profiles and the P-S calculations, Fig. 5, although the agreement did noticeably impair as x/δ_0 increased. The B-U calculations differ little from the Perry and Hoffmann values in the logarithmic region but the thermal "wake" function obtained from the calculation is significantly larger than the measured wake function.

A relatively stringent requirement for self-preservation of a thermal turbulent boundary layer would be that

$$\frac{\overline{v\theta}}{\overline{Q}_w} = f\left(\frac{y}{\Delta_T}\right)$$

where f is a universal function and

$$\Delta_T = \int_0^\infty \frac{T - T_1}{T_\tau}\,dy \tag{15}$$

is a length scale analogous to the Clauser thickness. In Fig. 7 the calculated distributions (using the B-U method) of $\overline{v\theta}/\overline{Q}_w$ at $x/\delta_0 \approx 18$ for the four test cases considered are in reasonable agreement with each other but differ significantly from distributions obtained in a thermal layer which has essentially the same origin as the momentum layer. Good agreement is observed between the results of Pimenta, et al. [17] for a rough wall thermal layer and those of Fulachier [9] obtained with no unheated starting length. In the case of Perry and Hoffmann [10], the B-U calculation was run for values of x/δ_0 as high as 85. It is clear from the figure that the calculated profiles only become self-preserving in the range $40 < x/\delta_0 < 60$. This is approximately the range in which Perry and Hoffmann's distribution of $\sqrt{\overline{\theta^2}}/T_\tau$ became a universal function of y/Δ_T. It was found in Antonia, et al. [12] that $\overline{v\theta}$ profiles became approximately self-preserving at $x/\delta_0 > 40$ and it was speculated that some aspects of the thermal interface may attain self-preserving behaviour only when $x/\delta_0 \approx 100$. The above results all seem to indicate that the relaxation distance for the thermal layer is large. This should place the onus on experimentalists to obtain data, particularly heat flux distributions, at values of x/δ_0 of order 100 in experiments dealing with a step change in surface heating conditions.

Acknowledgment

R.A.A. would like to acknowledge the support of the Australian Research Grants Committee. He is also grateful to Mr. P. Bradshaw for making the Bradshaw-Unsworth program available to him.

References

1 Reynolds, W. C., "Computation of Turbulent Flows," *Annual Review of Fluid Mechanics*, Vol. 8, Van Dyke, M., Vincenti, W. G., and Wehausen, J. V., eds., Ann. Rev. Inc., Palo Alto, California, 1976, pp. 183–208.

2 Reynolds, W. C., Cebeci, T., "Calculation of Turbulent Flows," *Topics in Applied Physics: Turbulence*, Vol. 12, ed. Bradshaw, P., Springer-Verlag, Berlin, 1976, pp. 193–229.

3 Launder, B. E., "Heat and Mass Transport," *Topics in Applied Physics: Turbulence*, Vol. 12, ed. Bradshaw, P., Springer-Verlag, Berlin, 1976, pp. 231–287.

4 Bradshaw, P., Ferriss, D. H., Atwell, N. P., "Calculation of Boundary Layer Development using the Turbulent Energy Equation," *Journal of Fluid Mechanics*, Vol. 28, 1967, pp. 593–616.

5 Bradshaw, P., Ferriss, D. H., "Calculation of Boundary Layer Development using the Turbulent Energy Equation IV: Heat Transfer with Small Temperature Differences," NPL Aero Report 1271, A.R.C. 30 300, 1968.

6 Bradshaw, P., Unsworth, K., "An Improved Fortran Program for the Bradshaw-Ferriss-Atwell Method of Calculating Turbulent Shear Layers," I.C. Aero Report 74-02, Imperial College, London, 1974.

7 Patankar, S. V., Spalding, D. B., *Heat and Mass Transfer in Boundary Layers*, 2nd Edn., Intertext Books, London, England, 1970.

8 Blom, J., "An Experimental Determination of the Turbulent Prandtl Number in a Developing Temperature Boundary Layer," 1970, Ph.D. Thesis, Department of Physics, Technical University, Eindhoven, Holland.

9 Fulachier, L., "Contribution à l'étude des Analogies des Champs Dynamique et Thermique dans une Couche Limite Turbulente," 1972, Thèse Docteur ès Sciences, Université de Provence, France.

10 Perry, A. E., Hoffmann, P. H., "An Experimental Study of Turbulent Convective Heat Transfer from a Flat Plate," Report FM 7, Fluid Mechanics Group, Department of Mechanical Engineering, University of Melbourne, Australia, 1976.

11 Reynolds, W. C., Kays, W. M., Kline, S. J., "Heat Transfer in the Turbulent Incompressible Boundary Layer II: Step Wall-Temperature Distribution," NASA Memo 12-2-58 SW, 1958.

12 Antonia, R. A., Danh, H. Q., Prabhu, A., "Response of a Turbulent Boundary Layer to a Step Change in Surface Heat Flux," *Journal of Fluid Mechanics*, Vol. 80, 1977, pp. 153–177.

13 Antonia, R. A., Danh, H. Q., "Calculation of a Turbulent Boundary Layer Downstream of a Step Change in Surface Heat Flux," *Institution of Engineers*

Proceedings of Thermofluids Conference, Hobart, Tasmania, Dec. 1-3, 1976, pp. 94-97.

14 Johnson, D. S., "Velocity and Temperature Fluctuation Measurements in a Turbulent Boundary Layer Downstream of a Stepwise Discontinuity in Wall Temperature," *Journal of Applied Mechanics, Trans. A.S.M.E.,* Vol. 26, 1959, pp. 325-336.

15 Swenson, G. G., "The Structure of Turbulence in a Boundary Layer in the Presence of Heat Transfer," 1973, Ph.D. Thesis, University of Sydney, Australia.

16 Kader, B. A., Yaglom, A. M., "Heat and Mass Transfer Laws for Fully Turbulent Wall Flows," *International Journal of Heat and Mass Transfer,* Vol. 15, 1972, pp. 2329-2351.

17 Pimenta, M. M., Moffat, R. J., Kays, W. M., "The Turbulent Boundary Layer. An Experimental Study of the Transport of Momentum and Heat with the Effect of Roughness," Report No. HMT-21, Thermosciences Division, Department of Mechanical Engineering, University of Stanford, California, 1975.

18 Klebanoff, P. S., "Characteristics of Turbulence in a Boundary Layer with Zero Pressure Gradient," N.A.C.A. Report No. 1247, 1955.

19 Wassel, A. T., Catton, I., "Calculation of Turbulent Boundary Layers over Flat Plates with Different Phenomenological Theories of Turbulence and Variable Turbulent Prandtl Number," *International Journal of Heat and Mass Transfer,* Vol. 16, 1973, pp. 1547-1563.

20 Reynolds, A. J., "The Prediction of Turbulent Prandtl and Schmidt Numbers," *International Journal of Heat and Mass Transfer,* Vol. 18, 1975, pp. 1055-1069.

21 Trinité, M., Valentin, P., "Couche Limite Turbulente avec Discontinuité de Température et de Concentration à la Paroi," *International Journal of Heat and Mass Transfer,* Vol. 15, 1972, pp. 1337-1354.

22 Kays, W. M., *Convective Heat and Mass Transfer,* McGraw-Hill, New York, p. 242, 1966.

B. K. Meena
Research Student.

G. Nath
Associate Professor.

Department of Applied Mathematics,
Indian Institute of Science,
Bangalore-560012, India

Laminar Boundary Layer Swirling Flow with Heat and Mass Transfer in Conical Nozzles and Diffusers

The flow and heat transfer for a steady axisymmetric laminar incompressible boundary layer swirling flow with mass transfer in a conical nozzle and a diffuser have been studied. The partial differential equations governing nonsimilar flow have been solved numerically using an implicit finite-difference scheme after transforming them into new coordinates having finite ranges. The results indicate that, both for the nozzle and diffuser, swirl exerts a strong influence on the longitudinal skin friction, but its effect on the tangential skin friction and heat transfer is comparatively small. In the case of the nozzle, even for a small value of the dissipation parameter at the inlet, the heat transfer rapidly increases near the end of the nozzle; whereas in the case of the diffuser, no such trend is observed. Suction increases the skin friction and heat transfer, but injection does the reverse. The results are found to be in good agreement with those of the local nonsimilarity and momentum integral methods except near the end of the nozzle or diffuser, but they differ appreciably from those of the local similarity method except near the inlet.

Introduction

Swirling flows are encountered in many engineering devices such as swirl atomizers used in agricultural spraying machinery and in oiled fired furnaces, dust collectors, moisture separators, turbines, pumps, fans, compressors and other rotodynamic machines [1–3]. The study of the swirling flow through nozzles and diffusers which are important components in these devices is of considerable importance. Although most of the applications mentioned above involve turbulent flow, the flow and heat transfer results obtained on the basis of laminar model are, to a large extent, expected to exhibit most of the characteristics of the actual problem. Swirling flows in nozzles and diffusers are, in general, governed by a set of nonlinear partial differential equations which are rather difficult to solve exactly. Hence, most of the investigators have obtained solutions of the governing equations using approximate methods.

The velocity field for an incompressible laminar boundary layer swirling flow through a conical convergent nozzle was first studied by Taylor [2] who considered the case when the tangential flow is superimposed upon a secondary axial flow. Binnie and Harris [4] extended Taylor's approach to include radial as well as swirling flow in a conical venturi geometry. Wilks [5] restudied the problem of [2] under the assumption that the flow field is composed of a central inviscid core flow and a thin boundary layer flow at the walls of the swirl chamber. He found velocity overshoot in longitudinal velocity profiles. Houlihan and Hornstra [6] followed the approach analogous to that of Wilks [4] but they included the effect of boundary layer growth upon the tangential and axial velocities in the freestream. As a result, they found that there is no velocity overshoot in longitudinal (axial) velocity profiles. It may be remarked that all the authors have studied only velocity flow field without mass transfer using the momentum integral method which is an approximate method with no means of assessing the error involved other than by comparison with an exact solution.

Unlike convergent nozzles, where the flow experiences a favorable pressure gradient, the flow in diffusers is against an adverse pressure gradient and therefore the main flow is liable to separate from the boundary. Moreover, in swirling diffuser flows "vortex breakdown" can also occur if swirl exceeds a certain critical value [7]. The detailed description of the phenomenon of vortex breakdown is given in an excellent review article by Hall [7]. However, the separation or vortex breakdown in diffusers can be prevented by applying suction [7]. The amount of suction required to prevent vortex breakdown or separation throughout the entire length of a diffuser depends on several factors such as swirl, cone angle, etc. Most research work in diffusers is experimental and deals mainly with performance characteristics of straight walled two-dimensional radial, conical or annular diffusers [8]. The swirling flows in conical diffusers have been experimentally studied by McDonald, et al. [9] and So [3]. The theoretical studies in rotationally symmetric flow passages including conical diffusers using boundary layer approximation have been carried out by Schlichting and Gersten [10]. Both experimental and theoretical studies mentioned above have stressed the performance characteristics and design problems. None of the authors has done a detailed study of the flow and heat transfer problem in swirling diffuser flows.

In the present paper, we have studied both the flow and heat transfer with mass transfer in a steady axisymmetric laminar incompressible boundary layer swirling flow through a conical convergent nozzle and a diffuser. The partial differential equations governing

---

Contributed by the Heat Transfer Division for publication in the JOURNAL OF HEAT TRANSFER. Manuscript received by the Heat Transfer Division March 16, 1978.

the flow have been transformed into new coordinates with finite ranges and the resulting equations have been solved numerically using an implicit finite-difference scheme [11–12]. The results have also been compared with those of the local similarity, local nonsimilarity and momentum integral methods [6, 13–15]. The results presented here are the first heat and mass transfer calculations for swirling nozzle and diffuser flows. The flow in nozzles and diffusers will remain laminar if the swirl is weak; however, for a strong swirl the flow may not remain laminar along the whole length but is likely to become turbulent near the outlet region. Nevertheless, the results obtained on the basis of laminar model can still be useful and can also form the basis of analysis with turbulent model.

Governing Equations

The governing equations in dimensionless form for steady laminar incompressible boundary layer swirling flow through an axisymmetric surface of arbitrary cross section (see Fig. 1) with free-vortex imposed on the longitudinal flow are [5–6]

$$f''' + ff'' + \beta(X)(1 - f'^2) + \alpha(X)(1 - s^2) = 2X(f'f_X' - f''f_X) \quad (1)$$

$$s'' + fs' = 2X(f's_X - s'f_X) \quad (2)$$

$$\mathrm{Pr}^{-1}g'' + fg' + (u_e{}^2/h_e)[f''^2 + (v_e/u_e)^2 s'^2] = 2X(f'g_X - g'f_X) \quad (3)$$

The boundary conditions are

$$f(X, 0) = f_w, f'(X, 0) = s(X, 0) = g(X, 0) = 0$$
$$f'(X, \infty) = s(X, \infty) = g(X, \infty) = 1 \quad (4)$$

where

$$Z = ru_e z/(2X)^{1/2}, X = \nu \int_0^x u_e r^2 dx$$

$$\psi = (2X)^{1/2} f(X, Z), u = r^{-1}(\partial\psi/\partial z), w = -r^{-1}(\partial\psi/\partial x)$$
$$f' = u/u_e, s = v/v_e, g = (T - T_w)/(T_\infty - T_w) \quad (5a)$$

$$\alpha(X) = (-2X/r)(dr/dX)(v_e/u_e)^2, \beta(X) = (2X/u_e)(du_e/dX)$$
$$h_e = C_p(T_\infty - T_w) \quad (5b)$$

$$f_w = -(2X)^{-1/2} \int_0^x (w)_w r dx \quad (5c)$$

The skin-friction coefficients along x and y directions and heat-transfer coefficient in the form of Nusselt number can be expressed as

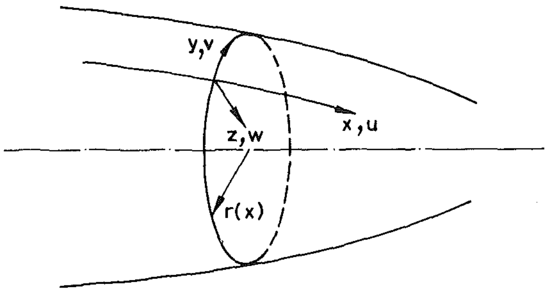

Fig. 1 Coordinate system and velocity components for axisymmetric flow through a surface with arbitrary cross section (*x* is the longitudinal distance along surface, *y* is the tangential (circumferential) distance around surface, and *z* is the distance normal to surface)

$$C_f = 2\tau_x/\rho u_e{}^2 = (2/X)^{1/2}\nu r f_w''$$
$$\overline{C}_f = 2\tau_y/\rho u_e{}^2 = (2/X)^{1/2} r\nu (v_e/u_e) s_w'$$
$$\mathrm{Nu} = x(\partial T/\partial z)_w/(T_\infty - T_w) = (\mathrm{r u_e x})(2X)^{-1/2} g_\mathrm{w}' \quad (6)$$

For a conical convergent nozzle with straight generators (see Fig. 2) [6]

$$r/L = (1 - \overline{x}) \sin\lambda, \overline{x} = x/L, u_e = b/r^2, v_e = \Gamma/r, X = \nu b x \quad (7a)$$

$$\alpha(\overline{x}) = 2\overline{x}(1 - \overline{x})(v_e/u_e)_i{}^2, \beta(\overline{x}) = 4\overline{x}/(1 - \overline{x}), X(\partial/\partial X) = \overline{x}(\partial/\partial\overline{x})$$
$$u_e{}^2/h_e = (u_e{}^2/h_e)_i(1 - \overline{x})^{-4}, (v_e/u_e)^2 = (v_e/u_e)_i{}^2(1 - \overline{x})^2 \quad (7b)$$

$$f_w = A(\overline{x})^{1/2}(1 - \overline{x}/2), A = -(w)_w L^{3/2} \sin\lambda/(2\nu b)^{1/2} \quad (7c)$$

where $A \gtrless 0$ according to whether there is suction or injection.

Similarly, for a truncated conical diffuser with straight generators (see Fig. 2)

$$r/L = b_1[1 + (\overline{x}/b_1)\sin\lambda], b_1 = a_1/L \quad (8a)$$

$$\alpha(\overline{x}) = -2(\overline{x}/b_1)\sin\lambda[1 + (\overline{x}/b_1)\sin\lambda](v_e/u_e)_i{}^2$$
$$\beta(\overline{x}) = -4(\overline{x}/b_1)\sin\lambda/[1 + (\overline{x}/b_1)\sin\lambda]$$
$$u_e{}^2/h_e = (u_e{}^2/h_e)_i[1 + (\overline{x}/b_1)\sin\lambda]^{-4},$$
$$(v_e/u_e)^2 = (v_e/u_e)_i{}^2[1 + (\overline{x}/b_1)\sin\lambda]^2 \quad (8b)$$

$$f_w = A(\overline{x}/b_1)^{1/2}[1 + (\overline{x}/2b_1)\sin\lambda],$$
$$A = -(w)_w a_1{}^{3/2}/(2\nu b)^{1/2} \quad (8c)$$

Other expressions are same as those for the nozzle.

From equations (7*c*) and (8*c*), it is evident that the parameter A will be a constant if the surface mass transfer $(w)_w$ is taken as a constant, because L, λ, ν, a_1 and b are all constants. Consequently, f_w will

Nomenclature

a, a_1, A, b, b_1 = constants
$C_f, \overline{C}_f$ = skin-friction coefficients along x and y directions, respectively
C_p = specific heat at a constant pressure
f_w = mass transfer parameter
f' = dimensionless longitudinal velocity
f_w'', s_w' = surface skin-friction parameters along x and y directions, respectively
g = dimensionless temperature
g_w' = surface heat-transfer parameter
h = enthalpy
L = length of the nozzle or diffuser measured along x direction
Nu = Nusselt number
Pr = Prandtl number
r = surface radius
s = dimensionless swirl velocity
T = temperature
u, v, w = velocity components along x, y and z directions, respectively
$u_e{}^2/h_e$ = viscous dissipation parameter
x, y, z = longitudinal, tangential and normal directions, respectively
$\overline{x}$ = dimensionless longitudinal distance
X, Z = transformed coordinates, equation (5*a*)
α, β = swirl and longitudinal acceleration parameters, respectively
Γ = constant circulation
$\eta, \overline{\eta}$ = transformed normal distances
λ = semi-vertical angle of the nozzle or diffuser
ν = kinematic viscosity
ρ = density
τ_x, τ_y = shear stresses along x and y directions, respectively
ψ = dimensional stream function

Subscripts

e = denotes condition at the edge of the boundary layer
i = denotes inlet condition
w = denotes condition at the surface $Z = \eta = 0$

Superscripts

$'$ = prime denotes differentiation with respect to Z

vary according to expression given in equation (7c) or (8c). Here, the mass transfer on the surface is taken to be so small that the potential flow at the edge of the boundary layer is not affected by it, and therefore the potential flow velocity components u_e and v_e given in equation (7a), which have been derived on the assumption of no mass transfer, can be assumed to hold good in the present case also.

It may be remarked that the solutions for incompressible nozzle flows are rather limited as the flow velocities increase with x and they tend to become compressible for large x.

It may be noted that equations (1) and (2) are uncoupled from (3) and, at $X = 0$ (or $\bar{x} = 0$), they reduce to well-known similarity (Blasius) equations. Further, they reduce to those of nonswirling flows when $\alpha(X) = 0$ and $(v_e/u_e)_i = 0$. Further, it may be remarked that both for nozzles and diffusers $f_w = 0$ at $\bar{x} = 0$ for all values of A (see equations (7c) and (8c)). The parameter v_e/u_e gives a measure of the relative magnitudes of the swirl and longitudinal flow. It is evident from equation (7b) that in the case of a nozzle the longitudinal flow dominates the swirl flow as the vertex is approached ($\bar{x} \rightarrow 1$), although at the inlet ($\bar{x} = 0$) the swirl flow is greater than the longitudinal flow ($(v_e/u_e)_i > 1$). On the other hand, in the case of a diffuser, as is evident from equation (8b), swirl flow dominates the longitudinal flow throughout the length of the diffuser if $(v_e/u_e)_i \geqslant 1$. It may also be remarked that swirl is assumed to be imposed upon the longitudinal flow when swirl is small, but for a large swirl ($(v_e/u_e)_i > 1$) it may be regarded as other way around.

Transformation to Finite Coordinates

The governing equations (1–3) are transformed to a new system of coordinates by means of a transformation [11]

$$\eta = 1 - \exp(-aZ), a > 0 \tag{9}$$

wherein the infinite range of integration $(0, \infty)$ on Z is replaced by a finite range $(0, 1)$ on η. The scaling factor, a, provides an optimum distribution of nodal points across the boundary layer [11]. We define $\partial f/\partial Z = F$, $a(1 - \eta) = \bar{\eta}$ and change the variable Z to η. As a result, equations (1) to (3) become

$$\bar{\eta}^2 F_{\eta\eta} + \bar{\eta}(f - a)F_\eta + \beta(X)(1 - F^2) + \alpha(X)(1 - s^2) = 2X(FF_X - \bar{\eta} f_X F_\eta) \tag{10}$$

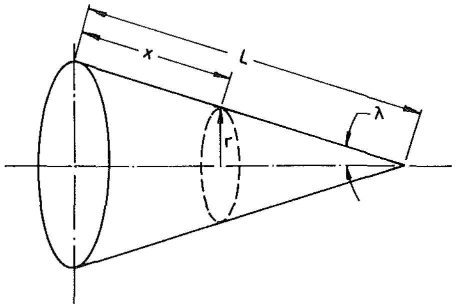

(a) Conical nozzle with straight generators

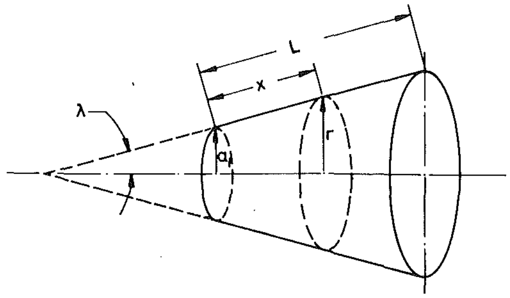

(b) Truncated conical diffuser with straight generators

Fig. 2 Conical nozzle and truncated conical diffuser

$$\bar{\eta}^2 s_{\eta\eta} + \bar{\eta}(f - a)s_\eta = 2X(Fs_X - \bar{\eta} f_X s_\eta) \tag{11}$$

$$\mathrm{Pr}^{-1}\bar{\eta}^2 g_{\eta\eta} + \bar{\eta}(f - a\mathrm{Pr}^{-1})g_\eta + (u_e{}^2/h_e)\bar{\eta}^2[F_\eta{}^2 + (v_e/u_e)^2 s_\eta{}^2] = 2X(Fg_X - \bar{\eta} f_X g_\eta) \tag{12}$$

with

$$\mathrm{f} = \int_0^\eta \frac{F}{a(1 - \eta)} d\eta + f_w \tag{13}$$

where f_w is given by equations (5c). The boundary conditions (4) are now transformed to

$$F(X, 0) = s(X, 0) = g(X, 0) = 0, F(X, 1) = s(X, 1) = g(X, 1) = 1 \tag{14}$$

The parameters f_w'', s_w' and g_w' occurring in (6) can be written as

$$f_w'' = a(F_\eta)_w, s_w' = a(s_\eta)_w, g_w' = a(g_\eta)_w \tag{15}$$

Method of Solution

The governing equations (10–12) under conditions (14) along with (7) or (8) were converted into a set of implicit finite-difference equations, and the resulting linear tridiagonal matrix equations were solved by the use of Thomas algorithm [16]. The method is the same as that employed by Marvin and Sheaffer [11] and Vimala and Nath [12], except that the fully implicit finite-difference scheme instead of Crank-Nicholson finite-difference scheme, and Thomas algorithm instead of the algorithm given by Varga, [17] were used. Since the method is described in full detail in [11–12], for the sake of brevity it is not described here. It may be noted that the use of Thomas's algorithm for the solution of tridiagonal matrix equations takes less computer time as compared to the matrix inversion method [16].

The computations were carried out for $(u_e{}^2/h_e)_i = 0.01$, $(v_e/u_e)_i{}^2 = 1, 10$; $A = 0, 1, -1$ (for nozzle) and 2 (for diffuser), $\lambda = 0.1, 0.2$ (in radians). Here Pr is taken as 0.7, $b_1 = 0.5$ and $a = 0.6217$. The step sizes $\Delta\eta = 0.005$ and $\Delta\bar{x} = 0.05$ have been used for computation and further reduction in them does not change the results up to the third decimal place. The accuracy of the method was also tested by comparing our results for $X = 0$ (i.e., similarity equations) with those obtained using forward integration scheme, and our results agreed to within 4 decimal places tabulated in [13]. It is evident from (7b) that $\beta(\bar{x})$ and $u_e{}^2/h_e$ tend to infinity as $\bar{x}$ tends to 1. Hence the solutions are not valid as $\bar{x}$ approaches 1. In order to compare our results with those of the local similarity, local nonsimilarity (three-equation model) and momentum integral methods [6, 13–15], we have also solved our equations using these methods.

Results and Discussion

Conical Convergent Nozzle. Some representative velocity and temperature profiles (f', s, g) are shown in Figs. 3–4. It is evident from these figures that the profiles become very steep when $\bar{x}$ increases. The profiles also become steep when A or $(v_e/u_e)_i$ increases, however they are not shown for lack of space. Since $\alpha = \beta = f_w = 0$ at $\bar{x} = 0$, the profiles at $\bar{x} = 0$ are unaffected by the change of these parameters. It may be remarked that there is no velocity overshoot in longitudinal velocity profiles f'. Similar behavior has also been observed by Houlihan and Hornstra [6].

The variation of f_w'', s_w' and g_w' with $\bar{x}$ for various values of A and $(v_e/u_e)_i$ is shown in Figs. 5–7 which also contain results obtained by the local similarity, local nonsimilarity (three-equation model) and momentum integral methods. The results show that swirl exerts a strong influence on f_w'' whereas its effect on s_w' and g_w' is comparatively small. It is also observed that f_w'', s_w' and g_w' increase along the nozzle whatever may be the values of A and $(v_e/u_e)_i$, but g_w' increases rapidly towards the end of the nozzle. This increase in g_w' for large $\bar{x}$ is due to the viscous dissipation parameter $u_e{}^2/h_e$. Even a small value of $(u_e{}^2/h_e)_i$ (say 0.01) can give rise to large increase in g_w' for large $\bar{x}$. The effect of suction ($A > 0$) is to increase f_w'', s_w' and g_w' while injection ($A < 0$) does the reverse. For non-swirling flows (i.e., $\alpha = 0$, $(v_e/u_e)_i = 0$), the values of f_w'', s_w' and g_w' are nearly same as those of swirling flows with $(v_e/u_e)_i = 1$, and, therefore, they could

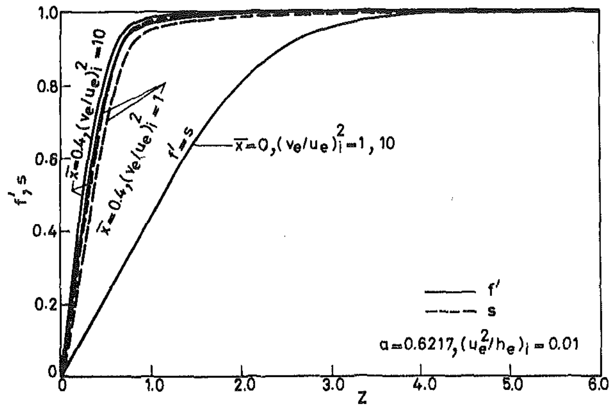

Fig. 3 Longitudinal and swirl velocity profiles (nozzle)

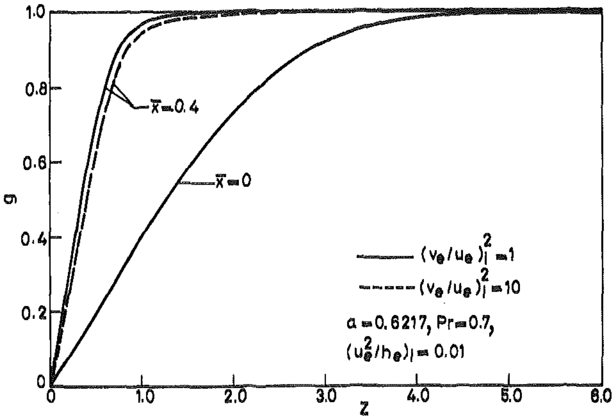

Fig. 4 Temperature profiles (nozzle)

not be shown in Figs. 5–7. The reason for small change in f_w'', s_w' and g_w' is that when $(v_e/u_e)_i = 1$, α is small $(0 \leqslant \alpha \leqslant 0.5)$ for $0 \leqslant \bar{x} \leqslant 0.8$ (see equation (7b)), hence small change in α is not expected to produce significant change in f_w'', s_w' and g_w'. This implies that it takes a lot of swirl to get a strong influence. The results indicate that there exists a critical value of the injection rate A depending upon the swirl parameter at the inlet $(v_e/u_e)_i$ beyond which separation occurs. For example, when $(v_e/u_e)_i = 1$ and $A = -1.8$, separation occurs near $\bar{x} = 0.1$. However, for $(v_e/u_e)_i{}^2 = 10$ and $A = -1.8$, separation does not occur. This implies that separation can be prevented by increasing the swirl velocity at the inlet.

In the inlet (throat) region, the skin friction (both longitudinal and tangential) is little affected by swirl when $(v_e/u_e)_i = 1$, but significant increase is observed when $(v_e/u_e)_i{}^2 = 10$. Near the end of the nozzle, the effect of swirl tends to diminish. On the other hand, the effect of swirl does not significantly increase the heat transfer in the inlet region. Similar trend has been observed experimentally, which is important from a design viewpoint [18].

We have compared our results (see Figs. 5–7) with those obtained by the local similarity, local nonsimilarity and momentum integral methods, and we find that except very near the inlet region (i.e., $\bar{x} \simeq 0$) the local similarity results are not in good agreement with the present (finite-difference) results and the difference increases as $\bar{x}$ increases. It may be noted that the local similarity solution of equation (2) or (11), when $f_w = 0$ or a constant, reduces to that of the similarity solution. Hence $s_w' = 0.4696$ for all $\bar{x}$ when $A = 0$ $(f_w = 0)$ and it is not shown in Fig. 6. In the present problem, the nonsimilar terms of equations (1–3) or (10–12) (i.e., right hand side) are not small for large $\bar{x}$ and therefore the local similarity method, in which the nonsimilar terms are neglected, is not expected to give satisfactory results especially for large $\bar{x}$. On the other hand, the local nonsimilarity and momentum integral results are in good agreement with the finite-difference results (present method) in the entire region except near the end of the nozzle. However, the local nonsimilarity method gives more accurate results compared to the momentum integral method.

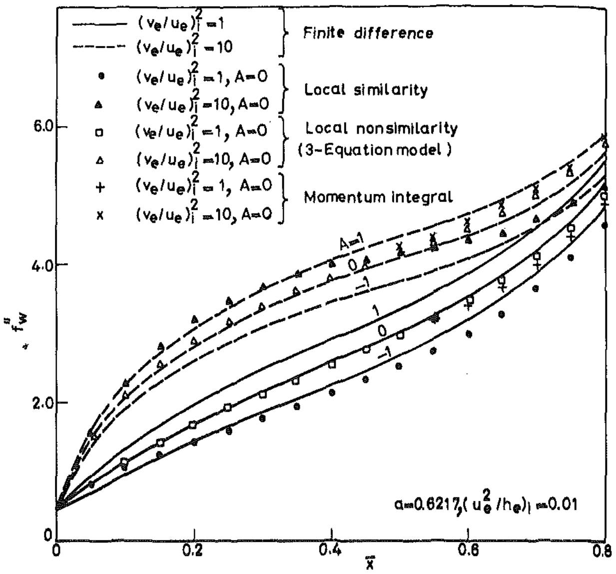

Fig. 5 Variation of longitudinal skin friction with $\bar{x}$ (nozzle)

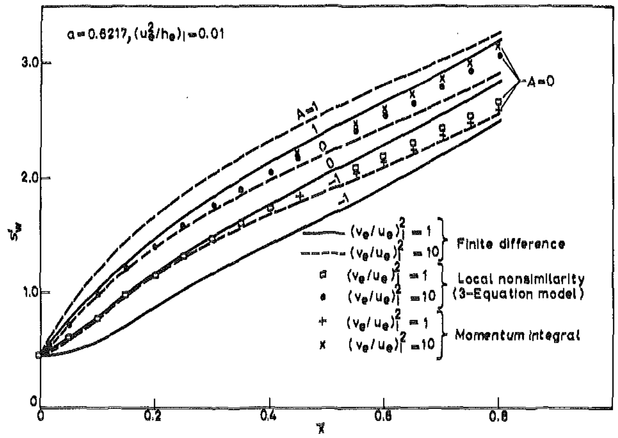

Fig. 6 Variation of tangential skin friction with $\bar{x}$ (nozzle)

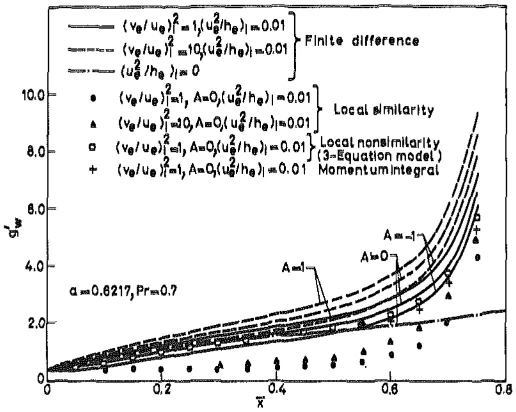

Fig. 7 Variation of heat transfer with $\bar{x}$ (nozzle)

Conical Diffuser. As mentioned earlier, the flow in diffusers is against an adverse pressure gradient and, therefore, separation even occurs near the inlet. The results show that for $A = 1.2$ and $(v_e/u_e)_i{}^2 = 10$, separation occurs near $\bar{x} = 0.2$, but for $(v_e/u_e)_i = 1$ and $A = 1.2$, no separation occurs. This indicates that the swirl critically affects separation, and this has also been observed experimentally [3, 9]. Since separation increases energy losses and leads to very nonuniform velocity profiles at the exit, the problem of designing diffusers with minimum energy losses is important. For the values of parameters used in the present analysis, we have found that separation throughout the entire length of the diffuser can be prevented by taking the suction parameter $A = 2$ and then the solution can be obtained for the entire range $(0 \leqslant \bar{x} \leqslant 1)$.

The velocity and temperature profiles (f', s, g) at $\bar{x} = 0.5$ and 1.0 are given in Fig. 8. Since the profiles at $\bar{x} = 0$ are the same as those of nozzles given in Figs. 3–4, they are not shown here. Like those of nozzles, they also become steep as $\bar{x}$ increases. The skin-friction and heat-transfer parameters (f_w'', s_w', g_w') are shown in Figs. 9–10. As in the case of a nozzle, swirl $(v_e/u_e)_i$ affects f_w'' significantly, but its effect on s_w' and g_w' is small. In fact, g_w' is little affected and it was not possible to show it in Fig. 10. Unlike those of nozzles, f_w'', s_w' and g_w' are reduced as $(v_e/u_e)_i$ increases. It is observed that g_w' is little affected by the dissipation parameter $(u_e{}^2/h_e)_i$, whereas in the case of nozzles the effect is very significant. It is also seen that s_w' and g_w' are more affected by the cone angle λ as compared to f_w''. As observed for nozzles, f_w'', s_w' and g_w' for nonswirling flows (i.e., $\alpha = 0$, $(v_e/u_e)_i = 0$) in diffusers are nearly same as those of swirling flows with $(v_e/u_e)_i = 1$. We have compared our results (see Figs. 9–10) with those obtained by the local similarity, local nonsimilarity and momentum integral methods, and we have found that they are in good agreement with those of the local nonsimilarity (three-equation model) and momentum integral methods except near the outlet, but that they differ appreciably from the local similarity results except near the inlet. In fact, the difference is much more pronounced compared to that of nozzles. Therefore, the local similarity method is not suitable for swirling nozzle or diffuser flows.

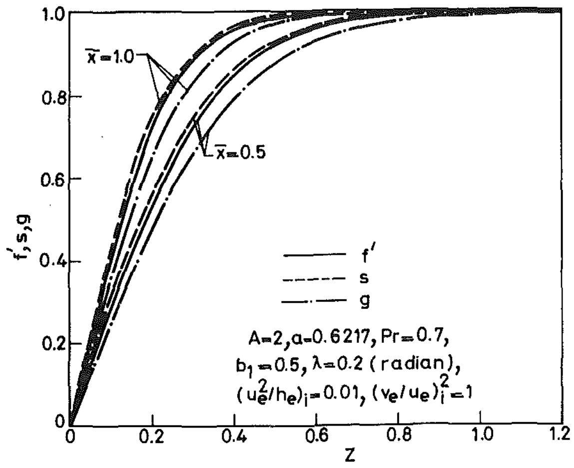

Fig. 8 Velocity and temperature profiles (diffuser)

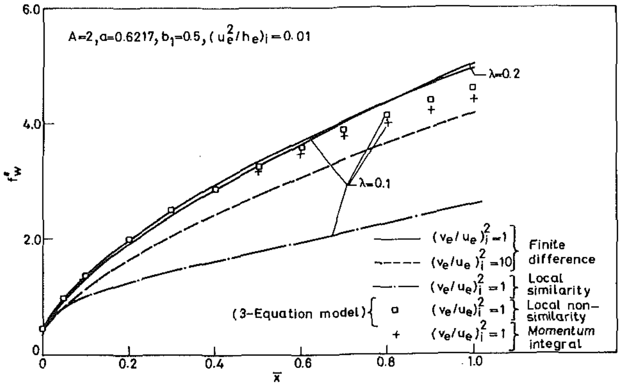

Fig. 9 Variation of longitudinal skin friction with $\bar{x}$ (diffuser)

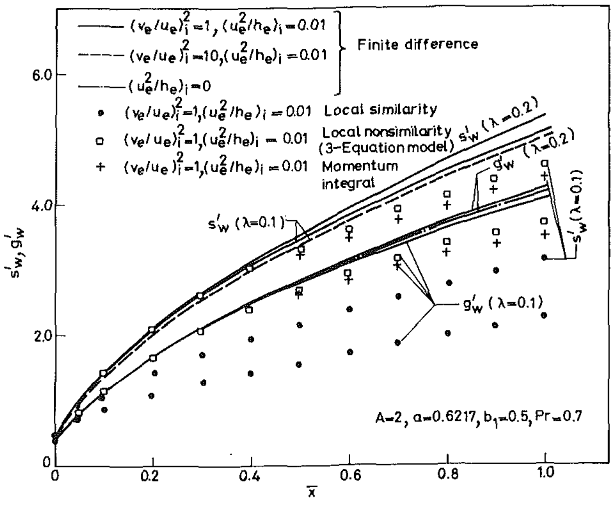

Fig. 10 Variation of tangential skin friction and heat transfer with $\bar{x}$ (diffuser)

Conclusions

Both for nozzles and diffusers, swirl exerts a strong influence on the longitudinal skin friction, but its effect on the tangential skin friction and heat transfer is comparatively small. It has also been found that the effect of small swirl on the skin friction and heat transfer is minor and that large swirl is required to produce strong influence. In the case of the nozzle, even for a small value of the dissipation parameter at the inlet, the heat transfer rapidly increases near the end of the nozzle, whereas in the case of the diffuser no such trend is observed. For the nozzle, the longitudinal skin friction is more than the tangential skin friction, but for the diffuser the reverse is true. Suction increases the skin friction and heat transfer, whereas injection does the reverse. The separation in the diffuser can be prevented by applying suction. The results are found to be in good agreement with those of the local nonsimilarity and momentum integral methods except near the end of the nozzle or diffuser, but they differ appreciably from those of the local similarity method except near the inlet.

Acknowledgment

One of the authors (G.N.) would like to thank the Council for International Exchange of Scholars, Washington, for the award of a fellowship, and the Ohio State University for providing the facilities. The author is also grateful to Professors O. R. Burggraf, M. R. Foster and other members of the Department of Aeronautical and Astronautical Engineering for useful discussion.

References

1 Lewellen, W. S., "A Review of Confined Vortex Flows," NASA CR-1772, 1971.

2 Taylor, G. I., "The Boundary Layer in the Converging Nozzle of a Swirl Atomizer," *Quart. J. Mech. Appl. Math.*, Vol. 3, No. 2, June 1950, pp. 129–139.

3 So, K. L., "Vortex Phenomena in a Conical Diffuser," *AIAA Journal*, Vol. 5, No. 6, June 1967, pp. 1072–1078.

4 Binnie, A. M., Harris, D. P., "The Application of Boundary Layer Theory to Swirling Liquid Flow Through a Nozzle," *Quart. J. Mech. Appl. Math.*, Vol. 3, No. 1, March 1950, pp. 89–106.

5 Wilks, G., "Swirling Flow Through a Convergent Funnel," *J. Fluid Mech.*, Vol. 34, Dec. 1968, pp. 575–593.

6 Houlihan, T. M., Hornstra, D. J., "Boundary Layer Velocity Profiles in a Swirling Convergent Flow Field," *J. Fluid Mech.*, Vol. 52, No. 2, March 1972, pp. 357–367.

7 Hall, M. G., "Vortex Breakdown," *Annual Review of Fluid Mechanics*, Vol. 4, Annual Reviews Inc., 1972, pp. 195–218.

8 Sovran, G., Klomp, E., "Experimentally Determined Optimum Geometries for Rectilinear Diffusers with Rectangular, Conical or Annular Cross Section," *Fluid Mechanics of Internal Flow*, ed., G. Sovran, Elsevier Publishing Company, Amsterdam, 1967, pp. 270–319.

9 McDonald, A. T., Fox, R. W., Van Dewolstine, R. V., "Effects of Swirling Inlet Flow on Pressure Recovery in Conical Diffusers," AIAA Paper No. 71-84, 1971, pp. 1–9.

10 Schlichting, H., Gersten, K., "Calculation of the Flow in Rotationally Symmetric Diffusers with the Aid of Boundary Layer Theory," *Z. Flugwiss.*, Vol. 9, No. 1, Jan. 1961, pp. 135–140.

11 Marvin, J. G., Sheaffer, Y. S., "A Method for Solving Nonsimilar Laminar Boundary Layer Equations Including Foreign Gas Injection," NASA Tech. Note—5516, 1969.

12 Vimala, C. S., Nath, G., "Unsteady Laminar Boundary Layers in Compressible Stagnation Flow," *J. Fluid Mech.*, Vol. 70, No. 3, Aug. 1975, pp. 561–572.

13 Dewey, C. F. Jr., Gross, J. F., "Exact Similar Solutions of the Laminar Boundary Layer Equations," *Advances in Heat Transfer*, Vol. 4, Academic Press, New York, 1967, pp. 317–446.

14 Sparrow, E. M., Quack, H., Boerner, C. J., "Local Nonsimilarity Boundary Layer Solutions," *AIAA Journal*, Vol. 8, No. 11, Nov. 1970, pp. 1936–1942.

15 Sparrow, E. M., Yu, H. S., "Nonsimilarity Thermal Boundary Layer Solutions, ASME JOURNAL OF HEAT TRANSFER, Vol. 93, No. 4, Nov. 1971, pp. 328–334.

16 Ames, W. F., *Numerical Methods for Partial Differential Equations*, Thomas Nelson, London, 1969, p. 32.

17 Varga, R. S., *Matrix Iterative Analysis*, Prentice-Hall, Englewood Cliffs, N. J., 1962, pp. 194–197.

18. Massier, P. F., "Heat Transfer by Convergent-Divergent Nozzles from Ionized Argon," *Jet Propulsion Laboratory Space Programme Summary* No. 37-24, Vol. IV, 1963, pp. 105–108.

H. R. Velkoff
Department of Mechanical Engineering,
The Ohio State University,
Columbus, Ohio 43210
Mem. ASME

R. Godfrey
Owens Corning Fiberglas Technical Center,
Granville, Ohio

Low-Velocity Heat Transfer to a Flat Plate in The Presence of a Corona Discharge in Air[1]

A study was conducted to determine the enhancement in convection heat transfer that could be achieved using the corona wind over a range of stream velocities. A heated flat plate mounted in a flow channel was placed in a Mach-Zehnder interferometer. Corona wires were placed above the active plate surface. Data were taken over a range of stream velocities. The results showed the expected large increase in heat transfer at low velocities and that this gain in heat transfer decreased to zero at high stream velocities.

Background

Enhanced heat transfer by the application of an applied electrostatic field has often been demonstrated. Increases in heat and mass transfer due to the actions of a corona discharge have been shown for condensation and frost formation and in free and forced convection. These actions have taken place in still air or nearly still air [1–12]. Industrial applications have centered on heating and cooling industrial parts in manufacturing processes, flame spraying, or in baking bread. Experimental efforts have been centered largely on the electrostatic-free convection interaction. Industrial uses likewise have centered on low-velocity processes.

The fivefold increase in heat transfer found with electrostatic-free convection in air is uniquely related to the fluid mechanics involved in the interaction [1, 2]. This mechanism is described briefly as follows. Consider a sharp, pointed electrode aimed at a flat plate. If a high voltage is applied between the point and the plate, at high enough voltages an electrostatic corona will form around the point. The air near the point will become ionized and these ions will be unipolar. The electrical field created by the applied voltage will drive these ions toward the plate. In their transit they will collide with the neutral air molecules and cause a streaming of the air. In air at atmospheric conditions, this electric wind can reach velocities of the order of 2 m/s. This slight wind created by the corona discharge can be used as any other air jet of the same velocity. If the electric wind is directed at a heated surface located in still air, the result will be more rapid cooling. The heat transfer increases as the free convection is changed to forced convection.

By analogy, the electric wind can be used to enhance mass transfer, and this has been demonstrated in freezing and condensation processes if the transport to the surface is the rate limiting step [8, 11]. Thus, one can see that the electrostatic action in air of a corona point is generally that of substituting an electrostatic air pump for a fluid mechanic air pump. Although a case might be made for the change in the fluid properties due to the charged specie within the zone of corona wind, the concentration of the charge is so small relative to the neutrals, of the order of one ion to 10^{10} neutrals, that any change in average physical properties, thermal conductivity or viscosity, should be very small. Prior experimental and analytical studies have indicated that the changes to free convection and frost formation can be explained quite closely on the basis of fluid mechanics rather than changes to physical properties [1, 2, 3, 6, 11]. The effects of temperature on the electrical properties is discussed in the Appendix.

In addition to "free-convection" interactions, studies have been made of electrostatic actions within channel flow. Tests of laminar flows of gases in round and flat channels have revealed large increases in friction factor [5] and increased heat-transfer coefficients. To account for these increased values, possible mechanisms have been studied extensively, and it has been concluded that the actions were due to electrostatically induced secondary flows that caused mass mixing of the low and high-velocity regions in the channel [12]. These secondary flows are directly related to the pressure gradients generated by the corona discharge electric wind. In the channel flow tests, it was found that the increases in friction factor and heat transfer vanished as the velocity increased and the flow became fully turbulent.

Because of the increases found in the "free-convection" region of heat and mass transfer, and in the low-velocity, forced-convection channel flow, it was considered logical to investigate the corona wind interactions with an ordinary flat-plate boundary layer and the associated heat transfer. This paper addresses a study of the possible existence, nature, and range of corona interactions with a flat-plate boundary layer.

Experimental Investigation

A Mach-Zehnder interferometer was used to measure the effect of a corona discharge on the heat transfer from a heated plate. The plate

---

[1] This work was conducted under sponsorship of the U.S. Army Research Office, Durham, North Carolina.

Contributed by the Heat Transfer Division and presented at the Winter Annual Meeting, New York, New York, December 5–10, 1976 of THE AMERICAN SOCIETY OF MECHICAL ENGINEERS. Manuscript received by the Heat Transfer Division, April 15, 1977. Paper No. 76-WA/HT-47.

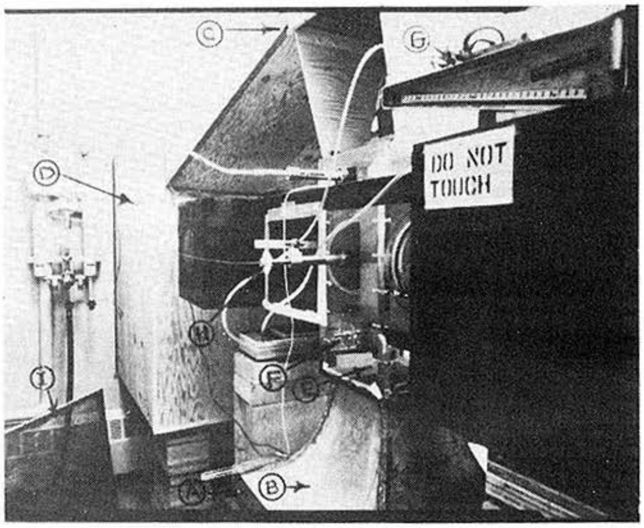

Fig. 1(*a*) Experimental arrangement. (*a*) Overall view of flow channel and interferometer (A) settling chamber, (B) nozzle, (C) hinged diffuser walls, (D) acoustic isolation chamber, (E) nylon cord, (F) pitot-static tube, (G) inclined manometer, (H) free-stream thermocouple, and (I) damping screen

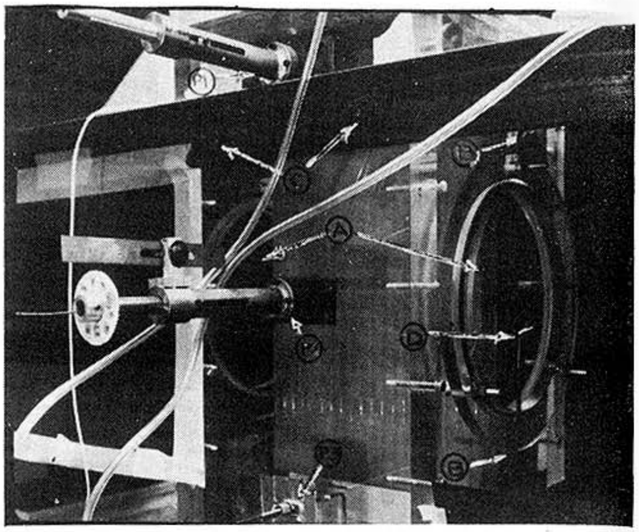

Fig. 1(*b*) Test section (A) optical flats, (B) plate supports, (C) vertical axis adjustment, (D) reference length "*T*"; P1, P2, and P3 are pressure tap locations

was mounted in a channel and air was passed over the plate [13]. The overall arrangement is shown in Figs. 1(*a*) and 1(*b*).

A flow channel is mounted so that the working test section is located in the active leg of the interferometer. Air flowed into the channel through a large area (50.8 × 76.2 cm) entry. This entry contained 14 × 18 mesh screens in the settling chamber. The flow then passed through a 9:1 contraction to the 20.3 × 25.4 cm cross section of the test section. The air flowed vertically upward through the test section and over the heated plate. The air then entered a diffuser, passed through turning vanes, entered an acoustic isolation settling chamber, and then was exhausted outside the building by two blowers. The acoustic chamber was incorporated to minimize the disturbances to the flow and heat transfer caused by the upstream propagation of pulsations caused by the blowers.

The heated plate was mounted in the center of the test section in a vertical position with the leading edge facing down. The air flow was directed up the plate as shown in Fig. 2. With this arrangement the upward streaming due to free convection would be in the same direction as the primary stream to minimize stream mixing effects. A grid of 0.0006 in. (0.0152 cm) stainless steel corona wires was stretched parallel to the plate surface and aligned with the fluid stream (Fig. 2). To minimize flow disturbance, a bayonet beam was mounted in the large entry plenum. The corona wires were attached at their lower ends to this bayonet. At their upper ends, the wires were mounted to a beam placed across the exit of the cross section. The alignment of

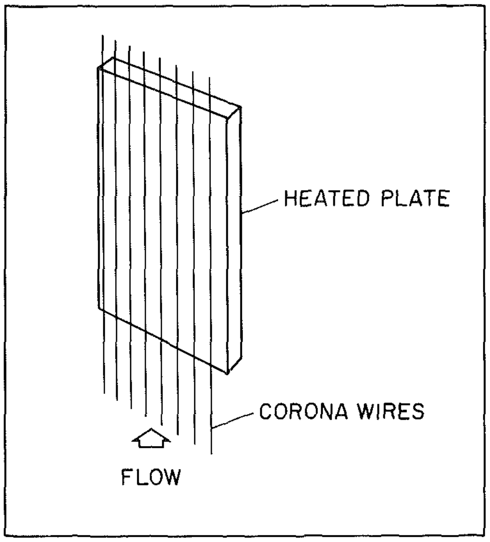

Fig. 2 Test plate with corona wires

Nomenclature

A = cross-sectional area
a = constant in equation for viscosity
b = constant in equation for thermal conductivity
C = constant in corona current equation
C_v = specific heat at constant volume
E = electrical field strength
G_z = Graetz Number along z
h = heat transfer coefficient
K = thermal conductivity
k = ion mobility
m = mass of a gas molecule
Nu = Nusselt number, hz/K
n = number of molecules per unit volume
p = pressure
T = temperature
T_w = plate temperature
T_∞ = ambient temperature
V = voltage
V_0 = cut-in voltage
v = velocity perpendicular to plane of corona wires
w = flow velocity along plate
W_∞ = flow velocity in free stream
$W_{f\max}$ = maximum volume of free convection velocity
y = distance perpendicular to plate
z = distance along the plate (measured from the front edge)
δ = boundary layer thickness
δ' = distance-subtangent to wall along y
ϵ = dielectric constant
η = Blasius distance transform, $-(y/z)(G_z/4)^{1/4}$
λ = mean free path of a molecule
μ = viscosity
ρ = density of air
ρ_c = electric charge density

the wires and their horizontal spacing from the plate could be adjusted by means of traversing screws located at the upper and lower beams. All grid wires were put into tension, and the uniformity of tension was noted by the pitch of the sound when each wire was plucked.

When the corona discharge takes place, a streaming of the air results from each corona wire. When the parallel streams impinge on the plate and form rolls along the surface of the plate the spacing of the rolls is directly related to the spacing of the wires. This action has been shown previously [1, 4]. In the case when the wire spacing is close, it is possible for the pressure field generated to cause fluid instability and the resulting fluid motion can also lead to enhanced heat transfer. In these tests the wire spacing was wide enough that it could be expected that individual corona wind streams could result. If a horizontal mounting of the wires had been used, it would have been possible to observe the effects on the temperature field of the individual corona wind streams. This had been done in previous work where the separate actions of the corona streams on the thermal field were clearly shown [1]. When electric wind would be initiated the free convection would change to forced convection, and the "rolls" would change their character completely making the interpretation of data difficult. To minimize the difficulty in interpretating the results as the flow field changed from free convection to forced convection the wires were placed in a vertical position.

Grid current was supplied by a Sorensen 5038-4 high-voltage source. Current from the source was measured on the high-voltage side by a Westinghouse-type PX-161 micro-ammeter contained within a plexiglas box. A neon bulb protection circuit was placed in series with the meter to guard the meter against damage from sparking. The grid voltage was measured by a Singer model SEH electrostatic voltmeter. The wire-wire and grid-plate spacings used in these tests were 0.50 and 0.25 in. (1.27 and 0.635 cm), respectively.

The heated test plate was made of aluminum, 19 in. long and 9-7/8 in. wide (48.3 cm × 25.1 cm). The top surface was flat within ±0.005 in. (0.0127 cm) overall with a sand-blasted finish. The leading edge had a $\frac{1}{8}$ in. (0.3175 cm) radius tangent to both the top surface and the 30 deg slope of the bottom cover plate. Twenty-five iron-constantan thermocouples were potted in drilled holes on the bottom surface of the top plate in rows of five with Sauerisen electric heater cement.

The heating element was made of nichrome alloy wire, with a resistance of 5.3 Ω/ft. The heater contained eight separate 46.4 Ω circuits, giving a total heater flux of 1100 W at 80 V R.M.S. over an area of one square foot per side. The plate temperature was monitored by a Leeds-Northrup millivolt potentiometer using an ice bath for reference.

Side rails fitted to the bottom cover plate were slotted to allow adjustment of the plate so it could be viewed at different positions up to 14 in. (35.6 cm) from the leading edge.

The optics of the Mach-Zehnder interferometer were modified for the channel flow arrangement. In the vertical side walls of the test section, optical flats were mounted to provide a smooth closed surface for the flow, and also provide a precise undistorted path for the light beam into and out of the test chamber. To compensate for these optical flats in the test chamber, two 1 in. (2.6 cm) optical flats were incorporated in the reference leg of the interferometer. Useful fringe patterns were achieved by readjusting the flats and the corona mirrors. The light source was a Baird Atomic D-9 interference filter with a peak wavelength for the green line of mercury of 5460 Å and a tolerance of +15, −0 Å.

A Speed Graphic camera fitted with a Polaroid 4 × 5 film holder was used in conjunction with a shutter to form a camera. Polaroid 200 speed film was exposed at $\frac{1}{25}$ shutter speed.

The stream velocity was determined by making pitot-static measurements. For low velocities, the pressure difference was measured using a traversing microscope to read a micromanometer. At higher velocities, a 0 to 3 in. (0 to 7.6 cm) inclined manometer was used.

Test Procedure

The following procedure was used throughout the tests to obtain the greatest accuracy. The plate was positioned so that the region of interest was in view, and the plate was parallel to the test section walls. Parallelism was checked with a depth gauge micrometer at three points on the plate using the front wall of the test section as a reference. When the three points were within 0.005 in. (0.0127 cm), parallelism was considered accomplished.

A similar procedure was used to locate the wire plane parallel to the plate. Using the plate surface as a reference, the beams were adjusted until the four grid-plate spacings were within one grid wire diameter of each other.

A glass probe was moved up to the plate surface. The camera was positioned so that the object plane coincided with the center of the plate to reduce refraction error. The fringes were focused at the object plane. The test section was then rotated about its vertical axis until the probe appeared just to touch the plate at its tip. The displacement fringes were made perpendicular to the plate by adjusting the mirror.

The flow was adjusted to give the desired rate. The plate was then heated and the heaters adjusted so that the surface temperature was uniform within 1°F. At high free-stream velocities, the surface temperature varied ±1.5°F across the plate from side to side. Since the heater circuits ran from side to side, no adjustment could be made to reduce this 3 deg maximum cross plate temperature variance. When steady-state temperature was reached, a no-current picture was taken. Grid voltage was then adjusted until the desired grid current was obtained. If the plate temperature varied, it was adjusted to no-current conditions. After steady-state had been reached with the current on, all thermocouples were read and recorded at each test condition as well as stream velocity and temperature. Barometric pressure and wet and dry bulb temperatures were taken at the beginning of each test.

Evaluation of Interferograms

Temperature profiles were obtained by careful measurement of fringe displacement. To accomplish this, the following procedure was used. A reference length T located in the interferogram was measured with a machinist rule. Since the actual length of the cross bar of the T was known, the photomagnification could be determined. The interferogram was placed on the stage of a Gaertner comparator traversing microscope.

The technique used to evaluate the interferograms consisted of scribing a line tangent to the linear portion of the fringe. The crosshairs of the comparator were moved along the line and the intersections of the line with the fringes recorded. The temperature corresponding to each fringe was calculated by comparing conditions in the test section with known conditions in the reference leg [13–15]. The results were checked with photographs taken by Kennard and were found to agree within 1°F.

A free convection test was run and the temperature profile determined by this method. The results are shown in Fig. 3, where the Pohlhausen solution is shown for reference. The correlation is considered to be good, and deviation appears only in the region very close to the plate where it is difficult to interpret the fringes.

Evaluation of Test Apparatus

To present the test results effectively, the data were reduced to dimensionless form. The quantities in the dimensionless group $(T - T_\infty)/(T_w - T_\infty)$ were determined as follows: $T - T_\infty$ was calculated by the measurements of the interferograms; T_w was determined from an average thermocouple reading in the region of interest; and T_∞ was taken to be room temperature as read on a mercury bulb thermometer. A thermocouple placed in the stream was found to give erratic readings. The quantity $\eta = \eta(W_\infty, z, y)$ was calculated for the two positions investigated (z = 7 and 8 in.). The term W_∞ was determined from a pitot-static reading in the main stream ahead of the plate. To account for the area reduction caused by the plate, a pressure profile was taken at the test site and compared with concurrent readings ahead of the plate. The velocity corresponding to the flat portion of the curves was taken as W_∞. The kinematic viscosity ν was evaluated at the mean temperature $(T_w + T_\infty)/2$; z was measured from the leading edge.

Local Nusselt numbers were calculated from the temperature profiles as follows (15). Nusselt number is defined as $N_u = hz/k$, where

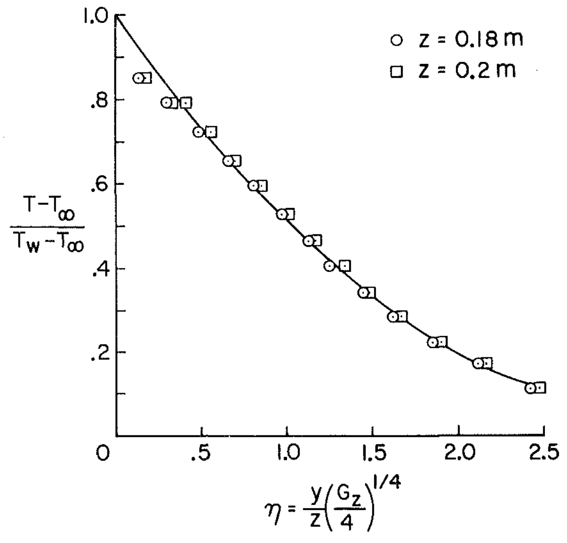

Fig. 3 Experimental points for the free-convection test plotted against Pohlhausen's solution

z is a characteristic dimension (for the plate, the distance from the leading edge), h is the local film heat transfer coefficient at the surface defined as $(k/\Delta T)(dT/dy)|_w$. The temperature gradient $(dT/dy)_w$ on the surface can be determined from the temperature profile. The subtangent to this profile, denoted by δ^1, is $\Delta T/(dT/dy)_w$. Substituting δ^1, the Nusselt number is simply the ratio of two lengths, z/δ^1, where z is predetermined for any case chosen and δ^1 can be obtained from the temperature profile.

The accuracy of this method of determining the Nusselt number depends on the accuracy with which the tangent can be drawn on the temperature profile. The subtangent to the test profiles was constructed assuming a linear profile from 70° to 80°F ΔT.

The maximum velocity in a free convective boundary layer ($W_{f\max}$) was calculated by assuming that the maximum value of $W/2\sqrt{gz}\sqrt{T_\infty/(T_w - T_\infty)}$ was 0.275, as shown by Schlichting [16]. For $\Delta T = 80°\text{F}$, $W_{f\max}$ was 0.925 and 0.988 ft/s (28.2 and 30.1 cm/s) at 7 and 8 in. (17.8 and 20.3 cm) from the leading edge, respectively.

The flow conditions in the test section were determined by running pitot-static traverses across the channel. A typical result is shown in Fig. 4. It can be seen that the flow in the mainstream is quite uniform at the test site (7 in. or 17.8 cm from the leading edge of the plate).

To further check the operation of the entire test assembly, runs were made with no applied voltage but at several flow velocities. The no-corona profiles were plotted against the Blasius solution for a laminar boundary layer in forced convection. Typical results are shown in Figs. 5 and 6. A plot of $\log_{10}[1 - (T - T_\infty)/(T_w - T_\infty)]$ versus $\log_{10}(y/\delta)$ for a turbulent boundary layer should have a slope of 1/7 [17]. Such a plot was made for the 15.4 and 19.1 m/s tests. Their slopes ranged from 1/4.8 to 1/6.0. It appeared that the boundary layer was in transition from laminar to turbulent in this velocity range. This trend can also be noted in Figs. 5 and 6, where the profiles become fuller at larger velocities as one would expect when the boundary layer becomes turbulent.

Experimental Results with Current

After the channel flow velocity had been set and the plate temperature stabilized, the voltage would be applied and increased until the desired corona current was reached. After the plate temperatures had stabilized, a picture of the fringe pattern was taken. The temperature profiles that resulted from the application of the voltage and the consequent corona current are shown in Figs. 7–10.

The data are presented at various values of corona current because for a given wire configuration current is directly related to the pressure rise generated by the electric wind. Typically

$$\Delta p = J/k$$

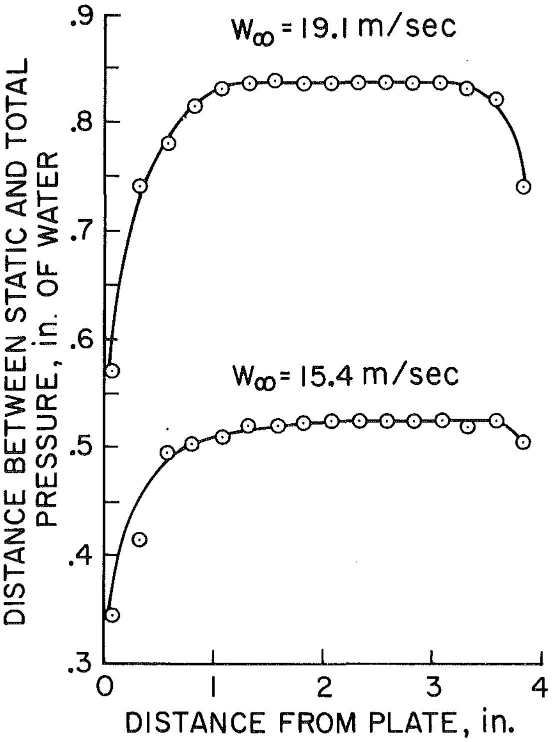

Fig. 4 Pitot-static pressure profile at test site

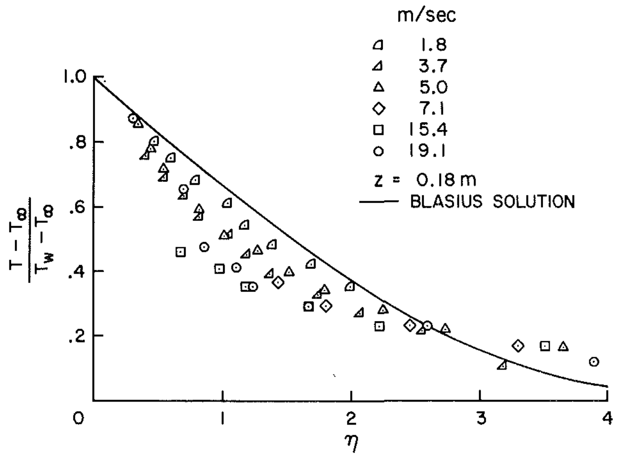

Fig. 5 Experimental temperature profiles plotted against the Blasius solution

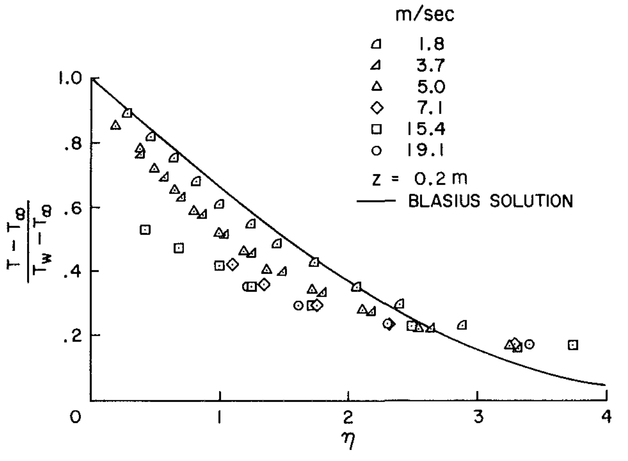

Fig. 6 Experimental temperature profiles plotted against the Blasius solution

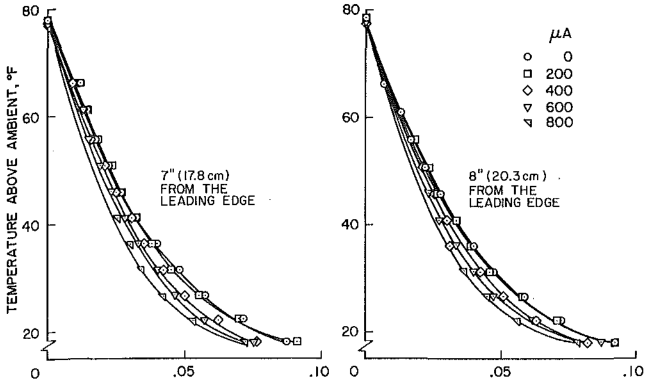

Fig. 7 Effects of corona discharge on the temperature profile. Free-stream velocity, 16.3 ft/s (5.0 m/s), grid-plate spacing, 0.236 in. (0.60 cm), wire-wire spacing, 0.5 in. (1.27 cm)

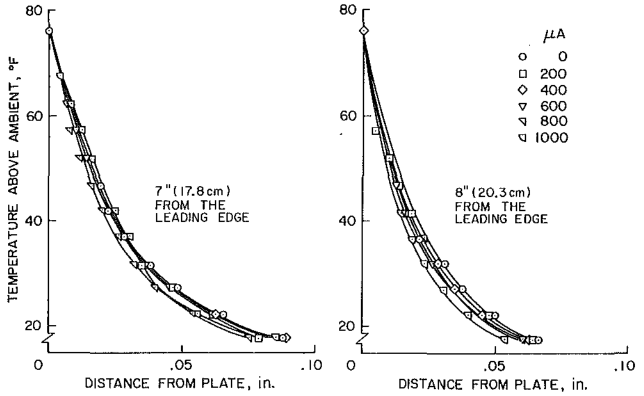

Fig. 8 Effects of corona discharge on the temperature profile. Free-stream velocity, 23.4 ft/s (7.1 m/s), grid-plate spacing, 0.236 in. (0.60 cm), wire-wire spacing, 0.5 in. (1.27 cm)

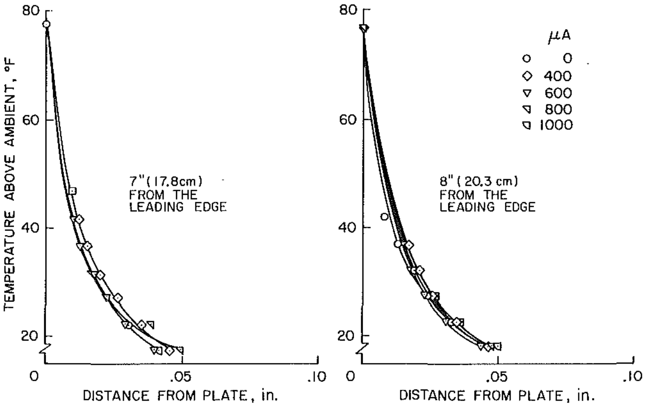

Fig. 9 Effects of corona discharge on the temperature profile. Free-stream velocity, 50.6 ft/s (15.4 m/s), grid-plate spacing, 0.236 in. (0.60 cm), wire-wire spacing, 0.5 in. (1.27 cm)

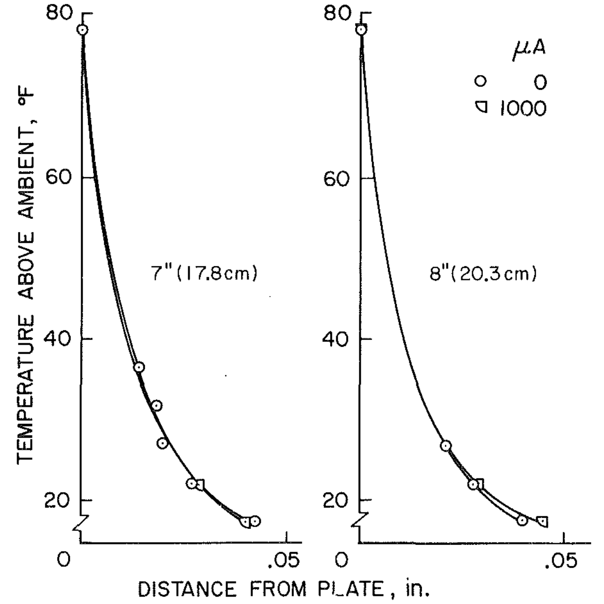

Fig. 10 Effects of corona discharge on the temperature profile. Free-stream velocity, 62.5 ft/s (19.1 m/s), grid-plate spacing, 0.236 in. (0.60 cm), wire-wire spacing, 0.5 in. (1.27 cm)

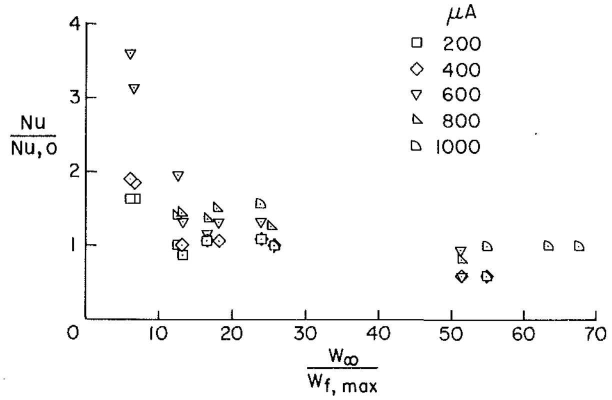

Fig. 11 Dimensionless plot showing the effect of corona discharge at various free-stream velocities; $W_{f\max}$ is the maximum free convective velocity at the same ΔT, subscript 0 indicates no current condition.

where J is current density and k is ion mobility. If voltage is used, it is necessary to obtain the cut-in voltage under each test condition. Atmospheric changes affect the cut-in voltage, V_0. The common corona relationship is

$$i = CV(V - V_0)$$

where i is current, C is a constant and V is voltage. The choice of using V and V_0, or using current is somewhat arbitrary, but since the fluid interaction is driven by the pressure and the pressure is a direct function of current, current has been used. In past experiments no actions could be discerned until a current was measured no matter what the voltage was [2].

Examination of the figures shows that, at the lowest velocities, the slope of the temperature profile becomes more steep as the corona current is increased. Such a steepening of the temperature profile implies an increased heat transfer coefficient. Also note that, as the stream velocity increases, the differences in the temperature profiles tend to disappear.

These findings are more graphically portrayed in Fig. 11, where the ratio of the Nusselt number with corona to the Nusselt number without current is plotted. The abscissa is the ratio of stream velocity to the peak velocity of a free convection profile at the same ΔT (plate to freestream temperature difference). This figure indicates that, at very low stream velocities, the heat transfer is doubled, but at high stream velocities, the effect of the corona on heat transfer disappears. The magnitude of the velocities involved can be seen by recalling that $W_{f\max}$ was 0.925 ft/s and 0.988 ft/s (28.2 and 20.1 cm/s) for z = 7 and 8 in. (17.8 and 20.3 cm), respectively.

To check the accuracy of the conclusion that the effects of corona disappeared at higher velocities, an additional test was run at 62.5 ft/s

(19.1 m/s). The plate temperature was recorded before high voltage was applied. Then a voltage was applied so that a corona current of 1000 μA was indicated. No changes were made in the power being supplied to the plate. The setup was left undisturbed for 30 min. The plate temperature was again recorded and was found to be identical to that taken before the voltage was applied. The heat balance was unaffected by the corona discharge. It can be concluded that the ratio of Nusselt numbers before and after the voltage was applied is one.

To further aid in the interpretation of the results, the temperatures for a velocity of 5.9 ft/s (1.8 m/s) are plotted against the Blasius boundary-layer distance parameter in Fig. 12. The profiles with corona current are fuller than the no current case and heat transfer is increased greatly by corona at this low velocity. If one now examines Fig. 5, where the no-current velocity profiles are plotted at various stream velocities, it can be seen that the profiles with corona at the lower velocity, 5.9 ft/s (1.8 m/s), resemble the higher velocity no-current profiles as they tend to become turbulent.

Thus, the interpretation of Figs. 11 and 12 lends credence to the concept that the action of the corona is to promote mixing of the boundary-layer flow and the free-stream in a manner somewhat analogous to turbulent flow. This result supports the conclusions drawn from extensive tests of the electrostatically induced changes in channel flow of gases [11]. In those tests it was deduced that electrostatically induced secondary flows caused the low and high-velocity fluids to mix in the channel with a subsequent increase in the friction factor and heat-transfer coefficient.

Conclusions

The study has indicated that the enhanced heat transfer found in the past with corona wind-free convection also exists at low air velocities over a flat heated plate. The increases found were of the same order of magnitude as those found with free convection so long as the stream velocity was no more than an order of magnitude larger than the characteristic free convection velocity. At higher stream velocities, the increase in heat transfer was found to lessen until enhancement no longer existed. This result is in agreement with the concept that the increases in heat transfer result directly from the electric wind induced by a corona discharge [21]. Since the characteristic velocity of the electric wind is low, it can be expected that the region of application of electrostatically enhanced heat transfer due to corona discharge in gases will exist under conditions where the stream velocity is of the order of the corona-wind velocity or less.

APPENDIX

Concern is sometimes expressed over the mechanisms involved in the electric field actions on heat transfer in gases, particularly about property variations. If significant fluid property variations were induced by the ion wind or the E field, then the assumption that the effect on heat transfer was due to the electric wind induced by the corona could be questioned. In the case of liquids, dielectric effects could exist as well as charge effects. With gases the dielectric influence usually is small. The effects on viscosity and thermal conductivity of the air caused by the corona discharge should be small. There are about 10^{10} neutrals per ion in the electric wind near the plate. The influence of these energetic particles on the net transport properties, μ (viscosity) and K (thermal conductivity) is small. If we look at $\mu = anmu\,\lambda$ and $K = bnmu\lambda C_v$ then if a change in μ or K were to occur with $n_{\text{ion}}/n_{\text{neutral}} = 10^{-10}$, then the product $(u\lambda)$ would have to be of the order of 10^{10}. This is just not possible since u, the velocity of the particle, is of the order 10^4 to 10^5 cm/s between collisions and the mean free path, λ, is of the order of 10^{-6} cm.

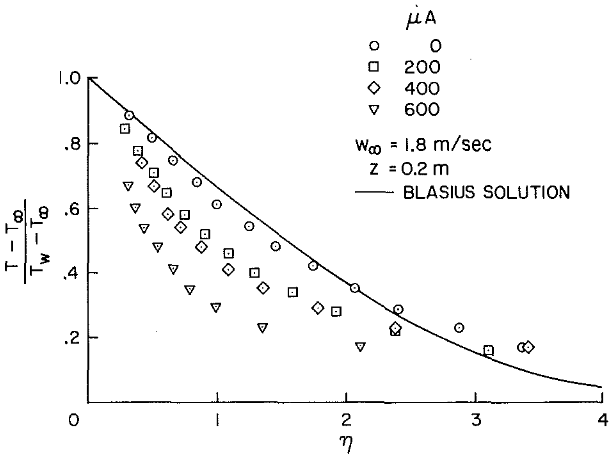

Fig. 12 Temperature profiles for different corona currents.

The electrical properties that could be affected by temperature variations include the dielectric constant and the conductivity. If one uses a typical expression for the variation of dielectric constant [18],

$$(\epsilon - 1)_T/(\epsilon - 1)_{20} = (1 + 0.003411\,(T - 20))^{-1}$$

for an average mean temperature increase of 17°C (30°F) found in the tests, the dielectric constant would decrease by about 10 percent.

The influence of temperature on the electrical conductivity of ionized air arises through the change in density. The product ρk is constant where ρ is density and k is ion mobility [19, 20]. Thus $k \infty \frac{1}{T}$ for constant pressure and it can be seen that the mobility is directly proportional to temperature. Electrical conductivity can be written as

$$\sigma = \rho_c k$$

where ρ_c is charge density. It can be shown that for the parallel wire geometry that $\rho_c \propto (i/\mathrm{k})^{1/2}$ and hence that $\sigma \propto (\epsilon k)^{1/2}$. For a change in temperature of 17°C (30°F) the change in conductivity would be less than 1 percent.

The impact of changes in dielectric constant on the electric wind process and hence on heat transfer should be small. Though electrostatic pressure rise can be written as $\frac{1}{2}\,\epsilon E^2$, it is more relevent to consider the pressure rise due to electric wind in the form

$$\Delta p = {}^{i}/kA$$

where A in the area of the plate under the wires. A temperature increase of 17°C (30°F) would result in a reduction in pressure rise of about 6 percent due to the increase in mobility.

From these considerations it can be expected that the temperature effects of the electric wind processes will be small, and hence should not affect the results and conclusions of the body of the paper.

References

1 Velkoff, H. R., "Electrofluidmechanics, Investigation of the Effects of Electrostatic Fields on Heat Transfer and Boundary Layers," ASD-TDR-62-650, Aeronautical System Division, Air Force Systems Command WPAFB, OH, 1962.

2 Velkoff, H. R., and Marco, S. M., "Effect of Electrostatic Fields on Free-Convection Heat Transfer from Flat Plates," ASME Paper 62-HT-9, ASME-AICHE Joint Meeting on Heat Transfer, Boston, Mass., Aug. 1963.

3 O'Brien, R. J. and Shine, A. J., "Some Effects of an Electric Field on Heat Transfer from a Vertical Plate on Free Convection," ASME JOURNAL OF HEAT TRANSFER, Vol. 84, No. 1, Feb. 1967.

4 Franke, M. E., "Effect of Vortices Induced by Corona Discharge on Free Convection Heat Transfer from a Vertical Plate," ASME JOURNAL OF HEAT TRANSFER, Vol. 89, Aug. 1969, pp. 427–433.

5 Velkoff, H. R., "The Effects of Ionization on the Flow and Heat Transfer of a Dense Gas in a Transverse Electrical Field," *Heat Transfer and Fluid Mechanics Institute Proceedings,* Stanford University Press, Palo Alto, Calif., 1964.

6 Chuang, T. and Velkoff, H., "Analytical Studies of the Effects of Ionization on Fluid Flows," The Ohio State University Research Foundation Rep. RF-1864-6, Columbus, OH, June 1967.

7 Reynolds, B. L. and Holmes, R. E., "Heat Transfer Between a Finned Tube and Air in the Presence of a Corona Discharge," WA/HT-18, Winter Annual Meeting, ASME, N.Y., N.Y., Dec. 1975.

8 Velkoff, H. R. and Miller, J., "Condensation of Vapor on a Vertical Plate with a Transverse Electrostatic Field," ASME JOURNAL OF HEAT TRANSFER, Vol. 87, May 1965.

9 Choi, H. Y., "Electrohydrodynamic Condensation Heat Transfer," ASME

JOURNAL OF HEAT TRANSFER, Vol. 90, Feb. 1968.

10 Holmes, R. E. and Chapman, A. J., "Condensation of Freon-114 in the Presence of a Strong Non-Uniform Alternating Electric Field," ASME Paper 70-HT-6, June 1970.

11 Chuang, T. H. and Velkoff, H. R., "Forst Formation in a Non-Uniform Electric Field," Sixty-Third Annual Meeting, AICHE, Chicago, Ill., Dec. 1970.

12 Velkoff, H. R., Pejack, E. J., and Chuang, T. H., "Electrostatically Induced Secondary Flows in a Channel," Sixty-Ninth National Meeting, AICHE, Cincinnati, OH, May 1971.

13 Godfrey, R. and Velkoff, H. R., "An Interferometric Study of the Effects of Corona Discharge on the Temperature Profiles on a Flat, Uniform Temperature Plate in Forced Convection," The Ohio State University Research Foundation Rep. RF-1864-7, Columbus, OH, Aug. 1967.

14 Kennard, R. B., "An Optical Method for Measuring Temperature Distribution and Convective Heat Transfer," *Bureau of Standards Journal of Research,* Vol. 8, 1932.

15 Eckert, E. R. G. and Soehngen, E. E., "Studies on Heat Transfer in Laminar Free Convection with the Mach-Zehnder Interferometer," AF-TN 5747, U.S. Air Force Wright-Patterson AFB, OH.

16 Schlichting, H., *Boundary-Layer Theory,* McGraw-Hill, New York, N.Y., 1963.

17 Eckert, E. R. G., *Introduction to the Transfer of Heat and Mass,* McGraw-Hill, New York, N.Y., 1950.

18 *C.R.C. Handbook of Chemistry and Physics,* 49th Edition, C.R.C. Cleveland, OH. page E61, 1969.

19 Lawton, J. and Weinberg, F., *Electrical Aspects of Combustion,* Clarendon Press, Oxford, England, 1969.

20 Cobine, J. D., *Gaseous Conductors,* Dover Publications, New York, N.Y., 1958.

21 Yabe, A., Mori, Y., Hiyakata, "EHD Study of the Corona Wind between Wire and Plate Electrodes," *AIAA Journal,* Vol. 16, No. 4, April 1978, pp. 340–345.

Jiin-Iang Lee

Assistant Environmental Scientist, Energy and
Environmental Systems Division,
Argonne National Laboratory,
Argonne, Ill. 60439

Potential Weather Modification Caused by Waste Heat Release from Large Dry Cooling Towers

A numerical model of a cooling tower plume is employed to study the possible atmospheric effects of thermal plumes from natural draft dry cooling towers. Calculations are performed for both single and multiple towers, each of which can dissipate the waste heat from a nominal 1000 MWe power generating unit, and the results are compared with those for wet cooling towers associated with plants of the same generating capacity. Dry cooling tower plumes are found to have a higher potential for inducing convective clouds than wet cooling tower plumes, under most summertime meteorological conditions. This is due to the fact that both the sensible heat and momentum fluxes from a dry tower in summer are approximately one order of magnitude larger than those from a wet cooling tower.

Introduction

The availability of water supplies for cooling towers in much of the Southwestern and Western United States may be uncertain in the coming decades, according to a study by Peterson and Sonnichsen [1]. Consequently, large dry cooling towers may become viable cooling alternatives for power plants in these areas. The rising cost of cooling water coupled with increasing plant capabilities may make dry cooling towers attractive economic alternatives elsewhere as well.

In the many theoretical and observational studies that have been published about the atmospheric impacts of cooling tower operations [2, 3, 4, 5], it is frequently stated that dry cooling towers will have little environmental impact. Some authors even believe that the airborne heat release may have the beneficial effect of increased ventilation in inversion-prone areas [6]. However, under certain atmospheric conditions favorable to natural cloud formation, the buoyancy and momentum fluxes resulting from the dry cooling tower thermal effluent could initiate convective clouds or even induce large scale convective storms [2, 6, 7]. The water vapor in a dry cooling tower plume is convected from the relatively rich moisture content of the lower layer air mass surrounding the tower. This vapor condenses to form clouds and thus enhances the convective penetration through latent heat release. Koenig, et al. [8] found that heat released in sensible form is more likely to induce cloudiness and associated phenomena than heat released in latent form, assuming the same energy release spread over the same area.

This article examines the potential formation of convective clouds by thermal effluent from large natural draft dry cooling towers, based on state of the art tower design and performance data. Thus, the form and magnitude of the perturbations can be properly specified. A numerical model of a cooling tower plume, previously used to study the atmospheric effects of wet cooling tower effluents at power parks [9], is employed to simulate the possible induced cloud convection caused by the operation of a large dry cooling tower. For purposes of comparison, a parallel simulation is also performed for a wet cooling tower plume associated with the same plant capacity assumed for the dry tower.

Boyack and Kearney [10] have concluded that plumes from large dry cooling towers are not likely to produce large clouds, or clouds that cause substantial precipitation. While these statements are qualitatively true, one should be cautious in extrapolating them to general conclusions, since Boyack and Kearney's results are drawn from only 12 atmospheric soundings at three stations in the central United States. No attempt is made here to assess the general behavior of dry cooling tower plumes or to reassess Boyack and Kearney's conclusions, since the atmospheric effects of cooling tower plumes are site-specific, and require a study based on a considerable amount of climatological data. Instead, attention is focused on the points that have not been addressed, particularly the differences in induced cloud convections between dry and wet cooling tower plumes.

Model Description

The dynamics of plume convection are described by the so-called "shallow convection" equations for a quasi-incompressible fluid. The Boussinesq approximation is used to describe a steady-state buoyant plume. The system is set into axisymmetric coordinates natural to the bent-over plume with linearized perturbation equations derived

---

Contributed by the Heat Transfer Division for publication in the JOURNAL OF HEAT TRANSFER. Manuscript received by the Heat Transfer Division January 6, 1978.

from the first law of thermodynamics and the laws governing change of momentum and conservation of mass. With the assumption of similarity profiles for plume variables, the approximate equations of motion are obtained through integration over the radial direction. The perturbed pressure field is neglected; instead, a form drag term is included in the momentum equation. The change in momentum is caused by buoyancy force, entrainment, and form drag. The entrainment assumption used in the model is similar to that given by Morton, Taylor, and Turner [11] and to that used by Briggs [12]. The nonadiabatic energy source or sink in the first law of thermodynamics includes heat gained or lost due to phase changes of water and entrainment. The microphysical processes are simplified by Kessler's parameterization approach [13]. The detailed description and validation of the model have been reported previously [9].

The droplet spectra used in this study are those measured by Auer [14] in an induced cumulus cloud observed over a petroleum refinery in Wood River, Illinois. As these droplet spectra[1] pertain to an observed nonprecipitating cloud, the fallout of rainwater, Q_h, is essentially negligible and is not included in these calculations.

Cooling Tower Description

Unlike evaporative wet cooling tower systems, dry cooling is accomplished through a series of finned-tube heat exchangers. Since the air and water are not in direct contact as in wet cooling towers, the heat transfer is sensible in nature rather than evaporative. Dry cooling system performance is therefore dependent upon the ambient dry bulb air temperature, whereas evaporative systems are wet-bulb-temperature dependent.

In this study it is assumed that a single, natural-draft dry cooling tower is designed to dissipate 2227 MW of waste heat at a 24°C ambient temperature from a nominal 1000 MWe generating unit. The design conditions and tower dimensions are those used by Kearney and Boyack [6]. The tower has an exit diameter of 134 m and a height of 217 m.

The heat rejection rate and MWe output are determined according to the off-design performance curves given by Boyack and Kearney [10]. At a 32.2°C ambient temperature, the power output is approximately 940 MWe and the heat rejection rate is approximately 2300 MW.

For comparison, a nominal 940 MWe unit equipped with a natural draft wet cooling tower based on 32.2 °C design dry bulb and 23.9°C wet bulb temperature (a typical design condition in the Eastern U.S.) also is evaluated. The tower is 162 m high and has an exit diameter of 94 m. The off-design performance of the wet cooling tower is calculated by the method suggested by Winiarski, et al. [15].

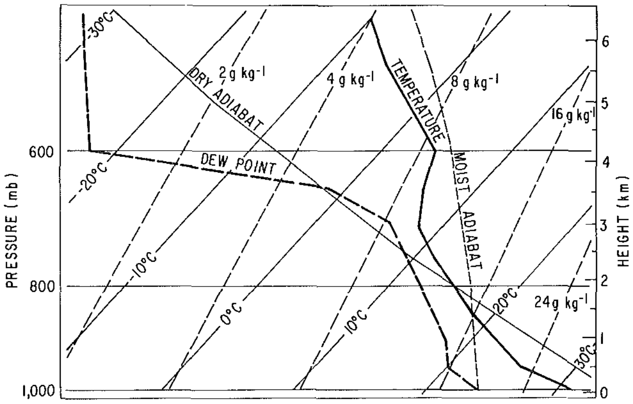

Fig. 1 Basic sounding for 0000 GMT August 24, 1960, Shreveport, Louisiana

Table 1 Average sounding for 0000 GMT July, Shreveport, Louisiana

Pressure mb	Height m	Temp. °C	R.H. percent	Wind Speed m/s	Wind Dir. deg
1004	0	31.8	54.7	4.5	161
950	489	26.7	61.1	4.3	168
900	957	22.7	67.4	4.4	181
850	1446	19.0	68.9	4.8	210
800	1959	15.9	62.0	5.2	236
750	2498	12.6	56.2	5.5	254
700	3069	9.2	50.0	5.7	282
600	4319	2.0	40.8	6.2	307
500	5757	−6.1	32.3	6.9	309

Numerical Experiments

The main objective of this article is to compare, through numerical simulation, the relative abilities to induce cloud convection of dry and wet cooling tower plumes. A meteorological candidate for this simulation is an atmospheric condition with convective instability;[2] thus an unstable convective cloud can be generated. The sounding for 0000 GMT August 24, 1960, taken at the Shreveport, Louisiana, National Weather Service station (as shown in Fig. 1) qualifies for use in the simulation. The wind was reported from the south-southeast at 5 m/s changing to northerly at 2 m/s at the 850 mb pressure level, then shifting to westerly at 650 mb with a speed of 6 m/s, and then veering back to northerly at the 450 mb level with a speed of 3 m/s. Theoretically, selecting one atmospheric sounding of this type (potentially unstable condition) is adequate. However, this might represent one extreme that rarely occurs. To obtain a result more typical of a summertime average, an average atmospheric sounding for the month of July, taken at the same station, was used for general comparison purposes and is listed in Table 1. The sounding was obtained by averaging soundings at fixed pressure levels taken at 0000 GMT for the month of July for a period of five years.

Cooling tower effluent conditions for both sounding cases are listed in Table 2. The exit relative humidities for dry cooling tower plumes are calculated by assuming that the exit air has the same moisture content as the ambient air, while the wet cooling tower plumes are assumed saturated.

Results of the simulation show that the energy released in the form of sensible heat from a single dry cooling tower of the proposed size could easily induce convective activity and form cumulus clouds reaching 3700 m in height for the case of the August 24, 1960 sounding. On the other hand, a saturated vapor plume from a single wet cooling tower associated with the same plant capacity would become unsaturated immediately after leaving the tower and decay rapidly,

---

[1] Using equation (12), [9], we obtain $\alpha = 2.769$ and $\gamma = 1.494$.

---

[2] The term convective instability (or potential instability) refers to the stability of a layer or column of air after the layer has been lifted to saturation. Accordingly, regardless of its initial temperature lapse rate, if a layer is unstable after lifting to saturation, it is said to be potentially unstable. The criterion for a potentially unstable air mass is its wet-bulb potential temperature decreasing with elevation.

Nomenclature

T_0 = ambient temperature
w = vertical velocity
ρ = density of the plume
g = gravitational acceleration
q' = specific humidity perturbation
Q_h = rainwater
T' = temperature excess
b = cloud radius
F_b = buoyancy flux
F_m = momentum flux

Table 2 Cooling tower effluent conditions

	Dry Tower	Wet Tower
1) 0000 GMT August 24, 1960 Sounding		
Exit Temperature, °C	46.2	38.6
Exit Velocity, m/s	5.2	3.2
Exit Relative Humidity, percent	30	100
2) Average July Sounding	Dry Tower	Wet Tower
Exit Temperature, °C	46.6	38.2
Exit Velocity, m/s	5.2	3.1
Exit Relative Humidity, percent	27	100

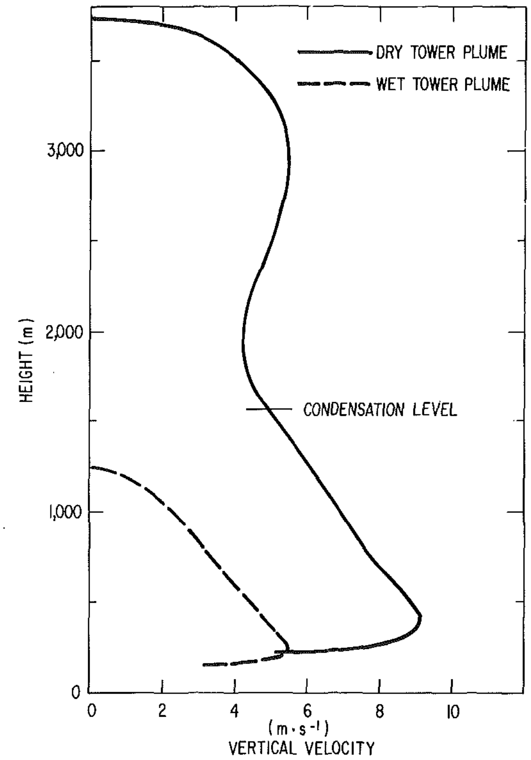

Fig. 2 Variation of vertical velocity with height, August 24, 1960 sounding

reaching a height of only 1200 m for the same sounding condition. The behavior of this thermal plume from a dry tower is discussed in detail below. Values of all plume parameters calculated by the model represent the mean at a given height.

The rate of sensible heat release from the dry tower in this case is approximately 2290 MW. At the top of the tower, this buoyant plume has already gained a significant momentum (an exit velocity of 5.2 m/s with a temperature excess of 14.7°C above the ambient temperature). As the plume leaves the top of the tower, it continues to gain momentum through the acceleration caused by the buoyancy force in the unstable atmospheric layer and reaches a maximum vertical velocity of 9.1 m/s at about 400 m (957 mb). Thereafter, the plume enters a slightly stable layer and the vertical velocity decreases. As the plume continues to rise, it cools rapidly through entrainment and adiabatic expansion. Finally, it reaches a temperature slightly below that of the ambient air (approximately 0.37°C below), and saturates at 1567 m in height; condensation begins, and the cloud forms.

The warming of the cloud resulting from the latent heat of condensation reactivates the ability of cloud penetration. Vertical velocity reaches a second peak of 5.4 m/s at a height of about 3040 m. Finally, the cloud enters a dry and stable layer, and stops at a height of 3700 m. The cloud is about 950 m in radius near the top. Fig. 2 shows the variations of vertical velocity with height of this convective plume from the dry cooling tower; for comparison, predictions for the wet cooling tower plume also are shown. Fig. 3 shows the predicted temperature excesses as functions of height for both dry and wet cooling tower plumes. The maximum total liquid water content is about 2.08 g/kg. This value would usually be associated with moderate cumulus clouds observed in nature.

Using the cooling tower performance data, the different behaviors of both cooling tower plumes, under the condition used in this study, will be compared. At an ambient temperature of 31.7°C, a dry cooling tower will dissipate 2290 MW of waste heat at only 940 MWe generating capacity, while a wet cooling tower operating at the same rate capacity rejects only 1760 MW of waste heat, 23 percent less than the dry tower does. Only 10.6 percent (187 MW) of the reject heat from a wet cooling tower is in sensible form. From the effluent condition listed in Table 2, it can be seen that the initial sensible heat flux of a dry tower plume is approximately 11 times larger than that of a wet tower plume, and the initial momentum flux of the dry tower plume (6.79×10^5 kg·m/s^2) is more than eight times greater than that of a wet tower plume (8.23×10^4 kg·m/s^2). Figs. 4 and 5 show the variation

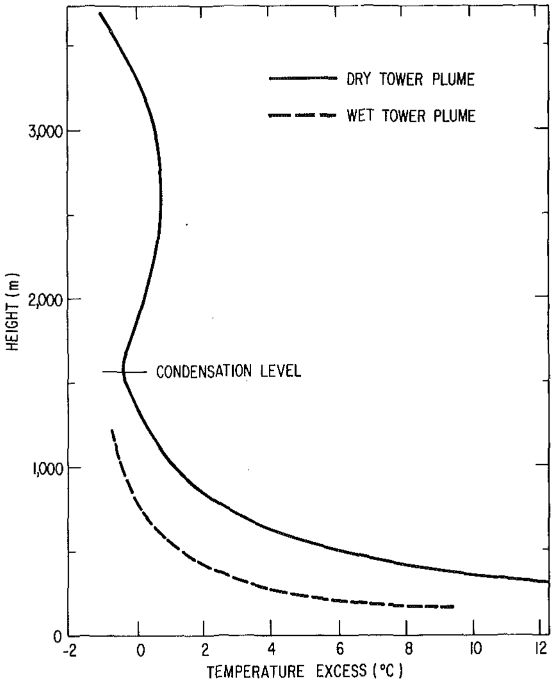

Fig. 3 Variation of temperature excess with height, August 24, 1960 sounding

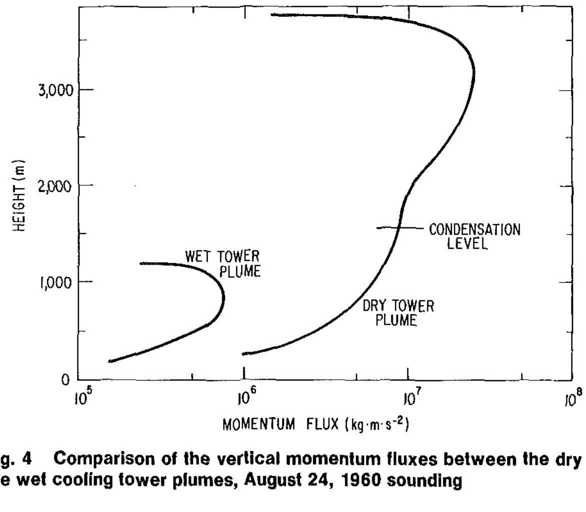

Fig. 4 Comparison of the vertical momentum fluxes between the dry and the wet cooling tower plumes, August 24, 1960 sounding

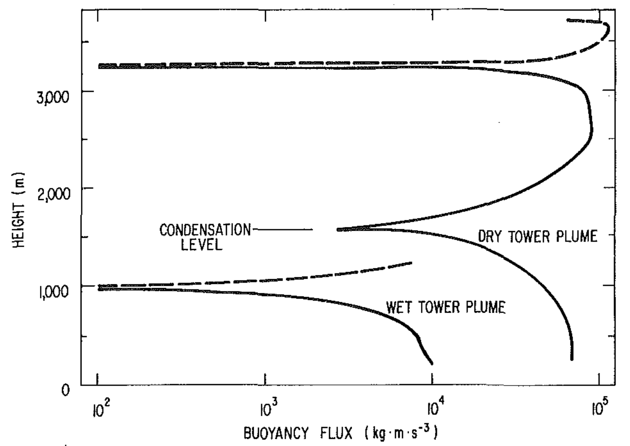

Fig. 5 Comparison of the buoyancy fluxes between the dry and the wet cooling tower plumes, August 24, 1960 sounding

of vertical momentum flux, F_m, and buoyancy flux, F_b, with height for both the dry and the wet cooling tower plumes. These fluxes are defined as:

$$F_m = \pi \rho\, w^2 b^2, \tag{1}$$

and

$$F_b = \pi \rho g b^2\, w \frac{T'}{T_o} (1 + 0.61q') \tag{2}$$

where ρ is the density of the plume, w the vertical velocity, b the cloud radius, g the gravitational acceleration, T' and T_0 the temperature excess and ambient temperature, respectively, and q' the specific humidity perturbation. The buoyancy flux defined above is actually an energy transformation rate, i.e., the rate of transformation from available potential energy to kinetic energy, or vice versa, per unit height of a slice of buoyant plume. In Fig. 5, the negative buoyancy fluxes near the top of the dry and wet plumes are plotted in absolute magnitude (shown as dashed lines). These large differences in vertical momentum and buoyancy fluxes are due to the combination of higher vertical velocity and temperature excess, and larger plume size, for the dry tower plume.

The height of the plume rise is an important factor that determines whether the plume will reach the condensation level and form clouds, and lead to further enhanced convective activity. It is generally true that the larger the magnitude of the perturbation (such as vertical velocity, temperature excess, etc.), the higher the plume rises. However, the difference in behavior between the dry and the wet cooling tower plumes is not a simple function of the type, intensity, and scale of perturbation, and the type of atmospheric structure. Table 3 lists the predicted plume heights and cloud water at various initial radii for both modes of cooling using the same heat rejection rate and, for a given mode of cooling, a fixed initial sensible heat flux and initial volume flow rate at various initial plume sizes. It can be seen that within the scale of the possible design cooling tower sizes, the height of plume rise and the intensity of convection depend on the initial specific buoyancy and momentum, and are not sensitive to the size of the initial impulse in the atmospheric condition used in this work. It should be noted that the insensitivity of the results to the initial radius is true only under the constraints imposed in Table 3. No convective cloud is generated by a wet cooling tower plume if the initial radius is 100 m or less. If the initial radius of perturbation is greater than 100 m, the decrease in the moisture dissipation rate causes the ascending plume to reach saturation before the momentum is completely consumed. Once the condensation takes place, the convection is enhanced through the conversion of latent heat back to sensible heat. The cloud finally grows to a size comparable to that of a cloud generated by the same heat rejection rate in a purely sensible form. This result substantiates those stated by Koenig, et al. [8].

A more general comparison of the relative possibility of generating convective clouds via heat rejection for both modes of cooling tower can be obtained by simulating atmospheric convection from multiple towers clustered in a small area (a possible arrangement in future power parks). The criteria and assumptions for the merger of multiple plumes are given in [9]. A similar approach has been used by Hanna [16]. To see the effect more typical of an average for a given location, an average sounding for the month of July taken at Shreveport, Louisiana, was used as the ambient condition. The sounding and the associated cooling tower effluent conditions are listed in Tables 1 and 2, respectively.

Fig. 6 shows the predicted plume heights as functions of the number of towers in a group, for both dry and wet cooling towers, at three different tower spacings. Again, dry cooling tower plumes are found to be more likely to form cumulus clouds than wet cooling tower plumes, for similar plant capacities. In addition, the larger the tower spacings, the less likely the plumes are to induce convective clouds. However, once the clouds can be generated, the larger the tower spacing, the more intense the resulting convective activity.

Conclusions

It is frequently stated and generally true that dry cooling towers

Table 3 Comparison of plume behavior for two different cooling modes based on same amount of reject heat

	Dry Cooling Mode		Wet Cooling Mode	
Initial Radius m	Plume Height m	Cloud Water g kg^{-1}	Plume Height m	Cloud Water g kg^{-1}
47	3,706	1.75	1,262	No Cloud
83	3,660	1.89	1,262	No Cloud
100	3,653	1.93	1,262	No Cloud
150	3,664	2.01	3,509	1.75
200	3,694	2.01	3,515	1.90
250	3,737	2.01	3,643	1.94

Note: 1 Heat rejection rate = 1758 MW
2 For dry cooling, exit temp. = 44.3°C
exit volume flow = 1.06×10^5 m^3/s,
exit relative humidity = 31.4 percent.
For wet cooling, exit temp. = 38.5°C
exit volume flow = 2.34×10^4 m^3/s,
exit relative humidity = 100 percent.
3 Exit volume flow rate is kept constant for a given mode.

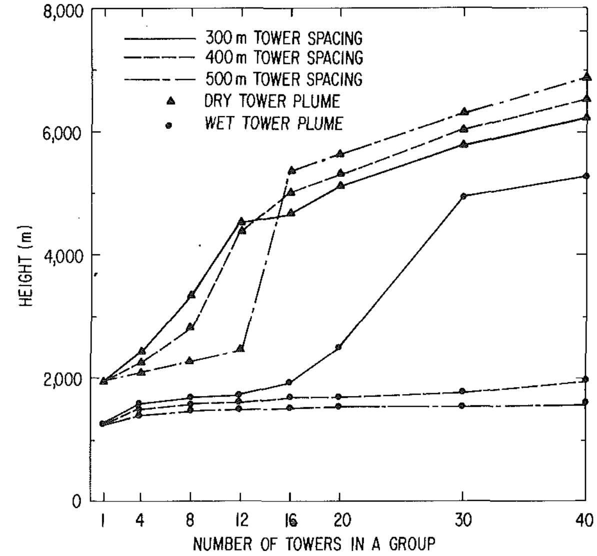

Fig. 6 Comparison of predicted plume heights as functions of tower number in a group between the dry and the wet tower plumes at various tower spacings, average July sounding

will not cause environmental problems such as the fogging, icing, drift deposition, blowdown, long visible plume, or snow augmentation frequently experienced with wet cooling towers. However, under potentially unstable atmospheric conditions and other conditions favorable to natural formation of cumulus convection, a large dry cooling tower has a higher potential for inducing convective clouds than does a wet cooling tower associated with the same generating capacity.

Dry cooling operation with conventional turbines is less efficient than evaporative cooling. Therefore, for a given plant capacity, a dry cooling tower rejects more waste heat than does a wet cooling tower. Furthermore, only about 10 percent of the reject heat from a wet cooling tower is in the sensible heat form on hot summer days. The sensible heat flux from a dry tower is approximately one order of magnitude larger than that of an evaporative wet cooling tower. Consequently, a dry cooling tower plume (also having a larger specific momentum and buoyancy force) has a higher lifting potential, and is more likely to create cumulus clouds or convective storms, given an existing atmospheric convective instability. For present cooling tower sizes, the moisture released from the wet cooling tower in the form of latent heat will usually disperse downwind without causing any atmospheric effects during warm seasons. The latent heat can, in some situations, convert into sensible heat if the wet tower plume condenses; then, the atmospheric effects of the latent heat plume are similar to those of the sensible heat plume in a potentially unstable atmosphere.

Acknowledgments

The author would like to thank J. E. Carson and R. J. Yamartino of Argonne National Laboratory for their critical reading of the manuscript, and D. M. Rote and T. Yamada of Argonne National Laboratory and F. C. Chen of Oak Ridge National Laboratory for their valuable discussions. The author is particularly grateful to the reviewers and the editor, Prof. E. M. Sparrow, whose comments led to major improvements in this article. K. S. Macal of Argonne made the final editorial corrections. The research discussed was partially supported by the U.S. Department of Energy.

References

1 Peterson, D. E., Sonnichsen, J. C., "Assessment of Requirements for Dry Towers," HEDL-TME 76-82, UC-12, Hanford Engineering Development Laboratory, Richland, WA, Sept. 1976.

2 Carson, J. E., "Atmospheric Impacts of Evaporative Cooling Systems," ANL/ES-53, Argonne National Laboratory, Argonne, IL, Oct. 1976.

3 McVehil, G. E., Heikes, K. E., "Cooling Tower Plume Modeling and Drift Measurements, A Review of the State-of-the-Art," *Trans. ASME,* New York, N. Y., 1975.

4 "Environmental Effects of Cooling Towers," Proceedings of a Symposium held at the CERL, Leatherhead, Sarrey, Great Britain, March 27-28, 1973. *Atmospheric Environment,* Vol. 8, No. 4, Apr. 1974, pp. 305-440.

5 "Cooling Tower Environment-1974," ERDA Symposium Series, CONF-740302, NTIS Springfield, VA, 1975, 638 pp.

6 Kearney D. W., Boyack, B. E., "Plume Behavior and Potential Environmental Effects of Large Dry Cooling Towers," *Dry and Wet/Dry Cooling Towers for Power Plants,* ASME JOURNAL OF HEAT TRANSFER, Vol. 6, 1973, pp. 35-48.

7 Rotty, R. M., "Waste Heat Disposal from Nuclear Power Parks," Tech. Memo. ERL ARL-47, National Oceanic and Atmospheric Administration, Sept. 1974.

8 Koenig, L. R., Murray, F. W., Tag, P. M., "Difference in Atmospheric Convection Caused by Waste Energy Rejected in the Forms of Sensible and Latent Heats," *Atmospheric Environment,* Vol. 12, 1978, pp. 1013-1019.

9 Lee, J.-L., "Potential Weather Modification from Cooling Tower Effluents at Conceptual Power Parks," *Atmospheric Environment,* Vol. 11, 1977, pp. 749-759.

10. Boyack, B. E., Kearney, D. W., "Plume Behavior and Potential Environmental Effects of Large Dry Cooling Towers," Gulf-GA-A12346, Gulf General Atomic Co., San Diego, CA, Feb. 1973.

11 Morton, B. R., Taylor, G. I., Turner, J. S., "Turbulent Gravitation Convection from Maintained and Instantaneous Sources," *Proceedings Royal Society of London,* A., Vol. 234, 1956, pp. 1-23.

12 Briggs, G. A., "Plume Rise," USAEC-TID-25075, Springfield, VA, 1969, pp. 28-34.

13 Kessler, E., "On the Distribution and Continuity of Water Substance in Atmospheric Circulations," *Meteorological Monographs,* Vol. 10, No. 32, American Meteorological Society, Nov. 1969, pp. 26-30.

14 Auer, A. H., Jr., "Observations of an Industrial Cumulus," *Journal of Applied Meteorology,* Vol. 15, Apr. 1976, pp. 406-413.

15 Winiarski, L. D., Tichenor, B. A., Byram, K. V., "A Method for Predicting the Performance of Natural Draft Cooling Towers," 16130 GKF 12/70, Environmental Protection Agency, Water Quality Office, Corvallis, OR, Dec. 1970.

16 Hanna, S. R., "Predicted Climatology of Cooling Tower Plumes from Energy Centers," *Journal of Applied Meteorology,* Vol. 16, No. 9, Sept. 1977, pp. 880-887.

journal of heat transfer

technical notes

This section contains shorter technical papers. These shorter papers will be subjected to the same review process as that for full papers.

A Note on Thermal Convection in a Saturated, Heat-Generating Porous Layer

F. A. Kulacki[1] **and R. G. Freeman**[2]

Introduction

Thermal convection in liquid-saturated porous layers with uniform internal energy generation has recently received attention in connection with certain geophysical and engineering heat transfer problems. Some specific problems in these areas include the determination of the post-accident heat removal rates in a heat generating particulate bed saturated with liquid sodium, heat transfer associated with deep storage of radioactive wastes, and heat recovery and loss in geothermal systems.

When viewing the horizontal layer as a model for more complicated heat transfer problems, one is concerned with the conditions required for the onset of convection, the relation between the Nusselt number and the Rayleigh number at the layer boundary, and the details of the convective flow within the layer. In this note, measurements of steady-state heat transfer coefficients are presented for a porous layer with a rigid, insulated lower boundary and a rigid, isothermal upper boundary. From these measurements, the critical Rayleigh number for the onset of convection is determined. We also compare our results for heat transfer to those of Buretta and Berman [1], Sun [2], Hardee and Nilson [3], and Rhee, Dhir and Catton [4], whose papers appear to be the only relevant literature at the present. The interesting feature of our results is that, while our range of Rayleigh numbers is essentially the same as that in [1–4], the Nusselt number versus Rayleigh number relation does not exhibit the discontinuity observed by Buretta and Berman and, in addition, lies close to the lower branch of their correlation over the entire range of Rayleigh number.

Experimental Apparatus

The convection chamber is that used by Kulacki and Emara [5] in a recent study of thermal convection in internally heated liquid layers. This chamber is 25.4 cm × 25.4 cm, and the depth of the porous layer is varied by changing spacers which support the upper surface. Randomly packed glass spheres of either 3 mm or 6 mm dia are used to form the porous layers treated in this study. A dilute solution of aqueous copper sulfate is used as the test fluid, and volumetric energy sources within the fluid are provided by passing 60 Hz alternating current between two copper electrodes in opposing side walls. The upper and lower surfaces of the layer contain thermocouples for the measurement of the overall temperature difference across the layer. A small resistance heater heater is embedded in the lower surface to maintain a zero heat-flux boundary condition. The upper surface comprises a channeled aluminum plate and is covered by a thin layer of Mylar to electrically insulate it from the test fluid. The aluminum plate is maintained at a constant temperature to within ±0.05°C by circulating water from a constant temperature bath. A 5.08 cm thick layer of Styrofoam insulation is provided on all exterior surfaces of the chamber to minimize heat losses. Additional details of the design and construction of the chamber are given by Kulacki and Emara and Freeman [6]. A simplified cross-sectional view of the chamber is presented in Fig. 1.

Steady-state heat transfer measurements have been made by starting each run with an isothermal layer. When the temperature of the lower surface reaches a steady-state value, several measurements of the lower and upper surface temperatures and the power input to the layer are recorded over a 30 min period. Prior to the recording of data in all runs, the resistance heater in the lower surface is adjusted to maintain the desired zero heat-flux boundary condition.

Results and Discussion

The Nusselt Number at the upper surface of the layer is defined in terms of layer depth, L, the area of the upper surface, A, and the overall temperature difference between the upper and lower surfaces, ΔT. Thus

$$\mathrm{Nu} = \frac{\dot{Q}_e L}{k_m A \Delta T} \tag{1}$$

where the mean thermal conductivity of the layer, k_m, is defined in terms of the porosity, ϵ, the thermal conductivity of the fluid, k_f, and the thermal conductivity of the glass matrix, k_g, by

$$k_m = \epsilon k_f + (1 - \epsilon) k_g. \tag{2}$$

The power input to the fluid, $\dot{Q}_e$, is corrected for heat losses through the walls of the chamber. These heat losses are generally small, with

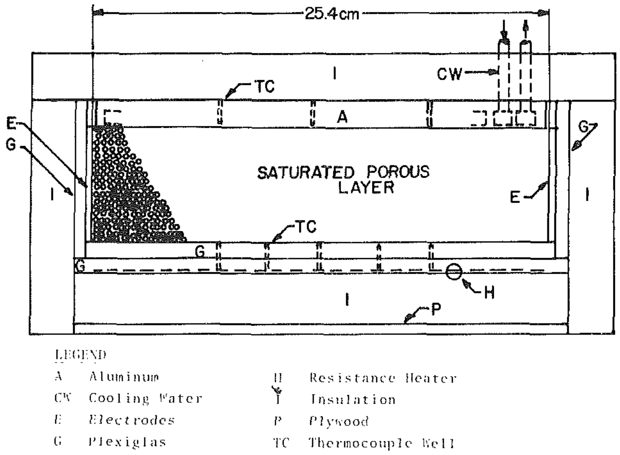

Fig. 1 Detail view of the convection chamber

---

[1] Department of Mechanical Engineering, The Ohio State University, Columbus, OH 43210, Mem. ASME.

[2] Department of Mechanical Engineering, The Ohio State University, Columbus, OH. Present address: Battelle Memorial Institute, Colombus, OH 43201.

Contributed by the Heat Transfer Division for publication in the JOURNAL OF HEAT TRANSFER. Manuscript received by the Heat Transfer Division April 21, 1978.

maximum values at the largest Rayleigh numbers on the order of 3 percent of the power input.

The Rayleigh number is defined in terms of the layer depth and the temperature difference, $HL^2/2k_m$, that would exist in the layer under conduction heat transfer. Thus

$$\mathrm{Ra} = \frac{g\beta L\kappa}{\alpha_m \nu_f}\frac{HL^2}{2k_m}, \tag{3}$$

where the thermal diffusivity, α_m, is defined in terms of k_m and $(\rho c_p)_f$ following Katto and Masuoka [7], and the permeability, κ, is estimated [1, 4] from

$$\kappa = 0.013\, D_h{}^2, \tag{4}$$

where D_h is the hydraulic void diameter. It should be noted that H is the energy generation rate averaged over the layer volume.

Measured maximum temperature differences across the layer as a function of Ra are presented in Fig. 2, the Nusselt numbers computed from these data are presented in Fig. 3.

The Nusselt number has been correlated with the Rayleigh number assuming a relation of the form

$$\mathrm{Nu} = \mathrm{Constant}\ \mathrm{Ra}^m. \tag{5}$$

A linear regression of ln(Nu) on ln(Ra) gives:

$$\mathrm{Nu} = 0.57\ \mathrm{Ra}^{0.35\pm0.03},$$

where

$$40 \le \mathrm{Ra} \le 1400, \quad 0.175 \le L/X \leqslant 0.200, \quad 4.74 \le \mathrm{Pr}_f \le 6.17, \tag{6}$$

and the coefficient of correlation is 0.93 for the fourteen observations. The thermophysical properties of the fluid are evaluated at the integrated mean temperature of the layer assuming a conduction temperature profile for a given energy source strength. The Prandtl number is not included in the correlation because it could not be controlled systematically. Layer depths of 4.45 cm and 5.08 cm have been used in developing equation (6).

If one assumes that the Nu-Ra relation is well established at moderately large values of Ra, then equation (6) can be used to predict the Rayleigh number at the onset of convection, Ra_c, by extrapolation to the conduction limit, Nu = 2. By this method, Ra_c = 36.1, and this value is listed with those obtained by other investigators in Table 1. It may be noted that the several measured values of Ra_c lie within +39 percent of the theoretical estimate based on variational principles given by Buretta and Berman [1]. This kind of agreement is, perhaps, to be expected owing to the difficulties inherent in the determination of the mean thermophysical properties of the saturated layer and the generally sparse data in the vicinity of Ra_c from which extrapolation to the conduction limit is obtained. For these reasons, also, the rather good agreement between the experimental values of Ra_c should be considered fortuitous. Rhee, et al. [4] present a graphical summary of the heat transfer data in the vicinity of the critical Rayleigh number.

Another possible factor that enters into the prediction of Ra_c from extrapolated convection data is the ratio of the conductivities of the fluid and the porous matrix. In all of the studies referenced in Table 1, except that of Rhee, et al. [4], the fluid and the matrix thermal conductivities are on the same order of magnitude. Rhee, et al. argue that for their experiments in which the matrix is inductively heated steel particles and the test fluid is water, the difference in the thermal conductivities of the matrix and the fluid could account for the variation of the measured values of Ra_c. However, no verification of this hypothesis is made by Rhee, et al., nor has any additional information appeared in the literature on this point.

The heat transfer correlation of the present study is compared to those of Buretta and Berman [1], Sun [2], Hardee and Nilson [3], and Rhee, et al. [4] in Fig. 4. Whereas Buretta and Berman have observed a branch in the Nusselt number versus Rayleigh number relation, no such branch is observed in the present study. Instead, our results tend to follow the lower branch of their correlation over the entire range of Ra. The results of the other investigators, however follow the upper branch of Buretta and Berman's correlation.

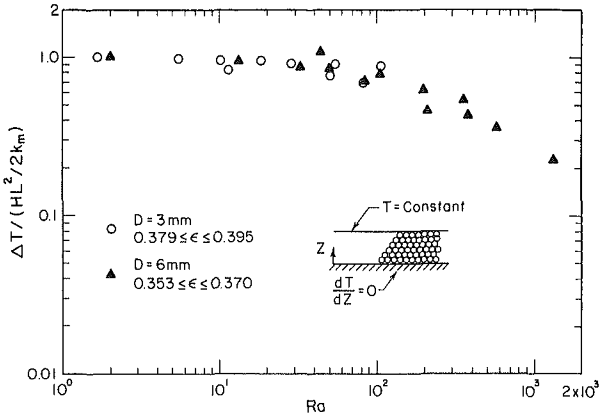

Fig. 2 Maximum temperature difference across the layer in steady convection

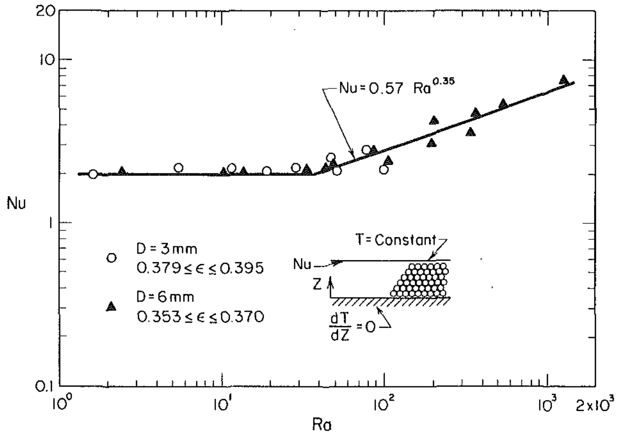

Fig. 3 Steady-state Nusselt numbers

Table 1 Rayleigh numbers for onset of convection

Ra_c	
32.4	Buretta and Berman [1]. Experimental. Lower branch of correlation.
34.9	Buretta and Berman [1]. Experimental. Upper branch of correlation.
32.8	Buretta and Berman [1]. Variational estimate.
43	Sun [2]. Experimental.*
32	Hardee and Nilson [3]. Experimental.
46	Rhee, et al. [4]. Experimental.
36.1	This study.

* This value was obtained by extrapolation of an approximate correlation of Sun's data [4] to the conduction limit. Sun, however, reported that convection was observed to begin at $Ra_c \approx 33$.

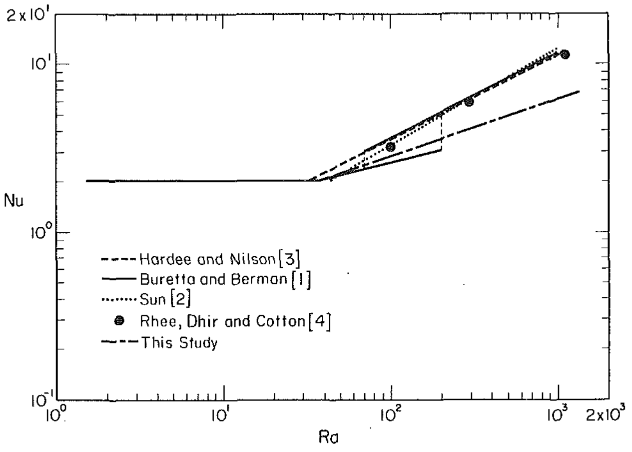

Fig. 4 Comparison of heat transfer results

An explanation for this apparent bifurcated behavior of the Nusselt number versus the Rayleigh number relation is difficult to offer at this time for several reasons. Each of the studies, with the exception of Buretta and Berman's study, does not contain a sufficiently large enough data base to permit a thorough comparison of the results. Ideally such a comparison should be made with full knowledge of the thermophysical properties of the porous matrix in each study, a complete description of the thermal boundary conditions and initial conditions of each study, and a detailed disclosure of the experimental procedures. In addition, it would be desirable to have heat transfer data made available for a wide range of permeabilities and porosities than at present. Such data could be used to statistically determine the effects of these parameters on the correlations. Finally, it would be helpful if data were available over a larger range of Rayleigh numbers. Hopefully such data could verify the lower branch of Buretta and Berman's and our results as being a real global feature of the energy transport process in the layer.

Error Estimates

The uncertainties in the Nusselt number and Rayleigh number are on the order of 7 percent and 9 percent, respectively. The largest portion of these uncertainties is attributed to the uncertainty in the average thermal conductivity of the porous layer (5 percent to 6 percent). This quantity is computed from measured values of the porosity, published values of the thermal conductivity of borosilicate glass [8, 9], and published values of thermal conductivity of water. Direct measurements of the mean thermal conductivity of the layer were not possible with the present apparatus.

Acknowledgment

The support of this work by the Department of Mechanical Engineering and the U.S. Nuclear Commission under Contract AT-(49-24)-0149 is appreciated.

References

1 Buretta, R. J., and Berman, A. S., "Convective Heat Transfer in a Liquid Saturated Porous Layer," ASME *Journal of Applied Mechanics,* Vol. 98, 1976, pp. 249–253.

2 Sun, W. J., "Convection Instability in Superposed Porous and Free Layers," Ph.D. Dissertation, University of Minnesota, 1973.

3 Hardee, H. C., and Nilson, R. H., "Natural Convection in Porous Media with Heat Generation," *Nuclear Science and Engineering,* Vol. 63, 1977, pp. 119–132.

4 Rhee, S. J., Dhir, V. K., and Catton, I., "Natural Convection Heat Transfer in Beds of Inductively Heated Particles," ASME JOURNAL OF HEAT TRANSFER, Vol. 100, 1978, pp. 78–85.

5 Kulacki, F. A., and Emara, A. A., "Steady and Transient Thermal Convection in a Fluid Layer with Uniform Volumetric Energy Sources," *Journal of Fluid Mechanics,* Vol. 83, 1977, pp. 375–395.

6 Freeman, R. G., "Experiments on Natural Convection Heat Transfer in a Porous Layer Saturated with a Heat Generating Fluid," M.Sc. Thesis in Mechanical Engineering, The Ohio State University, 1977.

7 Katto, Y., and Masuoka, T., "Criterion for the Onset of Convective Flow in a Porous Medium," *International Journal of Heat and Mass Transfer,* Vol. 10, 1967, pp. 297–309.

8 Shand, E. D., *Glass Engineering Handbook,* McGraw-Hill, New York, 1958.

9 Morey, G. W., *The Properties of Glass,* Reinhold, New York, 1954.

Numerical Solution of a Flow due to Natural Convection in Horizontal Cylindrical Annulus

M. C. Charrier-Mojtabi[1], A. Mojtabi[1] and J. P. Caltagirone[1]

Nomenclature

r_i, r_o = inner and outer cylinders' radii
$R = r_o/r_i$ = outer to inner cylinders' radius ratio
Ra = Rayleigh number, $\mathrm{Ra} = \rho_o g\beta(T_i - T_o)r_i^3/\mu a$, $\mathrm{Ra}_L = (R - 1)^3\mathrm{Ra}$
T = temperature, $T = (T' - T_o)/(T_i - T_o)$
T_i, T_o = inner and outer cylinders' temperatures
u = radial velocity component, $u = u'r_i/a$
v = tangential velocity component, $v = v'r_i/a$
ρ_0 = reference fluid density
ψ = stream function
ω = vorticity
subscript $'$ denotes real variables

Introduction

Flows due to natural convection between two horizontal coaxial cylinders with constant surface temperatures have been widely studied. Crawford and Lemlich [1] examine the steady two-dimensional flow for a Prandtl number of 0.74 and for radius ratios of 2, 8 and 57. Abbott [2] considers radius ratios close to unity. The numerical model of Powe, Carley and Carruth [3] shows, for $\mathrm{Ra}_L = 6000$, $R = 1.2$ and $\mathrm{Pr} = 0.7$, the existence of secondary phenomena in the form of small rolls turning in the opposite direction of the main cells. Kuehn and Goldstein [4] consider Rayleigh numbers between 100 and 50,000 and several radius ratios and confirm the secondary effects mentioned above. Most authors use an iterative scheme (Gauss Seidel). Recently, Custer and Shaughnessy [5] considered small Prandtl numbers by using a double perturbation expansion in powers of the Grashof and Prandtl numbers.

Numerous experimental data have also been obtained. Lui, et al. [6] show the existence of an oscillatory regime. Bishop, et al. [7] give some additional details on this. For high Rayleigh numbers, Powe, et al. [8] demonstrate the apparition of secondary phenomena, imposed on the stationary two-dimensional flow.

We solved the problem using the implicit alterning direction scheme [9] and the vorticity and stream function formulation, for Rayleigh numbers varying between 100 and 50,000, radius ratios between 1.2 and 5 and Prandtl numbers of either 0.7 and 0.02. In particular, the cases $\mathrm{Ra}_L = 6000$, $R = 1.2$ with $\mathrm{Pr} = 0.7$ and $\mathrm{Pr} = 0.02$ are studied. (For $\mathrm{Pr} = 0.02$, only a perturbation method solution is given in the literature [5, 10].)

Problem Formulation

The governing equations, in dimensionless form, are

$$\nabla^2\psi = -\omega \tag{1}$$

$$\frac{\partial\omega}{\partial t} = \mathrm{Pr}\,\nabla^2\omega + \mathrm{Ra}\,\mathrm{Pr}\left[\sin\phi\,\frac{\partial T}{\partial r} + \frac{\cos\phi}{r}\frac{\partial T}{\partial\phi}\right] - \left[u\,\frac{\partial\omega}{\partial r} + \frac{v}{r}\frac{\partial\omega}{\partial\phi}\right] \tag{2}$$

$$\frac{\partial T}{\partial t} = \nabla^2 T - \frac{1}{r}\left[\frac{\partial\psi}{\partial\phi}\frac{\partial T}{\partial r} - \frac{\partial\psi}{\partial r}\frac{\partial T}{\partial\phi}\right] \tag{3}$$

$$u = r^{-1}\partial\psi/\partial\phi \quad \text{and} \quad v = -\partial\psi/\partial r$$

ϕ is referenced against the descending vertical. The boundary conditions are:

$$r = 1 \qquad \psi = \partial\psi/\partial r = 0, \quad T = 1$$

$$r = R \qquad \psi = \partial\psi/\partial r = 0, \quad T = 0$$

The complete annular cylindrical space is considered, i.e., $\phi\epsilon\ (0.2\pi)$ and, for $\phi = 0$,

$$\psi = 0, \quad \partial T/\partial\phi = 0$$

There are no boundary conditions for the vorticity but, indirectly

$$\left.\begin{matrix} r = 1 \\ r = R \end{matrix}\right\} \quad \omega = -\partial^2\psi/\partial r^2 \tag{4}$$

$$\phi = 0 \quad \omega = 0$$

The local heat transfer is determined by the local Nusselt number $\mathrm{Nu} = (uT - \partial T/\partial r)r\ \mathrm{Log}\ R$.

---

[1] Laboratoire d'Aérothermique du C.N.R.S, 4 ter, route des Gardes, F 92190 Meudon, France

Contributed by the Heat Transfer Division for publication in the JOURNAL OF HEAT TRANSFER. Manuscript received by the Heat Transfer Division July 28, 1978.

An explanation for this apparent bifurcated behavior of the Nusselt number versus the Rayleigh number relation is difficult to offer at this time for several reasons. Each of the studies, with the exception of Buretta and Berman's study, does not contain a sufficiently large enough data base to permit a thorough comparison of the results. Ideally such a comparison should be made with full knowledge of the thermophysical properties of the porous matrix in each study, a complete description of the thermal boundary conditions and initial conditions of each study, and a detailed disclosure of the experimental procedures. In addition, it would be desirable to have heat transfer data made available for a wide range of permeabilities and porosities than at present. Such data could be used to statistically determine the effects of these parameters on the correlations. Finally, it would be helpful if data were available over a larger range of Rayleigh numbers. Hopefully such data could verify the lower branch of Buretta and Berman's and our results as being a real global feature of the energy transport process in the layer.

Error Estimates

The uncertainties in the Nusselt number and Rayleigh number are on the order of 7 percent and 9 percent, respectively. The largest portion of these uncertainties is attributed to the uncertainty in the average thermal conductivity of the porous layer (5 percent to 6 percent). This quantity is computed from measured values of the porosity, published values of the thermal conductivity of borosilicate glass [8, 9], and published values of thermal conductivity of water. Direct measurements of the mean thermal conductivity of the layer were not possible with the present apparatus.

Acknowledgment

The support of this work by the Department of Mechanical Engineering and the U.S. Nuclear Commission under Contract AT-(49-24)-0149 is appreciated.

References

1 Buretta, R. J., and Berman, A. S., "Convective Heat Transfer in a Liquid Saturated Porous Layer," ASME *Journal of Applied Mechanics,* Vol. 98, 1976, pp. 249–253.

2 Sun, W. J., "Convection Instability in Superposed Porous and Free Layers," Ph.D. Dissertation, University of Minnesota, 1973.

3 Hardee, H. C., and Nilson, R. H., "Natural Convection in Porous Media with Heat Generation," *Nuclear Science and Engineering,* Vol. 63, 1977, pp. 119–132.

4 Rhee, S. J., Dhir, V. K., and Catton, I., "Natural Convection Heat Transfer in Beds of Inductively Heated Particles," ASME JOURNAL OF HEAT TRANSFER, Vol. 100, 1978, pp. 78–85.

5 Kulacki, F. A., and Emara, A. A., "Steady and Transient Thermal Convection in a Fluid Layer with Uniform Volumetric Energy Sources," *Journal of Fluid Mechanics,* Vol. 83, 1977, pp. 375–395.

6 Freeman, R. G., "Experiments on Natural Convection Heat Transfer in a Porous Layer Saturated with a Heat Generating Fluid," M.Sc. Thesis in Mechanical Engineering, The Ohio State University, 1977.

7 Katto, Y., and Masuoka, T., "Criterion for the Onset of Convective Flow in a Porous Medium," *International Journal of Heat and Mass Transfer,* Vol. 10, 1967, pp. 297–309.

8 Shand, E. D., *Glass Engineering Handbook,* McGraw-Hill, New York, 1958.

9 Morey, G. W., *The Properties of Glass,* Reinhold, New York, 1954.

Numerical Solution of a Flow due to Natural Convection in Horizontal Cylindrical Annulus

M. C. Charrier-Mojtabi[1], A. Mojtabi[1] and J. P. Caltagirone[1]

Nomenclature

r_i, r_o = inner and outer cylinders' radii
$R = r_o/r_i$ = outer to inner cylinders' radius ratio
Ra = Rayleigh number, $\mathrm{Ra} = \rho_o g\beta(T_i - T_o)r_i^3/\mu a$, $\mathrm{Ra}_L = (R - 1)^3\mathrm{Ra}$
T = temperature, $T = (T' - T_o)/(T_i - T_o)$
T_i, T_o = inner and outer cylinders' temperatures
u = radial velocity component, $u = u'r_i/a$
v = tangential velocity component, $v = v'r_i/a$
ρ_0 = reference fluid density
ψ = stream function
ω = vorticity
subscript $'$ denotes real variables

Introduction

Flows due to natural convection between two horizontal coaxial cylinders with constant surface temperatures have been widely studied. Crawford and Lemlich [1] examine the steady two-dimensional flow for a Prandtl number of 0.74 and for radius ratios of 2, 8 and 57. Abbott [2] considers radius ratios close to unity. The numerical model of Powe, Carley and Carruth [3] shows, for $\mathrm{Ra}_L = 6000$, $R = 1.2$ and $\mathrm{Pr} = 0.7$, the existence of secondary phenomena in the form of small rolls turning in the opposite direction of the main cells. Kuehn and Goldstein [4] consider Rayleigh numbers between 100 and 50,000 and several radius ratios and confirm the secondary effects mentioned above. Most authors use an iterative scheme (Gauss Seidel). Recently, Custer and Shaughnessy [5] considered small Prandtl numbers by using a double perturbation expansion in powers of the Grashof and Prandtl numbers.

Numerous experimental data have also been obtained. Lui, et al. [6] show the existence of an oscillatory regime. Bishop, et al. [7] give some additional details on this. For high Rayleigh numbers, Powe, et al. [8] demonstrate the apparition of secondary phenomena, imposed on the stationary two-dimensional flow.

We solved the problem using the implicit alterning direction scheme [9] and the vorticity and stream function formulation, for Rayleigh numbers varying between 100 and 50,000, radius ratios between 1.2 and 5 and Prandtl numbers of either 0.7 and 0.02. In particular, the cases $\mathrm{Ra}_L = 6000$, $R = 1.2$ with $\mathrm{Pr} = 0.7$ and $\mathrm{Pr} = 0.02$ are studied. (For $\mathrm{Pr} = 0.02$, only a perturbation method solution is given in the literature [5, 10].)

Problem Formulation

The governing equations, in dimensionless form, are

$$\nabla^2\psi = -\omega \tag{1}$$

$$\frac{\partial\omega}{\partial t} = \mathrm{Pr}\,\nabla^2\omega + \mathrm{Ra}\,\mathrm{Pr}\left[\sin\phi\,\frac{\partial T}{\partial r} + \frac{\cos\phi}{r}\frac{\partial T}{\partial\phi}\right] - \left[u\,\frac{\partial\omega}{\partial r} + \frac{v}{r}\frac{\partial\omega}{\partial\phi}\right] \tag{2}$$

$$\frac{\partial T}{\partial t} = \nabla^2 T - \frac{1}{r}\left[\frac{\partial\psi}{\partial\phi}\frac{\partial T}{\partial r} - \frac{\partial\psi}{\partial r}\frac{\partial T}{\partial\phi}\right] \tag{3}$$

$$u = r^{-1}\partial\psi/\partial\phi \quad \text{and} \quad v = -\partial\psi/\partial r$$

ϕ is referenced against the descending vertical. The boundary conditions are:

$$r = 1 \qquad \psi = \partial\psi/\partial r = 0, \quad T = 1$$

$$r = R \qquad \psi = \partial\psi/\partial r = 0, \quad T = 0$$

The complete annular cylindrical space is considered, i.e., $\phi\epsilon\ (0.2\pi)$ and, for $\phi = 0$,

$$\psi = 0, \quad \partial T/\partial\phi = 0$$

There are no boundary conditions for the vorticity but, indirectly

$$\left.\begin{matrix} r = 1 \\ r = R \end{matrix}\right\} \quad \omega = -\partial^2\psi/\partial r^2 \tag{4}$$

$$\phi = 0 \quad \omega = 0$$

The local heat transfer is determined by the local Nusselt number $\mathrm{Nu} = (uT - \partial T/\partial r)r\,\mathrm{Log}\,R$.

---

[1] Laboratoire d'Aérothermique du C.N.R.S, 4 ter, route des Gardes, F 92190 Meudon, France

Contributed by the Heat Transfer Division for publication in the JOURNAL OF HEAT TRANSFER. Manuscript received by the Heat Transfer Division July 28, 1978.

Method of Solution

Equation (1) is modified in order to introduce a fictitious time, ρ,

$$\partial\psi/\partial\rho = \nabla^2\psi + \omega \qquad (1a)$$

Keeping the time dependent terms allows the introduction of the initial conditions naturally and the aquisition of a steady solution without necessarily being concerned with non-stationary behavior.

The finite difference formulation of equations (1a), (2) and (3) is solved using the A.D.I. method. For a given Ra_L, Pr and R, the computation within a time step is as follows: initial temperature and stream function fields are introduced, the vorticity boundary conditions at $r = 1$ and $r = R$ are calculated using the unsteady form of equation (4); equation (2) obtains the vorticity field and equation (1a) does the same for the stream function; then equation (3) is solved to obtain the temperature profile and, finally, the total Nusselt number is calculated. The nonlinear coupled equations (1a), (2), (3) are solved iteratively within the same time step.

On the convergence test we distinguish two different cases:

1) For Pr = 0.7, a convergence test based on the global Nusselt number stops all computations. However, we also calculate

$$\epsilon = \mathrm{Max}\left|\frac{\psi_{i,j}^{n+1} - \psi_{i,j}^{n}}{\psi_{i,j}^{n+1}}\right| \qquad i,j$$

and it remains close to 10^{-6}.

2) For Pr = 0.02 and high Rayleigh numbers, the convergence test based on the global Nusselt number is no longer used. We fix the time step at a size equal or higher than 120 in order to examine the unsteady or oscillatory character of the solution.

The network used is 49 × 49. For low Prandtl numbers (Pr = 0.02), and when we are sure of the flow's symmetry, we used a grid of 49 × 49 for half the annular area for each value of Ra.

Special care is taken to determine the vorticity boundary conditions. Equation (4) is solved using two different schemes. A first order discretization:

$$\omega(0) = \frac{-2}{h^2}\psi(h) + \sigma(h)$$

and a second order discretization:

$$\omega(0) = -\frac{8\psi(h) - \psi(2h)}{2h^2} + \sigma(h^2)$$

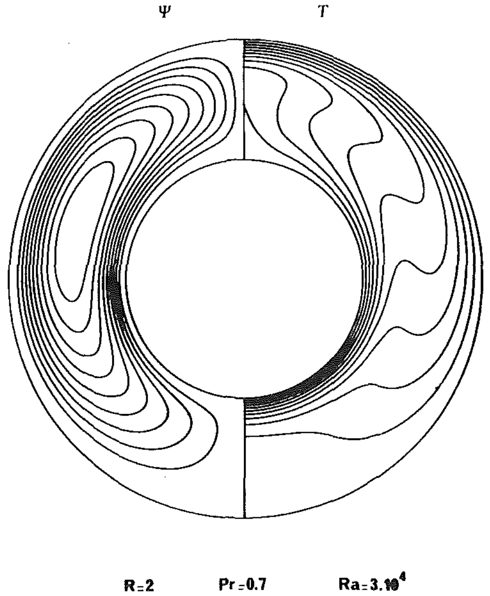

Fig. 1 Streamlines and isotherms for R = 2, Pr = 0.7, Ra = 3.10^4

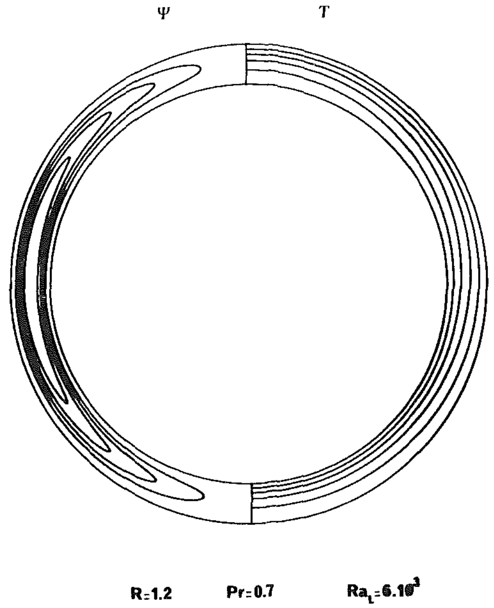

Fig. 2 Streamlines and isotherms for R = 1.2, Pr = 0.7, Ra_L = 6000

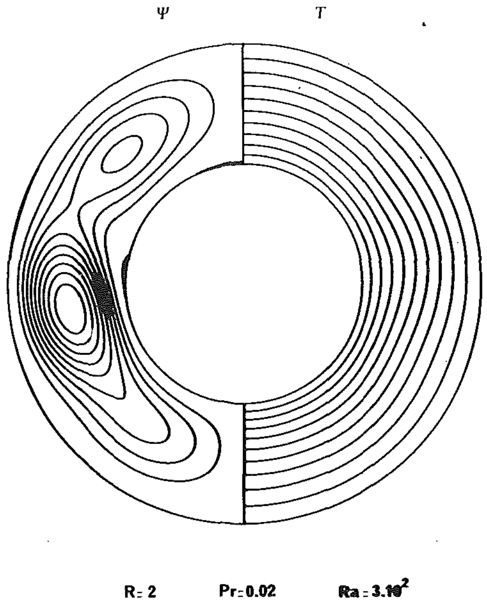

Fig. 3 Streamlines and isotherms for R = 2, Pr = 0.02, Ra = 300

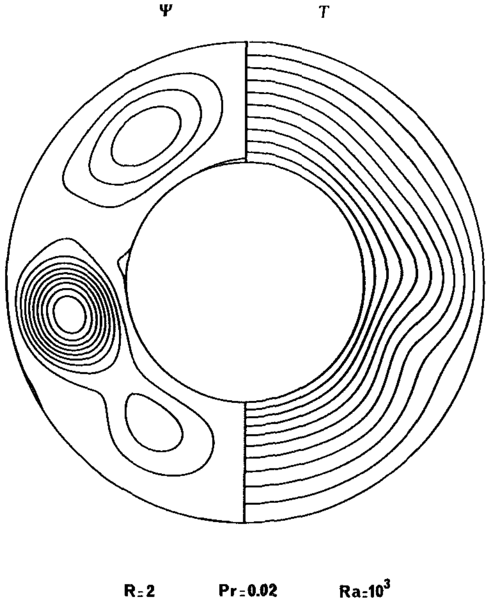

Fig. 4 Streamlines and isotherms for R = 2, Pr = 0.02, Ra = 1000

with tangential velocity subject to the condition:

$$V(h) = -\frac{4\psi(h) - 5\psi(0) + \psi(2h)}{4h} + \sigma(h^3)$$

in these expressions, 0 designates the boundaries and h is the step size in the radial direction $h = (R - 1)/48$. Actually, it can be shown that the two schemes are pratically equivalent.

To determine the vorticity boundary conditions, equation (4) is transformed into:

$$\frac{\partial \omega}{\partial t} + \omega + \frac{\partial^2 \psi}{\partial r^2} = 0 \qquad (4a)$$

where t is analogous to a relaxation parameter.

The linear systems, obtained by using the A.D.I. method, each of them with a tridiagonal matrix whose diagonal elements dominate, are solved explicitly by Gauss' method.

Results and Discussion

The following cases are considered:

1) A large annular space for Pr = 0.7:

$$R = 2 \quad \mathrm{Pr} = 0.7 \text{ and } \mathrm{Ra} = 100, 1000, 1700, 2500, 10^4, 3.10^4$$

$$R = 2.6 \ \mathrm{Pr} = 0.7 \text{ and } \mathrm{Ra}_L = 10^4, 5.10^4$$

For these cases our method gives identical results to those found by [1–4]. For small Rayleigh numbers, a pseudo-conduction regime with concentric isotherms predominates. As Ra increases, the convective phenomena become more important and the isotherms deform, especially in the upper region ($\phi = 180$ deg). The stream lines are always in the form of two thermoconvective cells, symmetrical with respect to the vertical axis (Fig. 1).

2) A small radius ratio for Pr = 0.7:

$$R = 1.2 \quad \mathrm{Pr} = 0.7 \quad \mathrm{Ra}_L = 6000, 7000$$

Here several initial conditions are considered. One of them is:

$$T_o(r, \phi) = 1 - \frac{\operatorname{Log} r}{\operatorname{Log} R} + \alpha \sin\left(\pi \frac{\operatorname{Log} r}{\operatorname{Log} R}\right) \cos(\gamma\phi)$$

α is an amplitude coefficient and γ is a wave number which permits to introduce either a symmetrical or non-symmetrical field with respect to the vertical axis.

The results obtained for these cases are in disagreement with the numerical results of [3] and [4] and with the experimental results of Powe, et al. [8]. For all initial conditions used, the same stationary two-dimensional solution is obtained. The phenomena is bicellular (Fig. 2). Experimentally, Powe, et al. [9] show the existence of a multicellular regime. This difference is most certainly due to the fact that our model is only two-dimensional. The cell length has a dominant influence on the flow's stability as shown in [11].

3) We also consider small Prandtl numbers:

$$R = 2 \quad \mathrm{Pr} = 0.02 \quad \mathrm{Ra}_L = 300, 1000$$

$$R = 5 \quad \mathrm{Pr} = 0.02 \quad \mathrm{Ra}_L = 150, 1230$$

For $\mathrm{Ra}_L = 300$, $R = 2$, $\mathrm{Pr} = 0.02$ we find two cells turning in the same direction (Fig. 3) while the perturbation method used by [10] predicts three counter rotating cells. Simultaneously, the regime begins to oscillate very slightly. As Ra increases, the stream function field changes, the cells turn counter rotatively, the oscillations amplify and the regime becomes unsteady. Fig. 4, ($\mathrm{Ra}_L = 1000$, $\mathrm{Pr} = 0.02$, $R = 2$).

For bigger radius ratio ($R = 5$) and small Rayleigh numbers ($\mathrm{Ra}_L = 150$) *a bicellular regime, similar to the one found in* [5] *is obtained.*

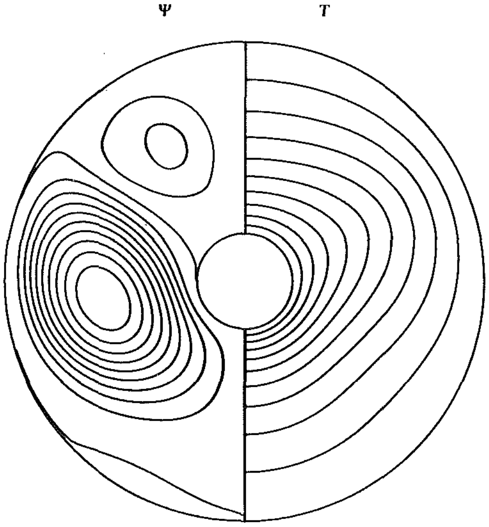

Fig. 5 Streamlines and isotherms for $R = 5$, Pr = 0.02, $\mathrm{Ra}_L = 1230$

As the Rayleigh number increases, our results differ from [5]. The regime becomes multicellular and begins to oscillate ($\mathrm{Ra}_L = 1230$, $R = 5$, Pr = 0.02). See Fig. 5.

To conclude, isotherms and streamlines as a function of the Rayleigh number are calculated. For Pr = 0.7, the results agree with the previous literature exept for a radius ratio close to unity where a multicellular regime is infirmed. The case Pr = 0.02 is studied; the perturbation method used in [5, 10] is only valid for small Ra. The present method permits a solution to be obtained for larger Ra values.

References

1 Crawford, L., Lemlich, R., "Natural Convection in Horizontal Concentric Cylindrical Annuli," *IEC Fundamentals*, Vol. 4, Nov. 1962, pp. 260–264.

2 Abbott, M. R., "Numerical Method for Solving the Equations of Natural Convection in a Narrow Concentric Cylindrical Annulus with a Horizontal Axis," *J. Mech. Applied Math.*, Vol. XVII, Part 4, 1964, pp. 471–481.

3 Powe, R. E., Carley, C. T., and Carruth, S. L., "A Numerical Solution for Natural Convection in Cylindrical Annuli," ASME JOURNAL OF HEAT TRANSFER, Vol. 93, 1971, pp. 210–220.

4 Kuhen, T. H., Goldstein, R. J., "An Experimental and Theoretical Study for Natural Convection in the Annulus Between Horizontal Concentric Cylinders," *J. Fluid Mech.*, Vol. 74, part 4, 1976, pp. 695–719.

5 Custer, J. R., Shaughnessy, E. J., "Thermoconvective Motion of Low Prandtl Number Fluids within a Horizontal Cylindrical Annulus," ASME. JOURNAL of HEAT TRANSFER, Vol. 99, Nov. 1977, pp. 596–602.

6 Lui, C. Y., Mueller, W. K., Landis, "Natural Convection Heat Transfer in Horizontal Cylindrical Annuli," *Int. developments in Heat Transfer, ASME*, 1961, pp. 976–984.

7 Bishop, E. H., Carley, C. T., Powe, R. E., "Natural Convection Oscillatory Flow in Cylindrical Annuli," *Int. J. Heat and Mass Transfer*, Vol. 11, 1968, pp. 1741–1752.

8 Powe, R. E., Carley, C. T., Bishop, E. H., "Free Convective Flow Pattern in Cylindrical Annuli," ASME JOURNAL OF HEAT TRANSFER, Vol. 91, 1969, pp. 310–314.

9 Roache, J., *Computational Fluid Dynamics*, Sect IIIC, 1972, pp. 139–145.

10 Mack, L. R., Bishop, E. H., "Natural Convection between Horizontal Concentric Cylinders for Low Rayleigh Numbers," *J. Mech. Applied Math.*, Vol. XXI, Part 2, 1968, pp. 223–241.

11 Mojtabi, A., Caltagirone, J. P., "Etude de la Stabilité d'un Écoulement de Convection Naturelle dans l'Espace Annulaire Horizontal," *J. de Meca.*, Vol. 18, No. 81, 1979.

Over-All Heat Transfer from Vertical Cones in Laminar Free Convection: an Approximate Method

Md. Alamgir[1]

Nomenclature

a_0, a_1 = constants given in equations (16) and (23)
Gr_L = Grashof number based on L, $g\beta(T_{w,\mathrm{ref}} - T_\infty)L^3 \cos\gamma/\nu^2$
$h(\eta)$ = velocity profile, equation (9)
L = slant height of the cone
n = temperature variation index, equation (13)
Pr = Prandtl number
r = radial distance from cone axis, $R = r/L$
T_w, $T_{w,\mathrm{ref}}$, T_∞ = wall temperature, reference wall temperature and ambient temperature
Δ = boundary layer thickness, $\delta = \Delta/L$
ϵ = curvature parameter, equation (18)
η = dimensionless boundary layer coordinate, $y/\Delta \equiv Y/\delta$
γ = half angle of cone

Introduction

Analytical and experimental studies of free convective heat transfer from vertical cones have been made by various investigators. Early workers approximated the distance to a point in the boundary layer from the cone axis by the local cone radius, thus neglecting the effects of curvature. The resulting boundary layer equations were found to possess similar solutions, [1–6].

The effect of radial curvature was first considered by Kuiken [7]. He found that heat transfer from the cone is augmented significantly for slender cones compared to the case when curvature is neglected. Oosthuizen and Wu [8] also considered curvature effects and solved the boundary layer equations with a finite difference technique. Experimental results for heat transfer from slender, isothermal vertical cones held in air have been reported by Oosthuizen and Donaldson [9].

In the present work an integral method is used to predict the over-all heat transfer from slender vertical cones having certain power-law wall temperature variations. A general expression is obtained for the mean Nusselt number in terms of Grashof number, Prandtl number, the power-law exponent and a parameter characterizing curvature.

Analysis

The coordinate system for the cone is shown in Fig. 1. The governing differential equations with Boussinesq approximation for axisymmetric natural convective flow over a vertical cone (see [8]) are nondimensionalized using $X = x/L$, $Y = y/L$, $R = r/L$, $\delta = \Delta/L$, $U = uL/\nu$, $V = vL/\nu$, $\theta = (T - T_\infty)/(T_w - T_\infty)$ and $\phi = (T_w - T_\infty)/(T_{w,\mathrm{ref}} - T_\infty)$. The result is

$$\frac{\partial(UR)}{\partial X} + \frac{\partial(VR)}{\partial Y} = 0 \tag{1}$$

$$U\frac{\partial U}{\partial X} + V\frac{\partial U}{\partial Y} = \phi\theta \mathrm{Gr}_L + \frac{1}{R}\frac{\partial}{\partial Y}\left(R\frac{\partial U}{\partial Y}\right) \tag{2}$$

$$\mathrm{Pr}\left[U\frac{\partial(\phi\theta)}{\partial X} + V\frac{\partial(\phi\theta)}{\partial Y}\right] = \frac{1}{R}\frac{\partial}{\partial Y}\left(R\frac{\partial(\phi\theta)}{\partial Y}\right) \tag{3}$$

Pressure variations across the boundary layer have been neglected and a constant ambient temperature is assumed. From Fig. 1, $R = X \sin\gamma + Y\cos\gamma$. Next the continuity equation (1) is used to replace V in equations (2) and (3) and the resulting equations are integrated across the boundary layer using the boundary conditions

$$U = V = 0, \quad \theta = 1 \text{ at } Y = 0$$
$$U = 0, \quad \theta = 0 \text{ at } Y = \delta \tag{4}$$

Here thermal and hydrodynamic boundary layer thicknesses are assumed to be equal. The integrated momentum and energy equations are

$$A\frac{d}{dx}\left[U_1{}^2X\delta\left(1 + \frac{B}{A}\frac{\delta}{X}\cot\gamma\right)\right] = C\mathrm{Gr}_L\phi X\delta\left(1 + \frac{D}{C}\frac{\delta}{X}\cot\gamma\right) - \frac{NU_1X}{\delta} \tag{5}$$

$$E\mathrm{Pr}\frac{d}{dx}\left[U_1\phi X\delta\left(1 + \frac{F}{E}\frac{\delta}{X}\cot\gamma\right)\right] = M\frac{\phi X}{\delta} \tag{6}$$

where $\eta = y/\Delta = Y/\delta$ and

$$U = U_1 h(\eta) \tag{7}$$

with U_1 a dimensionless characteristic velocity and

$$A = \int_0^1 h^2\,d\eta,\ B = \int_0^1 \eta h^2\,d\eta,\ C = \int_0^1 \theta\,d\eta,$$
$$D = \int_0^1 \eta\theta\,d\eta, \tag{8}$$

$E = \int_0^1 h\theta\,d\eta$, $F = \int_0^1 \eta h\theta\,d\eta$, $M = -\theta'(0)$ and $N = h'(0)$. In equations (5) and (6) the effect of curvature is represented by the terms containing cot γ. Kuiken [7] observed that similarity solutions to the boundary layer equations do not exist if the curvature effect is included.

As a first approximation solutions will be obtained with neglected curvature effects. Then these solutions will be used to get an approximation of the term $(\delta/X)\cot\gamma$, the latter to be introduced in equations (5) and (6) to obtain the complete solution. The velocity and temperature profiles chosen are

$$U = U_1 h(\eta) = U_1\eta(1 - \eta)^3 \tag{9}$$

$$\theta = (1 - \eta)^2 \tag{10}$$

which satisfy equation (4) and the additional boundary conditions $\partial U/\partial Y = \partial^2 U/\partial Y^2 = \partial\theta/\partial Y = 0$ at $Y = \delta$. The constants in equation (8) after evaluation using equations (9) and (10), are substituted in equations (5) and (6). After the terms containing cot γ are dropped, we have

$$\frac{d}{dX}[U_1{}^2X\delta] = 84\,\mathrm{Gr}_L\phi X\delta - 252\,U_1X/\delta \tag{11}$$

$$\frac{d}{dX}[U_1\phi X\delta] = (84/\mathrm{Pr})\phi X/\delta \tag{12}$$

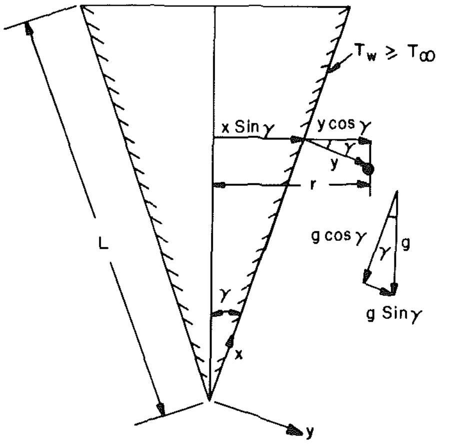

Fig. 1 Coordinate system for the cone

---

[1] Research Assistant, Boiling and Phase Change Laboratory, Mechanical Engineering Dept., University of Kentucky, Lexington, KY 40506

Contributed by the Heat Transfer Division for publication in the JOURNAL OF HEAT TRANSFER. Manuscript received by the Heat Transfer Division May 19, 1978.

Let the wall temperature variation be represented by

$$\phi = X^n \tag{13}$$

The following expressions for U_1 and δ, obtained by a method similar to that used for free convection from a vertical plate, (See [10], for example) satisfy equations (11) and (12).

$$\delta = a_0 \mathrm{Gr}_L{}^{-1/4} X^{(1-n)/4} \tag{14}$$

$$U_1 = \frac{336}{a_0{}^2 \mathrm{Pr}(5n+7)} \mathrm{Gr}_L{}^{1/2} X^{(1+n)/2} \tag{15}$$

where

$$a_0 = \left[\frac{1008[n+3+(5n+7)\mathrm{Pr}]}{[(5n+7)\mathrm{Pr}]^2}\right]^{1/4} \tag{16}$$

To obtain a solution which includes curvature effects we propose that the term $(\delta/X) \cot \gamma$ in equations (5) and (6) be replaced with the averaged quantity

$$[\overline{(\delta/\delta_{\mathrm{iso}})}][\overline{(\delta_{\mathrm{iso}}/X)}] \cot \gamma = \frac{16a_0}{4-n} \mathrm{Gr}_L{}^{-1/4} \cot \gamma \tag{17}$$

Both δ and δ_{iso} on the left hand side of equation (17) are evaluated from equations (14) and (16) and the subscript iso refers to the case of the isothermal wall, that is $n = 0$. The averaged quantities are evaluated as

$$\overline{(\delta/\delta_{\mathrm{iso}})} = (1/L) \int_0^L (\delta/\delta_{\mathrm{iso}})\, dx, \text{ etc.}$$

As a result of the aforementioned averaging, the results of this paper should be applied for the values of exponent n not too different from zero. Defining a curvature parameter

$$\epsilon = \frac{2}{\mathrm{Gr}_L{}^{1/4} \tan \gamma} \tag{18}$$

we find equations (5) and (6) reduce to

$$\left(1 + \frac{2.4a_0\epsilon}{4-n}\right) \frac{d}{dX} [U_1{}^2 X \delta] = 84 \left(1 + \frac{2a_0\epsilon}{4-n}\right) \phi X \delta - 252 \frac{U_1 X}{\delta} \tag{19}$$

$$\mathrm{Pr} \left(1 + \frac{2a_0\epsilon}{4-n}\right) \frac{d}{dX} [U_1 \phi X \delta] = 84 \frac{\phi X}{\delta} \tag{20}$$

which are similar to equations (11) and (12) except for the multiplicative constants. Following the discussion after equation (13), we find the expressions for δ and U_1 that satisfy equations (19) and (20) to be

$$\delta = a_1 \mathrm{Gr}_L{}^{-1/4} X^{(1-n)/4} \tag{21}$$

$$U_1 = \frac{336}{a_1{}^2 \mathrm{Pr}(5n+7)\left(1 + \frac{2a_0\epsilon}{4-n}\right)} \mathrm{Gr}_L{}^{1/2} X^{(n+1)/2} \tag{22}$$

$$a_1 = \left[1008 \frac{(n+3)\left(1 + \frac{2.4a_0\epsilon}{4-n}\right) + (5n+7)\left(1 + \frac{2a_0\epsilon}{4-n}\right)\mathrm{Pr}}{\left(1 + \frac{2a_0\epsilon}{4-n}\right)\left[(5n+7)\left(1 + \frac{2a_0\epsilon}{4-n}\right)\mathrm{Pr}\right]^2}\right]^{1/4} \tag{23}$$

Heat Transfer Results and Discussion

The local wall heat flux is

$$q = -k \left.\frac{\partial T}{\partial y}\right|_{y=0} = -k\theta'(0)(T_w - T_\infty)/L\delta \tag{24}$$

The over-all heat flux is obtained by integrating equation (24) over the lateral surface area of the cone and dividing it by the total lateral surface area

$$Q = \frac{1}{A_t} \int_S q ds = -\frac{2k\theta'(0)}{L} (T_{w,\mathrm{ref}} - T_\infty) \int_0^1 \frac{\phi X}{\delta} \tag{25}$$

where $A_t = \pi L^2 \sin \gamma$ and $ds = 2\pi x \sin \gamma\, dx$. A mean heat transfer coefficient is defined as

$$\bar{h} = \frac{Q}{T_{w,\mathrm{ref}} - T_\infty} \tag{26}$$

Using equations (10, 13, 21) and (25) in equation (26) we get the mean Nusselt number Nu_L $(= \bar{h}L/k)$ as

$$\mathrm{Nu}_L = \frac{4\mathrm{Gr}_L{}^{1/4}}{a_1} \int_0^1 X^{(5n+3)/4} dX = \frac{16\mathrm{Gr}_L{}^{1/4}}{a_1(5n+7)} \tag{27}$$

where a_1 is as given in equation (23).

Kuiken [7] obtained a series type solution for the isothermal vertical cone which included curvature effects. From his local heat transfer results it can be deduced that for Prandtl number of 0.7, $\mathrm{Nu}_L/\mathrm{Gr}_L{}^{1/4} = 0.51554 + 0.412\epsilon + 0.022\epsilon^2$. Both this result and $\mathrm{Nu}_L/\mathrm{Gr}_L{}^{1/4}$ obtained from the present work, equation (27), are plotted against the curvature parameter ϵ in Fig. 2. It is seen that the present approximate solution agrees quite well with Kuiken's solution.

The experimental data correlation of Oosthuizen and Donaldson [9] and the solution of Hering and Grosh [4] which neglects curvature are also shown. It can be seen that when the cone is a slender one or when the Grashof number Gr_L is not large, neglect of curvature may result in heat transfer predictions which may be too low (100 percent too low when $\epsilon = 1.2$, for example). From equations (10, 13, 21, 23), and (24) the local Nusselt number for an isothermal cone ($n = 0$) with negligible curvature ($\epsilon \rightarrow 0$) is given by

$$\mathrm{Nu}_x \mathrm{Gr}_x{}^{-1/4} = \frac{2}{a_0} \tag{28}$$

with $\mathrm{Nu}_x = qx/(k(T_w - T_\infty))$ and $\mathrm{Gr}_x = (g\beta(T_w - T_\infty)x^3 \cos \gamma)/\nu^2$, a_0 is given in equation (16). Hering [5] and Roy [6] have given numerical solutions for heat transfer from an isothermal cone at low and high Prandtl numbers, respectively, by neglecting curvature effects. In Fig. 3, $\log_{10} (\mathrm{Nu}_x/\mathrm{Gr}_x{}^{1/4})$ from equation (28) is plotted against $\log_{10}$ Pr. The solutions of [5] and [6] are also shown. The present solution demonstrates acceptable behavior over a wide range of Prandtl numbers in spite of the simplifying assumption that the thermal and hydrodynamic boundary layer thicknesses are equal. When $\mathrm{Pr} \leq 1$, equality of thermal boundary layer, δ_t, and velocity boundary layer, δ_h is a proper assumption. For $\mathrm{Pr} > 1$, $\delta_h > \delta_t$ and a separate calcu-

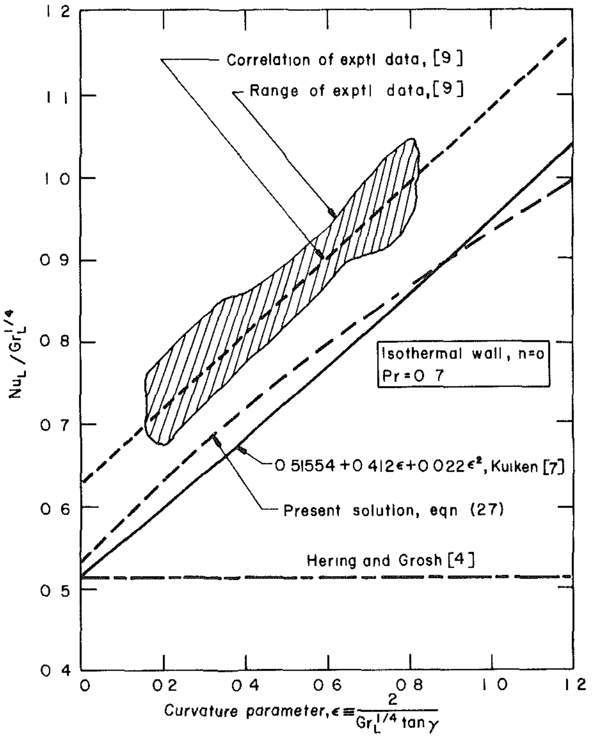

Fig. 2 Over-all heat transfer from an isothermal cone

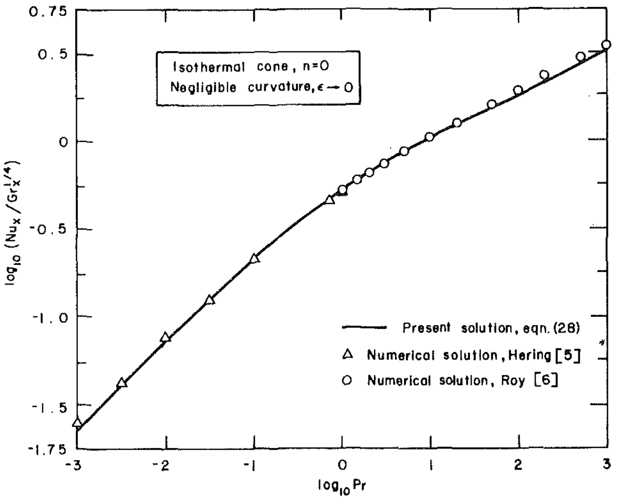

Fig. 3 Effect of Prandtl number on local heat transfer

lation was made to note the effect of unequal δ's on the Nusselt number. The boundary layer equations for an isothermal cone with neglected curvature effects were integrated up to δ_t assuming δ_t/δ_h to be independent of the streamwise coordinate. For Prandtl numbers up to 10^3, values of local Nusselt number differed by 9 percent, at most, from $\delta_t = \delta_h$ case.

Acknowledgment

The author is indebted to Professor R. Eichhorn and Professor John H. Lienhard for constructive suggestions and advice.

References

1 Merk, H. J., and Prins, J. A., "Thermal Convection in Laminar Boundary Layers I, II," *Appl. Sci. Res.*, A4, 1953–54, pp. 11–24, 195–206.

2 Braun, W. H., and Heighway, J. E., "An Integral Method for Natural Convection Flows at High and Low Prandtl Numbers," NASA, TN D-292, 1960.

3 Braun, W. H., Ostrach, S., and Heighway, J. E., "Free Convection Similarity Flows About Two-dimensional and Axisymmetric Bodies with Closed Lower Ends," *Int. J. Heat Mass Transfer*, Vol. 2, 1961, pp. 121–135.

4 Hering, R. G., and Grosh, R. J., "Laminar Free Convection From a Nonisothermal Cone," *Int. J. Heat Mass Transfer*, Vol. 5, 1962, pp. 1059–1068.

5 Hering, R. G., "Laminar Free Convection from A Non-Isothermal Cone at Low Prandtl Numbers," *Int. J. Heat Mass Transfer*, Vol. 8, 1965, pp. 1333–1337.

6 Roy, S., "Free Convection From a Vertical Cone at High Prandtl Numbers," ASME JOURNAL OF HEAT TRANSFER, Vol. 96, Feb. 1974, pp. 115–117.

7 Kuiken, H. K., "Axisymmetric Free Convection Boundary-layer Flow Past Slender Bodies," *Int. J. Heat Mass Transfer*, Vol. 11, 1968, pp. 1141–1153.

8 Oosthuizen, P. H., and Wu, E., "A Numerical Study of Some Laminar Free Convection Problems," Report 2-71, Thermal and Fluid Sciences Group, Queen's University, Kingston, Ontario, Canada, 1971.

9 Oosthuizen, P. H., and Donaldson, E., "Free Convective Heat Transfer From Vertical Cones," ASME JOURNAL OF HEAT TRANSFER, Vol. 94, Aug. 1972, pp. 330–331.

10 Eckert, E. R. G., and Drake, R. M., Jr., *Heat and Mass Transfer*, 2nd ed., McGraw-Hill, New York, 1959.

Heat Transfer Correlation for Subcooled Water Films on Horizontal Tubes

V. Sernas[1]

Nomenclature

g = acceleration due to gravity
h_1 = average heat transfer coefficient defined by equation (2)
h_θ = local heat transfer coefficient defined by equation (1)
k = thermal conductivity
Nu_δ = Nusselt number based on film thickness = $h_1\delta/k$
Pr = Prandtl number = ν/α
Re = film Reynolds number = $4\Gamma/\mu$
$\dot{q}$ = heat flux
T_{in} = water temperature in feed tray
T_w = wall temperature
α = thermal diffusivity
Γ = mass flow rate per side per unit axial length of tube
δ = film thickness $(3\nu\Gamma/g\rho)^{1/3}$
θ = angular position measured clockwise from top of tube
μ = dynamic viscosity
ν = kinematic viscosity
ρ = density

Introduction

Experimental studies of falling liquid film evaporation on horizontal tubes has been reported by Fletcher, et al. [1, 2]. In those studies, the operating conditions were such that the liquid film was always boiling making it difficult to separate the convective contribution to the heat transfer out from the results. Parken [3] has reported many experimental heat transfer results of a nonboiling subcooled water film on 5 cm and 2.5 cm dia horizontal tubes in the Appendix of his thesis. In these experiments, the water was carefully deposited on the horizontal tube to form laminar falling films. Furthermore, the experiments were run under conditions that produced little or no evaporation from the liquid film. In the body of his thesis Parken showed that these heat transfer results can be predicted very well by a finite difference computer model of the convective flow in the falling film. However, Parken did not arrive at a dimensionless correlation that would predict the average heat transfer coefficients for all of his experimental tests. That task has now been completed and is presented in this paper.

Apparatus

Parken's falling film tests were performed in the same facility that was used for the boiling film tests reported in [1] and [2]. Construction details of the facility can be found in Parken [3] and [4]. Only the construction of the horizontally heated tubes and the feed water tray differed from the previous studies [1] and [2].

The 5 cm dia horizontal tube was made from a thick walled brass tube that had eight axial grooves 25 cm long machined on its outside surface. Thermocouples were placed in these grooves and a 0.1 mm thick brass shim was soldered on top to form a smooth heat transfer surface that covered the complete perimeter of the tube and which was 15 cm long in the axial direction. The inside surface of the brass tube was lined with asbestos paper and a 30 cm long coiled electric heater was centered under the shim and pressed against the inside surface of the asbestos to provide a uniform heat flux to the tube. The 2.5 cm OD heated tube was constructed in the same manner.

The water feed tray shown in Fig. 1 contained a single slot 32.5 cm long and 0.56 mm wide for the 5 cm tube, and 0.38 mm wide for the 2.5 cm tube. The exit of the slot was centered over the heated tube and was kept approximately 3 mm above it. The water flow rate over the tube was changed by increasing the water head within the feed tray. This feed tray design produced a laminar sheet (or slot jet) of water at the top of the horizontal tube. This laminar slot jet split into half and formed two laminar films which slid down on the tube surface (one on either side of the tube) for a distance of only half a circumference of the horizontal tube (7.85 cm for the 5 cm tube). Wilke's study [5] has shown that carefully deposited laminar films at the top of vertical tubes turn turbulent only some 40 to 80 cm from the top of the tube if the Reynolds number is near the range of Parken's ex-

---

Assoc. Professor of Mechanical Engineering, Rutgers University, New Brunswick, N.J. 08903

Contributed by the Heat Transfer Division for publication in the JOURNAL OF HEAT TRANSFER. Manuscript received by the Heat Transfer Division October 4, 1978.

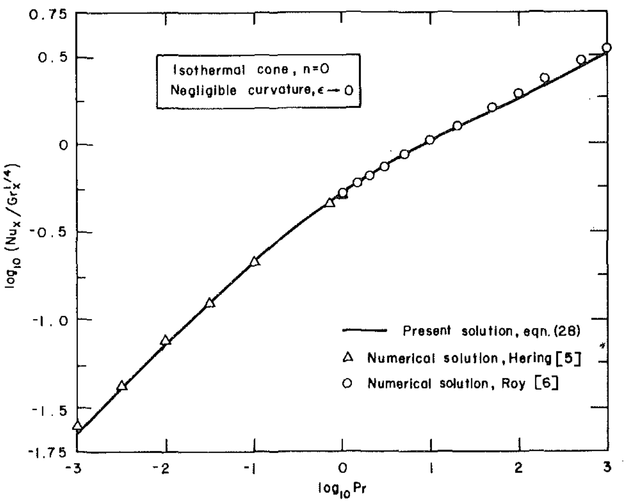

Fig. 3 Effect of Prandtl number on local heat transfer

lation was made to note the effect of unequal δ's on the Nusselt number. The boundary layer equations for an isothermal cone with neglected curvature effects were integrated up to δ_t assuming δ_t/δ_h to be independent of the streamwise coordinate. For Prandtl numbers up to 10^3, values of local Nusselt number differed by 9 percent, at most, from $\delta_t = \delta_h$ case.

Acknowledgment

The author is indebted to Professor R. Eichhorn and Professor John H. Lienhard for constructive suggestions and advice.

References

1 Merk, H. J., and Prins, J. A., "Thermal Convection in Laminar Boundary Layers I, II," *Appl. Sci. Res.*, A4, 1953–54, pp. 11–24, 195–206.

2 Braun, W. H., and Heighway, J. E., "An Integral Method for Natural Convection Flows at High and Low Prandtl Numbers," NASA, TN D-292, 1960.

3 Braun, W. H., Ostrach, S., and Heighway, J. E., "Free Convection Similarity Flows About Two-dimensional and Axisymmetric Bodies with Closed Lower Ends," *Int. J. Heat Mass Transfer*, Vol. 2, 1961, pp. 121–135.

4 Hering, R. G., and Grosh, R. J., "Laminar Free Convection From a Nonisothermal Cone," *Int. J. Heat Mass Transfer*, Vol. 5, 1962, pp. 1059–1068.

5 Hering, R. G., "Laminar Free Convection from A Non-Isothermal Cone at Low Prandtl Numbers," *Int. J. Heat Mass Transfer*, Vol. 8, 1965, pp. 1333–1337.

6 Roy, S., "Free Convection From a Vertical Cone at High Prandtl Numbers," ASME JOURNAL OF HEAT TRANSFER, Vol. 96, Feb. 1974, pp. 115–117.

7 Kuiken, H. K., "Axisymmetric Free Convection Boundary-layer Flow Past Slender Bodies," *Int. J. Heat Mass Transfer*, Vol. 11, 1968, pp. 1141–1153.

8 Oosthuizen, P. H., and Wu, E., "A Numerical Study of Some Laminar Free Convection Problems," Report 2-71, Thermal and Fluid Sciences Group, Queen's University, Kingston, Ontario, Canada, 1971.

9 Oosthuizen, P. H., and Donaldson, E., "Free Convective Heat Transfer From Vertical Cones," ASME JOURNAL OF HEAT TRANSFER, Vol. 94, Aug. 1972, pp. 330–331.

10 Eckert, E. R. G., and Drake, R. M., Jr., *Heat and Mass Transfer*, 2nd ed., McGraw-Hill, New York, 1959.

Heat Transfer Correlation for Subcooled Water Films on Horizontal Tubes

V. Sernas[1]

Nomenclature

g = acceleration due to gravity
h_1 = average heat transfer coefficient defined by equation (2)
h_θ = local heat transfer coefficient defined by equation (1)
k = thermal conductivity
Nu_δ = Nusselt number based on film thickness = $h_1\delta/k$
Pr = Prandtl number = ν/α
Re = film Reynolds number = $4\Gamma/\mu$
$\dot{q}$ = heat flux
T_{in} = water temperature in feed tray
T_w = wall temperature
α = thermal diffusivity
Γ = mass flow rate per side per unit axial length of tube
δ = film thickness $(3\nu\Gamma/g\rho)^{1/3}$
θ = angular position measured clockwise from top of tube
μ = dynamic viscosity
ν = kinematic viscosity
ρ = density

Introduction

Experimental studies of falling liquid film evaporation on horizontal tubes has been reported by Fletcher, et al. [1, 2]. In those studies, the operating conditions were such that the liquid film was always boiling making it difficult to separate the convective contribution to the heat transfer out from the results. Parken [3] has reported many experimental heat transfer results of a nonboiling subcooled water film on 5 cm and 2.5 cm dia horizontal tubes in the Appendix of his thesis. In these experiments, the water was carefully deposited on the horizontal tube to form laminar falling films. Furthermore, the experiments were run under conditions that produced little or no evaporation from the liquid film. In the body of his thesis Parken showed that these heat transfer results can be predicted very well by a finite difference computer model of the convective flow in the falling film. However, Parken did not arrive at a dimensionless correlation that would predict the average heat transfer coefficients for all of his experimental tests. That task has now been completed and is presented in this paper.

Apparatus

Parken's falling film tests were performed in the same facility that was used for the boiling film tests reported in [1] and [2]. Construction details of the facility can be found in Parken [3] and [4]. Only the construction of the horizontally heated tubes and the feed water tray differed from the previous studies [1] and [2].

The 5 cm dia horizontal tube was made from a thick walled brass tube that had eight axial grooves 25 cm long machined on its outside surface. Thermocouples were placed in these grooves and a 0.1 mm thick brass shim was soldered on top to form a smooth heat transfer surface that covered the complete perimeter of the tube and which was 15 cm long in the axial direction. The inside surface of the brass tube was lined with asbestos paper and a 30 cm long coiled electric heater was centered under the shim and pressed against the inside surface of the asbestos to provide a uniform heat flux to the tube. The 2.5 cm OD heated tube was constructed in the same manner.

The water feed tray shown in Fig. 1 contained a single slot 32.5 cm long and 0.56 mm wide for the 5 cm tube, and 0.38 mm wide for the 2.5 cm tube. The exit of the slot was centered over the heated tube and was kept approximately 3 mm above it. The water flow rate over the tube was changed by increasing the water head within the feed tray. This feed tray design produced a laminar sheet (or slot jet) of water at the top of the horizontal tube. This laminar slot jet split into half and formed two laminar films which slid down on the tube surface (one on either side of the tube) for a distance of only half a circumference of the horizontal tube (7.85 cm for the 5 cm tube). Wilke's study [5] has shown that carefully deposited laminar films at the top of vertical tubes turn turbulent only some 40 to 80 cm from the top of the tube if the Reynolds number is near the range of Parken's ex-

---

Assoc. Professor of Mechanical Engineering, Rutgers University, New Brunswick, N.J. 08903

Contributed by the Heat Transfer Division for publication in the JOURNAL OF HEAT TRANSFER. Manuscript received by the Heat Transfer Division October 4, 1978.

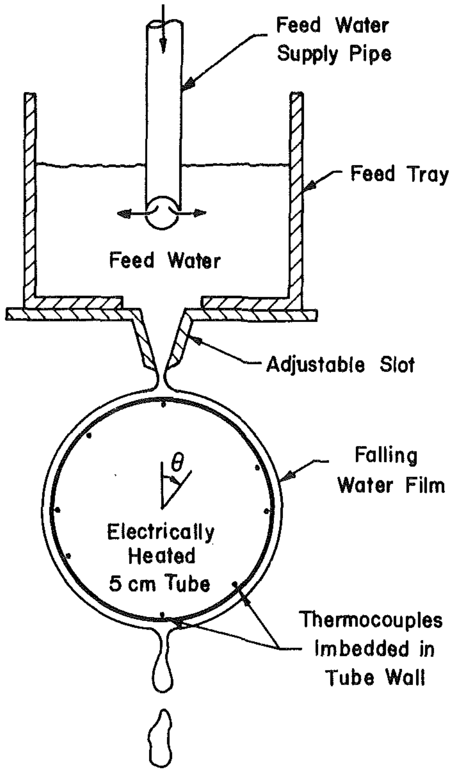

Fig. 1 Experimental arrangement for producing the falling water film on horizontal heated tube

periments. Oosthuizen and Cheung [6] also produced laminar films at the top of vertical tubes at Reynolds numbers about an order of magnitude larger than Parken's.

The water in the feed tray was always slightly subcooled because the pressure in the horizontal tube chamber was always kept slightly above the saturation pressure of the feed water.

Experimental Results

Parken's [3] experimental results are presented in the Appendix of his thesis as a table of measured temperatures and local conductances, h_θ, around the circumference of the heated tube for each test within the range specified in Table 1. The local conductance was defined as:

$$h_\theta = \dot{q}/(T_w - T_{in}) \tag{1}$$

where $\dot{q}$ was the constant heat flux produced by the internal electric heater, T_w was the local tube wall temperature, and T_{in} was the feed water temperature.

Before correlating Parken's data, an average heat transfer coefficient, h_1, for the entire tube was calculated for each test run. The average heat transfer coefficient was defined as:

$$h_1 = \frac{1}{2\pi}\int_0^{2\pi} h_\theta d\theta \tag{2}$$

where θ is the angle measured clockwise from the top of the tube. The average conductance for the 2.5 cm tube was obtained by averaging the local heat transfer coefficient measured at $\theta = 0$ deg, 45 deg, 90 deg, 135 deg, 160 deg, 225 deg, 270 deg, and 315 deg. The average conductance for the 5 cm tube was obtained by averaging the local heat transfer coefficient at $\theta = 0$ deg, 65 deg, 90 deg, 135 deg, 180 deg, 245 deg, 270 deg, and 315 deg. The average of the specified eight local conductances is a good estimate of h_1 because the location of these local conductances are approximately evenly spaced around the tube. The variation of h_θ with θ was found by Parken [3] to be quite large. It was largest at $\theta = 0$ deg and decreased continuously to about half that value (depending on flow rate) at the bottom.

It is indicated in Table 1 that six runs out of the 78 reported by Parken [3] were not used in the correlations. The accuracy of these tests was questioned either because their wall temperature distribution was unsymmetric, or because their $(T_w - T_{in})$ was small due to a small heat flux setting.

Table 1 Range of experimental conditions

	2.5 cm tube	5 cm tube
flow rate Γ, kg/s-m	0.133 to 0.292	0.222 to 0.375
Reynolds No., $4\Gamma/\mu$	1151 to 4594	1679 to 6044
inlet temp., °C	44.9 to 117	47.7 to 122.4
Prandtl No. ν/α	1.49 to 3.92	1.453 to 3.717
heat flux, kW/m^2	47 to 79	47 to 79
No. of tests used in correlation	33	39
No. of tests reported by Parken	36	42[1]

[1] Only those tests that were made on tube whose thermocouple locations are shown in Fig. 1.

Correlation of Results

It has become a common practice to express the Reynolds number for thin film flow at $4\Gamma/\mu$ where Γ is the mass flow rate in the film per unit width of surface, and μ is the dynamic viscosity of the fluid film. For horizontal tubes the mass flow rate supplied to the tube per unit length of tube is divided by two to obtain Γ because two films are established on the tube, one on each side. This definition of the Reynolds number implies that the characteristic length for the flow is 4δ which is the "hydraulic diameter" of the film and δ is the film thickness. It is therefore reasonable to define a Nusselt number based on the film thickness, i.e., $\mathrm{Nu}_\delta = h_1\delta/k$. The film thickness on a horizontal tube varies with angle θ, and is not an easily measureable quantity. It is known [7], however, that the laminar film thickness at steady state on a flat vertical surface is expressible in terms of easily measureable quantities, i.e., $\delta = (3\mu\Gamma/g\rho^2)^{1/3}$. Thus the dimensionless grouping $h_1(3\mu\Gamma/g\rho^2)^{1/3}/k = \mathrm{Nu}_\delta$ was adopted to serve as an average Nusselt number for the horizontal tube.

A dimensionless analysis revealed that the experimental data of each tube should be correlated by an equation of the form

$$\mathrm{Nu}_\delta = C\,\mathrm{Re}^m\mathrm{Pr}^n \tag{3}$$

where C, m, and n are constants, and Re and Pr are the Reynolds and Prandtl numbers respectively. A multiple linear regression analysis was performed separately on the 2.5 cm tube data and the 5 cm tube data. In the regression analysis the data were fitted to equation (3). It was found that the exponent of the Prandtl number was almost the same in both the 2.5 cm and 5 cm tube correlations. The 95 percent confidence interval for n was found to be (0.637 ± .045) for the 2.5 cm tube data and (0.687 ± .060) for the 5 cm tube data. Since the same exponent for Pr is highly desirable for both tube diameters, a common value of $n = 0.66$ was chosen because it fell about half way between the exponents for each tube and it was well within the 95 percent confidence limit for the exponent for each diameter.

The exponent for the Reynolds number in equation (3) was found by first a least square procedure for each tube diameter to fit

$$\frac{\mathrm{Nu}_\delta}{\mathrm{Pr}^{0.66}} = C\,\mathrm{Re}^m \tag{4}$$

and then by choosing a common exponent for both groups of data. In the linear regression analysis that fitted the data to equation (4) the 95 percent confidence interval for m was found to be (0.553 ± .028) for the 2.5 cm tube data, and (0.587 ± .033) for the 5 cm tube data. A common exponent of $m = 0.57$ was then chosen for both groups of data. This chosen value of m was in the middle between 0.553 and 0.587 and still within the 95 percent confidence interval of both sets of data.

The premultiplying constant C in equation (3) was found separately for each set of data by a procedure that is equivalent to the formula

$$C = \frac{1}{N}\sum_{i=1}^{N}\frac{\mathrm{Nu}_\delta}{\mathrm{Re}^{0.57}\mathrm{Pr}^{0.66}}$$

where the sum is taken over the 33 data points of the 2.5 cm tube to obtain the C for that tube, and over the 39 data points of the 5 cm tube

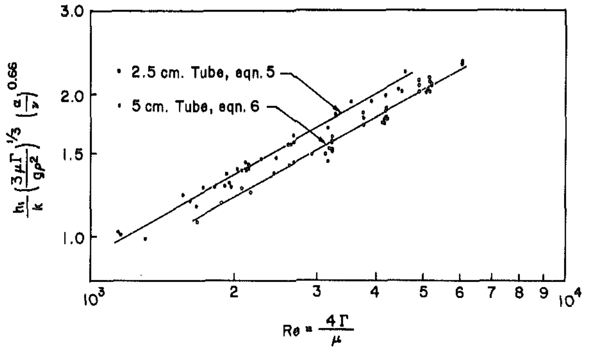

Fig. 2 Comparison of experimental data with equations (5) and (6)

to obtain the C for the 5 cm tube. The resultant correlations are as follows:

for the 2.5 cm diameter tube,

$$\frac{h_1}{k}\left(\frac{3\mu\Gamma}{g\rho^2}\right)^{1/3} = 0.01757\left(\frac{4\Gamma}{\mu}\right)^{0.57}\left(\frac{\nu}{\alpha}\right)^{0.66} \quad (5)$$

and for the 5 cm tube,

$$\frac{h_1}{k}\left(\frac{3\mu\Gamma}{g\rho^2}\right)^{1/3} = 0.01578\left(\frac{4\Gamma}{\mu}\right)^{0.57}\left(\frac{\nu}{\alpha}\right)^{0.66}. \quad (6)$$

These correlations (which are applicable only in the Re and Pr range given in Table 1) are plotted on Fig. 2 to show how well they fit the experimental data. The square root of the mean square error for the 2.5 cm tube correlation is only 3.1 percent and only one data point (out of 33) deviates from the correlation by more than 5 percent. The square root of the mean square error for the 5 cm tube is 3.3 percent, and only four data points (out of 39) deviate from the correlation by more than 5 percent.

It should be noted that in equations (5) and (6) the fluid properties are to be evaluated at the feed water temperature. It was found that the variation of the properties due to temperature was very small because the temperature differences were small. An estimate of the effect of the temperature variation of the properties was made by calculating a correction factor of the Sieder-Tate [8] type, i.e., $(\mu_m/\mu_w)^{0.14}$ where μ_m is the viscosity at the mean film temperature and μ_w is the viscosity at the average wall temperature. This correction factor was found to fall in the range between 1.006 and 1.025 for all the test runs. In view of the fact that this correction factor was close to unity it was not incorporated into equations (5) and (6).

It is possible to write equations (5) and (6) in terms of the commonly used dimensionless group, $h(\nu^2/g)^{1/3}/k$, by multiplying both sides of the equations by $(\mu/3\Gamma)^{1/3}$. The results are for the 2.5 cm tube

$$\frac{h_1}{k}\left(\frac{\nu^2}{g}\right)^{1/3} = .01925\left(\frac{4\Gamma}{\mu}\right)^{0.24}\left(\frac{\nu}{\alpha}\right)^{0.66} \quad (7)$$

and for the 5 cm tube

$$\frac{h_1}{k}\left(\frac{\nu^2}{g}\right)^{1/3} = .01729\left(\frac{4\Gamma}{\mu}\right)^{0.24}\left(\frac{\nu}{\alpha}\right)^{0.66} \quad (8)$$

References

1 Fletcher, L. S., Sernas, V., Galowin, L., "Evaporation from Thin Water Films on Horizontal Tubes", *Ind. Eng. Chem., Process Des. Develop.*, Vol. 13, 1974, pp. 265–269.

2 Fletcher, L. S., Sernas, V., and Parken, W. H., "Evaporation Heat Transfer Coefficients for Thin Sea Water Films on Horizontal Tubes," *Ind. Eng. Chem., Process Des. Develop.*, Vol. 14, No. 4, 1975, pp. 411–416.

3 Parken, W. H., Jr. "Heat Transfer to Thin Water Films on Horizontal Tubes," Ph.D. Thesis, Rutgers University, June 1975.

4 Fletcher, L. S., and Sernas, V., Report RU-TR 142-MIAE-H, Dept. of Mech., Ind., and Aero. Engineering, Rutgers University, July 1973.

5 Wilke, W., "Wärmeübergang an Rieselfilme," *VDI-Forschungsheft* 490, 1962.

6 Oosthuizen, P. H., and Cheung, T., "An Experimental Study of Heat Transfer to Developing Water Film Flow Over Cylinders," ASME JOURNAL OF HEAT TRANSFER, Vol. 99, 1977, pp. 152–155.

7 Bird, R. B., Stewart, W. E., and Lightfoot, E. N., *Transport Phenomena*, John Wiley & Sons, 1960, p. 40.

8 Sieder, E. N., and Tate, G. E., "Heat Transfer and Pressure Drop of Liquids in Tubes," *Ind. Eng. Chem.*, Vol. 28, p. 1429, 1936.

A Note on Combined Boiling and Evaporation of Liquid Films on Horizontal Tubes

J. J. Lorenz[1] and D. Yung[1]

Introduction

Relatively high heat fluxes can be attained with small temperature differences by evaporation of thin liquid films on horizontal tubes. If nucleate boiling accompanies film evaporation, even higher heat fluxes can be realized. Evaporators employing these heat transfer mechanisms have been used in refrigeration systems, desalination plants, and, more recently, have been proposed for use in Ocean Thermal Energy Conversion (OTEC) power plants. A design of particular interest for OTEC is the horizontal tube falling film evaporator, where a working fluid (e.g., ammonia) is vaporized on vertical banks of heated horizontal tubes.

Despite the importance of boiling and evaporation of liquid films on horizontal tubes, surprisingly little analytical and experimental work has appeared in the literature [1–5]. Much of the previous work was sponsored by the Office of Saline Water (OSW), presently the Office of Water Research and Technology (OWRT), and was directed toward desalination. In a recent study by the authors [6], a simple model was developed for predicting heat transfer by combined boiling and evaporation of liquid films on horizontal tubes. Predictions were shown to be in good agreement with the experimental data of Fletcher, et al., [1, 2] and Liu [3] for evaporating water films. Unfortunately no data for other working fluids, such as ammonia, was available at that time. Subsequently a number of investigators published experimental data for ammonia evaporating on horizontal tubes [7–9]. The purpose of this technical note is to provide a comparison between those data and our analytical model.

Analysis

Before presenting a comparison of predictions with the experimental data, a brief discussion of the model will be given. For the case of a single horizontal tube with outer diameter, D, the problem is treated by "unwrapping" the tube to form a vertical surface of length $L = \pi D/2$, see Fig. 1.[2] Within the length, L, two distinct convective heat transfer regions are defined: a thermal developing region and a fully developed region. If the superheat is sufficiently high, nucleate boiling can occur in the film. The overall heat transfer process is modelled as a superposition of the convective components and the boiling component.

Thermal Developing Region. Referring to Fig. 1, liquid at the saturation temperature T_s is fed at a flowrate (per unit axial length) 2Γ to the top of a heated tube, establishing a thin film on the surface. The feed flow splits evenly with Γ going to each side. A thermal developing length L_d is required for the film to be superheated from the saturation temperature to a fully developed linear profile. In the thermal developing region all of the heat transferred from the wall goes into superheating the liquid film and no evaporation occurs. The

---

[1] Components Technology Division, Argonne National Laboratory, Argonne, IL 60439

[2] Justification for this is partially by analogy to laminar film condensation where the average heat transfer coefficient calculated via Nusselt for a vertical plate with $L = \pi D/2$ is found to be only 15 percent different from the "exact" Nusselt solution for a horizontal tube. The simple approach was adopted in view of this and because the actual problem involves a number of complex phenomena which are not rigorously considered in the overall modelling (e.g., waves, ripples, splashing, and bubbles).

Contributed by The Gas Turbine Division for publication in the "JOURNAL OF HEAT TRANSFER. Manuscript received by The Heat Transfer Division August 17, 1978.

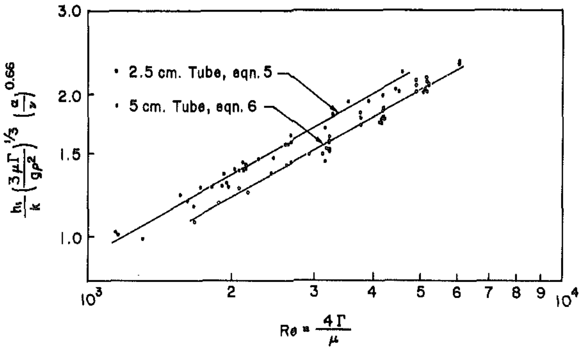

Fig. 2 Comparison of experimental data with equations (5) and (6)

to obtain the C for the 5 cm tube. The resultant correlations are as follows:

for the 2.5 cm diameter tube,

$$\frac{h_1}{k}\left(\frac{3\mu\Gamma}{g\rho^2}\right)^{1/3} = 0.01757\left(\frac{4\Gamma}{\mu}\right)^{0.57}\left(\frac{\nu}{\alpha}\right)^{0.66} \quad (5)$$

and for the 5 cm tube,

$$\frac{h_1}{k}\left(\frac{3\mu\Gamma}{g\rho^2}\right)^{1/3} = 0.01578\left(\frac{4\Gamma}{\mu}\right)^{0.57}\left(\frac{\nu}{\alpha}\right)^{0.66}. \quad (6)$$

These correlations (which are applicable only in the Re and Pr range given in Table 1) are plotted on Fig. 2 to show how well they fit the experimental data. The square root of the mean square error for the 2.5 cm tube correlation is only 3.1 percent and only one data point (out of 33) deviates from the correlation by more than 5 percent. The square root of the mean square error for the 5 cm tube is 3.3 percent, and only four data points (out of 39) deviate from the correlation by more than 5 percent.

It should be noted that in equations (5) and (6) the fluid properties are to be evaluated at the feed water temperature. It was found that the variation of the properties due to temperature was very small because the temperature differences were small. An estimate of the effect of the temperature variation of the properties was made by calculating a correction factor of the Sieder-Tate [8] type, i.e., $(\mu_m/\mu_w)^{0.14}$ where μ_m is the viscosity at the mean film temperature and μ_w is the viscosity at the average wall temperature. This correction factor was found to fall in the range between 1.006 and 1.025 for all the test runs. In view of the fact that this correction factor was close to unity it was not incorporated into equations (5) and (6).

It is possible to write equations (5) and (6) in terms of the commonly used dimensionless group, $h(\nu^2/g)^{1/3}/k$, by multiplying both sides of the equations by $(\mu/3\Gamma)^{1/3}$. The results are for the 2.5 cm tube

$$\frac{h_1}{k}\left(\frac{\nu^2}{g}\right)^{1/3} = .01925\left(\frac{4\Gamma}{\mu}\right)^{0.24}\left(\frac{\nu}{\alpha}\right)^{0.66} \quad (7)$$

and for the 5 cm tube

$$\frac{h_1}{k}\left(\frac{\nu^2}{g}\right)^{1/3} = .01729\left(\frac{4\Gamma}{\mu}\right)^{0.24}\left(\frac{\nu}{\alpha}\right)^{0.66} \quad (8)$$

References

1 Fletcher, L. S., Sernas, V., Galowin, L., "Evaporation from Thin Water Films on Horizontal Tubes", *Ind. Eng. Chem., Process Des. Develop.*, Vol. 13, 1974, pp. 265–269.

2 Fletcher, L. S., Sernas, V., and Parken, W. H., "Evaporation Heat Transfer Coefficients for Thin Sea Water Films on Horizontal Tubes," *Ind. Eng. Chem., Process Des. Develop.*, Vol. 14, No. 4, 1975, pp. 411–416.

3 Parken, W. H., Jr. "Heat Transfer to Thin Water Films on Horizontal Tubes," Ph.D. Thesis, Rutgers University, June 1975.

4 Fletcher, L. S., and Sernas, V., Report RU-TR 142-MIAE-H, Dept. of Mech., Ind., and Aero. Engineering, Rutgers University, July 1973.

5 Wilke, W., "Wärmeübergang an Rieselfilme," *VDI-Forschungsheft* 490, 1962.

6 Oosthuizen, P. H., and Cheung, T., "An Experimental Study of Heat Transfer to Developing Water Film Flow Over Cylinders," ASME JOURNAL OF HEAT TRANSFER, Vol. 99, 1977, pp. 152–155.

7 Bird, R. B., Stewart, W. E., and Lightfoot, E. N., *Transport Phenomena*, John Wiley & Sons, 1960, p. 40.

8 Sieder, E. N., and Tate, G. E., "Heat Transfer and Pressure Drop of Liquids in Tubes," *Ind. Eng. Chem.*, Vol. 28, p. 1429, 1936.

A Note on Combined Boiling and Evaporation of Liquid Films on Horizontal Tubes

J. J. Lorenz[1] and D. Yung[1]

Introduction

Relatively high heat fluxes can be attained with small temperature differences by evaporation of thin liquid films on horizontal tubes. If nucleate boiling accompanies film evaporation, even higher heat fluxes can be realized. Evaporators employing these heat transfer mechanisms have been used in refrigeration systems, desalination plants, and, more recently, have been proposed for use in Ocean Thermal Energy Conversion (OTEC) power plants. A design of particular interest for OTEC is the horizontal tube falling film evaporator, where a working fluid (e.g., ammonia) is vaporized on vertical banks of heated horizontal tubes.

Despite the importance of boiling and evaporation of liquid films on horizontal tubes, surprisingly little analytical and experimental work has appeared in the literature [1–5]. Much of the previous work was sponsored by the Office of Saline Water (OSW), presently the Office of Water Research and Technology (OWRT), and was directed toward desalination. In a recent study by the authors [6], a simple model was developed for predicting heat transfer by combined boiling and evaporation of liquid films on horizontal tubes. Predictions were shown to be in good agreement with the experimental data of Fletcher, et al., [1, 2] and Liu [3] for evaporating water films. Unfortunately no data for other working fluids, such as ammonia, was available at that time. Subsequently a number of investigators published experimental data for ammonia evaporating on horizontal tubes [7–9]. The purpose of this technical note is to provide a comparison between those data and our analytical model.

Analysis

Before presenting a comparison of predictions with the experimental data, a brief discussion of the model will be given. For the case of a single horizontal tube with outer diameter, D, the problem is treated by "unwrapping" the tube to form a vertical surface of length $L = \pi D/2$, see Fig. 1.[2] Within the length, L, two distinct convective heat transfer regions are defined: a thermal developing region and a fully developed region. If the superheat is sufficiently high, nucleate boiling can occur in the film. The overall heat transfer process is modelled as a superposition of the convective components and the boiling component.

Thermal Developing Region. Referring to Fig. 1, liquid at the saturation temperature T_s is fed at a flowrate (per unit axial length) 2Γ to the top of a heated tube, establishing a thin film on the surface. The feed flow splits evenly with Γ going to each side. A thermal developing length L_d is required for the film to be superheated from the saturation temperature to a fully developed linear profile. In the thermal developing region all of the heat transferred from the wall goes into superheating the liquid film and no evaporation occurs. The

---

[1] Components Technology Division, Argonne National Laboratory, Argonne, IL 60439

[2] Justification for this is partially by analogy to laminar film condensation where the average heat transfer coefficient calculated via Nusselt for a vertical plate with $L = \pi D/2$ is found to be only 15 percent different from the "exact" Nusselt solution for a horizontal tube. The simple approach was adopted in view of this and because the actual problem involves a number of complex phenomena which are not rigorously considered in the overall modelling (e.g., waves, ripples, splashing, and bubbles).

Contributed by The Gas Turbine Division for publication in the "JOURNAL OF HEAT TRANSFER. Manuscript received by The Heat Transfer Division August 17, 1978.

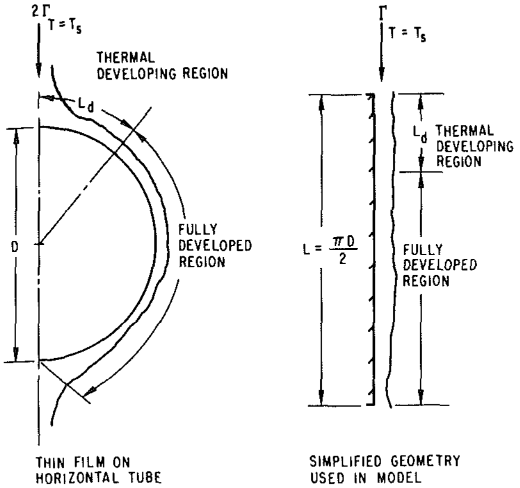

Fig. 1 Sketch of actual configuration and simplified geometry used in model

average heat transfer coefficient in this region was calculated from an energy balance as:

$$h_d = \frac{3}{8} C_p \frac{\Gamma}{L_d} \tag{1}$$

where C_p is the specific heat. For this calculation a fully developed laminar falling film velocity profile together with a linear temperature profile were assumed at the end of the developing region. The developing length, L_d, was estimated assuming a constant film thickness, given by the well-known Nusselt expression, and employing an approximate integral method, yielding:

$$L_d = \frac{\Gamma^{4/3}}{4\pi\rho\alpha}\sqrt{\frac{3\mu}{g\rho^2}} \tag{2}$$

where ρ is the density; α is the thermal diffusivity; and μ is the viscosity. A more exact treatment of the developing region could not be justified in view of the many complicating factors that come into play (e.g., waves, ripples, splashing, and bubbles). Fortunately many of these effects tend to cancel. Equations (1) and (2) apply strictly to laminar flow but have been successfully employed slightly within the turbulent region. Since most flow conditions of practical interest for horizontal tubes are either laminar or just slightly turbulent, these equations are generally applicable.

Fully Developed Region. In the fully developed region, convective heat transfer leads to evaporation at the vapor/liquid interface. Chun and Seban [10] developed the following correlations for heat transfer to evaporating liquid films on smooth vertical tubes:

Laminar:

$$h_c = 0.821 \left(\frac{\nu^2}{k^3 g}\right)^{-1/3} \left(\frac{4\Gamma}{\mu}\right)^{-0.22} \tag{3a}$$

Turbulent:

$$h_c = 3.8 \times 10^{-3} \left(\frac{\nu^2}{k^3 g}\right)^{-1/3} \left(\frac{4\Gamma}{\mu}\right)^{0.4} \left(\frac{\nu}{\alpha}\right)^{0.65} \tag{3b}$$

where k is the thermal conductivity and ν is the kinematic viscosity. Both correlations give the "local" heat transfer coefficient as a function of film Reynolds number, $4\Gamma/\mu$. In the laminar range, equation (3a) includes the influence of waves and ripples which have the effect of increasing heat transfer by reducing the effective film thickness. Equations (3a) and (3b) should apply equally well for either constant heat flux or constant wall temperature boundary conditions: in laminar flow h_c is essentially equal of k/δ, regardless of boundary conditions; and in turbulent flow the behavior should be essentially similar to that in pipes where it is known that $(\mathrm{Nu})_{T=\mathrm{const}}/(\mathrm{Nu})_{q/A=\mathrm{const}} \approx 0.9$ for $\mathrm{Pr} > 0.5$. The intersection of correlations (3a) and (3b) yields the following pseudo-transition Reynolds number:

$$\left(\frac{4\Gamma}{\mu}\right)_{tr} = 5800 \left(\frac{\nu}{\alpha}\right)^{-1.06} \tag{4}$$

This should not be regarded as an actual indication of the transition from laminar to turbulent but only as the point of transition from one correlation to the other. The actual transition to turbulence may be more accurately characterized by the Weber number [10].

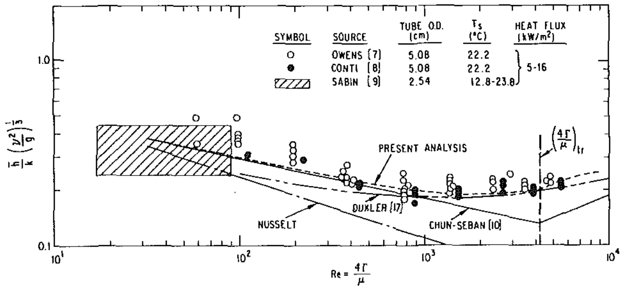

Fig. 2 Comparison of predictions with experimental data for ammonia evaporating on smooth horizontal tubes

Nucleate Boiling. If the superheat is sufficiently high, boiling may occur in the film. It has been found that greater heat fluxes are attainable with boiling in thin films than with boiling in pools, e.g., [11–13]. Nishikawa [12] developed a correlation for nucleate boiling in thin liquid layers, but falling films on tubes are generally so thin that they lie outside the validated range of his correlation. Rather than using an extrapolation of Nishikawa's correlation, it was decided to conservatively adopt a pool boiling correlation, such as that of Rohsenow [14, 15]:

$$h_b = \frac{\mu h_{fg}}{C_{sf}^3 \sqrt{\frac{g_0}{g}\frac{\sigma}{\rho}}} \left(\frac{C_p}{h_{fg} P_r{}^s}\right)^3 \Delta T^2 \tag{5}$$

where $s = 1$ for water and $s = 1.7$ for all other fluids. The parameter C_{sf} is a function of fluid-surface combination. Experimental data, when available, should be used in preference to this correlation.

Average Heat Transfer Coefficient. The overall heat flux is assumed to be a superposition of convective heat transfer and boiling. This procedure is essentially similar to that of Bergles and Rohsenow [16] for determining forced convective boiling heat transfer coefficients. The average heat transfer coefficient over the circumferential length, L, is then:

$$\bar{h} = h_b + h_d \frac{L_d}{L} + h_c \left(1 - \frac{L_d}{L}\right) \tag{6}$$

Since $\bar{h}$ is defined as the average heat transfer coefficient over the entire length, it should be evident that the quantities (L_d/L) and $(1 - L_d/L)$ in equation (6) merely weight the respective convective heat transfer components according to the length over which each is effective. Boiling is assumed to occur over the entire length and therefore the weighting factor for h_b is unity.[3] Equations (3a) and (3b) for h_c are evaluated assuming a constant flowrate, a procedure which does not take into account the thinning of the film. This assumption was found to be generally quite good, particularly when the rate of evaporation is small compared to the feed flowrate Γ.

Results

The experimental apparatus employed in [7–9] consist essentially of a feed tube which supplies ammonia liquid at T_s to an electrically heated horizontal tube on which vaporization occurs. Heat transfer coefficients were determined from the electrical input and thermocouples located circumferentially and axially along the tube. No boiling was observed in the ammonia film in any of the experimental studies. This is probably due to the fact that ammonia wets surfaces very well and floods out potential nucleation sites.

Figure 2 shows a comparison of predictions with experimental data. Results are plotted as dimensionless heat transfer coefficient versus

---

[3] A weighting factor of unity resulted in favorable agreement between equation (6) and the experimental data of Fletcher, et al., [1, 2] for boiling of thin water films on horizontal tubes. In using a weighting factor of unity it was assumed that the incipient boiling superheat was exceeded over the entire length. When the maximum active cavity size is known, the modelling can be refined by invoking an incipience criterion.

film Reynolds number. Note that considerable scatter exists for Re < 100. This reflects variability in the measured heat transfer coefficients resulting from random dry patches that form on the tube surface at very low feed flowrates. The present analysis is seen to be in good agreement with the data over the entire Reynolds number range. Since no boiling was experimentally observed, h_b was set equal to zero in the model. The trends indicated by the model are rather interesting. At low flowrates, the heat transfer coefficient is large because the film is relatively thin. As the flowrate increases, the film thickens and consequently the heat transfer coefficient decreases. At still higher flowrates heat transfer in the developing region becomes increasingly important, and the heat transfer coefficient gradually rises. The variance between the Chun-Seban correlation and the present model reflects the influence of the thermal developing region. Note the large divergence at high flowrates where the developing length is most important. Dukler's analysis [17] agrees favorably with the data at higher flowrates, but underpredicts the data at lower flowrates. Actually the Dukler prediction is remarkably good in view of the fact that the analysis, like that of Chun-Seban, was developed for falling films on vertical surfaces rather than on horizontal tubes. For reference, the Nusselt prediction is also plotted.

Conclusions

A simple model of combined boiling and evaporation of liquid films on horizontal tubes was developed. Predictions were shown to agree favorably with recent thin film evaporation data for ammonia. Previously [6] the model was shown to successfully predict published experimental data for evaporating (and boiling) water films. In view of the good agreement with experimental data, this model is expected to be a useful tool for the thermal design of horizontal tube falling film evaporators.

References

1 Fletcher, L. S., Sernas, V., and Galowin, L. S., "Evaporation from Thin Water Films on Horizontal Tubes," ASME Paper No. 73-HT-42, ASME-AIChE Heat Transfer Conference, Atlanta, Georgia, 1973.

2 Fletcher, L. S., Sernas, V., and Parken, W. H., *Ind. Eng. Chem., Process Des. Dev.*, Vol. 14, No. 4, 1975, pp. 411–416.

3 Liu, P., PhD Thesis, Dept. of Mech. Eng., Univ. of Wisconsin, Madison, Wisconsin, 1975.

4 Schultz, V. N., Edwards, D. K., and Catton, I., *AIChE Symposium Series*, Vol. 73, No. 164, 1977, pp. 223–227.

5 Moalem, D. and Sideman, S., *Int. J. Heat Mass Transfer*, Vol. 19, 1976, pp. 259–270.

6 Lorenz, J. J. and Yung, D., "Combined Boiling and Evaporation of Liquid Films on Horizontal Tubes," *Proceedings, Fifth Ocean Thermal Energy Conversion Conference*, Miami Beach, Florida, 1978.

7 Owens, W. L., "Correlation of Thin Film Evaporation Heat Transfer Coefficients for Horizontal Tubes," *Proceedings, Fifth Ocean Thermal Energy Conversion Conference*, Miami Beach, Florida, 1978.

8 Conti, R. J., "Experimental Investigation of Horizontal-Tube Ammonia Film Evaporators with Small Temperature Differentials," *Proceedings, Fifth Ocean Thermal Energy Conversion Conference*, Miami Beach, Florida, 1978.

9 Sabin, C. M. and Poppendiek, H. F., "Film Evaporation of Ammonia over Horizontal Round Tubes," *Proceedings, Fifth Ocean Thermal Energy Conversion Conference*, Miami Beach, Florida, 1978.

10 Chun, K. R. and Seban, R. A., ASME JOURNAL OF HEAT TRANSFER, Vol. 93, 1971, pp. 391–396.

11 Mesler, R., *AIChE Journal*, Vol. 22, No. 2, 1967, pp. 246–252.

12 Nishikawa, K., Kusada, H., Yamasaki, K., and Tanaka, K., *Bull. JSME*, Vol. 10, No. 38, 1967, pp. 328–338.

13 Marto, P. J., MacKensie, D. K., and Rivers, A. D., *AIChE Symposium Series*, Vol. 73, No. 164, 1977, pp. 228–235.

14 Rohsenow, W. M., *Trans. ASME*, Vol. 74, No. 6, 1952, pp. 969–976.

15 Rohsenow, W. M., ASME JOURNAL OF HEAT TRANSFER, Vol. 94, 1972, pp. 255–256.

16 Bergles, A. E. and Rohsenow, W. M., ASME JOURNAL OF HEAT TRANSFER, Vol. 86, 1964, pp. 365–372.

17 Dukler, A. E., *Chem. Eng. Prog. Symposium Series*, Vol. 56, No. 30, 1960, pp. 1–10.

An Analytical Estimate of the Microlayer Thickness in Nucleate Boiling

M. S. Plesset[1] **and S. S. Sadhal**[2]

Nomenclature

$m_s = R^2\dot{R}$ = source strength
$m = -R^2\dot{R}$ = sink strength
p = pressure
$R(t)$ = bubble radius
R_0 = maximum bubble radius
r = spherical distance from origin
t = time
t_0 = bubble lifetime
U = free-field radial velocity
u = radial velocity within the boundary layer
w = velocity normal to wall
z = distance normal to wall
δ = boundary layer thickness
δ_0 = microlayer thickness
$\langle\delta_0\rangle$ = average value of δ_0
$\eta = z(m/2\nu r^3)^{1/2}$ = similarity variable
ν = kinematic viscosity
ρ = density of liquid
ϕ = velocity potential

1 Introduction

Among the phenomena of interest in nucleate boiling at a solid surface is the enhanced heat transfer that takes place with the onset of such boiling. In the physical situation of present concern one has a large temperature gradient in the liquid in the neighborhood of the solid. Vapor bubbles grow and collapse at the solid with a lifetime of the order of a millisecond or less. These nucleate boiling bubbles have characteristically a maximum size of about 0.5 mm. The analysis of the dynamics of such vapor bubbles is important for the understanding of the physical mechanism of the increased heat transfer from a hot solid to a liquid in nucleate boiling conditions.

To explain the increased heat transfer with nucleate boiling two mechanisms have been suggested. The first supposes that the growing and collapsing of a bubble produces a stirring of the liquid in the region of the large temperature gradient near the solid. This "microconvection" is then supposed to produce the increase in heat transfer. Because of viscosity, the bubble growth and collapse have associated with them a viscous layer between the bubble base and the solid (see Fig. 1). This viscous layer is known as the "microlayer." The second mechanism supposes that the important contribution comes from the transport of latent heat. In this latter mechanism the heat from the hot wall is conducted through the microlayer and is transported from the bubble base to the cooler bubble cap in the form of latent heat of vaporization from the microlayer. The contribution of this latent heat transport in subcooled nucleate boiling has been studied by Plesset and Prosperetti [1].

In the determination of heat transfer rates due to these mechanisms the thickness of the microlayer plays an important role and has been the subject of several investigations. From a theoretical point of view the calculation of the thickness of the microlayer is a well-defined problem in fluid dynamics. However, previous attempts [2, 3] to solve this problem have led to solutions which have been developed and applied to slowly growing bubbles. These growing bubbles are observed in situations in which the temperature gradient in the liquid in the neighborhood of the solid is much smaller than the gradients which apply to nucleate boiling. The vapor bubbles which grow in such

---

[1] Division of Engineering and Applied Science, Department of Engineering Science, California Institute of Technology, Pasadena, CA 91125

[2] Division of Engineering and Applied Science, Department of Engineering Science, California Institute of Technology, Pasadena, CA 91125. Present Address: Department of Mechanical Engineering and Applied Mechanics, University of Pennsylvania, Philadelphia, PA 19104.

Contributed by the Heat Transfer Division for publication in the JOURNAL OF HEAT TRANSFER. Manuscript received by the Heat Transfer Division October 4, 1978.

film Reynolds number. Note that considerable scatter exists for Re < 100. This reflects variability in the measured heat transfer coefficients resulting from random dry patches that form on the tube surface at very low feed flowrates. The present analysis is seen to be in good agreement with the data over the entire Reynolds number range. Since no boiling was experimentally observed, h_b was set equal to zero in the model. The trends indicated by the model are rather interesting. At low flowrates, the heat transfer coefficient is large because the film is relatively thin. As the flowrate increases, the film thickens and consequently the heat transfer coefficient decreases. At still higher flowrates heat transfer in the developing region becomes increasingly important, and the heat transfer coefficient gradually rises. The variance between the Chun-Seban correlation and the present model reflects the influence of the thermal developing region. Note the large divergence at high flowrates where the developing length is most important. Dukler's analysis [17] agrees favorably with the data at higher flowrates, but underpredicts the data at lower flowrates. Actually the Dukler prediction is remarkably good in view of the fact that the analysis, like that of Chun-Seban, was developed for falling films on vertical surfaces rather than on horizontal tubes. For reference, the Nusselt prediction is also plotted.

Conclusions

A simple model of combined boiling and evaporation of liquid films on horizontal tubes was developed. Predictions were shown to agree favorably with recent thin film evaporation data for ammonia. Previously [6] the model was shown to successfully predict published experimental data for evaporating (and boiling) water films. In view of the good agreement with experimental data, this model is expected to be a useful tool for the thermal design of horizontal tube falling film evaporators.

References

1 Fletcher, L. S., Sernas, V., and Galowin, L. S., "Evaporation from Thin Water Films on Horizontal Tubes," ASME Paper No. 73-HT-42, ASME-AIChE Heat Transfer Conference, Atlanta, Georgia, 1973.

2 Fletcher, L. S., Sernas, V., and Parken, W. H., *Ind. Eng. Chem., Process Des. Dev.*, Vol. 14, No. 4, 1975, pp. 411–416.

3 Liu, P., PhD Thesis, Dept. of Mech. Eng., Univ. of Wisconsin, Madison, Wisconsin, 1975.

4 Schultz, V. N., Edwards, D. K., and Catton, I., *AIChE Symposium Series*, Vol. 73, No. 164, 1977, pp. 223–227.

5 Moalem, D. and Sideman, S., *Int. J. Heat Mass Transfer*, Vol. 19, 1976, pp. 259–270.

6 Lorenz, J. J. and Yung, D., "Combined Boiling and Evaporation of Liquid Films on Horizontal Tubes," *Proceedings, Fifth Ocean Thermal Energy Conversion Conference*, Miami Beach, Florida, 1978.

7 Owens, W. L., "Correlation of Thin Film Evaporation Heat Transfer Coefficients for Horizontal Tubes," *Proceedings, Fifth Ocean Thermal Energy Conversion Conference*, Miami Beach, Florida, 1978.

8 Conti, R. J., "Experimental Investigation of Horizontal-Tube Ammonia Film Evaporators with Small Temperature Differentials," *Proceedings, Fifth Ocean Thermal Energy Conversion Conference*, Miami Beach, Florida, 1978.

9 Sabin, C. M. and Poppendiek, H. F., "Film Evaporation of Ammonia over Horizontal Round Tubes," *Proceedings, Fifth Ocean Thermal Energy Conversion Conference*, Miami Beach, Florida, 1978.

10 Chun, K. R. and Seban, R. A., ASME JOURNAL OF HEAT TRANSFER, Vol. 93, 1971, pp. 391–396.

11 Mesler, R., *AIChE Journal*, Vol. 22, No. 2, 1967, pp. 246–252.

12 Nishikawa, K., Kusada, H., Yamasaki, K., and Tanaka, K., *Bull. JSME*, Vol. 10, No. 38, 1967, pp. 328–338.

13 Marto, P. J., MacKensie, D. K., and Rivers, A. D., *AIChE Symposium Series*, Vol. 73, No. 164, 1977, pp. 228–235.

14 Rohsenow, W. M., *Trans. ASME*, Vol. 74, No. 6, 1952, pp. 969–976.

15 Rohsenow, W. M., ASME JOURNAL OF HEAT TRANSFER, Vol. 94, 1972, pp. 255–256.

16 Bergles, A. E. and Rohsenow, W. M., ASME JOURNAL OF HEAT TRANSFER, Vol. 86, 1964, pp. 365–372.

17 Dukler, A. E., *Chem. Eng. Prog. Symposium Series*, Vol. 56, No. 30, 1960, pp. 1–10.

An Analytical Estimate of the Microlayer Thickness in Nucleate Boiling

M. S. Plesset[1] and S. S. Sadhal[2]

Nomenclature

$m_s = R^2\dot{R}$ = source strength
$m = -R^2\dot{R}$ = sink strength
p = pressure
$R(t)$ = bubble radius
R_0 = maximum bubble radius
r = spherical distance from origin
t = time
t_0 = bubble lifetime
U = free-field radial velocity
u = radial velocity within the boundary layer
w = velocity normal to wall
z = distance normal to wall
δ = boundary layer thickness
δ_0 = microlayer thickness
$\langle\delta_0\rangle$ = average value of δ_0
$\eta = z(m/2\nu r^3)^{1/2}$ = similarity variable
ν = kinematic viscosity
ρ = density of liquid
ϕ = velocity potential

1 Introduction

Among the phenomena of interest in nucleate boiling at a solid surface is the enhanced heat transfer that takes place with the onset of such boiling. In the physical situation of present concern one has a large temperature gradient in the liquid in the neighborhood of the solid. Vapor bubbles grow and collapse at the solid with a lifetime of the order of a millisecond or less. These nucleate boiling bubbles have characteristically a maximum size of about 0.5 mm. The analysis of the dynamics of such vapor bubbles is important for the understanding of the physical mechanism of the increased heat transfer from a hot solid to a liquid in nucleate boiling conditions.

To explain the increased heat transfer with nucleate boiling two mechanisms have been suggested. The first supposes that the growing and collapsing of a bubble produces a stirring of the liquid in the region of the large temperature gradient near the solid. This "microconvection" is then supposed to produce the increase in heat transfer. Because of viscosity, the bubble growth and collapse have associated with them a viscous layer between the bubble base and the solid (see Fig. 1). This viscous layer is known as the "microlayer." The second mechanism supposes that the important contribution comes from the transport of latent heat. In this latter mechanism the heat from the hot wall is conducted through the microlayer and is transported from the bubble base to the cooler bubble cap in the form of latent heat of vaporization from the microlayer. The contribution of this latent heat transport in subcooled nucleate boiling has been studied by Plesset and Prosperetti [1].

In the determination of heat transfer rates due to these mechanisms the thickness of the microlayer plays an important role and has been the subject of several investigations. From a theoretical point of view the calculation of the thickness of the microlayer is a well-defined problem in fluid dynamics. However, previous attempts [2, 3] to solve this problem have led to solutions which have been developed and applied to slowly growing bubbles. These growing bubbles are observed in situations in which the temperature gradient in the liquid in the neighborhood of the solid is much smaller than the gradients which apply to nucleate boiling. The vapor bubbles which grow in such

---

[1] Division of Engineering and Applied Science, Department of Engineering Science, California Institute of Technology, Pasadena, CA 91125

[2] Division of Engineering and Applied Science, Department of Engineering Science, California Institute of Technology, Pasadena, CA 91125. Present Address: Department of Mechanical Engineering and Applied Mechanics, University of Pennsylvania, Philadelphia, PA 19104.

Contributed by the Heat Transfer Division for publication in the JOURNAL OF HEAT TRANSFER. Manuscript received by the Heat Transfer Division October 4, 1978.

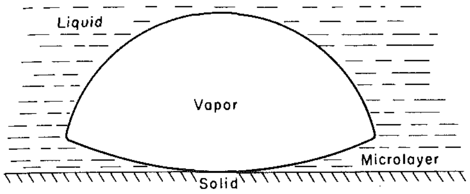

Fig. 1 (*a*) A diagrammatic representation of a typical nucleate boiling vapor bubble with a viscous microlayer

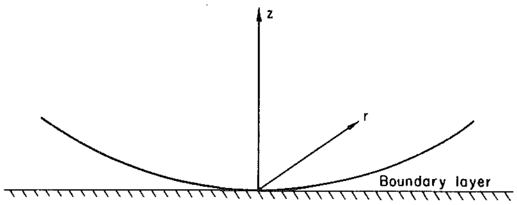

Fig. 1 (*b*) Mathematical model (point source or sink)

moderate temperature gradients not only grow much more slowly but also attain sizes of the order of several millimeters. These do not usually collapse on the solid but detach from it to collapse at a distance from it. Measurements of the microlayer thickness for such bubbles have been made by Jawurek [4] and by Voutsinos and Judd [5] with use of optical interferometry. For the small, short-lived nucleate boiling bubbles such measurements are not yet available.

For a spherical vapor bubble of radius $R(t)$ growing or collapsing in an unbounded liquid such as water the velocity potential in the liquid viewed as a perfect fluid is

$$\phi(r) = \frac{R^2\dot{R}}{r} \tag{1}$$

where $\dot{R} \equiv dR/dt$ is the velocity at the bubble boundary. This motion is the same as the motion produced by a point source (or a sink) of liquid of strength

$$m_s = R^2\dot{R} \tag{2}$$

Viscous effects for such unbounded spherical motion in water are unimportant. A bubble growing (collapsing) at a solid wall usually has a nearly hemispherical shape and the liquid motion away from the wall can be described by (1–2). At the wall, however, the no-slip condition applies and we have a viscous boundary layer. The motion of the liquid is similar to the case of a point source (sink) in an unbounded liquid where we introduce a rigid plane containing the point.

In the present analysis, we obtain an estimate of the microlayer thickness during the collapse of a bubble from the known solution [6] to the boundary layer equations for a constant point sink on a plane. That is to say, we simulate a bubble of time-varying radius $R(t)$ by a point sink of liquid on a rigid plane in a semi-infinite liquid (see Fig. 1). The strength of the sink is taken to be $m = -R^2\dot{R}$. An estimate of the microlayer thickness during the growth of the bubble could not be obtained in a corresponding way because of fundamental difficulties in the existence and the uniqueness of a boundary layer solution for a point source on a plane. A steady state boundary layer solution for a constant point sink is, however, available [6] and a calculation of the boundary layer thickness is used to give an estimate of the microlayer thickness for a collapsing bubble.

2 Boundary Layer Solution for a Point Sink on a Plane

The boundary layer solution presented by Rosenhead [6] is based on the general class of axisymmetric solutions by Mangler [7] and Geis [8]. The potential flow outside the boundary layer is given in terms of the free-field velocity U as

$$U = -\frac{m}{r^2} \tag{3}$$

where $m = -R^2\dot{R}$ is the strength of the point sink and r is the radial distance from the sink. From the momentum equation the pressure term, $-(1/\rho)(\partial p/\partial r)$, for inviscid flow is obtained as

$$-\frac{1}{\rho}\frac{\partial p}{\partial r} = U\frac{dU}{dr} = -\frac{2m^2}{r^5} \tag{4}$$

In the boundary layer approximation it is assumed that equation (4) describes the pressure distribution within the viscous layer as well as outside it. Therefore, the momentum equation within the boundary layer has the well known form [6]

$$u\frac{\partial u}{\partial r} + w\frac{\partial u}{\partial z} = -\frac{2m^2}{r^5} + \nu\frac{\partial^2 u}{\partial z^2} \tag{5}$$

where u is the radial velocity along the plane, w is the velocity normal to the plane, z is the distance normal to the plane, and ν is the kinematic viscosity of the liquid. The continuity equation in these coordinates is

$$\frac{\partial}{\partial r}(ru) + \frac{\partial}{\partial z}(rw) = 0 \tag{6}$$

By using the similarity variable

$$\eta = z\left(\frac{m}{2\nu r^3}\right)^{1/2}, \quad m = -R^2\dot{R} > 0 \tag{7}$$

and by expressing u in terms of an undetermined function $f(\eta)$ as

$$u = Uf'(\eta) \tag{8}$$

one obtains from equations (5) and (6)

$$f''' - ff'' + 4(1 - f'^2) = 0 \tag{9}$$

which is a special case of the Falkner-Skan equation. The no-slip and the zero normal velocity conditions require that

$$f(0) = f'(0) = 0 \tag{10}$$

and in order that $u \rightarrow U$ away from the plane, f has to satisfy the requirement

$$f'(\eta) \rightarrow 1 \quad \text{as} \quad \eta \rightarrow \infty \tag{11}$$

A numerical solution to this set of equations (9–11) is available [6], and it can be used to obtain the flow velocity at any point. It is appropriate to point out here that a similar boundary layer solution for a point source does not exist.

3 Microlayer Thickness

If the boundary layer thickness is defined as the distance in which the flow velocity has attained 99 percent of the potential flow velocity, then from (8) it follows that

$$f'(\eta) < 0.99 \tag{12}$$

From the numerical solution of (9–11) we find that (12) requires that

$$z\left(\frac{m}{2\nu r^3}\right)^{1/2} = \eta \lesssim 2 \tag{13}$$

Therefore, the boundary layer is the region

$$0 \leq z \lesssim 2\left(\frac{2\nu r^3}{m}\right)^{1/2} \tag{14}$$

and hence the boundary layer thickness is given by

$$\delta \simeq 2\left(\frac{2\nu r^3}{m}\right)^{1/2} \tag{15}$$

There is, of course, some arbitrariness in the determination of the boundary layer thickness. If the thickness is defined as $f'(\eta) = 0.999$, then one finds $\delta \simeq 3(2\nu r^3/m)^{1/2}$; and if one takes $f'(\eta) = 0.95$ one finds $\delta \simeq 0.9(2\nu r^3/m)^{1/2}$.

An estimate of the microlayer thickness δ_0 can be obtained if we find a suitable expression for m and then interpret δ as δ_0. The expression for m must be consistent with the assumption that it be a constant and it should fit the experimental data for $R(t)$.

The above results are valid only for the collapse of the bubble, and we take $t = 0$ as the time when the bubble radius $R(t)$ is a maximum R_0, i.e.,

$$R(0) = R_0 \tag{16}$$

If t_0 is taken as the total bubble lifetime, for growth and collapse, then we require

$$R(\tfrac{1}{2}t_0) = 0 \tag{17}$$

In addition, $R(t)$ must satisfy

$$R^2\dot{R} = -m \tag{18}$$

where m is taken to be a constant. We then find that

$$R(t) = R_0\left(1 - \frac{2t}{t_0}\right)^{1/3} \tag{19}$$

and

$$m = \frac{2}{3}\frac{R_0{}^3}{t_0} \tag{20}$$

which upon substitution into (15) gives the microlayer thickness as

$$\delta_0 \simeq 2(3\nu t_0)^{1/2}\left(\frac{r}{R_0}\right)^{3/2} \tag{21}$$

This expression may be averaged over the region beneath the bubble to give

$$\langle\delta_0\rangle \simeq \frac{8}{7}(3\nu t_0)^{1/2} \tag{22}$$

where $\langle\delta_0\rangle$ is the average value of δ_0.

4 Discussion

The information about the boundary layer thickness just described can be used to estimate the heat transfer rate due to evaporation from the microlayer. A question arises concerning the accuracy of the description of the collapse motion which is determined by taking m to be a constant. In Fig. 2, $R(t)/R_0$ from (19), which is a direct result of this assumption, is shown as a function of t/t_0 together with the data from the measurements by Gunther and Kreith [9] and by Gunther [10]; also plotted on the same graph are the best fits of these data. The assumption that m is a constant is fairly good for $0 \leq t \lesssim t_0/4$, but is less accurate as $t \rightarrow t_0/2$. We should also remark that the bubble velocity at the maximum radius for fixed m is not zero while for the growing and collapsing bubble $\dot{R} = 0$ at the maximum radius. The results given by (21) and (22) cannot be compared with any available experimental data because none of these deal with collapsing bubbles of nucleate boiling.

A valid solution for a time varying m would be of considerable value but it appears to be exceedingly difficult to obtain analytically. For a constant point source a solution of the boundary layer type does not exist and it appears that the exact solution is quite complicated. Presumably, the difficulty in the potential solution for a point source arises from the regions of reverse flows so that one does not have a monopole potential flow. The existence of such reverse flows can be inferred from the exact solutions of the Navier-Stokes equations for the viscous flows from a line source in a two-dimensional channel [11-13].

The analytical model presented here for the microlayer thickness has a significant advantage of simplicity. It also gives some useful information regarding the variation of the microlayer thickness along the solid boundary. We should reiterate that the description of the bubble motion by a source or a sink gives the fluid flow only in the potential region outside the viscous boundary layer on the solid. A legitimate question may be raised concerning the validity of the use of a source of constant strength for the bubble growth or a sink of constant strength for the collapse. The constant source does not have a boundary layer solution, as has been mentioned, presumably because the potential flow has regions of reverse flow. In addition, the use of a constant source does not give a physically acceptable description of the corresponding bubble growth since such a description would require the growth to begin with a large velocity. The constant sink solution is more useful not only because there is a boundary layer solution but also because the collapse motion is acceptably described. A flaw in the constant sink description of the collapse lies in the consequence that the collapse motion does not begin from rest when the bubble radius is at its maximum. This initial nonzero velocity while small does make an incorrect contribution to the boundary layer. The constant sink boundary layer description should be considered qualitative, and it presumably tends to overestimate somewhat the bubble collapse microlayer thickness.

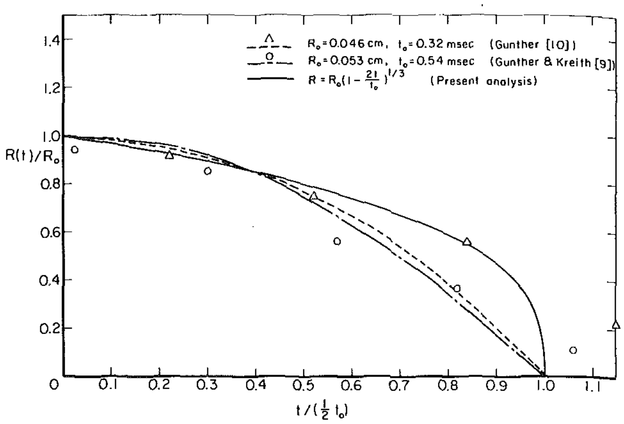

Fig. 2 **A comparison of $R(t)$ obtained by assuming constant m with experimental data and their best fits**

Acknowledgments

One of us (S.S.S.) wishes to express his appreciation to the Natural Sciences and Engineering Research Council Canada for a postgraduate scholarship. The study is part of the program supported by the National Science Foundation under Grant No. ENG 75-22676.

References

1 Plesset, M. S., and Prosperetti, A., "The Contribution of Latent Heat Transport in Subcooled Nucleate Boiling," *International Journal of Heat and Mass Transfer*, Vol. 21, 1978, pp. 725–734.

2 Cooper, M. G., and Lloyd, A. J., "The Microlayer Thickness in Nucleate Boiling," *International Journal of Heat and Mass Transfer*, Vol. 12, 1969, pp. 895–913.

3 Olander, R. R., and Watts, R. G., "An Analytical Expression for the Microlayer Thickness in Nucleate Boiling," ASME JOURNAL OF HEAT TRANSFER, Vol. 91, 1969, pp. 178–180.

4 Jawurek, H. H., "Simultaneous Determination of Microlayer Geometry and Bubble Growth in Nucleate Boiling," *International Journal of Heat and Mass Transfer*, Vol. 12, 1969, pp. 843–848.

5 Voutsinos, C. M., and Judd, R. L., "Laser Interferometric Investigations of the Microlayer Evaporation Phenomenon," ASME JOURNAL OF HEAT TRANSFER, Vol. 97, 1975, pp. 88–92.

6 Rosenhead, L., (Ed.), Laminar Boundary Layers, Oxford, 1963.

7 Mangler, W., "Boundary Layers on Bodies of Revolution in Symmetrical Flow," *Ber. Aerodyn. VersAnst. Göttingen*, 45/A/17, 1945.

8 Geis, T., "Ähnliche Grenzschichten an Rotationskörpern," 50 *Jahre Grenzschichtforschung* (Editors: Görtler, H., and Tollmien, W.), Vieweg, Braunschweig, 1955, pp. 294–303.

9 Gunther, F. C., and Kreith, F., "Photographic Study of Bubble Formation in Heat Transfer to Subcooled Water," Progress Report No. 4-120, Jet Propulsion Laboratory, Pasadena, 1950.

10 Gunther, F. C., "Photographic Study of Surface-Boiling Heat Transfer to Water with Forced Convection," *Journal of Applied Mechanics*, Vol. 18, 1951, pp. 115–123.

11 Jeffery, G., "The Two-Dimensional Steady Motion of a Viscous Fluid," *Philosophical Magazine*, (6) Vol. 29, 1915, pp. 455–465.

12 Hamel, G., "Spiralförminge Bewegungen zäher Flüssigkeiten," *Jber. dtsch. MatVer*, Vol. 25, 1917, pp. 34–60.

13 Rosenhead, L., "The Steady Two-Dimensional Radial Flow of Viscous Fluid Between Two Inclined Plane Walls," *Proceedings of the Royal Society*, Vol. A175, 1940, pp. 436–467.

The Influence of Geometric Asymmetry on the Flow Downstream of Row of Jets Discharging Normally into a Free Stream

D. Crabb[1] and J. H. Whitelaw[1]

Introduction

The present measurements comprise values of mean velocity and the mass concentration of a tracer in the flow downstream of a row of jets issuing normally into a free stream. The geometric configuration and velocity ratio are directly relevant to the combustion chamber of a gas turbine and the results were obtained to quantify the influence of asymmetry in the hole arrangement, on the down-stream mean-flow properties.

The quantification of the influence of nonuniform pitch is of direct practical relevance and, also, is important to the development of methods for the determination of combustor performance by the solution of appropriate three-dimensional equations. A complete specification of a flow pattern, for calculation purposes, requires knowledge of boundary conditions and it is normally presumed, see for example Jones, et al. [1], that flow symmetry exists and corresponds to geometric symmetry. This assumption is imposed in the absence of experimental confirmation but, because of limitations of computer storage and run time, is probably essential at the present time and for some time to come.

Flow Configuration and Measurement Techniques

The wind tunnel previously discussed by Kacker and Whitelaw [2] was used for the present investigation. It has an area contraction ratio of 7.1 with carefully established two-dimensional flow with a free stream turbulence intensity of less than 0.6 percent at the present free-stream velocity of 12.75 m/s.

Seven 25.4 mm ID tubes, of 0.76 m length and spaced at two diameters apart, allowed the injection of corresponding jets normal to the free stream. The seven jets were arranged across the 0.46 m width of the tunnel, which had a height of 0.3 m, and at a distance of 0.15 m downstream of an emery paper trip. The boundary layer at the leading edge of the jet had a thickness, to the 99 percent value, of approximately 6 mm. The jets were supplied from a centrifugal fan through a screened plenum chamber which resulted in fully-developed turbulent flow in the supply tubes. The velocity profiles in the plane of the pipe exits were measured, in the absence of the free stream velocity, and were each found to be symmetric about two orthogonal planes to better than 5 percent of the local velocity values. In addition, the centerline velocities of each of the seven jets were within 1 percent of the mean of the seven values. The present measurements were obtained with the ratio of average jet to free-stream velocity of 2.3. The maximum temperature difference between the two flows was less than 3°C.

In all cases, mean velocity values were obtained with a Pitot tube with external and internal diameters of 0.87 mm and 0.26 mm respectively. A transducer and time-averaging voltmeter allowed a reproducibility of measurement of better than ±1 percent. The same total head probe was used to pass samples of the wind tunnel air, plus a trace of helium which was injected into the central jet or into the central three jets, to a Servomex thermal conductivity cell, located in a constant-temperature oven. This allowed the measurement of the helium concentration to ±2 percent of the maximum value measured. Gas samples were also obtained through static-pressure holes located in the base plate of the tunnel in the manner previously described by Rastogi and Whitelaw [3] and in previous papers. The volume fraction of injected helium did not exceed 1 percent and, in the range of measurements, the calibration indicated that the relationship between the output voltage of the thermo-conductivity cell and helium concentration was linear.

To allow a controlled and quantitative investigation of the effect of the influence of asymmetry, the central pipe was arranged within two eccentric rings which permitted its adjustment in relation to its immediate neighbours. The present measurements were obtained with four locations of the central jet pipe. These corresponded to zero eccentricity and to eccentricities of 0.5, 0.25 and 0.1 dia. The precision of location of the central pipe was better than 0.005 dia.

Results

Fig. 1 presents measured values of mean velocity, normalized with the freestream velocity, and of mean concentration normalized with the concentration of helium in the central pipe which was the only pipe with a helium tracer. The results are presented at a downstream distance corresponding to 6D from the plane above the central line of the holes in vertical planes corresponding to 0.25, 1, 2 and 3 diameters above the base plate of the wind tunnel. As can be seen, the

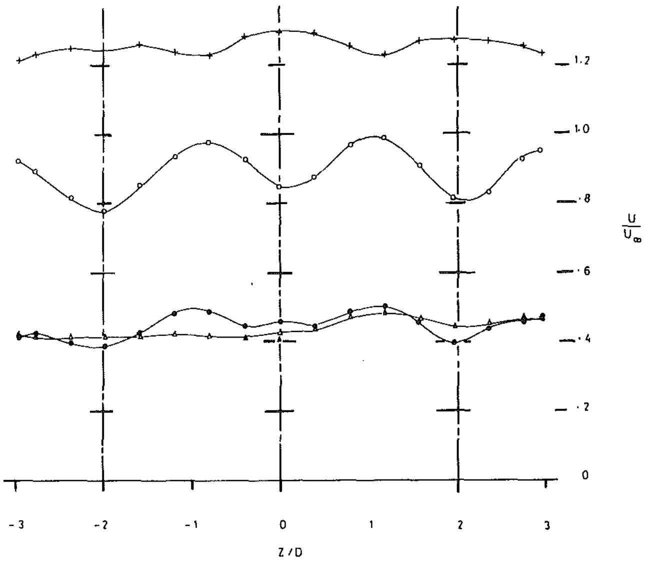

Fig. 1(*a*) Velocity distributions at X = 6 dia, no eccentricity

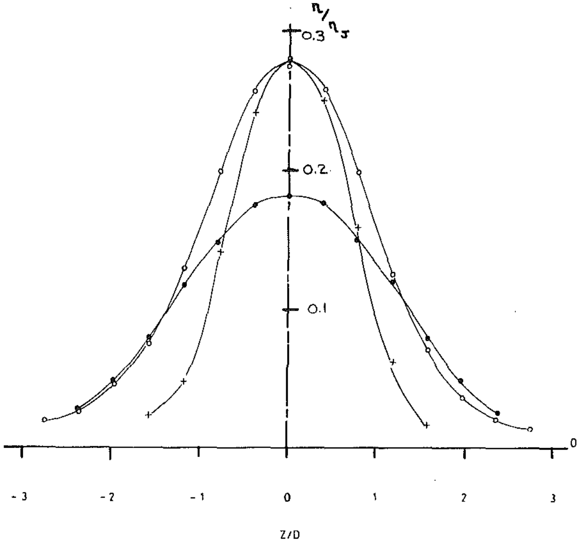

Fig. 1(*b*) Concentration distributions at X = 6 dia, no eccentricity

Y/D	
+	3
○	2
●	1
△	0.25

---

[1] Fluids Section, Department of Mechanical Engineering, Imperial College, London, England.

Contributed by the Heat Transfer Division for publication in the JOURNAL OF HEAT TRANSFER. Manuscript received by the Heat Transfer Division, June 9, 1978.

profiles are symmetrical within 6 percent of the maximum values of normalized velocity and 1% of normalized concentrations and were stable. Velocity distributions indicate peaks on either side of the hole centreline and indicate that the jets create a blockage to the oncoming flow and, as a result, create a downstream wake. This wake is present for values of Y/D of 1 but not at Y/D of 3 where the jet has already turned into the freestream to create maximum velocities along the lines of the hole centers. The concentration distributions indicate that, the mass of the tracer is greatest at Y/D of 2 although the forward momentum is significantly greater at Y/D of 3.

Figs. 2(*a*) and 2(*b*) correspond to an eccentricity of 0.5 dia, i.e. the central jet was moved 0.5 diameters to one side but in the same lateral plane as the other six jets. The four velocity distributions indicate the very considerable eccentricity in the mean-velocity field brought about by the eccentric location of the central jet. As can be seen, a large recirculation zone exists between the two neighbouring jets and extends beyond $6D$ downstream. This recirculation region is more than twice as long as that found in the immediate wake of a single jet of similar size and velocity ratio and implies that the two jets, whose centrelines are separated by 1.5 dia, form a large blockage around which the freestream flow passes producing a correspondingly wide and long downstream wake. Inspite of this, it is clear from Fig. 2(*b*) that the initially eccentric jet has moved rapidly towards the symmetric position and that, by 6 dia downstream, the maxima in the concentration profile are very close to the symmetric position.

Eccentricities of 0.5 dia and 0.25 dia (which indicated similar trends) are probably significantly greater than in gas turbine practice. As a consequence, results were obtained with an eccentricity of 0.1 dia which is the order of an eccentricity which may occur in gas turbine practice. The velocity distributions were significantly eccentric and the two closest jets again added as a single source of a downstream wake in the region of the potential core of the jets.

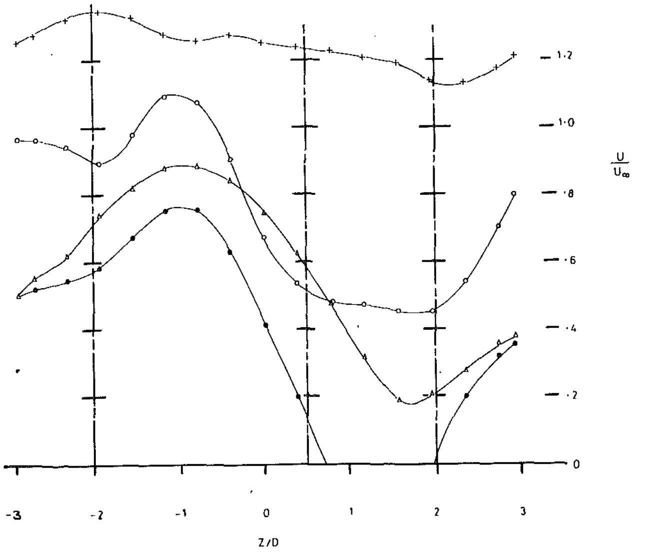

Fig. 2(*a*) Velocity distributions at X = 6 dia, eccentricity = 0.5 dia

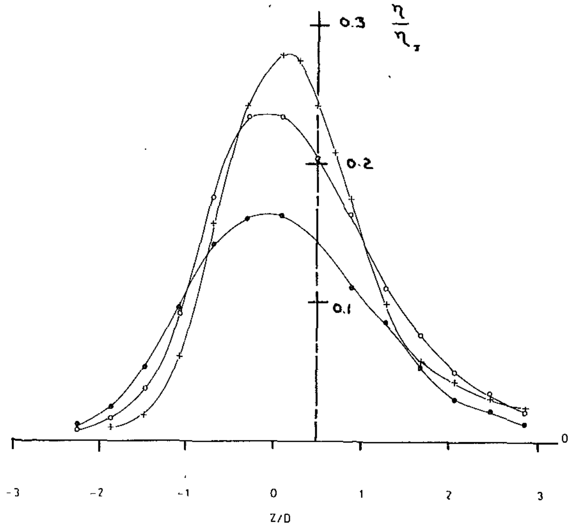

Fig. 2(*b*) Concentration distributions at X = 6 dia, eccentricity = 0.5 dia

Fig. 3 presents measured values of helium concentration obtained through the static pressure holes on the base plate of the wind tunnel with the helium tracer in the central three jets. They are presented for a symmetric arrangement of holes and for each of the eccentricities of the previous figures. It is clear that, although previous concentration distributions have indicated that the peak values rapidly return to a symmetric location, the wall values remain asymmetric at least to 8 dia downstream and to all values of eccentricity.

Concluding Remarks

The following summary conclusions may be extracted from the results of the preceding section.

1 The mean-flow characteristics downstream of a symmetrically arranged row of jets issuing normally into a free stream are symmetric and stable. It remains to determine whether this situation will remain with opposed rows of symmetrically arranged jets, as found in annular jet combustion chambers.

2 If one of the jets of a single row is eccentrically positioned with respect to its neighbors, it will tend to return to a symmetric position and will achieve this as far as the maximum value of a conserved scalar is concerned. It will, however, result in a large asymmetry in the velocity field and, although the peak of the scalar property may return to its symmetric location, the general pattern will remain asymmetric. With a pitch-to-diameter ratio of 2 and eccentricities between 0.25 and 0.5 dia, two jets with the smaller distance between them act as a blockage and cause a large region or recirculation immediately downstream. With an eccentricity of 0.1 dia, the region of recirculation does not exist at 6 dia downstream but the eccentricity in the velocity field is, nevertheless, significant.

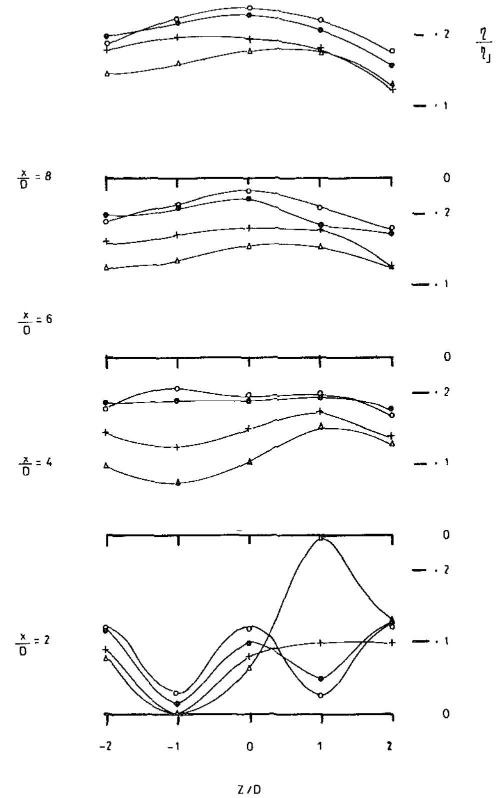

Fig. 3 Wall concentrations for eccentricity/diameter

○ 0
● 0.1
+ 0.25
△ 0.5

3 The results suggest that the asymmetries observed in the exit plane of gas turbine combustors are, at least in part, due to asymmetries in the location of the plunged primary and dilution holes. It is also clear that the calculation of gas-turbine combustor performance will be significantly in error unless account is taken of asymmetries in hole arrangements; it is unlikely that, even if the geometry of an asymmetric hole arrangement is unknown a priori, the corresponding boundary conditions can be correctly prescribed.

References

1 Jones, W. P., Clifford, W. C., Priddin, C. H., and de Chair, R., "A Comparison between Predicted and Measured Species Concentrations in Velocities in a Research Combustor," AGARD PEP, Paper 41, 50th Meeting. Symposium on High Temperature Problems in Gas Turbine Engines. Ankara, Turkey, Sept. 1977.

2 Kacker, S. C., and Whitelaw, J. H., "The Turbulence Properties of Wall-Jet and Wall-Wake Flows," *J. Appl. Mech.*, Vol. 38E, 1971, p. 239.

3 Rastogi, A. K., and Whitelaw, J. H., "The Effectiveness of Three-Dimensional Film-Cooling Slot Measurements," *Int. J. Heat and Mass Transfer*, Vol. 16, 1973, p. 1665.

Radiant Exchange for a Fin and Tube Solar Collector

T. F. Smith[1] and H. Y. Lee[2]

Nomenclature

H = convection to radiation, $h/\sigma T_t^3$
N = conduction to radiation, $kt/R^2\sigma T_t^3$
Q_f = fin heat transfer, $q_j/LW\sigma T_t^4$
Q_t = tube heat transfer, $q_t/\pi RW\sigma T_t^4/2$
S = solar energy to radiation, $S_0/\sigma T_t^4$
W = fin width, m
η = dimensionless distance, x/L
θ = dimensionless temperature, T/T_t
ζ = tube radius to fin half length, R/L

Introduction

Several contemporary flat plate solar energy collectors are of a design similar to that illustrated in Fig. 1. The collectors consist of several ducts separated by metallic sheets which act as fins. Current flat plate collector models [1, 2] do not adequately describe the collector performance as the tube spacing is decreased. The purposes of this study are to examine the heat transfer processes occurring within a fin and tube collector as well as the collector thermal efficiency for various tube spacings.

In the analysis, it is assumed that there is perfect thermal contact between the fins and the tubes and that the fin is of uniform thickness and is sufficiently thin so that a one-dimensional temperature distribution within the fin can be assumed. The tubes are taken to be isothermal. A solar flux normal to the fin surface irradiates uniformly both the fin and tube surfaces. The upper surfaces of the collector lose energy by two paths. Convective losses are given in terms of a convective heat transfer coefficient which is uniform over the fin and tube surfaces and based on air temperature T_a. Radiative losses are the result of radiant exchange between the fin and tube as well as with a surrounding surface at T_s. These temperatures could also be interpreted to represent the lower surface temperature of a cover above the fin and tube surfaces. For convenience, all surfaces are black for radiant exchange processes. In addition all properties are assumed constant and heat losses from the lower fin and tube surfaces are negligible.

Analysis

A steady-state energy balance for a differential fin element may be expressed as

$$\frac{d^2\theta}{d\eta^2} = \frac{1}{N\zeta^2}[H(\theta - \theta_a) + Q_r - S] \tag{1}$$

with boundary conditions of $\theta(0) = 1$ and $\theta'(1) = 0$. N, H and S may be interpreted to represent the importance of conduction, convection and solar energy relative to the black body emissive power at the tube temperature, respectively. In the absence of the radiative term, equation (1) may be solved for the fin temperature distribution [1] where the convective coefficient is replaced by a top loss coefficient. Representative values for the convective coefficient may be obtained from the Nusselt number correlations for inclined spaces [3]. The net radiant flux loss for equation (1) is obtained from an analysis presented by Sparrow and Eckert [4] but extended to include a non-zero environment temperature and is written as

$$Q_r = \theta^4 - \theta_s^4 - (F_{\eta-1} + F_{\eta-2})(1 - \theta_s^4) \tag{2}$$

where the view factors are available from [4]. The fin base heat transfer is given as

$$Q_f = -N\zeta^2\theta'(0) \tag{3}$$

A numerical scheme based on the fourth order Runge-Kutta integration method with a Newton-Raphson iteration method was employed to solve for the fin temperature distribution.

An energy balance on the upper one-quarter portion of the tube surface yields

$$Q_t = H(1 - \theta_a) + Q_{t,r} - \frac{2}{\pi}S \tag{4}$$

The tube radiant energy term is [4]

$$Q_{t,r} = \frac{2}{\pi}\left[(1 - \partial_s^4) + \frac{1}{\zeta}\int_0^1 (2 - \theta^4 - \theta_s^4)(F_{\eta-1} + F_{\eta-2})d\eta\right] \tag{5}$$

where the integral is performed by a numerical scheme.

An important factor which describes the collector thermal performance is the collector efficiency defined as the ratio of useful energy gained to incident solar energy. The useful energy gained consists of two terms related to the fin and tube heat transfer rates. The collector efficiency is expressed as

$$\eta_c = \frac{-[Q_f + Q_t\zeta\pi/2]}{S(1 + \zeta)} \tag{6}$$

As $\zeta \to 0$ implying small tubes or large separations, the integration for the tube radiative loss given by equation (5) is essentially over that portion of the fin surface where $\theta \approx 1$. The tube heat transfer becomes negligible in comparison with that for the fin and the collector efficiency reduces to

$$\eta_c = Q_f/S \tag{7}$$

At the opposite extreme of ζ, where $\zeta \to \infty$, the tubes are adjacent with no intervening fin. Thus, $Q_f = 0$ and the integration in equation (5) is discarded. The collector efficiency reduces to

$$\eta_c = 1 - \frac{(1 - \theta_s^4)}{S} - \frac{\pi}{2}\frac{H}{S}(1 - \theta_s) \tag{8}$$

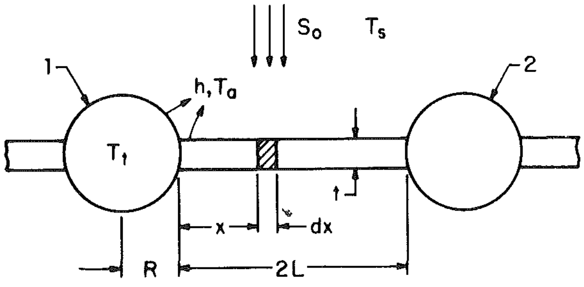

Fig. 1 Schematic diagram of a fin and tube collector

---

[1] Associate Professor. Division of Energy Engineering, The University of Iowa, Iowa City, Iowa 52242, Mem. ASME.

[2] Graduate Student. Division of Energy Engineering, The University of Iowa, Iowa City, Iowa 52242.

Contributed by the Heat Transfer Division for publication in the JOURNAL OF HEAT TRANSFER. Manuscript received by the Heat Transfer Division July 10, 1978.

3 The results suggest that the asymmetries observed in the exit plane of gas turbine combustors are, at least in part, due to asymmetries in the location of the plunged primary and dilution holes. It is also clear that the calculation of gas-turbine combustor performance will be significantly in error unless account is taken of asymmetries in hole arrangements; it is unlikely that, even if the geometry of an asymmetric hole arrangement is unknown a priori, the corresponding boundary conditions can be correctly prescribed.

References

1 Jones, W. P., Clifford, W. C., Priddin, C. H., and de Chair, R., "A Comparison between Predicted and Measured Species Concentrations in Velocities in a Research Combustor," AGARD PEP, Paper 41, 50th Meeting. Symposium on High Temperature Problems in Gas Turbine Engines. Ankara, Turkey, Sept. 1977.

2 Kacker, S. C., and Whitelaw, J. H., "The Turbulence Properties of Wall-Jet and Wall-Wake Flows," *J. Appl. Mech.*, Vol. 38E, 1971, p. 239.

3 Rastogi, A. K., and Whitelaw, J. H., "The Effectiveness of Three-Dimensional Film-Cooling Slot Measurements," *Int. J. Heat and Mass Transfer*, Vol. 16, 1973, p. 1665.

Radiant Exchange for a Fin and Tube Solar Collector

T. F. Smith[1] and H. Y. Lee[2]

Nomenclature

H = convection to radiation, $h/\sigma T_t^3$
N = conduction to radiation, $kt/R^2\sigma T_t^3$
Q_f = fin heat transfer, $q_j/LW\sigma T_t^4$
Q_t = tube heat transfer, $q_t/\pi RW\sigma T_t^4/2$
S = solar energy to radiation, $S_0/\sigma T_t^4$
W = fin width, m
η = dimensionless distance, x/L
θ = dimensionless temperature, T/T_t
ζ = tube radius to fin half length, R/L

Introduction

Several contemporary flat plate solar energy collectors are of a design similar to that illustrated in Fig. 1. The collectors consist of several ducts separated by metallic sheets which act as fins. Current flat plate collector models [1, 2] do not adequately describe the collector performance as the tube spacing is decreased. The purposes of this study are to examine the heat transfer processes occurring within a fin and tube collector as well as the collector thermal efficiency for various tube spacings.

In the analysis, it is assumed that there is perfect thermal contact between the fins and the tubes and that the fin is of uniform thickness and is sufficiently thin so that a one-dimensional temperature distribution within the fin can be assumed. The tubes are taken to be isothermal. A solar flux normal to the fin surface irradiates uniformly both the fin and tube surfaces. The upper surfaces of the collector lose energy by two paths. Convective losses are given in terms of a convective heat transfer coefficient which is uniform over the fin and tube surfaces and based on air temperature T_a. Radiative losses are the result of radiant exchange between the fin and tube as well as with a surrounding surface at T_s. These temperatures could also be interpreted to represent the lower surface temperature of a cover above the fin and tube surfaces. For convenience, all surfaces are black for radiant exchange processes. In addition all properties are assumed constant and heat losses from the lower fin and tube surfaces are negligible.

Analysis

A steady-state energy balance for a differential fin element may be expressed as

$$\frac{d^2\theta}{d\eta^2} = \frac{1}{N\zeta^2}[H(\theta - \theta_a) + Q_r - S] \tag{1}$$

with boundary conditions of $\theta(0) = 1$ and $\theta'(1) = 0$. N, H and S may be interpreted to represent the importance of conduction, convection and solar energy relative to the black body emissive power at the tube temperature, respectively. In the absence of the radiative term, equation (1) may be solved for the fin temperature distribution [1] where the convective coefficient is replaced by a top loss coefficient. Representative values for the convective coefficient may be obtained from the Nusselt number correlations for inclined spaces [3]. The net radiant flux loss for equation (1) is obtained from an analysis presented by Sparrow and Eckert [4] but extended to include a non-zero environment temperature and is written as

$$Q_r = \theta^4 - \theta_s^4 - (F_{\eta-1} + F_{\eta-2})(1 - \theta_s^4) \tag{2}$$

where the view factors are available from [4]. The fin base heat transfer is given as

$$Q_f = -N\zeta^2\theta'(0) \tag{3}$$

A numerical scheme based on the fourth order Runge-Kütta integration method with a Newton-Raphson iteration method was employed to solve for the fin temperature distribution.

An energy balance on the upper one-quarter portion of the tube surface yields

$$Q_t = H(1 - \theta_a) + Q_{t,r} - \frac{2}{\pi}S \tag{4}$$

The tube radiant energy term is [4]

$$Q_{t,r} = \frac{2}{\pi}\left[(1 - \partial_s^4) + \frac{1}{\zeta}\int_0^1 (2 - \theta^4 - \theta_s^4)(F_{\eta-1} + F_{\eta-2})d\eta\right] \tag{5}$$

where the integral is performed by a numerical scheme.

An important factor which describes the collector thermal performance is the collector efficiency defined as the ratio of useful energy gained to incident solar energy. The useful energy gained consists of two terms related to the fin and tube heat transfer rates. The collector efficiency is expressed as

$$\eta_c = \frac{-[Q_f + Q_t\zeta\pi/2]}{S(1 + \zeta)} \tag{6}$$

As $\zeta \to 0$ implying small tubes or large separations, the integration for the tube radiative loss given by equation (5) is essentially over that portion of the fin surface where $\theta \approx 1$. The tube heat transfer becomes negligible in comparison with that for the fin and the collector efficiency reduces to

$$\eta_c = Q_f/S \tag{7}$$

At the opposite extreme of ζ, where $\zeta \to \infty$, the tubes are adjacent with no intervening fin. Thus, $Q_f = 0$ and the integration in equation (5) is discarded. The collector efficiency reduces to

$$\eta_c = 1 - \frac{(1 - \theta_s^4)}{S} - \frac{\pi}{2}\frac{H}{S}(1 - \theta_s) \tag{8}$$

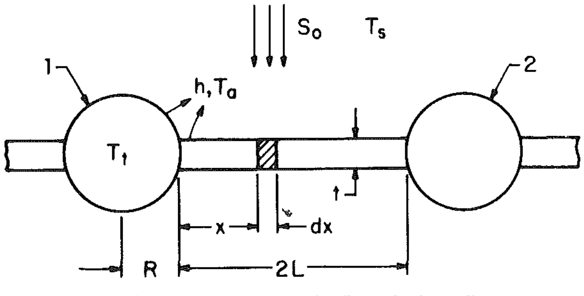

Fig. 1 Schematic diagram of a fin and tube collector

---

[1] Associate Professor. Division of Energy Engineering, The University of Iowa, Iowa City, Iowa 52242, Mem. ASME.

[2] Graduate Student. Division of Energy Engineering, The University of Iowa, Iowa City, Iowa 52242.

Contributed by the Heat Transfer Division for publication in the JOURNAL OF HEAT TRANSFER. Manuscript received by the Heat Transfer Division July 10, 1978.

For a fin with a large thermal conductivity, $N \rightarrow \infty$ and $\theta = 1$. Thus, the fin and tube heat transfer terms are respectively evaluated from

$$Q_{f,t} = H(1 - \theta_a) + (1 - \theta_s^4)\,[1 - (F_{f-1} + F_{f-2})] - S \qquad (9)$$

$$Q_{t,t} = H(1 - \theta_a) + \frac{2(1 - \theta_s^4)}{\pi}\left[1 + \frac{1}{\zeta}(F_{f-1} + F_{f-2})\right] - \frac{2}{\pi}S \qquad (10)$$

where the second subscript on Q denotes the fin at the tube temperature. The view factors are given in [4]. Another limiting case is that where surface radiant exchange is neglected [1].

Results and Discussion

Before numerical results are presented, it is instructive to examine values for the governing parameters as found in a fin and tube solar collector. Consider a collector where the following values are applicable: $t = 3$ mm, $L = 150$ mm, $R = 12.7$ mm, $k = 380$ W/m-K (copper), $T_t = 70°\text{C}$, $h = 2$ W/m^2 – K [3], $S_0 = 900$ W/m^2 and $T_a = T_s = 36°\text{C}$ (cover temperature). Hence, the dimensionless parameters acquire the following values: $\zeta = 0.08$, $N = 3090$, $H = 0.9$, $S = 1.1$ and $\theta_a = \theta_s = 0.9$. For a steel fin where $k = 50$ W/m-K, $N = 400$. Recognizing these values, results are presented for $1/\zeta = 0$ to 10, $N = 500$ and 3030, $H = 0.5$ to 2, $S = 0.5$ to 2 as well as $\theta_a = \theta_s = 0.85$ to 0.95. The air and surrounding surface temperatures were assumed identical as representative of the lower surface temperature of a cover.

As an aid to discussion regarding collector thermal performance, representative fin temperature distributions are displayed in Fig. 2 where results with surface radiant exchange included are applicable for $H = S = 1$ and $\theta_a = \theta_s = 0.95$. Temperature results are also presented for the analysis where surface radiation is neglected. For these latter results, a value of $H = 4$ was found to produce nearly identical temperature distribution as for results with $N = 3030$, $H = 1$ and where surface radiation is included. For the high conductance fin, tube spacings less than $2R$ yield nearly uniform fin temperatures. Thus, fin and tube heat transfer rates may be calculated from equations (9) and (10). A fin with a low conductance yields relatively large temperature variations sufficient to reduce collector efficiency as discussed later. Temperature results where surface radiation is neglected illustrate that the convective coefficient must be increased by a factor of four to account for neglection of radiation. However, as will be examined later, even though the fin temperature distributions are nearly identical, collector efficiencies differ significantly.

Collector efficiencies are illustrated in Fig. 3 for several values of the parameters. The overall trend of collector efficiency is to increase with tube spacings for small values of $1/\zeta$ followed by a decreasing behavior as the tube spacing is increased further. The maximum efficiency appears at smaller tube spacings for the higher efficiencies and generally occurs at tube spacings ($2L$) between 8 and $20R$. The lower efficiency for nearly adjacent tubes is attributed to the increased importance of tube surface area in determining convective losses even though the radiant exchange between two tubes is increasing. The decrease in efficiency with large tube spacings is the result of increased fin conductive resistance.

The influence of the various parameters may be examined by first considering efficiencies for $H = S = 1$ where $N = 500$ and 3030. For small tube spacing, the efficiency is insensitive to fin conductance but this changes drastically particularly when $1/\zeta = 10$ where the efficiency drops from 0.73 to 0.59. Thus, unless small tube spacings are designed into the collector, a fin with low thermal conductivity should be avoided from a thermal design criterion. The effect of H is as expected where a suppression of convective transfer produced higher efficiencies. Reduction of H from 1 to 0.5 yields about three percent gain in efficiency. An increase in solar energy produces higher efficiencies even though the fin temperature increases. As illustrated by results for $N = 3030$ and $H = S = 1$ with $\theta_a = \theta_s = 0.85$, 0.90 and 0.95, collector efficiencies are found to be very sensitive to the values for the surrounding temperatures. This illustrates the importance of a properly designed collector cover system.

In order to illustrate the importance of including radiative effects, efficiency results are presented in Fig. 4 when surface radiation is neglected as well as for the comprehensive model where $H = S = 1$. For the convection only model, efficiencies are shown for $H = 1$, 2 and 4 where the latter value of H produces efficiencies similar to those where surface radiation is included. At small tube spacings, the efficiencies with radiation included do not decrease as rapidly with

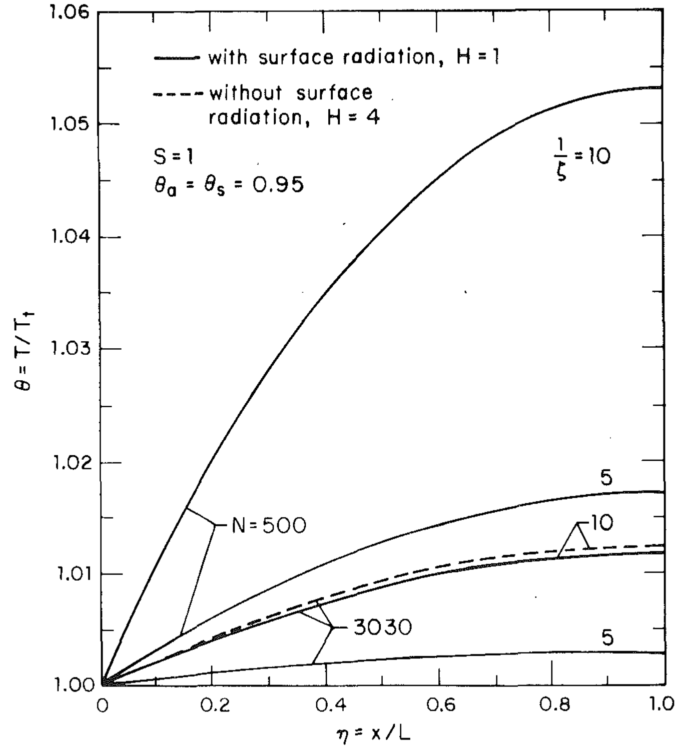

Fig. 2 Fin temperature distributions

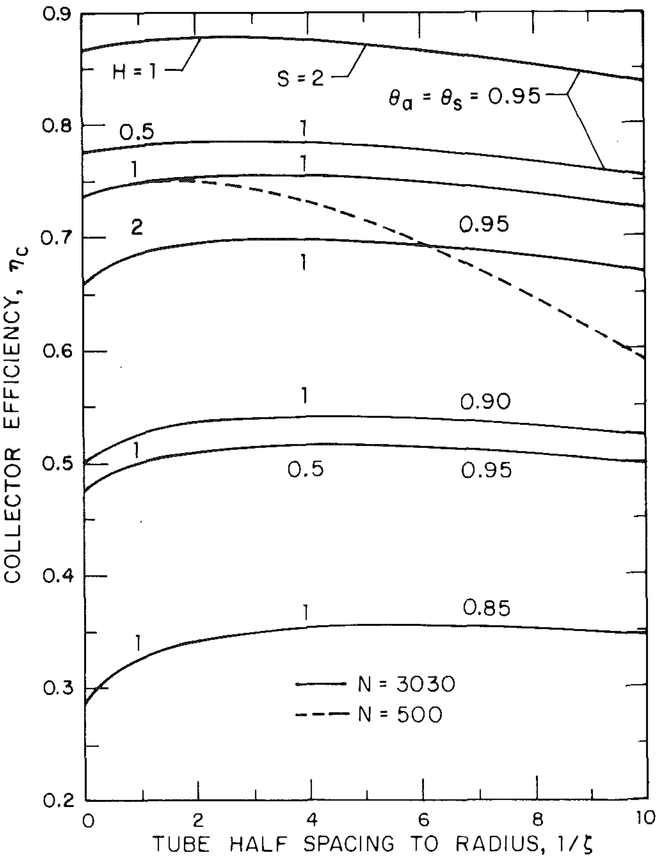

Fig. 3 Effect of system parameters on collector efficiencies

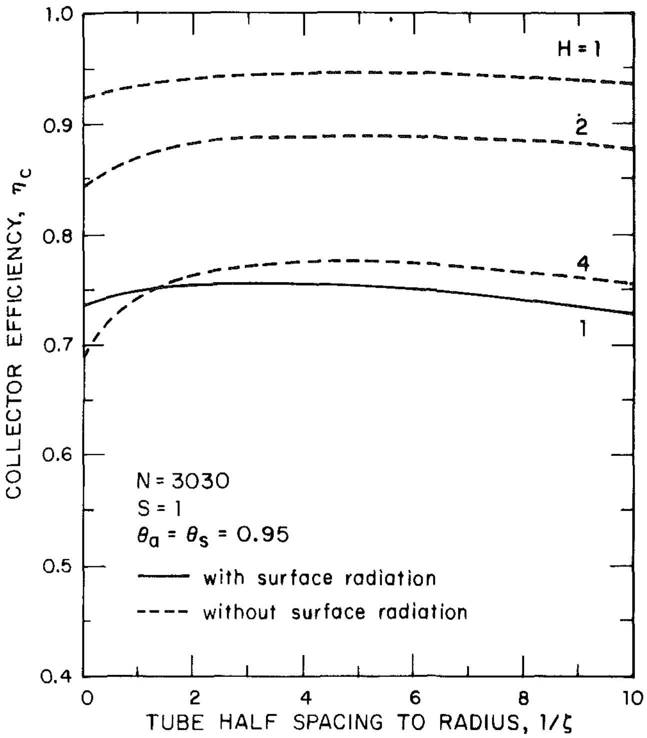

Fig. 4 Collector efficiencies with and without surface radiation

decreasing tube spacing as those for only convection. This finding is attributed to the radiant exchange between tubes for the smaller tube spacings. For adjacent tubes, the radiant trapping effect produces efficiencies which are higher by about five percent. For the larger tube spacing, it was shown in Fig. 2 that the fin temperature profiles nearly coincide with results for $H = 1$ (radiation) and $H = 4$ (no radiation). However, the efficiency for the latter results is higher by about three percent. The lower efficiency for the results with radiation is due to the radiation emission being proportional to the fourth power of temperature. The benefits of a selective coating applied to reduce the absorber infrared emittance is also illustrated by results in Fig. 4 for $H = 1$ with and without surface radiation. The latter results represent the limit of zero emittance and yield highest efficiencies. For a tube spacing of 2, the efficiency increases from 0.75 for a black absorber panel to 0.94 when surface radiation is suppressed.

Conclusions

An analysis has been presented to examine the radiant exchange phenomenon found in a fin and tube solar energy collector. The analysis demonstrates that the collector efficiency depends upon the tube spacing to radius ratio, fin conductance, convective coefficient, absorbed solar energy and air and surrounding surface temperatures which are employed to calculate convective and radiative losses. The collector efficiency was found to increase with tube spacing and then decrease as a result of increased fin conductive resistance. The model illustrated that accounting for surface radiation exchange yielded higher collector efficiencies at small tube spacings than those when surface radiation is neglected. Maximum collector efficiencies were found to occur for tube spacing to radius ratios between 8 and 20. Furthermore, the efficiencies were particularly sensitive to the values of air and surrounding surface temperatures.

Acknowledgment

This research was supported in part by a grant from the Iowa Energy Policy Council.

References

1 Duffie, J. A., and Beckman, W. A., *Solar Energy Thermal Processes*, John Wiley, 1974.

2 Rao, P. P., Francis, J. E., and Love, T. J., Jr., "Two-Dimensional Analysis of a Flat-Plate Solar Collector," *Journal Energy*, Vol. 1, 1977, pp. 324–328.

3 Buchberg, H., Catton, I. and Edwards, D. K., "Natural Convection in Enclosed Spaces—A Review of Application of Solar Energy Collection," ASME JOURNAL of HEAT TRANSFER, Vol. 98, 1976, pp. 182–188.

4 Sparrow, E. M. and Eckert, E. R. G., "Radiant Interaction Between Fin and Base Surfaces," ASME JOURNAL OF HEAT TRANSFER, Vol. 82, 1962, pp. 12–18.

journal of heat transfer

discussion

Heat Transfer and Fluid Flow Analysis of Interrupted-Wall Channels, with Application to Heat Exchangers[1]

R. K. Shah.[2] Heat transfer and flow friction characteristics of compact heat exchanger surfaces are mainly determined experimentally. Theoretical/analytical solutions that are available are primarily useful only for continuous cylindrical passage type compact surfaces. The authors of this paper are the first investigators to analyze the complex flows and heat transfer in one type of interrupted wall compact surface which is referred to as strip fin, serrated fin or offset fin.[3] Analyses of this type are long needed and are most welcome. My congratulations to the authors for their very fine and practical paper.

As the authors have clearly mentioned in their Introduction, the heat transfer coefficients in the entrance region of a duct are substantially higher than those at locations further downstream. This fact has motivated having heat exchanger surfaces interrupted in the flow direction. It is a common presumption that the shorter the interrupted length, the higher the performance of the surface and subsequently of the exchanger. The reduction in the strip length is presently limited by the manufacturing technology, although significant advances have been made by the industry in the past decade.

One simple way to predict the heat transfer performance of the strip fin may be the use of the conventional plain duct thermal entry length solutions. The idealizations made in such solutions are: uniform temperature profile and uniform (or developed) velocity profile at the start of each strip fin and the conventional boundary layer growth over it. The applicable theoretical mean Nusselt numbers correspond to those for the entrance region of a plain duct of length L. In Fig. 10, such $\mathrm{Nu}_{m,T}$ for the constant wall temperature boundary condition are plotted as a function of $L^* = L/(4H \mathrm{Re} \mathrm{Pr})$ for parallel plates for two flow conditions: developing velocity profiles, and fully developed velocity profiles [10]. Superimposed are $\overline{\mathrm{Nu}}_p$ from Table 1 of the paper for the periodic fully developed flow, and $\mathrm{Nu}_{m,T}$ ($=7.541$) for the fully developed flow through parallel plates. The following observations may be made from this figure:

1 For $L^* > 0.017$, the strip length mean Nusselt numbers associated with a periodic *fully* developed flow are greater than those for a simultaneously developing flow for parallel plates. The augmentation characteristics of the interrupted wall is clearly seen in this region.

2 As expected, periodic fully developed $\overline{\mathrm{Nu}}_p$ are always greater than 7.541 for the stable fully developed flow through parallel plates.

3 For $L^* < 0.0005$, $\overline{\mathrm{Nu}}_p$ for periodic fully developed flow are lower than those for the thermal entrance mean Nusselt numbers for parallel plates having a fully developed velocity profile. This is because of the differences in the temperature fields. The periodic fully developed region is thermally saturated, while the plain duct thermally developing region is unsaturated.

4 For a given RePr, the reduction in L/H increases the Nusselt numbers for the periodic fully developed flow; however, the increase diminishes and approaches an asymptotic value for lower values of L^*.

This last observation is very significant from an industrial viewpoint. This essentially contradicts the presumption mentioned earlier. There does not appear to be an advantage to reduce the strip length below certain value for a given application. From Fig. 10, an engineer should be able to decide himself for his application what is the optimum minimum strip length L from the heat transfer and manufacturing considerations.

In the analysis, I believe that the authors have neither considered the effect of vortices generated at the leading and trailing edges of the strips nor the effect of unstable laminar wake region downstream of the strips. If the vortices sweep the significant portion of the strip length, the boundary layer growth (considered in the analysis) may be only over a small portion of the strip. Hence, the applicability of the asymptotic $\overline{\mathrm{Nu}}_p$ of Fig. 10 (for the periodic fully developed flow) is questionable in a strip-fin heat exchanger. Would the authors comment on the qualitative effects of the neglected factors. Would

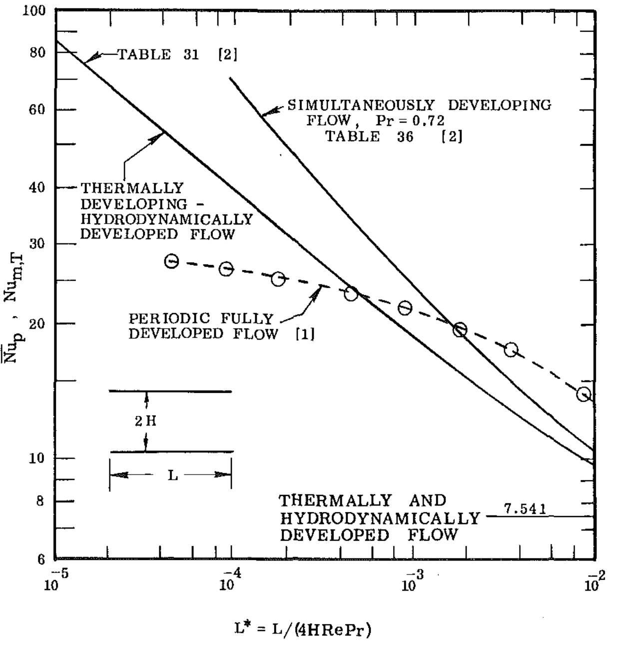

Fig. 10 A comparison of laminar mean Nusselt numbers for the plain duct thermal entrance region with those for periodic fully developed flow

---

[1] By E. M. Sparrow, B. R. Baliga, and S. V. Patankar, published in the Feb. 1977 issue of the ASME JOURNAL OF HEAT TRANSFER, Vol. 99, pp. 4-11.

[2] Technical Director of Research, Harrison Radiator Division, General Motors Corporation, Lockport, NY 14094, Member ASME.

[3] They have idealized a two-dimensional problem considering the fin height as infinity and the fin efficiency as 100 percent.

the authors also provide an approximate quantitative number for the accuracy of the numerical results.

Based on the authors' results of Figs. 8 and 9, the fully developed periodic flow is achieved at $x/L = 4$ and 30 for Re = 200 and 1600 respectively for $L/H = 1$. Would the authors first quantitatively define the periodic fully developed flow, and then provide the tabular values of x/L as functions of L/H and Re for $L/H = 0.2, 0.5, 1, 2$ and 5, and the covered range of Re.

A research task remains further refining the analytical model to correlate better the performance of interrupted wall surface with the experimental results. Subsequently, the more complex heat exchanger surfaces could be analyzed. In the meanwhile, this paper by Prof. Sparrow and his colleagues serves as a reminder that the flow and heat transfer phenomena in a compact heat exchanger are too complex to analyze. A better quantitative understanding of the flow phenomena is essential for better correlations and improved heat exchanger design.

Additional Reference

10 Shah, R. K., and London, A. L., *Laminar Flow Forced Convection in Ducts*, Supplement 1 to *Advances in Heat Transfer* Series, Academic Press, New York, 1977.

Authors' Closure

We are appreciative of the perspectives conveyed by Dr. Shah's Discussion. With regard to the role of vortices and wakes, there are, assuredly, conditions where they will affect both the heat transfer and friction. On the other hand, there are conditions for which no significant effect will be felt. Perspectives on these conditions are conveyed in references [11] and [12]. In connection with the identification of the periodically developed regime in Figs. 8 and 9, there is considerable latitude depending on the selected criterion. Since all portions of a velocity or temperature profile do not develop with equal rapidity, there are various criteria that can be employed. It was for this reason that we did not quote development lengths in the paper.

Additional References

11 Kottke, V., Blenke, H., and Schmidt, K. G., "The Influence of Nose Section and Turbulence Intensity on the Flow Around Thick Plates in Parallel Flow," *Wärme- und Stoffübertragung*, Vol. 10, 1977, pp. 159–174.

12 Loehrke, R. I., Roadman, R. E., and Read, G. W., ASME Paper 76-WA/HT-30, American Society of Mechanical Engineers, New York, N.Y., 1976.

Calculation of Shape Factors between Rings and Inverted Cones Sharing a Common Axis[1]

D. A. Nelson.[1] In a recent note, Minning presented analytical results for the shape factor between inverted conical frustrums and a differential element or ring. These results should be very useful for *rapid estimation of radiation from rocket plumes or flares but should* find other applications as well.

The purpose of this discussion is to point out how one of Minning's results can be generalized. In his analysis of the inverted conical frustrum, Minning has chosen to express his results in terms of four variables—the cone half angle β, the height of the frustrum h, the radial location of the differential element ρ, and the vertical distance from the differential element to the extended frustrums' vertex s. In my view, this last choice is not the natural one and indeed it obscures the generality of the result expressed by equation (7). The author has also introduced a source of possible confusion by requiring that s be negative in that equation.

It appears that a better choice of variable would be the radius of the frustrum in the plane of the element or ring, which is given by $r = -s \tan \beta$. If s is thereby eliminated from equation (7) in favor of r, then it becomes clear that the cone half angle is not restricted to positive values but can be anywhere within the range $-\tan^{-1}(r/h) \leq \beta \leq \pi/2$. Now, however, one must interpret the cone half angle as the absolute value of β, whereas β itself is an angular coordinate. When it is positive, the frustrum opens in the upward direction or is inverted as discussed by Minning. When β is negative, the direction of opening is downward, thus the frustrum is in an upright orientation. The particular value $\beta = -\tan^{-1}(r/h)$ yields the upright cone configuration. Minning's equation (7) then, when properly interpreted, is valid for the complete range of shape factors between conical frustrums and a differential element (or ring) located in a plane which intersects the conical surface. The use of shape factor algebra, of course, extends the geometric configurations to which this result can be applied.

With respect to this latter point, one may note, as was done for a cylinder by Sparrow, et al. [1] that the shape factor in question can be considered as the sum of two parts—one being a circular segment and, in this case, the other being a tilted triangular plate frustrum. Since the former is known [2], the latter can be readily obtained and subsequently expressed in variables more suitable for that configuration. This, of course, introduces new possibilities too numerous to mention.

Finally, since Minning does not mention any analytical checks of his result, it is pointed out that, when $\beta = 0$, it reduces to a form equivalent to that for the cylinder [1].

Additional References

1 Sparrow, E. M., Miller, G. B., and Jonsson, V. K., "Radiating Effectiveness of Annular-Finned Space Radiators, Including Mutual Irradiation between Radiator Elements," *Journal Aerospace Sciences*, Vol. 29, 1962, pp. 1291–1299.

2 Sparrow, E. M., "A New and Simpler Formulation for Radiative Angle Factors," ASME JOURNAL OF HEAT TRANSFER, Vol. 85, 1963, pp. 81–88.

Author's Closure

I appreciate Dr. Nelson's pointing out that the applicability of equation (7) is broader than originally indicated in my paper. I also agree with his contention that my original choice of variables is not the most convenient for the applications he has in mind. However, from the standpoint of clarity and visualization of the geometry, I find the use of both positive and negative values of β to be no less confusing than the use of both positive and negative values of s.

An alternate expression that avoids this confusion can be derived by substitution of the relation $r = -s \tan\beta$, as suggested by Dr. Nelson, and the relation $\alpha = (\pi/2) - \beta$ into equation (7). The result is as follows:

$$F_{dA_1-A_2} = \frac{\cos\alpha}{\pi}\mathrm{Tan}^{-1}\left[h\sqrt{\frac{1+\cot^2\alpha}{\rho^2-r^2}}\right] + \frac{1}{\pi}\mathrm{Tan}^{-1}\left[\sqrt{\frac{\rho+r}{\rho-r}}\right]$$
$$+ \frac{(h\cot\alpha + r)^2 - \rho^2 - h^2}{\pi\sqrt{[(h\cot\alpha+r)^2+\rho^2+h^2]^2 - 4\rho^2(h\cot\alpha+r)^2}}$$
$$\times\,\mathrm{Tan}^{-1}\left[\sqrt{\frac{[(h\cot\alpha+r)+\rho]^2}{[(h\cot\alpha+r)-\rho]^2}\cdot\left(\frac{\rho-r}{\rho+r}\right)}\right]$$

In this expression, α is the angle between the plane of dA_1 and the sloping side of the conical frustrum. Values of α are always positive and lie in the range $0 \leq \alpha \leq \pi$. For $0 \leq \alpha < \pi/2$, the frustrum opens upward away from the plane of dA_1. For $\pi/2 < \alpha \leq \pi$, the frustrum opens downward toward the plane of dA_1. The special case, $\alpha = \pi/2$,

---

[1] By C. P. Minning, published in the August, 1977 issue of the JOURNAL OF HEAT TRANSFER, Vol. 99, No. 3, pp. 492–494.

[2] The Aerospace Corporation, El Segundo, CA 90245.

the authors also provide an approximate quantitative number for the accuracy of the numerical results.

Based on the authors' results of Figs. 8 and 9, the fully developed periodic flow is achieved at $x/L = 4$ and 30 for Re = 200 and 1600 respectively for $L/H = 1$. Would the authors first quantitatively define the periodic fully developed flow, and then provide the tabular values of x/L as functions of L/H and Re for $L/H = 0.2, 0.5, 1, 2$ and 5, and the covered range of Re.

A research task remains further refining the analytical model to correlate better the performance of interrupted wall surface with the experimental results. Subsequently, the more complex heat exchanger surfaces could be analyzed. In the meanwhile, this paper by Prof. Sparrow and his colleagues serves as a reminder that the flow and heat transfer phenomena in a compact heat exchanger are too complex to analyze. A better quantitative understanding of the flow phenomena is essential for better correlations and improved heat exchanger design.

Additional Reference

10 Shah, R. K., and London, A. L., *Laminar Flow Forced Convection in Ducts*, Supplement 1 to *Advances in Heat Transfer* Series, Academic Press, New York, 1977.

Authors' Closure

We are appreciative of the perspectives conveyed by Dr. Shah's Discussion. With regard to the role of vortices and wakes, there are, assuredly, conditions where they will affect both the heat transfer and friction. On the other hand, there are conditions for which no significant effect will be felt. Perspectives on these conditions are conveyed in references [11] and [12]. In connection with the identification of the periodically developed regime in Figs. 8 and 9, there is considerable latitude depending on the selected criterion. Since all portions of a velocity or temperature profile do not develop with equal rapidity, there are various criteria that can be employed. It was for this reason that we did not quote development lengths in the paper.

Additional References

11 Kottke, V., Blenke, H., and Schmidt, K. G., "The Influence of Nose Section and Turbulence Intensity on the Flow Around Thick Plates in Parallel Flow," *Wärme- und Stoffübertragung*, Vol. 10, 1977, pp. 159–174.

12 Loehrke, R. I., Roadman, R. E., and Read, G. W., ASME Paper 76-WA/HT-30, American Society of Mechanical Engineers, New York, N.Y., 1976.

Calculation of Shape Factors between Rings and Inverted Cones Sharing a Common Axis[1]

D. A. Nelson.[2] In a recent note, Minning presented analytical results for the shape factor between inverted conical frustrums and a differential element or ring. These results should be very useful for rapid estimation of radiation from rocket plumes or flares but should find other applications as well.

The purpose of this discussion is to point out how one of Minning's results can be generalized. In his analysis of the inverted conical frustrum, Minning has chosen to express his results in terms of four variables—the cone half angle β, the height of the frustrum h, the radial location of the differential element ρ, and the vertical distance from the differential element to the extended frustrums' vertex s. In my view, this last choice is not the natural one and indeed it obscures the generality of the result expressed by equation (7). The author has also introduced a source of possible confusion by requiring that s be negative in that equation.

It appears that a better choice of variable would be the radius of the frustrum in the plane of the element or ring, which is given by $r = -s \tan \beta$. If s is thereby eliminated from equation (7) in favor of r, then it becomes clear that the cone half angle is not restricted to positive values but can be anywhere within the range $-\tan^{-1}(r/h) \leq \beta \leq \pi/2$. Now, however, one must interpret the cone half angle as the absolute value of β, whereas β itself is an angular coordinate. When it is positive, the frustrum opens in the upward direction or is inverted as discussed by Minning. When β is negative, the direction of opening is downward, thus the frustrum is in an upright orientation. The particular value $\beta = -\tan^{-1}(r/h)$ yields the upright cone configuration. Minning's equation (7) then, when properly interpreted, is valid for the complete range of shape factors between conical frustrums and a differential element (or ring) located in a plane which intersects the conical surface. The use of shape factor algebra, of course, extends the geometric configurations to which this result can be applied.

With respect to this latter point, one may note, as was done for a cylinder by Sparrow, et al. [1] that the shape factor in question can be considered as the sum of two parts—one being a circular segment and, in this case, the other being a tilted triangular plate frustrum. Since the former is known [2], the latter can be readily obtained and subsequently expressed in variables more suitable for that configuration. This, of course, introduces new possibilities too numerous to mention.

Finally, since Minning does not mention any analytical checks of his result, it is pointed out that, when $\beta = 0$, it reduces to a form equivalent to that for the cylinder [1].

Additional References

1 Sparrow, E. M., Miller, G. B., and Jonsson, V. K., "Radiating Effectiveness of Annular-Finned Space Radiators, Including Mutual Irradiation between Radiator Elements," *Journal Aerospace Sciences*, Vol. 29, 1962, pp. 1291–1299.

2 Sparrow, E. M., "A New and Simpler Formulation for Radiative Angle Factors," ASME JOURNAL OF HEAT TRANSFER, Vol. 85, 1963, pp. 81–88.

Author's Closure

I appreciate Dr. Nelson's pointing out that the applicability of equation (7) is broader than originally indicated in my paper. I also agree with his contention that my original choice of variables is not the most convenient for the applications he has in mind. However, from the standpoint of clarity and visualization of the geometry, I find the use of both positive and negative values of β to be no less confusing than the use of both positive and negative values of s.

An alternate expression that avoids this confusion can be derived by substitution of the relation $r = -s \tan\beta$, as suggested by Dr. Nelson, and the relation $\alpha = (\pi/2) - \beta$ into equation (7). The result is as follows:

$$F_{dA_1-A_2} = \frac{\cos\alpha}{\pi}\,\mathrm{Tan}^{-1}\left[h\sqrt{\frac{1+\cot^2\alpha}{\rho^2-r^2}}\right] + \frac{1}{\pi}\,\mathrm{Tan}^{-1}\left[\sqrt{\frac{\rho+r}{\rho-r}}\right] + \frac{(h\cot\alpha+r)^2-\rho^2-h^2}{\pi\sqrt{[(h\cot\alpha+r)^2+\rho^2+h^2]^2-4\rho^2(h\cot\alpha+r)^2}} \times \mathrm{Tan}^{-1}\left[\sqrt{\frac{[(h\cot\alpha+r)+\rho]^2}{[(h\cot\alpha+r)-\rho]^2}\cdot\left(\frac{\rho-r}{\rho+r}\right)}\right]$$

In this expression, α is the angle between the plane of dA_1 and the sloping side of the conical frustrum. Values of α are always positive and lie in the range $0 \leq \alpha \leq \pi$. For $0 \leq \alpha < \pi/2$, the frustrum opens upward away from the plane of dA_1. For $\pi/2 < \alpha \leq \pi$, the frustrum opens downward toward the plane of dA_1. The special case, $\alpha = \pi/2$,

---

[1] By C. P. Minning, published in the August, 1977 issue of the JOURNAL OF HEAT TRANSFER, Vol. 99, No. 3, pp. 492–494.

[2] The Aerospace Corporation, El Segundo, CA 90245.

corresponds to a vertical cylinder. For $\pi/2 < \alpha \leq \pi$, this expression is comparable to the analytical results derived by Holchendler and Laverty [1] for the same geometry.

Another interesting case is the situation where $\rho = r$. Here the alternate expression reduces to

$$F_{dA_1-A_2} = \frac{1}{2}\,[1 + \cos\alpha]$$

where it is seen that for $\alpha = \pi/2$, $F_{dA_1-A_2} = 0.5$, which is the well-known result for a circular cylinder.

Additional References

1 Holchendler, J. and Laverty, W. F., "Configuration Factors for Radiant Heat Exchange in Cavities Bounded at the Ends by Parallel Disks and Having Conical Centerbodies," ASME JOURNAL OF HEAT TRANSFER, Vol. 96, No. 2, 1974, pp. 254–257.